7 August 2009 | $10

Science

Industrial Chemistry

AAAS

INTERNATIONAL SCIENCE & ENGINEERING
VISUALIZATION CHALLENGE

COMPETITION DEADLINE APPROACHING

ENTRY DEADLINE: SEPTEMBER 15, 2009

SCIENCE AND ENGINEERING'S MOST POWERFUL STATEMENTS
ARE NOT MADE FROM WORDS ALONE

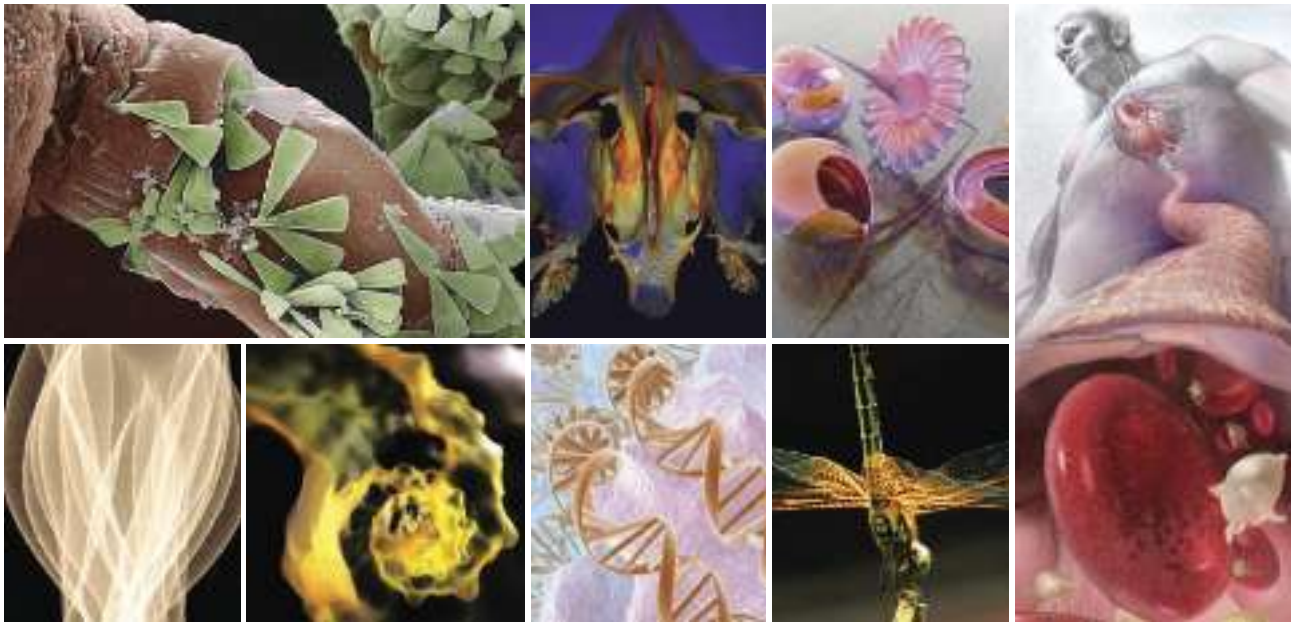

When the left brain collaborates with the right brain, science emerges with art to enhance communication and understanding of research results—illustrating concepts, depicting phenomena and drawing conclusions.

The National Science Foundation (NSF) and the journal *Science*, published by the American Association for the Advancement of Science, invite you to participate in the seventh annual International Science & Engineering Visualization Challenge. The competition recognizes scientists, engineers, visualization specialists and artists for producing or commissioning innovative work in visual communication.

Winners in each category will be published in the February 19, 2010 issue of *Science* and *Science* Online, and will be displayed on the NSF Web site.

Award Categories

- Photographs/Pictures
- Illustrations/Drawings
- Informational/Explanatory Graphics
- Interactive Media
- Non-Interactive Media

Complete Entry Information:
www.nsf.gov/news/scivis

AACR American Association for Cancer Research

www.aacr.org/meetingcalendar

Upcoming conferences

at the forefront of cancer prevention research:

Eighth Annual AACR
International Conference on
Frontiers in Cancer Prevention Research
December 6-9, 2009 • Houston, TX
Chairperson: Ernest T. Hawk
Abstract Submission Deadline:
September 28, 2009

AACR-IASLC Joint Conference
Molecular Origins of Lung Cancer:
Prospects for Personalized Prevention and Therapy
January 11-14, 2010 • Coronado, CA
Chairpersons: David P. Carbone and Roy S. Herbst

AACR 101st Annual Meeting 2010
April 17-21, 2010 • Washington, DC
Program Chairperson: Frank McCormick

Third AACR Conference on The Science of
Cancer Health Disparities
in Racial/Ethnic Minorities and the
Medically Underserved
September 30-October 3, 2010 • Miami, FL
Chairpersons to be announced

Comprehensive Coverage of Cancer Prevention Science

Through the AACR Cancer Prevention Journals Portal

Prevention-related articles from AACR journals:
- Cancer Prevention Research
- Cancer Epidemiology, Biomarkers & Prevention
- Cancer Research
- Clinical Cancer Research
- Molecular Cancer Therapeutics
- Molecular Cancer Research

Abstracts from AACR conferences:
- Frontiers in Cancer Prevention Research
- AACR Annual Meeting
- Science of Cancer Health Disparities

http://preventionportal.aacrjournals.org
For more information, contact marketing@aacr.org

Additional conference content:
- Session webcasts
- Education Book articles

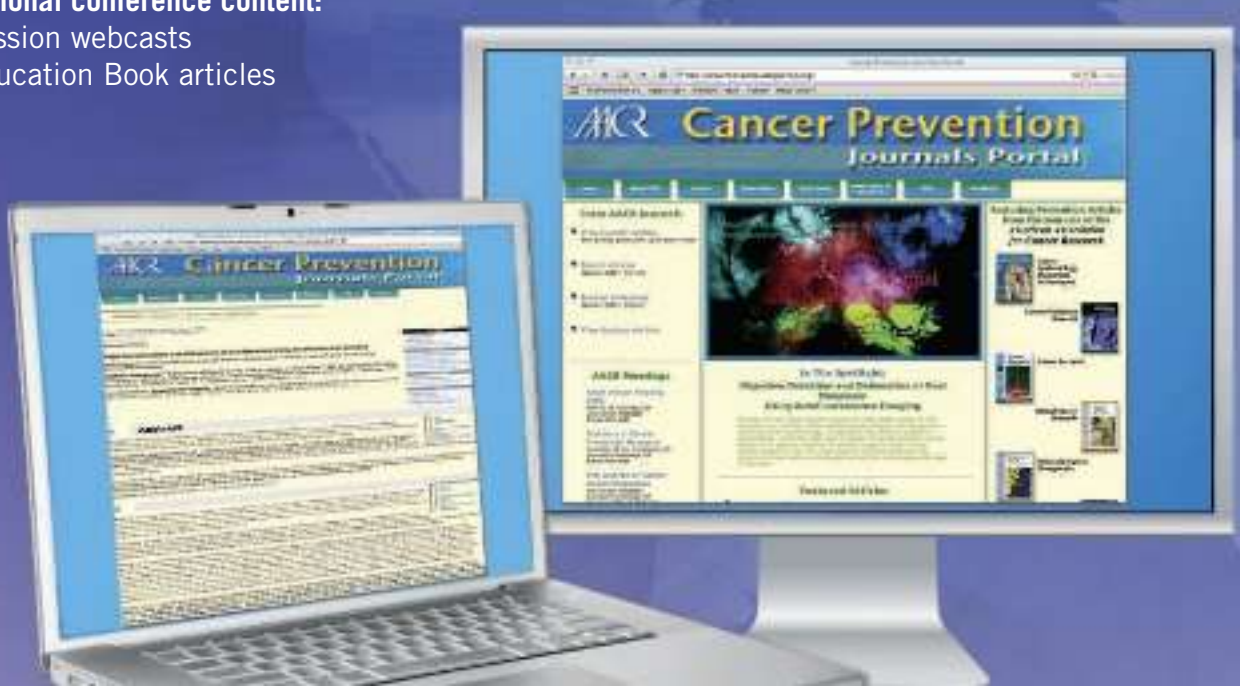

GE Healthcare

360° Service

"These days, productivity is everything in our business. Knowing that our scientists were losing valuable time due to service-related issues wasn't helping. To solve this problem and improve overall organizational efficiency, we looked at ways we could consolidate by purchasing from fewer suppliers. GE Healthcare was the only company that was happy to manage everything, regardless of the OEM; unbeatable flexibility that allows our teams to focus on what they are best at. Of course, GE Healthcare's track record in healthcare is world-class and it's a real benefit having a company that is happy to manage equipment of all types."

Richard Dickinson, Director of Operations, ERBI Ltd.

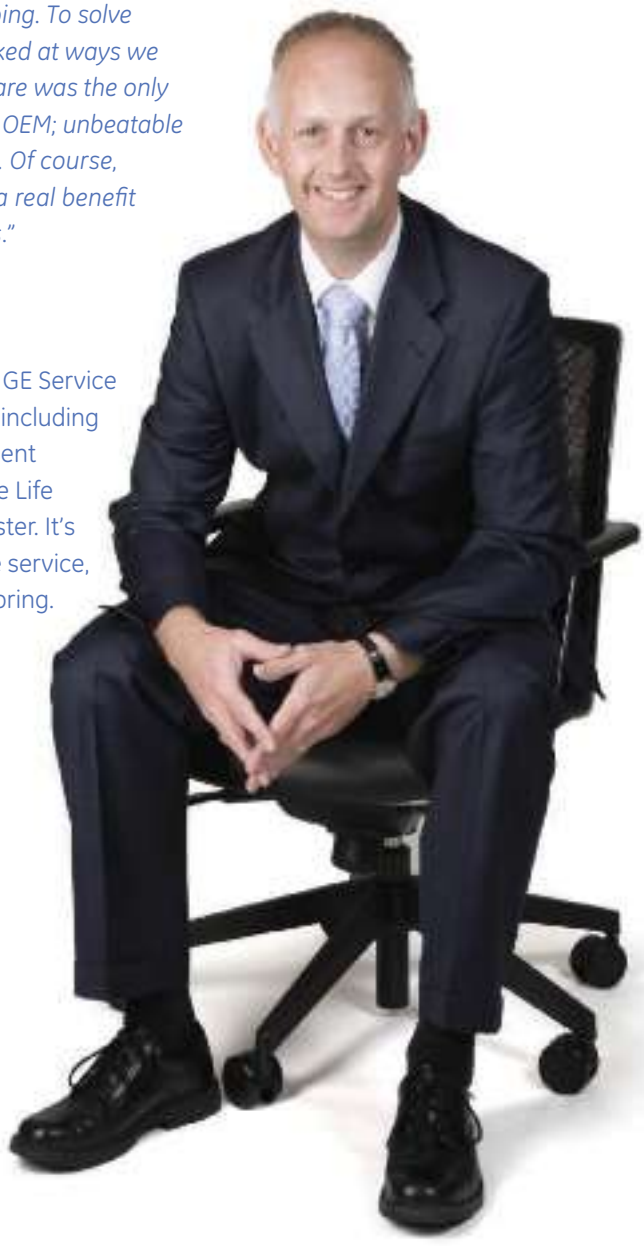

Pharmaceutical and biotech companies around the world rely on GE Service to deliver total coverage. From instrument service agreements — including systems from other manufacturers — to asset lifecycle management and facility validation. Now that's service in 360°. At GE Healthcare Life Sciences, our focus is on helping scientists achieve even more, faster. It's a commitment we have in our genes. And all this is backed by the service, support, and investment for the future that being part of GE can bring.

Find out more. Why not talk with us today.
Visit **www.gelifesciences.com/360service**

I ÄKTA I Amersham I Biacore I IN Cell I Whatman I **GE Service** I

imagination at work

First published June 2009
GE Healthcare Bio-Sciences AB, Björkgatan 30, 751 84 Uppsala, Sweden

GE07-09

SPECIAL SECTION

Industrial Chemistry

INTRODUCTION

NEWS

PERSPECTIVES

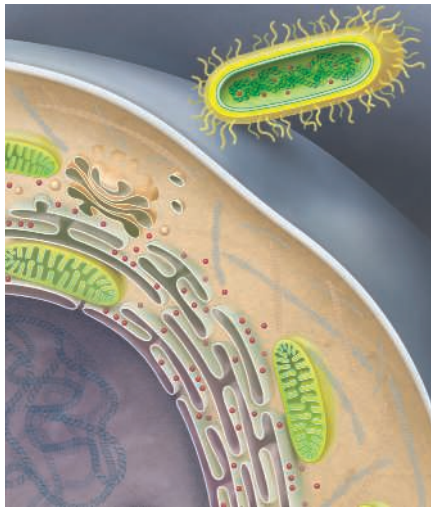

page 666

EDITORIAL

NEWS OF THE WEEK

NEWS FOCUS

LETTERS

BOOKS *ET AL.*

POLICY FORUM

PERSPECTIVES

CONTENTS continued >>

COVER

Among the contrasts in scale between academic and industrial chemistry is the latter field's use of raw materials by the trainload. This week's special section, beginning on page 691, elaborates on the challenges and opportunities in industrial chemistry as the field embarks on its second century of development.

Photo illustration: Yael Kats (photos: iStockphoto.com)

DEPARTMENTS

Published by AAAS

Gene expression and function analysis sample and assay technologies by QIAGEN

Enjoy first-time success

Rely on QIAGEN's manual and automated workflow solutions for:

- **Sample collection and disruption**
- **RNA stabilization and purification**
- **Real-time PCR and RT-PCR and gene expression assays**
- **RNAi and gene silencing**
- **miRNA purification and assays**
- **Methylation analysis in epigenetics research**
- **Protein sample preparation and assays**

Making improvements in life possible — www.qiagen.com

GEPart0309S1WW

QIAGEN®

Sample & Assay Technologies

BREVIA

RESEARCH ARTICLES

REPORTS

page 682

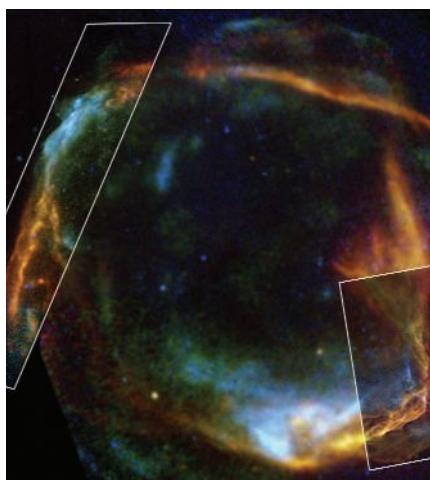

pages 683 & 719

CONTENTS continued >>

Published by AAAS

WHERE THE BASIC SCIENCE

WORLD MEETS WORLD

OF MEDICINE

Submit your work to *Science Translational Medicine* today!

This fall, AAAS and *Science* will launch *Science Translational Medicine*, a new journal focused on applications of basic research knowledge that will improve human health.

The goal of *Science Translational Medicine* is simple: to help the scientific community harness decades of progress in research at the basic level and translate these biological discoveries into medical advances. Take this opportunity to have your work recognized in this groundbreaking new journal.

Papers in the following areas will be reviewed and considered for publication:

- Animal & Human Studies
- Applied Physical Sciences
- Behavior
- Bioengineering
- Biomarkers
- Cancer
- Cardiovascular Disease
- Cell Culture
- Chemical Genomics/Drug Discovery
- Data Mining
- Drug Delivery
- Gene Therapy/Regenerative Medicine
- Imaging
- Immunology/Vaccines
- Infectious Diseases
- Medical Informatics
- Medical Nanotechnology
- Metabolism/Diabetes/Obesity
- Neuroscience/Neurology/Psychiatry
- Pharmacogenetics
- Policy
- Toxicology & Pharmacokinetics
- And other interdisciplinary approaches to medicine

To submit your work for consideration, please visit **www.submit2scitranslmed.org**

Science Translational Medicine AAAS

www.ScienceTranslationalMedicine.org

INTEGRATING MEDICINE AND SCIENCE

SCIENCEONLINE

SCIENCEXPRESS
www.sciencexpress.org

Entropy Landscape of Phase Formation Associated with Quantum Criticality in $Sr_3Ru_2O_7$
A. W. Rost et al.

The thermodynamic properties of strongly correlated electron systems can be probed near their quantum critical point.
10.1126/science.1176627

Complete Methods Set for Scalable Ion Trap Quantum Information Processing
J. P. Home et al.

Coupling of different ions creates states that are insensitive to stray magnetic fields and more robust for quantum computing.
10.1126/science.1177077

Risks of Climate Engineering
G. C. Hegerl and S. Solomon

Observations indicate that attempts to limit climate warming by reducing incoming shortwave radiation risk major precipitation changes.
10.1126/science.1178530

Cellular Basis of Itch Sensation
Y.-G. Sun et al.

Itch, but not pain sensation, is abolished by selective ablation of a small subpopulation of spinal neurons.
10.1126/science.1174868

Glucose Deprivation Contributes to the Development of *KRAS* Pathway Mutations in Tumor Cells
J. Yun et al.

Glucose deprivation can drive the acquisition of certain oncogenic mutations in human cancer cells.
10.1126/science.1174229

Poly(ADP-ribose)–Dependent Regulation of DNA Repair by the Chromatin Remodeling Enzyme ALC1
D. Ahel et al.

A chromatin remodeling complex targeted by poly(ADP ribosyl)ation plays a role in DNA repair.
10.1126/science.1177321

SCIENCENOW
www.sciencenow.org
Highlights From Our Daily News Coverage

Gorilla Virus in Our Midst
Gorilla version of AIDS virus found in human.

How Happy Is the Internet?
Researchers analyze blogs and song lyrics to gauge society's mood.

Researchers Grow New Teeth in Mice
Bioengineered molars could one day replace lost teeth in humans.

SCIENCESIGNALING
www.sciencesignaling.org
The Signal Transduction Knowledge Environment

RESEARCH ARTICLE: The Akt1-eNOS Axis Illustrates the Specificity of Kinase-Substrate Relationships in Vivo
M. Schleicher et al.

Akt mediates postnatal angiogenesis through eNOS signaling.

PERSPECTIVE: New Connections, New Components, Real Dynamics
J. S. Bader

Secrets of the yeast MAPK pathways continue to be revealed.

MEETING REPORT: Chemical Approaches to Nuclear Receptors in Metabolism
R. N. Margolis et al.

An NIH-sponsored workshop focused on innovative chemical methods for probing and modulating nuclear receptor pathways.

NETWATCH: Kinomer
Search and browse a library of kinases classified by family; in Protein Databases.

NETWATCH: Rel/NF-κB Transcription Factors
Explore NF-κB transcription factors and their regulation in this site by Thomas Gilmore; in Labs and People.

SCIENCECAREERS
www.sciencecareers.org/career_magazine
Free Career Resources for Scientists

The Ups and Downs of Doing a Postdoc in Europe
L. Laursen

A postdoc abroad can mean logistical hurdles, but also a rewarding experience.

Taken for Granted: Doing Something About the Postdoc Mess
B. L. Benderly

Two new initiatives seek to prepare postdocs for off-campus careers.

See also Industrial Chemistry news story p. 696

SCIENCEPODCAST
www.sciencemag.org/multimedia/podcast
Free Weekly Show

Download the 7 August *Science* Podcast to hear about designer DNA shapes, new technologies for toxicity testing, the origins of eukaryotes, and more.

ORIGINSBLOG
blogs.sciencemag.org/origins
A History of Beginnings

SCIENCEINSIDER
blogs.sciencemag.org/scienceinsider
Science Policy News and Analysis

SCIENCE**NOW**
A gorilla from Cameroon.

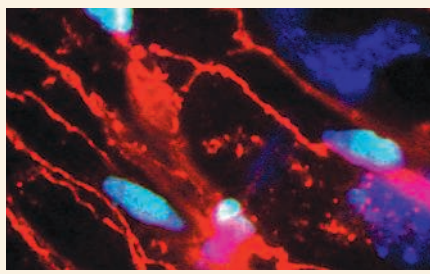

SCIENCE**SIGNALING**
Angiogenic endothelium.

SCIENCE**CAREERS**
A postdoc's ups and downs in Europe.

SCIENCE (ISSN 0036-8075) is published weekly on Friday, except the last week in December, by the American Association for the Advancement of Science, 1200 New York Avenue, NW, Washington, DC 20005. Periodicals Mail postage (publication No. 484460) paid at Washington, DC, and additional mailing offices. Domestic individual membership and subscription (51 issues): $146 ($74 allocated to subscription). Domestic institutional subscription (51 issues): $835; Foreign postage extra: Mexico, Caribbean (surface mail) $55; other countries (air assist delivery) $85. First class, airmail, student, and emeritus rates on request. Canadian rates with GST available upon request, GST #1254 88122. Publications Mail Agreement Number 1069624. **Printed in the U.S.A.**

Change of address: Allow 4 weeks, giving old and new addresses and 8-digit account number. **Postmaster:** Send change of address to AAAS, P.O. Box 96178, Washington, DC 20090–6178. **Single-copy sales:** $10.00 current issue, $15.00 back issue prepaid includes surface postage; bulk rates on request. **Authorization to photocopy** material for internal or personal use under circumstances not falling within the fair use provisions of the Copyright Act is granted by AAAS to libraries and other users registered with the Copyright Clearance Center (CCC) Transactional Reporting Service, provided that $20.00 per article is paid directly to CCC, 222 Rosewood Drive, Danvers, MA 01923. The identification code for *Science* is 0036-8075. *Science* is indexed in the *Reader's Guide to Periodical Literature* and in several specialized indexes.

AAAS
ADVANCING SCIENCE, SERVING SOCIETY

Published by AAAS

FROM START TO FINISH, ENDNOTE X3 KEEPS YOUR RESEARCH ON THE FAST TRACK.

Download your free demo or buy online today
www.endnote.com

With its world-class speed and track record, EndNote X3 puts your publishing in the lead and keeps you there. Out of the blocks with new features like faster start up times and seasoned favorites like our Cite While You Write™ technology, EndNote X3 is moving fast to deliver the world's most complete bibliographic solution.

It doesn't stop there. EndNote X3 is also meters ahead with a personal EndNote Web account that not only transfers groups swiftly between desktop and Web but also organizes your own publication list for the ResearcherID author community. You'll find new speed in Cite While You Write for Apple® Pages '09, Microsoft® Word, and now OpenOffice.org Writer 3 for Windows. EndNote X3 even sports new options for chemistry styles, multiple bibliographies within a Word document, and more.

Keep the lead, right to the finish line. Put EndNote X3 on your reference team today!

800-722-1227 • 760-438-5526 • rs.info@thomson.com

THOMSON REUTERS

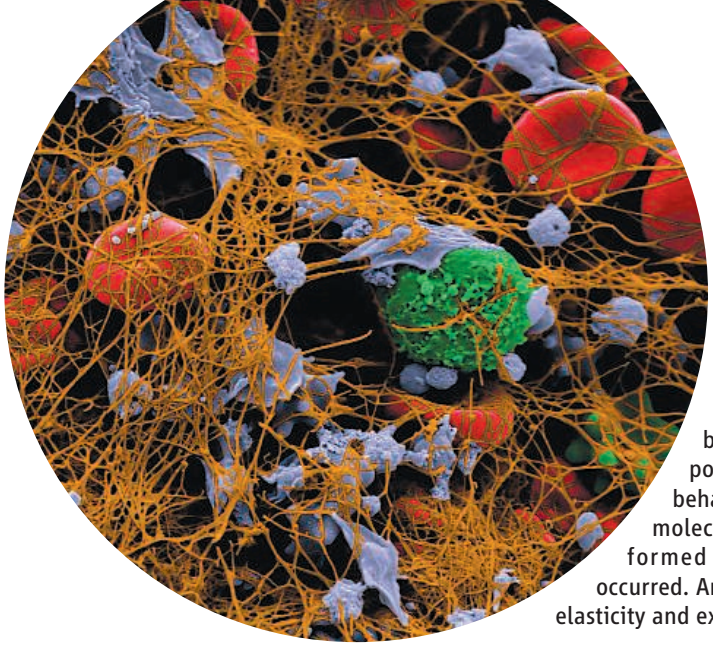

<< Focusing on Fibrin

Vascular injury initiates biochemical reactions that cause the blood protein, fibrin, to polymerize and help to stop bleeding and support wound healing. Fibrin can also be a scaffold for thrombi that lead to cardiovascular diseases. To maintain homeostasis, fibrin clots must be stiff, plastic, and, so that the network can be decomposed, permeable. **Brown *et al.*** (p. 741) investigated the behavior of fibrin clots at the macroscopic, single-fiber, and molecular scale. At relatively low strains, fibers aligned and formed bundles, and at higher strains, protein unfolding occurred. An integrated model provides a molecular basis for fibrin elasticity and extensibility.

The Melting Is in the Details

Global sea level rises and falls as ice sheets and glaciers melt and grow, providing an integrated picture of the changes in ice volume but little information about how much individual ice fields are contributing to those variations. Knowing the regional structure of ice variability during glaciations and deglaciations will clarify the mechanisms of the glacial cycle. **Clark *et al.*** (p. 710) compiled and analyzed more than 5000 radiocarbon and cosmogenic surface exposure ages in order to develop a record of maximum regional ice extent around the time of the Last Glacial Maximum. The responses of the Northern and Southern Hemispheres differed significantly, which reveals how the evolution of specific ice sheets affected sea level and provides insight into how insolation controlled the deglaciation.

Honing Bivalve History

What are the lasting effects of extinction, both persistent background extinctions and major events, on surviving lineages? **Roy *et al.*** (p. 733) examined the excellent fossil record of marine bivalves over the past 200 million years, which spans the end-Cretaceous extinction. Background extinctions tended to be higher within certain lineages and depended on the previous history of extinctions within those lineages. Cenozoic taxa are still reflecting the end-Cretaceous event.

Codifying Maize Modifications

Maize, one of our most important crop species, has been the target of genetic investigation and experimentation for more than 100 years. Crossing two inbred lines tends to result in "better" offspring, in a process known as heterosis. Attempts to map the genetic loci that control traits important for farming have been made, but few have been successful (see the Perspective by **Mackay**). **Buckler *et al.*** (p. 714) and **McMullen *et al.*** (p. 737) produced a genomic map of maize that relates recombination to genome structure. Even tremendous adaptations in very diverse species were produced by numerous, small additive steps. Differences in flowering time in maize among inbred lines were not caused by a few genes with large effects, but by the cumulative effects of numerous quantitative trait loci—each of which has only a small impact on the trait.

Cosmic Shock Waves

Cosmic rays are high-energy charged particles that bombard Earth from all directions in the sky; those originating from within our Galaxy are thought to be accelerated in the shockwaves produced by supernova explosions. **Helder *et al.*** (p. 719, published online 25 June; see the Perspective by **Raymond**) measured the velocity of a section of the blast wave created by supernova RCW 86, an exploding star believed to have been witnessed by Chinese astronomers in 185 A.D., and the post-shock proton temperature. The post-shock proton temperature was much lower than would be expected without any cosmic ray acceleration, which implies that the pressure induced by cosmic ray exceeds the thermal pressure behind the shock.

Higher-Level Quantum Emulation

At the heart of a quantum computer is the device on which information is to be encoded. This is typically done with a qubit, a two-level quantum system analogous to the two-level bit that encodes 0 and 1 in classical computers. However, there need not be just two quantum energy levels. There could be three (a qutrit), or more generally, *d*-levels (a qudit) in the device. **Neeley *et al.*** (p. 722; see the Perspective by **Nori**) demonstrate a five-level quantum device and show that their qudit can be used to emulate the processes involved in manipulating quantum spin. The use of multilevel qudits may also have potential in quantum information processing by simplifying certain computational tasks and simplifying the circuitry required to realize the quantum computer itself.

Stressful Self-Assembly

One way to control shape during the assembly of an object is to design in stresses that cause a planned amount of deformation. **Dietz *et al.*** (p. 725; see the Perspective by **Liu and Yan**) designed DNA helix bundles, arranged in honeycomb lattices, in which some of the helices have insertions or deletions relative to the other helices in the bundles. The stresses help the bundles assemble into objects on the scale of tens of nanometers. Both the direction and degree of bending could be controlled, and curvatures as tight as 6 nanometers achieved. Complex shapes, such as square-toothed gears, could be created by combining multiple curved elements.

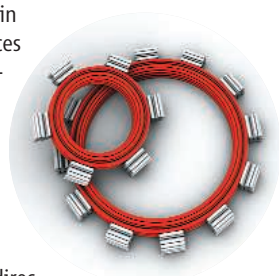

No NO

Isoprene, a five-carbon diene produced by plants, is the most abundant nonmethane hydrocarbon released into the atmosphere and plays

Continued on page 653

CREDITS (TOP TO BOTTOM): ANDRÉ E. X. BROWN *ET AL.*; HENRIK DIETZ

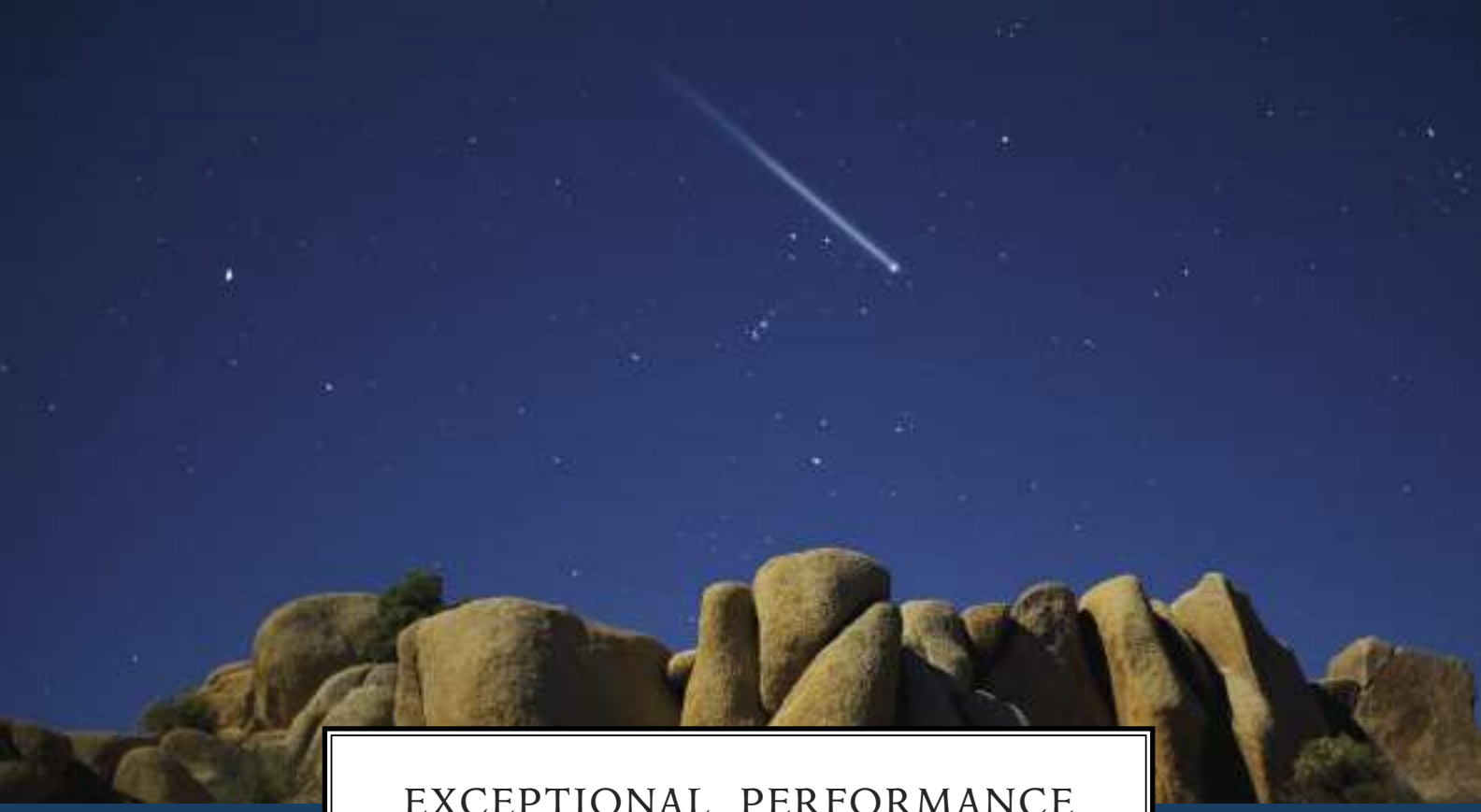

EXCEPTIONAL PERFORMANCE

Restriction Enzymes from New England Biolabs

With 35 years of experience in enzyme technology, New England Biolabs leads the industry in the study and improvement of restriction enzymes. NEB is pleased to introduce a line of High Fidelity (HF) enzymes that have been engineered for reduced star activity. HF enzymes bring a new level of flexibility when choosing reaction conditions, including volume, incubation time and buffer compatibility. Make NEB your first choice and experience the exceptional performance of this next generation in restriction enzyme technology.

Reduced star activity with HF Enzymes from NEB

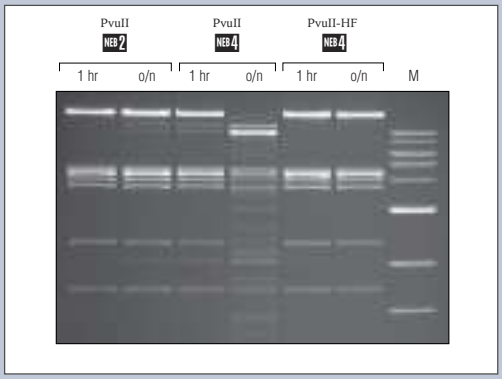

Recombinant PvuII, normally supplied in NEBuffer 2, exhibits star activity when used in extended incubations or in alternate buffers. Star activity is significantly reduced with PvuII-HF, even under extended incubation.

Advantages:

- **Selection** – More specificities than any other supplier
- **Convenience** – Optimal activity for over 160 enzymes in a single buffer NEB 4
- **Quality** – State-of-the-art production and stringent QCs
- **Innovation** – HF enzymes engineered for reduced star activity
- **Performance** – Guaranteed

NEW ENGLAND BioLabs® Inc.
enabling technologies in the life sciences

CLONING & MAPPING	DNA AMPLIFICATION & PCR	RNA ANALYSIS	PROTEIN EXPRESSION & ANALYSIS	GENE EXPRESSION & CELLULAR ANALYSIS

www.neb.com

Continued from page 651

an important role in tropospheric chemistry. Isoprene is also thought to affect climate by acting as a source of atmospheric aerosols. **Paulot *et al.*** (p. 730; see the Perspective by **Kleindienst**) now describe how isoprene may lead to the formation of secondary organic aerosols. In laboratory experiments, the photooxidation of isoprene in low-NO conditions, such as those which occur in vegetated regions far from anthropogenic influence, produced high yields of dihydroxy epoxides, a suspected precursor of the aerosols. This discovery could help to explain some of the more puzzling aspects of isoprene chemistry in remote regions.

Untangling Food Webs

The factors affecting the stability of food webs are important in conservation and ecological restoration. **Gross *et al.*** (p. 747) used a generalized modeling approach to evaluate billions of replicates of food webs in order to reveal the properties that stabilize (or destabilize) food webs. Variability in the strength of trophic links between predator and prey strength affected stability in different ways depending on the size of the web—stabilizing only in relatively small food webs and destabilizing in larger ones. Universal topological rules were extracted for the patterns of network links that enhance food-web stability.

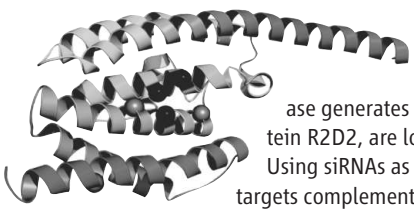

RNA Wars

During RNA interference (RNAi), the Dicer endonuclease generates small interfering (si)RNAs that, with the help of the protein R2D2, are loaded into the siRNA-induced silencing complex (RISC). Using siRNAs as guides, RISC, and specifically its Argonaute subunit, targets complementary RNAs for destruction. In order to identify other components of the RISC complex, **Liu *et al.*** (p. 750) reconstituted the core RISC activity, using purified *Drosophila* Dicer, R2D2, and Ago-2. The protein C3PO (component 3 promoter of RISC), which consists of heterodimer of Translin and Translin-associated factor X (Trax), was found to enhance RISC activity in this system, and in vivo, with the Trax endonuclease activity activating RISC through the removal of siRNA passenger strand cleavage products.

Jamming Protein Translocation

Antibiotics are tremendously important drugs in modern medicine, yet we are still learning precisely how they work. SecY is a bacterial membrane protein that is part of a complex that allows protein secretion across the membrane. **Van Stelten *et al.*** (p. 753; see the Perspective by **Breukink**) found in *Escherichia coli* cells that if the protein translocator complex becomes jammed with a protein that cannot pass through, the SecY protein is degraded by the protease FtsH, leading to cell death. Cells could be protected by increasing amounts of an inhibitor of FtsH, the YccA protein. Antibiotics that block protein translation also caused jamming of the SecY machinery and destruction of SecY, thus contributing to cell death.

Plastic Pain Perception

Drugs and endocannabinoids acting on cannabinoid (CB) receptors have potential in the treatment of certain types of pain. In the spinal cord they are believed to suppress nociception, the perception of pain and noxious stimuli. **Pernia-Andrade *et al.*** (p. 760) now find that endocannabinoids, which are released in spinal cord by noxious stimulation, may promote rather than inhibit nociception by acting on CB1 receptors. Endocannabinoids not only depress transmission at excitatory synapses in the spinal cord, but also block the release of inhibitory neurotransmitters, thereby facilitating nociception.

Taking Shape

DNA recombination mechanisms enable certain pathogens to modify the proteins on their outer surfaces by rearranging their genes and so avoid repeated detection by the immune system. **Cahoon and Seifert** (p. 764) have found that antigenic variation of a single genetic locus in the human pathogen *Neisseria gonorrhoeae* is triggered by a specific cis-acting DNA element. This 16–base pair DNA sequence formed an unusual DNA structure in vitro; a guanine quartet (G4), which has been implicated in only a few other biological processes. The G4 forming sequence is required for processing the gene conversion reaction leading to antigenic variation. These findings have implications both for understanding mechanisms of DNA recombination and its role in microbial pathogenesis.

CREDIT: LIU *ET AL.*

Published by AAAS

Future Energy Institutes

Paul G. Falkowski is a professor and director of the Rutgers Energy Institute, New Brunswick, NJ. E-mail: falko@marine.rutgers.edu

Robert M. Goodman is a professor and executive dean of the School of Environmental and Biological Sciences at Rutgers, the State University of New Jersey, New Brunswick, NJ. E-mail: execdean@aesop.rutgers.edu

THE LANDMARK ENERGY BILL WENDING ITS WAY THROUGH CONGRESS THIS SUMMER SEEKS TO reduce emissions of carbon dioxide and other greenhouse gases and supports the development of alternative energies, including solar and wind power. It's a bill that aims to create both a "green" U.S. economy and a sustainable environment. At this critical juncture, America must take an equally sustainable view toward investing in the brainpower required to confront the world's complex energy issues.

Three-quarters of students in the United States attend the country's public colleges and universities, but very few of these institutions have vigorous education, research, and outreach programs focused on energy and climate change. Without a major restructuring of these powerful institutions, we forego the intellectual power and entrepreneurial spirit that they could tap to solve the energy and climate problems we face. We propose the creation of a public "energy-grant university system" devoted to energy education and research. This new system would be modeled on the U.S. land-grant university system established in 1862 in the midst of the Civil War to promote public education in agriculture and the mechanical arts. In the 20th century, the 78 land-grant institutions became a major source of intellectual wealth for the production of food, fiber, and basic scientific knowledge. Federal appropriations for this system in 2009 were nearly $1 billion, multiplied many-fold by matching state appropriations.

Federal investments in an energy-grant university system could build on the existing infrastructure and framework embedded in the nation's comprehensive public research universities. In some cases, this could lead to expanding the mission of existing land-grant universities; in other cases, different comprehensive public research institutions or a consortium of such universities may be more appropriate. Support for at least one such institution in each state would provide, as it did for agriculture, new scientific knowledge and an extension service capable of advising every town on how best to reduce carbon footprints, increase energy efficiency, and promote sustainable economic growth.

To harness a vast untapped intellectual pool to drive the new green revolution, Congress should enact legislation that provides long-term funding through the Department of Energy to support research and extension services focused on energy issues at specific universities selected through a competitive process. A one-time investment of $5 billion could fund the construction of new buildings and facilities, and a $30 billion endowment would generate $1.5 billion in federal funding per year to support programs on energy research. As with the land-grant program, federal funding should be contingent on co-funding by each state, and it should provide strong incentives for corporate support from the energy industry. The new energy-grant institutions would become impartial advisers to local, state, and national policy-makers, and they would engage the country in building strong, science-based programs that focus on energy and climate, as their predecessors focused on agriculture over a century ago.

Developing global sustainable and scalable energy resources today is as critical to the future as strategically investing in agriculture once was to securing the national food system. Congressional action on the energy bill signals a new level of commitment to U.S. energy security. The 4-year America's Energy Future study launched by the U.S. National Academies in 2007, and the recent Brookings Institution proposal of a complementary network of "discovery-innovation institutes" to move breakthrough inventions to the marketplace, demonstrate broad high-level support for finding sustainable solutions.

The energy-grant university proposal thrusts the intellectual might of public research institutions into the national conversation about solving global energy and climate challenges. Energy and climate change aren't simply environmental issues; they're also social, economic, and political problems. The next generation of leaders must confront these issues. It's up to colleges and universities to lay the foundation for their success. **– Paul G. Falkowski and Robert M. Goodman**

10.1126/science.1176998

EDITED BY GILBERT CHIN AND JAKE YESTON

GEOLOGY

Salty Fingers

Convection of groundwater through porous rock plays a critical role in many geological processes in the crust. It occurs whenever groundwater density decreases with depth (on account of either a temperature or salinity gradient relative to overlying water layers) and the rock permeability and pore connectivity are sufficient to allow flow. Convection at ocean ridges is responsible for altering the composition of ocean crust globally; locally, convection is the basis for most geothermal energy systems. Despite the wide-ranging implications of the phenomenon, clear-cut visualization of convection in the field has proven difficult. Laboratory experiments have shown that stratified systems, in which salty water overlies fresh water, should produce interfingering of the layers at a wavelength of about twice the thickness of the system. In this context, Van Dam *et al.* studied a sabkha aquifer near Abu Dhabi, United Arab Emirates, where evaporation produces salty groundwater perched above fresh ancient water at depth. Electrical resistivity measurements, sensitive to the salt content of the groundwater, revealed prominent fingers of descending salt water that were generally consistent with predictions. — BH

Geophys. Res. Lett. **36**, L11403 (2009).

MICROBIOLOGY

Resistance on Tap

Antibiotic-resistant bacteria have become so common in aquatic ecosystems that some researchers suggest their genes should be considered environmental contaminants. Efforts to uncover the means whereby antibiotic resistance propagates are crucial in confronting the overall problem. Using a combination of broad-spectrum culturing methods and quantitative molecular techniques, Xi *et al.* characterized the prevalence of antibiotic-resistant bacteria, as well as the genes conferring resistance, at various points within water supply networks in the midwestern United States. In most municipalities they sampled, the abundance of antibiotic-resistant bacteria was higher in tap water than in finished water (i.e., water sampled directly after treatment). The quantity of antibiotic-resistant genes in tap water was also greater than in finished water and, remarkably, exceeded the quantities in original source waters as well. Water treatment plants and distribution systems may therefore unintentionally serve as incubators for growth of antibiotic-resistant bacteria and selectively increase antibiotic resistance of bacterial communities through horizontal gene transfer. — NW

Appl. Environ. Microbiol. **75**, 10.1128/AEM.00382-09 (2009).

MICROBIOLOGY

Paracrine Parable

Bacillus subtilis is a soil-dwelling organism that forms biofilms—extracellular matrices harboring a bacterial community. One way in which bacteria are known to coordinate their activities is via signaling molecules that are produced when the colony reaches a certain density, a phenomenon known as quorum sensing. Lopez *et al.* describe a distinct mode of social networking, referred to as paracrine signaling. Many of the cells in a *B. subtilis* biofilm secrete a small peptide called ComX. This peptide binds to a membrane-bound kinase and triggers the phosphorylation of an intracellular transcription factor, which goes on to initiate the synthesis and secretion of the peptide surfactin in a small group of cells. The authors have discovered that apart from being a surfactant, surfactin evokes extracellular matrix production in another group of cells. Surfactin producers do not make extracellular matrix themselves, whereas matrix producers do not become surfactin producers, because their response to ComX is blocked by the presence of matrix. Thus, populations of independently minded cells develop and coexist for prolonged periods, alongside others with yet other functions, defying the notion that bacterial cells cannot differentiate and specialize like eukaryotic cells do. — CA

Genes Dev. **23**, 1631 (2009).

BIOCHEMISTRY

A Scaffold for Interactions

The mitogen-activated protein kinase (MAPK) signaling pathway provides an example of the elaborate controls that are necessary when a cellular module regulates a huge range of processes from proliferation and survival to metabolism and cell motility. The enzymes of the MAPK cascade—the protein kinase Raf, which phosphorylates the kinase MEK, which in turn phosphorylates the MAPK ERK—are localized in

CREDITS (TOP TO BOTTOM): LOPEZ *ET AL.*, *GENES DEV.* **23**, 1631 (2009); JUPITERIMAGES

Published by AAAS

complexes by scaffold proteins, increasing the efficiency of interactions and stipulating the specificity of such events. McKay *et al.* have established the intricate choreography of interactions mediated by the scaffold protein KSR1. This protein was identified as a positive regulator of the small guanosine triphosphatase Ras, which initiates the activation of Raf and the rest of the MAPK cascade. KSR1 forms a ternary complex with Raf and MEK; this activates ERK, and the activation of ERK exposes a site that allows ERK to bind to KSR1, where it (ERK, that is) phosphorylates four sites each on KSR1 and Raf. When the binding site for ERK on KSR1 was disrupted or the sites that ERK phosphorylates on KSR1 were removed, though, the interaction of KSR with Raf1 was enhanced and signaling was prolonged. Thus, the authors conclude that ERK provides a negative-feedback signal that disrupts interaction of Raf and KSR1 and releases KSR1 from the cell membrane, thereby adjusting the intensity and duration of signaling through the MAPK cascade. — LBR

Proc. Natl. Acad. Sci. U.S.A. **106**, 11022 (2009).

BIOPHYSICS

Tugging at Heartstrings

One of the first lessons in learning to work with wood is that it exhibits a resistance to compression or tension that depends upon the direction in which force is applied. A macroscopic clue to this anisotropic behavior can be found by examining the wood grain. Bertz *et al.* demonstrate that this phenomenon can also be observed at the molecular level in their atomic force microscopy investigation of titin, a structural protein found in skeletal and cardiac muscle. In these tissues titin is subject to considerable force, and the end-cap protein,

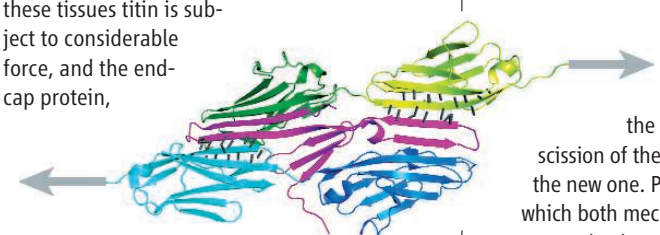

telethonin (red), grasps two titin molecules, binding to the N-terminal domain Z1 (dark green and blue) and the next interior one Z2 (light green and blue). Pulling apart this joint requires a force of 700 pN when applied to Z2 (that is, the normal physiological direction of pulling), but only one-third as much force need be applied to Z1; the difference is accounted for by directionally oriented hydrogen bonds (gray) between telethonin and the Z2 domain. — GJC

Proc. Natl. Acad. Sci. U.S.A. **106**, 10.1073/pnas.0902312106 (2009).

CREDIT: BERTZ *ET AL.*, *PROC. NATL. ACAD. SCI. U.S.A.* **106**, 10.1073/PNAS.0902312106 (2009)

BIOMEDICINE

Inhibiting Interactions

Although the genetic bases of many cancers have been identified, there remains the challenge of translating this knowledge into promising drug candidates. The discovery of the chromosomal translocation that fuses the *BCR* and *Abl* genes and leads to the development of chronic myeloid leukemia was followed by spectacular clinical data attesting the efficacy of the inhibitor imatinib mesylate in the late 1990s. Ewing's sarcoma family tumors are also caused by a chromosomal translocation, most commonly one that fuses the *EWS* and *FLI1* genes. The resulting EWS-FLI1 transcription factor both lacks enzymatic activity and is inherently disordered, making it difficult to screen chemical libraries for inhibitors. EWS-FLI1 does, however, bind to RNA helicase A, which acts as a transcriptional coactivator, and this interaction is important for tumorigenesis. Erkizan *et al.* designed a peptide to inhibit binding and used it to identify a small molecule (YK-4-279) that specifically blocked EWS-FLI1 binding to RNA helicase A and also decreased tumor growth in mouse xenograft assays. This strategy may be valuable for developing lead molecules in other cancers caused by similar types of fusion proteins. — HP

Nature Med. **15**, 750 (2009).

CHEMISTRY

Simultaneous Substitutions

There is a long-standing distinction in organic chemistry between unimolecular (S_N1) and bimolecular (S_N2) substitution mechanisms at carbon centers. The former involves departure of a substituent before arrival of its replacement, whereas the latter involves concomitant scission of the old bond and formation of the new one. Phan *et al.* explore a system in which both mechanisms appear to operate concurrently, depending on the identity of the attacking group, or nucleophile. Through careful kinetics measurements, they show that a series of benzhydryl bromides react with amines via an S_N2 pathway, while a competitive S_N1 pathway results in replacement of bromide with a dimethyl sulfoxide solvent molecule. Using a parameterized nucleophilicity/electrophilicity relation, the authors account for the results based on the lifetimes of benzhydrylium intermediates and the relative likelihood of having an amino or dimethyl sulfoxide molecule in the vicinity when bromide departs. — JSY

J. Am. Chem. Soc. **131**, 10.1021/ja903207b (2009).

www.sciencemag.org

Science

1200 New York Avenue, NW
Washington, DC 20005
Editorial: 202-326-6550, FAX 202-289-7562
News: 202-326-6581, FAX 202-371-9227
Bateman House, 82-88 Hills Road
Cambridge, UK CB2 1LQ
+44 (0) 1223 326500, FAX +44 (0) 1223 326501

Subscription Services For change of address, missing issues, new orders and renewals, and payment questions: 866-434-AAAS (2227) or 202-326-6417, FAX 202-842-1065. Mailing addresses: AAAS, P.O. Box 96178, Washington, DC 20090-6178 or AAAS Member Services, 1200 New York Avenue, NW, Washington, DC 20005

Institutional Site Licenses please call 202-326-6755 for any questions or information

Reprints: Author Inquiries 800-635-7181
Commercial Inquiries 803-359-4578

Permissions 202-326-7074, FAX 202-682-0816

Member Benefits AAAS/Barnes&Noble.com bookstore www.aaas.org/bn; AAAS Online Store www.apisource.com/aaas/ code MKB6; AAAS Travels: Betchart Expeditions 800-252-4910; Apple Store www.wapple/eppstore/aaas; Bank of America MasterCard 1-800-833-6262 priority code FAA3YU; Cold Spring Harbor Laboratory Press Publications www.cshlpress.com/affiliates/aaas.htm; GEICO Auto Insurance www.geico.com/landingpage/go51.htm?logo=17624; Hertz 800-654-2200 CDP#343457; Office Depot https://bsd.officedepot.com/portalLogin.do; Seabury & Smith Life Insurance 800-424-9883; Subaru VIP Program 202-326-6417; VIP Moving Services www.vipmayflower.com/domestic/index.html; Other Benefits: AAAS Member Services 202-326-6417 or www.aaasmember.org.

science_editors@aaas.org	(for general editorial queries)
science_letters@aaas.org	(for queries about letters)
science_reviews@aaas.org	(for returning manuscript reviews)
science_bookrevs@aaas.org	(for book review queries)

Published by the American Association for the Advancement of Science (AAAS), *Science* serves its readers as a forum for the presentation and discussion of important issues related to the advancement of science, including the presentation of minority or conflicting points of view, rather than by publishing only material on which a consensus has been reached. Accordingly, all articles published in *Science*—including editorials, news and comment, and book reviews—are signed and reflect the individual views of the authors and not official points of view adopted by AAAS or the institutions with which the authors are affiliated.

AAAS was founded in 1848 and incorporated in 1874. Its mission is to advance science, engineering, and innovation throughout the world for the benefit of all people. The goals of the association are to: enhance communication among scientists, engineers, and the public; promote and defend the integrity of science and its use; strengthen support for the science and technology enterprise; provide a voice for science on societal issues; promote the responsible use of science in public policy; strengthen and diversify the science and technology workforce; foster education in science and technology for everyone; increase public engagement with science and technology; and advance international cooperation in science.

Information for Authors
See pages 807 and 808 of the 6 February 2009 issue or access www.sciencemag.org/about/authors

EDITOR-IN-CHIEF **Bruce Alberts**
EXECUTIVE EDITOR **Monica M. Bradford**
NEWS EDITOR **Colin Norman**
MANAGING EDITOR, RESEARCH JOURNALS **Katrina L. Kelner**
DEPUTY EDITORS **R. Brooks Hanson, Barbara R. Jasny, Andrew M. Sugden**

Editorial senior editors/commentary Lisa D. Chong, Brad Wible; **senior editors** Gilbert J. Chin, Pamela J. Hines, Paula A. Kiberstis (Boston), Marc S. Lavine (Toronto), Beverly A. Purnell, L. Bryan Ray, Guy Riddihough, H. Jesse Smith, Phillip D. Szuromi (Tennessee), Valda Vinson, Jake S. Yeston; **associate editors** Kristen L. Mueller, Nicholas S. Wigginton, Laura M. Zahn; **research associate** Alexis Wynne Mogul; **online editor** Stewart Wills; **associate online editors** Robert Frederick, Tara S. Marathe; **web content developer** Martyn Green; **book review editor** Sherman J. Suter; **associate letters editor** Jennifer Sills; **editorial manager** Cara Tate; **senior copy editors** Jeffrey E. Cook, Cynthia Howe, Harry Jach, Barbara P. Ordway, Trista Wagoner; **copy editors** Chris Filiatreau, Lauren Kmec; **editorial coordinators** Carolyn Kyle, Beverly Shields; **publications assistants** Ramatoulaye Diop, Carlos L. Durham, Joi S. Granger, Jeffrey Hearn, Lisa Johnson, Scott Miller, Jerry Richardson, Jennifer A. Seibert, Brian White, Anita Wynn; **editorial assistants** Emily Guise, Michael Hicks, Patricia M. Moore; **executive assistant** Sylvia S. Kihara; **administrative support** Maryrose Madrid; **editorial fellow** Melissa R. McCartney

News deputy news editors Robert Coontz, Eliot Marshall, Jeffrey Mervis, Leslie Roberts; Contributing Editors Elizabeth Culotta, Polly Shulman; **news writers** Yudhijit Bhattacharjee, Adrian Cho, Jennifer Couzin, David Grimm, Constance Holden, Jocelyn Kaiser, Richard A. Kerr, Eli Kintisch, Andrew Lawler (New England), Greg Miller, Elizabeth Pennisi, Robert F. Service (Pacific NW), Erik Stokstad; **interns** Michael Torrice, Brittany Johnson, Preyanka Makadia; **contributing correspondents** Dan Charles, Jon Cohen (San Diego, CA), Daniel Ferber, Ann Gibbons, Robert Koenig, Mitch Leslie, Charles C. Mann, Virginia Morell, Evelyn Strauss, Gary Taubes; **copy editors** Linda B. Felaco, Melvin Gatling, Melissa Raimondi; **administrative support** Scherraine Mack, Fannie Groom; **bureaus** New England: 207-549-7755; San Diego, CA: 760-942-3252, FAX 760-942-4979; Pacific Northwest: 503-963-1940

Production director James Landry; **senior manager** Wendy K. Shank; **assistant manager** Rebecca Doshi; **senior specialists** Steve Forrester, Chris Redwood; **specialist** Anthony Rosen; **Preflight director** David M. Tompkins; **manager** Marcus Spiegler; **specialist** Jason Hillman

Art director Yael Kats; **associate art director** Laura Creveling; **senior illustrators** Chris Bickel, Katharine Sutliff; **illustrator** Yana Greenman; **senior art associates** Holly Bishop, Preston Huey, Nayomi Kevitiyagala; **art associates** Jessica Newfield, Matthew Twombly; **photo editor** Leslie Blizard

***Science* International**

Europe (science@science-int.co.uk) **editorial: international managing editor** Andrew M. Sugden; **senior editor/commentary** Julia Fahrenkamp-Uppenbrink; **senior editors** Caroline Ash, Stella M. Hurtley, Ian S. Osborne, Peter Stern; **associate editor** Maria Cruz; **locum editor** Helen Pickersgill; **editorial support** Deborah Dennison, Rachel Roberts, Alice Whaley; **administrative support** John Cannell, Janet Clements, Louise Moore; **news: europe news editor** John Travis; **deputy news editor** Daniel Clery; **contributing correspondents** Michael Balter (Paris), John Bohannon (Vienna), Martin Enserink (Amsterdam and Paris), Gretchen Vogel (Berlin)

Asia Japan Office: Asca Corporation, Eiko Ishioka, Fusako Tamura, 77 Tenjin-cho, Shinjuku, Tokyo 162-0808, Japan; +81 3 6802 4616, FAX +81 3 6802 4615, inquiry@sciencemag.jp; **asia news editor** Richard Stone (Beijing: rstone@aaas.org); **contributing correspondents** Dennis Normile [Japan: +81 (0) 3 3391 0630, FAX +81 (0) 3 5936 3531; dnormile@gol.com]; Hao Xin [China: +86 (0) 10 6307 4439 or 6307 3676, FAX +86 (0) 10 6307 4358; cindyhao@gmail.com]; Pallava Bagla [South Asia: +91 (0) 11 2271 2896; pbagla@vsnl.com]

EXECUTIVE PUBLISHER **Alan I. Leshner**
PUBLISHER **Beth Rosner**

Fulfillment Systems and Operations (membership@aaas.org); **director** Waylon Butler; **senior systems analyst** Nomuna Nyamaa; **customer service supervisor** Pat Butler; **specialists** Latoya Casteel, LaVonda Crawford, Vicki Linton, April Marshall; **data entry supervisor** Cynthia Johnson; **specialists** Shirlene Hall, Tarrika Hill, William Jones

Business Operations and Administration director Deborah Rivera-Wienhold; **assistant director, business operations** Randy Yi; **manager, business analysis** Eric Knott; **manager, business operations** Jessica Tierney; **financial analysts** Priti Pamnani, Celeste Troxler; **rights and permissions: administrator** Emilie David; **associate** Elizabeth Sandler; **marketing director** Ian King; **marketing managers** Allison Pritchard, Alison Chandler, Julianne Wielga; **marketing associates** Aimee Aponte, Mary Ellen Crowley, Adrian Parham, Wendy Wise; **marketing executive** Jennifer Reeves; **director, site licensing** Tom Ryan; **director, corporate relations** Eileen Bernadette Moran; **publisher relations, eresources specialist** Kiki Forsythe; **senior publisher relations specialist** Catherine Holland; **publisher relations, east coast** Phillip Smith; **publisher relations, west coast** Philip Tsolakidis; **fulfillment supervisor** Iquo Edim; **fulfillment coordinator** Carrie MacDonald; **marketing associate** Mary Lagnaoui; **electronic media: manager** Lizabeth Harman; **project manager** Trista Snyder; **assistant manager** Lisa Stanford; **senior production specialists** Christopher Coleman, Walter Jones; **production specialists** Nichele Johnston, Kimberly Oster

Advertising director, worldwide ad sales Bill Moran

Product (science_advertising@aaas.org); **midwest/west coast/w. canada** Rick Bongiovanni: 330-405-7080, FAX 330-405-7081; **east coast/e. canada** Laurie Faraday: 508-747-9395, FAX 617-507-8189; **uk/europe/asia** Roger Goncalves: TEL/FAX +41 43 243 1358; **japan** Mashy Yoshikawa: +81 (0) 3 3235 5961, FAX +81 (0) 3 3235 5852; **senior traffic associate** Deiandra Simms

Commercial Editor Sean Sanders: 202-326-6430

Project Director, Outreach Brianna Blaser

Classified (advertise@sciencecareers.org); **u.s.: sales manager** Daryl Anderson: 202-326-6543; **midwest** Tina Burks: 202-326-6577; **east coast** Alexis Fleming: 202-326-6578; **west/south central** Nicholas Hintibidze: 202-326-6533; **sales coordinators** Rohan Edmonson, Shirley Young; **international: sales manager** Tracy Holmes: +44 (0) 1223 326525, FAX +44 (0) 1223 326532; **sales** Susanne Kharraz, Dan Pennington, Alex Palmer; **sales assistant** Lisa Patterson; **japan** Mashy Yoshikawa: +81 (0) 3 3235 5961, FAX +81 (0) 3 3235 5852; **advertising support manager** Karen Foote: 202-326-6740; **advertising production operations manager** Deborah Tompkins; **senior production specialist/graphic designer** Amy Hardcastle; **senior production specialist** Robert Buck; **senior traffic associate** Christine Hall

AAAS Board of Directors retiring president, chair James J. McCarthy; **president** Peter C. Agre; **president-elect** Alice Huang; **treasurer** David E. Shaw; **chief executive officer** Alan I. Leshner; **board** Alice Gast, Linda P. B. Katehi, Nancy Knowlton, Cherry A. Murray, Julia M. Phillips, Thomas D. Pollard, David S. Sabatini, Thomas A. Woolsey

AAAS
ADVANCING SCIENCE, SERVING SOCIETY

EDITED BY ROBERT COONTZ

BLOGS: HAPPINESS BAROMETERS?

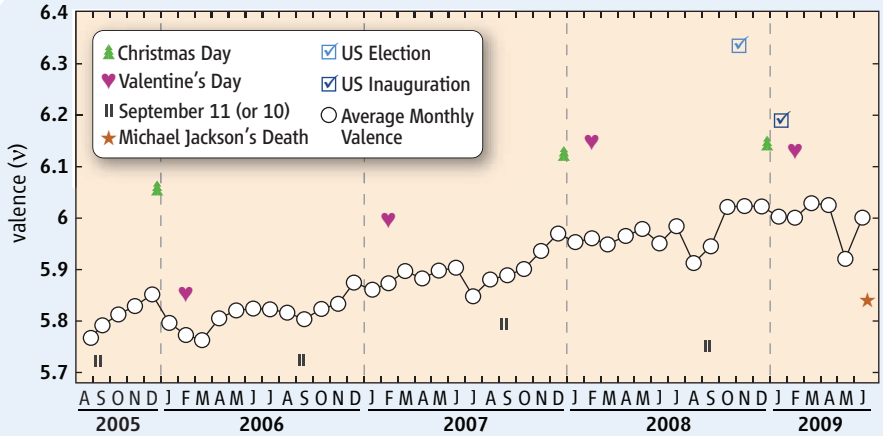

Day in, day out, bloggers pour their feelings onto the Web. Now researchers are mining those outpourings to track society's mood swings.

Peter Dodds and Christopher Danforth, applied mathematicians at the University of Vermont, Burlington, automatically searched 2.4 million blogs, via the Web site www.wefeelfine.org, for phrases containing the words "I feel." Their computers then scanned those phrases for 1034 emotionally charged words that a 1999 psychology study had ranked on a happiness scale from 1 (miserable) to 9 (ecstatic). From the words' frequency and scores, an algorithm calculated a net feel-good factor for each day and month.

For the past 4 years, happiness has steadily increased in the blogosphere, Dodds and Danforth reported online recently in the *Journal of Happiness Studies*. Spirits spike on Christmas and Valentine's Day but dip on 11 September. The happiest day since 2005 was 4 November 2008, the day of the U.S. presidential election. In contrast, Michael Jackson's death in June triggered a 3-day trough.

The Vermont scientists are now studying Twitter feeds. James Fowler, a social scientist at the University of California, San Diego, says the new method will enable scientists "to take the pulse of the whole world, assessing the mood of human society."

Easy as 1, 2, 3

New Caledonian crows, known for clever tool-making in the wild and in the lab (*Science*, 9 August 2002, p. 981), have added another first to their list of talents: using three tools in the correct order to bag a treat. Such sequential tool use has never been observed in any other untrained nonhuman animal, behavioral ecologist Joanna Wimpenny and others in Alex Kacelnik's lab at the University of Oxford in the United Kingdom report this week in *PLoS ONE*.

In the wild, the crows (*Corvus moneduloides*) regularly fashion barbs and hooks from leaves and twigs to extract grubs from holes and crevices. And in Kacelnik's lab, a wild-caught crow called Betty was famous for inventing tools. In the new experiment, Kacelnik's team gave each of seven crows a test tube stuffed with a tasty piece of meat that could be pried out only with a particular stick. To get at the meat, the birds had to do three things in the right order: pick up a short stick, available on the cage floor, and use it to pull a longer stick out of a second test tube; use that stick to extract an even longer stick from a third test tube; and then use this longest stick to get the prize.

Four crows took home the bacon. "Clearly, they were not selecting the sticks at random," Kacelnik says, because the birds usually swapped sticks for longer ones. Frans de Waal, a primatologist at Emory University in Atlanta, applauds the study as "absolutely essential to understand better what these crows are doing," although he suspects that they're solving the task via a trial-and-error process "closer to that of a capuchin monkey than an ape."

Life Tags Along

Could martian life have come from Earth or vice versa? The transpermia hypothesis suggests that life hopped planets on debris kicked up by asteroid impacts. Now researchers are gearing up to test whether that was possible.

The Living Interplanetary Flight Experiment (LIFE), designed and sponsored by the Planetary Society in Pasadena, California, will hitch a ride on a Russian sample-return mission to Mars's moon Phobos to see whether Earth life without special protection can survive a 34-month space voyage. "We view this as a simulated meteoroid," says Bruce Betts, the society's director of projects.

The scientists will fill a hockey puck–sized capsule with 10 different organisms, including *Bacillus subtilis* bacteria and the seeds of the mouse-eared cress plant (*Arabidopsis thaliana*). The tiny disk will launch in October aboard the Russian probe, nicknamed Phobos-Grunt. Phobos-Grunt will collect rocks and dirt from Phobos and return them and the LIFE capsule to Earth in 2012. Biologists will then examine how the tiny spacefarers fared.

How Sweet It Is

People whose early ancestors lived in Europe have the keenest biological sensitivity to sweet tastes, geneticists report.

Scientists led by Alexey Fushan at the National Institute on Deafness and Other Communication Disorders (NIDCD) in Bethesda, Maryland, asked 144 people from various ethnic backgrounds to rank the sweetness of nine solutions ranging from 0% to 4% sugar. The volunteers' sucrose sensitivity turned out to be strongly associated with two variants of a gene called *TAS1R3*, which plays a major role in encoding the main carbohydrate sweet taste receptor.

Consulting a reference collection of DNA from 1050 people from around the world held by CEPH, the French gene database, the scientists found that most Europeans have both of the sweetness-sensing variants. The variants are less widespread in people from Asia and the Middle East and are least prevalent in Africans, they report in the 11 August issue of *Current Biology*.

"People who study diet and evolution have pointed out most of the high sugar–containing plants like sugarcane are tropical plants," says NIDCD geneticist Dennis Drayna, a co-author of the study. "So in northerly latitudes, you have to be more sensitive to sugar to find calories." Molecular biologist Stephen Wooding of the University of Texas Southwestern Medical Center at Dallas says the reasons for such differences among populations aren't yet clear. "One possibility is that the mutations are adaptive," he says. "Figuring out whether this is the case will require some work."

CREDITS (TOP TO BOTTOM): COURTESY OF P. DODDS AND C. DANFORTH; THE PLANETARY SOCIETY; PHOTOS.COM

Published by AAAS

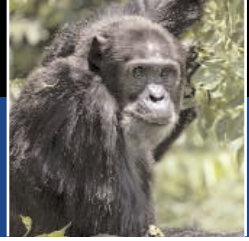

Malaria from chimps
663

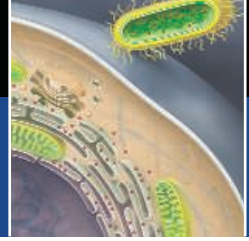

Origin of eukaryotes
666

It's back. Defying predictions, a vaccine-derived poliovirus—and an eradicated serotype to boot—has spawned a raging epidemic in Nigeria.

CREDIT: REUTERS/LANDOV

PUBLIC HEALTH

Type 2 Poliovirus Back From The Dead in Nigeria

In 1999, the Global Polio Eradication Initiative (GPEI) scored an unequivocal victory: It wiped one of three serotypes of wild poliovirus, type 2, off the face of the earth, except for samples stored in labs for study or vaccine creation. That triumph left just two foes to battle, poliovirus types 1 and 3, which have continued to put up quite a fight.

But now a version of type 2 has returned. Springing back to life from a weakened form of the pathogen used in a vaccine, poliovirus type 2 is causing a runaway outbreak in Nigeria, where types 1 and 3 are also raging. This type 2 virus had already caused 124 cases of paralysis by 26 July, up from 30 this time last year, and the case count is headed straight up, already exceeding that of the most feared type 1. "[The type 2 outbreak] is very much not under control," says Mark Pallansch, whose group does genetic analysis of poliovirus isolates at the U.S. Centers for Disease Control and Prevention (CDC) in Atlanta. In July, the World Health Organization (WHO) issued a global alert warning that type 2 poliovirus in Nigeria posed an "increasing risk of international spread."

It's a stunning setback for the initiative, now already 9 years past its original deadline for vanquishing the virus. "Type 2 is an eradicated pathogen. … No one wants to see the world reseeded" with a virus "the world got rid of 10 years ago," says Roland Sutter, who directs research at GPEI's headquarters at WHO in Geneva, Switzerland.

If type 2 was going to crop up somewhere, it's little surprise it happened in Nigeria, one of only four countries where transmission of types 1 and 3 has never been stopped. In 2008, nearly 50% of all global cases of types 1 and 3—roughly 1600—occurred in the chaotic, unstable northern part of the country, where opposition to the polio campaign continues and immunization rates are generally abysmal (*Science*, 6 February, p. 702).

The type 2 poliovirus in Nigeria is a slightly different beast than types 1 and 3, which are wild viruses that have never been quashed. Instead, it's a direct descendant of the weakened virus used to make the oral polio vaccine (OPV) that has mutated and regained its neurovirulent, dangerous state—in other words, a good virus gone bad.

Experts disagree on just how dangerous these circulating vaccine-derived polioviruses (cVDPVs) are. One school maintains that cVDPVs are wimpier than their wild counterparts, so any outbreak should be easier to control. But those analyzing the Nigerian VDPV outbreak—the largest and longest running ever observed—say it puts an end to that myth. "If there was any doubt that VDPVs pose risks, I think those doubts have essentially been dispelled," says molecular virologist Olen Kew of CDC.

Any distinction between a wild and vaccine-derived virus is "artificial," says Pallansch. "It is scientifically unacceptable to make a distinction. … This VDPV paralyzes children. It can only be stopped by immunization. Does it behave like a wild virus? Will it continue to spread indefinitely [without intervention]? Yes."

No one knew that a vaccine virus could pose such a threat, regaining not only the power to paralyze but also the ability to spread from person to person, until 2000, when CDC scientists investigating a suspicious outbreak of type 1 poliovirus in Hispaniola traced it to the use of OPV—specifically, to a single OPV dose in 1998 or 1999. That meant the vaccine-derived virus had been circulating undetected for years—and could do so in other settings as long as OPV was used.

Some program critics began immediately calling for a global switch from OPV to the inactivated polio vaccine, IPV, made from a killed virus. But GPEI officials in Geneva stuck with OPV for the eradication campaign: Not only was it cheap and easy to administer in drops, it had a proven track record at stamping out outbreaks in tropical settings. Its benefits far outweighed the risks, which could be managed, officials said. And that seemed to be the case in the handful of VDPV outbreaks detected since—until Nigeria.

The first case of vaccine-derived type 2 polio was detected in Nigeria in late 2005 (*Science*, 28 September 2007, p. 1842). It limped along in characteristic VDPV fashion for a few years, until January 2009, when it "just took off, for reasons we don't pretend to understand," says Sutter. The mutated vaccine virus could have become more transmissible, experts speculate, or, more likely, the pool of children susceptible to type 2 grew larger,

Published by AAAS

Sport: Knocks on the brain
670

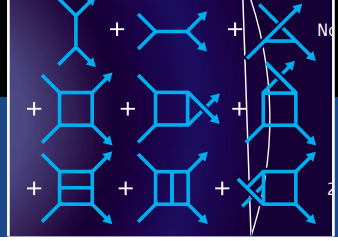

Unraveling string theory
673

providing a reservoir in which the virus could circulate.

Nigerians had been focused on fighting wild types 1 and 3, using monovalent vaccines that are more effective than trivalent OPV (tOPV) against these two serotypes. That was the right decision, says Kew, but as a result, population immunity to type 2 was low. In northern Nigeria, roughly 20% of children have never received a single dose of tOPV, which is very effective against type 2.

Despite the intensity of the outbreak, experts agree that because tOPV works so well against type 2, a couple of good rounds with that vaccine should "stop type 2 in its tracks," as Sutter says. Unfortunately, he adds, in Nigeria, "the biggest problem is whether we can reach enough kids." The country conducted one tOPV campaign in May, and another is scheduled for August. It's too soon to say how many children were immunized in May, but early signs are encouraging, says Kew. "I am still more worried about types 1 and 3," in large part because type 2 viruses tend to stay put geographically. Sutter agrees. "In Nigeria, type 2 should go first. If we can't get rid of this one, there is little hope of getting rid of the others."

Longer term, the Nigerian cVDPV outbreak is underscoring just how hard finishing the job of polio eradication will be. To prevent OPV from seeding new outbreaks, the world must stop using the vaccine, says GPEI head Bruce Aylward—when it figures out a way to do so safely. Plans are in flux, but that probably involves using a revamped IPV. With the vaccine-derived and wild-type viruses virtually indistinguishable, says Pallansch, "the job is not finished until all poliovirus is gone." **–LESLIE ROBERTS**

BIOSECURITY

Faulty Risk Analysis Puts Biofacility Plan in Jeopardy

Ever since the U.S. Department of Homeland Security (DHS) announced plans to replace the aging Plum Island Animal Disease Center with a mainland facility 4 years ago, the proposal has been attacked by environmental groups and lawmakers worried about the risk to livestock of an accidental release of deadly pathogens like the foot-and-mouth (FMD) virus. Now, as DHS prepares to build the $450 million National Bio and Agro-Defense Facility (NBAF) in Manhattan, Kansas, it has run into its stiffest challenge yet: a damning report from the Government Accountability Office (GAO) that accuses DHS of relying on a flawed risk analysis to push the project through.

Released last week, the GAO report provides ammunition not just to those who oppose NBAF on environmental grounds but also to a Texas consortium that wanted the facility. The consortium filed a lawsuit against DHS this spring alleging bias in the selection of the Kansas site. The House Energy and Commerce Subcommittee on Oversight and Investigations plans to hold a hearing this fall. "It is puzzling that DHS wants to transfer the foot-and-mouth virus from the relative isolation of Plum Island into the heart of cattle country," Representative John Dingell (D–MI), a subcommittee member, said in a press release announcing the GAO report.

The report points out a multitude of weaknesses in DHS's assessment of risk at the proposed facility. For one, the report says, the model DHS used to sketch the airborne spread of the FMD virus is suited to studying radiological dispersion, not the dispersion of viral particles. Nor did DHS model the risk of infectious spread from one farm to another, the report said.

"Our impression is DHS simply went through the motions," says Nancy Kingsbury at GAO. Based on the faulty analysis, she says, DHS concluded that all of the six sites under consideration—including Plum Island—were equally safe. So DHS focused on other selection criteria, such as community acceptance—which Kansas lawmakers, including Republican Senator Pat Roberts, played up in their lobbying efforts to win the competition (*Science*, 12 December 2008, p. 1620).

DHS officials say they used the best scientific data available and will not back down. "We intend to place the lab [in Kansas]," DHS Secretary Janet Napolitano told the Associated Press last week.

FMD experts contacted by *Science* say they generally agree with GAO's criticisms. If DHS "did not consider the network of direct and indirect contacts in the region that would be responsible for the spread of the disease," it is hard to put a lot of confidence in the agency's conclusions about the risks, says veterinarian Andres Perez of the University of California, Davis.

Barred. To some, a 2007 foot-and-mouth outbreak in the United Kingdom shows the wisdom of keeping FMD research off the mainland.

Matt Keeling, an FMD expert at the University of Warwick in the United Kingdom, thinks the GAO report may have underestimated problems with DHS's analysis, such as its failure to consider water-borne contamination of the environment. "I'd be worried about what we had in the U.K.," he says, referring to the 2007 FMD outbreak in Surrey caused by a leak of virus-laden water from the Pirbright animal facility (*Science*, 14 September 2007, p. 1486)

That's why some scientists favor keeping research on FMD and other animal diseases off the mainland. If an incident like the Pirbright leak were to happen "in Kansas and in Plum Island, which of those two releases would result in the largest number of outbreaks?" asks Perez, adding that common sense, not models, should dictate the answer. **–YUDHIJIT BHATTACHARJEE**

CREDIT: AFP/GETTY IMAGES/NEWSCOM

SWINE FLU OUTBREAK

Worries About Africa as Pandemic Marches On

In July 2002, more than 70% of the 2160 inhabitants of Sahafata, a small village in the rural highlands of southeastern Madagascar, came down with an acute respiratory illness, and 27 died. A few patient samples tested positive for influenza, but the viciousness of the outbreak led health authorities to suspect something worse and ask for assistance. In August, researchers from Atlanta, Paris, and Geneva, Switzerland, descended on the region.

They confirmed that the outbreak was caused by H3N2, one of the three influenza strains that circle the globe every year. Although there was nothing special about the Madagascar strain, a series of local factors—from an unusually cold winter to civil unrest and a poor health infrastructure—conspired to make the outbreak more intensive and lethal than usual, they hypothesized.

That episode—and a similar one in the Democratic Republic of the Congo (DRC) in 2003—showed just how little researchers know about flu's patterns of spread and severity in Africa, says Jean-Claude Manuguerra of the Pasteur Institute in Paris, who helped investigate the outbreak. And it suggests that, with its myriad of problems, Africa—especially south of the Sahara—might be harder hit by the 2009 H1N1 pandemic virus than any other continent. The virus has been detected in 19 African countries so far.

With HIV/AIDS, TB, malaria, and a host of other diseases competing for attention, influenza has never been high on most African countries' priority lists. Whether that is justified is not clear, says World Health Organization (WHO) flu scientist Keiji Fukuda, because nobody knows how much of the massive total burden of respiratory infections in Africa is due to flu.

Getting a handle on the spread of influenza viruses in Africa has long been problematic because laboratories and surveillance have been lacking. A 2002 survey by Barry Schoub and colleagues at South Africa's National Institute of Virology showed that only a handful of countries in sub-Saharan Africa had labs able to isolate and characterize influenza viruses. That has begun to change rapidly in the past few years, due mostly to the threat of H5N1 avian influenza, which has surfaced in 11 African countries. At so-called pledging conferences in 2006 and 2007 in Beijing, Bamako, and New Delhi, donors offered billions to fight avian influenza and promote pandemic preparedness in the developing world. Agencies such as the U.S. Centers for Disease Control and Prevention (CDC), the U.S. military, the Pasteur Institute, and WHO have begun providing African labs with training and equipment.

Today, 13 countries have a National Influenza Center accredited by WHO (see map); at least seven more have labs capable of testing for the pandemic virus. WHO wants to see the network expand further, says Fukuda. The new labs have already proven their worth in the current pandemic, says Mark Katz, head of the CDC-Kenya lab: Ethiopia and Tanzania, for instance, were able to identify their first cases themselves.

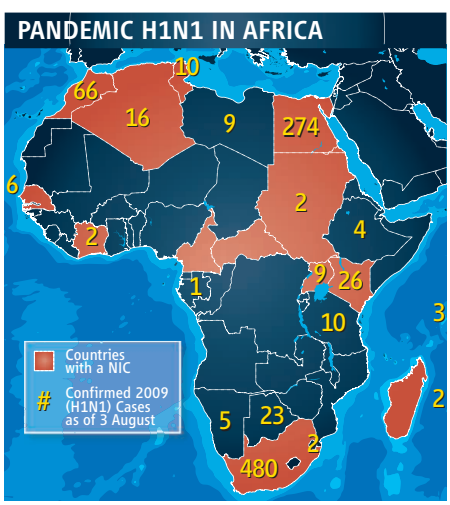

Test case. Lab scientist Sylvia Omolo at work at the CDC-Kenya lab in Nairobi. Only 13 countries in Africa have a WHO-accredited National Influenza Center (NIC).

Surveillance is also expanding. Lately, Rwanda, Kenya, Tanzania, Uganda, Zambia, and the DRC have joined a list of countries that have set up so-called sentinel flu surveillance systems, Katz says, in which doctors from selected sites send in samples from patients with flulike symptoms for testing. With that, "we should be able to pick up outbreaks of the novel H1N1 and document its spread," he adds.

Still, most countries have no lab capacity whatsoever, and surveillance systems cover only a tiny fraction of Africa's massive geography. "We really won't have a good idea what's happening," says Schoub, who is now executive director of the National Institute for Communicable Diseases in Johannesburg, South Africa. The absence of reported H1N1 cases in most African countries indicates that in most places, there's simply nobody looking.

Experts fear that the high HIV infection rates in many African countries could worsen the pandemic's impact. Although data are limited, studies in Western countries have suggested that HIV-infected seasonal flu patients are at higher risk of severe disease and death than those without HIV; South African studies have shown that they are also more likely to have secondary infections such as bacterial pneumonia, says Schoub.

Meanwhile, African health systems' capacity to cope with the pandemic is limited. Again, Madagascar's H3N2 outbreak offered a preview of problems that may play out across the continent. Patients were hard to reach, antibiotics to treat secondary infections were in short supply, intensive care units were nonexistent, and general awareness about influenza was minimal. An analysis of 35 African countries' national preparedness plans, published last year by Richard Coker and colleagues at the London School of Hygiene and Tropical Medicine, showed that preparation was wanting as well. Most plans were detailed when it came to detecting flu in animals but not on coping with a human pandemic. Operational details were scant, and some plans—such as Madagascar's seven pages—were rudimentary.

Vaccines could make a difference—in theory, at least. But setting up vaccination programs would be a massive logistical challenge, and besides, it's unclear whether developing nations will have much access to vaccines, despite efforts by WHO Director-General Margaret Chan. Manufacturers have reported disappointing yields, and most of their output is spoken for through deals with rich countries.

Add all of that up, and it seems inevitable that the death toll in Africa will be higher than elsewhere, says Manuguerra—but the patchy reporting and the difficulty of doing epidemiology suggest that we'll never know how much higher exactly. "We'll have some data on some spots here and there," says Manuguerra, "but we won't have the entire picture."

–MARTIN ENSERINK

CREDITS (TOP TO BOTTOM): CAROLYN BAER; WHO

Published by AAAS

PARASITOLOGY

Key Malaria Parasite Likely Evolved From Chimp Version

For centuries, the origin of the main parasite that causes malaria in humans has remained murkier than the stagnant water loved by the mosquitoes that transmit the killer pathogen. Now an international research team has uncovered compelling evidence that the parasite, *Plasmodium falciparum*, evolved from a relative called *P. reichenowi* that infects chimpanzees. The data support a provocative theory that as human red blood cells evolved a way to dodge *P. reichenowi*, they became highly vulnerable to *P. falciparum*.

CREDIT: MALCOLM LINTON

Descent of malaria. *P. reichenowi* from chimpanzees preceded the main human parasite.

Much debate has surrounded the relationship of *P. falciparum* to *P. reichenowi*, in part because for decades, scientists had only one isolate of the chimp parasite. But working with collaborators in Africa, a team led by Nathan Wolfe of Stanford University in Palo Alto, California, and Stephen Rich of the University of Massachusetts, Amherst, identified eight new isolates of *P. reichenowi* by examining tissue samples from 10 wild chimpanzees that had died in Côte d'Ivoire and blood from 84 captive chimps living in sanctuaries in Cameroon. A comparison of genes from all nine *P. reichenowi* isolates and 133 strains of *P. falciparum* showed that the chimp parasite has much more genetic diversity, indicating that *P. reichenowi* is older, the research team reports online 3 August in the *Proceedings of the National Academy of Sciences*. "It's the answer to a substantive mystery," says Wolfe, a virologist who runs Stanford's Global Viral Forecasting Initiative. Malaria is "one of the oldest diseases in humanity, and it's amazing to us that it took this long to nail down where it came from."

A phylogenetic analysis also shows that the two parasites are on the same branch of the *Plasmodium* family tree. "This is a huge step forward and places *P. falciparum* clearly in a cluster of chimp parasite species," says parasitologist Julian Rayner of the Wellcome Trust Sanger Institute in Hinxton, U.K.

In 1920, German researcher Eduard Reichenow claimed to have found *P. falciparum*—which in people causes what researchers call "malignant malaria"—in chimpanzees. But attempts to infect chimps with lab isolates failed, which led two British researchers, Donald Blacklock and Saul Adler, to inject themselves a few years later with blood taken from a *Plasmodium*-infected chimpanzee. Neither of them became ill, and they concluded that chimps had a different parasite, which they named *reichenowi*.

In the 1990s, Francisco Ayala, a co-author of the new paper and the former Ph.D. adviser of Rich, revived interest in the long-ignored chimp parasite. Not persuaded by a study that linked the human parasite's evolution to a *Plasmodium* found in birds, Ayala noticed that the analysis had ignored *P. reichenowi*. Three years later, his lab showed that it was actually the closest relative of the human parasite. But Ayala could not determine whether the two pathogens evolved from a common ancestor or if one came from the other—or when the split occurred.

The new study answers the first issue but leaves unsettled when *P. falciparum* appeared in humans. Its debut may be linked to a change in human red blood cells 2 million to 3 million years ago. In 2005, Rayner, working with a group led by Ajit Varki and Pascal Gagneux at the University of California, San Diego, School of Medicine, reported that a genetic mutation protects people from *P. reichenowi* and makes them more susceptible to *P. falciparum*. The mutation altered the surface of red blood cells, changing a sugar that *P. reichenowi* binds to during the infection process. As a result, a new sugar adorned human red blood cells that *P. falciparum* favors. "We escaped malaria from *P. reichenowi*, but we paid a price," says Gagneux.

Varki now suggests that the chimp parasite might work as a vaccine against *P. falciparum*, much in the way that cowpox immunizes against smallpox. Any way you go about it, researchers clearly have a bevy of new *P. reichenowi* isolates to examine. For malaria researchers, says Wolfe, "it's like the solar system is suddenly filled with planets that we never knew about." **–JON COHEN**

ScienceNOW.org

From *Science*'s Online Daily News Site

Gorilla Virus in Our Midst
Researchers are shaking up the HIV family tree again. For the first time, investigators have found what looks like a gorilla version of the AIDS virus in a person. They do not know how the woman became infected but suspect that other humans harbor a similar virus. The possibility that gorillas can transmit the virus to humans further underscores the danger of butchering the apes or keeping them as pets, which still occurs in some African communities. http://bit.ly/Io0Q7

Dinosaur Study Backs Controversial Find
When scientists reported 2 years ago that they had discovered intact protein fragments from a 68-million-year-old *Tyrannosaurus rex*, the skeptics pounced. They argued that one of the main lines of evidence, signatures of the protein fragments taken by mass spectrometry, was flawed. But now a reanalysis of that mass-spec data from an independent group of researchers backs up the original claim that dinosaur proteins have indeed survived the assault of time. http://bit.ly/q16Jn

Undoing the Damage of Glaucoma
In people suffering from glaucoma, damage to the optic nerve can slowly degrade peripheral vision and, in the worst cases, eventually lead to blindness. But eye drops containing nerve growth factor—a protein that promotes the survival and growth of neurons in the developing brain—appear to have prevented nerve damage in rats and restored some vision in three human glaucoma patients, the authors of a new study claim. Not everyone thinks the reported effect is real, however. http://bit.ly/JSxjm

Researchers Grow New Teeth in Mice
If you've lost a tooth to decay or injury, you may not have to rely on that dental bridge or implant forever. Japanese scientists have found a way to bioengineer new adult teeth. So far, the method works only in mice, but experts say it may one day take hold in humans. http://bit.ly/1186kX

Read the full postings, comments, and more on **sciencenow.sciencemag.org**.

Published by AAAS

SCIENCE AND COMMERCE

Systematics Researchers Want to Fend Off Patents

When an e-mail last week alerted David Hillis to U.S. Patent Application 20090030925, he thought it was a joke. A graduate student had stumbled across the 2-year-old application while looking for phylogenetics material on the Web. It seemed to be claiming the invention of techniques that Hillis, an evolutionary biologist at the University of Texas, Austin, has been using for years to discern how organisms were related to one another through evolutionary time, based on similarities in genetic sequence. "I had a hard time believing [the claim] was true at first," Hillis recalls. It sounded "like *The Onion* article about Microsoft trying to patent 1's and 0's."

But this Microsoft application is for real, and as word about it spreads, the phylogenetics community is increasingly worried. They think the patent is unlikely to pass muster at the U.S. Patent and Trademark Office because it seems obvious. However, should the application be approved, some researchers may find that they are doing work that infringes it. "It's frankly terrifying," says entomologist David Maddison of the University of Arizona, Tucson. "As patents enter this field, there is a very great danger that we will get bogged down in a legal morass."

Patenting basic research tools generally goes against the grain of systematists and evolutionary biologists, who are accustomed to sharing methods freely. Yet those innocent days may be waning. Just last month, a proposed patent for a DNA bar code threatened to derail a carefully crafted agreement about short DNA sequences to discriminate plant species (*Science*, 31 July, p. 526). "I suspect phylogenetics has simply been under the radar compared to things of interest to dot-coms, venture capitalists, and the tech industry," says Tamara Munzner, a computer scientist at the University of British Columbia in Vancouver, Canada. "I am concerned that this [Microsoft] application marks the beginning of the end for that state of grace."

Patent 20090030925 was filed by Microsoft researcher Stuart Ozer, an expert in databases, in July 2007. Ozer says he wanted to apply database technologies to complex problems in biological sciences: "I saw an opportunity to create a new approach in analyzing sequence data when phylogenetic information was available," he says.

The patent application describes a way to use biological data that has been organized according to evolutionary relatedness. It includes methods for counting evolutionary events and grouping positions within molecules. However, "this patent is written in such broad language that it appears to swallow up any activity that involves understanding biodiversity through phylogenetics," says William Piel, a phylogeneticist at Yale University. He points out that such analyses date back to Charles Darwin, who sketched the first evolutionary tree; today, more than 350 phylogeny software packages are available on the Web. "Microsoft might as well patent the multiplication tables," Piel says.

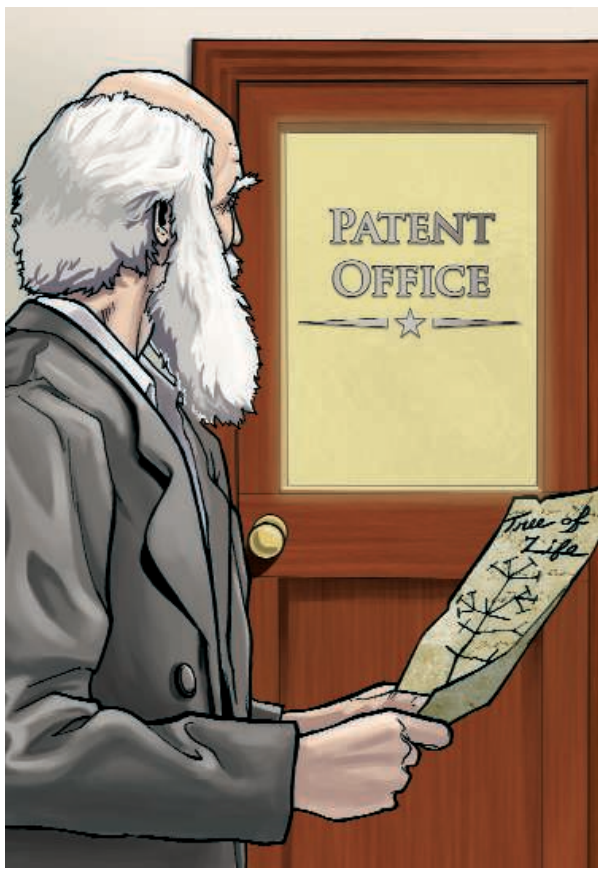

Ozer stresses that his patent does not apply to creating phylogenies or determining evolutionary trees, only to a technique for making further use of the variation seen among sequences used in such an analysis. "It is a novel approach applying specific mathematical methods to existing, phylogenetically annotated data to draw conclusions about relationships within a molecule," Ozer explains.

Several of the patents related to phylogenetics that have cropped up before now have met stiff resistance. In the mid-1990s, Willie Davidson, a molecular biologist at Simon Fraser University in Burnaby, Canada, caused a fuss when he and his colleague sought to patent the use of a piece of mitochondrial DNA to identify unknown specimens by comparing that specimen's DNA sequence with a database of DNA of known organisms. The pending patent was licensed to a French company called Atlangene, which challenged the right of the CSL Food Science Laboratory in Aberdeen, U.K., to use that approach to identify tuna species. The laboratory's scientists appealed to the systematics community for support. A senior researcher at the Natural History Museum in London, with backing from the U.K. government, challenged the patent application, which Davidson subsequently withdrew, he says.

Three times, the Barcode of Life project has grappled with patent applications. The latest involved Vincent Savolainen of the Royal Botanic Gardens, Kew, in Richmond, U.K., and colleagues. Savolainen had been a member of an independent committee of plant scientists trying to decide which pieces of DNA would work best for bar-coding plants. Not until the committee was on the verge of publishing its plan did the rest of the committee discover that Savolainen and a few colleagues had filed a patent application to cover the use of one of the pieces of DNA selected. When the Consortium for the Barcode of Life heard about the pending patent, "we were immediate and emphatic about asking [Savolainen] to withdraw the application," says consortium executive secretary David Schindel. Savolainen and his colleagues complied.

The interpretation—and fate—of Ozer's Microsoft patent is still undecided. But Hillis, Munzner, and others are keeping close watch on these and other patent developments. Says Schindel, "It's a constant threat requiring constant vigilance."

–ELIZABETH PENNISI

CREDIT: M. TWOMBLY/*SCIENCE*

INTELLECTUAL PROPERTY

Drug Metabolite Patents Prompt Legal Battle

U.S. medical groups are lining up this week against a biotech company in a rare federal court battle over whether a specific drug test can be patented. One side says the patents apply to aspects of the human metabolism that should not become private property. The other side says such patents are vital to foster further medical advances. The outcome is likely to affect an ongoing debate over patenting natural phenomena, a theme already before the U.S. Supreme Court (*Science*, 12 June, p. 1374).

On 5 August, the U.S. Court of Appeals for the Federal Circuit in Washington, D.C., heard oral arguments in a case that pits Prometheus Laboratories in San Diego, California, against the Mayo Clinic in Rochester, Minnesota. Prometheus runs a testing service that monitors responses to the drug azathioprine, which is used to treat autoimmune disorders. The Mayo Clinic wants to do the same kind of testing but doesn't have a relevant patent.

The American Medical Association and the American College of Medical Genetics have sided with Mayo, arguing that Prometheus's patents are based on mere observations of nature and seek ownership of a common metabolic response. Such "observational patents," according to Mayo, add to health-care costs and complicate research.

Prometheus and its allies respond that not only are the patents valid, but also that denying them could stifle innovation. The Biotechnology Industry Organization in Washington, D.C., warns in an *amicus* brief that voiding the patents could mean "promising innovative products that could benefit patients and consumers would be developed abroad, or not at all." The American Intellectual Property Law Association also supports Prometheus's position.

The issue arose 5 years ago after Mayo and its profitmaking subsidiary, Mayo Medical Laboratories (MML), proposed to do azathioprine metabolite testing. Doing the test itself would be faster and give doctors more options than sending samples to Prometheus, administrators decided. "We were not aware of Prometheus's intellectual-property claims," says MML Chief Administrative Officer David Herbert. Prometheus sued in U.S. court, asking Mayo to stop work. Mayo complied. But "we decided to take a stand," says Herbert. Mayo argued that the patents were invalid, and in 2008, the court agreed with Mayo. Prometheus appealed, leading to this week's hearing. Herbert says the legal fight has already cost Mayo more than it would have earned from selling its own test.

At issue is a procedure for adjusting the dose of azathioprine, an anti-inflammatory drug used to treat Crohn's disease and other autoimmune disorders. The drug has a narrow window of efficacy. Too little gives no benefit, but too much can be toxic to the liver or, in rare cases, suppress the bone marrow and cause death. The response is driven particularly by thiopurine methyltransferase (TPMT) enzymes, which are produced by a gene that may be present in a single copy, two copies, or none. People without the gene are most at risk.

It's possible to test patients for the TPMT gene, but Mayo doctors say it's often necessary to watch blood levels of azathioprine metabolites because TPMT isn't the only enzyme involved. The Prometheus patents (issued in 2002 and 2004) cover a simple procedure for adjusting the drug dose according to safe azathioprine metabolite levels seen in previous patients.

Although its critics say this approach is obvious, Prometheus defends the test's originality. After hearing arguments this week, the appellate judges may wait to act until the Supreme Court has ruled on a related case.

–ELIOT MARSHALL

CREDIT: NEWSCOM

Taking a stand. Mayo Clinic decided to fight patents on an azathioprine metabolite test controlled by Prometheus Laboratories, arguing that they apply to natural phenomena.

ScienceInsider

From the *Science* Policy Blog

The United States should begin **vaccinating its citizens this fall against the H1N1 influenza virus**, says an expert panel that guides the Department of Health and Human Services (HHS). The Advisory Committee on Immunization Practices proposed rationing the limited supplies of vaccine among high-priority groups representing roughly half the country's population. At the top of the list are people with underlying conditions that put them at risk for severe disease, pregnant women, those from 6 months to 24 years old, anyone who lives with infants under 6 months old, health-care workers, and emergency personnel. HHS hopes to have enough doses of the vaccine by October for everyone in these groups.

A mistake in handling manuscripts—not deliberate copying—led to an embarrassing use of borrowed text in a recent paper on the use of human embryonic stem cells, claims one of the authors, Karim Nayernia of Newcastle University in the United Kingdom. The journal's editor withdrew it after receiving an allegation of plagiarism, but Nayernia says the error occurred when a postdoc accidentally submitted the wrong draft for online publication.

A Senate appropriations panel has matched President Barack Obama's constrained **funding request for the National Institutes of Health** in 2010. The $442 million boost to $31.8 billion is less than half of the increase the House of Representatives approved last week. Legislators won't make a final decision on the spending bill until fall at the earliest.

In other news, epidemiologist **David Michaels**, known for studying nuclear workers' health risks, has been chosen to run the U.S. Occupational Safety and Health Administration, pending Senate confirmation. Meanwhile, **David Besser**, the former acting director of the Centers for Disease Control and Prevention, is moving to ABC News.

For more science policy news, go to **blogs.sciencemag.org/scienceinsider/**.

Published by AAAS

On the Origin of Eukaryotes

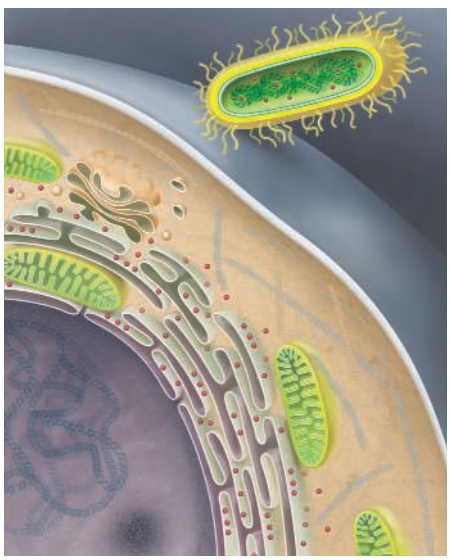

YOU MAY NOT FEEL AS THOUGH YOU HAVE much in common with a toadstool, but its cells and ours are strikingly similar. Animals and fungi both keep their DNA coiled up in a nucleus. Their genes are interspersed with chunks of DNA that cells have to edit out to make proteins. Those proteins are shuttled through a maze of membranes before they can float out into the cell. A cell in a toadstool, like your own cells, manufactures fuel in compartments called mitochondria. Both species' cells contain the same molecular skeleton, which they can break down and reassemble in order to crawl.

This same kind of cell is found in plants and algae; single-celled protozoans have the same layout as well. Other microbes, such as the gut bacterium *Escherichia coli*, lack it. All species with our arrangement are known as eukaryotes. The word is Greek for "true kernel," referring to the nucleus. All other living things that lack a nucleus, mitochondria, and the eukaryote LEGO-like skeleton are known as prokaryotes. "It's the deepest divide in the living world," says William Martin of the University of Düsseldorf in Germany.

The evolution of the eukaryote cell is one of the most important transitions in the history of life. "Without the origin of eukaryotes, we wouldn't be here to discuss the question," says T. Martin Embley of Newcastle University in the United Kingdom. Along with animals, eukaryotes gave rise to every other multicellular form of life. Indeed, when you look at the natural world, most of what you see are these "true kernel" organisms.

The fossil record doesn't tell us much about their origin. Paleontologists have found fossils of prokaryotes dating back 3.45 billion years. The earliest fossils that have been proposed to be eukaryotes—based on their larger size and eukaryotelike features on their surfaces—are only about 2 billion years old. Paleontologists have not yet discovered any transitional forms in the intervening 1.45 billion years, as they have for other groups, such as birds or whales. "One gets a bit of fossil envy," says Anthony Poole of Stockholm University. Fortunately, living eukaryotes and prokaryotes still retain some clues to the transition, both in their cell biology and in their genomes.

By studying both, researchers have made tremendous advances in the past 20 years in understanding how eukaryotes first emerged. A key step in their evolution, for example, was the acquisition of bacterial passengers, which eventually became the mitochondria of eukaryote cells. But some scientists now argue that the genes of these bacteria also helped give rise to other important features of the eukaryote cell, including the nucleus. "It's been a really cool journey," says Embley.

Unexpected ancestry

Scientists first divided life into prokaryotes and eukaryotes in the mid-1900s, using increasingly powerful microscopes to see the fine details of cells. But they couldn't say much about how prokaryotes and eukaryotes were related. Did the two groups branch off from a common ancestor? Or did eukaryotes evolve from a particular lineage of prokaryotes long after the evolution of the first prokaryotes?

An important step toward an answer to these questions was taken in the 1970s. Carl Woese of the University of Illinois, Urbana-Champaign, and his colleagues compared versions of an RNA molecule called 16*S* rRNA in a wide range of prokaryotes and eukaryotes. They reasoned that species with similar sequences were closely related and used that reasoning to draw a tree of life. Eukaryotes were all more closely related to one another than any were to prokaryotes, they found, which suggests that eukaryotes all belong to a single lineage and that the eukaryote cell evolved only once in the history of life.

But Woese and his colleagues got a surprise when they looked at the prokaryotes. The prokaryotes formed two major branches in their analysis. One branch included familiar bacteria such as *E. coli*. The other branch included a motley crew of obscure microbes—methane-producing organisms that can survive on hydrogen in oxygen-free swamps, for example, and others that live in boiling water around deep-sea hydrothermal vents. Woese and his colleagues argued that there were three major groups of living things: eukaryotes, bacteria, and a group they dubbed archaea. And most surprising of all, Woese and his colleagues found that archaea were more closely related to eukaryotes than they were to bacteria.

Although archaea and bacteria may seem indistinguishable to the nonexpert, Woese's discovery prompted microbiologists to take a closer look. They found some important differences, such as in the kinds of molecules archaea and bacteria use to build their outer membranes. A number of scientists began to study archaea to get some clues to the origins of their close relatives, the eukaryotes.

Many scientists assumed that after the ancestors of eukaryotes and archaea split apart, eukaryotes evolved all of their unique traits through the familiar process of small mutations accumulating through natural selection. But Lynn Margulis, a microbiologist now at the University of Massachusetts, Amherst, argued that a number of parts of the eukaryote cell were acquired in a radically different way: by the fusion of separate species.

Reviving an idea first championed in the early 1900s, Margulis pointed to many traits that mitochondria share with bacteria. Both are surrounded by a pair of membranes, for example. Mitochondria and some bacteria can also use oxygen to generate fuel, in the form of adenosine triphosphate (ATP) molecules. And mitochondria

THE YEAR OF DARWIN

This essay is the eighth in a monthly series. For more on evolutionary topics online, see the Origins blog at **blogs.sciencemag.org/origins**. For more on eukaryotes, listen to a podcast by author Carl Zimmer at **www.sciencemag.org/multimedia/podcast.**

CREDITS (TOP TO BOTTOM): KATHARINE SUTLIFF/*SCIENCE*; WIKIPEDIA/GEORGE RICHMOND, FROM ORIGINS, RICHARD LEAKEY AND ROBERT LEWIN

Published by AAAS

have their own DNA, which they duplicate when they divide into new mitochondria. Margulis argued that mitochondria arose after bacteria entered host cells and, instead of being degraded, became so-called endosymbionts.

Many studies have bolstered this once-controversial hypothesis. The genes in mitochondria closely resemble genes in bacteria, not those in any eukaryote. In fact, a number of mitochondrial genes point to the same lineage of bacteria, part of the alpha proteobacteria.

> "As soon as you've got one prokaryote inside another prokaryote, you've completely transformed the cell and what it can do."
>
> —Nick Lane, University College London

Additional evidence for the endosymbiont hypothesis comes from the genes in the eukaryote nucleus. Some of the proteins that carry out reactions in mitochondria are encoded in nuclear DNA. When scientists have searched for the closest relatives of these genes, they find them among bacterial genes, not eukaryote genes. It seems that after the ancestors of mitochondria entered the ancestors of today's eukaryotes, some of their genes got moved into the eukaryote's genome.

Mitochondria everywhere

Although most eukaryotes have mitochondria, a few don't—or so it once seemed. In 1983, Thomas Cavalier-Smith of the University of Oxford in the United Kingdom proposed that these eukaryotes branched off before bacteria entered the eukaryote cell and became mitochondria. According to his so-called archezoa hypothesis, mitochondria first evolved only after eukaryotes had already evolved a nucleus, a cellular skeleton, and many other distinctively eukaryotic features.

But a closer look at mitochondria-free eukaryotes raised doubts about the archezoa hypothesis. In the 1970s, Miklós Müller of the Rockefeller University in New York City and his colleagues discovered that some protozoans and fungi make ATP without mitochondria using structures called hydrogenosomes. (They named it for the hydrogen it produces as waste.) In 1995, scientists discovered mitochondrialike genes in eukaryotes that only had hydrogenosomes. Further research has now confirmed that hydrogenosomes and mitochondria descend from the same endosymbiont.

By 1998, Müller and Martin of the University of Düsseldorf were arguing that it was time to throw out the archezoa hypothesis. They maintained that the common ancestor of all living eukaryotes already carried an endosymbiont. They predicted that further study would reveal mitochondrialike structures in eukaryotes that seemed to be missing mitochondria at the time.

Based on the biochemistry of mitochondria and hydrogenosomes, Martin and Müller sketched out a scenario for how the original merging of two cells occurred. They pointed out that it is very common for bacteria and archaea to depend on each other, with one species producing waste that another species can use as food. "That sort of stuff is all over the bottom of the ocean," says Martin. Martin and Müller proposed that mitochondria descend from bacteria that fed on organic carbon and released hydrogen atoms. Their partner was an archaea that used the hydrogen to make ATP, as many archaea do today. Over time, the archaea engulfed the bacteria and evolved the ability to feed their newly acquired endosymbionts organic carbon.

In the 11 years since Martin and Müller proposed their "hydrogen hypothesis," scientists have come to agree that the common ancestor of living eukaryotes had an endosymbiont. "It is certain," says Eugene Koonin of the National Center for Biotechnology Information in Bethesda, Maryland.

One by one, exceptions have fallen away. Along with making ATP, mitochondria also make clusters of iron and sulfur atoms. While studying *Giardia*, a "mitochondria-free" eukaryote, Jorge Tovar of Royal Holloway, University of London, and his colleagues discovered proteins very similar to the proteins that build iron-sulfur clusters in mitochondria. The scientists manipulated the proteins so that they would light up inside *Giardia*. It turned out that the proteins all clumped together in a tiny sac that had, until then, gone unnoticed. In 2003, Tovar and his colleagues dubbed this sac a

Eukaryotes all! Tarsiers (*left*), toadstools (*top right*), and diatoms (*lower right*) are all made up of complex cells.

CREDITS (TOP TO BOTTOM): BUGWOOD NETWORK/FORESTRY IMAGES/TOLWEB.ORG; TARSIER SANCTUARY, CORELLA, BOHOL/TOLWEB.ORG; NOAA

Published by AAAS

mitosome. Scientists now agree that mitosomes are vestigial mitochondria.

Mosaic genomes

In 1984, James Lake of the University of California, Los Angeles, and his colleagues challenged Woese's three-domain view of life. Lake and his colleagues took a close look at ribosomes, the protein-building factories found in all living things. They classified species based on the distinctive lobes and gaps in their ribosomes. Based on this analysis, Lake and his colleagues found that eukaryotes do not form a distinct group on their own. Instead, they share a close ancestry with some lineages of archaea and not others. In effect, they found that there are only two major branches of life—bacteria and archaea. Eukaryotes are just a peculiar kind of archaea. Lake dubbed the archaeal ancestors of eukaryotes eocytes (dawn cells).

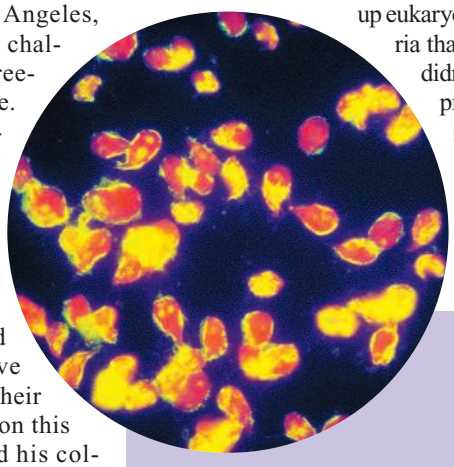

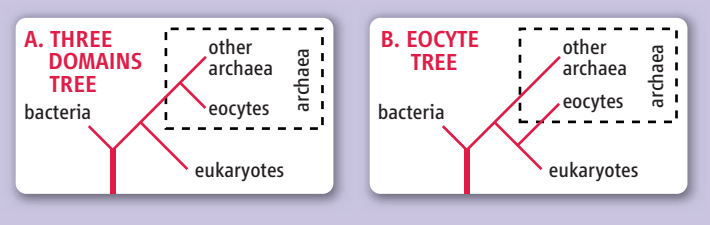

Unsettled origins. The two trees depict different views on the ancestry of eukaryotes, which include *Giardia* (*inset*), once thought to lack mitochondria.

Since then, a number of scientists have tried to choose among the three-domain hypothesis, the eocyte hypothesis, and several others. They've analyzed more genes in more species, using more sophisticated statistical methods. In the 12 August issue of the *Philosophical Transactions of the Royal Society*, Embley and his colleagues present the latest of these studies, comparing 41 proteins in 35 species. "It is the eocyte tree that is favoured and not the three-domains tree," they concluded.

Embley and his colleagues selected proteins that preserved the clearest signal of the deep ancestry of life. They have been carried down faithfully from ancestor to descendant for billions of years. But eukaryote genomes also include genes that have been imported from other species through a process called horizontal gene transfer. About 75% of all eukaryote genes are more closely related to genes found in bacteria than ones in archaea.

Scientists have tried to make sense of this genetic mélange by cataloging the kinds of jobs archaeal and bacterial genes do in our cells. Archaeal genes tend to be involved in information processing. Bacterial genes tend to be associated with metabolism and the structure of our cells. But the line is not always easy to draw between archaeal and bacterial genes. Koonin and his colleagues have found that the proteins that make up the walls of the nucleus are made up of both archaeal and bacterial genes.

One possible explanation for the mixed-up eukaryote genome is that the bacteria that gave rise to mitochondria didn't just shrivel up into ATP-producing factories. Instead, many of their genes were transferred to the nucleus of their archaeal host. Those genes then helped produce the eukaryote membranes, nucleus, and metabolism. Most of our genes, in other words, were transferred from an endosymbiont.

Having a second genome in such close quarters, Koonin and Martin have argued, may have posed a hazard to the survival of early eukaryotes. Along with protein-coding genes and other useful pieces of DNA, the genomes of many species also carry viruslike stretches of genetic material called mobile elements. Mobile elements can, on rare occasion, jump from one host genome to another. And once in their new host genome, they can make copies of themselves that are reinserted back in the genome. As mobile elements bombard a genome, they can disrupt the proper working of its genes.

Koonin and Martin suspect that with an endosymbiont in their midst, early eukaryotes would have been particularly vulnerable to attacks from mobile elements. They propose that the nucleus—the structure that gives eukaryotes their name—evolved as a defense against this attack. After mobile elements are transcribed into single-stranded RNA, they are copied back into the genome. With the invention of a nucleus, RNA molecules were moved across a barrier out of the nucleus in order to be translated into proteins. That wall reduced the chances of mobile elements being reinserted back into the genome.

Despite all the new insights into the origin of eukaryotes, scientists are far from agreed on all the details. In the July issue of *Bioessays*, for example, Yaacov Davidov and Edouard Jurkevitch of the Hebrew University of Jerusalem propose that the ancestors of mitochondria were not mutualists with archaea but predators that pushed their way into other prokaryotes and devoured them. Instead of killing their prey, Davidov and Jurkevitch argue, some predators took up residence there.

Scientists are also still debating how many bacterial genes eukaryotes got from the original endosymbiont. Prokaryotes sometimes pass DNA between distantly related species with the result that their genomes have become mosaics of genes. It's possible, some researchers argue, that many genes were transferred this way into the eukaryote genome from a variety of bacteria.

Testing these ideas will demand a better knowledge of the diversity of both prokaryotes and eukaryotes. It may also require new methods for reconstructing events that happened 2 billion years ago. "These are some of the hardest problems in biology," says Embley.

Whatever the exact series of events turns out to be, eukaryotes triggered a biological revolution. Prokaryotes can generate energy only by pumping charged atoms across their membranes. That constraint helps limit their size. As prokaryotes grow in size, their volume increases much faster than their surface area. They end up with too little energy to power their cells. Eukaryotes, on the other hand, can pack hundreds of energy-generating mitochondria into a single cell. And so they could get big, evolving into an entirely new ecological niche. "You don't have to compete for the same nutrients," says Nick Lane of University College London, author of *Life Ascending: The Ten Great Inventions of Evolution*. "You simply eat the opposition."

The eukaryote also opened the way to more complex species. Single-celled eukaryotes could evolve into multicellular animals, plants, and fungi. Individual cells in those organisms could evolve into specialized forms, such as muscles and neurons. "As soon as you've got one prokaryote inside another prokaryote," says Lane, "you've completely transformed the cell and what it can do."

–CARL ZIMMER

Carl Zimmer is the author of *Microcosm: E. coli and the New Science of Life*.

CREDITS (TOP TO BOTTOM): CDC/VISVESVARA; J. NEWFIELD/*SCIENCE*

Published by AAAS

NEWSMAKER INTERVIEW

Space Telescope's Chief Scientist Recalls How Hubble Was Saved

As he prepares to retire, David Leckrone reflects on the rescue effort that kept the observatory in orbit and on the prospects for humans in space

One day in October 2008, David Leckrone's cell phone rang shortly before he was to board a flight from Baltimore, Maryland, to Houston, Texas, to watch the launch of a long-awaited final mission to refurbish the Hubble Space Telescope. It was a call to inform the Hubble chief scientist that the 18-year-old telescope's computer had developed a snag, which meant the mission would have to be postponed. For Leckrone, the delay marked yet another heart-stopping moment on a roller-coaster ride that began with former NASA Administrator Sean O'Keefe's 2004 decision to cancel the final servicing mission.

O'Keefe's decision was reversed, and the mission launched successfully on 11 May 2009. The seven astronauts on board completed all the planned improvements and repairs: swapping out the Wide Field and Planetary Camera 2 for the more advanced Wide Field Camera 3, installing a new computer and the new Cosmic Origins Spectrograph, replacing gyroscopes and batteries, and fixing the Advanced Camera for Surveys (ACS), which had lost two of its three channels in 2006. Leckrone, who will retire this October after 17 years in the job, told *Science* last week that he expects all of Hubble's instruments to be doing science by early fall. He also shared some of the drama from the days leading up to—and during—the mission. His answers have been edited for brevity. **–YUDHIJIT BHATTACHARJEE**

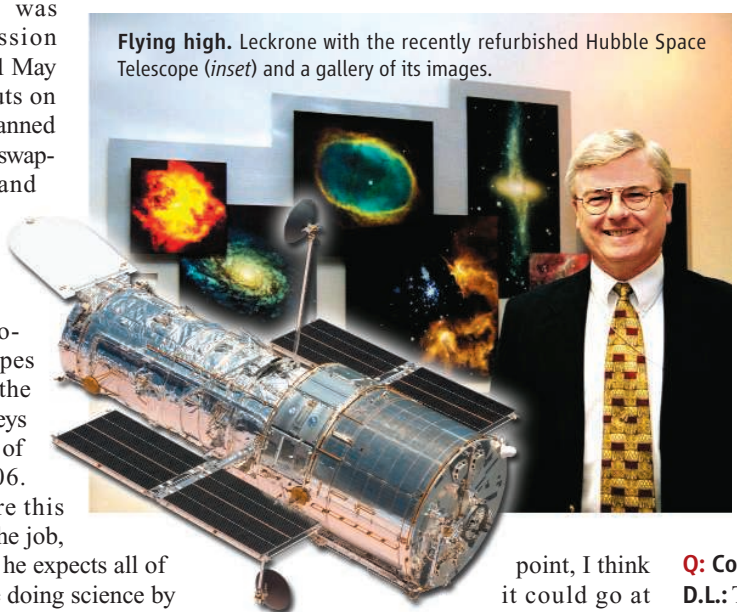

Flying high. Leckrone with the recently refurbished Hubble Space Telescope (*inset*) and a gallery of its images.

CREDITS (PHOTO AND INSET): NASA

Q: How is the Hubble doing?

D.L.: We are still in the midst of calibrating some of the old and new systems to make sure they run in an optimal fashion. The ACS is already doing science; the Wide Field Camera [3] will be doing so in 2 to 3 weeks. The Cosmic Origins Spectrograph will become operational after that.

Q: Have there been any issues to resolve?

D.L.: We had a couple of little hiccups. A cosmic ray particle hit the circuitry of the backup computer a few weeks after the mission ended, and some of the data arrived in all zeroes and all ones. We rebooted it, and it has been fine since. We created a software patch in the main computer to intervene if this ever happens again. We had a similar hiccup on the ACS. It's routine to have some trouble here and there, but we never panic.

Q: How long do you think the Hubble will stay afloat? Five years?

D.L.: The 5-year time frame is a budget number. From an engineering and science standpoint, I think it could go at least 10 years before starting to degrade. You always find clever scientists and engineers to keep the instruments going. As the spacecraft's ability diminishes, the creativity of the team on the ground increases.

Q: Did you and others give up hope of extending Hubble's life after Sean O'Keefe canceled the mission?

D.L.: It seemed like the mission was for certain gone. We went through a mourning period. NASA wanted us to tie off the work on the instruments at a logical stopping point, and some had the idea that the new instruments might be usable on other missions. That was not credible because they had been designed for Hubble.

The next thing that came along was this bright idea of servicing the mission robotically. It looked promising; our folks put in a substantial effort into developing a design for a robotic mission, but the time and costs for pulling it together would have been substantial. Fortunately, after Mike Griffin took over, he said, "Let's scuttle the robot idea and go back to what we know how to do."

Q: Was that difficult?

D.L.: We had to undo some of the steps from when NASA was thinking about using the instruments elsewhere. Also, many of our top-notch team members and contractors had gone off and taken other jobs. It took a little while to pull back the best people.

Q: Did the mission go smoothly?

D.L.: Mostly, yes. The worst moment came at the beginning of the first spacewalk when astronauts had to remove the Wide Field Camera 2. We had power tools to loosen the single bolt that was holding it in place. The crew tried three different torque settings; none of them was strong enough. At that point, I could see the whole mission crumbling into dust around my head.

Drew Feustel [one of the astronauts] saved our bacon. He went into manual mode, made sure that the tool was properly engaged, and applied some muscle. He was scared the bolt would break, which would have been a disaster. At the last minute, it popped loose. I felt like I came within 6 inches of being hit by a truck. It was a great example of what humans can do in space.

Q: Couldn't robots have done that?

D.L.: There's a limit to what robots can do; we are just not there technologically. One could argue that a robotic mission would have been only 50% as effective.

Q: What's your message to the panel that's reviewing the human space flight program [*Science*, 22 May, p. 999]?

D.L.: I have told the panel that it would be insane to do away with the human program. I hope the panel will recommend that whatever new architecture is developed will retain the capabilities that we have, including the ability to service large space observatories. That is the bedrock of our preeminence in space right now. Without humans in space, there is no NASA.

Published by AAAS

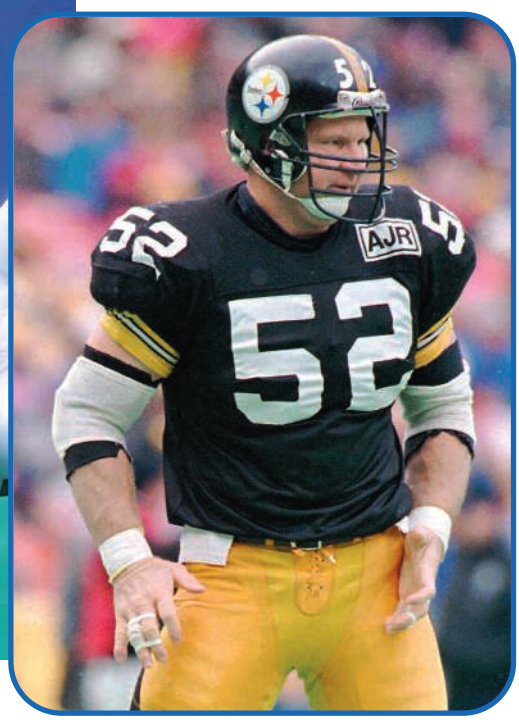

Dangerous play? Postmortem exams on former NFL players John Grimsley (blue jersey, *left*) and Mike Webster have found signs of neurodegeneration.

NEUROPATHOLOGY

A Late Hit for Pro Football Players

Emerging research suggests that hard knocks on the field may cause delayed brain damage in retired athletes

As a professional wrestler, Chris Nowinski had what those in the business call "natural heat." His ring persona, Chris Harvard, was an Ivy League snob who sometimes entered the ring reading a book. Fans loved to hate him. "I think I achieved greatness when I was in Mumbai, India, and had 20,000 people chanting 'Harvard sucks!'" Nowinski says.

Nowinski had in fact attended Harvard University, where he'd majored in sociology, been a standout defensive tackle on the football team, and graduated in 2000. A stint on *Tough Enough*, a reality TV show, led to a contract with World Wrestling Entertainment. But Nowinski's wrestling career was short-lived. He quit in 2003 after a series of concussions left him prone to memory lapses, irritability, sleeplessness, and persistent headaches. "After the last one, I just didn't bounce back," he says.

Nowinski took a job at a life sciences consulting firm near Boston, thinking he'd get back in the ring as soon as he felt better. But as weeks turned into months with little progress, he began combing the medical literature for information about the long-term effects of head injuries in athletes. What he found disturbed him. Studies dating back to the 1920s had documented dementia and neurodegeneration in boxers. But were other athletes at risk? Until recently, the literature had very little to say.

Now Nowinski is trying to use his knack for getting people riled up to change that. In 2007, he co-founded the Sports Legacy Institute, a nonprofit organization funded by donations that promotes research on sports-related head injuries. Last year, the institute announced the formation of a new research center in partnership with the Boston University School of Medicine to study neuropsychiatric symptoms in athletes and to examine donated brains for signs of pathology. Using his contacts in the sporting world, Nowinski has persuaded 134 football players and other athletes to donate their brains for research when they die. So far, the Boston group and other researchers working independently say they have found signs of pathology in a total of 12 former players in the National Football League (NFL), plus at least four wrestlers and one soccer player, many of whom died in their 40s. Only one postmortem exam of an NFL player has so far turned up negative: that of Damien Nash, a running back for the Denver Broncos, who died at age 24.

Although the number of cases is still very small, and most have yet to be published in peer-reviewed journals, the researchers insist their preliminary findings are cause for concern because this type of brain pathology is virtually unheard of in people this young. Nowinski has used these cases to generate considerable media attention. At this year's Super Bowl, he and colleagues held a press conference to announce new findings, including early signs of pathology in an 18-year-old high school football player.

As was the case in his wrestling days, not everyone likes his style. "Chris Nowinski is someone I don't want anything to do with," says Bennet Omalu, the neuropathologist who published the first case report on neurodegeneration in an NFL player in 2005. Omalu, who is currently the chief medical examiner in San Joaquin County in California, initially collaborated with Nowinski and the Boston group, but he withdrew from the project because he felt Nowinski was putting publicity ahead of research and failing to give him proper credit for his contributions.

Despite their differences, both men are passionate about the issue, and both see growing evidence that contact sports put athletes at risk for neurological problems years after they quit playing. If they can prove their case, sports leagues like the NFL will likely face more pressure to protect athletes on the field and take care of them after they retire, and parents and coaches will face troubling questions about the long-term hazards for younger athletes.

Troublesome tangles

At Ann McKee's office at the Veterans Administration Hospital in Bedford, Massachusetts, about a half-hour drive from Boston, the décor includes poster-sized images of dis-

CREDITS (LEFT TO RIGHT): RICK STEWART/GETTY IMAGES; GENE J. PUSKAR/AP

eased and injured brains and bobblehead dolls of football players. McKee is a neuropathologist on the faculty at Boston University and co-director of the new research center. She grew up in Wisconsin and says she's a loyal Green Bay Packers fan. Rummaging through drawers, she pulls together a tray of glass microscope slides and sets them down with a clink next to a microscope with two sets of eyepieces. Placing a slide on the scope, she invites a visitor to take a look. At first the view is a constellation of purple dots: the stained cell bodies of neurons. There's a dizzying blur as McKee moves the slide and centers the view on a cluster of brownish dots surrounding a blood vessel. Another blur brings another dark cluster into view, this one lining the depths of a sulcus, as the grooves in the cerebral cortex are called. "None of this should be here, just none of it," McKee says.

In the most extreme cases, "the extent of tau pathology is just unbelievable."

—DANIEL PERL, MOUNT SINAI SCHOOL OF MEDICINE

The dark spots indicate a high concentration of a protein called tau, a prime suspect in several neurodegenerative disorders, including Alzheimer's disease. But the brain tissue on the microscope didn't come from an elderly Alzheimer's patient; it belonged to a former NFL player who died at age 45. John Grimsley, a retired linebacker, shot himself in the chest while cleaning his gun in February 2008. His death was ruled an accident. After a call from Nowinski, Grimsley's wife agreed to allow McKee to examine his brain. Grimsley had started experiencing problems with memory and concentration at age 40, his family told the Boston researchers. Those symptoms worsened toward the end of his life, and he became emotionally volatile.

Grimsley's brain lacks the clumps of amyloid protein that are a hallmark of Alzheimer's disease, and the distribution of tau is different, McKee and colleagues reported in the July issue of the *Journal of Neuropathology and Experimental Neurology*. His pathology fits another diagnosis, chronic traumatic encephalopathy (CTE), that has previously been reported in boxers but only recently in other athletes.

Long-term neurological problems in boxers were first described in a 1928 paper in *The Journal of the American Medical Association* written by a New Jersey pathologist named Harrison Martland. After consulting with a fight promoter, Martland compiled a list of "punch drunk" fighters and described their symptoms. In the ensuing decades, researchers reported more cases and published neuropathological exams showing extensive brain damage in boxers. The condition became known as *dementia pugilistica*, and more recently as CTE, to acknowledge newer evidence that boxers are not the only athletes at risk.

Omalu was the first to document CTE in a football player. One Saturday morning in late September 2002, he recalls, he had the television on as he was getting ready to go to work at the Allegheny County medical examiner's office, near Pittsburgh, Pennsylvania. The morning news included the death of former Pittsburgh Steelers center Michael "Iron Mike" Webster. At his peak in the 1970s and '80s, Webster was considered one of the best to ever play his position. But after retiring in 1990, Webster fell on hard times, going through a divorce and periods of depression, drug abuse, and homelessness. He died at age 50. Omalu wondered whether the hits Webster sustained in his 17 seasons in the NFL might have contributed to his troubles. He had no idea he was about to get a chance to investigate.

"I went to work and lo and behold, Mike Webster was on my autopsy table," says Omalu. Webster had died of a heart attack, but postconcussion syndrome was listed as a contributing factor. At first glance, Webster's brain looked normal, Omalu says. But closer examination revealed protein deposits similar to those found in patients with Alzheimer's disease, including dense tangles of tau and a smattering of amyloid plaques. (Webster's case may be unusual; most subsequent studies of football players have found only tau.)

Omalu and colleagues' case report on Webster, published in *Neurosurgery* in 2005, elicited a flurry of letters to the editor. One was a lengthy rebuttal from members of the NFL's committee on mild traumatic brain injury, who argued that the paper should be retracted or substantially revised because the researchers had misinterpreted their neuropathological findings and failed to present an adequate clinical history. Other letters were more supportive and joined the call for more research. One of these was from Robert Cantu, a sports neurologist and leading authority on concussion in Concord, Massachusetts, who happened to be Chris Nowinski's doctor and later became a co-founder of the Sports Legacy Institute.

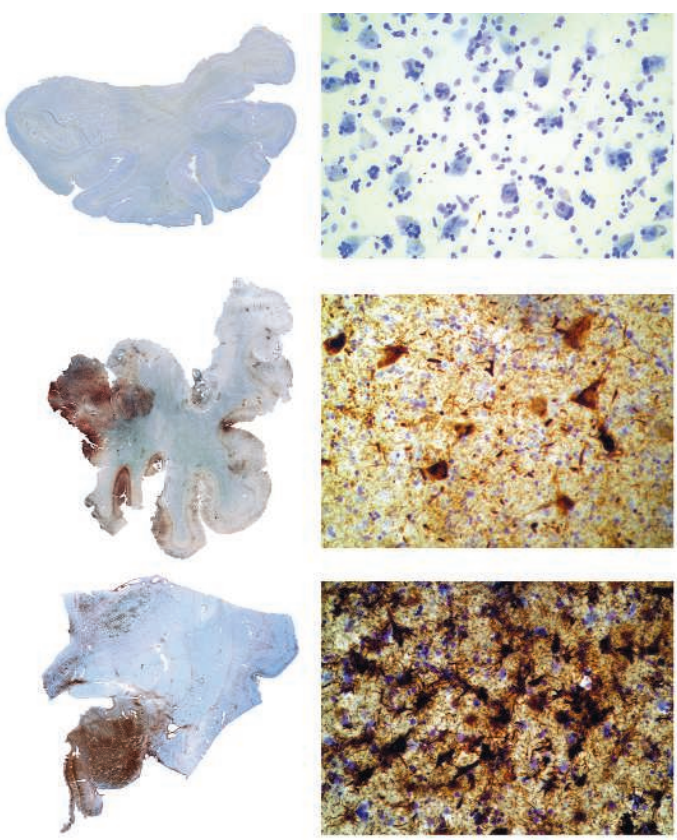

Signs of trouble. Concentrations of tau protein (dark brown regions) are absent in the brain of a nonathlete who died at age 65 (*top*) but present in the brains of NFL player John Grimsley (*middle*) and a professional boxer (*bottom*).

CREDIT: ANN MCKEE

Gaining ground

Although Omalu's report on Webster was initially greeted with skepticism, other evidence soon began to bolster the case that something was going wrong in the brains of some football players. In 2006, Omalu published a second *Neurosurgery* paper describing signs of CTE in another Steeler, Terry Long, who committed suicide by drinking antifreeze in 2005. Like Webster, Long had struggled in his post-football life.

In all, Omalu says he has found CTE in the brains of eight of the nine professional football players he's examined. (Nash

Ringleader. Former professional wrestler Christopher Nowinski wants more research on the neurological consequences of playing contact sports.

was the sole exception.) In Boston, McKee says she has found CTE in all four former pros she has examined. Something is clearly abnormal in these athletes' brains, says Daniel Perl, a veteran neuropathologist at Mount Sinai School of Medicine in New York City, who recently began collaborating with the Boston researchers. In the most extreme cases, says Perl, "the extent of tau pathology is just unbelievable."

Studies with living players hint at problems too. A survey of 2552 retired professional football players, led by Kevin Guskiewicz, a neuroscientist and research director of the Center for the Study of Retired Athletes at the University of North Carolina, Chapel Hill, found that those who reported three or more concussions in the course of their careers were five times more likely than those who reported no concussions to show signs of mild cognitive impairment, a frequent prelude to Alzheimer's disease. The researchers published the findings in *Neurosurgery* in 2005. In the same group, those with more concussions were more likely to have received a diagnosis of depression, Guskiewicz and colleagues reported in 2007 in *Medicine and Science in Sports and Exercise.*

Critics, including members of the NFL's committee on mild traumatic brain injury, dismissed the study because it relied on retirees' self-reported history of concussions and subsequent symptoms, Guskiewicz says. He and colleagues have begun a follow-up study in which retirees spend 2 days in Chapel Hill for a battery of tests to gauge their cognitive and psychological well-being more directly. They will also undergo magnetic resonance imaging scans to look for brain abnormalities. Guskiewicz says the preliminary work suggests that NFL players, particularly those who suffer more concussions, are at risk of depression and cognitive impairments later in life.

Looking downfield

It's a possibility the NFL has been quick to dismiss in the past, Guskiewicz and others say. The league did, however, invite McKee and others to present their findings at a meeting of its committee on mild traumatic brain injury in June. She says the response was polite but skeptical. The use of performance-enhancing anabolic steroids was raised as an alternative cause of pathology, McKee says. "I tried to make the case that the common denominator here is repetitive head trauma and that a number of these individuals never used anabolic steroids."

"There is neuropathological evidence that there's something going on, but exactly what the etiology is is not all that clear," says Ira Casson, the co-chair of the NFL committee on mild traumatic brain injury. He says the NFL is conducting its own study to examine 120 retired players; it will include detailed histories and cognitive and psychological tests and will use a variety of neuroimaging methods to look for signs of brain damage. As a control group, the study will include 60 players who tried out for the NFL but didn't see significant playing time—a comparison that would presumably distinguish any effects of playing football in general from effects of playing in the NFL per se.

One of the many major questions is whether all football players—or other people subjected to repeated blows to the head—are susceptible to CTE. After all, thousands of former hard-hitting athletes appear to be just fine. The number and severity of blows, and their proximity in time, are almost certainly a factor, says Cantu. Drug use and genetics may be important, too. For example, a handful of studies have suggested that a certain version of the apolipoprotein E gene, called *APOE4*, may make people more susceptible to ill effects from brain injuries. (*APOE4* also appears to up the risk of Alzheimer's disease in the general population.)

Exactly how repetitive brain trauma might cause delayed neurodegeneration is not known. Although tangles of tau protein contribute to neurodegeneration in a number of diseases, very little is known about what causes the protein to aggregate, says John Trojanowski, who studies mechanisms of neurodegeneration at the University of Pennsylvania. He notes that Swedish researchers reported in the *Annals of Neurology* in 2006 that amateur boxers have elevated levels of tau in their cerebrospinal fluid 7 to 10 days after a fight. But why? Rodent studies suggest that inflammation and oxidative stress after brain injuries encourage the buildup of amyloid protein. The same may be true for tau, Trojanowski says, but the experiments have yet to be done.

Perhaps the most worrisome of the findings to date is the presence of tau in the brain of the high school football player who died. "An 18-year-old should have a pristine brain," McKee says. For Nowinski, the case raises the question of how young is too young to play contact sports and underscores the urgency of studying CTE. "We want to figure out something to do before kids who didn't need to get this do [get it] because someone thought it was a good idea for them to start bashing their heads at 6 years old," he says.

–GREG MILLER

CREDITS (TOP TO BOTTOM): CHRIS O'MEARA/AP; WIKIPEDIA

Published by AAAS

THEORETICAL PHYSICS

Can Gravity and Quantum Particles Be Reconciled After All?

One group of intrepid theorists thinks the answer to that question may be "yes," and if they're right, one argument in favor of string theory unravels

Zvi Bern's epiphany came in October 2005 when he read in the newspaper about that year's Nobel Prize in physiology or medicine. Barry Marshall and J. Robin Warren took the honors for discovering that peptic ulcers are caused not by stress or diet but by a bacterium. When skeptics scoffed at the idea, Marshall gave himself the bug—and an ulcer—and cured himself with antibiotics. From the tale, "it was clear that in science the big money is in overturning the accepted beliefs," says Bern, a theoretical physicist at the University of California, Los Angeles. So he decided to return to a project that might upend a pillar of physics lore: the belief that standard quantum theory and gravity don't mix.

More precisely, many theorists think it is impossible to make a quantum theory of pointlike particles—a "quantum field theory"—that also incorporates Einstein's theory of general relativity. Try it, they say, and the theory will go mathematically haywire, spitting out meaningless infinities. That supposed inevitability has been a prime motivation for string theory, which assumes that every particle is actually an infinitesimal string vibrating in nine-dimensional space—and which is inherently immune to these infinities.

But point particles and gravity may be compatible after all. For several years Bern, Lance Dixon of SLAC National Accelerator Laboratory in Menlo Park, California, and colleagues have tried to show that one particular quantum field theory of gravity known as $N = 8$ supergravity gives sensible answers. In a paper in press at *Physical Review Letters*, they take another step to show that this theory works mathematically.

"It's a remarkable result," says Kellogg Stelle, a string theorist at Imperial College London, who had bet Bern a bottle of Italian Barolo wine that the latest calculation would "blow up," as physicists like to say. "I thought they would find infinities, and I lost fair and square."

The work doesn't disprove string theory, but it has string theorists backpedaling a bit in their criticism of quantum field theory. "At certain points, our understanding has been incomplete, and we may have said things that weren't right," says John Schwarz of the California Institute of Technology in Pasadena. "That being said, the fact is that we still need string theory."

Physicists have a "hand-waving" argument for why quantum field theory can't jibe with gravity, whereas string theory can. According to general relativity, massive objects like Earth bend space and time, or spacetime, to produce the effect we call gravity. But quantum mechanics says that spacetime should suffer from quantum uncertainty so that at the smallest scales, it should erupt into a frothy "quantum foam," in which *where* and *when* lose precise meaning. That should send any theory of point particles spiraling out of control.

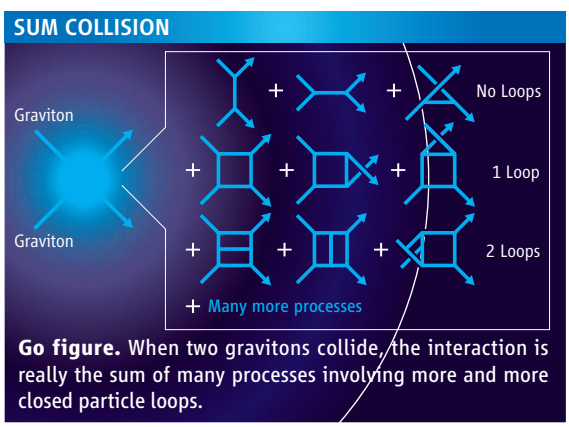

Go figure. When two gravitons collide, the interaction is really the sum of many processes involving more and more closed particle loops.

In contrast, strings would stretch over the bubbles in foam. So calculations in string theory should work, whereas those in quantum field theory should fail.

Except that $N = 8$ supergravity seems to give finite answers anyway. To show that, Bern and Dixon, who first considered the problem in the late 1990s, analyzed the behavior of gravitons, massless particles that make up gravitational fields just as photons make up light. To prove that the theory avoids unwanted infinities, the team need only show that it gives a finite answer for the probability that one graviton will bounce or "scatter" off another.

In practice, that calculation is hugely complicated. Gravitons can deflect one another by exchanging a particle, such as another graviton (see diagram). But they can also exchange more particles in evermore complicated processes in which the intermediary particles form closed loops in the little "Feynman diagrams" that theoretical physicists use to sort through the mathematics. The more loops a process has, the more likely it is to produce infinities. In 2007, the team showed that together, the diagrams with three loops yielded a finite answer. In the new paper, they extend the result to four loops.

The numbers don't balloon out of control because $N = 8$ supergravity is laden with symmetries: ways in which the underlying variables can be changed without changing the overarching equations. In particular, it is the quantum field theory of gravity with the most "supersymmetry," which relates particles of different inherent spins. The symmetries keep the infinities in check, Bern says. "There are correspondences betweens the various pieces [of the calculation], and when you add them all up, there are cancellations."

$N = 8$ supergravity is just a mathematical testing ground, not a realistic theory, Dixon cautions. "It's not the real world, it's a toy model," he says. Still, if it gives finite answers, then more-realistic quantum field theories of gravity might, too.

But that's a big if, says Stelle, who notes that the researchers have to prove that the theory yields finite results for *any* number of loops, or "to all orders." Stelle says he's willing to bet (again) against the proposition: "If $N = 8$ supergravity were finite to all orders, it would be a miracle."

What's more, Schwarz says, even if $N = 8$ supergravity is finite to all orders, it still wouldn't be a fully coherent theory of gravity. Like any theory, it would still need an extra bit called a "nonperturbative completion," and Schwarz and his colleagues argue that the nonperturbative completion of $N = 8$ supergravity is, in fact, string theory.

Still, physicists may need to rethink the assumption that quantum field theories of gravity are doomed to produce infinities as their pointlike particles sink into the quantum foam. "There was no proof, and it just got repeated over and over," Bern says. Now, the notion may be fading like the idea of an enchilada-induced ulcer.

–ADRIAN CHO

CREDIT: M. TWOMBLY/*SCIENCE*, SOURCE: ADRIAN CHO

Published by AAAS

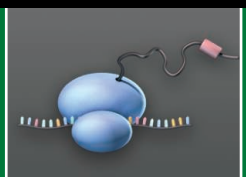

LETTERS

edited by Jennifer Sills

Droplet Data Not New

CONTRARY TO THE IMPLICATION IN A. CHO'S NEWS OF THE Week story "Water droplets grow faster than expected" (24 April, p. 453), the results are not new. The reported relationship between the volume of an isolated droplet and time to the power of 3/2 is a result of "Maxwellian" diffusion-limited growth (*1*), first examined by James Clerk Maxwell in the 19th century (*2*). Also well known is the reported reduction in growth rate when the droplets are crowded together, a situation commonly found in clouds. This reduction occurs because each droplet depletes the surrounding air of water vapor, effectively maintaining the local vapor pressure at a value near equilibrium (*3*). The transition observed by Sokuler and co-workers occurs when the droplet growth is no longer limited by local diffusion to isolated droplets, but by larger-scale diffusion to the ensemble. The 3/2 law is familiar to cloud physicists, and the linear growth rate of crowded droplets on a substrate is well known to researchers who study "breath figures" or aggregate growth on a surface (*4*).

NEIL J. BACON[1]* AND JON NELSON[2]

[1]Nion Company, Kirkland, WA 98033, USA. [2]Department of Electrical Engineering, Ritsumeikan University, Kusatu, Japan.

*To whom correspondence should be addressed. E-mail: neiljulianbacon@yahoo.com

References

1. Y.-S. Zou, N. Fukuta, *Atmos. Res*. **52**, 115 (1999).
2. J. C. Maxwell, *The Scientific Papers of James Clerk Maxwell, Vol. 2* (Dover reprint, New York, 1890).
3. R. R. Rogers, M. K. Yau, *Short Course in Cloud Physics* (Butterworth-Heinemann, Oxford, ed. 3, 1989).
4. D. Fritter, C. M. Knobler, D. A. Beysens, *Phys. Rev. A* **43**, 2858 (1991).

Cholera Vaccine Will Reduce Antibiotic Use

IN THEIR POLICY FORUM ("THE CHOLERA CRISIS in Africa," 15 May, p. 885), S. Bhattacharya *et al*. articulate important reasons for advocating vaccine development and deployment as a primary response to cholera epidemics in Africa and elsewhere. There is one more reason: Preventing cholera outbreaks through the use of vaccines also reduces the need to use antibiotics to treat the disease.

In parts of the world with suboptimal sanitation and water supply, antibiotics are widely used to shorten the period in which infectious bacteria are shed and thereby curtail transmission of *Vibrio cholerae* during epidemics. They have also been misused as prophylactics in cholera epidemics. In the past four decades, Africa's cholera epidemics are frequently initiated by drug-resistant strains. Even more commonly, resistance to drugs of choice emerges during the course of the epidemic. When antibiotics are ineffective, the number of individuals infected, as well as mortality rates, can rise (*1*, *2*). Moreover, the repertoire of resistance genes and elements in cholera bacteria is expanding, and some strains carry multiple genes conferring resistance to a single drug (*3*).

Effective vaccines offer longer-term protection than antibiotic drugs and therefore, in spite of higher delivery cost, would be more cost-effective in difficult-to-access or displaced populations, who are the most likely victims of repeated epidemics. In Africa, where the infectious disease burden means that overall selective pressure for resistance is unavoidably high, cholera vaccines for epidemic deployment could help to extend the life of valuable antibacterials.

IRUKA N. OKEKE

Department of Biology, Haverford College, Haverford, PA 19041, USA. E-mail: iokeke@haverford.edu

References

1. A. K. Siddique *et al*., *Lancet* **345**, 359 (1995).
2. A. Dalsgaard *et al*., *J. Clin. Microbiol*. **38**, 3774 (2000).
3. J. A. Opintan, M. J. Newman, O. A. Nsiah-Poodoh, I. N. Okeke, *J. Antimicrob. Chemother*. **62**, 929 (2008).

How to Improve U.S. Education

IN A RECENT NEWSMAKER INTERVIEW ("ARNE Duncan hopes a team approach will improve U.S. schools," J. Mervis, 10 April, p. 159), Education Secretary Arne Duncan responded to a question about whether there is a consensus regarding what students should know about science before leaving high school. He replied that "…across the board, we need to get clearer, higher, fewer standards." He is apparently unaware of the K–12 science learning goals developed in an unprecedented undertaking by the American Association for the Advancement of Science (AAAS) (*1*–*3*) or of those formulated by the National Academy of Sciences (NAS) (*4*). Duncan must understand that we simply do not need another definition of what students have to know before they leave high school in order to move ahead with substantial reform.

The windfall monies now available to the

Letters to the Editor

Letters (~300 words) discuss material published in *Science* in the previous 3 months or issues of general interest. They can be submitted through the Web (www.submit2science.org) or by regular mail (1200 New York Ave., NW, Washington, DC 20005, USA). Letters are not acknowledged upon receipt, nor are authors generally consulted before publication. Whether published in full or in part, letters are subject to editing for clarity and space.

Published by AAAS

Folding and bending DNA

685

Mapping maize traits

688

U.S. Department of Education (ED) and the National Science Foundation (NSF) can potentially put the United States on track to realize fundamental and lasting improvements in the quality and availability of science education. But the funds may well be wasted if they are invested in an array of panic-driven quick fixes. Thus, ED and NSF must work together to design a long-term plan of action that focuses on the attainment of the learning goals in the AAAS and NAS documents (*1*–*4*); interrelates programs for improving teacher preparation, redesigning school science curricula (*5*), and developing teaching materials and assessment instruments; carries out the serious cognitive research and data collection needed to inform those undertakings; and takes into account the lessons of the past, both positive and negative (*6*, *7*).

Achieving these goals will not be easy, but it is possible and even necessary—and the leadership of AAAS and *Science* can be crucial to the success of this agenda.

F. JAMES RUTHERFORD

1089 8th Street, Berkeley, CA 94710, USA. E-mail: fjrbwr@gmail.com

References and Notes

1. American Association for the Advancement of Science, *Science for All Americans* (Oxford Univ. Press, New York, 1989).
2. American Association for the Advancement of Science, *Benchmarks for Science Literacy* (Oxford Univ. Press, New York, 1993).
3. American Association for the Advancement of Science, *Atlas of Science Literacy* (National Science Teachers Association Press, Washington, DC, 2001).
4. National Research Council, *National Science Education Standards* (National Academy Press, Washington, DC, 1996).
5. American Association for the Advancement of Science, *Designs for Science Literacy* (Oxford Univ. Press, New York, 2000).
6. S. L. Helgeson, R. E. Stake, I. R. Weiss *et al.*, *The Status of Pre-College Science, Mathematics, and Social Studies Educational Practices in U.S. Schools: An Overview and Summaries of Three Studies* (U.S. Government Printing Office, Washington, DC, 1978).
7. F. J. Rutherford, *J. Sci. Ed. Technol.* **14**, 4 (2005).
8. The author is a former Chief Executive Officer of AAAS.

China Fights Against Statistical Corruption

PARTICULARLY IN THE CURRENT FINANCIAL crisis, many countries rely on statistics released by the Chinese government for production and trade of bulk commodities, exchange rates, and economic stimulus. However, the credibility of China's statistics has long been questioned. On 1 May, a new regulation, *Rules on Punishment for Violation of Laws in Statistics*, was put in effect by the Ministry of Supervision, Ministry of Human Resources and Social Security, and the National Bureau of Statistics (*1*).

Statistical corruption has been found in China for years, largely for two reasons. First, economic growth is a key factor determining the promotion of government officials. Statistical data and numbers are regarded as a reflection of economic growth, which is used to evaluate the performance of the officials.

This is the so-called "numbers make leaders" phenomenon ("shu zi chu guan" in Chinese). Second, the statistical organizations are not independent entities in China. They are a part of the government and hence are vulnerable to government interference. Without specific laws and regulations to punish statistical corruption, government leaders can intervene in statistical reporting with low political risks. They may tailor statistics for different purposes, such as inflating statistical numbers that indicate economic achievements and decreasing statistical numbers for environmental pollution and damage (*2*). This is the so-called "leaders make numbers" phenomenon ("guan chu shu zi" in Chinese).

The previous Statistics Law in China has been in effect since 1983, but it was too vague to enforce. Although it stated the penalty for illegal acts, the law did not clearly specify the types of the illegal acts and the extent to which penalties should be imposed. In contrast, the new regulation lists four types of statistics cheating: revising statistics without permission, or making up statistics; forcing or ordering statistics departments or individuals to revise or make up statistics or refuse to report statistics; retaliation against individuals who refuse to issue false statistics; and retaliation against individuals who report statistics violations (*3*). The degree of punishment depends on consequences of the violations, and the punishments include a warning, recording a demerit, or even removing officials from their positions.

The new regulation is an important step in the fight against statistical corruption in China. Nevertheless, to eradicate illegal acts in statistical work, further actions are needed, such as reform of the evaluation system for officials and the establishment of independent statistical organizations. Without progress in these areas, the goal of an 8% GDP growth rate for 2009 announced by the Chinese government could be merely another number created by leaders.

JUNGUO LIU[1]* AND HONG YANG[2]

[1]School of Nature Conservation, Beijing Forestry University, Beijing, 100083, China. [2]Eawag, Swiss Federal Institute of Aquatic Science and Technology, 8600 Duebendorf, Switzerland.

*To whom correspondence should be addressed. E-mail: water21water@yahoo.com

References

1. Xinhua News Agency, "*Rules on punishment for violation of laws in statistics*" (Xinhua News Agency News, 2009); http://news.xinhuanet.com/newscenter/2009-04/28/content_11275709.htm).
2. H. Yang, K. C. Abbaspour, *Desalination* **212**, 238 (2007).
3. Ministry of Supervision, Ministry of Human Resources and Social Security, National Bureau of Statistics, *Rules on Punishment for Violation of Laws in Statistics* (Order No. 18, 2009); www.stats.gov.cn/tjfg/gz/t20090428_402555151.htm.

Organics: Evidence of Health Benefits Lacking

MANY CONSUMERS CITE "HEALTH AND NUTRITIONAL concerns" as the primary reason for purchasing organic food (*1*). There are several hypotheses to explain why organic foods might be nutritionally superior to conventionally produced foods, including (i) the idea that nutrient uptake is enhanced because organic fertilizers release nutrients slowly, and (ii) the theory that conventional pesticides and herbicides may disrupt nutrient absorption or synthesis, potentially lowering nutrient levels in crops. However, systematic literature reviews over three decades, including a very recent one (*2*), have demonstrated neither consistent nor meaningful differences in nutrient levels.

Furthermore, almost all reviews and much of the original research report only the statistical significance of the differences in nutrient levels—not whether they are nutritionally important (*3*). To determine the latter, nutrient comparisons must be made on a per serving basis and then set against a standard, such as the FDA/USDA requirement that a nutrient must be 10% higher than it is in a comparison product to make the claim that the product has more of the nutrient.

Levels of phytochemicals—compounds found in plants that are not classified as nutrients but appear to play a role in reducing the risk of certain diseases—are frequently reported to be higher in organic foods compared with conventional foods. Although the production environment appears to affect the level of phytochemicals by as much as 30% [e.g., (*4*)], the genotype (variety) can vary the composition by a factor of three to ten, or more [e.g., (*5*)]. Therefore, cultivar selection may be as important or more important than the production method in increasing overall intake of these important compounds. However, data on phytochemical content are generally insufficient, and standards on which to base diet recommendations are lacking. Studies demonstrate that it is the total amount of dietary phytochemicals, not the amounts of individual compounds in a single food, that is important in reducing the chronic disease risk (*6*).

As Magkos *et al*. (*7*) state, "the quality of a food product should be considered as the result of the general quality of its production system." We can't stress enough the many potential public health and environmental benefits from organic production methods and the consumption of organic foods (e.g., low pesticide residues and reduced soil loss). Given these important benefits, supporting unsubstantiated claims of nutritional superiority is an unwise and unnecessary argument for promoting dietary change. For now, we urge scientists, producers, and others to carefully "identify the boundaries of accurate messaging" (*8*) and not to mislead themselves and the public.

KATE CLANCY,[1] MICHAEL HAMM,[2] ALLEN S. LEVINE,[3]* JENNIFER WILKINS[4]

[1]Minnesota Institute for Sustainable Agriculture, University of Minnesota, St. Paul, MN 55108–6074, USA. [2]Community, Agriculture, Recreation, and Resources, Michigan State University, East Lansing, MI 48824–1222, USA. [3]College of Food, Agricultural, and Natural Resource Sciences, University of Minnesota, St. Paul, MN 55108–6074, USA. [4]Division of Nutritional Sciences, Cornell University, Ithaca, NY 14853–4401, USA.

*To whom correspondence should be addressed. E-mail: aslevine@umn.edu

References

1. L. Demeritt, *Org. Process.* **4**, 12 (2007).
2. A. D. Dangour *et al., Am. J. Clin. Nutr.* 10.3945/ajcn.2009.20841 (published online 29 July 2009).
3. C. Benbrook, X. Zhao, J. Yanez, N. Davies, P. Andrews, "New evidence confirms the nutritional superiority of plant-based organic foods (The Organic Center, 2008); www.organic-center.org/reportfiles/5367_Nutrient_Content_SSR_FINAL_V2.pdf.
4. D. Asami, Y.-J. Hong, D. Barret, A. Mitchell, *J. Agric. Food Chem*. **51**, 1237 (2003).
5. M. W. Farnham, P. E. Wilson, K. K. Stephenson, J. W. Fahey, *Plant Breed.* **123**, 60 (2004).
6. R. Liu, *Am. J. Clin. Nutr.* **78** (suppl.), 517 (2003).
7. F. Magkos, A. Fotini, A. Zampelas, *Int. J. Food Sci. Nutr*. **54**, 357 (2003).
8. D. Conner, M. C. Heller, S. Cocciarelli, M. W. Hamm, "Opportunities in grazing dairy farms: Assessing future options" (2007); http://mottgroup.msu.edu/Portals/0/Opportunities%20in%20Grazing%20Dairy%20Farms.pdf.

CORRECTIONS AND CLARIFICATIONS

Reports: "Avian paternal care had dinosaur origin" by D. J. Varricchio *et al*. (19 December 2008, p. 1826). Incorrect Akaike weights and evidence ratios were used in the comparison of clutch volume–body mass data of three nonavian dinosaurs (Troodon, Citipati, and Oviraptor) to four a priori models generated from extant archosaurs. Erroneous Akaike information criterion values were calculated using base 10 rather than the natural logarithm. The corrected Akaike weights for the four models are bird-paternal, 0.698; bird-maternal, 0.174; crocodile-maternal, 0.093; and bird-biparental, 0.036. Thus, clutch volume–adult body mass ratios of these dinosaurs are 4.0, 7.5, and 19.5 times more likely to fit the bird-paternal model than the bird-maternal, crocodile-maternal, and bird-biparental models, respectively. These corrected values do not alter but instead lend greater support to the original interpretation.

Letters: "Optimizing ecosystem services in China" by W. J. Mitsch *et al*. (24 October 2008, p. 528). The distance between the Three Gorges Dam and Chongqing city center is 600 km, not 300 km. Chongqing province and the site of our investigations, however, is well within 300 km of the dam. Flooding in the pool behind the dam is currently being investigated so that it will be lower than originally predicted 600 km upstream at Chongqing city.

ARCHAEOLOGY

Imagining Our Ancient Future

Christopher E. Forth

Knossos and the Prophets of Modernism

by Cathy Gere

University of Chicago Press, Chicago, 2009. 287 pp. $27.50, £19. ISBN 9780226289533.

The palace of Knossos on the island of Crete has long fired the imaginations of Westerners raised on classical mythology. Many will recall stories of Theseus and Ariadne defeating the Minotaur, of the famous Labyrinth that was the monster's home, of Daedelus (the Labyrinth's designer) fashioning wings to escape the island, and of his son Icarus, who paid a terrible price for flying too high. Less well known is the extent to which ideas about Crete have informed perceptions of the origins and aims of Western civilization itself. When the English industrialist and amateur classicist Arthur Evans began to excavate the site in 1900, the Aegean Bronze Age was already generating new interest among writers, artists, and philosophers, many of whom looked to antiquity for ways of weathering the challenges of the present. Such appropriation of history for present-day purposes was vividly displayed in Evans's own "reconstruction" of the palace, which stylistically owed as much to modern architecture as it did to antiquity.

This merger of past and present is at the heart of Cathy Gere's richly textured and well-written cultural history, *Knossos and the Prophets of Modernism*. For her, Evans's speculative reconstruction of Knossos is emblematic of modern culture's tendency to sift through the ruins of the past for clues to approaching the future. Such exercises in "retrospective prophecy" were common among those who began to imagine ancient Crete as a matriarchal and pacifist precursor to modern Europe. Facing the spiritual malaise and geopolitical strife that seemed to characterize Western society around 1900, and which only worsened as the century unfolded, some proposed that the only way forward was to return to the paradise of this lost golden age. After all, the "fact" of ancient harmony proves that such things are indeed possible. This is how images of an idealized Crete found their way into numerous "alternative" movements in the 20th century, from feminism, ecopolitics, and the peace movement to New Age spiritualism and Afrocentrism. By assembling an impressive cast of characters—from Friedrich Nietzsche and Sigmund Freud to Robert Graves and Martin Bernal—Gere (a historian of science at the University of California, San Diego) engagingly reveals how fantasies about a peaceful human past were intimately bound up with speculations about the future of the West.

For much of its 20th-century history, Minoan society has been played off against the Greek mainland, with the belligerence of pre-Hellenic Mycenae functioning as a counterpoint to the peacefulness of Crete. Gere's story thus starts with Heinrich Schliemann, whose excavation of Troy was appropriated by Aryan racial theorists for "proof" of a Germanic link to classical heroes, and the philosopher Nietzsche, who argued that the great tragic age of Dionysian Greece was rudely ended with the advent of Socratic rationalism. Nietzsche's celebration of Dionysian ecstasy would inspire countless artists, intellectuals, and activists to look to antiquity for solutions to the current predicament of Western civilization.

Contrasting Crete to the belligerence of Mycenae, Evans offered it as a woman-centered, pacifist alternative to the religious and nationalist strife he saw all around him. Partly inspired by earlier theories of an ancient matriarchy brutally overturned by patriarchal political structures, he went so far as to repress archaeological evidence of Minoan bellicosity to promote his vision of a lost island paradise. Not long after Evans began his excavation, the classicist Jane Ellen Harrison (one of the first women to break into the profession) did much to popularize the idea of a Cretan Mother Goddess whose rule was unjustly overturned by the patriarchal Olympian god Zeus. Such ideas would become especially attractive when set against the mounting international tensions of the 1930s. Ariadne became a recurring image in the paintings of Giorgio de Chirico, while Minotaurs turned up frequently on the canvases of Pablo Picasso and the surrealists.

The Aegean Bronze Age came to be seen as the pagan precursor of European modernity (the innocent "childhood" of the "race"), and Gere shows how actual childhoods could be implicated in such ideas. Freud, who often used archaeological metaphors to describe how psychoanalysis worked, suggested that matriarchal Crete corresponded to a pre-Oedipal stage of Western civilization and thus the infantile stratum of the European psyche. He found support for this idea in his analysis of the modernist poet H.D. (Hilda Doolittle), whose obsessive interest in Greece and the Mother Goddess he circuitously traced to an unresolved mother fixation. And Evans, who had lost his own mother at an early age, seemed to have been symbolically reunited with her in his alleged discovery of the Great Goddess.

Myths about ancient matriarchy and of the

"Horns of Consecration" at Knossos. Evans's huge concrete replica of a characteristic Minoan symbol.

CREDIT: MICHAEL NICHOLSON/CORBIS

The reviewer is at the Humanities and Western Civilization Program, University of Kansas, Lawrence, KS 66045–7574, USA. E-mail: cforth@ku.edu

Published by AAAS

Mother Goddess found new purchase after the genocidal and nuclear horrors unleashed by the Second World War. Beatnik, peacenik, and feminist extensions of these ideas would gain momentum from the 1950s onward and would soon be joined by the claims of George Wells Parker, Chiekh Anta Diop, and Martin Bernal that Crete had in fact been colonized by the black African culture of Egypt. In some respects the "Black Athena" thesis poured old wine into new skins: as opposed to the militaristic and patriarchal culture of Mycenae, Diop argued, the black Minoans were still just as matriarchal, agricultural, and peaceful as the "white" ones imagined by Evans and others.

While controversy over such claims rocked academia in the 1990s, for decades archaeologists had been revealing a very different side to ancient Crete. Evidence of ancient fortifications, guard houses, deadly weapons, human sacrifice, and possibly even cannibalism effectively destroyed the utopian fantasy Evans had created. By the end of the Cold War, Gere writes, "the Minoan doves and Mycenaean hawks of the first half of the twentieth century began to look like the same species of bird after all."

The implications of this fascinating book extend far beyond the island that is its focus. In her conclusion, Gere acknowledges that using the past as a way of imagining the future is a very old practice. And as far as such retrospective prophecies go, she considers the Cretan fantasy to be pretty benign. More worrying for her are the prophecies currently at work in the human sciences' sometimes reductive tendency to seek in DNA and evolutionary development a framework for thinking about the future of humanity. Although some might disagree with Gere's suspicion that these are merely reassertions of old racialist tendencies "returned with all of the force of the long repressed," history shows just how problematic claims about the past can be as blueprints for the future.

10.1126/science.1175676

PUBLIC UNDERSTANDING

Selling Science

Jerry Coyne

In *Unscientific America*, a book slight in both length and substance, science writers Chris Mooney and Sheril Kirshenbaum argue that America's future is deeply endangered by the scientific illiteracy of its citizens and that this problem derives from two failings of scientists themselves: their vociferous atheism and their ham-handed and ineffectual efforts to communicate the importance of science to the public. According to Mooney and Kirshenbaum, atheistic scientists such as Richard Dawkins and P. Z. Myers [who runs the immensely popular science blog Pharyngula (*1*)] drive people away from science by forcing them to choose between the facts and their faith. Further, most scientists are neither trained nor deeply interested in selling their work to the public, Congress, or Hollywood. This disconnect could be fixed, say the authors, if scientists would just keep quiet about their atheism and if universities would train a new generation of scientists in public outreach, producing more "[h]ip, fun, trailblazing research pioneers."

Unscientific America
How Scientific Illiteracy Threatens Our Future

by Chris Mooney and Sheril Kirshenbaum

Basic Books, New York, 2009. 223 pp. $24, £13.99, C$30.50. ISBN 9780465013050.

Indeed, Americans' knowledge of science seems pretty dismal. Only half of us know that Earth goes around the Sun once per year, acceptance of evolution hovers at a dismaying 45%, and only 46% realize that electrons are smaller than atoms. But when Mooney and Kirshenbaum venture beyond such well-known data, their enterprise dissolves. Ironically for a book that aims to improve science literacy, *Unscientific America* is woefully short of evidence to support its claims. Does science illiteracy really endanger our country or our standard of living? This is not discussed. America still leads the world in funding and research output, and we're inundated with foreigners seeking scientific training. Yes, China and India are catching up in measures such as the proportion of all doctoral degrees that are in science, but should we really be afraid of that? After all, this is what happens when less-developed countries aspire to more, and surely the rising scientific tide will lift all of us.

Mooney and Kirshenbaum also fail to support their contention that the knowledge gap between scientists and the public is increasing. In fact, the only relevant statistic they provide shows no such thing: the proportion of Americans who believe that humans were created instead of evolved has not budged for three decades. This constancy undermines the authors' claim that scientific illiteracy once was ameliorated by people like Carl Sagan and Stephen Gould but is now exacerbated by the "new atheists." Instead of data, Mooney and Kirshenbaum rely on anecdotes. They make much, for example, of Carl Sagan's failure to secure tenure at Harvard or membership in the National Academy of Sciences: "In their treatment of Sagan, the nation's leading scientists had made clear their view of popularizers within their ranks, and of public outreach generally. It was a fateful position." Hardly. Yes, some scientists were jealous or scornful of Sagan's popularity, but he received dozens of awards from scientific organizations, including the National Academy's Public Welfare Medal for contributions to the public good. And how many Americans even knew about these things, anyway?

Other data contradict Mooney and Kirshenbaum's claim that American ignorance of scientific issues reveals a failure of outreach. As the authors themselves note, "college-educated Democrats are now more than twice as likely as college-educated Republicans to believe that global warming is real and is caused by human activities." Surely educated Democrats and Republicans experience similar exposure to scientific facts. All this suggests that the problem of an "unscientific America" may be far more complex than the authors let on. The public's reluctance to accept scientific facts may reflect not just a lack of exposure but a willful evasion of facts due to conflicting economic agendas (e.g., the case of global warming), personal agendas (vaccines), or religious agendas. A recent Pew survey, for instance, found that 55% of Americans see science and religion as often in conflict, and 64% said that if scientists were to disprove a particular religious belief, they would reject the scientific facts in favor of their faith. One could argue, in fact, that overcoming America's resistance to evolution could be accomplished more effectively by weakening religion than by teaching Darwinism.

But *Unscientific America* prescribes just

The reviewer is at the Department of Ecology and Evolution, University of Chicago, 1101 East 57th Street, Chicago, IL 60637–1573, USA. E-mail: j-coyne@uchicago.edu

the opposite: science illiteracy would diminish if vocal atheists like Richard Dawkins would just keep quiet about religion, a sanction that the authors don't impose on publicly religious scientists such as Francis Collins. Unfortunately, Mooney and Kirshenbaum provide no evidence that this prescription would work. Do they really think that if Dawkins had not written *The God Delusion* (*2*), Americans would wholeheartedly embrace evolution and vaccination and finally recognize the threat of global warming?

Mooney and Kirshenbaum's other proposed solution, training scientists in public outreach, does seem like a good idea, though hardly a novel one. After all, who among us wouldn't want Carl Sagan's ability to communicate the joy of science? But the authors fail to tell us how such training should be implemented and, more important, why (given the complex nexus of religious, political, and educational issues that affect the acceptance of science) more outreach is the best solution—or even an effective solution. What good is producing more "renaissance scientists" if nobody listens to them?

More than at any time in my life, I see Americans awash in popular science. Bookstores teem with volumes by Stephen Gould, Steven Pinker, Brian Greene, Steven Weinberg, Richard Dawkins, Michio Kaku, Edward O. Wilson, and Jared Diamond; natural history museums have become user friendly; and entire television channels are devoted to science and nature. Science education is readily available to anyone who is curious. And yes, we scientists need—and want—to share our love of science with the public. Still, we must compete with the infinite variety of claims on people's time and interests, including sports, movies, and reality shows. No matter how much atheists stifle themselves, no matter how many scientists reach out to the public via new media, we may not find the appetite for science infinitely elastic. This does not mean, of course, that we should refrain from feeding it. But figuring out where and how to intervene will take a lot more work than the shallow and unreflective analysis of *Unscientific America*.

References

1. http://scienceblogs.com/pharyngula.
2. R. Dawkins, *The God Delusion* (Bantam, London, 2006); reviewed in (*3*).
3. M. Shermer, *Science* **315**, 463 (2007).

10.1126/science.1179131

THEATER: EVOLUTION

Bridging an Ocean

Claire Thomas

> I am conscious that I am in an utterly hopeless muddle. I cannot think that the world, as we see it, is the result of chance; & yet I cannot look at each separate thing as the result of Design.
> –Charles Darwin to Asa Gray, 26 Nov. 1860

The American botanist Asa Gray was one of the first people in whom Darwin confided his theory on the origin of species; Darwin even discussed his doubts with Gray. Now, archived letters between the two have been brought back to life in Craig Baxter's play *Re:Design*, which tracks the intersection of their lives and their science. The playwright constructed most of the piece with quotes taken verbatim from the prolific correspondence between the two scientists. He has stitched them into a compelling story that traces the growth of Darwin's theories and his friendship with Gray. Baxter notes that "[Gray] made Darwin's ideas acceptable to the religious side in the States. He was very significant in the spread of [evolutionary] ideas to that continent."

Re:Design

by Craig Baxter; directed by Paul Bourne

Menagerie Theatre Company, ADC Theatre, University of Cambridge, UK. July 2009. Darwin Festival Fringe Programme.

The play opens with the two men flanking the stage, pacing their respective rooms on opposite sides of the Atlantic as they muse on their letters. A modern-day character, Jemma, sits center stage, trying to make sense of the letters while researching a video project. The scientists strike up their correspondence in 1855, when Darwin asks Gray for information about the distribution of plants in North America. They bond over shared interests, and later Darwin tentatively tells Gray of his new theories on evolution.

Gray is at first uncertain about natural selection. However, after he receives a copy of *On the Origin of Species*, he is impressed and, despite his faith in Christianity, almost becomes convinced by Darwin's work. When the book sparked great controversy in American scientific and religious circles, Gray played a key role in getting Darwin's ideas accepted in the United States. A public statement of his greatly calmed the opposition: "[We] cannot be expected to let the old belief about species pass unquestioned.… A new theory, like a new pair of breeches, is sure to have hard-fitting places." Darwin, who was not disposed to fight the intense debates surrounding his work, felt indebted to Gray and wrote thankfully: "I should have been fairly annihilated had it not been for four or five men, including yourself.… By myself I should be powerless."

Darwin and Gray continued their correspondence through the U.S. Civil War and the following decades. Apart from science, they exchanged comments on politics, their families, and their health.

First written in 2007 on commission from the Darwin Correspondence Project (*1*), the play has been recast in several formats—from short, 40-minute renditions for scientific conferences to full-length theatrical versions. Baxter explains that the new addition of the contemporary character Jemma was intended to attract more nonscientific audiences. She occasionally steps into Darwin and Gray's time to help remove an overcoat or take a photograph. Although some of these exchanges jar slightly, her presence brings a domestic quality, making the 19th-century scenes seem more accessible.

Voicing Darwin. Terry Molloy as Darwin in *Re:Design*. He also delivered excerpts from Darwin's letters at the start of the Darwin Festival's morning sessions.

The friendship and obvious warmth between the protagonists is the play's most touching aspect. Despite their differences, Darwin and Gray always manage to find common ground. Baxter found their relationship inspirational, because they did not come to loggerheads over evolution versus religion—an all-too-often polarizing topic. He hopes that their example can teach us much about "how intellectual debate can be."

References and Notes

1. www.darwinproject.ac.uk.
2. For additional coverage of the recent Darwin festival in Cambridge, see our evolution blog, http://blogs.sciencemag.org/origins.

10.1126/science.1179422

The reviewer was recently an intern in *Science*'s Cambridge, UK, office. E-mail: clairemmt@hotmail.com

CREDIT: MENAGERIE THEATRE COMPANY

ENVIRONMENTAL SCIENCE

Digital Soil Map of the World

Increased demand and advanced techniques could lead to more refined mapping and management of soils.

Pedro A. Sanchez,[1]* Sonya Ahamed,[1] Florence Carré,[2] Alfred E. Hartemink,[3] Jonathan Hempel,[4] Jeroen Huising,[5] Philippe Lagacherie,[6] Alex B. McBratney,[7] Neil J. McKenzie,[8] Maria de Lourdes Mendonça-Santos,[9] Budiman Minasny,[7] Luca Montanarella,[2] Peter Okoth,[5] Cheryl A. Palm,[1] Jeffrey D. Sachs,[1] Keith D. Shepherd,[10] Tor-Gunnar Vågen,[10] Bernard Vanlauwe,[5] Markus G. Walsh,[1] Leigh A. Winowiecki,[1] Gan-Lin Zhang[11]

Soils are increasingly recognized as major contributors to ecosystem services such as food production and climate regulation (*1*, *2*), and demand for up-to-date and relevant soil information is soaring. But communicating such information among diverse audiences remains challenging because of inconsistent use of technical jargon, and outdated, imprecise methods. Also, spatial resolutions of soil maps for most parts of the world are too low to help with practical land management. While other earth sciences (e.g., climatology, geology) have become more quantitative and have taken advantage of the digital revolution, conventional soil mapping delineates space mostly according to qualitative criteria and renders maps using a series of polygons, which limits its resolution. These maps do not adequately express the complexity of soils across a landscape in an easily understandable way.

Maps can provide soil inputs (e.g., texture, organic carbon, and soil-depth parameters) to models predicting land-cover changes in response to global climatic and human disturbances.

The Food and Agriculture Organization (FAO) of the United Nations (UN) and the UN Educational, Scientific and Cultural Organization (UNESCO) published the first world soil map in 1981, using a single soil classification terminology (*3*). The map has been utilized in many global studies on climate change, food production, and land degradation. But its low resolution (1:5 million scale) is not suitable for land management decisions at field or catchment scales. One of the most-cited soil degradation studies, the *Global Assessment of Human Induced Soil Degradation*, is based on expert judgment by a few individuals, has very low resolution (1:50 million scale), and lacks quantitative information on soil properties that indicate the degree of soil degradation (*4*). At present, 109 countries have conventional soil maps at a scale of 1:1 million or finer, but they cover only 31% of the Earth's ice-free land surface, leaving the remaining countries reliant on the FAO-UNESCO map (*5*). [See supporting online material (SOM) for more history.]

To address these many shortcomings, soil scientists should produce a fine-resolution, three-dimensional grid of the functional properties of soils relevant to users. We call for development of a freely accessible, Web-based digital soil map of the world that will make georeferenced soil information readily available for land-users, scientists, and policy-makers. A foundation for such an effort is being laid by the GlobalSoilMap.net (GSM) project. This effort originated in 2006 (*6*) in response to policy-makers' frustrations at being unable to get quantitative answers to questions such as: How much carbon is sequestered or emitted by soils in a particular region? What is its impact on biomass production and human health? How do such estimates change over time?

The GSM consortium's overall approach consists of three main components: digital soil mapping, soil management recommendations, and serving the end users—all of them backed by a robust cyberinfrastructure. [See fig. S1, expanded from (*7*).] Specific countries may add their own modifications.

Digital Soil Mapping

Digital soil mapping began in the 1970s (*8*) and accelerated significantly in the 1980s because of advances in information and remote-sensing technologies, computing, statistics and modeling, spatial information and global positioning systems, measurement systems (such as infrared spectroscopy), and in more recent times, online access to information. Experimentation with these technologies is leading toward consensus (*7*, *9*–*12*), and operational systems are being implemented.

A digital soil map is essentially a spatial database of soil properties, based on a statistical sample of landscapes. Field sampling is used to determine spatial distribution of soil properties, which are mostly measured in the laboratory. These data are then used to predict soil properties in areas not sampled. Digital soil maps describe the uncertainties associated with such predictions and, when based on time-series data, provide information on dynamic soil properties. They also differ from conventional, polygon-based maps, in that they are pixel-based and can be more easily displayed at higher resolutions currently used by other earth and social sciences.

There are three main steps in digital soil mapping. Step 1, data input, starts with the production of base maps, assembling and calibrating spatially contiguous covariates from available data [e.g., the 90- × 90-m resolution digital terrain models from Shuttle Radar Topography Mission (SRTM v.3)]. Covariates, reflecting state factors of soil forma-

[1]Earth Institute at Columbia University, 61 Route 9W, Palisades, NY 10964, USA. [2]Joint Research Centre, European Commission, 21020 Ispra, VA, Italy. [3]ISRIC–World Soil Information, 6700 AJ, Wageningen, Netherlands. [4]National Soil Survey Center, U.S. Department of Agriculture Natural Resources Conservation Service, Lincoln, NE 68508, USA. [5]Tropical Soil Biology and Fertility Institute of the International Center for Tropical Agriculture, Post Office Box 30677, Nairobi, Kenya. [6]Laboratoire d'Étude des Interactions Sols-Agrosystèmes-Hydrosystèmes, L'Institut National pour la Recherche Agronomique, Institut de Recherche pour Développement, SupAgro, 34060 Montpellier 1, France. [7]Faculty of Agriculture, Food and Natural Resources, The University of Sydney, Sydney, NSW 2006, Australia. [8]Commonwealth Scientific and Industrial Research Organization (CSIRO) Land and Water, Government Post Office Box 1666, Canberra, ACT, 2601, Australia. [9]EMBRAPA–Brazilian Agricultural Research Corporation, The National Center of Soil Research, Rua Jardim Botânico, 1024, 22.460-000, Rio de Janeiro, Brazil. [10]World Agroforestry Centre, Post Office Box 30677–00100, Nairobi 00100, Kenya. [11]State Key Laboratory of Soil and Sustainable Agriculture, Institute of Soil Science of the Chinese Academy of Sciences, Nanjing, China.

*Author for correspondence. E-mail: psanchez@ei.columbia.edu

Published by AAAS

tion (*13*–*15*), include climate information (e.g., temperature, rainfall, evaporation); land cover (e.g., Normalized Difference Vegetation Index); a range of digital terrain variables; and geological variables relating to soil parent materials (e.g., airborne gamma radiometric spectroscopy).

In developed countries, there may be sufficient point soil observations to allow putting a fraction aside to subsequently test and cross-validate the map for "ground truth." In Africa, ground-truthing has been built into the system. Over the next 4 years, experimental sites will be established in 60 sentinel landscapes, which have been randomized across an 18.1 million km^2 of sub-Saharan Africa.

Collection of legacy soils data (preexisting, georeferenced field or laboratory measurements) is an important part of step 1. Major investment in new soil measurement will be required in countries having sparse soil legacy data.

Step 2 involves estimation of soil properties, expressed as probabilities of occurrence (*16*). They are derived by using quantitative relations between point soil measurements and the spatially continuous covariates. This results in maps of soil properties, such as the ones selected by the GSM consortium as the minimum data set—clay content, organic carbon content, pH, estimated cation-exchange capacity, electrical conductivity, and bulk density (to convert carbon and nutrients on a mass basis to a land-surface-area basis for biogeochemical modeling). This process enables production of maps that use a range of soil classification systems.

In step 3, spatially inferred soil properties are used to predict more difficult-to-measure soil functions, such as available soil water storage, carbon density, and phosphorus fixation. This is achieved using pedotransfer functions (*11*), including those in the Fertility Capability Classification system (*17*, *18*), such as aluminum toxicity, or those included in environmental models (*15*). These soil functions largely determine the capacity of soils to deliver various provisioning and regulating ecosystem services. The overall uncertainty of the prediction is assessed by combining uncertainties of input data, spatial inference, and soil functions.

Soil Management Recommendations

After the three-step soil-mapping process, data from reliable, georeferenced field trials are compiled in step 4. This step is analogous to the data capture of step 1, except that the covariates in this case are "social": digital maps of land use, agroecological zones, farming systems, crop yields, poverty, road density, and input supply networks, as well as crop models, such as those being assembled by HarvestChoice (*19*). These social covariates address additional state factors of soil formation: organisms (other than vegetation), time, and human activities (*13*, *14*). Legacy data from field trials are used to develop models and transfer functions for specific soil management recommendations. (See SOM for further information.)

Serving the End Users

Step 5 is to develop evidence-based soil management recommendations. This relies on analysis of soil functions of step 3 and the legacy data, social covariates, and new experimental data obtained in step 4. Resulting maps and management recommendations form a baseline against which changes can be monitored and evaluated over time. Principal user groups are typically agricultural extension workers and policy-makers whose main task is to reverse soil degradation, to preserve and maintain soil health, and to improve food security and household livelihoods. Other users include research and modeling communities, farmer associations, environmental extension services, agribusinesses, and nongovernmental and civil society organizations. The cyberinfrastructure should encourage feedback, with appropriate quality standards developed for the incorporation of such information.

Products will be tailored to specific needs of end users. For commercial farmers and national planners, the basic 90-m resolution is appropriate (roughly equivalent to 1:90,000 scale). The basic product for smallholder farmers might be at 30-m resolution. For some research, for example, studies of nutrient cycling, resolution may need to be finer, whereas for a study of global fertilizer policy a 1-km resolution may suffice.

Effective irrigation is another application requiring high-quality soil information. For example, in order to alleviate droughts in the central North China Plain, more water is often pumped into fields than the soil can hold. In the long run, irrigation must be tuned to local soil conditions (e.g., profile water storage and permeability) to alleviate water scarcity.

Developments in geographic information systems, online services, and mobile technologies are providing new ways to build, leverage, and disseminate spatial information. The intergovernmental Group on Earth Observations (GEO) is building the cyberinfrastructure needed to link numerous emerging systems for monitoring and predicting global environmental change. GEO is orchestrating these efforts through the Global Earth Observation System of Systems (GEOSS), a network of content providers intended to support a wide variety of end users (*20*). Digital soil information is likely to be welcomed by such groups. For example, GSM will focus on providing soil inputs (e.g., texture, organic carbon, and soil-depth parameters) to Soil-Vegetation-Atmosphere Transfer models that are used to predict land-cover changes in response to anticipated climatic and human disturbances across the globe.

A new generation of soil scientists must be trained in this approach. The resultant new maps and management recommendations will help address some of the main challenges of our time: food security, climate change, environmental degradation, water scarcity, and threatened biodiversity.

References and Notes

1. C. A. Palm, P. A. Sanchez, S. Ahamed, A. Awiti, *Annu. Rev. Environ. Resour.* **32**, 99 (2007).
2. Millennium Ecosystems Assessment, *Ecosystems and Human Well-Being* (Island Press, Washington, DC, 2005).
3. FAO-UNESCO, "Soil map of the world: Revised legend (with corrections and updates)" (World Soil Resources Report 60, FAO, Rome, 1988).
4. L. R. Oldeman, R. T. A. Hakkeling, W. G. Sombroek, *World Map of the Status of Human-Induced Soil Degradation: Explanatory Note* (ISRIC–UN Environment Programme, Wageningen, 1991).
5. F. O. Nachtergeale, E. van Ranst, in *Evolution of Tropical Soil Science, Past and Present*, G. Stoops, Ed. (Koninklijke Academie voor Overzeese Wetenschnappen, Brussels, p. 107–126 (2003).
6. A. E. Hartemink, A. B. McBratney, M. L. Mendonça-Santos, Eds., *Digital Soil Mapping with Limited Data* (Springer, New York, 2008).
7. B. Minasny, A. B. McBratney, R. M. Lark, in (*6*), pp. 15–30.
8. R. Webster, P. A. Burrough, *J. Soil Sci.* **23**, 210 (1972).
9. P. Lagacherie, A. B. McBratney, M. Volz, Eds., *Digital Soil Mapping: An Introductory Perspective* (Elsevier, Amsterdam, 2007).
10. Third Global Workshop on Digital Soil Mapping, Bridging Research, Production and Environmental Applications, 30 September to 3 October 2008, Logan, Utah (CD).
11. B. Minasny, A. B. McBratney, F. Carré, in *Encyclopedia of Soil Science*, R. Lal, Ed. (CRC Press, Boca Raton, FL, 2008).
12. N. J. McKenzie, M. J. Grundy, R. Webster, A. J. Ringrose-Voase, *Guidelines for Surveying Soils and Land Resources* (CSIRO Publishing, Melbourne, ed. 2, 2008), 557 pp.
13. H. Jenny, *Factors of Soil Formation* (McGraw-Hill, New York, 1941).
14. H. Jenny, *Soil Sci. Soc. Am. Proc.* **25**, 385 (1961).
15. A. B. McBratney, M. L. Mendonça-Santos, B. Minasny, *Geoderma* **117**, 3 (2003).
16. F. Carré, A. B. McBratney, T. Mayr, L. Montanarella, *Geoderma* **142**, 69 (2007).
17. P. A. Sanchez, W. Couto, S. W. Buol, *Geoderma* **27**, 283 (1982).
18. P. A. Sanchez, C. A. Palm, S. W. Buol, *Geoderma* **114**, 157 (2003).
19. HarvestChoice, www.harvestchoice.org.
20. GEO–Group on Earth Observations, www.earthobservations.org (2008).

21. The authors are grateful to the Bill & Melinda Gates Foundation, the Alliance for a Green Revolution in Africa and the authors' institutions for providing support. B.M. and A.B.M. were funded by the Australian Research Council for their contributions to methodology for the project.

Supporting Online Material

www.sciencemag.org/cgi/content/full/325/5941/680/DC1

10.1126/science.1175084

ECOLOGY

Barcoding of Plants and Fungi

Mark W. Chase and Michael F. Fay

DNA barcoding enables rapid and accurate identification of species in many groups of organisms, but cannot always distinguish between closely related species of land plants or fungi.

Rapid identification of biological specimens or fragments of biological origin has always been desirable, but has rarely been possible owing to a shortage of natural history specialists. Very often, for a particular group of organisms there is only one expert worldwide, and no one person can be expected to identify every organism that is relevant to ecological studies. Also, environmental samples (for example, from water or soil) that contain mixtures of minute organisms with few morphological traits pose great identification challenges. Short, standardized DNA regions—or "barcodes"—have been used to identify biological material from many groups of animals (*1*–*3*). The barcoding approach also has great potential for identifying plants (*4*, *5*) and fungi (*6*), but faces different challenges when applied to these groups.

For animals and algae, a fragment of mitochondrial cytochrome oxidase I—often called *coxI* or COI—has been developed as a universal DNA barcode (*7*). In this fragment, the level of variation between species (interspecific) is much larger than that within a species (intraspecific). This DNA "barcode gap" (*8*) usually enables clear-cut identification, because even closely related species are easily distinguished. In the context of conservation and restoration ecology, the first relevant question is which species are present, and DNA barcoding is well suited to addressing this question quickly and accurately for many organisms.

In most land plants and fungi, the standard region of *coxI* is not suitable for use as a DNA barcode, because the mitochondrial genes in these groups evolve too slowly to allow accurate discrimination between species. In addition, in fungi these genes are subject to duplications. Thus, other alternatives have been sought. In fungi, the internal transcribed spacers (ITS) of nuclear ribosomal DNA have been selected as the best alternative DNA region (*9*), whereas in land plants, two short coding regions of plastid DNA (*matK* and *rbcL*) have been selected (*10*). The biggest problem with these regions is that in many plants and fungi, there is no barcode gap (*11*): There are relatively few differences between the barcodes for closely related species, making identification in these groups less definitive.

Rapid identification. *Fritillaria meleagris*, the snake's head fritillary, is a rare plant in southern England. The barcode for this species, based on the gene *rbcL*, enables rapid identification of this and other plant species.

Nonetheless, most species can be distinguished through the use of these alternative markers. For example, the CBOL Plant Working Group has recently shown that in plants, an average of 72% of species can be distinguished (*10*); by restricting the scope of the reference database to those known to occur in a specific habitat or region, a much greater degree of discrimination is possible—probably close to 100% in many cases (*12*). Not all close relatives of a given species occur in the area under study, so the inability to easily distinguish these other species from those in the study zone is irrelevant.

Theoretically, barcoding based on nuclear DNA, which is inherited from both parents, would provide much more information than barcoding based on organellar DNA, which is inherited from only one parent. Nevertheless, all standard barcoding regions used in plants and animals to date are based on organellar DNA, for reasons of a practical nature: It is easier to sequence without the need for cloning and is less likely to occur in multiple copies than most nuclear loci (*5*).

Uniparentally inherited markers as DNA barcodes have limitations: For example, in the case of plants, hybrids will go unrecognized and will be identified as their plastid donor parent (the maternal parent in nearly all flowering plants). But the great advantages of rapid identification of potentially thousands of individuals outweighs the inability to identify hybrids. In the future, use of multiple regions of nuclear low-copy genes (which are present in 1 to less than 10 copies) should permit identification of hybrids and probably also overcome the lower levels of discrimination afforded by the use of more slowly evolving DNA regions in plants and fungi (*5*, *13*).

A second question of relevance in conservation studies and restoration ecology relates to the place of origin of individual genotypes within the range of the species in question, particularly if the species is widespread. Provenance is often an issue in conservation and restoration, because knowing its geographical origin provides clues about how best to conserve that species and where a given geographical variant might be best able to survive if it is to be placed in a habitat undergoing restoration. Lukhtanov *et al*. have shown that in the case of the rapidly evolving *coxI*, many animals and algae exhibit some degree of geographical variation (*14*), providing at least some capacity to address the issue of provenance. In the case of land plants and fungi, the DNA markers evolve much less quickly than *coxI*, substantially reducing the possibilities for addressing the question of provenance.

DNA barcoding is in its infancy. The currently used DNA markers are crude tools relative to the biological complexity we wish to identify. Many mistakes will no doubt be made, and the limitations of these DNA markers must be kept in mind. In particular, hybrids and multiple closely related species occupying the same area pose currently insurmountable obstacles to the goal of both rapid and highly accurate identification.

Nonetheless, the obvious benefits of rapid identification of massive numbers of samples makes it imperative to push forward and develop the reference databases needed to make DNA barcoding as effective as pos-

Jodrell Lab, Royal Botanic Gardens Kew, Kew, Richmond, Surrey TW9 3DS, UK. E-mail: m.fay@rbgkew.org.uk

sible (*15*). In the not too distant future, alternative barcodes based on more rapidly evolving nuclear regions may allow provenance to be determined and hybrids to be identified (*5*, *13*). Together with the current uniparentally inherited regions, these nuclear regions may yield a DNA barcoding system sophisticated enough to deal with the biological complexities facing biodiversity scientists.

References

1. P. D. N. Hebert *et al.*, *PLoS Biol.* **2**, e312 (2004).
2. R. D. Ward *et al.*, *Philos. Trans. R. Soc. London Ser. B* **360**, 1847 (2005).
3. M. Hajibabaei *et al.*, *Proc. Natl. Acad. Sci. U.S.A.* **103**, 968 (2006).
4. W. J. Kress *et al.*, *Proc. Natl. Acad. Sci. U.S.A.* **102**, 8369 (2005).
5. M. W. Chase *et al.*, *Philos. Trans. R. Soc. London Ser. B* **360**, 1889 (2005).
6. L. Tedersoo *et al.*, *New Phytol.* **180**, 479 (2008).
7. P. D. N. Hebert *et al.*, *Proc. R. Soc. London Ser. B.* **270**, 313 (2003).
8. M. Wiemers, K. Fiedler, *Front. Zool.* **4**, 8 (2007).
9. T. R. Horton, T. D. Bruns, *Mol. Ecol.* **10**, 1855 (2001).
10. CBOL Plant Working Group, *Proc. Natl. Acad. Sci. U.S.A.* 10.1073/pnas.0905845106 (2009).
11. R. Lahaye *et al.*, *Proc. Natl. Acad. Sci. U.S.A.* **105**, 2923 (2008).
12. J. R. Starr *et al.*, *Mol. Ecol. Res.* 10.1111/j.1755-0998.2009.02640.x (2009).
13. K. K. Dasmahapatra, J. Mallet, *Heredity* **97**, 254 (2006).
14. V. Lukhtanov *et al.*, *Mol. Ecol. Res.* 10.1111/j.1755-0998.2009.02577.x. (2009).
15. C. Thomas, *Science* **324**, 1632 (2009).

Published online 30 July 2009;
10.1126/science.1176906
Include this information when citing this paper.

ASTRONOMY

Cosmic-Ray Acceleration in Supernova Remnants

John C. Raymond

Combined x-ray and optical observations of a supernova remnant reveal details of the origin and mechanism of cosmic-ray acceleration.

Cosmic rays are ubiquitous in our Galaxy and exhibit a power-law spectrum in their energy distribution up to a "knee" at around 10^{15} eV, where the power law steepens. It is generally accepted that cosmic rays up to the knee are accelerated by the strong shock waves in supernova remnants, but the efficiency of this acceleration process remains largely unknown. On page 719 of this issue, Helder *et al*. (*1*) combine x-ray and optical observations of a supernova remnant to obtain a lower limit to the acceleration efficiency in a fast shock.

The belief that cosmic-ray acceleration occurs in supernova remnants rests partly on the fact that the power needed to maintain the cosmic rays corresponds to about 10% of the kinetic energy dissipated by supernova shocks. Simply, no obvious alternative exists. A supernova remnant shock origin is also supported by radio and x-ray observations of supernova remnants, showing power-law spectra from synchrotron emission by electrons at least up to 10^{14} eV, and by theoretical models that predict efficient particle acceleration in fast shock waves (termed "diffusive shock acceleration") (*2*).

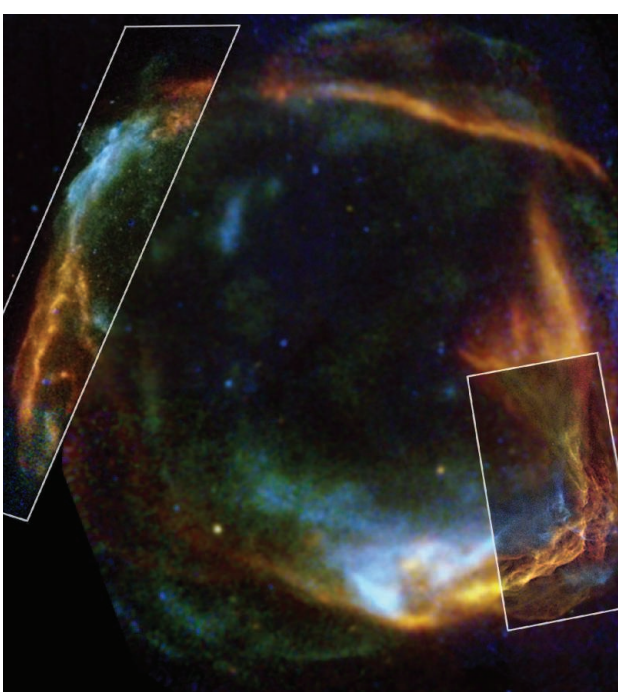

CREDIT: CHANDRA, NASA/CXC/UNIV. OF UTRECHT/J. VINK *ET AL.*

Shocking energetics. Composite x-ray image of RCW 86. Low-resolution data for the full remnant are from the XMM-Newton satellite; the higher-resolution data in the rectangles are from Chandra. The lower energies (red) are largely thermal emission, whereas the higher energies (blue) are dominated by synchrotron emission from relativistic electrons (*11*).

However, although models of the diffusive shock acceleration process predict a power-law spectrum of energetic particles, they do not yet make a robust prediction for the acceleration efficiency—the fraction of energy dissipated in the shock that goes into energetic particles. Because electrons account for only about 1% of the cosmic rays, x-ray and radio measurements of the synchrotron spectrum cannot directly address this problem. Gamma rays from supernova remnants are sometimes attributed to interactions between relativistic protons and nuclei in the ambient interstellar medium (*3*). This interpretation remains ambiguous (*4*), but observations with the recently launched FERMI satellite will help to resolve the issue. Measurements of shocks in the solar wind should pin down the physics of particle acceleration, but those shocks do not reach the extreme energies seen in supernova remnants.

Therefore, a number of indirect estimates of acceleration efficiency have been made. One method uses the compression of the postshock gas, which is stronger if a substantial fraction of the shock energy goes in to relativistic particles (*5*). In another method, the shock speed is estimated from the supernova remnant distance and the motion of shock filaments across the sky, giving the total shock energy available; any difference between that energy and the postshock thermal energy is ascribed to cosmic rays (*6*, *7*). A limitation of this method is that it relies on the electron temperature measured from the thermal x-ray spectrum to determine the postshock energy, and the electron and proton temperatures can differ (*8*).

Helder *et al*. apply a different method to obtain the postshock thermal energy. When a shock moves through partially neutral gas, H atoms do not feel the shock itself, because they do not respond to electromagnetic fields or plasma turbulence. However, some of the neutral atoms undergo charge transfer reactions with protons downstream, producing a population of neutral atoms with a velocity distribution similar to that of the shocked protons. These atoms can emit Hα photons during the charge transfer process or during subsequent collisional excitation, producing a broad Hα profile that can be used to determine the proton temperature (*9*, *10*).

RCW 86 is a fairly young, well-studied supernova remnant believed to have originated

Harvard-Smithsonian Center for Astrophysics, 60 Garden Street, Cambridge, MA 02138, USA. E-mail: raymond@cfa.harvard.edu.

with an explosion in 185 CE (*11*, *12*) (see the figure). Helder *et al*. now combine x-ray and optical observations of RCW 86 to determine the acceleration efficiency. They measured the shock speed from the motion of the shock front seen in x-ray images obtained by the Chandra satellite in 2004 and 2007, and they find a surprisingly high shock speed of 6000 ± 2800 km/s. They also analyze a Hα profile obtained with the European Southern Observatory's Very Large Telescope. The width of the broad Hα profile yields a proton temperature of only 2.3 keV. The high shock speed and modest proton temperature imply that more than half of the shock energy goes into cosmic rays, enough to match the requirements of cosmic-ray acceleration by supernova shocks.

It is important to verify this new result. Another Chandra image in a year or two would drastically reduce the uncertainty in the shock speed. The efficiency of shock acceleration is likely to depend on the angle between the shock and the magnetic field (*13*), so observations at different positions around RCW 86 or in other supernova remnants will be valuable. The efficiency may also depend on the neutral fraction in the preshock gas or on the plasma density, so observations of other Hα filaments will be important.

References

1. E. A. Helder *et al*., *Science* **325**, 719 (2009); published online 25 June 2009 (10.1126/science.1173383).
2. R. A. Blandford, D. Eichler, *Phys. Rep.* **154**, 1 (1987).
3. E. G. Berezhko, G. Pühlhofer, H. Völk, http://arxiv.org/abs/0906.5158 (2009).
4. B. Katz, E. J. Waxman, *J. Cosmol. Astropart. Phys.* 10.1088/1475-7516/2008/01/018 (2008).
5. J. S. Warren *et al*., *Astrophys. J.* **634**, 376 (2005).
6. J. P. Hughes *et al*., *Astrophys. J.* **543**, L61 (2000).
7. G. Salvesen, J. C. Raymond, R. J. Edgar, http://arxiv.org/abs/0812.2515 (2008).
8. P. Ghavamian, J. M. Laming, C. E. Rakowski, *Astrophys. J.* **654**, L69 (2007).
9. R. A. Chevalier, J. C. Raymond, *Astrophys. J.* **225**, L27 (1978).
10. M. van Adelsberg *et al*., *Astrophys. J.* **689**, 1089 (2008).
11. J. Vink *et al*., *Astrophys. J.* **648**, L33 (2006).
12. F. Aharonian *et al*., *Astrophys. J.* **692**, 1500 (2009).
13. G. Cassam-Chenai *et al*., *Astrophys. J.* **680**, 1180 (2008).

10.1126/science.1177743

CELL BIOLOGY

Lethal Traffic Jam

Antibiotics activate a pathway that disables protein secretion in bacteria.

Eefjan Breukink

The antibiotics chloramphenicol and tetracycline were discovered in the late 1940s shortly after the introduction of penicillin (*1*). Elucidation of the structure of the ribosome (*2*, *3*) revealed how they bind to this target structure and inhibit protein synthesis. On page 753 in this issue, van Stelten *et al*. (*4*) demonstrate another mode of action for these antibiotics, involving the destruction of a complex that allows proteins to be translocated across (or into) the bacterial membrane (*5*).

Protein translocation across (or into) the bacterial inner membrane requires the combined action of several secretory (Sec) proteins that function in a single membrane-associated complex. A protein that is destined for secretion possesses a signal sequence at its amino terminus, which directs it to a translocator complex that is formed by SecY, E, G, and A proteins (see the figure) (*6*–*8*). In principle, cytoplasmic proteins can also be secreted if they are "tagged" with a signal sequence. However, apart from successful translocation of such hybrid proteins into the periplasm, two other scenarios are possible, both of which depend on folding characteristics of the fusion protein. One is that misfolding of the protein after its translocation into the periplasm can lead to the formation of toxic aggregates. Another possibility is that a fast-folding hybrid protein can jam the translocator complex, which also leads to cell death (because all protein secretion is inhibited). The build-up of aggregates in the periplasm triggers a stress response (mediated by the two-component Cpx regulatory system) which, among other effects, leads to the production of a periplasmic protease (DegP) that removes the toxic aggregates.

Both of the latter scenarios can occur upon synthesis of a fusion protein used by van Stelten *et al*., composed of a cytoplasmic

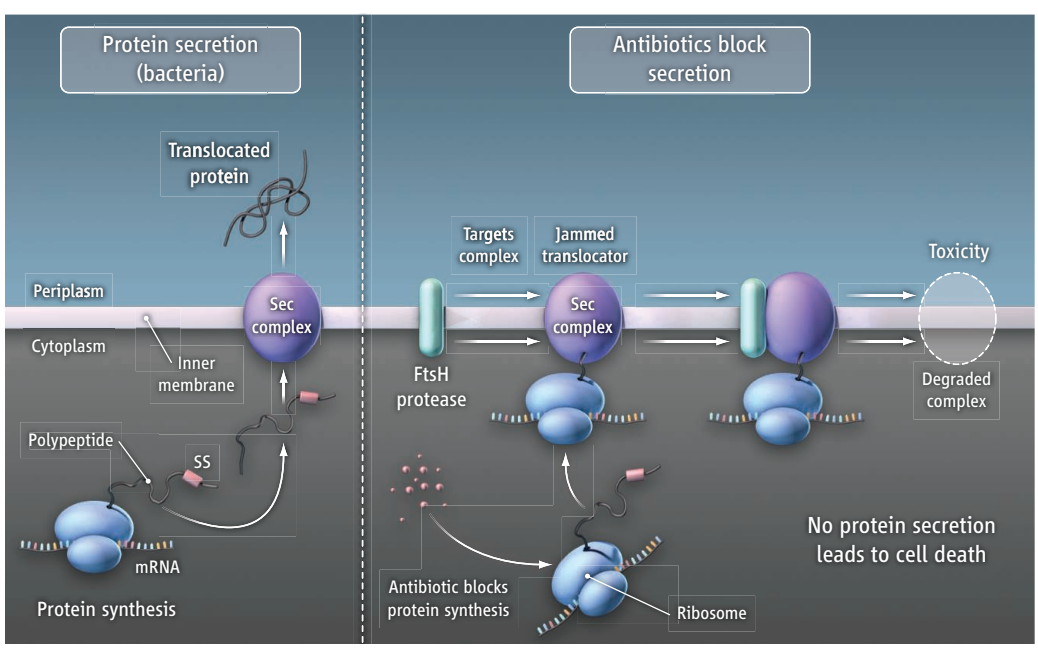

Traffic jam. (**Left**) Proteins that are transported across the bacterial membrane are synthesized as precursors with an amino-terminally located signal sequence (SS). Under normal conditions these are directed toward the protein translocator (Sec complex) formed by Sec A, Y, E, and G (posttranslational protein translocation is shown). (**Right**) When bacteria are treated with antibiotics (chloramphenicol or tetracycline), ribosomes synthesizing precursor proteins are targeted to the Sec complex and cause it to become jammed. This jamming event activates FtsH, which degrades the SecY and E components of the translocation machinery.

CREDIT: C. BICKEL/*SCIENCE*

Department of Chemical Biology and Organic Chemistry, Utrecht University, Padualaan 8, 3584 CH Utrecht, Netherlands. E-mail: e.j.breukink@uu.nl

enzyme β-galactosidase (LacZ) and a signal sequence. Robust synthesis of the fusion protein jammed the Sec translocator, leading to cell death. Relieving this effect caused the proteins to form toxic aggregates in the periplasm, also toxic to the cell. The lethality of both situations could be overcome by activating the Cpx-mediated stress response (which leads to DegP production). But if DegP only exerts its effect in the periplasm, then an additional factor that is also Cpx related must relieve translocator jamming. The additional factor turns out to be the protein YccA. YccA is a substrate for FtsH, a membrane-embedded protease that functions in the quality control of membrane proteins. Van Stelten *et al*. show that when the translocator gets jammed, FtsH degrades SecY, and to a lesser extent SecE. This is an apparent suicide attempt by the bacterium because functional SecY in the membrane (as part of the Sec complex) is required for the newly synthesized SecY to translocate and insert into the membrane. Regulating FtsH activity is thus essential because uncontrolled degradation of SecY is lethal. YccA is the bacterial homolog of Bax inhibitor–1, a human protein involved in the stress response within the endoplasmic reticulum (*9*). Overexpression of YccA in bacteria relieved lethal jamming of the Sec translocator, further demonstrating that SecY degradation is the main cause of the lethality of the jamming event.

Why would treatment of bacteria with chloramphenicol or tetracycline lead to degradation of SecY? These antibiotics stop the translation of messenger RNA into protein, leaving incomplete polypeptides that are firmly attached to ribosomes (see the figure). Ribosomes bearing polypeptides with a signal sequence are as effective in lethally jamming the translocator complex as are the fast-folding cytoplasmic proteins that are fused to a signal sequence; both induce translocator degradation. A key question is the extent to which the antibiotic-induced degradation of SecY contributes to the efficacy of the antibiotics.

Because of its indispensability and uniqueness, the bacterial protein secretion machinery has long been recognized as an attractive drug target (*10*–*12*). Yet after almost 20 years of research, there are still no successful candidates that target this pathway. This makes the discovery of an additional mode of action of chloramphenicol and tetracycline even more interesting. Apparently, this pathway was already (albeit indirectly) targeted by clinically used antibiotics—we just didn't realize it. This raises the question of whether other ribosomal-targeting antibiotic classes also cause degradation of the translocator. The aminoglycoside antibiotics such as gentamycin and kanamycin induce serious errors in proteins during their synthesis that result in misfolded proteins. These antibiotics also trigger the Cpx system (*13*) due to the accumulation of misfolded proteins in the plasma membrane or periplasm. Whether this also leads to SecY degradation is not yet known, but in view of the results of van Stelten *et al*., this seems highly likely.

The manner in which the protein translocation pathway is affected by FtsH also marks a potentially therapeutic route to target bacteria. Successful dysregulation of the cytoplasmic protease ClpP by acyldepsipeptide antibiotics leads to uncontrolled proteolysis (*14*). Thus, in cases where direct action of antibiotics on the translocation machinery seems out of reach, dysregulation of FtsH may be an alternate mode of action for a new class of antibiotics.

References

1. C. Walsh, *Nat. Rev. Microbiol.* **1**, 65 (2003).
2. M. Pioletti *et al*., *EMBO J.* **20**, 1829 (2001).
3. F. Schlünzen *et al*., *Nature* **413**, 814 (2001).
4. J. van Stelten, F. Silva, D. Belin, T. J. Silhavy, *Science* **325**, 753 (2009).
5. A. R. Osborne, T. A. Rapoport, *Cell* **129**, 97 (2007).
6. A. J. Driessen, N. Nouwen, *Annu. Rev. Biochem.* **77**, 643 (2008).
7. T. A. Rapoport, *Nature* **450**, 663 (2007).
8. J. Zimmer, Y. Nam, T. A. Rapoport, *Nature* **455**, 936 (2008).
9. F. Lisbona *et al*., *Mol. Cell* **33**, 679 (2009).
10. A. Economou, *Expert Opin. Ther. Targets* **5**, 141 (2001).
11. R. Misra, T. J. Silhavy, in *Emerging Targets in Antibacterial and Antifungal Therapy*, J. Sutcliffe, N. Georgopapadakou, Eds. (Chapman & Hall, New York, 1992), pp. 163–175.
12. C. Stephens, L. Shapiro, *Chem. Biol.* **4**, 637 (1997).
13. M. A. Kohanski, D. J. Dwyer, J. Wierzbowski, G. Cottarel, J. J. Collins, *Cell* **135**, 679 (2008).
14. H. Brotz-Oesterhelt *et al*., *Nat. Med.* **11**, 1082 (2005).

10.1126/science.1178424

CHEMISTRY

Designer Curvature

Complex nanostructures can be created by systematically tuning the bending and twisting of synthetic DNA assemblies.

Yan Liu[1,2] and Hao Yan[1,2]

Biological systems create marvelous devices with nanometer-scale dimensions and precisely controlled three-dimensional (3D) architectures. Scientists have long dreamed of creating artificial nanostructures that mimic nature's elegance. One example is DNA nanotechnology (*1*), which uses DNA as a molecular engineering material to create nanostructures with controlled geometries, topologies, and periodicities and to organize matter with nanometer precision. On page 725 of this issue, Dietz *et al*. (*2*) report an elegant strategy for transforming 3D DNA nanostructures into complex geometric shapes with systematically controlled curvatures. It is as if DNA has been subjected to the practice of yoga to display a variety of difficult postures at the nanoscale.

Self-assembly of DNA nanostructures with controlled 3D architectures has long been a central goal of DNA nanotechnology (*3*) and has recently begun to see some success (*4*–*10*). However, methods for creating programmable, quantitatively controlled bending and twisting of 3D DNA nanostructures have remained elusive. This fundamental design capability is necessary to construct sophisticated molecular machines that can mimic, or even rival, structures built in the biological and macroscopic worlds.

Natural DNA molecules can assume tightly bent and twisted conformations (*11*). For example, in eukaryotic cells, DNA is packed into nucleosomes, in which DNA bends around histone proteins with a radius of curvature as small as ~4.3 nm (much smaller than its persistence length of ~50 nm, which measures the stiffness of the double-helical DNA polymer). DNA is also tightly bent by many proteins that regulate transcription processes. These natural examples show that DNA is mechanically flexible, with bending and twisting generally facilitated by externally bound protein molecules.

Dietz *et al*. (*2*) now show that DNA curvature can be controlled in synthetic systems by self-assembly of longer double helices laterally coupled to shorter ones whose axes are parallel to those of the longer ones—reminiscent of adjacent lanes on a curving sprint

[1]The Biodesign Institute, Arizona State University, Tempe, AZ 85287, USA. [2]Department of Chemistry and Biochemistry, Arizona State University, Tempe, AZ 85287, USA. E-mail: hao.yan@asu.edu

track. Thus, the forces required for bending are transmitted by adjacent DNA double helices rather than by DNA binding proteins.

The principal building block is based on a multilayer 3D DNA nanostructure developed earlier this year by the same group (*9*). In that work, the authors devised a DNA folding strategy to create geometrically complex 3D DNA nanostructures. In doing so, they extended the 2D "scaffolded DNA origami" technique (*12*) to a third dimension.

In the original 2D technique, a long single-stranded viral genome (the "scaffold strand") is laid out in a 2D plane following a designated folding path. Next, hundreds of short oligonucleotide "staple strands" hybridize with the scaffold strand through complementary base pairing to form branched DNA junctions between adjacent helices.

To create 3D DNA nanostructures, Shih and co-workers (*9*) packed parallel corrugated multihelical DNA sheets into honeycomb lattices, with neighboring DNA helices connected by staple strands crossing over from one to another in a 3D space. In these structures, repeating DNA double-helical units of 7 base pairs are brought together by staple strands crossing over in 3D space (see the figure, panel A). Relaxed double-stranded DNA forms a right-handed double helix with ~10.5 base pairs per turn. Thus, a 7–base pair block of a DNA double helix corresponds to two-thirds of one turn, and staple-strand crossovers implemented every 7 base pairs along a helix cross-link that helix to its three nearest neighbors at 120° intervals. By tuning the number, arrangement, and length of each helix, the authors constructed a variety of 3D shapes.

To enable the 3D DNA nanostructure to bend or twist, Dietz *et al*. (*2*) varied the number of base pairs in the building blocks at selected positions, such that the local DNA helical structure deviates from 10.5 base pairs per turn. To introduce a global twist, selected layers of 7–base pair units along the bundle of helices are extended to 8 base pairs or reduced to 6 base pairs, resulting in a local under- or over-twisting of DNA helices, respectively (see the figure, panel B). These local strains can be relieved somewhat by a global twisting of the entire structure in the opposite direction (see the figure, panel C).

To bend the structure, Dietz *et al*. (*2*) modified a layer of 7–base pair units by deleting base pairs on one side and inserting base pairs on the other side, which results in contraction on the concave face and expansion on the convex face, respectively (see the figure, panel D). By manipulating the number of insertions and deletions, bending over a 98–base pair length can be precisely tuned from 0° to 180°, with a 5° dynamic range. At the 180° bending angle, the structure bends with a radius of curvature of only ~6 nm on its inner layer of helices (see the figure, panel E). The authors further assembled these well-controlled bent structures into sophisticated constructions (see the figure, panels F to H).

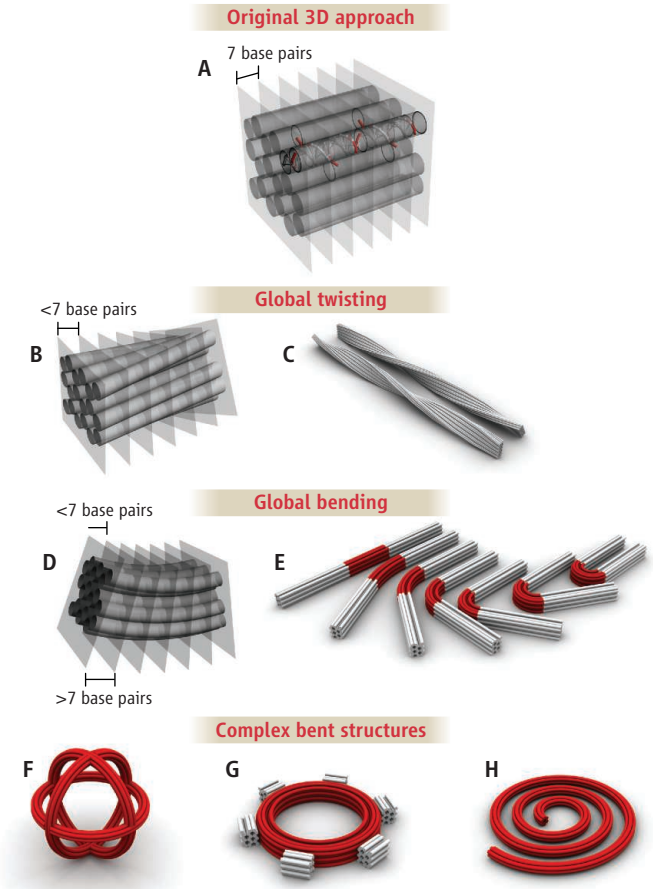

Designer curvatures with DNA nanostructures. (**A**) Multihelix 3D DNA origami packed on a honeycomb lattice. The rods are the DNA helices; the crossover points along any helix to the three nearby helices are restricted to the planes perpendicular to the axis of the helices, evenly spaced by 7 base pairs. (**B**) A global twist is generated by changing the distance between selected neighboring planes to >7 base pairs for a right-handed twist or <7 base pairs for a left-handed twist (shown here). (**C**) Right- and left-handed global twists are created by linking multiple DNA units end to end. (**D**) A global bend is generated by varying the distance between neighboring planes to <7 base pairs on one side and >7 base pairs on the opposite side. (**E**) The curvature can be tuned by changing the gradient of the base pair difference across the structure. Bent DNA units with appropriate curvatures are further assembled to form the beach ball (**F**) and the square-toothed gear (**G**). The spiral DNA multihelix bundle (**H**) is created from six semicircles of decreasing curvature.

There are other approaches for creating DNA nanostructures with curved features. For example, Mao and co-workers (*6*) have shown that simple DNA branched junctions can be used to hierarchically assemble 3D polyhedral objects such as tetrahedra, dodecahedra, and fullerene structures by tuning the branching numbers and the bending curvature of the junction core. Andersen *et al*. (*8*) and Ke *et al*. (*10*) created boxlike 3D objects by connecting different 2D DNA origami domains through sharp interfaces. The study by Dietz *et al*. (*2*) is different in that the curvature continuously connects different DNA nanostructure domains and can be quantitatively controlled. All these methods may be combined to construct increasingly sophisticated, precisely engineered geometric objects, the scope of which will be limited only by the human imagination.

Additional studies are needed to establish the stability of curved versus relaxed DNA nanostructures. Methods should be developed to assess the defect rates and improve the yields of the hierarchically engineered structures. A better understanding of the mechanical properties, and whether 3D packing parameters can affect them, is also necessary to translate them into practical applications.

References and Notes

1. N. C. Seeman, *Nature* **421**, 427 (2003).
2. H. Dietz *et al*., *Science* **325**, 725 (2009).
3. N. C. Seeman, *J. Theor. Biol.* **99**, 237 (1982).
4. W. M. Shih, J. D. Quispe, G. F. Joyce, *Nature* **427**, 618 (2004).
5. R. P. Goodman *et al*., *Science* **310**, 1661 (2005).
6. Y. He *et al*., *Nature* **452**, 198 (2008).
7. F. A. Aldaye, H. F. Sleiman, *J. Am. Chem. Soc.* **129**, 13376 (2007).
8. E. S. Andersen *et al*., *Nature* **459**, 73 (2009).
9. S. M. Douglas *et al*., *Nature* **459**, 414 (2009).
10. Y. Ke *et al*., *Nano Lett.* **9**, 2445 (2009).
11. H. G. Garcia *et al*., *Biopolymers* **85**, 115 (2007).
12. P. W. Rothemund, *Nature* **440**, 297 (2006).
13. We thank C. Lin for help preparing the figure. The authors are financially supported by grants from the NSF, NIH, Office of Naval Research, Air Force Office of Scientific Research, Army Research Office, and Sloan Research Fellowship.

10.1126/science.1178328

CHEMISTRY

Epoxying Isoprene Chemistry

Laboratory experiments show how the gas-phase and aerosol chemistry of isoprene may be connected.

Tadeusz E. Kleindienst

It seems that every few months we read about another missing aspect of atmospheric chemistry—from missing products and missing reactivity to missing sources and missing understanding. The report by Paulot *et al*. on page 730 of this issue (*1*) thus comes as a relief: It provides more answers than questions on a topic of considerable interest to atmospheric scientists, the formation of gas- and aerosol-phase products from the atmospheric oxidation of isoprene.

Worldwide emissions of isoprene (C_5H_8) from vegetation (see the figure) have been estimated to exceed 500 teragrams per year (*2*). Given these massive emissions, this compound arguably has the most important chemistry of any single nonmethane hydrocarbon. It reacts very quickly with hydroxyl radicals (OH), leading to a daytime half-life of less than 2 hours. In urban and rural areas, reactions with nitric oxide (NO) produce carbonyl and organic nitrate compounds that are important in ozone chemistry (*3*). In remote or tropical environments, where NO can be less than 50 parts per trillion, cross reactions by intermediate peroxy radicals tend to dominate (*4*). Many recent studies have aimed to elucidate this low-NO regime; this is also what Paulot *et al*. address.

In recent years, research into the atmospheric chemistry of isoprene has followed roughly two tracks. The first of these tracks began with the 2004 article by Claeys *et al*. (*5*), who argued, based on the detection of two chemical tracers (2-methylthreitol and 2-methylerythritol), that aerosol collected in the Amazon rainforest contain a substantial portion of products from the photooxidation of isoprene. It had been known for more than 30 years that isoprene is produced in high abundance in locations where deciduous trees are plentiful. But how could such a small molecule undergo atmospheric reactions to form compounds of sufficiently low volatility to condense onto submicrometer particles at measurable levels? Given that organic aerosol of this type can influence Earth's radiation budget as well as promote the formation of cloud condensation nuclei, it became essential to establish the details of the phenomena and determine its atmospheric importance.

Among the flurry of laboratory experiments that followed, Edney *et al*. (*6*) showed that the tracer compounds detected by Claeys *et al*. (*5*) were indeed generated in laboratory photooxidations of isoprene, and that the aerosol formation yield was considerably enhanced in the presence of acidic aerosol. Kroll *et al*. (*7*) provided the essential laboratory data to conduct the first global model of isoprene aerosol formation. Isoprene is now thought to be an important contributor to global aerosol formation (*8*).

What these studies lacked was a mechanistic rationale for their findings. In their laboratory studies, Paulot *et al*. have now irradiated isoprene under NO_x conditions similar to those found in the tropics. Through the use of chemical ionization mass spectrometry (CIMS), the authors were able to measure gas-phase organic hydroperoxides similar to those probably formed in the atmosphere. Moreover, the CIMS technique was shown to measure not only the hydroperoxides but, through tandem mass spectrometry, organic epoxides as well.

The authors report a remarkably high (75%) epoxide yield. The measured epoxides have previously been proposed to be stable intermediates in isoprene aerosol formation. The authors also conducted molecular dynamics calculations, which showed that the reaction energetics were consistent with epoxide formation, giving additional plausibility to the findings. With respect to isoprene aerosol formation, Paulot *et al*. find that similar epoxides are readily taken up by acidic aerosol, and, once incorporated in the aerosol, can form polymers; Kalberer *et al*. have previously reported evidence for polymers in ambient aerosol (*9*).

Moving on to the gas phase, Paulot *et al*. show that the same mechanism that generates the epoxide also regenerates OH radicals. This is the second very active track of isoprene chemistry research. The conventional wisdom had been that radical-radical reactions forming organic peroxides were completely chain terminating. A chain-propagating mechanism has already been examined in field (*10*, *11*) and laboratory studies (*12*, *13*) and on theoretical (*14*) grounds. The laboratory studies have found direct (*12*) and indirect (*13*) evidence for OH regeneration from reactions of HO_2 with peroxy radicals. By contrast, the theoretical study (*14*) relied on isomerization reactions of the isoprene intermediates to regenerate OH. The mechanisms and yields of the low-NO isoprene chemistry still have considerable uncertainty, but these findings from peroxy-radical reactions will close the gap between model results and atmospheric measurements of OH levels (*15*, *16*).

Perhaps the most important aspect of the Paulot *et al*. work is its practical value. Air quality models for secondary organic aerosol

CREDIT: CHRIS GERON/U.S. EPA

Measuring isoprene emissions. As in the Amazon, isoprene emissions in southeastern United States forests are among the highest in the world. The photo shows a view of the forest canopy from a sampling tower at Duke Forest near Chapel Hill, North Carolina. Paulot *et al*. (*1*) elucidate the reaction chemistry of this compound.

National Exposure Research Laboratory, Office of Research and Development, U.S. EPA, Research Triangle Park, NC 27711, USA. E-mail: kleindienst.tad@epa.gov

Published by AAAS

formation used by regulatory agencies, such as the U.S. EPA, are generally limited in their predictive power by relying on experiments that give parameterized aerosol yields from reacting precursor compounds. Incorporation of the chemical mechanisms derived experimentally by Paulot *et al*. into deterministic models of gas-aerosol chemistry should help to improve their predictive capabilities.

References

1. F. Paulot *et al*., *Science* **325**, 730 (2009).
2. A. Guenther *et al*., *J. Geophys. Res.* **100**, 8873 (1995).
3. B. J. Finlayson-Pitts, J. N. Pitts Jr., *Science* **276**, 1045 (1997).
4. C. E. Reeves, S. A. Penkett, *Chem. Rev.* **103**, 5199 (2003).
5. M. Claeys *et al*., *Science* **303**, 1173 (2004).
6. E. O. Edney *et al*., *Atmos. Environ.* **39**, 5281 (2005).
7. J. H. Kroll *et al*., *Environ. Sci. Technol.* **40**, 1869 (2006).
8. D. K. Henze, J. H. Seinfeld, *Geophys. Res. Lett.* **33**, (2006).
9. M. Kalberer *et al*., *Science* **303**, 1659 (2004).
10. J. Lelieveld *et al*., *Nature* **452**, 737 (2008).
11. A. Hofzumahaus *et al*., *Science* **324**, 1702 (2009).
12. T. J. Dillon, J. N. Crowley, *Atmos. Chem. Phys.* **8**, 4877 (2008).
13. M. E. Jenkin *et al*., *Phys. Chem. Chem. Phys.* **10**, 4274 (2008).
14. J. Peeters *et al*., *Phys. Chem. Chem. Phys.* **11**, (2009).
15. J. A. Thornton *et al*., *J. Geophys. Res.* **107**, 4146 (2002).
16. X. Ren *et al*., *J. Geophys. Res.* **113**, D05310 (2008).

10.1126/science.1178324

GENETICS

A-maize-ing Diversity

Analysis of a new maize resource reveals that a large number of genetic loci with small effects may underlie the wide variation seen in traits such as flowering time.

Trudy F. C. Mackay

Maize (*Zea mays*)—corn—is a staple food source in much of the world, as well as a source of cooking oil, grain alcohol, livestock feed, and biofuel. There is enormous quantitative variation among maize strains for traits of agronomic importance, due to allelic variation at multiple quantitative trait loci (QTLs) with effects that are sensitive to the environment. Knowledge of the genetic basis of this variation (see the figure) would be a major boon to selective breeding programs, but has been hindered by the difficulty of mapping the underlying QTLs. On pages 714 and 737 of this issue (*1*, *2*), Buckler and colleagues describe the genetic properties of a new resource for mapping maize quantitative traits (*3*), and discuss the genetic architecture of a key trait—flowering time—derived from it.

The molecular basis of quantitative genetic variation remains unclear because accurate phenotypes and high-density molecular marker genotypes for tens of thousands of individuals are needed to map QTLs whose effects are not large. In addition, the resolution of DNA recombination—the exchange of genetic material between homologous chromosomes—must be high enough to identify the genes involved. Linkage mapping can readily detect chromosomal regions containing one or more QTLs that affect a trait, with samples of several hundred individuals and molecular markers, but it is difficult to precisely localize the QTLs (*4*). This approach usually relies on crosses between two strains, thus capturing only a tiny fraction of genetic diversity in the population. By contrast, association mapping widely samples genetic diversity and requires fewer individuals (*4*), but has less power to detect QTLs when alleles are not common. Thus, precision of localization comes at the expense of high-resolution genotyping. Association mapping is also highly sensitive to spurious false positives that result from recent mixing of populations with different allele frequencies and values of the quantitative trait.

Buckler and colleagues combine the benefits of linkage and association mapping in a single population through a nested association mapping (NAM) approach. The maize NAM population was derived by crossing a common reference sequence strain to 25 different maize lines. Individuals resulting from each of the 25 crosses (families) were self-fertilized for four further generations, to produce 5000 NAM recombinant inbred lines. This NAM population can be used for initial QTL detection using linkage mapping with moderate numbers of markers, followed by a second stage of high-resolution association mapping in QTL regions that capitalizes on a high-density marker map within each diverse strain. Because all individuals within a given recombinant inbred line are nearly genetically identical, the phenotype of the same quantitative trait can be scored for multiple individuals of the same genotype, increasing the accuracy of estimating the true genotypic value of each line. The same lines can also be evaluated for many quantitative traits and in multiple environments, providing a valuable resource for understanding the genetic basis of pleiotropy (single gene effects on multiple traits) and genotype-environment interactions.

Diverse corn. The genetic diversity of maize can explain the vast phenotypic variation observed across strains.

McMullen *et al*. (*1*) genotyped 4699 lines of the NAM population for 1106 single-nucleotide polymorphisms (SNPs), giving a composite genetic map with an average marker density of one SNP per 1.3 cM and a total of 136,000 recombination events. From 63 to 74% of the SNPs were polymorphic in any given family. Substantial variation in recombination was not attributable to QTLs with general effects on recombination, but rather to numerous and localized regions of variation in recombination that are specific to each family. Unfortunately, variation in recombination confounds combining linkage and association mapping of QTLs—the intention of the NAM design—which assumes constant recombination frequencies across populations. Otherwise, the NAM population is an excellent resource for QTL mapping, with nearly equal representation of genetic material from both founder lines in all of the 25 families in the NAM population.

Buckler *et al*. (*2*) used the NAM population to map QTLs affecting flowering time in nearly 1 million plants representing all the NAM lines, and also in a separate set of 282 strains that represent maize diversity, in each of four different environments and in two different years. Depending on the analysis performed, a range of 29 to 56 QTLs were found to affect flowering time. Most were shared among multiple families; however, the effects varied among families, which suggests that common QTLs with different low-frequency alleles affect

Department of Genetics, Campus Box 7614, North Carolina State University, Raleigh, NC 27695, USA. E-mail: trudy_mackay@ncsu.edu

variation in flowering time. The effects of all QTLs were, however, small. Tests for epistasis and genotype-environment interactions revealed very little contribution of context-dependent effects to the genetic architecture of flowering time.

Using the NAM population for high-resolution recombination mapping will not be possible until the parent strains are genotyped for a dense panel of molecular markers. The large numbers of QTLs, small effects, and likelihood of identifying novel genes affecting quantitative traits from dissection of natural genetic variation pose a challenge for functional validation.

The observation of large numbers of QTLs with small effects on flowering time is consistent with results from mice, flies (*Drosophila melanogaster*), and humans for many different quantitative traits (*5*). However, the lack of QTLs with large effects is in contrast to the genetic architecture of flowering time in rice, barley, sorghum, and the model flowering plant *Arabidopsis thaliana*, where large-effect QTLs account for most of the observed variance (*6*–*9*). The trivial contribution of epistasis is also in contrast to epistatic interactions affecting flowering time in *Arabidopsis* (*10*) and rice (*11*), as well as the common occurrence of epistasis affecting quantitative traits in *Drosophila* and mice (*5*). Genotype-environment interaction is also a typical feature of the genetic architecture of quantitative traits in *Drosophila* and mice (*5*). The extent to which mating system, demography, sampling, experimental design, and relationship to fitness contribute to the genetic architecture of quantitative traits is an open question.

Genetic variation for most quantitative traits in most organisms may well be attributable to large numbers of loci with small effects. What, then, is the future of genetic dissection of complex traits? Rather than analyzing one gene at a time, we will need to understand how molecular variants affect quantitative traits through correlated networks of transcripts, proteins, and metabolites. The NAM population joins the mouse Collaborative Cross (*12*), the *Drosophila* Genetic Reference Panel (*13*), and the *Arabidopsis* 1001 Genomes Project (*14*) projects as a community resource population suitable for such systems' genetics analysis (*15*, *16*).

References and Notes

1. M. D. McMullen *et al.*, *Science* **325**, 737 (2009).
2. E. S. Buckler *et al.*, *Science* **325**, 714 (2009).
3. J. Yu *et al.*, *Genetics* **178**, 539 (2008).
4. T. F. C. Mackay, *Annu. Rev. Genet.* **35**, 303 (2001).
5. J. Flint, T. F. C. Mackay, *Genome Res.* **19**, 723 (2009).
6. C. Alonso-Blanco, S. E. El-Assal, G. Coupland, M. Koornneef, *Genetics* **149**, 749 (1998).
7. M. Yano *et al.*, *Theor. Appl. Genet.* **95**, 1025 (1997).
8. A. Turner, J. Beales, S. Faure, R. P. Dunford, D. A. Laurie, *Science* **310**, 1031 (2005).
9. Y. R. Lin, K. F. Schertz, A. H. Paterson, *Genetics* **141**, 391 (1995).
10. M. E. El-Lithy *et al.*, *Genetics* **172**, 1867 (2006).
11. N. Uwatoko *et al.*, *Euphytica* **163**, 167 (2008).
12. G. A. Churchill *et al.*, *Nat. Genet.* **36**, 1133 (2004).
13. www.hgsc.bcm.tmc.edu/project-species-i-Drosophila_genRefPanel.hgsc?pageLocation=Drosophila_
14. D. Weigel, R. Mott, *Genome Biol.* **10**, 107 (2009) s.Medline
15. S. K. Sieberts, E. E. Schadt, *Mamm. Genome* **18**, 389 (2007).
16. M. V. Rockman, *Nature* **456**, 738 (2008).

17. Supported by NIH research grant GM45146.

10.1126/science.1178420

PHYSICS

Quantum Football

Franco Nori

A superconducting circuit passes a quantum state between several energy levels like a football is passed between players.

Quantum information processing is usually based on two-level quantum systems, called quantum bits or qubits, but the use of additional quantum levels can simplify some quantum computations. It can also allow the emulation of other quantum systems, in which one quantum system acts as an analog of another and allows it to be better understood by reproducing its dynamics in a more controllable manner. On page 722 of this issue, Neeley *et al.* (*1*) demonstrate the operation of a superconducting circuit with five quantum levels, and show how to manipulate and measure its quantum states. They used this circuit to emulate the dynamics of single spins with various quantum numbers, including the measurement of their geometric phases that result from spin rotations. This extension of the two-level qubit to a multilevel "qudit" opens possibilities for richer quantum computing architectures and better emulations of other quantum systems.

Superconducting circuits can behave like atoms, in that both systems have discrete energy levels, and coherent quantum oscillations can occur between those levels. Such circuits can perform microscopic quantum mechanics at macroscopic scales and can be used to conduct atomic-physics experiments on a silicon chip (*2*–*4*). However, whereas transitions between electronic energy levels in atoms are controlled with visible or microwave photons, transitions in the artificial atoms are driven by currents, voltages, and microwave photons.

Quantum circuits can be lithographically designed to have specific characteristics, such as a large dipole moment (*2*–*5*) or particular transition frequencies. This tunability is an important advantage over natural atoms for several applications. For example, quantum circuits can produce photons (*6*–*8*), can be cooled (*9*–*11*) like natural atoms, can form molecules (*12*), and can be used for quantum memories (*13*, *14*).

For applications in quantum computing, quantum circuits have been designed to store and manipulate information as two-level quantum systems, called qubits (*2*, *3*). The greater complexity and flexibility of a many-level quantum system can be illustrated by making analogies with a classical system, that of a game of football (soccer). The main characters in standard quantum information processing are two players (two energy levels that form a qubit) with player numbers $|0\rangle$ and $|1\rangle$. The state of the quantum system—the football—can be written as the sum of $a\cdot|0\rangle + b\cdot|1\rangle$, where a and b are complex numbers that can vary in time but always satisfy the normalization condition $|a|^2 + |b|^2 = 1$. For instance, when ball state = $|0\rangle$, the ball is with player $|0\rangle$. In general, the quantum ball is in a superposition state: It is shared between both players.

Now, consider quantum information with several states. In the experiment by Neeley *et al.*, the states in their quantum circuits can emulate a particle with spin s, which can be described as a vector rotating on a sphere. When a spin rotates as it moves around a closed path, the spin state that describes it is multiplied by a phase factor, often referred to as Berry's phase. This phase factor depends on the solid angle enclosed by the path. For a 2π rotation, integer spins are unchanged, whereas half-integer spins are multiplied by -1. This parity difference leads to the symmetric statistics

Advanced Science Institute, RIKEN, Wako-shi, Saitama 351-0198, Japan, and Department of Physics, University of Michigan, Ann Arbor, MI 48109, USA. E-mail: fnori@riken.jp

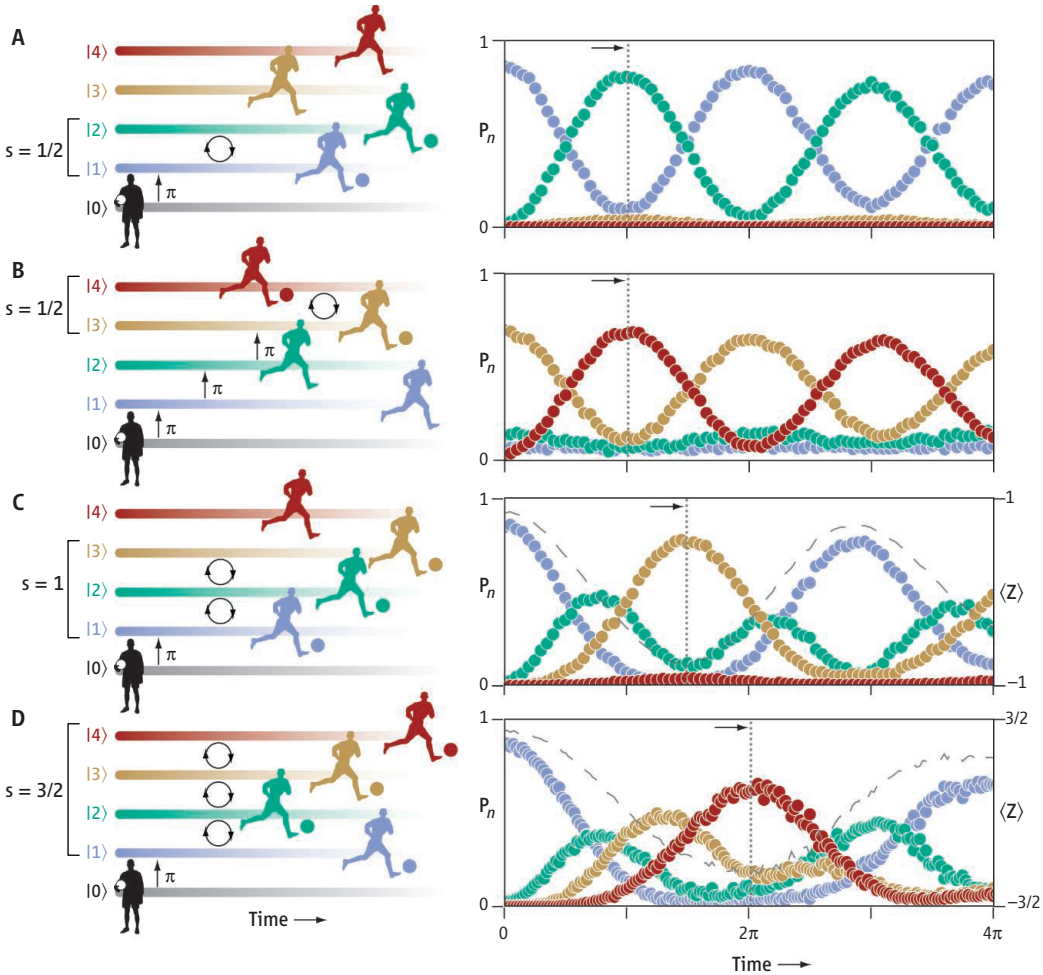

All players have some of the ball. In quantum football, this statement is literally true, because the occupied state, or quantum football, is probabilistic in nature—it can be at more than one place at any given time. The left side of each panel shows the sequences of operations that transfers the occupied state between five discrete energy levels of an artificial atom based on superconducting circuits. Each state $|n\rangle$ can be thought of as a player in football. On the right side, the occupancy of the energy levels as a function of time is expressed as a probability P_n, which corresponds to having the ball. Transitions between levels correspond to passes between players. The $|0\rangle$ state serves as a reference; in the football analogy, it is the goalkeeper. (**A**) Player $|0\rangle$, the goalkeeper, passes the ball to a defender, player $|1\rangle$; this pass is called "π shift" because it corresponds to a π rotation of the ball's quantum state. Afterward, defenders $|1\rangle$ and $|2\rangle$ repeatedly pass the ball to each other; these passes correspond to Rabi oscillations (shown as a black circle) and emulate a spin-1/2 system. The probability that other players have the ball is almost zero. (**B**) A series of π shifts gets the ball to the midfielders, $|3\rangle$ and $|4\rangle$, who repeatedly pass the ball to each other. The probability of player $|4\rangle$ controlling the ball at time π is lower than that for player $|2\rangle$ at the same time in (A). (**C**) A quantum ball repeatedly passed among three players can simulate a spin-1 system. (**D**) Repeatedly passing the ball among four players can simulate a spin-3/2 system. In (C) and (D), the circuit drives multiple transitions simultaneously to emulate spin operators. The expectation value $\langle Z\rangle$ that sums over all of these probabilities (far right) evolves sinusoidally (gray dashed curve), as expected for a rotating spin. The vertical dotted lines in the four right-side panels indicate the times when one of the players is more likely to have the ball.

of bosons and antisymmetric statistics of fermions under particle exchange.

Neeley *et al*. measured the phase factor and spin parity for spin-1/2, spin-1, and spin-3/2, at all solid angles, using their superconducting circuit as a quantum simulator. Their circuit reproduced the quantum phase acquired by each spin under closed-path rotations, in particular the even parity of integer spins and odd parity of half-integer spins under 2π rotation. This demonstration opens possibilities for using qudits in quantum information processing.

In the football analogy, the ball, which represents the occupied state, can be shared between many energy levels (players). Microwave pulses drive transitions between levels. For example, a π shift transfers the state completely, as happens when the goalkeeper $|0\rangle$ throws the ball to his defender $|1\rangle$ (see the figure, panel A). It is also possible to induce Rabi oscillations that allow the occupied state to oscillate between two energy levels and emulate a spin-1/2 state; this would correspond to two players passing the ball between them as they head upfield (see the figure, panels A and B). Adding more Rabi oscillations emulates higher spin states, corresponding to three or four players sharing the quantum football (see the figure, panels C and D). Unlike ordinary football, the quantum football has a probabilistic nature, so at no time can we be sure who has the ball.

Future directions and extensions of this work include developing qudit tomography, which would provide snapshots of the quantum states, as well as understanding decoherence in qudits and controlling the coupling and entangling of qudits. Applications of qudits include enhanced quantum memory and quantum logic relative to qubits, quantum cryptography with many quantum levels, and analog quantum simulations, in which controllable quantum systems emulate the dynamics of other quantum systems and explore new physical phenomena. If two players have been able to "score" so many exciting results in qubit quantum systems, then many players should be able to score even more results and win more challenging matches.

References and Notes

1. M. Neeley *et al*., *Science* **325**, 722 (2009).
2. J. Q. You, F. Nori, *Phys. Today* **58** (11), 42 (2005).
3. J. Clarke, F. K. Wilhelm, *Nature* **453**, 1031 (2008).
4. R. J. Schoelkopf, S. M. Girvin, *Nature* **451**, 664 (2008).
5. C. M. Wilson *et al*., *Phys. Rev. Lett.* **98**, 257003 (2007).
6. M. A. Sillanpaa *et al*., *Nature* **449**, 438 (2007).
7. F. Deppe *et al*., *Nat. Phys* **4**, 686 (2008).
8. M. Hofheinz *et al*., *Nature* **459**, 546 (2009).
9. S. O. Valenzuela *et al*., *Science* **314**, 1589 (2006).
10. F. Nori, *Nat. Phys.* **4**, 589 (2008).
11. M. Grajcar *et al*., *Nat. Phys.* **4**, 612 (2008).
12. T. Yamamoto *et al*., *Phys. Rev. B* **77**, 064505 (2008).
13. A. M. Zagoskin *et al*., *Phys. Rev. Lett.* **97**, 077001 (2006).
14. M. Neeley *et al*., *Nat. Phys.* **4**, 523 (2008).
15. Supported in part by the Laboratory for Physical Sciences, the National Security Agency, the Army Research Office, and the National Science Foundation.

10.1126/science.1178828

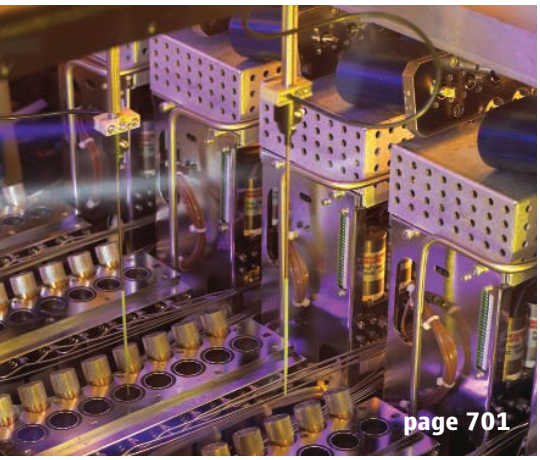
page 701

INTRODUCTION

Chemistry Writ Large

MANY PEOPLE ENCOUNTER THE APPARATUS OF A CHEMISTRY LABORATORY AT SOME stage in their education. They might recall performing a simple ion exchange reaction in a flask and then isolating the powdery product by vacuum filtration. Comparatively few see the scaled-up industrial versions of such tools, though they make ample use of the products—the fuels, pharmaceuticals, plastics, paints, cosmetics, and countless other components of modern life prepared through chemical synthesis. The lab bench and plant floor are similar in some respects: At the molecular level, atomic bonds break and form in much the same way whether the bulk material is being collected in fractions of a milligram or hundreds of kilograms. Yet numerous additional concerns arise at industrial scale. Cost becomes a major factor; waste streams must be processed efficiently; flow and mixing rates start to dominate reaction productivities. This special section explores the current dynamics of industrial chemistry. After a century of rapid development, where is the field headed?

Four Perspectives highlight different facets of the enterprise. Dudukovic (p. 698) discusses the general design of chemical reactors, noting that in practice, most reactors have tended to be optimized empirically after assembly rather than constructed from the outset to maximize reaction efficiency at a large scale. He argues that increasingly sophisticated computational fluid dynamics models, coupled with experimental tracer studies, should offer improved design principles. In pharmaceutical synthesis, drug leads pass through three stages of development, from preliminary exploration through clinical trials to commercialization, and often the synthetic process changes dramatically at each stage. Davies and Welch (p. 701) emphasize the benefits of a more consistent approach, facilitated by the adoption of versatile reaction protocols, or platforms, that are optimized by high-throughput experimentation and then applied broadly to multiple targets at multiple scales. Hustad (p. 704) discusses recent efforts to tune the properties of polyethylene, the most abundantly synthesized plastic. He highlights the often competing virtues of selectivity and productivity, and the creative approaches from both academic and industrial research directed toward reconciling them. Willems (p. 707) examines the opportunities and challenges inherent in efforts to replace petroleum—long the chemical industry's primary feedstock—with biomass.

Beyond process optimization factors, industrial chemists must consider societal concerns about the potential toxicity of marketed products and discarded by-products. Two News stories describe how some of these issues are playing out in the United States. Service (p. 692) discusses the prospects for revising a once-vaunted comprehensive environmental law affecting industrial compounds, the Toxic Substances Control Act. Stokstad (p. 694) explores the quest for faster, more effective toxicological tests to gauge how synthetic compounds affect living cells.

Finally, there are the people themselves, engaged in pushing the field forward. In a *Science* Careers feature by Petkewich (p. 696), young chemists offer impressions and advice to others planning to make the leap from academia to careers in industry.

– JAKE YESTON AND ROBERT COONTZ

CREDIT: I. W. DAVIES AND C. J. WELCH

Industrial Chemistry

CONTENTS

News

Perspectives

Science

Published by AAAS

NEWS

A New Wave of Chemical Regulations Just Ahead?

The United States's aging flagship law for controlling toxic compounds is ripe for overhaul, and chemical companies—or some of them—want to play a major role in shaping what comes next

IN 1976, SHORTLY AFTER CONGRESS PASSED A law designed to regulate toxic chemicals, Russell Train, then the administrator of the U.S. Environmental Protection Agency (EPA), called the new law "one of the most important pieces of 'preventive-medicine' legislation" ever passed by Congress. The Toxic Substances Control Act (TSCA), Train said, would help regulators identify chemicals hazardous to human health and phase them out.

TSCA led to restrictions on a handful of chemicals, including a ban on polychlorinated biphenyls and limits on certain uses of metalworking fluids. But then came asbestos. In 1989, EPA used TSCA to ban the persistent ultrafine fibers that numerous studies had linked to lung diseases. But TSCA stipulates that chemicals should be restricted using the least burdensome regulations available. And because EPA couldn't convince a U.S. appeals court that banning asbestos was the least burdensome way to regulate it, in 1991 the court overturned the ban. In the 18 years since, EPA has not banned a single chemical.

"TSCA has essentially failed," says Richard Denison, a senior scientist with the Environmental Defense Fund in Washington, D.C. The way TSCA has been interpreted has raised the bar for restricting a chemical so high that it has effectively gutted the law, Denison and others say. It's a sentiment that has spread far beyond environmental organizations, prompting widespread calls—even within the U.S. chemical industry—for the law's reform.

"There is general agreement that some change is needed in TSCA," says J. Clarence Davies, a senior fellow with Resources for the Future in Washington, D.C., who also helped craft the original TSCA legislation. "But there is a big difference of opinion on how much." Just how that question gets answered could have a major effect not just on chemical manufacturers and consumers but also on a broad range of scientists who could be called on to revamp the way chemicals are tested and gauge their risk.

TSCA was designed to regulate chemicals and chemical mixtures, with the exception of food, drugs, cosmetics, and pesticides. It gives EPA the authority to require reporting and testing, and then to restrict substances that present an unreasonable health risk. But the law is widely viewed as having major loopholes. When TSCA was written, Davis notes, it allowed tens of thousands of existing compounds to be grandfathered in without comprehensive health and safety testing. Companies still had to report health and safety data for new chemicals. But they were able to claim much of their submissions as confidential to protect proprietary chemical recipes for their products. The provision made it nearly impossible for scientists and environmentalists to challenge the release of new chemicals.

Even when EPA does have the authority under TSCA to collect data on chemicals of potential concern, it rarely does so. To ask manufacturers to submit health data, EPA must first verify that the chemical poses a health risk to the public. "It is the epitome of a Catch-22," Davies says. The result, according to a 2006 report by the Government Accountability Office (GAO), is that of the 62,000 chemicals in use when TSCA went into effect in 1976, EPA has required testing of fewer than 200 and has either banned or limited production of only five. In a follow-up report earlier this year, GAO concluded: "Without greater attention to EPA's efforts to assess toxic chemicals, the nation lacks assurance that human health and the environment are adequately protected."

That ineffectiveness isn't for lack of concern. Consumers have become increasingly anxious about several classes of compounds on the market. They include phthalates, commonly found in children's toys; flame retardants; and bisphenol A, an organic compound used in the plastic coatings that line food cans and other items, which has been found to have estrogenic effects. Numerous studies have raised red flags about all of these compounds. Biomonitoring studies have revealed that most people have trace amounts of many industrial compounds in their blood. For example, a 2004 study by the Washington, D.C.–based Environmental Working Group, which fights children's exposure to toxic chemicals, found a total of 287 industrial chemicals in the umbilical cord blood of 10 newborn babies. They included chemicals used in fast-food packaging, stain repellents in textiles, flame retardants, and pesticides.

No one is sure whether those compounds are harmful in such small doses, but it is clear that toxics create a significant personal and financial burden. Last year, for example, a study by researchers at the University of California, Berkeley, and UC Los Angeles found that preventable chemical- and pollution-

CREDITS (CLOCKWISE, FROM LEFT): ISTOCKPHOTO; JUPITERIMAGES (3); GETTY IMAGES/VISUALS UNLIMITED

Published by AAAS

Second glance. Rising concerns about compounds in many products are prompting calls for an overhaul of the law regulating toxic chemicals.

related diseases in California alone (not including air pollution) cost the state's insurers, businesses, and families $2.6 billion a year in direct and indirect expenses.

The effects are far-reaching. According to Maureen Gorsen, the former head of California's Department of Toxic Substances Control, 57% of landfills in California are leaking hazardous waste into groundwater. TSCA reform wouldn't stop all such leaks, as landfills contain many substances, such as used oil, that are unlikely to be restricted. Nevertheless, Gorsen notes that the problem is prompting expensive cleanups that must be paid for out of the cash-strapped state's general fund. "It's a losing battle," Gorsen said at a recent meeting at UC Berkeley. "We can't keep going on the way we have been for the past 40 years."

TSCA's perceived ineffectiveness, combined with growing public concerns about chemical exposures, has spurred government agencies in the European Union and several U.S. states to launch their own alternatives. By far the most comprehensive is the European Union's effort, abbreviated REACH (for "Registration, Evaluation, Authorisation, and Restriction of Chemical substances"). It requires chemical manufacturers and importers in Europe to submit health and safety data on all compounds they sell in the European Union in excess of 1 million metric tons per year. Most notably, the act shifts the burden of carrying out health and safety screens from government regulators to companies themselves.

States are also jumping into the fray. California, Washington, Maine, Massachusetts, and Michigan have all recently passed laws increasing their control over toxics. These initiatives largely fall into two camps: one set banning chemicals such as phthalates, cadmium, and lead from children's products; the other promoting "green chemistry" to find safer alternatives to toxic compounds used in manufacturing processes and consumer products. "The states are way ahead of the federal government at this point," says Joel Tickner, a chemical regulations policy expert at the University of Massachusetts, Lowell. Some industry representatives agree. "We look at [the state initiatives] in large part as a lack of public confidence in the safety of these materials that can be attributed to a lack of confidence in the regulatory process," says Calvin Dooley, president and CEO of the American Chemistry Council (ACC), a trade group in Arlington, Virginia.

According to Dooley, Tickner, and Denison, the combination of the new state laws, REACH, and declining consumer confidence in the safety of household products has prompted many large chemical manufacturers (such as the multinationals that make up most of ACC's membership) to embrace TSCA reforms. The current patchwork of regulations that have arisen is becoming an increasing burden for companies doing business across U.S. state lines and national borders. And many are hoping that new TSCA reforms would preempt state laws. Smaller companies, however, have been less pleased with the idea of reforms. The Society of Chemical Manufacturers and Affiliates (SOCMA)—which is made up of small to midsize chemical companies—reflected the split in a position paper it issued in March: "Sweeping revisions of TSCA … could be highly detrimental to innovation and quality of life, yet paradoxically not produce major changes in our ability to protect health or the environment."

Just how sweeping any change would be isn't yet clear. But at least one potential revision is on the table. In 2008, Senator Frank Lautenberg (D–NJ) and Representative Henry Waxman (D–CA) sponsored the Kid-Safe Chemicals Act, which is aimed at reducing children's exposure to toxic compounds. The proposed act would not initially evaluate all chemicals, but it would shift the onus to companies to demonstrate that chemicals they sell are safe rather than have the government prove they are harmful. The bill would also make safety data available to consumers through an Internet database in hopes of encouraging public oversight of the process. Last year, the Kid-Safe Chemicals Act made little progress in Congress thanks to a promised veto threat from President George W. Bush. But Lautenberg and Waxman have said they plan to reintroduce the bill this term, possibly as early as this fall.

In April, SOCMA President Joseph Acker said, "The Kid-Safe Chemicals Act would bring an unproven REACH-like system to the U.S." that would be overly burdensome to chemical manufacturers. But Dooley argues that the law doesn't go far enough. "Let's not take a piecemeal approach," he says. "Consumers would be much better served with a more-comprehensive reform of TSCA rather than focusing on one section: children." Dooley says his organization is comfortable with shifting the burden of providing safety data on chemicals from EPA to companies and with other major changes such as allowing businesses to make fewer secrecy claims. SOCMA favors more cautious changes.

Both ACC and SOCMA argue that REACH goes too far in requiring complete health and safety data for all chemicals sold in the European Union. Instead, the groups say, chemicals should be ranked for review by a formula that considers both potential hazard and potential exposure. Tickner agrees that any federal TSCA reforms are likely to incorporate that type of risk-based approach.

So far, the Obama Administration's position on the specifics of toxics reform remains unclear. Lisa Jackson, the Administration's newly appointed EPA director, has listed reform of chemical regulation as one of her five top priorities. In a January memo to EPA employees, she wrote: "It is now time to revise and strengthen EPA's chemical management and risk assessment programs." With such clear signals coming from a high level, there's a good chance TSCA in its current form will soon find itself phased out. **–ROBERT F. SERVICE**

STATE TOXIC CHEMICALS INITIATIVES

State	Year Passed/ Proposed	Title	Goal
California	2007	California Green Chemistry Initiative	Identify chemicals of concern and propose alternatives
Maine	2008	Act to Protect Children's Health	Reduce toxic chemicals in toys
Massachusetts	1989	Toxics Use Reduction Act	Reduce hazardous chemical use
Michigan	2006	Michigan Green Chemistry Directive	Support R&D for nontoxic chemicals
Washington	2008	Children's Safe Products Act	Eliminate phthalates, lead, and cadmium in toys

Stepping in. With the Toxic Substances Control Act seen increasingly as ineffective, several states have begun passing their own laws to control chemical exposures.

SOURCE: ADAPTED FROM UNIVERSITY OF MASSACHUSETTS, LOWELL, CHEMICALS POLICY INITIATIVE

NEWS

Putting Chemicals on a Path To Better Risk Assessment

Industry and regulators are embracing new technologies to move beyond slow, expensive, and perplexing animal tests

PRACTICALLY EVERY BOTTLE OF SUNSCREEN contains ethylhexyl methoxycinnamate, a compound that blocks ultraviolet rays. But there's a slight risk that it could pose a health hazard of its own, because the compound is weakly estrogenic. Last summer, researchers with the U.S. National Toxicology Program (NTP), which is led by the National Institute of Environmental Health Sciences, proposed to investigate with a time-honored toxicological test: a large, multigenerational study of rodents. To get a dose comparable to what might harm humans, they would feed large amounts of ethylhexyl methoxycinnamate to rats and mice. "What does this mean, really?" wonders Kim Boekelheide, a toxicologist at Brown University, who reviewed the proposal for the study. "It's a difficult question."

Many researchers and policymakers are asking similar questions about how chemicals are evaluated for safety. The current mainstay of toxicity testing—giving animals large doses of chemicals—is slow and expensive, and its relevance to humans is often unclear. "We have a system that many people regard as broken," says Melvin Andersen of the Hamner Institutes for Health Research in Research Triangle Park, North Carolina.

As the U.S. Congress mulls legislation that might tighten regulations for chemicals (see p. 692), companies and government agencies are already seeking new approaches for testing them. In March, the Environmental Protection Agency (EPA) issued a 20-year strategic plan. It incorporates much of the advice of a major report* issued in 2007 by the National Academies' National Research Council (NRC): Use computers to predict toxicity and gather data from high-throughput, rapid assays of human cells rather than animal tests. The report has "created incredible momentum," says Tina Bahadori of the American Chemistry Council, an industry trade group in Arlington, Virginia, that is spending $9 million this year on research related to interpreting data from new testing methods.

The transition won't be quick or easy. Basic research to figure out how cellular assays indicate signs of human disease could cost $1 billion to $2 billion over a decade or two. There are significant questions, such as how to ensure that cellular tests truly reveal information about the risk of human disease. "The ultimate, total replacement of existing animal toxicity tests with these new high-throughput methods is likely a long way off," says James Bus, who directs toxicology and environmental research at Dow Chemical Co. in Midland, Michigan.

But EPA Administrator Lisa Jackson has made improving the assessment and management of chemicals a top priority. And that focus will likely end up affecting companies. Because EPA calls the shots on what kinds of data it requires, the agency's position determines what kinds of tests companies have to conduct, says Dan Newton of the Society of Chemical Manufacturers and Affiliates in Washington, D.C. "For the first time in a very long time, the prominence of attention being paid to chemical issues within the agency has risen significantly," says Richard Denison of the Environmental Defense Fund, an advocacy group in Washington, D.C.

**Toxicity Testing in the 21st Century: A Vision and a Strategy*, National Academy Press, 2007

Costly cornerstones

The current system of toxicity testing in the United States dates back to a 1937 tragedy, when a company advertised an antimicrobial drug called "Elixir of Sulfanilamide." More than 73 people died from toxic side effects. In the following uproar, Congress passed the Food, Drug, and Cosmetic Act, which required toxicity testing in animals. A decade later, another law required animal testing of pesticides—a process that EPA has overseen since it was formed in 1970.

Most toxicity testing is done by companies. For example, under EPA's voluntary program called the High Production Volume (HPV) Challenge, companies have provided the agency with minimal safety data on more than 1400 chemicals that are manufactured in quantities of 450,000 kg or more a year. Denison and other environmentalists criticize the program for not gathering more data; Europe's REACH program requires safety and exposure data for any chemical manufactured in or imported into the European Union in quantities of just 10,000 kg per year, with more tests for HPV chemicals.

In 2005, EPA asked NRC how it could do a better job in assessing the health risk of chemicals. The resulting report envisions new streams of data coming from rapid tests of chemicals on human cells. Warning signs of toxicity would come from disturbances in cellular signaling pathways. The tests would be expensive to create but also fast and cheap to operate so that many kinds of chemicals

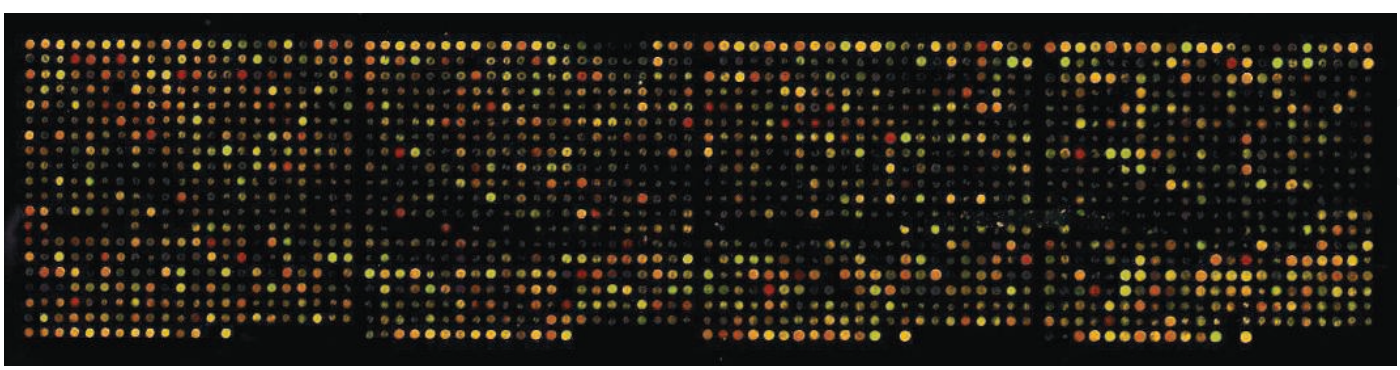

CREDIT: NHGRI

Snapshot. Microarrays reveal which genes are active in a cell at one particular instance, but much more research is needed to figure out which are signs of toxicity.

Published by AAAS

and even mixtures could be run through them.

Making the vision real, of course, will require discovering all the pathways and the ways in which chemicals can perturb them. No one knows for sure how many such pathways exist, but estimates range up to 200. It's such a big job that the NRC panel, chaired by epidemiologist Daniel Krewski of the University of Ottawa, recommended a new national institute be founded with an annual budget on the order of $100 million. The institute would also develop high-throughput screening tests that could identify these perturbations.

EPA began heading in that direction in 2005, when it started its National Center for Computational Toxicology (NCCT). One part of the center is EPA's ToxCast program, which has subjected 309 well-characterized chemicals, mostly pesticides, to 467 different high-throughput tests, examining various measures that could indicate toxicity (*Science*, 22 August 2008, p. 1036). NCCT is collaborating with NTP and the National Institutes of Health's Chemical Genomics Center, which is also running high-throughput tests. "The agency has made huge progress with ToxCast," says Krewski. In July, it received from Pfizer the first of nearly 120 compounds that failed for toxicity reasons in clinical trials, along with data on animal studies and on toxicity in patients. The goal is to use these data to investigate how well cellular results can predict toxicity in humans. "It's an incredible thing that they're doing this," says Robert Kavlock, who directs NCCT. "Normally, these are tightly held company secrets." Kavlock says as many as four other pharmaceutical companies will also provide data.

It's not just the pharmaceutical industry that has invested in improving testing. Agrochemical companies, for example, also use high-throughput techniques to rapidly screen new chemicals for biochemical or genetic signs of toxicity. Computer models that analyze chemical structure, called quantitative structure-activity relationship models, are also commonly used to eliminate compounds likely to be toxic. George Daston, a toxicologist at Procter & Gamble, described at a May meeting at the National Academy of Sciences how researchers at the company are working on genomic tests to screen for compounds that might disrupt hormone signaling. "This is really where the action is in terms of taking these from simple preliminary exercises to being the cornerstone of assessment of potential toxicity," he said.

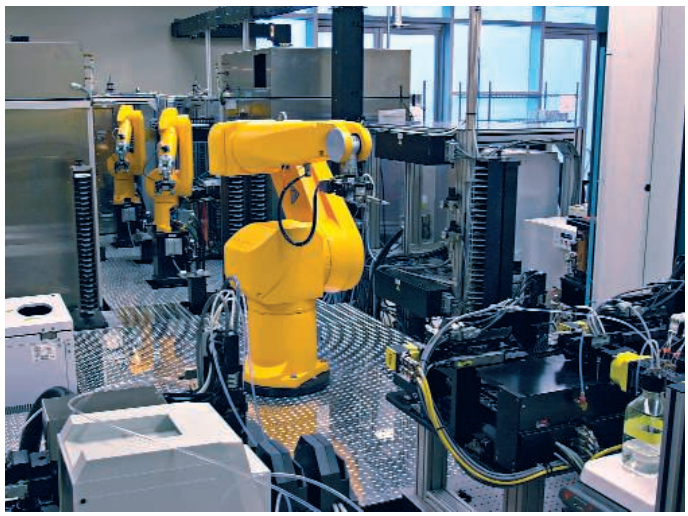

Automate. A toxicology test of a single compound can require more than 1000 animals and cost several hundred thousand dollars. Robots, like these at the NIH Chemical Genomics Center, could quickly detect signals in human cells.

CREDITS (TOP TO BOTTOM): © UNDERSTANDING ANIMAL RESEARCH/WELLCOME IMAGES; J. MAINQUIST/NHGRI

Long road ahead

Many questions remain about tests based on toxicity pathways in human cells. One is exactly which chemicals to examine. Because chemicals often break down inside the body into other compounds, researchers need a way to predict the metabolites. Dosage is another key variable; little is known about exposure to many chemicals, although biomonitoring can help narrow the data gap (*Science*, 25 June 2004, p. 1892). Another major issue is how to identify which cellular signals are true signs of an adverse effect. Some changes might be so-called adaptive responses, part of a natural coping mechanism that doesn't necessarily indicate harm. And the human body may have ways to manage toxic chemicals that aren't apparent if cells are tested in isolation.

Perhaps the biggest question of all is how to validate the new tests. Kavlock and other researchers say that rodent tests are a useful point of comparison. "I think we can use the animal data to build confidence," Kavlock says. But others, such as Krewski, see a danger: "If we spend all our time focusing on trying to replicate what happens in animals, we miss the chance to focus on toxicity pathways in humans." He envisions a comprehensive suite of data from cellular tests, epidemiology in some cases, and computational models—such as NCCT's nascent Virtual Liver—as a way to validate pathway-based toxicity tests of the future. Not everyone shares Krewski's enthusiasm. "I think it's a very long road to do that," says Dale Hattis, a toxicologist at Clark University in Worcester, Massachusetts. "They're going to consume a huge amount of resources that might have better uses."

Peter Preuss, head of EPA's National Center for Environmental Assessment, recognizes the pace of change at EPA is likely to be quite slow, comparing it with changing the course of an aircraft carrier. Kenneth Ramos of the University of Louisville in Kentucky says a large constraint is resources: EPA's research budget has declined about 30% in real terms in the past decade.

There are other challenges in moving new tests into the regulatory process, as Lynn Goldman of Johns Hopkins Bloomberg School of Public Health in Baltimore, Maryland, relates in what she calls a "cautionary tale." In 1996, Congress passed two laws that required EPA to develop ways to test chemicals for the potential to disrupt the endocrine system. But it was only this April that the agency released a final proposal for 67 chemicals to be screened. The program was delayed not just by a lack of funding, Goldman says, but also by opposition from industry and lack of political will. Although there is more support overall for developing a radically new system of toxicity testing—animal-rights groups are enthusiastic about the concept, for example—the research challenge is also far greater.

–ERIK STOKSTAD

Published by AAAS

SCIENCECAREERS

Young Industrial Chemists Find The Learning Curve Never Ends

Academia teaches technical skills, but scientists in the private sector say landing a job and thriving there is an education in itself

WHEN MATERIALS CHEMIST DANIELA RADU STARTED LOOKING FOR A JOB in her field, she decided to stay flexible. Her Ph.D. adviser at Iowa State University in Ames told her she would be competitive for faculty positions, but her postdoc adviser at the Scripps Research Institute in San Diego, California, said her research questions were more suited to a career in industry. She interviewed for both kinds of jobs.

When you're looking for a job and a new place to live, Radu notes, at a certain point you just feel at home. "That is the way I felt when I came to the Experimental Station at DuPont," says Radu, who was born in Romania. She has been working at the lab in Wilmington, Delaware, for almost 2 years, developing photovoltaic materials. She is, she says, "very happy" there.

Other young Ph.D. chemists we spoke to—at companies large and small, specializing in fields as wide-ranging as pharmaceuticals and petrochemicals—agree that life in the private sector has a lot going for it. Some say it offers a better work-life balance; others relish the challenge of developing real-world products designed to change people's lives for the better. All say their academic training prepared them well to ask good questions, set up experiments, and solve chemistry problems. But they still had much to learn, they say, about other skills needed to succeed in an industrial career, as well as major adjustments to make on leaving the research environment and culture of their universities.

Teamwork, deadlines, and bottom lines

Teamwork, a focus on products, and real deadlines were other important differences the chemists noticed in moving from academia into industry. Organometallic chemist Neil Strotman has worked in process catalysis at Merck in Rahway, New Jersey, for about 2 years. The atmosphere there, he says, is worlds away from the individual-oriented achievement he experienced while working on his Ph.D. at the University of Wisconsin, Madison, and postdoc at the Massachusetts Institute of Technology in Cambridge. In academic science, Strotman says, you generally work with one adviser on one project; in industry, "you are working with an entire team, and everything you do has a very collaborative nature."

The driving force behind the work is different, too, says Dustin Levy, a physical chemist with Smiths Detection in Danbury, Connecticut: "The whole reason you are there is to make a profit, and you are not doing pure science anymore." People who want to explore a subject completely can get very frustrated in industry, Levy says.

For solid-state chemist Michael Hurrey, a big chunk of the difference boils down to a technical phrase: "fit for purpose." Hurrey earned a Ph.D. in analytical chemistry from the University of North Carolina, Chapel Hill, in 2004 and now works on physical and materials chemistry projects at Vertex Pharmaceuticals in Cambridge. In industry, he explains, "fit for purpose" means doing exactly what the project requires—and no more. For example, Hurrey says, his current project at Vertex "honestly could be a dissertation." But "I will get to a certain point that is good enough and move on to something else."

Industry's emphasis on patents brings with it other constraints, Catherine Faler says. At ExxonMobil Chemical's Baytown, Texas, plant, Faler uses her synthetic skills to improve catalysts that turn petroleum distillates into polymers. ExxonMobil permits its scientists to give presentations at conferences and publish in scientific journals but only after the intellectual property has been patent-protected. "Everything I do is proprietary," she says. It's a stark contrast to her academic training at the University of Pennsylvania, where, she says, if she had an "interesting and cool" result, she would immediately share the details with her chemistry buddies.

Tailoring the message

Knowing the differences among audiences and tailoring the message to each is a crucial part of an industry job and one that's difficult to learn before you start working in industry, Hurrey says. Even when communicating inside your company, what you say and how you say it depends on whom you're talking to; peer scientists, administrators, lawyers, and engineers each have their own information needs. Addressing people outside the company—scientists at conferences, competitors, and customers—requires altogether different messages, he adds.

Levy, a product manager at Smiths Detection, had to learn on the job how to communicate scientific and technical ideas to nontechnical customers. He completed a Ph.D. in physical chemistry at the University of Maryland, Baltimore County, in 2005, then did a postdoc in optical spectroscopy at the National Institute of Standards and Technology in Gaithersburg, Maryland. In graduate school, he says, his main communication challenge was explaining to microbiologists how a laser spectrometer operates. Today, his customers are hazmat technicians, firefighters, police officers, and postal workers, many of whom have no technical background.

CREDITS (TOP TO BOTTOM): KERRY HARRISON PHOTOGRAPHY/DUPONT; SMITHS DETECTION

Published by AAAS

Scale it up and write it down

Strotman's job in process chemistry requires a different kind of translation: translation of scale. He develops catalytic methods aimed at reducing cost and environmental impact while increasing the efficiency and reliability of processes such as new drug syntheses for HIV and diabetes. His academic experience prepared him to do small-scale chemical reactions, but he had to learn large-scale development from more experienced colleagues at Merck. Issues such as purification and fire hazards become far more relevant as scale increases, he says. The work involved in making drugs is highly regulated for patient safety and requires careful documentation. Today, Christopher Ciolli is a process chemist at Ricerca Biosciences, a contract research organization in Concord, Ohio. But his first industry post, which he started just 4 days after finishing his Ph.D. at the University of Wisconsin, Madison, was in a "current good manufacturing practices" (cGMP) facility at Abbott Laboratories in Illinois, where the work is closely scrutinized by the U.S. Food and Drug Administration.

In graduate school, Ciolli says he "picked a bottle off the shelf and recorded the amount used" in his lab notebook. In a cGMP environment, he says, the same chemical first had to have specifications established, be tested for purity, and be approved by quality assurance as meeting those specifications. Then he had to document the internally assigned reference number, the lot, the expiration/retest date, and the lab number in which the chemical was used.

Online
sciencecareers.org
Visit our Web site for articles, advice, and more on science careers.

Such restrictions aren't unique to pharmaceutical companies; industry in general requires more stringent safety, regulatory, and environmental training and documentation than academic facilities do, says Jinkun Huang, an organic chemist in process research and development at Amgen in Thousand Oaks, California.

Postdocs and internships

Although an academic postdoc is always good experience to have, an industry internship may be better preparation for understanding industry. To get a head start on skills unique to industry, several young chemists strongly recommend summer internships or co-ops in addition to postdoctoral research. Vertex's Hurrey completed an internship at Eastman Chemical in Kingsport, Tennessee, during the summer between college and graduate school. Being immersed in the "culture of a very large organization" was beneficial, he says, even though he ended up in a very different industry.

Adam Myers grew up in Indianapolis knowing several scientists at pharma giant Eli Lilly. He studied chemistry at Purdue University, interned for three summers at Eli Lilly, and earned his Ph.D. in organic chemistry at Purdue in 2005. As a result of his internships, he says he treated documentation "a little more from an industrial perspective during my graduate school than an academic perspective." He also took opportunities to handle group finances when his Ph.D. adviser was on sabbatical, which gave him some valuable experience, he says.

After earning his Ph.D., Myers worked as a manufacturing chemist and chemical safety officer with a medical diagnostics start-up called Quadraspec in West Lafayette, Indiana, until a layoff in 2007. He is currently working on pharmaceutical analysis at a contract research organization called BASi in West Lafayette.

Breaking in, staying on

The chemists we interviewed say there are many ways to land a job in industry. On-campus recruiting worked for DuPont's Radu and Merck's Strotman. Levy found an ad for the job at Smiths Detection in a chemistry magazine. Faler connected with ExxonMobil by contacting the manager of the catalyst group at Baytown after being tipped off by a friend. Myers and Ciolli searched broadly and networked their ways to their first and second jobs.

Myers recommends "casting a wide net" when exploring companies and job postings. That means looking beyond obvious industry sectors and job-title keywords. "You can be surprised at what will actually be out there that is perfect for your skill set but may not have the particular label you thought it would," he says.

Persistence pays. Ciolli interviewed with Abbott Laboratories during the fall on-campus recruiting process. The on-campus interview was a dead end. While at the recruiting event, however, Ciolli heard an Abbott human resources representative offer to return to his campus to give a seminar on resumé and interview preparation. "At the time, I was coordinating a student-run seminar series on campus," Ciolli says. He arranged a seminar with the human resources rep, who passed his resumé on to a hiring manager for an internally posted position. "Without that little piece of networking, I wouldn't have gotten the job there," he says.

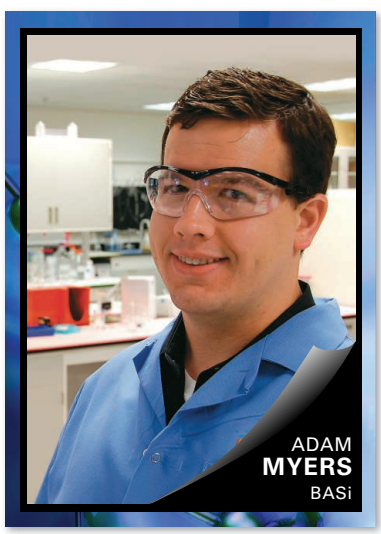

For his second job, Ciolli wanted to move into process chemistry, applied to scale-up. He also wanted to move from Illinois to Ohio to be closer to extended family. "I'd been looking for about a year just to see if there was something that met both personal and professional needs," he says. A local online jobs site listed only a very brief job description. "I didn't know who the hiring company was until they called me back," he says. He knew the company, having researched Ricerca during his previous job search. He was "ecstatic" to start there last year.

Help and humility

Once on board, Ciolli advises, new employees should be ready to learn. Everybody in industry, from receptionists to research managers, "knows more about that industry than you do walking in," he says. If you keep the right attitude, people will show you the ropes. "Check the ego at the door," he says, and "most people are willing to help."

"One of the things I think was critical to me being successful at Abbott and earning the job here at Ricerca early on in my career was just to stay humble and ask questions and listen to what the people around me have to say," Ciolli says. "But they aren't going to spoon-feed you everything. You have to get out there, … talk to people, and help move things along."

–RACHEL PETKEWICH

Rachel Petkewich writes from Oakland, California.

CREDITS (TOP TO BOTTOM): AARON STRYK/EXXONMOBIL CORP.; BASI

Published by AAAS

PERSPECTIVE

Frontiers in Reactor Engineering

Milorad P. Dudukovic

The key challenge for reactor engineering is to establish the scientifically based sustainable technologies necessary for meeting the future energy, environmental, and materials needs of the world. This goal requires advancing our scientific understanding of multiscale kinetic transport interactions to enable better reactor choice and to ensure higher reactor and process efficiencies.

Reactor technology is involved in all chemical transformations by which raw materials—renewable, nonrenewable, and intermediates derived therefrom—are converted to products such as fuels, basic and specialty chemicals, materials for construction and communications, fibers for clothing, fertilizers, pharmaceuticals, and a variety of consumer products (Fig. 1). The selection of a particular process chemistry and an associated reactor technology determines the energy and mass efficiency of the process, as well as its environmental impact.

Chemical reaction engineering emerged early in the last century, when it became apparent that economical large-scale continuous production of chemicals and fuels required more than the knowledge of chemistry. To enable the reactant molecules in a large-scale reactor to undergo chemical transformations at conditions mimicking those achieved in the laboratory, it was necessary to engineer the flow of reactants and their mixing and to provide for adequate addition or removal of heat. In heterogeneous systems, which are prevalent in industrial use, it was necessary to understand the contact between the phases involved and to describe the transport of reactants, intermediates, and products within a phase and between phases. Thus, reaction engineering developed as a discipline by introducing the scientific principles that quantify the interactions between chemical kinetics and the transport of momentum, heat, and mass (*1*–*3*). The resulting multiscale methodology (Fig. 2) provides the means for comparison of different reactor types by the quantitative assessment of various measures of performance, such as productivity, yield, selectivity, energy efficiency, and environmental impact, as a function of operating and feed variables. This approach is applicable to all chemical transformations (*4*). The quantitative description on each scale (Fig. 2) can be obtained at different levels of knowledge, and hence provides different levels of certainty. As we increase the level of scientific understanding at each scale, we move farther to the right on the bars indicated in Fig. 2.

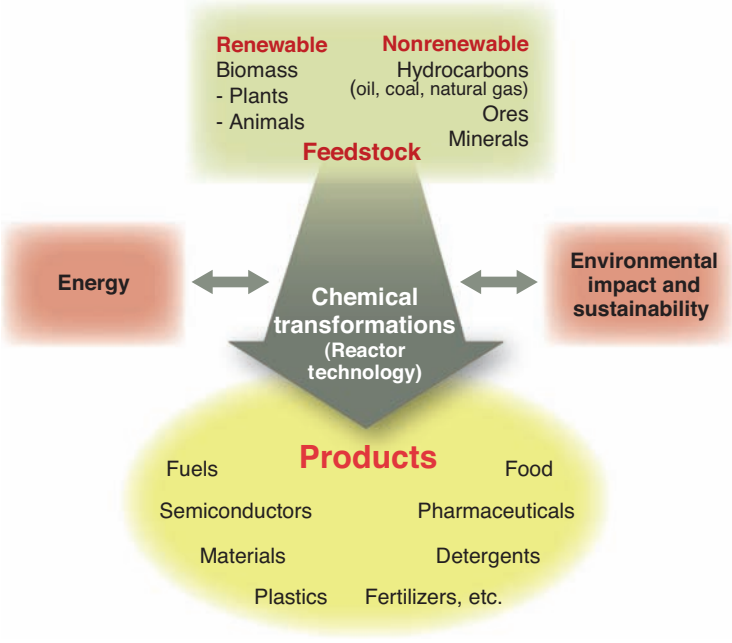

Fig. 1. Inputs and outputs of chemical reactor processes.

After the Second World War, reaction engineering played a pivotal role in the successful development of various reactor technologies in the petrochemical industry, and then spread to the manufacture of polymers, composites, semiconductors, and optical fibers; to biotechnology and the production of antibiotics; and to the synthesis of specialty chemicals. The scientific knowledge used at each scale (Fig. 2) in all of these applications was often rudimentary. It did not go much beyond empirical rate forms at the molecular scale, basic quantification of the effect of catalyst pellet size on catalytic performance at the particle (meso) scale, and assumptions of ideal flow patterns (plug flow or perfect mixing) at the reactor scale. Reaction engineering was practiced as a combination of science and empiricism using what might be called the "principle of optimum sloppiness." This meant that reactor designers did not search for an ideal reactor to best meet the chemistry requirements, nor did they design commercial units a priori. Instead, the reactor type with which a company was most familiar was generally applied, either through repurposing of existing plant infrastructure or through the use of established empirical scale-up procedures to reproduce performance achieved at the bench scale. Scale-up in parallel (i.e., replication of multiple units identical to the small-scale prototype) was favored as less risky than vertical scale-up, the latter requiring a change in reactor dimensions. As a consequence, currently available "best reactor technologies" may not be optimal.

Notably, even the rudimentary application of reaction engineering concepts in the petrochemical industry led to much smaller amounts of unwanted products produced per unit of desired product (lower E-factors) than were encountered in industries that did not make use of such concepts. Nonetheless, the global negative environmental impact of commodity-scale processes is too large to ignore. We are greatly in need of a new generation of reactor technology, even though many of the old technologies are kept profitable by moving them to the developing world. This will require increased levels of scientific understanding of the mesoscale and large-scale kinetic transport interactions. The use of basic reaction engineering concepts is currently spreading to emerging areas such as biomaterials, drug delivery, bionanotechnology, biomass conversion in supercritical water, chemical looping combustion, carbon dioxide sequestration, methane activation, biodiesel synthesis, and hydrogen production (*5*). Many claim that the emphasis on diverse applications testifies to the maturity of the discipline, which in turn implies incorrectly that all the important scientific developments have already been accomplished. That view does not reflect reality well.

Our current increased awareness of the finiteness of our resources raises the bar for future reactor technology. Instead of continuing the application of principles at the rudimentary level, the main task now is to provide an improved scientific basis for conducting chemical transformations in an environmentally acceptable, energy-efficient, and sustainable manner. This means that products that minimize damage to the environment should be identified first (via life-cycle analysis) (*6*). Then, reaction pathways to create these products—preferably from renewable

Chemical Reaction Engineering Laboratory, Department of Energy, Environmental and Chemical Engineering, Washington University, St. Louis, MO 63130, USA. E-mail: dudu@wustl.edu

resources—should be synthesized on the basis of green chemistry principles. The effectiveness of the multiscale approach in developing green technologies for such pathways has been illustrated by the Center for Environmentally Beneficial Catalysis at the University of Kansas.

To reduce the risk of scale-up failure for new technologies, increased levels of scientific understanding will be required at each scale (Fig. 2). On a molecular scale, quantum and molecular dynamics calculations coupled with microkinetic concepts will yield a more detailed understanding of surface chemistry and catalysis, leading to improved mechanisms and better kinetic rate description. On the micro- to mesoscale, further advances are needed to describe the interactions of turbulent mixing with the kinetics, mass transfer, and heat transfer of multicomponent, multiphase systems (*7*, *8*). On the reactor scale, developments in computational fluid dynamics (CFD) codes are making inroads (*9*, *10*), replacing ideal-flow models. Simulations in multiphase systems are vastly aided by imaging tools for the assessment of phase distributions and flows, which provide needed validations for the codes. Quantification of the mesodomains on the basis of first principles is resulting in better design of reactor internals through assessment of the role of films in trickle beds or reactors with structured packing. All of this is done with the aim of obtaining higher rates per unit reactor volume and better selectivity at higher mass and energy efficiency (*11*).

Currently there is a good scientific basis for a number of such process intensification schemes (*12*), such as combining reaction and separation in one unit to overcome equilibrium limitations, adopting a dynamic mode of reactor operation to increase productivity and selectivity, miniaturizing the reactor in order to enhance all transport rates by reducing distances for transport, and conducting the reaction at supercritical conditions with more rapid diffusion. All of these approaches reduce waste and positively affect the environment. For example, in equilibrium limited reactions it is highly advantageous to remove the product in situ or adopt a dynamic mode of operation. The former can be effectively accomplished by reactive distillation (e.g., Eastman Chemicals commercial methyl-acetate synthesis) (*13*), by catalytic distillation (*14*) as used in a number of refinery processes [e.g., (*15*)], or by selective product removal via membranes (*16*). Using in situ adsorption, 100% conversion of syngas to methanol has been demonstrated in an adiabatic reactor (*17*). The reverse-flow dynamic operation of adiabatic packed beds, in which the feed direction is periodically reversed for an exothermic reaction, results in an exit conversion far exceeding that achievable in steady-state operation (*18*). This idea of periodic operation of packed bed reactors, with feed switching from end to end, can be extended by coupling an exothermic reaction (e.g., methane combustion) with an endothermic one (e.g., methane steam reforming), leading to high thermal efficiency and productivity (*19, 20*). This reactor-regenerator concept has potential uses in solar energy storage and clean coal combustion. Successful periodic operation has been commercially demonstrated for a number of systems that use UOP's pressure swing adsorption-desorption process (*21*).

Additionally, because microreactors have high surface-to-volume ratios, they offer enhanced mass and heat transfer coefficients by up to two orders of magnitude at laminar flow conditions and low pressure drop. They offer high volumetric productivity, low manufacturing and operating costs, and increased safety because of the small amount of chemical compounds they contain at any given time (*22, 23*). Successful bench-scale direct fluorinations, chlorinations, sulfonations, and hydrogenations have been demonstrated. Each of these applications relies on the advantage of scale-up by multiplication of individual reactors (scale-up by numbering up). It has been shown (*23*) that multichannel integrated design enables scale-up to large production rates even for highly exothermic reactions such as the direct fluorination of aromatics. Siemens-Axiva, Clariant, Evonik (formerly Degussa), Velocys, and others are in hot pursuit of commercialization of microreactor technology. Despite all the advantages of the microreactors (and the availability of technologies to mass-produce them in silicon, glass, and steel or other metals), they are not widely used even after two decades of intense research. In part this is because they require very fast reactions and active, stable catalysts—an uncommon combination. More important, microreactors are more prone to clogging and to leaks between channels because of their small dimensions, and their reliability and life onstream are unknown. All of these are potentially solvable problems on a case-by-case basis. However, the perceived risk factor is too large for them to replace existing large-scale installations. Most likely, acceptance of microdevices will occur first in highly energetic fast reactions and in situ production of hazardous chemicals, followed by applications in consumer products and distributed power systems.

Most reactors used in commercial applications with the largest environmental footprints are multiphase in character and are large. To reduce their footprint, there is a need for advancing the sci-

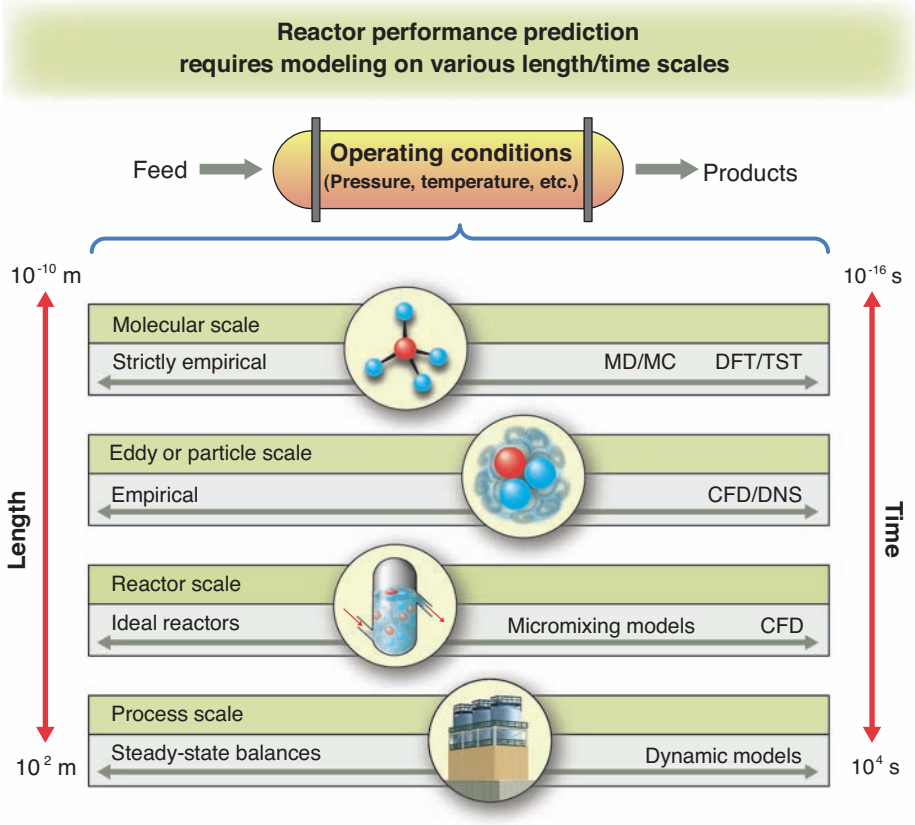

Fig. 2. The time and length scales involved in different facets of a reactor process, from individual molecular interactions to flow dynamics at a catalyst surface, interactive flows of reactant and product streams in the reactor, and ultimately, integrated considerations in the full plant. Modeling techniques developed for rigorous analysis at each scale are noted at the right [molecular dynamics and Monte Carlo (MD/MC) simulations, density functional theory and transition state theory (DFT/TST), and computational fluid dynamics and direct numerical simulation (CFD/DNS)].

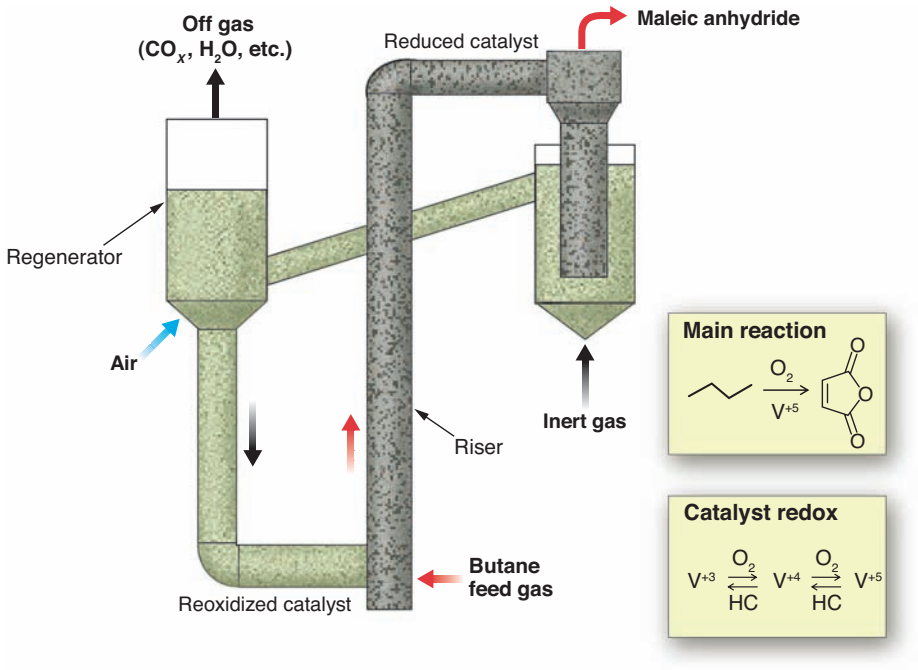

Fig. 3. Schematic of a circulating fluidized bed reactor for maleic anhydride synthesis.

entific basis for scale-up of such units (i.e., packed beds, trickle beds, fluidized beds, mixed slurry systems, bubble columns) (*24*, *25*). In particular, the currently assumed ideal flow pattern (i.e., perfect mixing or plug flow) must be replaced by more realistic descriptions. Although CFD programs for multiphase systems are available, their predictions must be validated. Noninvasive techniques that can provide data in such opaque systems have been developed (*26*). The suggested procedure for the development of scientifically based reactor models for scale-up and design is as follows: The physics and statistics of flow are captured experimentally over a range of conditions; the CFD model is tuned to represent a set of data and then tested for predictability on a new set of conditions; upon validation, the CFD model is used to generate information needed for the development of an appropriate flow model to be coupled with kinetics. The success of this approach has been demonstrated for stirred tanks, bubble columns, and fluidized beds and risers (*24*).

The need for such an advanced approach in describing the solid-flow field in the riser of the circulating fluidized bed (CFB) is illustrated by an example from the fuel-processing field. Currently, worldwide licensed alkylation processes for the production of high-octane fuels make use of strong mineral acids (HF and H_2SO_4) as catalysts, which present environmental hazards. A liquid-solid riser for solid acid–catalyzed alkylation offers an environmentally friendlier alternative. The alkylation reaction takes place in the riser, and the solid acid catalyst is regenerated in a fluidized bed of the CFB system. The flow pattern in the riser affects catalyst activity and selectivity. The prevailing knowledge base (heuristics) suggests that both liquid and solids can be assumed in plug flow. A fully validated CFD model predicts close to plug flow of liquid but indicates a backflow of solids (documented by radioactive particle tracking) (*27*). Thus, riser design based on existing heuristics would lead to the wrong conclusion regarding the state of the catalyst in the riser, and a more detailed description of the flow is needed for proper design and scale-up.

Another example to consider in this light is production of maleic anhydride by partial oxidation of butane, which is often described as a green process because it results in much higher theoretical mass and atom efficiencies (100% for carbon) (*28*). Ultimately, a green process can be achieved here only if the developed vanadium-phosphorus-oxide (VPO) catalyst stays highly selective and active. However, this VPO catalyst does not stay highly selective and active in wall-cooled, packed tubular reactors operating at steady state—the traditional setup used because of its ease of scale-up in parallel. Catalyst selectivity is much improved in transient operation, arguing for a CFB arrangement (Fig. 3) (*29*). The oxidized catalyst meets butane in the riser, where partial oxidation takes place; upon separation of the products, the catalyst is reoxidized in the fluid bed of the CFB. Excellent conversion and selectivity are obtained at laboratory and pilot plant scales, so the key issues in scale-up to a commercial unit are maintenance of the same contact time and variance of the solids residence times. Mean contact time depends in turn on the solids fraction in the riser and its circulation rate through the system. Unfortunately, neither parameter was readily available for a CFB (*30*). In the absence of that information, scale-up was risky and could not be based on scientific prediction. Hence, green chemistry did not result in a green commercial process.

This experience raised doubts about the viability of CFB technology. Data are now available for the true solids residence time distributions and the statistics for solids velocities in the riser (*30*) and await suitable CFD codes that can provide adequate predictions. Such development in turn requires a better scientific description of dense gas-particle flows. Only then can the risk of CFB scale-up be reduced, thereby allowing reliable implementation of this promising technology in partial oxidations, coal and biomass gasification, chemical looping combustion, and redox catalysis.

The creation of new reactor technology thus requires not only an improved understanding of molecular interactions, but also a further advance in the theories of turbulent flows, encompassing reaction, mass, and heat transfer on all scales in complex multiphase systems; the currently used models are more than 50 years old. Reaction engineering is a versatile discipline that will without question be used to solve a number of pressing problems in energy, clean fuels, and materials processing. The question remains whether the economic, political, and regulatory environment will provide the impetus needed for the development of increased levels of scientific understanding in our multiscale methodology in order to use reaction engineering to its fullest potential for the betterment of human society.

References and Notes

1. International Symposia on Chemical Reaction Engineering (www.iscre.org).
2. O. Levenspiel, *Chemical Reaction Engineering* (Wiley, New York, 1962).
3. H. Kramers, K. R. Westerterp, *Elements of Chemical Reactor Design and Operation* (Academic Press, New York, 1964).
4. J. J. Lerou, K. M. Ng, *Chem. Eng. Sci.* **51**, 1595 (1996).
5. J. P. Schouten, *Chemical Reaction Engineering: History, Recent Developments, Future Scope*, Book of Abstracts, 20th International Symposium on Chemical Reaction Engineering (ISCRE 20), Kyoto, 7 to 10 September 2008, pp. 6–7.
6. H. Bauman, A.-M. Tillman, *The Hitch Hiker's Guide to LCA* (Studentlitteratur, Lund, Sweden, 2004).
7. R. D. Fox, *Computational Methods for Turbulent Reacting Flows* (Cambridge Univ. Press, New York, 2003).
8. H. E. A. van den Akker, *Adv. Chem. Eng.* **31**, 151 (2006).
9. J. A. M. Kuipers, V. Van Swaaij, *Adv. Chem. Eng.* **24**, 227 (1998).
10. V. Ranade, *Computational Flow Modeling for Chemical Reactor Engineering* (Academic Press, San Diego, CA, 2002), vol. 5.
11. J. C. Charpentier, *Comput. Chem. Eng.* **33**, 936 (2009).
12. A. Stankiewicz, J. A. Moulijn, *Chem. Eng. Prog.* **96**, 22 (2000).
13. V. H. Agreda, L. R. Partin, U.S. Patent 4435595 (1984).
14. K. Sundmacher, A. Kienle, *Reactive Distillation: Status and Future Directions* (Wiley, New York, 2003).
15. L. A. Smith Jr., U.S. Patent 5345006 (1994).
16. R. Struis, S. Stucki, M. Wiedorn, *J. Membr. Sci.* **113**, 93 (1996).
17. K. R. Westerterp, M. Kuczynski, *Chem. Eng. Sci.* **42**, 1871 (1987).

18. Y. Matros, *Catalytic Processes Under Unsteady State Conditions* (Elsevier, New York, 1989).
19. M. S. Kulkarni, M. P. Dudukovic, *Chem. Eng. Sci.* **52**, 1777 (1997).
20. M. van Sint Annaland *et al.*, *Chem. Eng. Sci.* **57**, 855 (2002).
21. R. T. Maurer, U.S. Patent 5171333 (1992).
22. K. F. Jensen, *Chem. Eng. Sci.* **56**, 293 (2001).
23. V. Hessel *et al.*, *Ind. Eng. Chem. Res.* **44**, 9750 (2005).
24. M. P. Dudukovic *et al.*, *Catal. Rev. Sci. Eng.* **44**, 123 (2002).
25. M. P. Dudukovic, *Ind. Eng. Chem. Res.* **46**, 8674 (2007).
26. J. F. Chaouki *et al.*, *Ind. Eng. Chem. Res.* **36**, 4476 (1997).
27. S. Roy *et al.*, *AIChE J.* **51**, 802 (2005).
28. D. T. Allen, D. T. Shonnard, *Green Engineering: Environmentally Conscious Design of Chemical Processes* (Prentice Hall, Englewood Cliffs, NJ, 2002).
29. R. M. Contractor *et al.*, in *New Developments in Selective Oxidations II*, V. C. Corberan, S. V. Beloon, Eds. (Elsevier, New York, 1994), pp. 233–242.
30. S. Bhusarapu, M. H. Al-Dahhan, M. P. Dudukovic, *Powder Technol.* **163**, 98 (2006).

31. I thank N. Dudukovic-Kuhl, S. Mueller, and E. Redekop for providing suggestions as to how to reach the non–reaction engineering audience via this brief text and visual aids. I am indebted to my graduate students and industrial colleagues who provided so many opportunities for demonstrating the power of reaction engineering.

10.1126/science.1174274

PERSPECTIVE

Looking Forward in Pharmaceutical Process Chemistry

Ian W. Davies and Christopher J. Welch

Core activities of process chemistry involve the synthesis of drug candidates at a scale that supports clinical evaluations and the creation of a manufacturing process that is safe, robust, and cost effective. Innovative problem solving has always been a key element in process chemistry and will be increasingly important for addressing emerging challenges in science, globalization, and commoditization. The acquisition and creation of platform chemical technologies that enable rapid problem solving through the use of high-throughput experimentation will continue to be an important focus going forward. Linking and deploying platforms throughout the discovery-development continuum is expected to enable drug discovery. Increasing collaboration with academia will also become more important for accessing technical solutions and providing the next generation of innovative problem solvers.

Pharmaceutical process chemistry involves the creation of an efficient and cost-effective synthetic route that can be used for the commercial production of a molecule designed for function by medicinal chemists (*1*). This inherent focus on efficiency and economic viability requires a deep understanding of innovative chemical problem solving at the molecular level and places process chemistry at the center of the determination of whether a preclinical candidate will remain a laboratory phenomenon or advance to the marketplace and realize its potential to profoundly affect human health.

Process chemistry embraces three core activities, each critically important in the development of a new drug. First, the drug candidate, which was previously available in only very small quantities from medicinal chemistry, must be synthesized in kilogram-level quantities so as to provide material for Good Laboratory Practices (GLP) safety studies and to enable early clinical investigations. Second, increased quantities of the candidate, which are typically several hundred kilograms but sometimes much more depending on dose and study size, are prepared in collaboration with chemical engineers. This material supports the ongoing clinical program and other activities such as the development of a commercially viable formulation. Third, process chemistry must create a synthetic route for manufacture of the commercial drug that is appropriately safe, robust, and cost effective. The synthetic routes used for preparing the initial lead, the first kilogram, the material for clinical trials, and the commercial product are often substantially different from one another, reflecting the different drivers at the various stages of development. Speed and expediency are most important in discovery and early development, and production cost, safety, environmental impact, and robustness constitute the key drivers for manufacture and commercialization.

Successful innovation in process chemistry has historically involved the thoughtful application of synthetic, separation, and analysis technologies in order to quickly converge on an optimal synthesis. In the most impressive cases, completely new chemistries have been invented to solve the most challenging problems. In addition, process chemists have always been quick to identify and appropriate promising solutions from any quarter, be it internal or external, vendor or academic.

As large pharma organizations emerged in the mid-20th century, they assembled into vertically integrated enterprises capable of carrying out all aspects of chemical discovery, development, and manufacturing. Recent years have brought about alternatives to this model, with contract companies emerging to service practically all stages of drug discovery and development, from design and synthesis of discovery libraries all the way through conducting the pivotal trials that support registration. Speed and operational efficiency are differentiators for some activities, cost and unique scientific capabilities for others. This disaggregation of chemistry activities parallels the globalization in other industries that leverage cost, but also recognizes that innovation and talent are no longer confined to any one country or geography.

A range of business models are emerging that span the spectrum from the internal execution of all activities to the virtual research and development approach, in which all chemistry activities are outsourced. In between these extremes, models will leverage off-shoring to lower-cost geographies, where in addition to cost considerations capability arbitrage can now be used to access the imagination of the expanding global pool of talent.

Open-source innovation models are also becoming increasingly important and allow traditionally internal activities such as brainstorming, troubleshooting, or problem solving to be sourced. It is clear that in the next few years, global competition will drive the industry toward Darwinian outcomes. The successful companies will adopt an innovation model that evolves internal sources of competitive advantage faster than can occurr externally while developing business processes that are capable of accessing and leveraging external sources of innovation.

As the business environment changes at the macro level, a remarkable change in the practice of chemistry can also be anticipated. Innovation in the external environment is currently growing at a rapid pace, with an increasing number of academics now working on the fundamental discovery of reactions or on the development of greener, more efficient processing technologies (*2*). In addition to new approaches coming from academia, a number of new supplier companies that cater to the specialized needs of the pharmaceutical process chemist enter the marketplace each year. The result is a sometimes bewildering array of potential solutions, highlighting the increasing need for intelligent triage.

In addition to reagents and reactions, the importance of analytical, automation, and purification tools and technologies cannot be overstated. Although the image of a robot scientist toiling away in front of a chemistry fume hood has not yet been realized, the use of high-throughput experimentation, with which reactions are first discovered then optimized by use of multiparallel-reaction screening tools, is already a practical re-

Merck, 126 East Lincoln Avenue, Rahway, NJ 07065–0900, USA.

ality within pharma (Fig. 1). This high-throughput experimentation capability affects all three traditional areas of process chemistry: initial scale-up to produce the first kilogram, mid-scale preparation of materials in order to support clinical trials, and creation of an efficient and cost-effective manufacturing route. The ability to make progress rapidly and efficiently with high-throughput experimentation and to extract meaning from the experiments through rapid analysis requires a suite of diverse tools and technologies that are currently in a state of rapid evolution.

High-throughput experimentation enables the creation of platform tools and technologies for the support of pharmaceutical process chemistry. In this context, a platform represents a generalized solution that can be applied to an entire class of complex problems whenever they are encountered (Fig. 2). Platform solutions often incorporate a "user-friendly" simplifying layer that masks an underlying layer of complexity. Tools that allow the user to rapidly screen a selection of catalysts (*3*), enzymes (*4*), purification media (*5*), or crystallization conditions (*6*) are already generating substantial benefits.

Current trends in the area of platform development include a drive not only toward increased speed and throughput but also toward a miniaturization of reaction discovery and optimization. That scientists working on the development of synthetic routes for multiton commercial production would have need for miniaturized experimentation tools at first seems counterintuitive. This seeming paradox becomes understandable when one considers that process chemists need to make the most of small amounts of material when pursuing new route discovery, and miniaturized platforms allow the parallel evaluation of a wide range of routes and reaction conditions. In this context, the invention of a single chemical process typically involves the exploration of several different five- to 10-step synthetic routes, with an extremely limited availability of almost all substrates and intermediates. This increasing use of automation in process chemistry not only enables high-value work but also removes lower-value repetitive tasks from the day-to-day experience of the chemist. Overall, platform building allows resources to be extracted and repurposed for innovation.

It is easy to understand that the synthetic routes used for initial discovery and commercial manufacturing of a pharmaceutical will differ. However, it may seem puzzling why different synthetic routes are used for the preparation of the first milligram and the first kilogram. Part of the answer is because initial discovery syntheses are designed to generate families of related compounds at a very small scale with minimal regard to cost or scarcity of materials and reagents. As a single lead compound for development is identified, substantial improvements in the synthetic process often become possible. Process chemists have historically preferred to get a head start on the challenge of defining a commercial synthesis, often using the synthesis of the first kilogram as a proving ground for trying out new ideas and approaches. There is currently a growing interest in seamlessly scaling the reactions used in discovery chemistry to speed early development. This change will require enhanced collaboration between medicinal and process chemists and is expected to enable discovery by linking and deploying platforms throughout the discovery-development continuum. The goal will be not to constrain but to expand the range of chemical transformations accessible by all chemists.

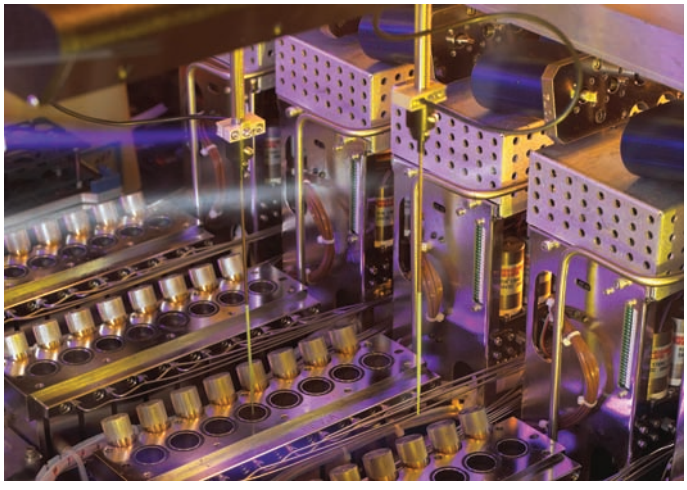

Fig. 1. Multiparallel reactors enable high-throughput evaluation of conditions for carrying out pressurized reactions. Shown above is an individual six-by-eight-cell reactor module with integrated liquid-handling, mixing, temperature (to 200°C) and pressure control (to 500 psi) with operating volume of 2.5 mL.

Prediction of the scale-up behavior of chemistry has always been a concern in process research, especially for highly exothermic reactions or chemistries in which stirring, mixing, or heat transfer issues are critical to performance or process safety. Some of the platform reactions and operations that are used in process chemistry are easily scaled, allowing the confident prediction of performance at a large scale on the basis of microscale evaluations (*7*). Microanalytical approaches that improve the ability to identify and understand scale-up concerns at an early stage will become increasingly important, as will the replacement of poorly scaled technologies with more robust and predictable platforms.

Catalytic processes hold enormous promise for process chemistry because they address synthetic efficiency through high turnover and exceptional selectivity, which reduces costs through both minimization of cycle time and environmental impact. In addition, catalytic processes have the potential to exponentially expand the range of synthetic strategies and complex structural diversity that can be accessed by both discovery and development chemists. For example, remarkable progress has been made in recent years in the development of robust catalysis technologies for performing stereoselective synthesis, which allows process chemists to more effectively access increased diversity.

Process chemists have been somewhat slow to embrace the use of catalysis and biocatalysis as the preferred synthetic approach for pharmaceutical manufacturing. A risk-averse and cautious culture has sometimes limited the use of transition metal–catalyzed processes or complexity-building steps late in the synthetic sequence. Although catalyst application is on the increase, most manufacturing processes still incorporate only a limited number of catalytic transformations. Use of patented catalysts has sometimes presented an impediment to adoption, but with an increased experience in working together, pharma and institutional intellectual property (IP) offices are becoming more adept at the construction of licensing arrangements that facilitate convenient and timely access, for example by incorporating IP access into the purchase price of the catalyst. As industry pricing pressures continue to escalate, the increased adoption of catalytic methodologies can be anticipated.

In the past, high product margins were possible because of the overall market pricing for pharmaceuticals in the developed world. Reinnovation of the synthetic route so as to extract efficiencies during the patented life cycle of a product was sometimes avoided because of regulatory burden and the fact that available resources of process chemists were focused on emerging new products rather than on life-cycle management of inline products. There is now an increasing drive to substantially reduce the cost of active ingredients in order to both accommodate the need for cost containment in the developed world and to enable broader access to emerging markets, and this trend is expected to intensify.

Generic manufacturers, long accustomed to competing on the basis of price and quality, have often been extremely innovative, adopting newer synthetic technologies that were unavailable for deployment by the original innovator at the time of product launch. A case in point is the steady stream of improved processes that emerged for the popular pain reliever ibuprofen after the patent expired, each route being more efficient and cost effective than the last (*8*). When ibuprofen was launched in the late 1960s, the synthetic route involved a six-step reaction sequence and was

characterized by the use of excess reagents and the production of large amounts of unwanted byproducts. Nevertheless, the synthetic route was suitable for meeting commercial demand. Because ibuprofen was approved for generic and over-the-counter use in many markets, the need to supply a substantially expanded volume at commodity prices became a business reality for manufacturers. Through the use of catalysts rather than excess of reagents to drive the reactions, the number of steps in the ibuprofen-manufacturing process was reduced while yield and efficiency were increased. This was not only good for the patient but also good for the environment.

In contrast to some other chemical industries, pharmaceutical manufacturing typically involves a multistep synthesis of compounds with considerable stereochemical complexity and requires substantial regulatory oversight to ensure patient safety. Nevertheless, the general approach to process research is the same as in other industries, and lessons from successful commodity chemical manufacturing (such as intensive process optimization and continuous processing for cost reduction) can be applied in pharmaceutical process research.

Whole-cell fermentation and semisynthesis have long been used for the cost-effective production of complex drugs with cultured organisms such as yeast, fungi, or bacteria. A new wave of innovation in this field is being fueled by an increased understanding of biosynthetic pathways, the ability to achieve production in an expanded suite of organisms, and greatly improved synthesis tools. Isolated enzymes are also emerging as preferred tools for carrying out industrial-scale catalytic processes, with recent successes in the uses of enzymes obtained via directed evolution (*4*) leading to remarkable selectivity and efficiency as well as cost and environmental advantages. Additional development in directed evolution and assembly of designed enzyme arrays will emerge to parallel the biosynthetic reaction assemblies used in nature in order to accomplish multiple transformations in series.

In the field of organocatalysis, small-molecule catalysts are emerging as promoters of useful transformations and cascades that do not rely on transition metals (*9*). The emerging area of C-H functionalization (*10*) holds considerable promise for substantially changing synthetic strategy. Other recent advances use flow chemistry to carry out multiple linked steps via flow-through immobilized catalyst beds. The application of these and other exciting technologies to emerging problems in pharmaceutical process chemistry holds considerable promise, but to install them and capture full value will require a change in the culture.

As chemical processes based on these emerging technologies are introduced into the manufacturing arena, the focus will become increasingly dominated by considerations of the cost, compliance, and integrity of the global supply. Lean manufacturing approaches will dominate rather than production according to forecast schedules that have been incumbent in pharmaceutical manufacturing. Continuous processes are likely to be used to drive down unit cost and facilitate changes in product volume. Logistical controls may be required to assure product quality, necessitating closer collaboration with suppliers. Quality by Design (*11*) will become increasingly important, ensuring a thorough understanding of the process, including risks and mitigation strategies.

The relationship between process chemists and academia is also changing as more formalized mechanisms emerge to improve access to both innovation and talent. Efficient scouting for the identification of useful tools and technologies coming from academic labs is clearly needed, but process chemistry will also need to develop improved mechanisms for alerting academics and funding agencies to emerging areas of greatest opportunity. Funded collaborations will become more structured and transparent with clearer goals and deliverables than in the past. Pharma will continue to compete for the best, brightest, and most innovative graduates for careers in chemistry. Although the skills required for handcrafting individual molecules will still be valuable, an underlying core competency of innovative problem solving is likely to become increasingly important.

Academia has only recently begun to embrace the labor-saving tools adopted in industry,

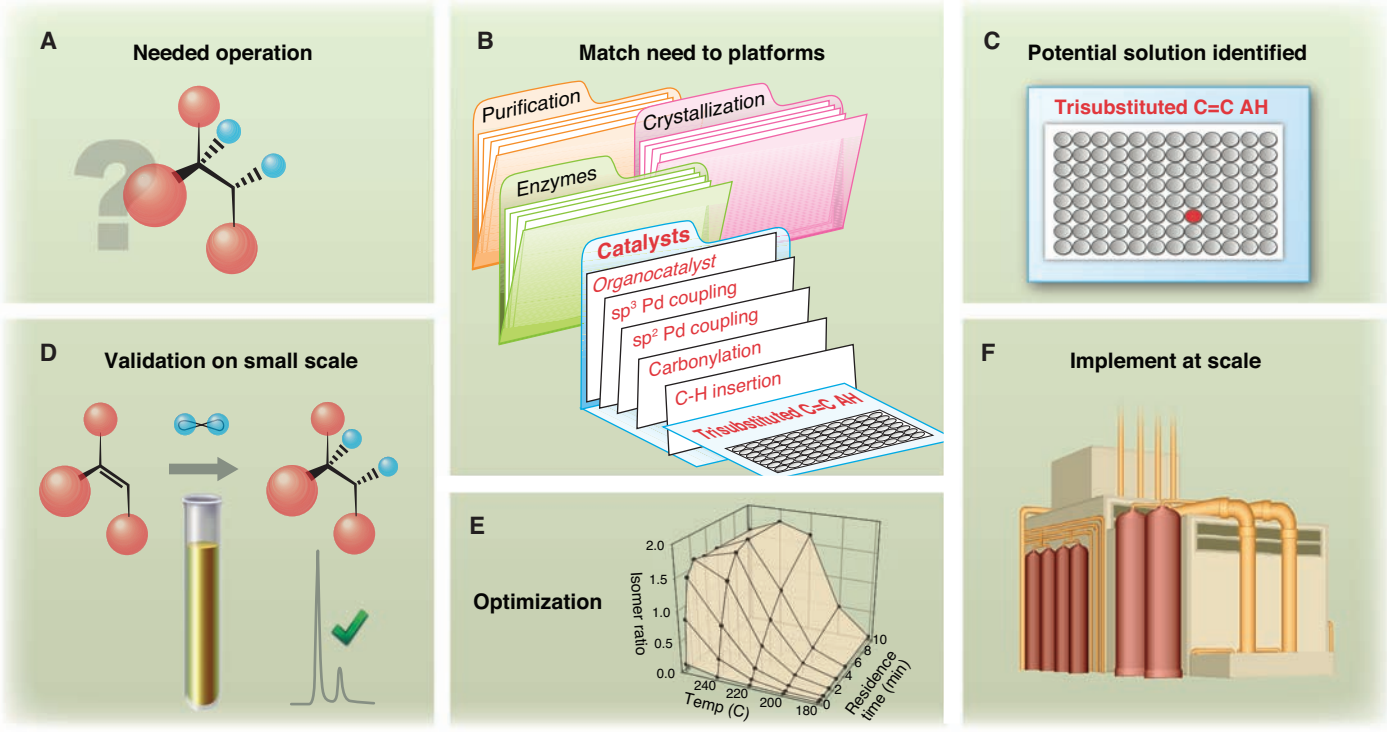

Fig. 2. Use of platform tools facilitates modern pharmaceutical process chemistry. Needed transformations [(**A**) exemplified here by an asymmetric olefin hydrogenation] are matched against available platform tools (**B**). A potential solution is first identified (**C**), then validated on small scale (**D**), optimized (**E**), and implemented at scale (**F**).

previously relying on armies of graduate students as a source of readily available labor. In the past, major discoveries in natural product total-synthesis and methodology development were made possible by these large numbers of talented students who toiled in the academic labs in anticipation of a bright future and stable employment in pharma. The training mission of academia and the development of a robust research infrastructure will need to be refreshed and scaled appropriately in order to thrive in a global innovation environment. Going forward, it will become increasingly important for academia to embrace high-throughput experimentation and platform tools, not only to increase innovation productivity but also to produce graduates with the relevant skills and problem-solving capability that will be needed in the next decade. To be successful in the long term, chemists will not only need to be smart, innovative, and vastly imaginative, but also will need to possess a variety of other nonscientific competencies. Open-mindedness and continuous learning are essential, as are the outstanding communication and collaboration skills that are needed for working on global project teams that involve both internal collaborators and external partners.

The best discoveries in biomedical research are yet to come, and enormous challenges and major unmet medical need exist across a wide range of therapeutic areas. These challenges will be overcome through scientific innovation and collaboration across many disciplines. Process chemistry can be one of those disciplines that help strengthen the value proposition of medicines to patients and payers. The old ways are simply too slow, too expensive, and have an unacceptably low probability of success. There has never been a more challenging or exciting time for process chemistry.

References

1. H. J. Federsel, *Acc. Chem. Res.* **42**, 671 (2009).
2. www.epa.gov/greenchemistry.
3. C. S. Shultz, S. W. Krska, *Acc. Chem. Res.* **40**, 1320 (2007).
4. R. J. Fox, G. W. Huisman, *Trends Biotechnol.* **26**, 132 (2008).
5. C. J. Welch *et al.*, *Org. Process Res. Dev.* **12**, 81 (2008).
6. P. J. Desrosiers, *Mod. Drug Disc.* **7**, 40 (2004).
7. C. J. Welch *et al.*, *Org. Process Res. Dev.* **12**, 674 (2008).
8. K. D. Rainsford, *Ibuprofen: A Critical Bibliographic Review* (CRC Press, Cincinnati, OH, 1999).
9. D. W. C. MacMillan, *Nature* **455**, 304 (2008).
10. H. M. L. Davies, J. R. Manning, *Nature* **451**, 417 (2008).
11. www.fda.gov/AboutFDA/CentersOffices/CDER/ucm128080.htm.

10.1126/science.1174501

PERSPECTIVE

Frontiers in Olefin Polymerization: Reinventing the World's Most Common Synthetic Polymers

Phillip D. Hustad

Synthetic polymers are vital to our society, affecting practically every aspect of modern life. The ubiquitous nature of these materials is a result of years of collaboration between basic and applied researchers across many disciplines, resulting in economic routes to materials that meet customer needs. These considerations are exemplified by recent developments in the synthesis of block copolymers from simple olefins. The practical application of creative chemistry has produced materials with a favorable balance of desirable polymer properties and process economics.

Nearly a century has passed since the introduction of Bakelite (Leo Baekaland, Yonkers, New York), the first commercial, synthetic polymer. Since then, the broader class of carbon-based polymeric materials has become so prevalent that it is hard to imagine life without these materials. The rapid growth of polymers is a result of tremendous collaborative effort in both fundamental and applied research at the interface of chemistry, materials science, and polymer engineering. It is clear to those working in the field that it would have been impossible to develop such a broad portfolio of successful materials without this collaborative effort.

The invention of any material begins with an important chemical breakthrough, but the development of a commercially useful material presents distinct challenges. Though serendipity can play an important role, the path to success is clearest when materials are born from market need. This need subsequently defines the specific function of the target material. And, of course, the cost of the material must be reasonable with respect to the application. For example, fluoroelastomer o-rings are used as high-performance seals, despite a material cost that is nearly 15 times higher than the nitrile rubber that is used for less demanding applications. Finding the balance between performance and price is critical to commercial success, as the customer will almost always adopt the cheapest solution that meets the performance criteria.

Once a need is identified and the target material is defined, the polymer chemist can begin to consider what molecular structure will achieve the desired performance and whether or not the synthesis is feasible from a chemistry and capital standpoint. Polymeric materials are often sought to replace existing products. In this case, the success of the new material will depend on the customer's motivation for change; higher performance and lower cost will be key attributes of a successful substitute. When all of these issues (market need, structure/function relations, synthetic challenge, and cost) are considered, it becomes clear that the successful launch of a commercial synthetic polymer relies heavily on creative thought, practical problem solving, careful lab work, timing, and to some degree, luck.

Many polymeric materials are born in academic laboratories and subsequently developed into commercial products in industry; this pathway is not especially surprising. Industrial and academic R&D differ in a number of ways, most notably the motivation behind them. Industrial polymer research has as its driving force the invention of materials that people will pay to adopt. Academic R&D has a very different mission: defining the newest advances, challenging preconceived notions, and educating the next generation of researchers. The difference between the two missions is evident in the way success is measured. In industry, success comes with commercial sales of the material, but in academia, success is measured by winning grants and publication of results in high-quality, peer-reviewed journals. The academic researcher is less constrained with respect to practicality, scalability, or final product price; creativity is the bottom line. The industrial researcher, on the other hand, knows that even the most creative scientific breakthrough must ultimately lead to a commercially viable product for the company to realize an economic benefit. Certainly, a combination of the best qualities of both approaches—unlimited creativity and constrained pragmatism—would be ideal.

The story of polyolefins represents the quintessential example of the convergence of creativity and practicality leading to the commercial launch of new materials. Polyolefins, the generic name for synthetic polymers based on ethylene, propylene, and α olefins, have become the world's

The Dow Chemical Company, 2301 North Brazosport Boulevard, B-3827, Freeport, TX 77541, USA. E-mail: pdhustad@dow.com

most common synthetic polymers, with current annual capacity in excess of 70 billion kg. The tremendous volume and broad utility of polyolefins is related to the ability to make many different kinds of material, from rigid thermoplastics to flexible elastomers to waxes, from a very simple set of inexpensive building blocks. This growth has been fueled by a series of breakthroughs in synthesis of differentiated materials, with contributions from academic and industrial researchers alike.

Polyethylene was originally commercialized by Imperial Chemical Industries (London, England) in the 1930s with the use of a high-pressure free-radical polymerization process (*1*) that produced a highly branched material with a limited range of properties and applications. In the 1950s, the application space was broadened substantially after Ziegler *et al.* (*2*) and Natta *et al.* (*3*) discovered heterogeneous olefin polymerization catalysts. The linear chain structures of these homopolymers and copolymers resulted in differentiated properties and enabled many market opportunities. Another polyolefin revolution began in the 1980s with Sinn and Kaminsky's discovery of efficient activators for metallocene catalyst systems (*4*). These homogeneous catalysts, bearing organic ligands that can be tailored to influence polymerization characteristics, have expanded the utility of polyolefins even further. These catalyst systems have enabled finely tuned preparation of microstructures such as soft, flexible materials useful in many elastomer applications. With these advances, polyolefins are now widely used in applications as varied as milk jugs, food-packaging films, cable jackets, flexible tubing, automotive dashboards, and even artificial hip joints.

Given all of these tremendous advances over more than 70 years of development, many researchers are beginning to view polyolefins as simple, large-volume commodity materials with little to no room for further breakthrough. The polymer science community is trending toward more sophisticated polymer systems, but opportunities for continued polyolefin development can be identified in the limitations of current materials. For example, the aforementioned materials are composed of statistical copolymer structures that present some unfortunate property correlations; increasing comonomer content gives a more flexible material with a concomitant decrease in use temperature. These tradeoffs preclude the use of these olefin-based copolymers in thermoplastic elastomer applications requiring higher levels of performance, currently served in part by styrenic block copolymers (SBCs) (*5*). Nonetheless, there was much speculation that olefin-based block copolymers bearing both semicrystalline and amorphous blocks could provide a means to break these long-standing property correlations and extend polyolefins into more demanding application spaces. Olefin-based materials could be cost-advantaged over SBCs and have potential for further performance enhancements that may allow competition against even higher-value materials.

A combination of this market pull and the tremendous synthetic challenge has made synthesis of block copolymers from simple olefins one of the long-standing goals of polymer synthesis, attracting the attention of many researchers in both academia and industry. The predominant approach toward this goal has focused on living-polymerization systems, similar to the processes for the production of SBCs. In living polymerizations, chains are grown without termination, which enables synthesis of block copolymers by sequential monomer addition (*6*). In the 1980s, Bates *et al.* used living anionic polymerization coupled with hydrogenation to prepare model olefin-based block copolymers (*7*). These materials have provided a tremendous wealth of fundamental knowledge, but the range of potential polymer structures is somewhat limited.

These limitations could be overcome by adapting Ziegler-Natta catalysts for these synthetic processes, but unfortunately, these systems are susceptible to termination, and they also release, or transfer, many chains during polymerization. By designing systems that suppress these processes, advanced catalysts have been used to make block copolymers with sequential monomer addition techniques (Fig. 1) (*8*). These systems have produced many new block copolymers with precise structures (*9*), but, unfortunately, the fundamental features that enable precision synthesis also make the processes very inefficient and, thus, commercially impractical. Conventional catalysts produce hundreds to thousands of chains per metal center, but these living systems produce only one. To understand the magnitude of this limitation, consider the chain efficiency of the titanium bis(phenoxyimine) system developed independently by Tian *et al.* (*10*) and Saito *et al.* at Mitsui Chemicals (Tokyo, Japan) (*11*). In synthesis of a polymer with a number-average molecular weight of 100,000 g/mol, 1 g of precatalyst yields only ~100 g of polymer. Commercial olefin polymerization catalysts are typically one thousand times more productive. SBCs are produced by similar living-polymerization techniques, but the required initiators are much less expensive than these transition metal complexes. Because of this efficiency limitation, these materials will not be able to compete with SBCs in the targeted applications, but this does not imply that they are not valuable. Living systems have produced new materials that have provided fundamental understanding of key structure-property relations, advancing the field considerably. Materials from these methods may also find commercial use, but they will always be limited to high-value, low-volume applications.

Several alternatives to the one-chain-per-catalyst route have been developed in attempts to surmount this efficiency limitation. Coates and Waymouth presented a breakthrough toward catalytic block copolymer synthesis in 1995 with an

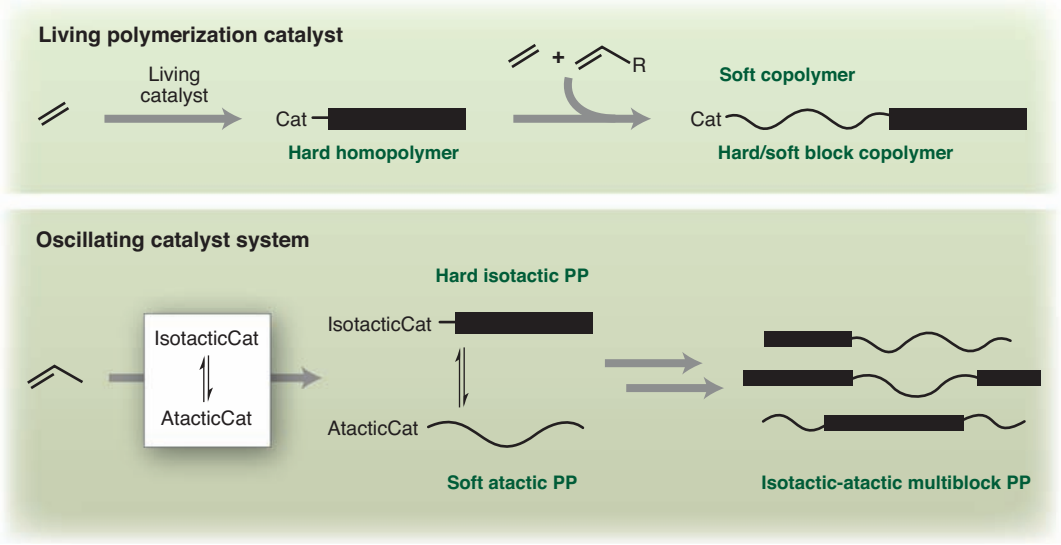

Fig. 1. Schematics of living-polymerization and oscillating-catalyst approaches to hard/soft block copolymers from simple olefin feedstocks. Cat, catalyst; R, alkyl group.

oscillating-catalyst system (*12*). These catalysts reversibly switch stereoselectivity on the time scale of polymerization, producing polypropylenes (PPs) containing both hard isotactic and amorphous atactic segments (Fig. 1). This system produces multiple chains per catalyst through chain release, but it also has a major limitation tied to a fundamental property. Atactic PP has a relatively high glass-transition temperature, and whereas these materials are tough, flexible elastomers at room temperature, they become brittle glasses below 0°C. This elegant catalyst system remains a creative example of polymerization catalysis and has served as inspiration for many researchers. Regardless, these materials have yet to find commercial applications because of this key deficiency against the targeted applications.

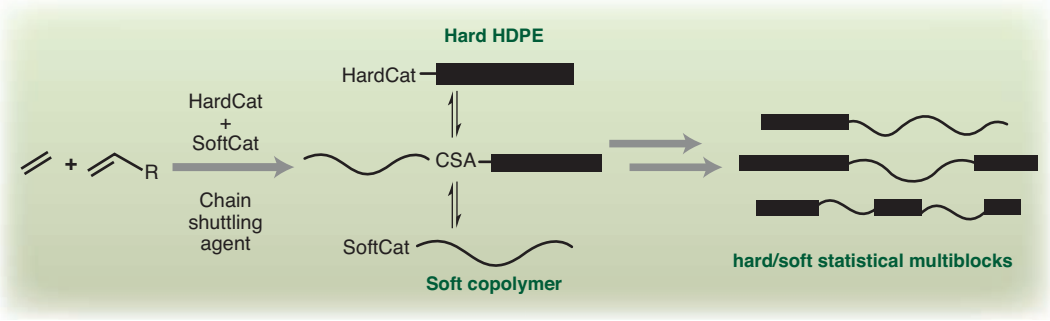

Fig. 2. Schematic of Dow's chain shuttling statistical multiblock process and products. HDPE, high-density polyethylene; CSA, chain-shuttling agent.

Industrial researchers have also undertaken the block copolymer challenge with a focus on producing materials with potential commercial utility. Researchers at ExxonMobil Chemical Company (Baytown, Texas) devised a dual catalyst technology to produce hard or soft materials with comb branch-block architectures in catalytic fashion with the use of a macromonomer approach (*13*). This system uses one catalyst to form a hard semicrystalline polymer with a polymerizable vinyl end group and a second catalyst that copolymerizes ethylene, an α olefin, and the macromonomer. The process can be carried out in either single- or dual-reactor schemes to produce comb branch-block copolymers with soft backbones and hard side chains.

A team from Dow (Freeport, Texas; South Charleston, West Virginia; and Midland, Michigan) tackled the challenge under the additional constraint that the chemistry should scale to existing capital assets. This restriction, although very limiting in scope, was enacted for economic reasons; grassroots process developments are far more complicated, expensive, and time-intensive to commercialize. Working under these constraints, the Dow team actually used chain transfer to their advantage for the practical synthesis of block copolymers. The inventive process, referred to as chain shuttling, uses two catalysts in a single reactor with a reversible chain-transfer mechanism to produce linear statistical multiblocks that have hard and soft segments with differing physical properties (Fig. 2). Pelletier *et al.* (*14*) and Britovsek *et al.* (*15*) had observed evidence of reversible chain-transfer in lanthanocene/magnesium and iron/zinc systems, respectively. However, the relatively low reaction temperatures used in these systems resulted in precipitation that limited production to fairly low molecular weights.

Recognizing these limitations, the Dow team set out to identify a pair of catalysts with reversible chain-transfer characteristics that also maintained high efficiency at high polymerization temperatures. They employed high-throughput screening tools (*16*) to evaluate a library of catalyst options, resulting in rapid identification of a system that fulfilled all of the desired criteria (*17*). The resulting system is highly efficient, producing hundreds of chains per catalyst molecule. The shuttling chemistry and continuous process produce materials with distributions of block length and molecular weight. Perhaps most importantly from an industrial standpoint, the chemistry is amenable to Dow's existing processes, thereby reducing process development costs and timelines. These factors ultimately led to Dow's introduction of a new product line, INFUSE (Midland, Michigan) Olefin Block Copolymers (OBCs), which are expanding olefin elastomers into a wide range of innovative market applications.

As these examples demonstrate, the development of polymeric materials is much more challenging when practical constraints are imposed and success is defined by commercial viability. It is often the case that overcoming one obstacle simply leads to another, but useful innovations can stem from explorations of these perceived contradictions. For example, both the oscillating-catalyst and chain-shuttling systems sacrifice structural precision for efficiency. It is common sentiment that "precise" and "useful" are directly correlated in polymeric materials (*18*). This may be true for many applications, but the required level of precision ultimately depends on the material's desired function. With biological systems, a single mistake can have drastic consequences, but in simpler polymeric materials, the penalties for imperfections are far less grave. For commercial success, the key is understanding the application's required level of precision and cost tolerance. Polymers from living-polymerization techniques are often described as precise, as they are composed of sets of nearly identical molecules. OBCs from chain shuttling have a distribution of architectures and are therefore fundamentally different materials that provide a new range of properties.

Some commercial applications may require precise structures from living polymerization, but the costs associated with such precision may limit their economic viability. Zhang and Sita have recently demonstrated a potential solution to this dilemma by combining attributes of living-polymerization and reversible chain-transfer processes, enabling catalytic synthesis of polyolefins with narrow molecular-weight distributions (*19*). This is an excellent example of academic research directed at a practical problem. In other instances, these structural "imperfections" actually prove to be beneficial. For example, Dow researchers recently demonstrated the dramatic effect of block-length distribution on phase behavior (*20*) in self-assembled diblock OBCs (*21*), resulting in films that act as partial one-dimensional photonic crystals (*22*). In this case, the practical solution produced a result that expanded a fundamental understanding in the field of polymer chemistry.

These examples demonstrate some of the tremendous progress that has been made toward synthesis of olefin-based block copolymers, but these synthetic feats represent only the first step toward commercialization. Contributions from process engineers, materials scientists, applications specialists, and many others are necessary for these materials to achieve commercial success. These fields are also experiencing exciting developments that are extending the reach of polyolefins. For example, advanced nucleation technologies are broadening the use window of PPs by increasing processing speeds and improving properties and aesthetics (*23*). Multilayer processing technologies are allowing polyolefins to be used in combination with other materials for innovative food packaging technologies. Researchers are also developing petroleum-free routes of olefin feedstocks, and both Braskem (São Paulo, Brazil) and a joint venture between Dow and Crystalsev (São Paulo, Brazil) are targeting the production of "green" polyethylene derived from sugarcane. It is clear that the last century witnessed many tremendous developments, but if these advances are any indication, perhaps the real fun is about to begin.

References and Notes

1. E. W. Fawcett, R. O. Gibson, M. W. Perrin, J. G. Patton, E. G. Williams, B Patent 471,590 (1937).
2. K. Ziegler, E. Holzkamp, H. Breil, H. Martin, *Angew. Chem.* **67**, 426 (1955).
3. G. Natta *et al.*, *J. Am. Chem. Soc.* **77**, 1708 (1955).
4. H. Sinn, W. Kaminsky, *Adv. Organomet. Chem.* **18**, 99 (1980).
5. G. Holden, in *Encyclopedia of Polymer Science and Technology*, vol. 5, J. I. Kroschwitz, Ed. (Wiley, New York, 1987), pp. 416–430.
6. M. J. Szwarc, *Polym. Sci. Part A Polym. Chem.* **36**, ix (1998).
7. F. S. Bates, H. E. Bair, M. A. Hartney, *Macromolecules* **17**, 1987 (1984).
8. G. W. Coates, P. D. Hustad, S. Reinartz, *Angew. Chem. Int. Ed.* **41**, 2236 (2002).
9. G. J. Domski, J. M. Rose, G. W. Coates, A. D. Bolig, M. Brookhart, *Prog. Polym. Sci.* **32**, 30 (2007).
10. J. Tian, P. D. Hustad, G. W. Coates, *J. Am. Chem. Soc.* **123**, 5134 (2001).
11. J. Saito *et al.*, *Chem. Lett.* **6**, 576 (2001).
12. G. W. Coates, R. M. Waymouth, *Science* **267**, 217 (1995).
13. E. J. Markel, W. Weng, A. J. Peacock, A. H. Dekmezian, *Macromolecules* **33**, 8541 (2000).
14. J.-F. Pelletier, A. Mortreux, X. Olonde, K. Bujadoux, *Angew. Chem. Int. Ed. Engl.* **35**, 1854 (1996).
15. G. J. P. Britovsek, S. A. Cohen, V. C. Gibson, P. J. Maddox, M. Van Meurs, *Angew. Chem. Int. Ed.* **41**, 489 (2002).
16. V. Murphy *et al.*, *Chem. Rec.* **2**, 278 (2002).
17. D. J. Arriola, E. M. Carnahan, P. D. Hustad, R. L. Kuhlman, T. T. Wenzel, *Science* **312**, 714 (2006).
18. C. K. Ober *et al.*, *Macromolecules* **42**, 465 (2009).
19. W. Zhang, L. R. Sita, *J. Am. Chem. Soc.* **130**, 442 (2008).
20. N. A. Lynd, A. J. Meuler, M. A. Hillmyer, *Prog. Polym. Sci.* **33**, 875 (2008).
21. P. D. Hustad, R. L. Kuhlman, D. J. Arriola, E. M. Carnahan, T. T. Wenzel, *Macromolecules* **40**, 7061 (2007).
22. P. D. Hustad, G. R. Marchand, E. I. Garcia-Meitin, P. L. Roberts, J. D. Weinhold, *Macromolecules* **42**, 3788 (2009).
23. D. Libster, A. Aserin, N. Garti, *Polym. Adv. Technol.* **18**, 685 (2007).
24. I thank L. Vosejpka, P. Roberts, N. Aboelella, L. Fan, J. Patt, A. Taha, P. Vosejpka, J. Carnahan, and J. Weinhold for helpful discussions.

10.1126/science.1174927

PERSPECTIVE

The Biofuels Landscape Through the Lens of Industrial Chemistry

Paul A. Willems

Replacing petroleum feedstock with biomass in the production of fuels and value-added chemicals carries considerable appeal. As in industrial chemistry more broadly, high-throughput experimentation has greatly facilitated innovation in small-scale exploration of biomass production and processing. Yet biomass is hard to transport, potentially hindering the integration of manufacturing-scale processes. Moreover, the path from laboratory breakthrough to commercial production remains as tortuous as ever.

A century's worth of innovation in industrial chemistry has afforded the plethora of fertilizers, pharmaceuticals, coatings, fabrics, and packaging materials so integral to modern society. The history of these developments, arising largely from a steady supply of petroleum-based feedstock, offers an enlightening perspective on the challenges and opportunities facing nascent projects to prepare a full range of commodity-scale fuels and chemicals from biomass sources.

As the name implies, industrial chemistry has predominantly been the domain of major corporations, rather than universities or small companies. The road to commercialization is typically a long one, on the order of 10 years from initial invention to broad commercial application. Along the way, a great many innovations fall by the wayside, not so much because the initial idea was flawed but rather because some ancillary aspect prevented economical deployment on a large scale. Issues range from minor impurities or compositional variations in real-world raw materials, which can disrupt the manufacturing process, to market imbalances in byproduct streams, to mismatches of the product properties with marketplace specifications. Only large companies have traditionally had the capacity and capability to weather these scale-up storms.

The process typically goes through several stages: investigation of various unit operations at the lab scale; development of computer models to analyze and scale up the results; construction of an intermediate-scale asset (a so-called pilot or demonstration plant), which integrates the various operations into a fully functioning facility, including recycle streams; a scale up from pilot plant to the first full-scale commercial facility; and finally, replication of that facility into multiple commercial assets. In reality of course, the process is not linear, and multiple iterations through some of these steps are often required. Given the time frames involved in the design, construction, and operation of the various stages, it is not difficult to arrive at the 10-year projection noted above. From a business perspective, initial innovation is relatively easy and cheap; most of the risk resides in the expensive and lengthy scale-up and commercialization process. Therefore, choosing which innovations to take forward becomes a critical question.

Despite industrial chemistry's extensive history, many practitioners in the field will attest that innovation has actually been accelerating over the past 10 years. This has been due in large measure to the advent of high-throughput experimentation (HTE) capacity. The capability to do many small-scale experiments in parallel relatively quickly has opened up vast avenues for investigation. Initially, HTE was used primarily for "needle-in-a-haystack" searches: trial-and-error exploration of multiparameter combinatorial problems such as new catalyst compositions or new product formulations. Attractive leads discovered through this process were then subjected to the conventional development process. As the technology has become more sophisticated, however, applications have emerged to systematically explore process parameters for optimization purposes and even to derive kinetic information. In this regard, HTE is improving not only the initial discovery step in the innovation process but also the rate at which the early commercialization steps can proceed. At the same time, it has become clear that the machines can quite quickly generate more data than humans can process and interpret. The blind application of HTE merely results in data overload.

As the cost of HTE capability has come down, the technology has reintroduced the academic community as well as some small companies to the innovation landscape in industrial chemicals. HTE in effect lowered the barrier to entry into the innovation space. The problem of how to get from the lab to commercial application has not fundamentally changed, however. Most of the cost, time, and risk still reside in the scale-up process; we now just have more good ideas competing at the beginning of the queue.

Another feature of industrial chemistry is the highly integrated nature in which the industrial processes and value chains have evolved. Driven by the need to make the most out of every barrel of petroleum and to create maximum economic value at minimum cost, the industry has evolved manufacturing complexes with shared infrastructure, in which the byproduct of one process becomes the raw material for another. Well-defined and globally accepted product specifications allow for tight integration along the value chain. This standardization has created value for buyers and suppliers alike, though it also tends to create barriers to entry for new products seeking to displace an incumbent one, because they need to meet at least the same specifications and performance expectations while conserving (or ideally lowering) costs.

Energy Biosciences Institute, 326 Calvin Laboratory, MC 5230, BP Group, University of California, Berkeley, CA 94720–5230, USA.

CREDIT: DUAL FREQ/WIKIMEDIA

So where do the emerging efforts in the industrialization of biofuels and biomass-derived chemicals stand in this context? Lignocellulosic biomass is one of the most widely available raw materials on Earth, and its conversion to liquid transportation fuels, basic chemicals, and specialty materials is a thriving international research theme. If we are successful in making the conversion of biomass to value-added products an economical proposition, then it will be an important contributor in the fight against global warming. It will also potentially satisfy other political objectives: increasing the security of energy supplies and supporting rural communities and agriculture in general. The issue here is not whether the task is technically feasible, but whether it can be done economically and sustainably.

Some believe that biomass-based production pathways will gradually substitute for petroleum-based routes, and that a similar industry will arise from a different raw material—hence the concept of biorefineries. Yet biomass is quite different from petroleum. Biomass is a bulky solid with relatively high water content. The range over which it can be economically transported to a manufacturing facility is on the order of 40 to 80 km. This supply constraint limits the scale of processing facilities, in contrast to petroleum-based manufacturing, whose scale is currently limited purely by our technical ingenuity. Scale factors in turn limit how many products can be economically produced in the biorefinery, because their range and quantity are limited by the size of the raw material supply. It is therefore unlikely that we will see manufacturing complexes arise with the same degree of integration seen in refining and petrochemical processing. It is also unlikely that the existing petrochemical complexes will be retrofitted to process biomass, because they are for the most part distant from the raw material supply. The inherently local nature of biomass will probably result in distributed processing plants spread across the country rather than in megacenters. A long-term symbiotic relationship will have to exist between the processing plant and the surrounding farming community, as they are effectively locked in together.

Tight product specifications are also likely to stand in the way of the market penetration of new biomass-based chemicals and polymers. The polymer segment is likely to be especially difficult, because products are generally sold on the basis of their processing and performance characteristics, which will be difficult to match unless the biomass-based material is chemically identical to the incumbent petroleum-based product. In this respect, the barrier to entry for lignocellulosic fuels is lower than for bulk and fine chemicals. Because gasoline and diesel are already mixtures of varying composition, new components can be integrated, and in the long run we might be able to produce biofuels at large scale that comprise hydrocarbons similar to those in petroleum-based fuels. Even in the fuel sector, however, questions remain over which biomass crops to grow; how to maximize agricultural productivity and sustainability; how to harvest, store, and transport the raw material efficiently; and how to transition from annual crops to perennials.

Once the biomass arrives at the manufacturing site to be processed into biofuels, we are in territory similar that of contemporary industrial chemistry. What can we learn from the world of industrial chemistry that might be relevant to biofuels? The biofuels innovation landscape is crowded with multiple academic and government labs, as well as venture capital–backed small companies. This situation is due to the relatively low barriers to entry enabled by biological HTE and data accumulation techniques similar to the chemical ones noted earlier. It is relatively easy to come up with an innovation that might be of importance in future conversion processes. However, the road from initial innovation to full commercial deployment remains as long and arduous in the biofuels case as in the industrial chemistry case. As time goes by, a gradual transition in lead roles from start-up companies to a few major corporations therefore seems likely.

There are also many competing technologies in the biofuels arena: (thermo)chemical conversion processes, biochemical strategies based on a huge (and growing) range of microorganisms and enzyme packages, and various different molecular product targets (each with associated pros and cons). Time will be necessary to determine which of these approaches ultimately proves superior. Because no one organization has the capacity to seriously invest in all the possibilities, each prospective commercialization effort carries a substantial risk that the chosen pathway might become technically obsolete. This in turn magnifies the risk profile of the scale-up process. A typical industrial chemistry asset needs at least a 20-year useful economic life in order to produce an attractive return on investment. A $500 million asset that becomes technically obsolete in 5 years is bad news from an investor's perspective. Meanwhile, regulators and legislators are pushing for faster and larger-scale implementation and are providing (temporary?) financial incentives to help push the process along. Taken all together, these factors produce a rather intimidating landscape in which to make prudent investment decisions. Only time will tell how things settle out in the end.

10.1126/science.1175502

Kepler's Optical Phase Curve of the Exoplanet HAT-P-7b

W. J. Borucki,[1]* D. Koch,[1] J. Jenkins,[2] D. Sasselov,[3] R. Gilliland,[4] N. Batalha,[5] D. W. Latham,[3] D. Caldwell,[2] G. Basri,[6] T. Brown,[7] J. Christensen-Dalsgaard,[8] W. D. Cochran,[9] E. DeVore,[2] E. Dunham,[10] A. K. Dupree,[3] T. Gautier,[11] J. Geary,[3] A. Gould,[12] S. Howell,[13] H. Kjeldsen,[8] J. Lissauer,[1] G. Marcy,[6] S. Meibom,[3] D. Morrison,[1] J. Tarter[2]

One of several methods for detecting exoplanets is to measure sequences of transits (*1*). To date, about 50 transiting exoplanets have been discovered by ground-based observations and CoRoT (*2*), among them HAT-P-7b (*3*). The Kepler mission (*4*) was launched on 6 March 2009 to detect Earth-size exoplanets. We collected 10 days of photometric data on 52,496 stars during the commissioning phase, which included data for HAT-P-7b. The data were processed by using the standard Kepler pipeline (*4*).

To estimate the detectability of the occultation of HAT-P-7b when it passes behind the star, we fit the data with an empirical model (Fig. 1) consisting of a transit of a limb-darkened star, a non–limb-darkened occultation, and a sinusoid for the phase variation between transits (*4*). The fit resulted in an orbital period of 2.204802 ± 0.000063 days, a transit depth of 6726 ± 11 parts per million (ppm), and an occultation depth of 130 ± 11 ppm, corresponding to an 11.3σ event for the combined set of four occultations. The residuals following this fit have a root mean square of 60 ppm. The peak in the phase variation of the planet is 122 ppm above the flux level just outside of transit. The phase variation represents the combination of the light reflected by the atmosphere of the planet as well as the thermal emission of the atmosphere. The flux levels near transit and during occultation are within 1σ.

Kepler's photometric detection of the optical phase curve and occultation of HAT-P-7b confirms the prediction based on theoretical models (*3*, *5*, *6*). The depth of the occultation and the shape and amplitude of the phase curve indicate that HAT-P-7b could have a strongly absorbing atmosphere and inhibited advection to the night side. If the planet has a completely absorbing atmosphere, its dayside temperature is estimated to be 2650 ± 100 K. The position in phase of the occultation is consistent with zero orbital eccentricity, as expected from the radial velocity variation. Analogous detections of emitted and reflected light and an occultation were reported for the very hot exoplanets CoRoT-1b (*7*) and CoRoT-2b (*8*).

The detection of the occultation without systematic error correction demonstrates that Kepler is operating at the level required to detect Earth-size planets. The signal from a Sun-Earth analog (~84 ppm) in an Earth-like orbit of a 12th-magnitude star will be at a comparable level of statistical significance.

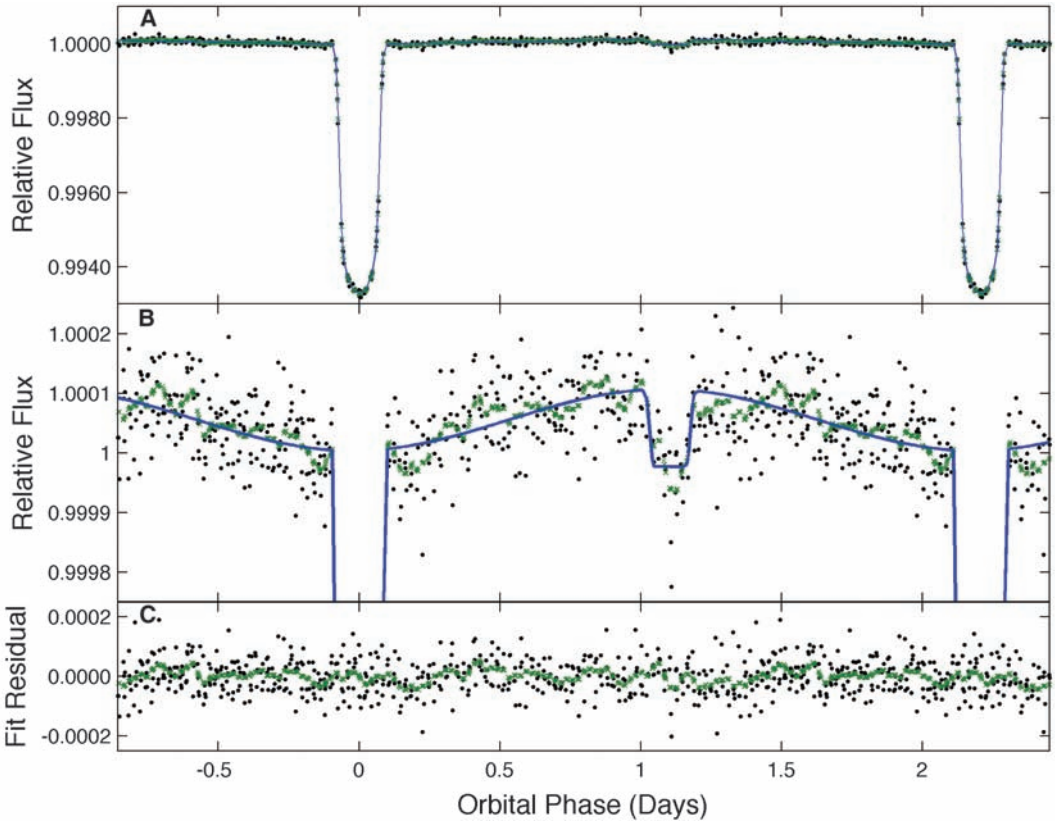

Fig. 1. Light curve for HAT-P-7b obtained by folding 10 days of data by the fitted orbital period. The black dots are the measurements. The green × marks are 0.1-day moving averages over the data. The blue line is a simple fit. (**A**) Light curve showing full depth of transit. (**B**) Expanded view to show phase curve and occultation. (**C**) Residuals from fit.

References and Notes

1. W. J. Borucki, A. L. Summers, *Icarus* **58**, 121 (1984).
2. http://exoplanet.eu
3. A. Pal *et al*., *Astrophys. J.* **680**, 1450 (2008).
4. Materials and methods are available on *Science* Online.
5. M. Lopez-Morales, S. Seager, *Astrophys. J.* **667**, L191 (2007).
6. J. J. Fortney, K. Lodders, M. S. Marley, R. S. Freedman, *Astrophys. J.* **678**, 1419 (2008).
7. I. A. G. Snellen, E. J. W. de Mooij, S. Albrecht, *Nature* **459**, 543 (2009).
8. R. Alonso *et al*., http://arxiv.org/abs/0906.2814v1 (2009).
9. We acknowledge the contributions of hundreds of individuals across NASA, Ball Aerospace, and the scientific community who made this mission possible. Funding was provided by the NASA Discovery program.

Supporting Online Material

www.sciencemag.org/cgi/content/full/325/5941/709/DC1
Materials and Methods
References

26 June 2009; accepted 22 July 2009
10.1126/science.1178312

[1]NASA Ames Research Center, Moffett Field, CA 94035, USA. [2]SETI Institute, Mountain View, CA 94043, USA. [3]Harvard-Smithsonian Center for Astrophysics, Cambridge, MA 02138, USA. [4]Space Telescope Science Institute, Baltimore, MD 21218, USA. [5]San Jose State University, San Jose, CA 95192, USA. [6]University of California, Berkeley, Berkeley, CA 94720, USA. [7]Las Cumbres Observatory Global Telescope, Goleta, CA 93117, USA. [8]Aarhus University, 8000 Aarhus, Denmark. [9]University of Texas, Austin, TX 78712, USA. [10]Lowell Observatory, Flagstaff, AZ 86001, USA. [11]Jet Propulsion Laboratory/California Institute of Technology, Pasadena, CA 91109, USA. [12]Lawrence Hall of Science, Berkeley, CA 94720, USA. [13]National Optical Astronomy Observatory, Tucson, AZ 85719, USA.

*To whom correspondence should be addressed. E-mail: william.j.borucki@nasa.gov

The Last Glacial Maximum

Peter U. Clark,[1]* Arthur S. Dyke,[2] Jeremy D. Shakun,[1] Anders E. Carlson,[3] Jorie Clark,[1] Barbara Wohlfarth,[4] Jerry X. Mitrovica,[5] Steven W. Hostetler,[6] A. Marshall McCabe[7]

We used 5704 ^{14}C, ^{10}Be, and ^{3}He ages that span the interval from 10,000 to 50,000 years ago (10 to 50 ka) to constrain the timing of the Last Glacial Maximum (LGM) in terms of global ice-sheet and mountain-glacier extent. Growth of the ice sheets to their maximum positions occurred between 33.0 and 26.5 ka in response to climate forcing from decreases in northern summer insolation, tropical Pacific sea surface temperatures, and atmospheric CO_2. Nearly all ice sheets were at their LGM positions from 26.5 ka to 19 to 20 ka, corresponding to minima in these forcings. The onset of Northern Hemisphere deglaciation 19 to 20 ka was induced by an increase in northern summer insolation, providing the source for an abrupt rise in sea level. The onset of deglaciation of the West Antarctic Ice Sheet occurred between 14 and 15 ka, consistent with evidence that this was the primary source for an abrupt rise in sea level ~14.5 ka.

The Last Glacial Maximum (LGM) is conventionally defined from sea-level records as the most recent interval in Earth history when global ice sheets reached their maximum integrated volume (*1*). Because sea level is an integrated signal, however, it does not distinguish between globally synchronous ice-sheet maxima that may have been in equilibrium throughout this interval and temporally variable regional ice-sheet maxima that combined to produce a millennia-long sea-level lowstand. Resolving the timing of regional variability in ice-sheet maxima is also important for understanding ice-sheet sensitivity to regional and global climate change, as well as in establishing ice-sheet–climate feedbacks. In particular, key questions that remain widely debated are what initiated the last deglaciation of the global ice sheets and what was their subsequent role during deglaciation in climate change, questions that are best assessed from the record of individual ice sheets rather than the integrated sea-level record.

We drew on 4271 ^{14}C ages and 475 terrestrial cosmogenic nuclide (TCN) ages that span the interval from 10,000 to 50,000 years ago (10 to 50 ka) to constrain the timing of maxima in global ice-sheet extent (Fig. 1). For all but the Barents-Kara and Greenland Ice Sheets, the spatial distribution of ages is sufficient to evaluate regional variability in the timing of maxima for different sectors of individual ice sheets. Because ice-sheet extent scales with ice volume (*2*), our constraints on regional variability in ice-sheet maxima allow us to evaluate the temporal evolution of individual ice-sheet contributions to global sea-level change. Because mountain glaciers are highly sensitive to climate change, we used an additional 172 ^{14}C ages and 786 TCN ages to constrain mountain-glacier fluctuations from five widely distributed regions of the world (Fig. 1), allowing a more comprehensive assessment of the response of the cryosphere to climate change.

The LGM sea-level lowstand. We used existing relative sea level (RSL) data from far-field sites to constrain the timing of the LGM as occurring from 26.5 to 19.0 ka (Fig. 2) (*3*–*5*). The sea-level change at these sites will differ from the eustatic change because of the spatially varying gravitational, deformational, and rotational perturbations in sea level driven by the ice-ocean mass transfer (*6*). In order to evaluate these effects, we used a state-of-the-art theory that includes a realistic glaciation phase to predict the RSL change at these far-field sites (*7*). Our ice model is characterized by a peak eustatic sea-level fall of ~130 m over the LGM (Fig. 2), which is in agreement with independent estimates (*3*, *8*).

We find that in the prediction for Barbados, peripheral bulge dynamics and, to a lesser extent, the continental (lithospheric) levering effect dominate the anti-syphoning effect during the LGM (*7*), leading to a net sea-level fall of ~3 m. In contrast, the remaining four sites lie well outside the peripheral bulges, and the sea-level rise due to anti-syphoning dominates; the net result is a ~4- to 5-m rise in sea level at these sites. Thus, across the LGM period, when the modeled ice history shows no change in the ice volume, the differential sea-level change between Barbados and the other sites approaches 10 m (Fig. 2 and fig. S1).

Global ice-sheet history. Our compilation of radiometric ages suggests that there is considerable regional variability in the timing of when ice sheets (and various sectors of ice sheets) first reached their local last glacial maxima (LLGM) (*9*). Within uncertainties, the earliest maxima were reached by several ice sheets (or sectors of ice sheets) sometime between 29 to 33 ka (Fig. 3B and figs. S2 and S3). This early response included large and small ice sheets at mid- and high northern latitudes, as well as the West Antarctic Ice Sheet (WAIS) in the Southern Hemisphere. Over the next 2500 years, the remaining ice sheets [and sectors of the Laurentide Ice Sheet (LIS)] continued to grow, so that by 26.5 ka, nearly all ice sheets had attained their maximum extents, corresponding to the onset of the LGM sea-level lowstand (Fig. 3C). In the context of the global sea-level record, we find that this expansion of ice sheets to their maximum extent can explain much of the global sea-level fall from intermediate levels during marine isotope stage (MIS) 3 to the LGM lowstand (*7*).

Based on the youngest possible age for ice-sheet maxima derived from our uncertainty assessment (*7*), most of the LIS, the northwest Cordilleran Ice Sheet (CIS), the Barents-Kara Ice Sheet (BKIS), the British-Irish Ice Sheet

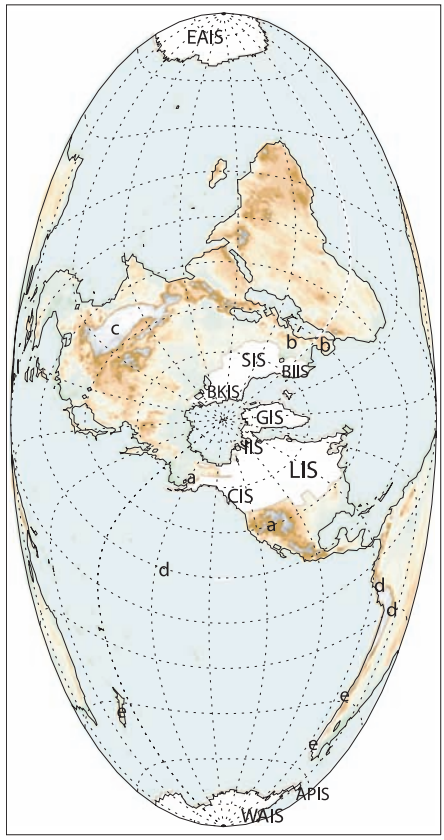

Fig. 1. Distribution of ice sheets at the LGM (*51*). APIS, Antarctic Peninsula Ice Sheet; EAIS, East Antarctic Ice Sheet. Also shown are areas of mountain glaciation discussed in the text (a, western North America; b, Europe; c, Tibet; d, tropics and subtropics; e, Southern Hemisphere).

[1]Department of Geosciences, Oregon State University, Corvallis, OR 97331, USA. [2]Geological Survey of Canada, 601 Booth Street, Ottawa, Ontario K1A 0E8, Canada. [3]Department of Geology and Geophysics, University of Wisconsin, Madison, WI 53706, USA. [4]Department of Geology and Geochemistry, Stockholm University, SE-10691, Stockholm, Sweden. [5]Department of Earth and Planetary Sciences, Harvard University, Cambridge, MA 02138, USA. [6]U.S. Geological Survey, Department of Geosciences, Oregon State University, Corvallis, OR 97331, USA. [7]School of Environmental Science, University of Ulster, Coleraine, County Londonderry, BT52 1SA, UK.

*To whom correspondence should be addressed. E-mail: clarkp@onid.orst.edu

(BIIS), and the Scandinavian Ice Sheet (SIS) had begun to retreat from their maxima between 19 and 20 ka (*10*) (Fig. 3B). Although the onset of Greenland Ice Sheet (GIS) retreat from the LLGM is poorly constrained by existing ^{14}C and TCN ages (fig. S3B), marine records of GIS runoff suggest that GIS retreat may have commenced ~20 ka (*11*). This evidence for widespread ice-margin retreat occurring between 19 and 20 ka indicates that the 19-ka meltwater pulse, which represents a rapid 10-m rise in sea level from the LGM lowstand sometime between 19 and 20 ka (Fig. 3C) (*8*, *12*), originated from these Northern Hemisphere ice sheets (*13*).

In the Southern Hemisphere, the best-dated record from Antarctica is for the WAIS in the Ross Sea region (fig. S3A). Stratigraphic relations of ^{14}C ages to ice-margin history suggest an onset of retreat from the WAIS maximum extent in the Ross Sea between 13.9 and 15.2 ka (*7*) which, within dating uncertainties, corresponds to the rapid rise in sea level ~14.5 ka referred to as meltwater pulse 1A (MWP-1A) (*14*–*19*).

Mountain glaciation. There is information suggesting that in many places, mountain glaciers were near or at their maximum extent by ~30 ka, which is broadly contemporaneous with the interval when global ice sheets first began to reach their maxima (Fig. 3B) (*7*). Within uncertainties (*7*), the TCN-based geochronology suggests that mountain glaciers in western North America, Europe, and the tropics began to retreat from their LLGM positions before those in Tibet and the mid-latitudes of the Southern Hemisphere (Fig. 3A and fig. S4) (*20*–*22*). Moreover, the earlier retreat of Northern Hemisphere mountain glaciers is synchronous, within error, with retreat from most Northern Hemisphere LLGM ice-sheet margins at ~19 ka. The retreat of tropical glaciers may also be synchronous, but because the differences in scaling factors are greatest in the tropics (fig. S4), it is equally likely that tropical-glacier retreat occurred earlier (Fig. 3A).

Discussion and conclusions. We have shown that the duration of the LGM sea-level lowstand (26.5 to 19 ka) is in excellent agreement with the duration of maximum extent of most of the global ice sheets, suggesting that most of the global ice sheets were in near-equilibrium with climate during this 7500-year interval (*23*). We have also documented specific ice-sheet contributions to several key events in the evolution of the integrated global sea-level record into and out of the LGM, including a Northern Hemisphere ice-sheet source for the 19-ka MWP and a significant Antarctic ice-sheet contribution to MWP-1A. Insofar as these two MWP's represent a substantial flux of freshwater into the surrounding ocean, the geographic sources of these events are consistent with inducing the ocean and climate changes that occurred at these times (*12*, *24*).

Our constraints in support of an extended LGM sea-level lowstand provide important insights into the origin of the carbonate $\delta^{18}O$ signal measured in benthic foraminifera ($\delta^{18}O_c$), which is often used directly as a proxy for sea-level change. Disentangling global changes in seawater $\delta^{18}O$ ($\delta^{18}O_{sw}$) from regional changes in seawater temperature ($\delta^{18}O_T$) and water-mass $\delta^{18}O$, however, remains largely unresolved (*25*–*27*), adding considerable uncertainty in interpreting the phase relationship of this proxy to other climate parameters. Comparison of the reasonably well-established global sea-level record for the past 35,000 years (35 ky) (Fig. 4A) with several benthic $\delta^{18}O_c$ records from the Pacific and Atlantic basins (Fig. 4B) clearly demonstrates that the $\delta^{18}O_{sw}$ signal has been compromised by these other effects, and that their relative contribution varies between sites.

We derive a first-order estimate of the $\delta^{18}O_{sw}$ contribution to the global $\delta^{18}O_c$ signal, as represented by the Lisiecki and Raymo (LR04) stack (*28*), by scaling the glacial-interglacial $\delta^{18}O_{sw}$ change of 1.0 ± 0.1 per mil (‰) (*27*) to the corresponding sea-level change of 127.5 ± 7.5 m

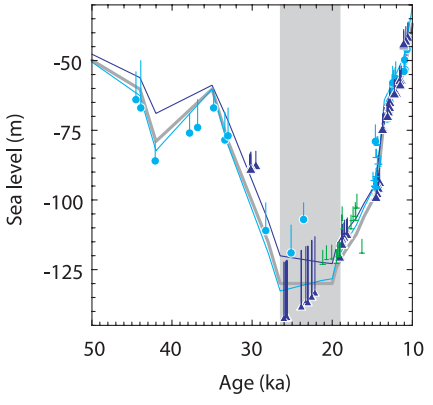

Fig. 2. Sea-level predictions for New Guinea (blue line) and Barbados (purple line) compared to RSL data with depth uncertainty for the interval from 10 to 50 ka from New Guinea (blue circles) (*4*, *52*, *53*), Barbados (purple triangles) (*5*, *54*), the Bonaparte Gulf (green half-pluses representing age and depth uncertainty) (*8*), and the Sunda Shelf (blue half-pluses) (*55*). Eustatic sea-level time series are shown as a gray line. The vertical gray bar indicates the time of the LGM as defined from the RSL data.

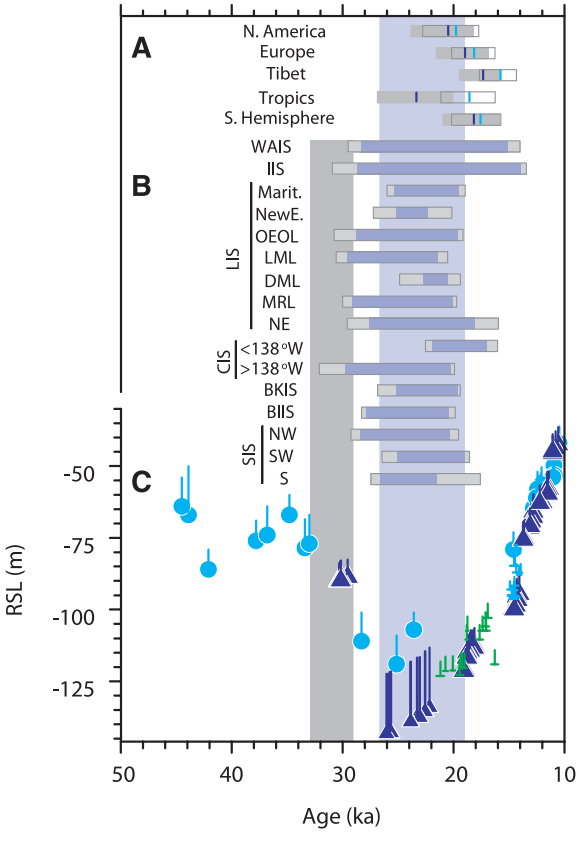

Fig. 3. Summary of glacier and ice-sheet chronologies for LLGM with RSL data constraining the time of the LGM. The vertical purple bar represents the time of the LGM as defined from the RSL data, whereas the vertical gray bar represents the earliest interval when sea level began to fall to the LGM lowstand, corresponding to the time when the first ice-sheet LLGM were reached. (**A**) Summary of the timing of regional deglaciation from the LLGM for the five regions of mountain glaciation evaluated in this paper (small horizontal bars) (fig. S4). In those bars, the vertical purple segment and associated horizontal gray segment represent the mean age and the 1σ age range for the onset of deglaciation based on the scaling factor that delivers the oldest age for the region, whereas the vertical blue segment and associated area outlined in gray represent the mean age and the 1σ age range for the onset of deglaciation based on the scaling factor that delivers the youngest age for the region (*7*). (**B**) Summary of the timing of the LLGM for each of the ice-sheet sectors and ice sheets shown in figs. S2 and S3, with the small horizontal purple bars with gray bars on either end representing the time of the LLGM and associated error, respectively (*7*). The seven LIS sectors are Maritimes (Marit.), New England (NewE.), the Ohio-Erie-Ontario Lobe (OEOL), the Lake Michigan Lobe (LML), the Des Moines Lobe (DML), the Mackenzie River Lobe (MRL), and the northeastern margin (NE). The three SIS sectors are northwest (NW), southwest (SW), and south (S). (**C**) RSL data with depth uncertainty for the interval from 10 to 50 ka from New Guinea (blue circles) (*4*, *52*, *53*), Barbados (purple triangles) (*5*, *54*), the Bonaparte Gulf (green half-pluses representing age and depth uncertainty) (*8*), and the Sunda Shelf (blue half-pluses) (*55*).

(*5*, *8*) (Fig. 4A). In doing so, we adopt ice-sheet model results that suggest that the $\delta^{18}O$ of global ice sheets that contributed to glacial-interglacial sea-level changes was relatively homogenous and thus did not cause any significant temporal changes in this relation (*29*).

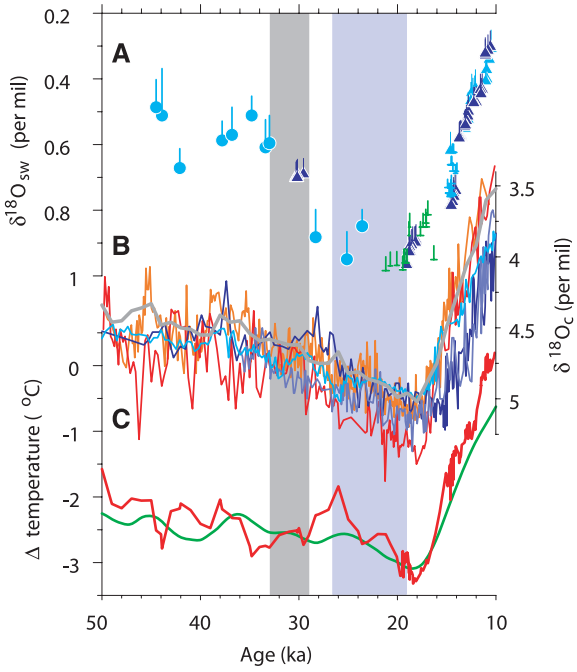

Fig. 4. Constraints on changes in sea level and deep ocean temperature. The vertical purple bar represents the time of LGM as defined from the RSL data, whereas the vertical gray bar represents the earliest interval when sea level began to fall to the LGM lowstand, corresponding to the time when the first ice-sheet LLGM were reached (Fig. 3). (**A**) RSL data for the interval from 10 to 50 ka (Fig. 3), converted to $\delta^{18}O_{sw}$ by scaling the glacial-interglacial $\delta^{18}O_{sw}$ change of 1.0 ± 0.1‰ (*27*) to the corresponding sea-level change of 127.5 ± 7.5 m (*5*, *8*). (**B**) Time series of $\delta^{18}O$ measured in benthic foraminifera from marine cores from the Pacific and North Atlantic basins, as well as the LR04 $\delta^{18}O$ stack (gray line) (*28*). Records are from Pacific core V19-30 (purple line) (*26*), Pacific core TR163-31B (dark purple line) (*25*), Pacific core W8709A-13PC (blue line) (*56*), North Atlantic core NA87-22 (red line) (*26*), and North Atlantic core MD99-2042 (orange line) (*57*). (**C**) The red line shows our estimate of global average deep sea temperature derived by subtracting the sea-level component of seawater in the RSL data (Fig. 4A) from the LR04 benthic $\delta^{18}O$ stack (*28*) (Fig. 4B), with the residual $\delta^{18}O$ converted to temperature using a relation of 0.28‰ $°C^{-1}$. The green line shows the modeled changes in deep ocean temperature from (*29*).

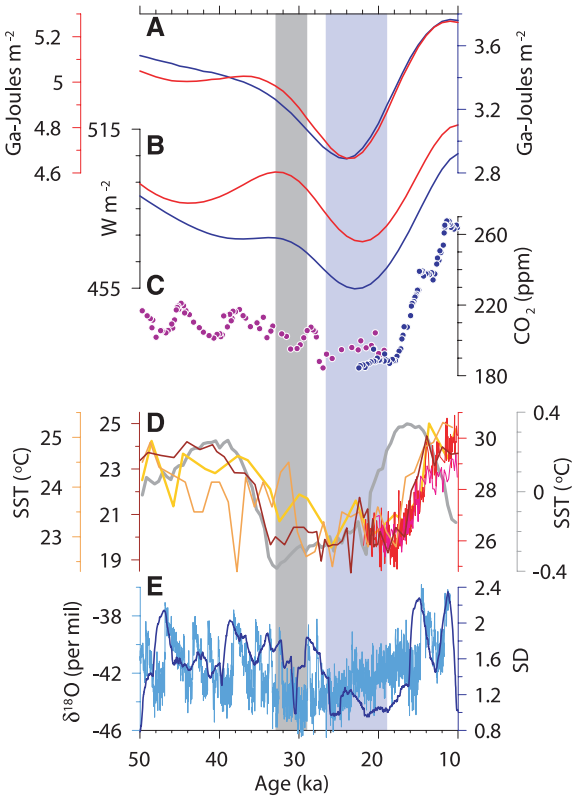

Fig. 5. Temporal relation between the LGM and various climate-forcing factors. The vertical purple bar represents the time of the LGM as defined from the RSL data, whereas the vertical gray bar represents the earliest interval when sea level began to fall to the LGM lowstand, corresponding to the time when the first ice-sheet LLGM were reached (Fig. 3). (**A**) Summer energy for 45°N (red line, $\tau = 400$) and 65°N (purple line, $\tau = 400$). (**B**) 21 June–20 July insolation for 45°N (red line) and 65°N (purple line) (*58*). (**C**) Atmospheric CO_2 from the Dome C ice core (light purple circles) (*59*) and Byrd ice core (dark purple circles) (*60*). (**D**) The 500-year average NINO3 index from the Zebiak-Cane model forced with orbital-scale solar variations (gray line) (*37*) compared to SST records from the tropical Pacific [deep yellow, RC13-110 (*34*); ruby red, ODP 846B (*35*); light orange, TR163-19 (*31*); magenta, MD98-2176 (*40*); red, MD98-2181 (*40*)]. (**E**) The 20-year-resolution $\delta^{18}O$ record from the Greenland NGRIP ice core (*61*) (blue line) and the SD of that record calculated with a centered, 3-ky sliding window (purple line).

We interpret the residual $\delta^{18}O$ signal ($\delta^{18}O_c - \delta^{18}O_{sw}$) as recording the change in mean deep ocean temperature ($\delta^{18}O_T$) (Fig. 4C). Based on a relation of 0.28 ‰ $°C^{-1}$, this analysis suggests a maximum cooling of the mean deep ocean temperature of 3.25 ± 0.55°C, which, for a current mean deep ocean temperature (>2000 m) of 1.3°C (*30*), would place the average temperature of deep ocean waters (–2.2°C) near the freezing point, similar to previous data analyses (*1*, *26*, *27*) and model results (*29*) (Fig. 4C). Within the context of the LGM, however, two additional features of this analysis stand out: Average deep ocean temperatures must have warmed by nearly 1°C during the interval when ice sheets were reaching their maximum extent, followed by a cooling trend through the LGM that culminated in maximum cooling occurring well after the LGM (Fig. 4C). We emphasize that the LR04 stack does not capture regional variability in $\delta^{18}O_T$ and that Skinner and Shackleton (*25*) argued that the Atlantic temperature minimum leads that of the Pacific, as is apparent from the $\delta^{18}O_c$ records shown in Fig. 4B. In contrast, however, these same $\delta^{18}O_c$ records indicate that there are no substantial regional phase offsets in the evolution of temperature leading into and during the LGM, suggesting a more uniform change in the global ocean heat budget during this time.

Our well-established timing of the LGM also allows us to address the forcing mechanisms that induce changes in ice volume and feedbacks with the climate system. Of particular interest is the role that high northern latitude insolation plays in these changes relative to other mechanisms internal to the climate system (*31*, *32*). We focus on three of the more widely proposed mechanisms: high northern latitude insolation, atmospheric CO_2, and tropical Pacific sea surface temperatures (SSTs) (Fig. 5). In evaluating insolation, we include the summer energy index, defined as the sum of insolation at a given latitude on days when a threshold insolation value corresponding to 0°C is exceeded (*33*). Because the relation between temperature and insolation will vary depending on, for example, albedo, elevation, and atmospheric greenhouse gas concentrations, we established the LGM threshold insolation value from an atmospheric general circulation model (AGCM) simulation with glacial boundary conditions (fig. S5) (*7*).

A combination of these three forcing mechanisms appears to explain the growth phase of ice sheets to their LLGM positions. The initial phase of sea-level lowering toward the LGM lowstand, accompanied by the time of earliest LLGM ice-sheet maxima (33 to 29 ka), occurred at the same time that northern summer insolation began to decline (Fig. 5B) and as summer energy was decreasing, particularly at 45°N, where ablation rates along the southern LIS margin would have been most sensitive to this index (Fig. 5A), thus supporting a northern latitude insolation control on ice-sheet growth. This insolation control may have been augmented by additional radiative

forcing from a small (~15 parts per million) decrease in atmospheric CO_2 (Fig. 5C).

There is also a strong temporal relationship between SST changes in the eastern equatorial Pacific and ice growth, which suggests that the 2° to 4°C cooling that occurred between 38 and 30 ka (Fig. 5D) (*31*, *34*, *35*) may have played a role in ice-sheet growth. SST records from the western equatorial Pacific indicate that surface waters in the warm pool had already cooled to LGM values by ~60 ka (*31*, *36*), suggesting that the decrease in SSTs in the eastern equatorial Pacific between 38 and 30 ka reflects a decrease in the equatorial zonal SST gradient, resulting in a more La Niña–like SST field. A model of the response of the NINO3 index (the SST anomaly averaged over 150°W to 90°W and 5°S to 5°N) to orbital forcing indicates that this cooling may have been caused by changes in low-latitude precession-related insolation (*37*) (Fig. 5D).

Regardless of their cause, AGCM simulations show that these changes in tropical Pacific SSTs would have induced a significant increase in the mass balance of Northern Hemisphere ice sheets (*38*) and thus were an important factor in explaining the ice-sheet growth phase. We used these simulations to estimate the possible sea-level response to a cooling of the tropical Pacific. For example, in the case of an intermediate-sized (MIS 3) LIS, cooling of the tropical Pacific induces a mass balance increase of 0.17 m $year^{-1}$ (*38*), which integrated over the area of the ice sheet for 6500 years (33.0 to 26.5 ka) results in a global sea-level fall of ~24 m (*39*). It is likely, however, that as the LIS expanded, the additional ice-sheet area added mass as well. Assuming that a similar mass balance increase (0.17 m $year^{-1}$) applied to the LIS expanding in area at an average rate of 611 km^2 $year^{-1}$ results in a sea-level fall of ~31 m. This analysis thus indicates that tropical Pacific SST cooling probably played an important role in causing the 32 to 38 m of sea-level fall associated with the growth of the LIS to its LLGM extent that we estimated from area-volume scaling relations (*7*). AGCM simulations further show that other Northern Hemisphere ice sheets responded similarly to tropical Pacific cooling (*38*) and may have caused an additional 13 m of sea-level fall in the 6500-year growth interval. The WAIS also reached its LLGM extent early in this growth interval (Fig. 3B), with its growth explaining much of the remaining sea-level fall to the LGM lowstand. In this case, recent analyses have shown that local changes in austral spring insolation control (*40*) or the duration of summer at high southern latitudes (*41*) may have induced climate changes that favored ice-sheet growth.

In contrast to the multiple controls that may have induced ice-sheet growth, our geochronology for the LGM clearly demonstrates that only northern insolation led the termination and was thus the primary mechanism for triggering the onset of Northern Hemisphere deglaciation (Fig. 5). Moreover, the fact that ice sheets of all sizes, as well as Northern Hemisphere mountain glaciers, began to retreat at approximately the same time (19 to 20 ka) (Fig. 3, A and B) suggests that the primary insolation control on initial deglaciation was through increased summer ablation, which can substantially reduce the long response times of large ice sheets by enabling dynamical processes that lead to rapid mass loss. When considering the onset of the LGM, we note that most Northern Hemisphere LGM ice sheets were in equilibrium (mass balance) as long as summer insolation was within 10 W m^{-2} (or 0.2 GJ m^{-2} for summer energy) of the minimum value (Fig. 5). The maximum ice sheets may themselves have reinforced this equilibrium condition by maintaining near-constant freshwater fluxes to the oceans and high albedo and orography, thereby reducing their role in causing climate variability (*42*) (Fig. 5E).

Simulated precessional forcing of tropical SSTs (*37*) suggests that the warming of the eastern tropical Pacific should have occurred 4 to 5 ky earlier than it actually began (Fig. 5D), indicating modulation of the SST response to precession by some other mechanism. Insofar as a key element of this simulated response involves the seasonal position of the Intertropical Convergence Zone (ITCZ) (*37*), one possible mechanism may involve high-latitude cooling induced by expansion of ice sheets and sea ice during the LGM and the effect of this cooling in steepening the pole-to-equator temperature gradient and thus shifting the mean position of the ITCZ (*43*). At the same time, this extratropical forcing associated with glacial boundary conditions may have directly caused cooler tropical SSTs (*44*), thus changing the sensitivity of the tropical Pacific to precessional forcing. In any event, warming of tropical Pacific SSTs did not begin until after 19 ka (Fig. 5D) and thus did not contribute to the termination of the LGM.

The onset of deglaciation of some ice sheets and mountain glaciers from their maxima was delayed until after 19 ka (Fig. 3), suggesting the existence of regional controls on glacier mass balance that modulated their response to insolation (*45*). Dyke and Prest (*46*) attributed the lag of the LLGM of the main body of the CIS with respect to the LLGM of the LIS (Fig. 3B) to atmospheric feedbacks associated with the influence of the growing LIS on the surface mass balance of the CIS and vice versa. Initial retreat of the northeastern LIS margin may have started near 19 ka, but retreat rates through the deglaciation were low (*47*), so that the climatic effects of the lingering ice sheet in this region induced a longer LLGM for the adjacent Inuitian Ice Sheet (IIS). The onset of retreat of the WAIS ~14.5 ka was substantially later than the start of regional warming throughout much of the Southern Hemisphere ~18 to 19 ka (*48*, *49*), and its large contribution to MWP-1A (*19*) suggests a nonlinear response to this warming, perhaps through the collapse of buttressing ice shelves.

Finally, we consider the timing of the LGM retreat of mountain glaciers in Tibet and the Southern Hemisphere, which occurred between 16 and 18 ka (Fig. 3A). One possible explanation for the delayed deglaciation in Tibet is that it was due to the strong influence of the East Asian monsoon, which remained unchanged throughout the LGM until it abruptly weakened ~17.5 ka (*50*). This weakening may have resulted in a reduction in moisture delivered to the glacier, causing a shift to negative mass balance. The initial retreat of Southern Hemisphere mountain glaciers, on the other hand, is consistent with the onset of Southern Hemisphere warming (*21*).

Although the lead-lag relationships established here by the timing of the LGM point to northern latitude insolation as the primary trigger of initial deglaciation of most Northern Hemisphere ice sheets and glaciers, subsequent increases in atmospheric CO_2 and tropical Pacific SSTs (Fig. 5, C and D) demonstrate the importance of carbon cycle and ocean feedbacks in amplifying the deglacial response and causing global warming. Whether these changes in CO_2 and SSTs were induced by deglaciation of Northern Hemisphere ice sheets (*12*) or high southern latitude insolation (*40*, *41*), however, remains an open question.

References and Notes

1. A. C. Mix, E. Bard, R. Schneider, *Quat. Sci. Rev.* **20**, 627 (2001).
2. W. S. B. Paterson, *The Physics of Glaciers: 3rd Edition* (Pergamon, New York, 1994).
3. K. Lambeck, J. Chappell, *Science* **292**, 679 (2001).
4. K. B. Cutler *et al.*, *Earth Planet. Sci. Lett.* **206**, 253 (2003).
5. W. R. Peltier, R. G. Fairbanks, *Quat. Sci. Rev.* **25**, 3322 (2006).
6. G. A. Milne, J. X. Mitrovica, *Quat. Sci. Rev.* **27**, 2292 (2008).
7. Materials and methods are available as supporting material on *Science* Online.
8. Y. Yokoyama, K. Lambeck, P. De Deckker, P. Johnston, L. K. Fifield, *Nature* **406**, 713 (2000).
9. We distinguish the LLGM from the LGM to emphasize the regional variability in the timing of ice-sheet and glacier fluctuations relative to the globally integrated sea-level record used to define the LGM.
10. There is evidence that some ice margins experienced small (tens of kilometers) fluctuations while at or near their LLGM position, such as the New England margin at Martha's Vineyard or the margin of the Ohio-Erie lobe in Ohio (7). We define the termination of the LLGM on the basis of when the margin began a sustained retreat from its LLGM position.
11. A. E. Carlson, J. S. Stoner, J. P. Donnelly, C. Hillaire-Marcel, *Geology* **36**, 359 (2008).
12. P. U. Clark, A. M. McCabe, A. C. Mix, A. J. Weaver, *Science* **304**, 1141 (2004).
13. The CIS and IIS remained at their maxima until after 19 ka. The southern margin of the CIS (where dating constraints are best) retreated from its maximum extent between 16 and 17 ka, whereas the IIS was the last of the global ice sheets to start to retreat from its maximum extent at ~13.5 ka (Fig. 3B).
14. Several additional lines of evidence support a significant change in WAIS volume at this time. The isotopic (δD and $\delta^{18}O$) records from two ice cores bordering the Ross Sea (the Siple and Taylor Domes) show an abrupt warming at 14.5 ka (*15, 16*), which may reflect

ice-surface lowering or some regional climate change induced by ice-surface lowering. If attributed solely to a change in ice-surface elevation, the 3° to 4°C warming at Siple Dome (*16*) would indicate 500 to 650 m of ice-surface lowering, assuming a free atmospheric lapse rate of 6°C per 1000 m. This magnitude of lowering is supported by ice-sheet modeling, which suggests thinning of Siple Dome ice by 350 m between 14 and 15 ka (*17*). Within the large dating uncertainties of dated marine samples, widespread retreat of the Antarctic Peninsula Ice Sheet margin on the continental shelf also occurred at this time (*18*). These lines of direct evidence for WAIS retreat at the time of MWP-1A are consistent with geophysical modeling of the noneustatic component of the sea-level rise during MWP-1A, which suggests a dominant source from Antarctica (*19*).

15. E. J. Steig *et al*., *Science* **282**, 92 (1998).
16. E. J. Brook *et al*., *Quat. Sci. Rev.* **24**, 1333 (2005).
17. S. F. Price, H. Conway, E. D. Waddington, *J. Geophys. Res. Earth Surf.* **112**, F03021 (2007).
18. D. C. Heroy, J. B. Anderson, *Quat. Sci. Rev.* **26**, 3286 (2007).
19. S. E. Bassett, G. A. Milne, J. X. Mitrovica, P. U. Clark, *Science* **309**, 925 (2005).
20. Based on a larger data set, the mean age for regional deglaciation of mid-latitude Southern Hemisphere mountain glaciers (17.7 ka) is not significantly different from the previously reported mean age (17.3 ka), using the same scaling factor (*21*). Nevertheless, the age of regional deglaciation in the mid-latitude Southern Hemisphere is significantly younger than the regional deglaciation age established for LLGM glaciers at northern mid-latitudes (Fig. 3A), a finding counter to the conclusion that deglaciation in the two hemispheres was synchronous (*21*). The source of this disagreement appears to be that Schaefer *et al*. (*21*) identified "outer LGM" and "inner LGM" moraines in any given region, which in western North America are typically 20 to 21 ka and 16.5 to 17.5 ka, respectively (*22*). In these cases, and to be consistent with the concept of LLGM, we used the TCN ages of the "outer" moraines to mark the onset of regional deglaciation from the LLGM, whereas we viewed the "inner" moraines as recording a subsequent millennial-scale ice-margin fluctuation that is unrelated to the termination of the LLGM.
21. J. M. Schaefer *et al*., *Science* **312**, 1510 (2006).
22. J. M. Licciardi, P. U. Clark, E. J. Brook, D. Elmore, P. Sharma, *Geology* **32**, 81 (2004).
23. Heinrich event 2 (H2), which occurred during the LGM ~24 ka, is generally thought to represent an instability of the LIS. In either case, we view H2 as an anomalous and short-lived event with respect to the 7500-year-long LGM interval, during which time ice sheets were otherwise largely in equilibrium with climate.
24. A. J. Weaver, O. Saenko, P. U. Clark, J. X. Mitrovica, *Science* **299**, 1709 (2003).
25. L. C. Skinner, N. J. Shackleton, *Quat. Sci. Rev.* **24**, 571 (2005).
26. C. Waelbroeck *et al*., *Quat. Sci. Rev.* **21**, 295 (2002).
27. D. P. Schrag, G. Hampt, D. W. Murray, *Science* **272**, 1930 (1996).
28. L. Lisiecki, M. E. Raymo, *Paleoceanography* **20**, PA1003 (2005).
29. R. Bintanja, R. S. W. van de Wal, *Nature* **454**, 869 (2008).
30. S. Levitus, *World Ocean Atlas 1994* (U.S. Government Printing Office, Washington, DC, 1994).
31. D. W. Lea, D. K. Pak, H. J. Spero, *Science* **289**, 1719 (2000).
32. J. Imbrie *et al*., *Paleoceanography* **8**, 699 (1993).
33. P. Huybers, *Science* **313**, 508 (2006).
34. M. Feldberg, A. C. Mix, *Paleoceanography* **18**, 10.1029/2001PA000740 (2003).
35. I. Martinez, L. Keigwin, T. T. Barrows, Y. Yokoyama, J. Southon, *Paleoceanography* **18**, PA000877 (2003).
36. L. Stott, C. Poulsen, S. Lund, R. Thunell, *Science* **297**, 222 (2002).
37. A. C. Clement, R. Seager, M. A. Cane, *Paleoceanography* **14**, 441 (1999).
38. P. U. Clark, S. W. Hostetler, N. G. Pisias, A. Schmittner, K. J. Meisner, in *Ocean Circulation: Mechanisms and Impacts*, A. Schmittner, J. Chiang, S. Hemming, Eds. (Geophysical Monograph 173, American Geophysical Union, Washington, DC, 2007), pp. 209–246.
39. To estimate this mass increase, we used the area of the LIS at 13 ka (7.35×10^6 km^2) multiplied by the mass balance increase of 0.17 m year^{-1} over 6500 years, resulting in 24 m of sea-level equivalent. The LIS expanded to its LGM area of 11.63×10^6 km^2 over 6500 years, resulting in an average annual rate of area increase of 611 km^2 year^{-1}. The assumption that the mass balance increase of 0.17 m year^{-1} applied to this expanding area over 6500 years results in an additional 7 m of sea-level equivalent.
40. L. Stott, A. Timmermann, R. Thunell, *Science* **318**, 435 (2007).
41. P. Huybers, G. Denton, *Nat. Geosci.* **1**, 787 (2008).
42. P. U. Clark, R. B. Alley, D. Pollard, *Science* **286**, 1104 (1999).
43. J. C. H. Chiang, C. M. Bitz, *Clim. Dyn.* **25**, 477 (2005).
44. A. B. G. Bush, S. G. H. Philander, *Science* **279**, 1341 (1998).
45. We examined the possibility that the perturbation to the threshold in summer energy (τ) due to LGM boundary conditions (*7*) may have induced a summer energy budget that favored mountain glaciation LLGM at times other than the LGM, but this did not prove to be the case.
46. A. S. Dyke, V. K. Prest, *Geogr. Phys. Quat.* **XLI**, 237 (1987).
47. J. P. Briner, G. H. Miller, P. T. Davis, R. C. Finkel, *Can. J. Earth Sci.* **42**, 67 (2005).
48. K. Pahnke, R. Zahn, H. Elderfield, M. Schulz, *Science* **301**, 948 (2003).
49. T. Blunier, E. J. Brook, *Science* **291**, 109 (2001).
50. Y. J. Wang *et al*., *Science* **294**, 2345 (2001).
51. W. R. Peltier, *Annu. Rev. Earth Planet. Sci.* **32**, 111 (2004).
52. R. L. Edwards *et al*., *Science* **260**, 962 (1993).
53. J. Chappell, *Quat. Sci. Rev.* **21**, 1229 (2002).
54. E. Bard, B. Hamelin, R. G. Fairbanks, A. Zindler, *Nature* **345**, 405 (1990).
55. T. Hanebuth, K. Stattegger, P. M. Grootes, *Science* **288**, 1033 (2000).
56. A. C. Mix *et al*., in *Mechanisms of Global Climate Change at Millennial Time Scales*, P. U. Clark, R. S. Webb, L. D. Keigwin, Eds. (Geophysical Monograph 112, American Geophysical Union, Washington, DC, 1999), pp. 127–148.
57. N. J. Shackleton, M. A. Hall, E. Vincent, *Paleoceanography* **15**, 565 (2000).
58. J. Laskar, P. Robutel, M. Gastineau, A. C. M. Correia, B. Levrard, *Astron. Astrophys.* **428**, 261 (2004).
59. J. Ahn *et al*., *J. Geophys. Res.* **109**, D13305 (2004).
60. J. Ahn, E. J. Brook, *Science* **322**, 83 (2008).
61. A. Svensson *et al*., *Clim. Past* **4**, 47 (2008).
62. The authors thank J. Licciardi, N. Pisias, and an anonymous reviewer for their constructive comments, and J. Bockheim, B. Hall, and P. Huybers for discussions. This work was supported by NSF (P.U.C., J.D.S., A.E.C., and S.W.H.), the Geological Survey of Canada Climate Change Program (A.S.D.), the University of Wisconsin (A.E.C.), the Swedish Nuclear Fuel and Waste Management Co. (B.W.), and the Canadian Institute for Advanced Research (J.X.M.).

Supporting Online Material

www.sciencemag.org/cgi/content/full/325/5941/710/DC1
Materials and Methods
SOM Text
Figs. S1 to S5
References

27 February 2009; accepted 23 June 2009
10.1126/science.1172873

The Genetic Architecture of Maize Flowering Time

Edward S. Buckler,[1,2,3]* James B. Holland,[1,4]* Peter J. Bradbury,[1,2] Charlotte B. Acharya,[2] Patrick J. Brown,[2] Chris Browne,[1,5] Elhan Ersoz,[2] Sherry Flint-Garcia,[1,5] Arturo Garcia,[1,5] Jeffrey C. Glaubitz,[6] Major M. Goodman,[4] Carlos Harjes,[7] Kate Guill,[1,5] Dallas E. Kroon,[2] Sara Larsson,[3] Nicholas K. Lepak,[1,3] Huihui Li,[8,2,9] Sharon E. Mitchell,[2] Gael Pressoir,[2] Jason A. Peiffer,[3] Marco Oropeza Rosas,[4] Torbert R. Rocheford,[10,11] M. Cinta Romay,[2,12] Susan Romero,[2] Stella Salvo,[1,4] Hector Sanchez Villeda,[5,13] H. Sofia da Silva,[10] Qi Sun,[14] Feng Tian,[2] Narasimham Upadyayula,[10] Doreen Ware,[1,15] Heather Yates,[2] Jianming Yu,[16] Zhiwu Zhang,[2] Stephen Kresovich,[2]* Michael D. McMullen[1,5]*

Flowering time is a complex trait that controls adaptation of plants to their local environment in the outcrossing species *Zea mays* (maize). We dissected variation for flowering time with a set of 5000 recombinant inbred lines (maize Nested Association Mapping population, NAM). Nearly a million plants were assayed in eight environments but showed no evidence for any single large-effect quantitative trait loci (QTLs). Instead, we identified evidence for numerous small-effect QTLs shared among families; however, allelic effects differ across founder lines. We identified no individual QTLs at which allelic effects are determined by geographic origin or large effects for epistasis or environmental interactions. Thus, a simple additive model accurately predicts flowering time for maize, in contrast to the genetic architecture observed in the selfing plant species rice and *Arabidopsis*.

The nature of standing genetic variation and its relation to phenotypic variation in plants affects our understanding of evolution (*1*), sustainable agriculture, and preservation of inter- and intraspecific variation in times of environmental change. Maize inbred lines have an average nucleotide diversity in genic regions around 1% (π = 1 to 1.4%) (*2*, *3*),

similar to the divergence between humans and chimpanzees (*4*). It is not uncommon to find maize haplotypes that are 5% divergent from one another (*5*), which indicates that the maize gene pool reaches back 2 to 4 million years (with one generation per year).

Maize is adapted to a range of environments from the lowland tropics to the Andean highlands and has been widely introduced worldwide into both temperate and tropical regions. Maize's genetic architecture for flowering time has evolved as its wild relatives adapted to distinct ecological zones in elevations differing by more than 3000 m in Mexico and then under both natural and artificial selection over the last 7000 years, with especially intense selection over the past century. This genetic architecture has evolved under a predominantly outcrossing mating system in a species with little population differentiation (*6*).

Flowering time reflects the adaptation of a plant to its environment by tailoring vegetative and reproductive growth phases to local climatic effects. Maize landraces vary widely, from 2 to 11 months, for the time required to mature (*7*). In addition, asynchrony of male and female flowering in maize may be adaptive in some cultivars, but can result in losses under drought conditions, especially in modern uniform varieties (*8*). Flowering time has been extensively studied in the predominantly self-fertilizing species *Arabidopsis*. Like maize, *Arabidopsis* grows across a wide range of latitudes and has flowering time controlled by the interaction of the photoperiod (light sensing and circadian rhythm), vernalization, and autonomous flowering and gibberellic acid–response pathways (*9*, *10*). In grasses, which include maize, wheat, and rice, some of the same genes are involved in flowering, but they have different functions (*11*–*13*).

In maize, diversity-based dissection of flowering time has been hindered by tight linkage of the trait to population structure and by the lack of a reference genome. However, putative orthologs for flowering-time genes identified in other species have been identified through QTL meta-analyses (*14*), although only one major maize flowering-time QTL has been positionally cloned [*vegetative to generative transition 1* (*vgt1*) (*15*)].

Experimental design. We used the maize NAM population (*16*) of 200 recombinant inbred lines (RILs) from 25 crosses between diverse inbred lines and B73 (each referred to as a family), which resulted in a total of 5000 lines (*17*). Because maize has rapid linkage disequilibrium (LD) decay, joint linkage analysis of the maize NAM population was used to evaluate complex trait genetic architecture, as we have insufficient marker density for a genome-wide association study (GWAS). The 5000 lines plus 500 checks—nearly one million plants—were evaluated in four locations over 2 years. We scored days to silking (DS, female flowering) and days to anthesis (DA, male flowering), and we calculated the anthesis-silking interval (ASI). We estimated heritability to be 94% for DS and DA and 78% for ASI; within-cross heritability averaged 83 to 84% for DS and DA and 68% for ASI (table S1). Overall, our phenotypic data were highly heritable, and substantial replication across environments reduced environmental effects on the phenotypic mean values of the lines.

Genetic architecture of flowering. We mapped QTLs both within the 25 families separately (using stepwise regression and inclusive composite interval mapping) and in joint analyses that combined information across all families (joint stepwise regression and joint inclusive composite interval mapping, JICIM (*17*). These methods produced concordant results in terms of the magnitude of effects; however, they have different power and resolution capabilities. Joint linkage QTL analysis identifies nearly twice as many significant effects compared with individual family analyses. The multiple-family joint stepwise regression method identified 36 and 39 QTLs that explained 89% of the total variance for DA or DS, respectively, whereas 29 QTLs explained 64% of the ASI variance (Fig. 1, top). JICIM generally found evidence for an additional 20 minor QTLs for each trait (Fig. 1, bottom). These findings are concordant with the evidence for 50 or more QTLs identified that affect oil content in a large maize population (*18*). Six major QTL regions previously identified in meta-analysis of maize flowering (*14*) were concordant with QTLs identified here. Robust QTL mapping with NAM permitted unprecedented estimation of the genetic architecture in terms of the magnitude of gene effects, epistasis, gene-environment interactions, and pleiotropy.

The number of days to silk emergence varied by 32 days among NAM founder lines and by 28 days among NAM RILs. However, relative to B73, the largest effect DS QTL allele had an additive effect of only 1.7 days (Fig. 2A), whereas the largest ASI effect was 0.4 days. Over 98% of the QTL alleles affected DS by less than 1 day (Fig. 2A). In contrast, in *Arabidopsis*, crosses between lines that flower at roughly the same time can segregate for QTLs that have 3- to 18-day effects (*19*). Rice and barley, both self-fertilizing species, also exhibit larger additive effects for variation in flowering time (*20*, *21*). *Ma1*, the major photoperiod-sensitivity locus in sorghum, has an additive effect of 40.3 days and explains 85.7% of the phenotypic variance for flowering time in a close interspecific (*Sorghum bicolor* × *S. propinquum*) mapping family (*22*).

Our results demonstrate that large differences in flowering time among inbred maize lines are not caused by a few genes of large effect, but by the cumulative effects of numerous QTLs (Fig. 2B), each with only a small impact on the trait. The latest flowering lines had significant allele effects at 24 QTLs, of which 75% delay flowering; the earliest had significant allele effects at 18 QTLs, with 66% of the QTLs accelerating flowering. In outbreeding species, flowering of individual plants must be substantially synchronous within a local population to ensure mating success. Selection may have favored a genetic architecture of additive small-effect QTLs, so that most offspring are likely to have partially synchronous flowering times to ensure fitness. The dispersion of heritable effects across 50 to 100 of these small-effect QTLs may permit the adaptation to a wide range of environments by accumulation of alleles that consistently increase or decrease flowering time.

We tested all pairwise marker combinations for epistatic interactions within each family separately. Epistatic interactions were detected for DS and DA and only within two families. We also tested all marker pairs for epistasis in a joint analysis of all populations, which resulted in detection of epistasis for two marker pairs for ASI, which, combined, explained only 2% of the phenotypic variation. The low epistasis detected for these traits was surprising because flowering time in plants results from interactive molecular pathways (*10*), and epistatic effects have been observed in *Arabidopsis* (*23*) and rice (*24*).

In general, the vast majority of flowering QTLs we identified showed largely consistent results across environments. Although 59% of QTLs had significant environmental (E) interactions, the genetic variation was many times larger than QTL×E interaction variation (Fig. 3A). Overall, this suggests a stable genetic architecture across environments. ASI appeared more sensitive to genotype-by-environment interactions (G×E) than the other flowering phenotypes observed here. Our testing environments had substantial differences in temperatures and rainfall, but day lengths were consistently longer than the critical photoperiod for short-day maize. Therefore, we

[1]U.S. Department of Agriculture (USDA)–Agricultural Research Service (USDA-ARS). [2]Institute for Genomic Diversity, Cornell University, Ithaca, NY 14853, USA. [3]Department of Plant Breeding and Genetics, Cornell University, Ithaca, NY 14853, USA. [4]Department of Crop Science, North Carolina State University, Raleigh, NC 27695, USA. [5]Division of Plant Sciences, University of Missouri, Columbia, MO 65211, USA. [6]Laboratory of Genetics, University of Wisconsin, Madison, WI 53706, USA. [7]Monsanto Company, Leesburg, GA 31763, USA. [8]School of Mathematical Science, Beijing Normal University, Beijing 100875, China. [9]Institute of Crop Science, Chinese Academy of Agricultural Sciences, Beijing 100081, China. [10]Department of Crop Sciences, University of Illinois, Urbana, IL 61801, USA. [11]Department of Agronomy, Purdue University, Urbana, IL 61801, USA. [12]Mision Biologica de Galicia, (CSIC), Pontevedra 36080, Spain. [13]CIMMYT, INT, Crop Research Laboratory, Carretera Mex-Veracruz, CP 56130, Mexico. [14]Computational Biology Service Unit, Cornell University, Ithaca, NY 14853, USA. [15]Cold Spring Harbor Laboratory, Cold Spring Harbor, NY 11724, USA. [16]Department of Agronomy, Kansas State University, Manhattan, KS 66506, USA.

*To whom correspondence should be addressed. E-mail: esb33@cornell.edu (E.S.B.); james_holland@ncsu.edu (J.B.H.); sk20@cornell.edu (S.K.); mcmullenm@missouri.edu (M.D.M.)

expect that G×E interactions may be stronger if tested under both short and long day length environments.

This study was able to investigate pleiotropy by correlating the allelic effects on multiple traits of each QTL across a robust sample of founders. We observed that 100% of DS and DA QTLs have correlated effects on both male and female flowering (average $r = 0.90$ across all loci). In contrast, only about 70% of ASI QTLs had correlated effects on DS, and only 14 to 21% of the ASI QTLs had correlated effects on DA. Overall, genetic control of male and female flowers appears to involve the same set of genes (although magnitudes of effects likely vary). However, the asymmetry between DA-ASI and DS-ASI correlations resulted from the higher variation in the DS phenotype.

We used the significant NAM QTL additive effect estimates to predict the timing of flowering of the NAM founder lines and were able to accurately predict parental flowering time (R^2 = 87 to 91%) (Fig. 3B). This suggests that NAM QTL results are more reliable than individual family QTL effect estimates (*25*) and provides further evidence that epistasis is relatively unimportant. By including nonsignificant additive effect estimates in the model, analogous to genome selection, our predictive ability increases to R^2 = 95%. Although we cannot extend these predictions to unrelated lines because of insufficient marker density, our results suggest that with large enough samples, additive QTL models can accurately predict phenotype.

Our maize founder lines represent a wide range of latitudinal variation (tropical ↔ temperate dent ↔ Northern Flint). We tested the correlation between QTL effect estimates of each founder allele with quantitative estimates of their relation to families of origin to determine whether population structure is defined by the allelic effects at any individual QTL (*26*). QTL effects at 26% of the loci were correlated ($P < 0.05$) with the tropical-temperate cline. The large effects observed for the QTLs on chromosome 10 were highly correlated with tropical origin, yet only 3 of the 16 lines with substantial tropical origin carried alleles at this locus that increased time to flowering by more than 0.4 days. Overall, allelic effects at many loci were weakly correlated with population structure, but tropical origin was not defined by specific QTL alleles; instead, it appears that numerous loci work in concert to produce latitudinal adaptations (Fig. 4A).

QTL and allele frequency. Thirty percent of the polymorphisms in maize were found to be unique to a single founder line (Fig. 4B), which indicates that rare sequence variants are common in diverse maize. We tested whether the phenotypic variation observed across families was mostly due to many rare variants (segregating in only one family) or to a smaller number of loci causing variation in multiple families. As each founder line gave rise to 200 offspring RILs, represented by about 40,000 plants, our design provided sufficient power to detect rare QTLs and to distinguish between these alternative

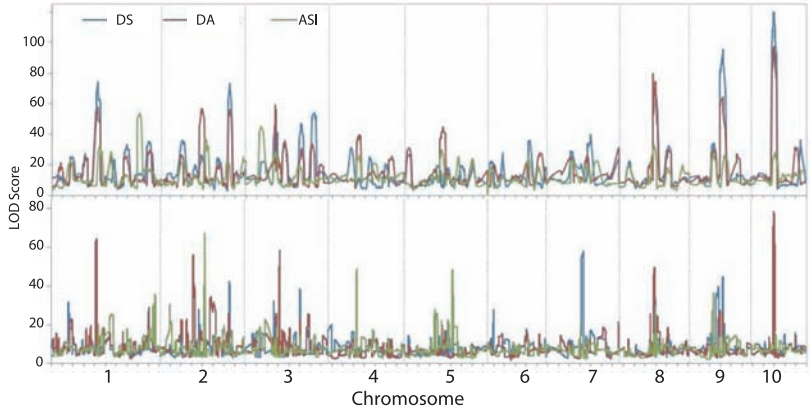

Fig. 1. Joint QTL mapping results across the genome for DS, DA, and ASI. The vertical lines indicate the breaks between the chromosomes. (**Top**) Scanning of the whole genome by using the joint General Linear Model (GLM). (**Bottom**) The whole genome scanned by JICIM.

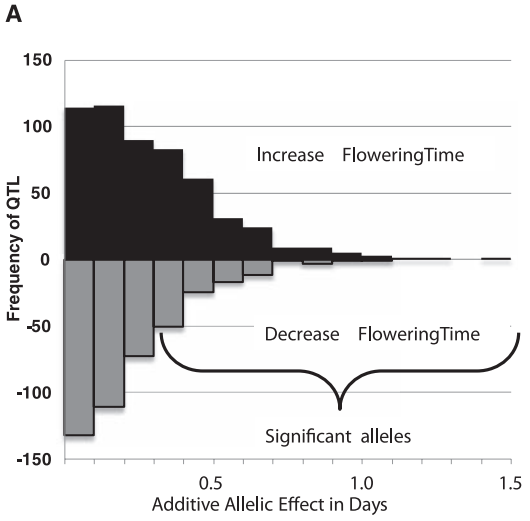

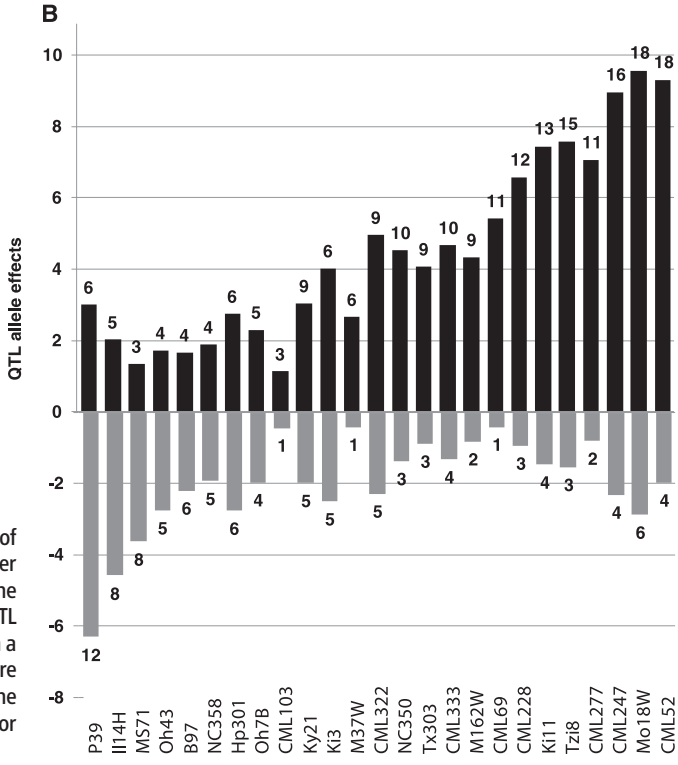

Fig. 2. All QTL allele effects were relatively modest. (**A**) Histogram of additive allele estimates for the 39 days to silking QTLs for all 25 founder lines relative to B73. Count of effects increasing flowering time above the line, and decreasing flowering time below the line. There were 333 QTL alleles that were significant at $P < 0.05$. Only seven (2.1%) had more than a 1-day effect on flowering time. (**B**) Large differences in the parental lines are the product of stacking large numbers of modest-effect QTL. Sums of the estimated additive positive and negative QTL allele effects for each line for DS. Number of QTLs next to each bar.

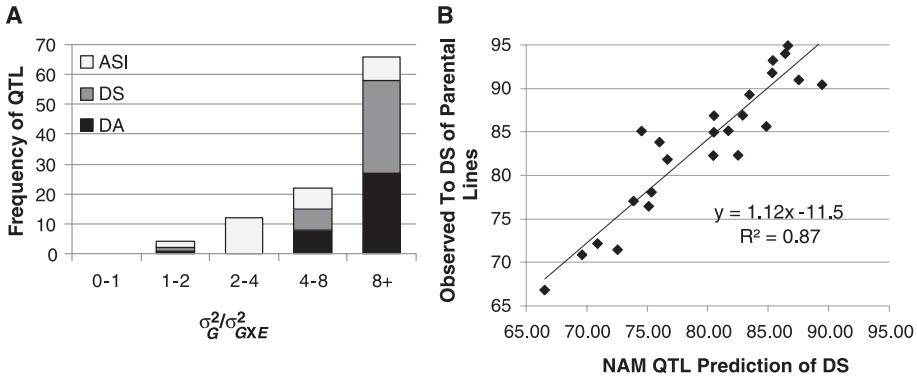

Fig. 3. (**A**) Ratio of genetic variance to genotype by environmental variance by trait. All traits were dominated by genetic variance, but Q×E was more important for ASI. (**B**) Parental flowering can be predicted well from the NAM QTL estimates. All significant QTL effects ($P < 0.05$) for DS were summed and added to observed B73 flowering to predict parental flowering. A consistent underestimate of the slope is likely because of epistasis. The fit increased when nonsignificant alleles were included to $R^2 = 0.95$.

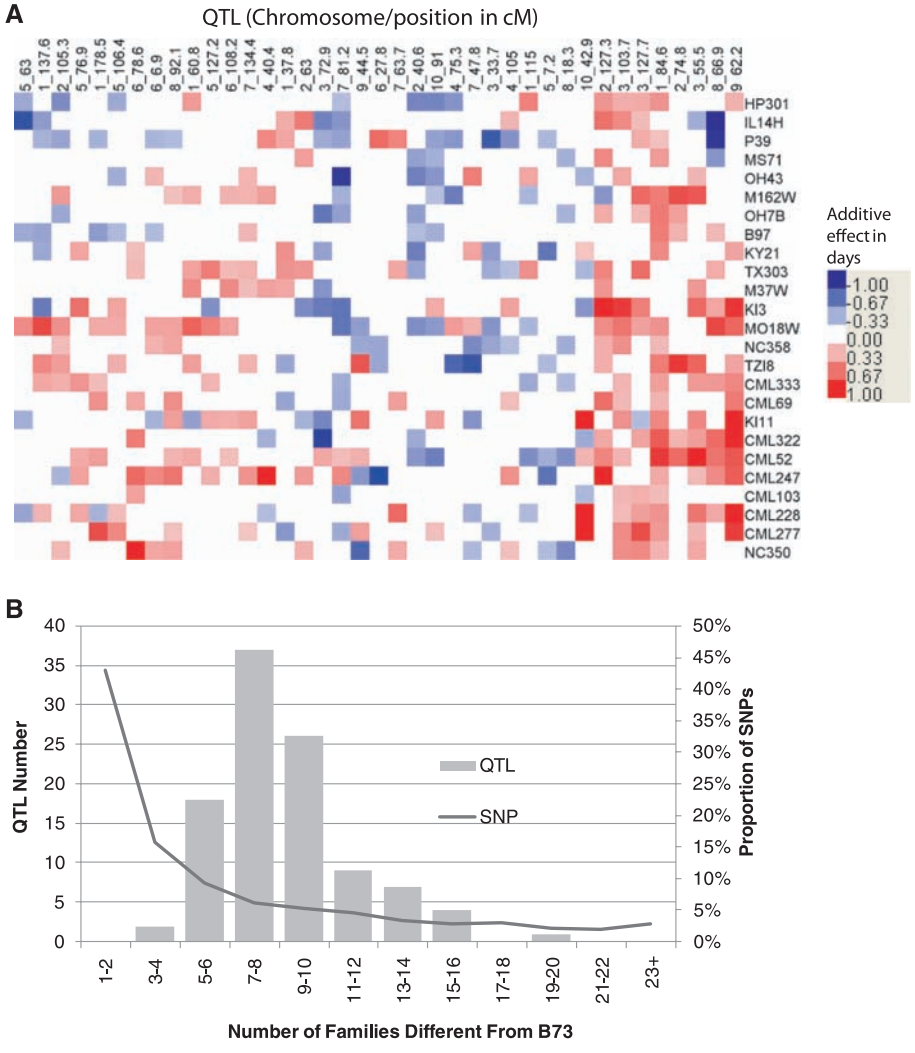

Fig. 4. (**A**) Heat map for DS QTL effects by chromosomal position and allele donor. Of the QTLs, 69% had both positive and negative effects relative to B73, which suggests that allelic series are important for maize flowering-time variation. The QTLs and population were clustered and sorted to show maximal population differentiation of QTLs and lines. Although some QTLs certainly are more common in tropical or temperate lines, no QTL sharply defined these differences. (**B**) The distribution of QTLs and SNPs across families was extremely different, with biases toward QTLs of intermediate frequencies. The QTL and SNP frequency among the NAM families for the three combined traits (DA, DS, and ASI) showed similar distributions. The SNP line indicates the observed frequency of SNP differences from a set 3641 SNPs identified through sequencing these lines.

hypotheses (>90% power for 1-day effect even in single-family analysis). Most QTLs were shared among multiple families (Fig. 4B), with many QTLs showing effects among seven to eight families (30% frequency). Our data partially support the common gene hypothesis for flowering-time genetic architecture, which proposes that variation at common loci causes phenotypic variation across different families. This result is striking because the sharing of QTLs across families contrasts with the high frequency of rare single-nucleotide polymorphisms (SNPs) in maize (Fig. 4B). This discrepancy cannot be due to bias in detecting QTLs of modest frequency for several reasons. (i) Although lower than that for common QTLs, our design provides enough power to detect QTLs segregating in two to four families; nevertheless, we observed few QTLs distributed in this way. (ii) NAM can statistically detect QTLs unique to B73 (common QTLs in this reference design, but rare QTL alleles in the species). However, only 1% of the QTLs were found in 17 or more families compared with 10% of the SNPs. (iii) Additional QTLs can be identified within individual families, but when they were added to the joint family analysis models, they showed significant effects in additional families. And (iv), retesting the final joint population QTLs model by jackknifing the families (leaving one or two families out sequentially) resulted in reduced significance for some of the QTLs, but none became insignificant.

Although many QTLs appear to be shared across families, we also found evidence for allelic series at most loci. Because our founders were crossed to a common reference line, we tested for and observed allelic series, including both positive and negative effects, at the same locus for 69 to 72% of the QTLs (Fig. 4A), depending on the trait. Such allelic series have previously been observed in maize (*27*). Although rare alleles dispersed across multiple tightly linked QTLs may also be misclassified as an allelic series in some cases, our association analysis suggests an allelic series for flowering-time effects at *vgt1* (below). Our results suggest a model of common genes with uncommon variants controlling flowering to explain our observation of a relatively small number of QTLs (e.g., <100), with many functionally distinct alleles at each locus, each occurring at low frequency. GWAS studies and fine-mapping multiple alleles per QTL will be needed to test this hypothesis.

Genes underlying this architecture. To evaluate the power and reliability of NAM, we

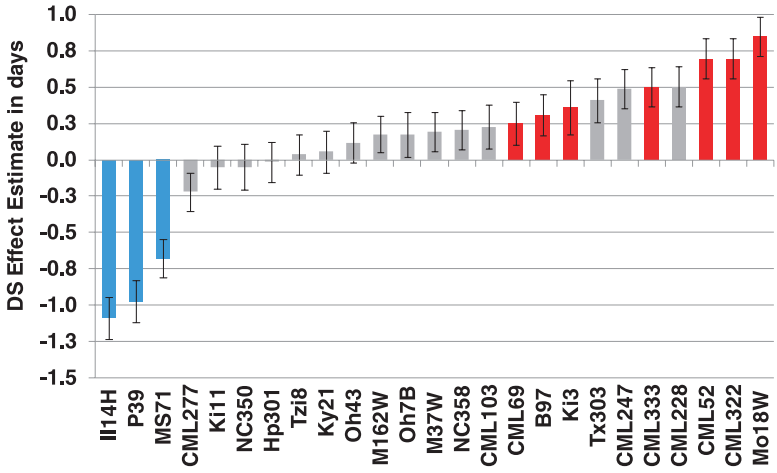

Fig. 5. Estimated DS effects and standard errors for the *vgt1* region of chromosome 8. Estimates are relative to B73 allele flowering. The blue alleles have the MITE at *vgt1* (the Mo17 family, also scored at the same time, also carries the polymorphism and equivalent effect). A simple *t* test of founder-effect estimate for MITE versus non-MITE was significant ($P = 2 \times 10^{-8}$). The red alleles identify lines that carry polymorphisms at *vgt1* target gene *rap2.7,* which also differs significantly ($P = 6 \times 10^{-4}$).

tested a QTL previously shown to affect flowering time in maize. The maize *vgt1* locus contains an *AP2*-like gene, *rap2.7*, involved in the timing of flowering under regulatory control of an enhancer region about 70 kb from the gene (*15*). We confirmed the presence of a QTL in the region of *vgt1* (DA: $P = 4 \times 10^{-44}$; DS: $P = 7 \times 10^{-40}$). Prior QTL mapping efforts (*28*) revealed an early flowering QTL about 5 centimorgans (cM) from *vgt1* that also may be contributing to the effects detected in this region; marker saturation across this interval permitted resolution into two linked QTLs. By controlling for the rest of the genome and estimating the effects of founder alleles at *vgt1*, we observed a distinct allelic series at this locus (Fig. 5).

A previously identified *vgt1* allele from northern germplasm associated with a miniature transposon (MITE) (*15*) was segregating in four of the NAM families (crosses involving Il14H, P39, MS71, and Mo17). In confirmation of previous results, this allele was strongly associated with early flowering in NAM (Fig. 5). Absence of this MITE did not explain the late flowering *vgt1* alleles, but sequencing of founder lines in this region identified SNPs at the *rap2.7* gene itself that were associated with this late-flowering effect (Fig. 5). Associations of both the MITE at the upstream regulator region (*vgt1*) and the SNPs within the *rap2.7* gene with flowering time were confirmed in a separate diverse maize inbred association panel (MITE: $P = 6 \times 10^{-4}$; *rap2.7* SNP: $P = 0.01$).

Natural variation at the *zfl2* locus also significantly affects flowering time (*29*). Although the null mutants of this gene previously observed in natural populations (*29*) did not segregate among these NAM families, we nevertheless found a QTL at the *zfl2* locus (DA: $P = 3 \times 10^{-10}$; DS: $P = 1 \times 10^{-15}$). One line, Ky21, had a phenotype associated with a 16–amino acid deletion in the proline-rich domain of this protein. In addition, other lines showing large effects have a 7-bp deletion 1 bp before the ATG start site of *zfl2*.

Marker saturation of RILs with recombinant chromosome blocks around the largest-effect QTL on chromosome 1 resolved the QTL to a region that includes a homolog of the recently cloned *Ghd7* gene from rice (*12*). On chromosome 1, the *bif2* gene, which is involved in auxin transport (*30*), overlaps with a QTL for ASI. Association analysis in unrelated lines implicates *bif2* in the timing of flowering (*31*). In addition, maize flowering mutant *id1* and homologs of the barley photoperiod genes (*Ppd-H1*) (*21*) fall within our QTL intervals. As there are over 1000 homologs of *Arabidopsis* flowering-time genes in maize, our study demonstrates a means by which to reliably relate maize QTLs to candidate genes.

Implications. Our study of QTLs controlling flowering time with NAM provides insight into the genetic architecture of adaptive traits. Our results suggest that for the outcrossing species maize, the genetic architecture of flowering time is dominated by small additive QTLs with few genetic or environmental interactions (within the tested range of environments). Human height may have a similar genetic architecture (*32*), but in the case of flowering time, these architectures are distinct from *Arabidopsis* and rice, self-fertilizing plant species, where flowering-time variation is controlled by fewer genes with larger effects, epistasis, and environmental interactions (*9*, *11*, *13*, *23*). This suggests that the mating system and demographics influence the genetic architecture of adaptive traits.

For maize, we now have some of the best genetic tools to conduct research of complex genetic architectures. We currently have nearly 15,000 genetic stocks for manipulation and isolation of the genetic variation throughout the entire species. We predict that soon it will be possible to more fully examine the genetic architecture of other traits of interest in maize. Such studies can be applied to improving the world's food security and to making maize production more environmentally sustainable.

References and Notes

1. T. Mitchell-Olds, J. Schmitt, *Nature* **441**, 947 (2006).
2. M. I. Tenaillon *et al.*, *Proc. Natl. Acad. Sci. U.S.A.* **98**, 9161 (2001).
3. S. I. Wright *et al.*, *Science* **308**, 1310 (2005).
4. The Chimpanzee Sequencing and Analysis Consortium, *Nature* **437**, 69 (2005).
5. A. M. Henry, C. Damerval, *Mol. Gen. Genet.* **256**, 147 (1997).
6. M. T. Hamblin, M. L. Warburton, E. S. Buckler, *PLoS One* **2**, e1367 (2007).
7. N. N. Kuleshov, *J. Am. Soc. Agron.* **25**, 688 (1933).
8. J. Bolanos, G. O. Edmeades, *Field Crops Res.* **48**, 65 (1996).
9. T. Izawa, Y. Takahashi, M. Yano, *Curr. Opin. Plant Biol.* **6**, 113 (2003).
10. Y. Komeda, *Annu. Rev. Plant Biol.* **55**, 521 (2004).
11. M. Yano, T. Izawa, in *Rice Genetics V: Proceedings of the Fifth International Rice Genetics Symposium*, 19 to 23 November 2005, Manila, Philippines (IRRI, World Scientific, Singapore, 2005), pp. 177–190.
12. W. Xue *et al.*, *Nat. Genet.* **40**, 761 (2008).
13. J. Cockram *et al.*, *J. Exp. Bot.* **58**, 1231 (2007).
14. F. Chardon *et al.*, *Genetics* **168**, 2169 (2004).
15. S. Salvi *et al.*, *Proc. Natl. Acad. Sci. U.S.A.* **104**, 11376 (2007).
16. M. D. McMullen *et al.*, *Science* **325**, 737 (2009).
17. Materials and methods are available as supporting material on *Science* Online.
18. C. C. Laurie *et al.*, *Genetics* **168**, 2141 (2004).
19. C. Alonso-Blanco, S. E. El-Assal, G. Coupland, M. Koornneef, *Genetics* **149**, 749 (1998).
20. M. Yano *et al.*, *Theor. Appl. Genet.* **95**, 1025 (1997).
21. A. Turner, J. Beales, S. Faure, R. P. Dunford, D. A. Laurie, *Science* **310**, 1031 (2005).
22. Y. R. Lin, K. F. Schertz, A. H. Paterson, *Genetics* **141**, 391 (1995).
23. M. E. El-Lithy *et al.*, *Genetics* **172**, 1867 (2006).
24. N. Uwatoko *et al.*, *Euphytica* **163**, 167 (2008).
25. C. C. Schon *et al.*, *Genetics* **167**, 485 (2004).
26. K. Liu *et al.*, *Genetics* **165**, 2117 (2003).
27. C. E. Harjes *et al.*, *Science* **319**, 330 (2008).
28. S. Salvi *et al.*, *Plant Mol. Biol.* **48**, 601 (2002).
29. K. Bomblies, J. F. Doebley, *Genetics* **172**, 519 (2006).
30. P. McSteen *et al.*, *Plant Physiol.* **144**, 1000 (2007).
31. G. Pressoir *et al.*, *Plant J.* **58**, 618 (2009).
32. P. M. Visscher, *Nat. Genet.* **40**, 489 (2008).

33. We thank the Buckler, Holland, Kresovich, McMullen, and Rocheford labs for their efforts in creating the populations, phenotyping the lines, and scientific input; L. R. Lirette for technical editing of the manuscript; and J. Doebley for managing the NSF project. This work was supported by U.S. NSF Plant Genome Program (DBI-9872631, DBI-0321467, DBI-0820619 to E.S.B., M.M.G. (98,03), J.B.H. (03,08), M.D.M. (03,08), S.K. (03,08), D.W. (03); DBI-0604923 to T.R.R.; U.S. Department of Agriculture–Agricultural Research Service (to E.S.B., J.B.H., M.D.M.), and Spanish Ministry for Education and Science (AP-2004-6033, fellowship to M.C.R.).

Supporting Online Material

www.sciencemag.org/cgi/content/full/325/5941/714/DC1
Materials and Methods
Tables S1 to S5
References

31 March 2009; accepted 26 June 2009
10.1126/science.1174276

Measuring the Cosmic-Ray Acceleration Efficiency of a Supernova Remnant

E. A. Helder,[1*] J. Vink,[1] C. G. Bassa,[2,3] A. Bamba,[4] J. A. M. Bleeker,[1,2] S. Funk,[5] P. Ghavamian,[6] K. J. van der Heyden,[7] F. Verbunt,[1] R. Yamazaki[8]

Cosmic rays are the most energetic particles arriving at Earth. Although most of them are thought to be accelerated by supernova remnants, the details of the acceleration process and its efficiency are not well determined. Here we show that the pressure induced by cosmic rays exceeds the thermal pressure behind the northeast shock of the supernova remnant RCW 86, where the x-ray emission is dominated by synchrotron radiation from ultrarelativistic electrons. We determined the cosmic-ray content from the thermal Doppler broadening measured with optical spectroscopy, combined with a proper-motion study in x-rays. The measured postshock proton temperature, in combination with the shock velocity, does not agree with standard shock heating, implying that >50% of the postshock pressure is produced by cosmic rays.

The main candidates for accelerating cosmic rays up to at least 10^{15} eV are shell-type supernova remnants (SNRs), which are the hot, expanding plasma shells caused by exploded stars (supernovas). To maintain the cosmic-ray energy density in the Galaxy, about three supernovae per century should transform 10% of their kinetic energy in cosmic-ray energy. Indeed, ~10^{14} eV electrons have been detected at forward shocks (*1*, *2*) and possibly at reverse shocks (*3*, *4*) of several shell-type remnants by their x-ray synchrotron emission, and particles with TeV energies have been detected in several SNRs by Cherenkov telescopes (*5*, *6*).

If SNRs transform a substantial amount of their kinetic energy into cosmic rays, this should affect the kinematics of the remnant. One imprint of energy losses by cosmic rays is a higher compression factor of the postshock plasma (*7*), for which indications have been found in both the Tycho SNR and SN 1006 (*8*, *9*). Another signature of the energy absorbed by cosmic rays is a lower postshock temperature (*10*–*13*). For shocks with conservation of mass, momentum, and energy, in the absence of cosmic rays, the postshock temperature (T_i) for species with mass m_i relates to the shock velocity (v_s) as

$$kT_i = \frac{3}{16} m_i v_s^2 \qquad (1)$$

in the case of no thermal equilibrium (i.e., the several atomic species do not have the same temperature), in which protons carry most of the thermal energy. In the case of fast thermal equilibration, this relation becomes $kT = \frac{3}{16}\mu m_p v_s^2$ ($\mu \cong 0.6$ for cosmic abundances). Indications for a lower postshock electron temperature have been found in the Magellanic Cloud remnant 1E 0102-72 (*14*), which may constitute only a minor part of the thermal pressure. Here we derive the postshock proton temperature and the shock velocity of the northeast rim of the shell-type SNR RCW 86 based on optical and x-ray observations.

RCW 86 (*15*) was detected in TeV energies by the HESS telescope (*16*) and is probably the remnant of the supernova witnessed by Chinese astronomers in 185 C.E. (*17*, *18*). It has been suggested that it evolves in a stellar-wind–blown cavity, where the southwest corner has already hit the cavity wall (*19*). The northeast side still expands in a less dense medium, and its x-ray spectrum is dominated by synchrotron radiation, which is an indication of efficient cosmic-ray acceleration.

The optical spectrum of the northeast rim of RCW 86 is dominated by hydrogen lines, with no [NII] line emission (*20*). The lack of [NII] indicates that the hydrogen line emission is not a result of strong cooling, but results from excitation processes immediately behind the shock front. The hydrogen lines from these shocks consist of two superimposed Gaussian line profiles: One, caused by direct excitation, has the thermal width of the interstellar medium (ISM), whereas the other is emitted after charge exchange between hot postshock protons and cold incoming neutral hydrogen and hence has the thermal width of the postshock protons. Hα emission and efficient cosmic-ray acceleration are likely to anticorrelate because incoming neutral species are likely to damp plasma waves, which are essential for shock acceleration (*21*) and because cosmic rays escaping ahead of the shock ionize the surrounding ISM and decrease the amount of Hα emission. In RCW 86, the Hα emission occurs all along the rim, including, although with weak emission, the parts coinciding with x-ray synchrotron emission, where efficient cosmic-ray acceleration is likely to occur

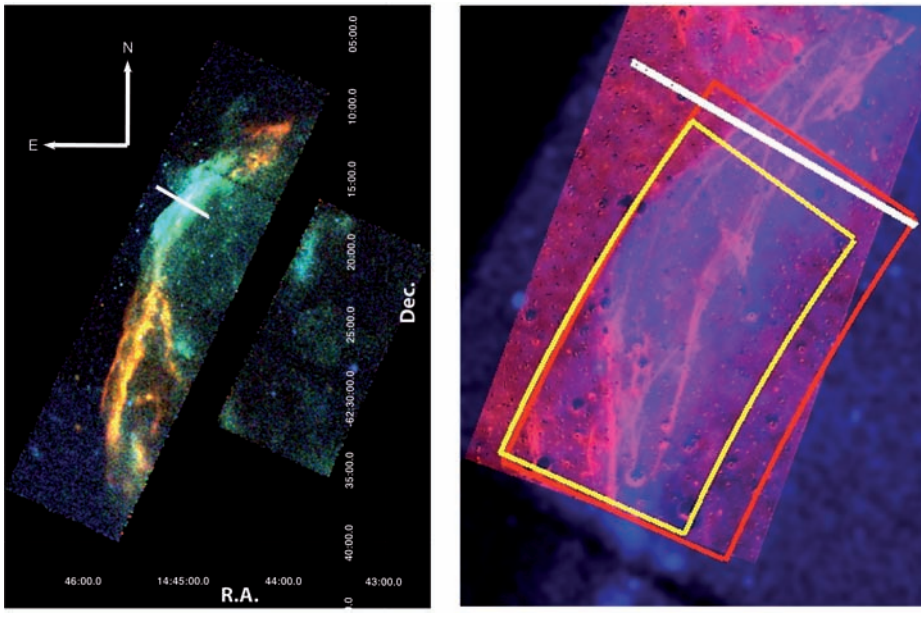

Fig. 1. (**Left**) The eastern rim of RCW 86, as observed in 2007 with Chandra. Red indicates the 0.5- to 1.0-keV band; green, the 1.0- to 1.95-keV band; and blue, the 1.95- to 6.0-keV band. The northern part has relatively more flux in the higher-energy bands, which is characteristic for synchrotron emission. (**Right**) Blue is the broadband keV Chandra image; red is the image as observed with the VLT through a narrow Hα filter. The regions (yellow and red) indicate where we measured the proper motion. In both panels, the location where we took the optical spectrum is indicated with a white line.

[1]Astronomical Institute Utrecht, Utrecht University, Post Office Box 80000, NL-3508 TA Utrecht, Netherlands. [2]SRON Netherlands Institute for Space Research, Sorbonnelaan 2, NL-3584 CA Utrecht, Netherlands. [3]Department of Astrophysics, Radboud University Nijmegen, Post Office Box 9010, Nijmegen, Netherlands. [4]Institute of Space and Astronautical Science–Japan Aerospace Exploration Agency, Department of High Energy Astrophysics 3-1-1, Yoshinodai, Sagamihara, Kanagawa 229-8510, Japan. [5]Kavli Institute for Particle Astrophysics and Cosmology, Stanford, CA 94025, USA. [6]Space Telescope Science Institute, 3700 San Martin Drive, Baltimore, MD 21218, USA. [7]Astronomy Department, University of Cape Town, Private Bag X3, Rondebosch 7701, South Africa. [8]Department of Physical Science, Hiroshima University, Higashi-Hiroshima, Hiroshima 739-8526, Japan.

*To whom correspondence should be addressed. E-mail: e.a.helder@uu.nl

(Fig. 1). The only other remnant in which Hα emission is seen all along the shell, including regions with x-ray synchrotron emission, is the SN 1006 SNR (*22*).

The right panel in Fig. 1 shows both the Hα and the x-ray emission of the northeast rim of RCW 86. The Hα emission marks the onset of the x-ray synchrotron radiation, which indicates that they are from the same physical system.

To measure the proton temperature, we used long-slit spectra obtained with the visual and near ultraviolet Focal Reducer and low-dispersion Spectrograph (FORS2) instrument on the Very Large Telescope (VLT) (*23*). We first imaged the northeast side of RCW 86, where the x-ray spectrum is dominated by synchrotron emission. Using this image as a guide, we pointed the slit at a location where the Hα emission is bright (Fig. 1 and table S1).

The spectrum's (Fig. 2) measured full width at half maximum is 1100 ± 63 km/s [see supporting online material (SOM) for further details], corresponding to a σ_v = 467 ± 27 km/s and implying a postshock temperature of 2.3 ± 0.3 keV.

To measure the shock velocity of the northeast rim of RCW 86, we observed it with the Chandra X-Ray Observatory in June 2007 and matched it with an observation taken in June 2004 (*18*). To make both observations as similar as possible, we used the same observation parameters as in 2004 (table S2). We measured the proper motion of the shock at the location of the slit of the Hα spectrum by comparing the positions of the shock in the two images (see SOM for further details). A solid estimate of the proper motion is 1.5 ± 0.5″ in 3 years' time (Fig. 3 and fig. S1), implying a shock velocity of (6.0 ± 2.0) × 10^3 km/s at a distance of 2.5 kpc (*24*, *25*). The statistical error on the measured expansion is on the order of 0.2″. However, when calculating the proper motions, we found that small details, such as slightly changing the angle in which we made the profile, tended to give a different proper motion, with a difference larger than the 0.2″ statistical error that we measured. However, in none of the measurements did we find a proper motion below 1.0″. Because the proper motion is higher than expected (*18*), we verified that it is consistent with data taken in 1993 with the Position Sensitive Proportional Counter (PSPC) on board the Roentgen Satellite (ROSAT) compared with the 2007 observation (Fig. 3 and fig. S1). Although the proper motion, using the nominal pointing of the ROSAT PSPC, is statistically highly significant, the large pointing error of ROSAT (~4″) results in a detection of the proper motion at the 2σ level.

Compared to other remnants of a similar age, the shock velocity is surprisingly high. Recent models (*26*) predict v_s ~ 5000 km/s after 2000 years for SNRs evolving in a wind-blown bubble (*27*). This fits with the scenario in which RCW 86 is evolving in a cavity and the southwest corner, which has a slower shock velocity (*28*, *29*) and a mostly thermal (*3*) x-ray spectrum, has already hit the cavity shell. Shock acceleration theory suggests that only shocks with velocities exceeding 2000 km/s emit x-ray synchrotron emission (*18*, *30*), which is also consistent with observations (*31*).

An additional uncertainty in the shock velocity is in the distance to RCW 86, which is based on converging but indirect lines of evidence. RCW 86 was found to be in the same direction as an OB association, at a distance of 2.5 kpc (*32*). Because high-mass stars are often found in such associations, the progenitor of RCW 86 may well have formed in this one, provided that RCW 86 is the remnant of an exploded massive star. Other studies (*24*, *25*) found a distance of 2.3 and 2.8 kpc, respectively, based on the line-of-sight velocity of ISM swept up by the remnant, combined with an observationally determined rotation curve of the Galaxy (*33*). The third argument supporting a distance of 2.5 kpc is the molecular supershell seen in CO emission in the direction of RCW 86, whose line-of-sight velocity agrees with that of RCW 86 (*34*). In further calculations, we take the distance toward RCW 86 to be 2.5 ± 0.5 kpc, leading to a shock velocity of 6000 ± 2800 km/s.

The relation between shock velocity and measured postshock proton temperature has been extensively studied (*20*, *29*, *35*–*37*), including the cross sections for excitation and charge exchange as function of v_s. Although recent studies show that there can be a substantial effect of cosmic rays on the postshock proton spectrum (*38*), until now, there was no need to include cosmic-ray acceleration in the interpretation of the postshock temperature, possibly because most of the Hα spectra are taken from the brightest rims of SNRs. Because Hα emission and efficient cosmic-ray acceleration are likely to anticorrelate (*21*), these rims probably have low cosmic-ray acceleration efficiency. A possible exception is "knot g" in the Tycho SNR, where indications for cosmic-ray acceleration in the form of a precursor have been found (*39*–*41*). Additionally, for some SNRs (*22*, *42*), the distance has been determined by using the postshock proton temperature in combination with the proper motion, using theoretical models that do not take into account energy losses and cosmic-ray pressure. This procedure leads to an underestimate of the distance if cosmic-ray acceleration is present. Thus, unless the distance is accurately determined in an independent way, there will be no discrepancy between the predicted v_s, based on *kT* and Eq. 1, and the actual shock velocity.

The shock velocity of the x-ray synchrotron rim implies a postshock temperature of 70 keV (assuming no thermal equilibrium) or 42 keV (assuming equilibrium), whereas the measured postshock temperature is 2.3 keV. This measurement is at least a factor 18 less than the postshock temperature estimated from the shock velocity, which can now be used to constrain current theoretical shock-heating models (*12*, *13*). Additionally, this proton temperature is close to the electron temperature at the same location (*18*), implying fast thermal equilibration between both species, breaking the trend between the shock velocity and the measure of thermal equilibrium seen in previous observations (*36*, *37*).

To translate this discrepancy into the energy and pressure in cosmic rays, we followed the approach of (*11*), which is based on standard shock equations for plane-parallel, steady-state shocks, modified by additional pressure and loss terms [see

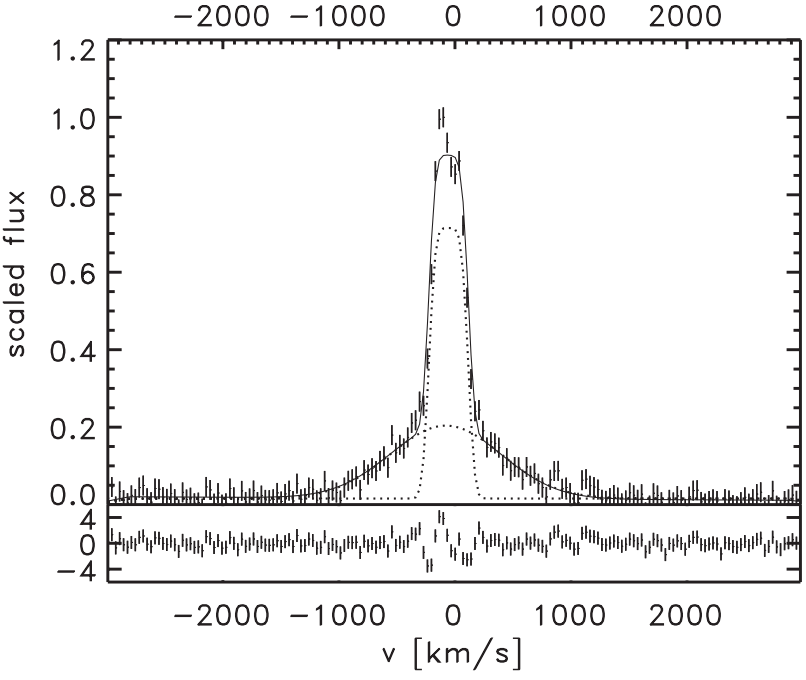

Fig. 2. The Hα spectrum, with broad and narrow components (dotted lines). The best-fitting spectrum is overplotted. The lower panel shows the residuals divided by the errors.

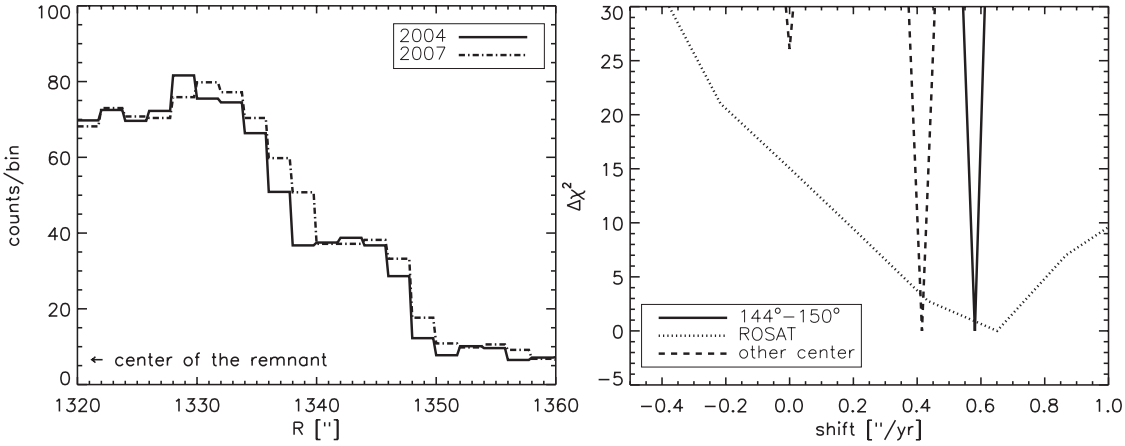

Fig. 3. (**Left**) Steep gradient in the radial profiles for the 2004 and 2007 observations, adaptively binned with the Haar method (*47*), so that each bin has a signal-to-noise ratio of at least 4, with a maximum bin width of 2″. (**Right**) χ^2 statistics of the proper motion measurement. (Details of the used radial profiles are in the SOM.)

also (*7*, *43*, *44*)]. The loss term is defined in terms of the incoming energy flux: $\varepsilon_{CR} \equiv F_{CR}/\frac{1}{2}\rho_0 v_s^3$, where F_{CR} is the amount of energy flux in cosmic rays that escapes from the system and ρ_0 is the preshock density. The parameter that indicates the fraction of the pressure induced by cosmic rays in the total postshock pressure is w_{CR} [$w_{CR} \equiv P_{NT}/(P_T + P_{NT})$], where P_T is the pressure in particles with a thermal and P_{NT} with a nonthermal energy distribution (i.e., CRs). We plot the modified equations (listed in the SOM) in Fig. 4 and indicate the region where the combination of kT and v_s of the northern rim of RCW 86 resides for thermal equilibrium as well as for no thermal equilibrium. As Fig. 4 shows, a postshock temperature and a shock velocity do not give a unique solution for w_{CR} and ε_{CR}. However, the cosmic rays significantly change the shock dynamics, because the combination solution is far away from $w_{CR} = 0$ and $\varepsilon_{CR} = 0$ (Fig. 4).

There are two ways to further constrain w_{CR} and ε_{CR}. First, an additional estimate of the compression ratio (χ) of the postshock plasma would exactly determine w_{CR} and ε_{CR}. For certain SNRs this is done by determining the distance between the supernova ejecta and the outer shock; a higher compression ratio implies that the swept-up ISM forms a thinner shell and hence the ejecta will be closer to the shock front (*8*, *9*). However, ejecta and swept-up ISM are distinguished only by their thermal spectra, which is (almost) absent in the x-ray synchrotron–dominated rim [~15% of the total x-ray emission (*18*)].

Another way is to invoke a dependency of w_{CR} on ε_{CR}. According to nonlinear shock acceleration theory (*12*, *45*), $\varepsilon_{CR}/w_{CR} = \frac{2}{\lambda}(1-1/\chi)^2$, in which χ is the compression ratio of the postshock plasma and $\lambda = 1,2$ indicates the (w_{CR},ε_{CR}) relation for a cosmic-ray spectrum with $f(p) \propto p^{-3}$,$p^{-3.5}$, respectively, with p the momentum of the cosmic rays. The $\lambda = 2$ line gives an upper limit to the energy losses, because it is valid for the most efficient cosmic-ray acceleration by cosmic-ray–modified shocks (*46*). For $f(p) \propto p^{-4}$, $\lambda = \ln(p_{max}/mc)$ (*12*), which can be large and does not provide a lower limit to ε_{CR}. Taking the $\lambda = 2$ line as an upper limit for ε_{CR}, we find a value for w_{CR} of $\geq 50\%$. One remaining question is whether we should include the effects of the turbulent magnetic field. The average magnetic field pressure in RCW 86 has been estimated to be $P_B = B^2/8\pi = 2.3 \times 10^{-11}$ dyn/cm^2, for a magnetic field of 24 μG (*18*). This is an order of magnitude below the thermal pressure, which we estimate to be $P_T = nkT = 3.7 \times 10^{-10}$ dyn/cm^2, for $n = 0.1$ (*18*) and $kT = 2.3$ keV. In reality, the magnetic field pressure may be higher if one takes full account of its unknown, turbulent spectrum.

In summary, our observations show that the postshock temperature of the northeast rim of RCW 86 is lower than expected from standard shock relations using the measured shock velocity. The high velocity (6000 ± 2800 km/s) of the shock implies a local low ISM density, which can be expected in a cavity blown by a stellar wind. Cosmic-ray acceleration decreases the postshock proton temperature in RCW 86 by a factor of 18, implying that ≥50% of the postshock pressure is due to cosmic rays.

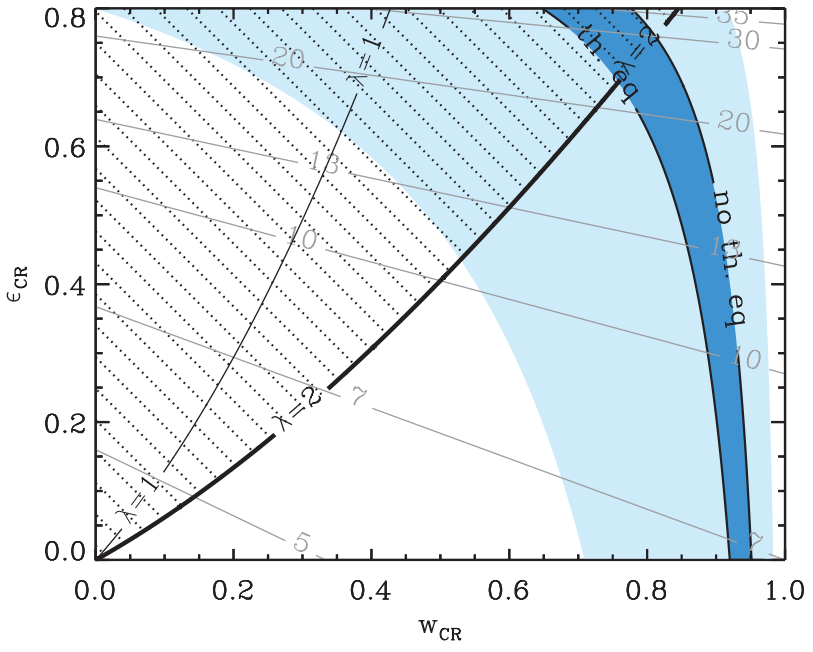

Fig. 4. Measurements of the shock velocity and postshock proton temperature for the northeast shock of RCW 86 in terms of w_{CR} and ε_{CR}. The dark blue area is the area allowed according to the modified equations, limited by full thermal equilibrium and no thermal equilibrium for the nominal values of kT = 2.3 keV, v_s = 6000 km/s. The light blue area shows the area of the kT and v_s with all uncertainties taken into account. The thin lines indicate the compression ratio (χ) of the postshock plasma. Within the allowed region, $\lambda = 2$ line provides an upper limit on ε_{CR} and a lower limit on w_{CR}.

References and Notes

1. K. Koyama *et al.*, *Nature* **378**, 255 (1995).
2. A. Bamba, R. Yamazaki, T. Yoshida, T. Terasawa, K. Koyama, *Astrophys. J.* **621**, 793 (2005).
3. J. Rho, K. K. Dyer, K. J. Borkowski, S. P. Reynolds, *Astrophys. J.* **581**, 1116 (2002).
4. E. A. Helder, J. Vink, *Astrophys. J.* **686**, 1094 (2008).
5. F. A. Aharonian *et al.*, *Nature* **432**, 75 (2004).
6. J. Albert *et al.*, *Astron. Astrophys.* **474**, 937 (2007).
7. E. G. Berezhko, D. C. Ellison, *Astrophys. J.* **526**, 385 (1999).
8. J. S. Warren *et al.*, *Astrophys. J.* **634**, 376 (2005).
9. G. Cassam-Chenaï, J. P. Hughes, E. M. Reynoso, C. Badenes, D. Moffett, *Astrophys. J.* **680**, 1180 (2008).

10. A. Decourchelle, D. C. Ellison, J. Ballet, *Astrophys. J.* **543**, L57 (2000).
11. J. Vink, in *High Energy Gamma-Ray Astronomy: Proceedings of the 4th International Meeting on High Energy Gamma-Ray Astronomy* (American Institute of Physics, College Park, MD, 2008), vol. 1085, pp. 169–180.
12. L. O'C. Drury, F. A. Aharonian, D. Malyshev, S. Gabici, *Astron. Astrophys.* **496**, 1 (2009).
13. D. J. Patnaude, D. C. Ellison, P. Slane, *Astrophys. J.* **696**, 1956 (2009).
14. J. P. Hughes, C. E. Rakowski, A. Decourchelle, *Astrophys. J.* **543**, L61 (2000).
15. G315.4-2.3, MSH 14-*63*.
16. F. Aharonian *et al*., *Astrophys. J.* **692**, 1500 (2009).
17. F. R. Stephenson, D. A. Green, *Historical Supernovae and Their Remnants*, International Series in Astronomy and Astrophysics, vol. 5 (Oxford Univ. Press, Oxford, 2002).
18. J. Vink *et al*., *Astrophys. J.* **648**, L33 (2006).
19. J. Vink, J. S. Kaastra, J. A. M. Bleeker, *Astron. Astrophys.* **328**, 628 (1997).
20. R. A. Chevalier, R. P. Kirshner, J. C. Raymond, *Astrophys. J.* **235**, 186 (1980).
21. L. O'C Drury, P. Duffy, J. G. Kirk. *Astron. Astrophys.* **309**, 1002 (1996).
22. P. F. Winkler, G. Gupta, K. S. Long, *Astrophys. J.* **585**, 324 (2003).
23. I. Appenzeller *et al*., *Messenger* **94**, 1 (1998).
24. M. Rosado, P. Ambrocio-Cruz, E. Le Coarer, M. Marcelin, *Astron. Astrophys.* **315**, 243 (1996).
25. J. Sollerman, P. Ghavamian, P. Lundqvist, R. C. Smith, *Astron. Astrophys.* **407**, 249 (2003).
26. V. V. Dwarkadas, *Astrophys. J.* **630**, 892 (2005).
27. The effects of cosmic ray acceleration on the evolution of the forward shock are small; see (*13*).
28. K. S. Long, W. P. Blair, *Astrophys. J.* **358**, L13 (1990).
29. P. Ghavamian, J. Raymond, R. C. Smith, P. Hartigan, *Astrophys. J.* **547**, 995 (2001).
30. F. A. Aharonian, A. M. Atoyan, *Astron. Astrophys.* **351**, 330 (1999).
31. S. Katsuda, H. Tsunemi, K. Mori, *Astrophys. J.* **678**, L35 (2008).
32. B. E. Westerlund, *Astrophys. J.* **74**, 879 (1969).
33. J. Brand, L. Blitz, *Astron. Astrophys.* **275**, 67 (1993).
34. K. Matsunaga *et al*., *Publ. Astron. Soc. Jpn.* **53**, 1003 (2001).
35. K. Heng, R. McCray, *Astrophys. J.* **654**, 923 (2007).
36. M. van Adelsberg, K. Heng, R. McCray, J. C. Raymond, *Astrophys. J.* **689**, 1089 (2008).
37. P. Ghavamian, J. M. Laming, C. E. Rakowski, *Astrophys. J.* **654**, L69 (2007).
38. J. C. Raymond, P. A. Isenberg, J. M. Laming, *Astrophys. J.* **682**, 408 (2008).
39. P. Ghavamian, J. Raymond, P. Hartigan, W. P. Blair, *Astrophys. J.* **535**, 266 (2000).
40. J.-J. Lee *et al*., *Astrophys. J.* **659**, L133 (2007).
41. A. Y. Wagner, J.-J. Lee, J. C. Raymond, T. W. Hartquist, S. A. E. G. Falle, *Astrophys. J.* **690**, 1412 (2009).
42. R. C. Smith, R. P. Kirshner, W. P. Blair, P. F. Winkler, *Astrophys. J.* **375**, 652 (1991).
43. R. A. Chevalier, *Astrophys. J.* **272**, 765 (1983).
44. A. M. Bykov, K. Dolag, F. Durret, *Space Sci. Rev.* **134**, 119 (2008).
45. M. A. Malkov, L. Drury, *Rep. Prog. Phys.* **64**, 429 (2001).
46. M. A. Malkov, *Astrophys. J.* **511**, L53 (1999).
47. J.-L. Starck, F. Murtagh, A. Bijaoui, *Image Processing and Data Analysis. The Multiscale Approach* (Cambridge Univ. Press, Cambridge, 1998).

48. We thank A. Achterberg for a useful discussion of the current literature on the theory of shock heating. E.A.H. and J.V. are supported by the Vidi grant to J.V. from the Netherlands Organization for Scientific Research (NWO). This work was supported in part by Grant-in-Aid for Scientific Research from the Japanese Ministry of Education, Culture, Sports, Science and Technology, no. 194014 (A.B.) and no. 19047004 and 21740184 (R.Y.). S.F. is supported by Smithsonian Astrophysical Observatory grant G07-8073X. P.G. is supported by the Space Telescope Science Institute grant GO-11184.07. This paper is based in part on observations made with European Southern Observatory Telescopes at the Paranal Observatories under program ID 079.D-0735.

Supporting Online Material

www.sciencemag.org/cgi/content/full/1173383/DC1
SOM Text
Fig. S1
Tables S1 and S2
References

11 March 2009; accepted 15 June 2009
Published online 25 June 2009;
10.1126/science.1173383
Include this information when citing this paper.

Emulation of a Quantum Spin with a Superconducting Phase Qudit

Matthew Neeley,[1] Markus Ansmann,[1] Radoslaw C. Bialczak,[1] Max Hofheinz,[1] Erik Lucero,[1] Aaron D. O'Connell,[1] Daniel Sank,[1] Haohua Wang,[1] James Wenner,[1] Andrew N. Cleland,[1] Michael R. Geller,[2] John M. Martinis[1]*

In quantum information processing, qudits (*d*-level systems) are an extension of qubits that could speed up certain computing tasks. We demonstrate the operation of a superconducting phase qudit with a number of levels *d* up to *d* = 5 and show how to manipulate and measure the qudit state, including simultaneous control of multiple transitions. We used the qudit to emulate the dynamics of single spins with principal quantum number *s* = 1/2, 1, and 3/2, allowing a measurement of Berry's phase and the even parity of integer spins (and odd parity of half-integer spins) under 2π-rotation. This extension of the two-level qubit to a multilevel qudit holds promise for more-complex quantum computational architectures and for richer simulations of quantum mechanical systems.

Quantum computers are typically thought of as being composed of qubits, or two-level quantum systems (*1*). However, one can also use qutrits (three-level systems) or more generally qudits (*d*-level systems), which can simplify some quantum computations (*2*, *3*) and improve quantum cryptography (*4*). The advantages of qudits are also evident when one considers using a quantum computer not to perform computations but rather to emulate another quantum system by the direct implementation of an analogous physical Hamiltonian. This requires a map between the Hilbert space and unitary operators of the emulator and the target system. If the target system contains parts with $d > 2$ levels, then it maps much more naturally to a set of qudits, making a qudit emulator potentially more efficient.

We describe the operation of a superconducting phase qudit with full unitary control and measurement of the state (*5*, *6*). This device, one of a family of superconducting quantum information–processing devices (*7*), is typically operated as a qubit (*8*, *9*) by restricting it to the two lowest-energy eigenstates. By relaxing this restriction, we can operate it as a qudit in which the number of levels *d* can be chosen as desired, in this case up to $d = 5$.

Emulation of spin, or intrinsic angular momentum, naturally calls for qudits with $d > 2$. A spin state is described by two quantum numbers (*10*), the principal quantum number $s = 0, 1/2, 1, 3/2,...$ and the azimuthal quantum number *m*, limited to the $d = 2s + 1$ values $m = s, s - 1,..., -s$. For a given *s*, the general spin states $|\psi\rangle = \sum_m c_m|s,m\rangle$ span a *d*-dimensional Hilbert space, so that although qubits can be used to model spin-1/2 physics a qudit allows one to model spins $s \geq 1$ ($d \geq 3$).

When rotated about a closed path (Fig. 1), a spin state $|s,m\rangle$ acquires a phase factor $\exp(-im\Omega)$, where Ω is the solid angle enclosed by the path, as predicted by Berry (*11*–*13*). For a 2π-rotation ($\Omega = 2\pi$), integer spins are unchanged, whereas half-integer spins are multiplied by −1. This parity difference leads to the symmetric statistics of bosons (or antisymmetric statistics of fermions) under exchange, as described by the spin-statistics theorem (*14*, *15*). The effect of 2π-rotations was first observed on spins $s = 1/2$ via neutron interferometry (*16*, *17*) and later for $s = 1$ and $s = 3/2$ in nuclear magnetic resonance (*18*). In superconducting qubits, the spin-1/2 parity (*19*) and Berry's phase (*20*) have been measured. We measured Berry's phase and spin parity for spin-1/2, spin-1, and spin-3/2 at all solid angles using our qudit emulation (*21*).

Our flux-biased phase qudit (Fig. 2A) is a nonlinear resonator formed by a Josephson junction, inductor, and capacitor. Applied magnetic flux produces a cubic potential as a function of the junction phase δ, with barrier height ΔU that can be tuned so as to change the number of energy levels in the well (Fig. 2B). The cubic anharmonicity is crucial for qubit operation (*22*), allowing microwaves at frequency $\omega_{10} = (E_1 - E_0)/\hbar$ to drive transitions between $|0\rangle$ and $|1\rangle$ while minimizing "leakage" to $|2\rangle$ and higher (*23*). For measurement, a brief current pulse $I_{\mathrm{meas}}^{(1)}$ is ap-

[1]Department of Physics, University of California at Santa Barbara (UCSB), Santa Barbara, CA 93106, USA. [2]Department of Physics and Astronomy, University of Georgia, Athens, GA 30602, USA.

*To whom correspondence should be addressed. E-mail: martinis@physics.ucsb.edu

plied to lower the barrier and cause $|1\rangle$ (but not $|0\rangle$) to tunnel out of the well. An on-chip superconducting quantum interference device (SQUID) detects this tunneling (*24*).

For qudit operation, anharmonicity is again crucial because it ensures that all transition frequencies $\omega_{n,n-1} = (E_n - E_{n-1})/\hbar$ are distinct, allowing frequency-selective control of all qudit states. In the present sample, transition frequencies are ~6 GHz and separated from each other by ~200 MHz (Fig. 2B). This separation is large enough that transitions can be selectively driven with fast pulses (as compared with the state lifetimes) but small enough that the total bandwidth required is within that of our microwave control (*13*). This selective control of transitions between neighboring levels allows for the construction of arbitrary unitary gates on the d-level qudit manifold (*25*).

To measure the qudit, $d-1$ pulse amplitudes $I^{(1)}_{\mathrm{meas}} > I^{(2)}_{\mathrm{meas}} > \ldots > I^{(d-1)}_{\mathrm{meas}}$ are chosen (Fig. 2C), with each pulse $I^{(n)}_{\mathrm{meas}}$ adjusted so that the upper states $|n\rangle$, $|n+1\rangle$,... tunnel out of the well whereas the lower states $|n-1\rangle$, $|n-2\rangle$,... do not. Each tunneling measurement is repeated ~10^3 times on identically prepared qudit states in order to obtain the cumulative tunneling probability $P_{\geq n}$. From these, we obtain the individual occupation probabilities $P_n = P_{\geq n} - P_{\geq n+1}$, which are the diagonal elements $P_n = \rho_{nn}$ of the qudit density matrix $\rho_{mn} = \langle m|\hat{\rho}|n\rangle$.

Arbitrary unitary gates combined with state measurement make this system a universal single qudit (*5*, *25*). By applying an appropriate set of unitaries before measurement, one could for example reconstruct the entire qudit density matrix, similar to previously demonstrated single- and coupled-qubit state tomography (*8*, *9*). Qudit-qudit coupling (*25*) is also possible but beyond the scope of this work.

We calibrated the qudit one transition at a time from the ground state upwards. First, as for qubit operation, we initialized the system in $|0\rangle$, and a standard protocol (*23*) was used to find $I^{(1)}_{\mathrm{meas}}$ and ω_{10} and to calibrate a π-pulse $|0\rangle \rightarrow |1\rangle$. Next, we applied this π-pulse so as to initialize the system in $|1\rangle$ and repeated the protocol so as to find $I^{(2)}_{\mathrm{meas}}$ and ω_{21} and to calibrate a π-pulse $|1\rangle \rightarrow |2\rangle$. This process may be repeated as desired, in this case up to $|d-1\rangle = |4\rangle$. Each π-pulse has a 16-ns envelope (*13*), with the amplitudes scaled to equalize the rotation rates (Fig. 3, A to C), thus calibrating the transition matrix elements $\delta_{n,n-1} = \langle n|\hat{\delta}|n-1\rangle$. The measured lifetimes of the excited states are $T_1 = 610$ ns, $T_2 = 320$ ns, $T_3 = 220$ ns, and $T_4 = 170$ ns, which is in good agreement with the $T_n = T_1/n$ scaling seen in harmonic oscillators (*26*, *27*) because of the weak anharmonicity.

Evolution of the qudit state is best described in the basis of moving eigenkets $|n'\rangle = \exp(-iE_n t/\hbar)|n\rangle$. In this basis, microwaves at $\omega_{n,n-1}$ appear as off-diagonal elements in the Hamiltonian

$$H' = \begin{pmatrix} 0 & A^*_{10} & 0 & 0 \\ A_{10} & 0 & A^*_{21} & 0 \\ 0 & A_{21} & 0 & A^*_{32} \\ 0 & 0 & A_{32} & 0 \end{pmatrix} \quad (1)$$

where the $A_{n,n-1}$ are arbitrary complex numbers giving the amplitude and phase of the microwaves at $\omega_{n,n-1}$, and we have made the usual rotating-wave approximation by discarding off-resonant terms. The calibration shown in Fig. 3, A to C, ensures that the $A_{n,n-1}$ are calibrated relative to each other.

To emulate a spin rotation, the applied qudit Hamiltonian should be the appropriate rotation generator. The generators of rotation about X for $s = 1/2$, 1, and 3/2 (*10*) are

$$X^{(1/2)} = \begin{pmatrix} 0 & 1 \\ 1 & 0 \end{pmatrix}$$

$$X^{(1)} = \begin{pmatrix} 0 & 1 & 0 \\ 1 & 0 & 1 \\ 0 & 1 & 0 \end{pmatrix}$$

$$X^{(3/2)} = \begin{pmatrix} 0 & \frac{\sqrt{3}}{2} & 0 & 0 \\ \frac{\sqrt{3}}{2} & 0 & 1 & 0 \\ 0 & 1 & 0 & \frac{\sqrt{3}}{2} \\ 0 & 0 & \frac{\sqrt{3}}{2} & 0 \end{pmatrix} \quad (2)$$

where the largest element in each matrix has been normalized to 1. Generators of Y-rotation are similar but have imaginary off-diagonal terms. These operators all have the form Eq. 1 of microwave-drive Hamiltonians, allowing us to use microwaves to emulate spin rotations about X, Y, or any other axis in the X-Y plane.

The evolution of the qudit state under emulated spin rotation is shown in Fig. 3 for spin-1 (Fig. 3D) and spin-3/2 (Fig. 3E). In both cases, the ground state $|0\rangle$ is reserved as a phase reference, so the spin is mapped to $|1\rangle \equiv |s,s\rangle$, $|2\rangle \equiv |s,s-1\rangle$,..., $|1+2s\rangle \equiv |s,-s\rangle$. The spin starts in $|1\rangle$, rotates to $|3\rangle$ (spin-1) or $|4\rangle$ (spin-3/2), then back to $|1\rangle$ and so on. Although the state populations evolve in a complicated fashion, the expectation value $\langle \hat{Z} \rangle = \sum_m m\, P_{|s,m\rangle}$ evolves sinusoidally (dashed line), as is expected for a rotating spin. Compared with spin-1/2 (Fig. 3, A to C), the rotation is slowed by a factor of $\sqrt{2}$ (spin-1) or 2 (spin-3/2), which is in agreement with direct exponentiation of the matrices in Eq. 2.

Next, these emulated spin rotations are used to measure Berry's phase, as described in Fig. 1. We made the phase measurement using Ramsey interference with $|0\rangle$ as a reference. First, we applied a $\pi/2$-pulse in order to prepare the superposition $(|0\rangle + |1\rangle)/\sqrt{2}$. Then,

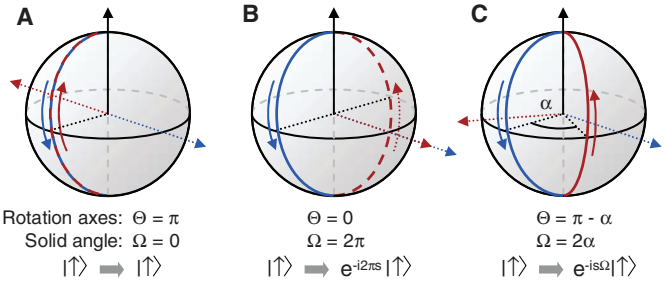

Fig. 1. Effect of rotation on a spin. The spin begins in the up state $|\uparrow\rangle = |s,+s\rangle$. After two π-rotations (blue and red) with angle Θ between the rotation axes (dotted arrows), the spin returns to $|\uparrow\rangle$ with a phase factor depending on Θ and s. In (**A**), the second rotation reverses the first, giving a phase factor 1, which leaves the spin state unchanged. In (**B**), both rotations are about the same axis. The spin traces out a great circle and acquires a phase factor $\exp(-i2\pi s)$. For integer spins (bosons), this has no effect, but for half-integer spins (fermions) this gives a factor of -1. In the general case (**C**), the acquired phase factor is $\exp(-is\Omega)$, where $\Omega = 2\alpha$ is the enclosed solid angle.

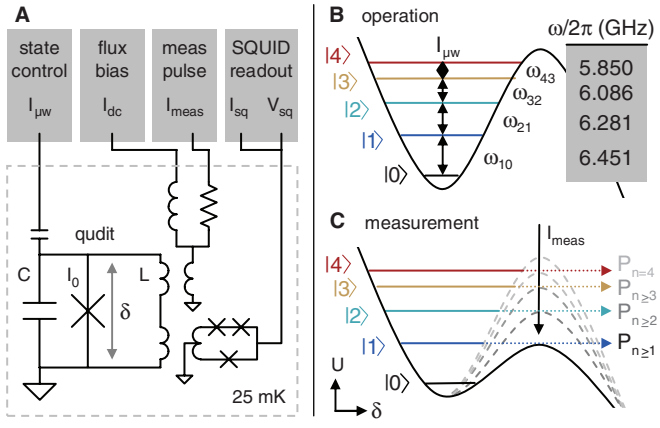

Fig. 2. Operation and measurement of a superconducting phase qudit. (**A**) Schematic of qudit circuit and control electronics. Current I_{dc} biases the junction, microwave drive $I_{\mu\mathrm{w}}$ manipulates the qudit state, and an on-chip SQUID detects tunneling events for readout. (**B**) The potential energy as a function of junction phase δ forms a well with several energy levels. The frequencies $\omega_{n,n-1} = (E_n - E_{n-1})/\hbar$ are distinct, allowing transitions to be driven independently. (**C**) For measurement, a brief current pulse $I^{(1)}_{\mathrm{meas}}$ is applied so as to lower the potential energy barrier, causing states $|n\rangle$, $|n+1\rangle$,... to tunnel out of the well. For each n, this is repeated ~10^3 times in order to obtain a probability.

we applied two emulated π-pulses with angle Θ between their rotation axes, rotating the spin component $|1\rangle \equiv |s,s\rangle$ about a closed path and giving the state $[|0\rangle + \exp(-is\Omega)|1\rangle]/\sqrt{2}$. Finally, we applied a second π/2-pulse in order to detect the phase of $|1\rangle$. Because the rotation axis ϕ of the latter π/2-pulse is varied, P_1 traces out a sinusoid—a Ramsey fringe—whose phase corresponds to the acquired spin phase.

The result of this experiment is shown in Fig. 4. For spin-0, no π-rotations are performed (the rotation generator is $X^{(0)} = 0$), so the Ramsey fringes are stationary. For s = 1/2, 1, and 3/2, the Ramsey fringes shift by −2π, −4π, and −6π, respectively, as Θ increases from 0 to 2π (Ω changes by 4π), which is in agreement with the predicted Berry phase factor $\exp(-is\Omega)$. The slices at Θ = π (Ω = 0) and Θ = 0 (Ω = 2π) clearly show the parity difference between integer spins s = 0, 1, and half-integer spins s = 1/2, 3/2, with in- and out-of-phase Ramsey fringes, respectively.

The Ramsey fringes show reduced contrast when higher qudit states are used in the sequence, which is largely due to the reduced lifetimes $T_n \approx T_1/n$ of the higher states. In addition, the use of higher states leads to imperfections in the microwave control because of the large bandwidth required and the effect of off-resonant terms dropped from Eq. 1. Ongoing work to reduce decoherence in superconducting quantum circuits (*28*) will improve the state lifetimes, and the off-resonant terms could be taken into account so as to improve the fidelity of qudit operation (*22*).

We have shown that the superconducting phase qubit can be extended to operate as a qudit up to d = 5 levels. The qudit state can be readily manipulated and measured with our existing control electronics, allowing us to perform nontrivial qudit protocols in order to emulate spins s = 1/2, 1, and 3/2. We reproduced the quantum

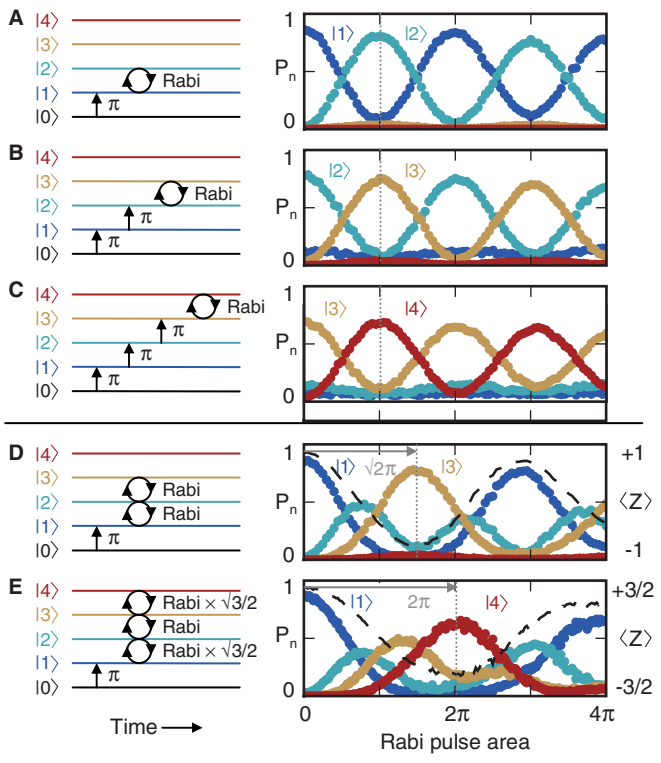

Fig. 3. Manipulation of the qudit state with microwaves. **(A)** (Left) The pulse sequence used to calibrate microwaves $|1\rangle \rightarrow |2\rangle$. A π-pulse excites the qubit to $|1\rangle$, then a second pulse drives Rabi oscillations between $|1\rangle$ and $|2\rangle$. (Right) Occupation probabilities P_n plotted versus the integrated area of the Rabi pulse, where π corresponds to a standard 16-ns pulse envelope with amplitude adjusted so as to create a π-rotation (swap) from $|1\rangle$ to $|2\rangle$. **(B** and **C)** Similar calibration for $|2\rangle \rightarrow |3\rangle$ and $|3\rangle \rightarrow |4\rangle$. **(D)** (Left) The pulse sequence for generating spin-1 rotations by simultaneously driving $|1\rangle \rightarrow |2\rangle$ and $|2\rangle \rightarrow |3\rangle$. (Right) A plot of P_n versus the integrated pulse area of the single drives. The spin-1 π-rotation (from $|1\rangle$ to $|3\rangle$) is $\sqrt{2}$ longer than a spin-1/2 rotation. The dashed line shows $\langle \hat{Z} \rangle$, which varies sinusoidally. **(E)** Generation of spin-3/2 rotations by driving three transitions, with the outer drives scaled by $\sqrt{3}/2$. The π-rotation is 2 times as long as a spin-1/2 rotation. The dashed line shows $\langle \hat{Z} \rangle$.

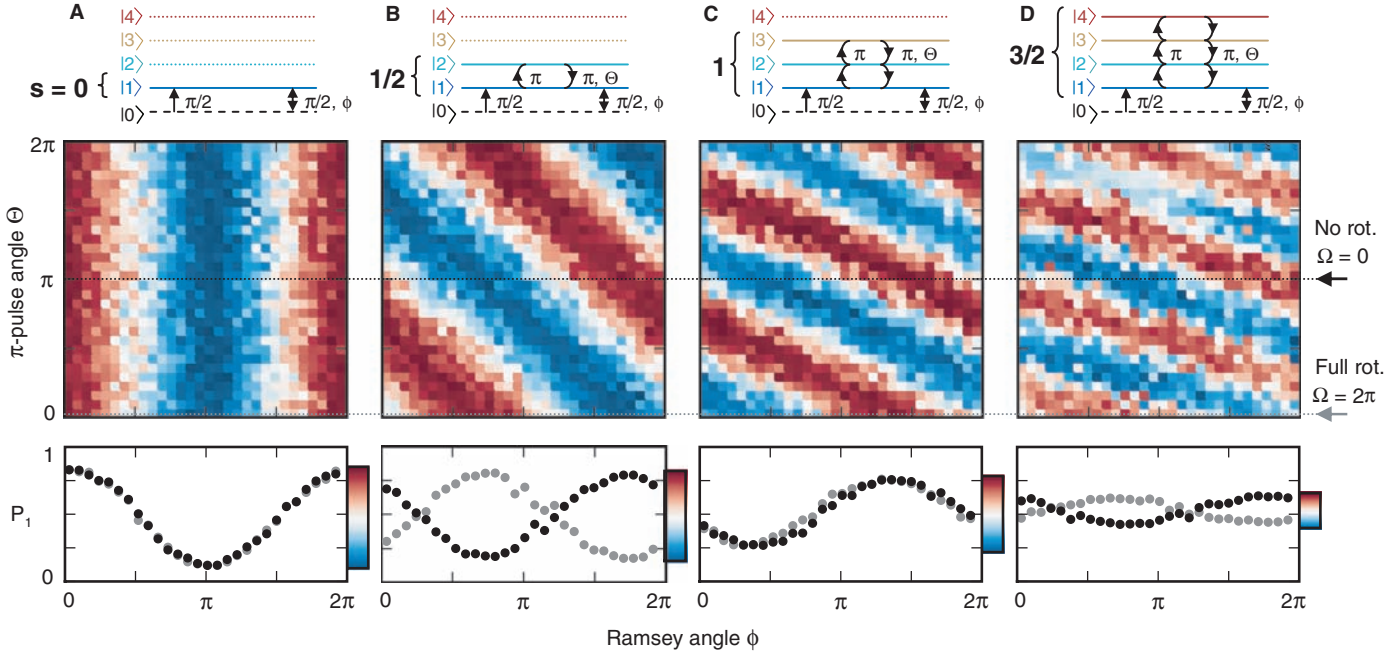

Fig. 4. Measurement of spin parity. The top panels show the microwave control sequence: The central π-pulses implement a closed-path spin rotation, whereas the outer π/2-pulses use Ramsey interference so as to detect the phase shift of $|1\rangle$. For spin-0, no π-rotations are applied. The middle panels show P_1 in color as a function of the angle Θ between the π-pulse rotation axes and the angle ϕ between the π/2-pulse rotation axes. The bottom panels show Ramsey fringe slices at Θ = π (Ω = 0 or no rotation; black) and Θ = 0 (Ω = 2π or one full rotation; gray), giving the relative phase shift due to a 2π-rotation. In-phase fringes (integer spins **A** and **C**) indicate a relative phase factor of 1, whereas out-of-phase fringes (half-integer spins **B** and **D**) indicate a relative phase factor of −1.

phase acquired by each spin under closed-path rotation, in particular the even parity of integer spins (and odd parity of half-integer spins) under 2π-rotation. This demonstration opens possibilities for using phase qudits in quantum information processing.

References and Notes

1. M. A. Nielsen, I. L. Chuang, *Quantum Computation and Quantum Information* (Cambridge Univ. Press, Cambridge, 2000).
2. A. Muthukrishnan, C. R. Stroud, *Phys. Rev. A* **62**, 052309 (2000).
3. B. Lanyon *et al.*, *Nat. Physics* **5**, 134 (2009).
4. I. Bregman, D. Aharonov, M. Ben-Or, H. S. Eisenberg, *Phys. Rev. A* **77**, 050301 (2008).
5. D. P. DiVincenzo, *Fortschr. Phys.* **48**, 771 (2000).
6. D. P. O'Leary, G. K. Brennen, S. S. Bullock, *Phys. Rev. A* **74**, 032334 (2006).
7. J. Clarke, F. K. Wilhelm, *Nature* **453**, 1031 (2008).
8. M. Steffen *et al.*, *Phys. Rev. Lett.* **97**, 050502 (2006).
9. M. Steffen *et al.*, *Science* **313**, 1423 (2006).
10. J. J. Sakurai, *Modern Quantum Mechanics* (Addison-Wesley, Reading, MA, 1994).
11. M. V. Berry, *Proc. R. Soc. Lond. A Math. Phys. Sci.* **392**, 45 (1984).
12. We worked in a rotating frame and chose the axis of rotation to be always perpendicular to the instantaneous spin direction $\langle \hat{\mathbf{S}} \rangle$, so that the dynamical phase is zero (*13*).
13. Materials and methods are available as supporting material on *Science* Online.
14. W. Pauli, *Phys. Rev.* **58**, 716 (1940).
15. I. Duck, E. C. G. Sudarshan, *Am. J. Phys.* **66**, 284 (1998).
16. H. Rauch *et al.*, *Phys. Lett.* **54A**, 425 (1975).
17. S. A. Werner, R. Colella, A. W. Overhauser, C. F. Eagen, *Phys. Rev. Lett.* **35**, 1053 (1975).
18. R. Kaiser, *Can. J. Phys.* **56**, 1321 (1978).
19. A. O. Niskanen *et al.*, *Science* **316**, 723 (2007).
20. A. Fragner *et al.*, *Science* **322**, 1357 (2008).
21. Because the global phase of a quantum system is undetectable, qudit states $|1\rangle$ and higher are used to emulate the spin, whereas the ground state $|0\rangle$ is reserved as phase reference. Hence, we emulated only up to spin-3/2, even though the 5-level qudit would map to an isolated spin-2.
22. M. Steffen, J. M. Martinis, I. L. Chuang, *Phys. Rev. B* **68**, 224518 (2003).
23. E. Lucero *et al.*, *Phys. Rev. Lett.* **100**, 247001 (2008).
24. M. Neeley *et al.*, *Phys. Rev. B* **77**, 180508 (2008).
25. G. K. Brennen, D. P. O'Leary, S. S. Bullock, *Phys. Rev. A* **71**, 052318 (2005).
26. H. Wang *et al.*, *Phys. Rev. Lett.* **101**, 240401 (2008).
27. M. Brune *et al.*, *Phys. Rev. Lett.* **101**, 240402 (2008).
28. J. M. Martinis *et al.*, *Phys. Rev. Lett.* **95**, 210503 (2005).

29. Devices were made at the UCSB Nanofabrication Facility, a part of the NSF-funded National Nanotechnology Infrastructure Network. This work was supported by the Intelligence Advanced Research Projects Activity (grant W911NF-04-1-0204) and NSF (grant CCF-0507227).

Supporting Online Material

www.sciencemag.org/cgi/content/full/325/5941/722/DC1
Materials and Methods
SOM Text
Figs. S1 and S2
References

12 March 2009; accepted 8 June 2009
10.1126/science.1173440

Folding DNA into Twisted and Curved Nanoscale Shapes

Hendrik Dietz,[1,2]* Shawn M. Douglas,[1,2,3] William M. Shih[1,2,3]†

We demonstrate the ability to engineer complex shapes that twist and curve at the nanoscale from DNA. Through programmable self-assembly, strands of DNA are directed to form a custom-shaped bundle of tightly cross-linked double helices, arrayed in parallel to their helical axes. Targeted insertions and deletions of base pairs cause the DNA bundles to develop twist of either handedness or to curve. The degree of curvature could be quantitatively controlled, and a radius of curvature as tight as 6 nanometers was achieved. We also combined multiple curved elements to build several different types of intricate nanostructures, such as a wireframe beach ball or square-toothed gears.

The sequences of DNA molecules can be engineered so that complex higher-order structures form as multiple double-helical segments connected through numerous turn regions. Programmable self-assembly based on DNA directed to branch in this way offers an attractive route to creating particular shapes on the 1- to 100-nm scale (*1*–*4*), as evidenced by its use in constructing two-dimensional (2D) crystals (*5*), nanotubes (*6*–*11*), and 3D wireframe polyhedra (*12*–*17*). More recently, oligonucleotide–"staple-strand"–assisted folding of a multiple-kilobase "scaffold strand" has been introduced as a powerful method to direct the self-assembly of custom-shaped, megadalton-scale, planar arrays of antiparallel helices connected through turn regions (*18*). In this "scaffolded–DNA-origami" method, each staple strand base pairs along part of its length with a complementary segment of the scaffold strand and then abruptly switches to base pair with another complementary scaffold segment that may be quite distant in the scaffold primary sequence. A single staple strand may pair with several scaffold-strand segments, in accordance with this switching strategy. Association with hundreds of such staple strands constrains the scaffold strand to helical paths that raster back and forth into a target antiparallel-array arrangement.

We recently extended DNA origami to 3D nanoconstruction with a design strategy that can be conceptualized as stacking corrugated sheets of antiparallel helices (*19*). The resulting structures resemble bundles of double helices constrained to a honeycomb lattice (an example is shown in Fig. 1A; also see figs. S7 to S24 for detailed examples of how staple strands can be programmed to link the scaffold strand into an antiparallel array of honeycomb-pleated helices). The number, arrangement, and individual lengths of helices can be tuned to produce a variety of 3D shapes; we have developed a graphical software tool to aid in the design process (*20*). In this experiment, we expand the design space of accessible DNA-origami shapes to include a rich diversity of nanostructures with designed twist and curvature.

In our honeycomb-array framework, every double helix has up to three nearest neighbors (Fig. 1A) and is designed to connect to each by antiparallel strand crossovers, which are covalent phosphate linkages in the same form as that found in naturally occurring Holliday junctions. For explanatory purposes, here we assume that only staple strands, and not the scaffold strand, can cross over to form a Holliday junction between adjacent double helices (*19*). Every 7 base pairs (bp), the helical path of a strand rotates by 240°, assuming a B-form–DNA twist density of 10.5 bp per turn. Therefore, 14 bp gives rise to a rotation of 120° plus 360°, and 21 bp gives rise to a rotation of 0° plus two times 360°. As a result, antiparallel strand crossovers to one of the three nearest neighbors at 0°, 120°, and 240° can be engineered to occur once every 7 bp. Thus, along the helical axis of the whole honeycomb array, crossovers only can occur at positions that coincide with conceptual planes perpendicular to that axis spaced at 7-bp intervals.

These crossover planes can be used as a reference to conceive the honeycomb-pleated helix bundle as a 3D array of cells that by default each contain a 7-bp-long double-helical DNA fragment (Fig. 1B) that is mechanically coupled to its nearest neighbors. This abstraction of the DNA bundle as a collection of array cells is key for understanding how site-directed insertions and deletions of base pairs in the bundle can control twist and curvature.

We systematically adjusted the number of base pairs in selected subsets of array cells to realize DNA shapes that globally twist or bend along their helix-parallel axes. Because any array-cell DNA fragment is physically constrained by its neighbors in the honeycomb array, deletion of a base pair results in a local overwinding and tensile strain for that fragment, which causes it to exert a left-handed torque and a pull on its neighbors (Fig. 1C, top). The overwind strain can be relieved by a compensatory global left-handed twist of the bundle along its

[1]Department of Cancer Biology, Dana-Farber Cancer Institute, Boston, MA 02115, USA. [2]Department of Biological Chemistry and Molecular Pharmacology, Harvard Medical School, Boston, MA 02115, USA. [3]Wyss Institute for Biologically Inspired Engineering, Harvard University, Cambridge, MA 02138, USA.

*Present address: Physik Department and CiPSM, Technische Universität München, D-85748 Garching bei München, Germany. †To whom correspondence should be addressed. E-mail: william_shih@dfci.harvard.edu

helix-parallel axis, whereas the tensile strain can be relieved by a compensatory global bend of the bundle toward that fragment along its helix-parallel axis. In the same way, insertion of a base pair into an array cell results in a local underwinding and compressive strain (Fig. 1C, bottom) that can be relieved by a compensatory global right-handed twist and bend away from the fragment along the helix-parallel axis.

Destructive cancellation of compensatory global bend deformations and constructive reinforcement of compensatory global twist deformations can be implemented, for example, by distribution of only deletions or only insertions in the bundle, as depicted in Fig. 1D. The bundle with only deletions is analogous to the architecture of protein coiled coils, where overwinding of right-handed α helices from 3.6 to 3.5 amino acids per turn, enforced by heptad-repeat phasing, is compensated by a global left-handed twist. Conversely, destructive cancellation of global twist deformations and constructive reinforcement of global bend deformations can be implemented, for example, by distribution of a gradient of deletions to insertions of base pairs through a bundle's cross section, as depicted in Fig. 1E. Steeper gradients of deletions to insertions can be implemented to achieve greater degrees of curvature.

To assess whether global twisting can be implemented, we chose as a model system a 10-row, 6-helix-per-row (10-by-6) bundle composed of 60 tightly interconnected DNA double helices (Fig. 2) that we previously had identified as a well-behaved folding architecture (*19*, *20*) and whose ribbonlike (as opposed to tubelike) structure makes observation of twisting more facile. We designed three versions of this bundle. In the default version that is designed not to twist, 19 crossover planes are spaced evenly in 7-bp steps across a length of 126 bp, or 12 complete turns at 10.5 bp per turn. We designed a second version of the 10-by-6 bundle in which we deleted a single base pair from every third array cell along each helix. Thus, one-third of all array cells contain overtwisted DNA fragments, resulting in a bundle with a length of 120 bp and an average twist density of 10 bp per turn. Additionally, we designed a third version of the 10-by-6 bundle in which we added a single base pair to every third array cell, resulting in a shape with a length of 132 bp and an average twist density of 11 bp per turn (see figs. S7 to S9 for design details).

The 10 by 6 bundles were folded by a two-step process. The first step involved initialization of the system by incubation at 80°C of the appropriate mixture of scaffold and staple strands in buffered solution. The second step involved gradual cooling of the strand suspension to room temperature. Next, the sample was subjected to agarose-gel electrophoresis. The fastest migrating band (excluding the free staple strands) typically represented the monomeric species. Thus, excision of this band from the gel, followed by recovery of the embedded particles by centrifugation through a cellulose-acetate filter, resulted in enrichment of well-folded particles. These gel-purified particles were then imaged by negative-stain transmission electron microscopy (TEM) (see note S1 for imaging methods and fig. S3 for additional zoom-out images). As previously reported, no systematic deformations were found in the default 10.5 bp per turn version of the bundle (Fig. 2A, bottom left) (*19*). However, particles designed with locally overtwisted DNA (Fig. 2B, bottom left) or locally undertwisted DNA (Fig. 2C, bottom left) appear to exhibit a global twist deformation when oriented so that they are viewed down the helical-axis interface or down the six-helix-wide side. The deformed appearance is not obvious for particles that are oriented with the 10-helix-wide side oriented parallel to the grid surface. Surprisingly, the 11 bp per turn designed twist density improved overall folding quality (Fig. 2F) of the 10-by-6 bundle. We speculate that the increased spacing between crossover planes may allow greater electrostatic-repulsion–driven bowing out of helices that, therefore, is easier to achieve. An alternative speculative explanation derives from the observation that, for helices surrounded by three neighbors in the honeycomb array, crossovers occur every 7 bp. An increased spacing of 8 bp may improve stability of these segments in a manner that affects the rate-limiting steps for folding. Systematic experiments in the future will be required for elucidating the determinants of folding speed and quality.

To verify the apparent twist, we separately polymerized each of the 10-by-6 bundle versions along the helical axes to form ribbons. When made up of bundles designed with only default 7-bp array cells, the resulting ribbons appeared to be completely straight with no detectable global twist (Fig. 2A, top right). In contrast, for both the versions with locally overtwisted and locally undertwisted DNA fragments, we consistently observed ribbons that clearly twist (see fig. S3 for additional zoom-out image data). To determine the chirality of these twisted ribbons, we collected tilt-pair images by rotating the TEM goniometer

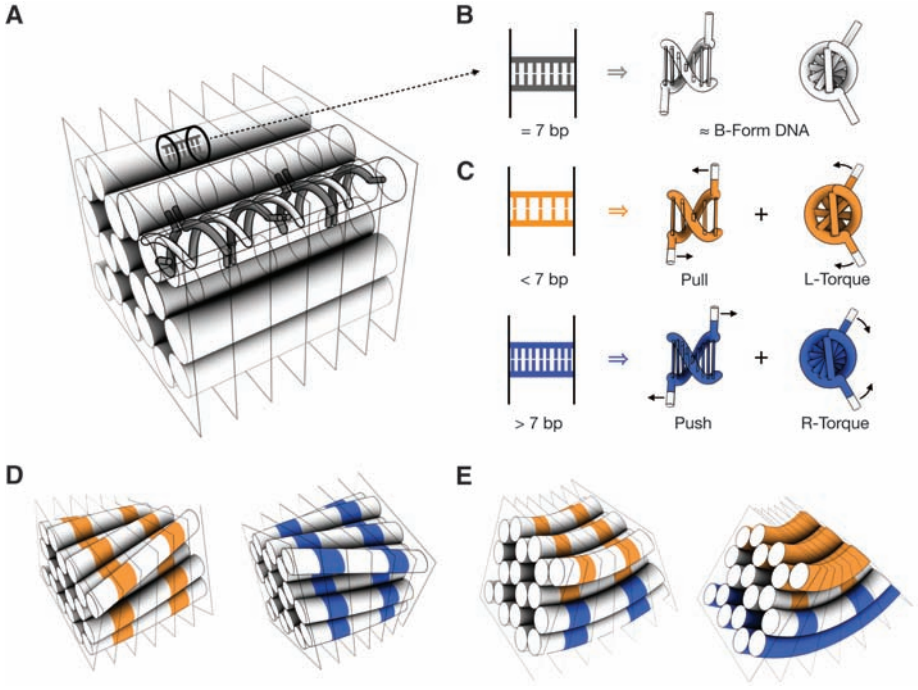

Fig. 1. Design principles for controlling twist and curvature in DNA bundles. (**A**) Double helices are constrained to a honeycomb arrangement by staple-strand crossovers. Semi-transparent crossover planes mark the locations of strand crossovers between neighboring helices, which are spaced at 7-bp intervals along the helical axis. From left to right, each plane contains a class of crossovers rotated in-plane by 240° clockwise with respect to the preceding plane. The crossover planes divide the bundle conceptually into helix fragments that can be viewed as residing in array cells (one cell is highlighted). (**B**) Array cell with default content of 7 bp, which exerts no stress on its neighbors. (**C**) Above, array cell with content of 5 bp, which is under strain and therefore exerts a left-handed torque and a pull on its neighbors. Below, array cell with content of 9 bp, which is under strain and therefore exerts a right-handed torque and a push on its neighbors. Force vectors are shown on only two of the four strand ends of the array-cell fragment for clarity. (**D**) (Left) Site-directed deletions installed in selected array cells indicated in orange result in global left-handed twisting with cancellation of compensatory global bend contributions; (right) site-directed insertions in selected array cells (shown in blue) result in global right-handed twisting. (**E**) Site-directed base-pair deletions (indicated in orange) and base-pair insertions (indicated in blue) can be combined to induce tunable global bending of the DNA bundle with cancellation of compensatory global twist contributions.

(Fig. 2, D and E). For ribbons polymerized from bundles with locally undertwisted DNA, we observed that the nodes consistently moved upward on an 80° counterclockwise sample-plane rotation. The experimental geometry (Fig. 2D, bottom) provides an unequivocal identification of the global twist as right-handed. Conversely, for ribbons constructed from bundles with locally overtwisted DNA, we observed that the ribbon nodes consistently moved downward on the same sample rotation, thus revealing a global left-handed twist.

We quantified the twist frequency by measuring the distance between consecutive nodes for multiple ribbons (Fig. 2G) and then plotting global twist per turn as observed for each version of the 10-by-6 bundles versus initially imposed double-helical twist density (Fig. 2H). Different architectures probably will exhibit global twisting that will vary in absolute magnitude but not in sign from the values observed for the 10-by 6-bundle because of differences in resistance to torsion as a function of cross-sectional shape. For example, a 60-helix bundle with a more extended cross section (e.g., 30 by 2 helices) would be expected to exhibit more global twist at the same initially imposed local double-helical twist density due to the lower torsional stiffness. We also experimentally observed global twist for a 3-by-6 bundle architecture, but because of the squarelike cross section, it was difficult to determine the location of the nodes and thereby quantify the magnitude of twisting.

These results imply that average double-helical twist density must be carefully considered during DNA-nanostructure design to avoid unwanted global twist deformations. Global twisting has been observed for DNA nanotubes assembled from oligonucleotide-based tiles with double-helical twist densities deviating from 10.5 bp per turn (*21*, *22*). Planar DNA origami (*18*) has been designed with an average twist density of 10.67 bp per turn. Intrinsic global twist of such designs as exists in solution, however, might not be obvious from image analysis of particles flattened by adhesion to surfaces.

We next explored the use of balanced gradients of insertions and deletions to produce global bend with no global twist by constructing seven versions of a three row, six-helix-per-row (3-by-6) bundle (Fig. 3A). The design contains 61 crossover planes evenly spaced along the helical axis. Between 15 crossover planes in the middle of the bundle, we implemented gradients of insertions and deletions across the short axis of the cross section (red segment in the models in Fig. 3, A to G; see figs. S10 to S18 for design details). We implemented increasingly steep gradients (Fig. 3H and figs. S10 to S18) up to extreme deviations from native B-form–DNA twist density, where one side of the 3-by-6 bundle has an average twist density of only 6 bp per turn, whereas the opposite side has a twist density as high as 15 bp per turn. We used a toy model that considers DNA as a continuum rod with elastic bending, stretch-compression, and twist-stretch coupling (see note S2 and fig. S1) and an iterative refinement procedure to identify gradients that produce bend angles from 30° to 180° in 30° steps with radii of curvature ranging from 64 to 6 nm.

Folding of five of the seven 3-by-6 bundle versions resulted in products that migrate as

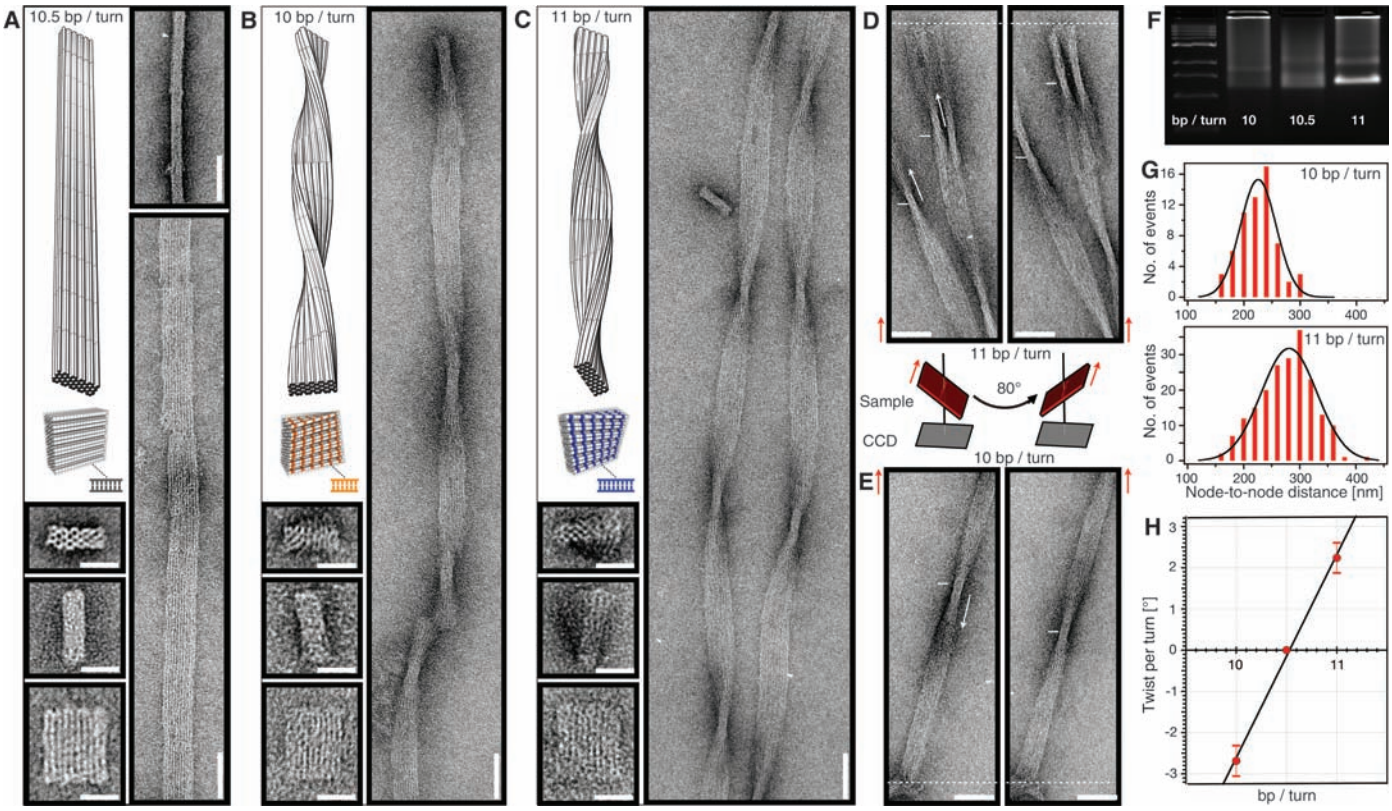

Fig. 2. Deviations from 10.5 bp per turn twist density induce global twisting. (**A** to **C**) (Top left) Models of a 10-by-6–helix DNA bundle (red) with 10.5, 10, and 11 bp per turn average double-helical twist density, respectively, and models of ribbons when polymerized (silver). (Bottom left) Monomeric particles as observed by negative-stain TEM. Scale bars, 20 nm. (Right) Polymeric ribbons as observed by TEM. Scale bars, 50 nm. (**D** and **E**) Tilt-pair images of twisted ribbons polymerized from 11 bp per turn (D) and 10 bp per turn (E); 10-by-6–helix bundles, recorded at goniometer angles of 40° and −40°. Arrows indicate the observed upward (for 11 bp per turn) or downward (for 10 bp/turn) direction of movement of the twisted-ribbon nodes. The dashed line provides a reference point (ends of ribbons remain stationary on goniometer rotation). CCD, charge-coupled device. (**F**) Ethidium-bromide–stained 2% agarose gel, comparing migration of unpurified folded bundles. (**G**) Histograms of the observed node-to-node distance in twisted ribbons, as observed in negative-stain TEM micrographs. Left- and right-handed ribbons undergo half-turns every 235 ± 32 nm (n = 62 internode distances measured) and 286 ± 48 nm (n = 197), respectively (numbers after the ± sign indicate SD). (**H**) Plot of observed global compensatory twist per turn versus double-helical twist density initially imposed by design. A value of 0.335 nm per bp was used to calculate global twist per turn from values obtained in (G). Error bars indicate SD.

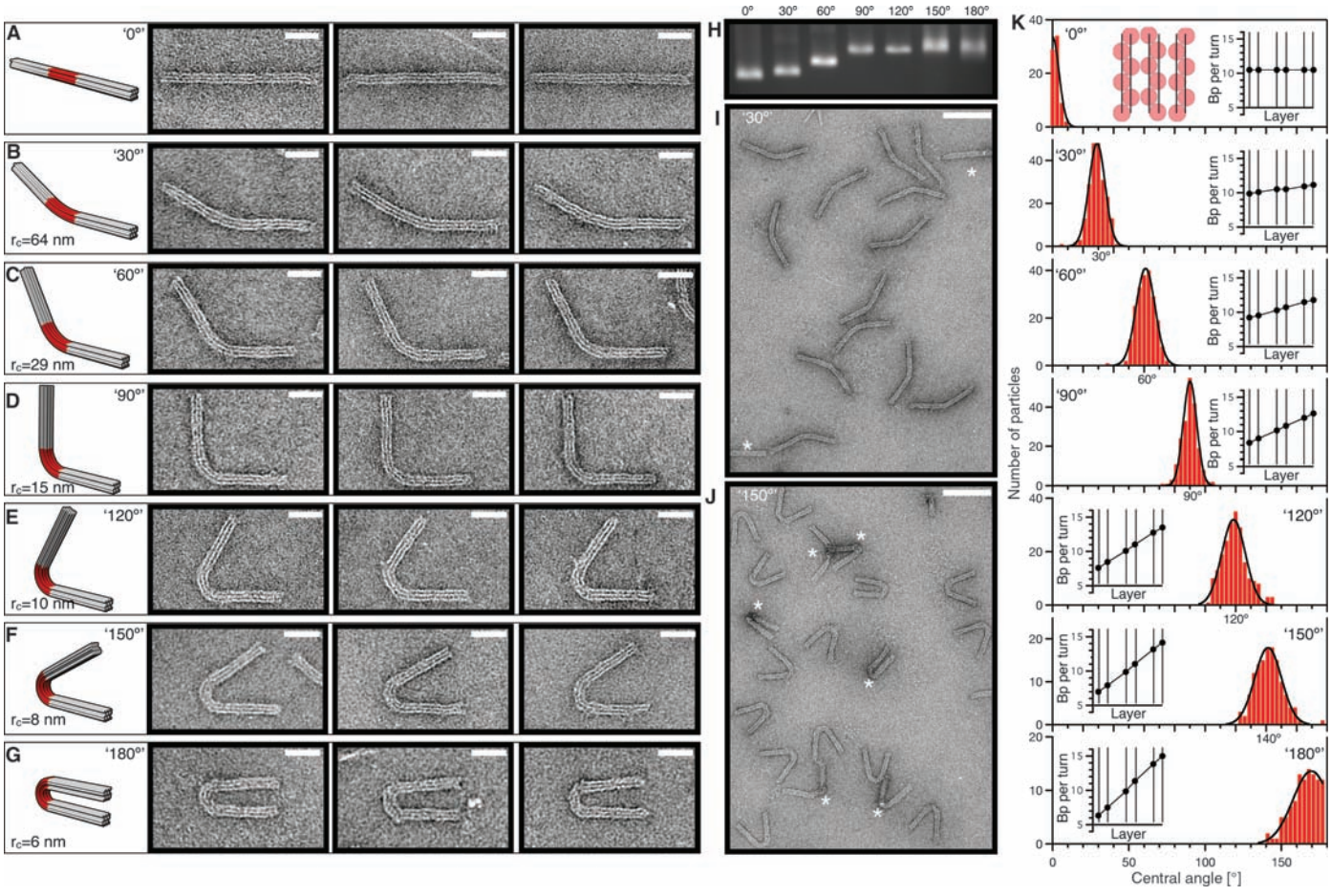

Fig. 3. Combining site-directed insertions and deletions induces globally bent shapes. (**A** to **G**) Models of seven 3-by-6–helix-bundle versions programmed to different degrees of bending and typical particles, as observed by negative-stain TEM. r_c, radius of curvature. Scale bars, 20 nm. (**H**) Ethidium-bromide–stained 2% agarose gel comparing migration of unpurified folding products of the seven differently bent bundles. (**I** and **J**) Low-magnification TEM micrographs of the bundle versions programmed to bend by 30° and 150°, respectively. Asterisks indicate defective particles, identified by the lack of three well-defined stripes at the bend. Scale bars, 100 nm. (**K**) Histograms of bend angles as observed in individual particles for the seven different bundle versions. Average bend angles were determined to be 0° ± 3° (n = 74), 30.7° ± 5.4° (n = 212), 62.4° ± 5.9° (n = 208), 91.3° ± 5.2° (n = 206), 121° ± 8.4° (n = 212), 143.4° ± 9° (n = 131), and 166° ± 9° (n = 106) (numbers after the ± sign indicate SD). (Insets) Plots of average double-helical twist density through the cross section of the bent segment that results from the pattern of insertions and deletions installed to induce bending.

sharp bands on a 2% agarose gel (Fig. 3H), indicating folding into an overall homogeneous shape, whereas the 150° and 180° versions migrate as more fuzzy bands, which suggests that a greater degree of shape heterogeneity is present. The latter two versions coincide with the two steepest insertion/deletion gradients. Such stark deviations from B-form DNA twist density apparently compromise folding quality and increase the frequency of defective particles. Moreover, the gel mobility decreases with increasing gradient of insertions and deletions, indicating pronounced changes in the aspect ratio of the particles.

We used negative-stain TEM to study the appearance of the particles (Fig. 3, A to G). The particles mainly adsorbed in two orientations on the TEM grids and exhibited a smooth appearance when oriented with the long axis of the bundle cross section parallel to the grid, but exhibited three pronounced stripes when oriented with the short axis parallel to the TEM grid (see note S4 and fig. S2 for a more detailed explanation of the origin of the stripes, as well as fig. S4 for image data with multiple particle orientations). The orientation giving rise to the "stripy" appearance allows for a direct assessment of the extent of the induced bending.

Bend angles ranging from 30° to 180°, as well as sharply bent radii of curvature down to 6 nm, close to the extreme bending of DNA found in the nucleosome (*23*), could be realized. Figure 3, I and J, gives a sense of the shape homogeneity exemplified by two bundle versions designed to bend at 30° and 150°, respectively. Additional zoom-out image data for each version of the 3-by-6 helix bundles is provided in fig. S4.

We quantified the distribution of bend angles for each version in the series of bundles. To avoid bias from obviously defective particles, we analyzed only those where three pronounced stripes were clearly discernible along the entire length. As an example, particles marked with an asterisk in Fig. 3, I and J, do not satisfy that criterion. We observed that the fraction of particles that failed this criterion was ~50% for radii of curvature above 10 nm but increased as a function of tightness of radii of curvature above 10 nm (fig. S4). Histograms of bend angles observed for the seven different 3-by-6 bundle versions are shown in Fig. 3K. The distributions each have a half-width at half maximum of 5° to 9°. Our toy model predicts thermally induced angular fluctuations with a SD from the mean bend angle of ~2.5° (see note S2 and fig. S1). The discrepancy between expected and observed distribution widths may be due to defects. Defective helices confer bending "individuality" to each particle, because defects change the effective gradient of insertions and deletions, as well as the compliance of a defective helix in the bundle. A future challenge will be to improve folding quality so that thermal fluctuations alone determine the angular precision of any produced shape. Our toy model can identify insertion and deletion patterns to an accuracy of 3° for desired mean bend angles less than or equal to 120°, although changes in environmental conditions may require adjustment of

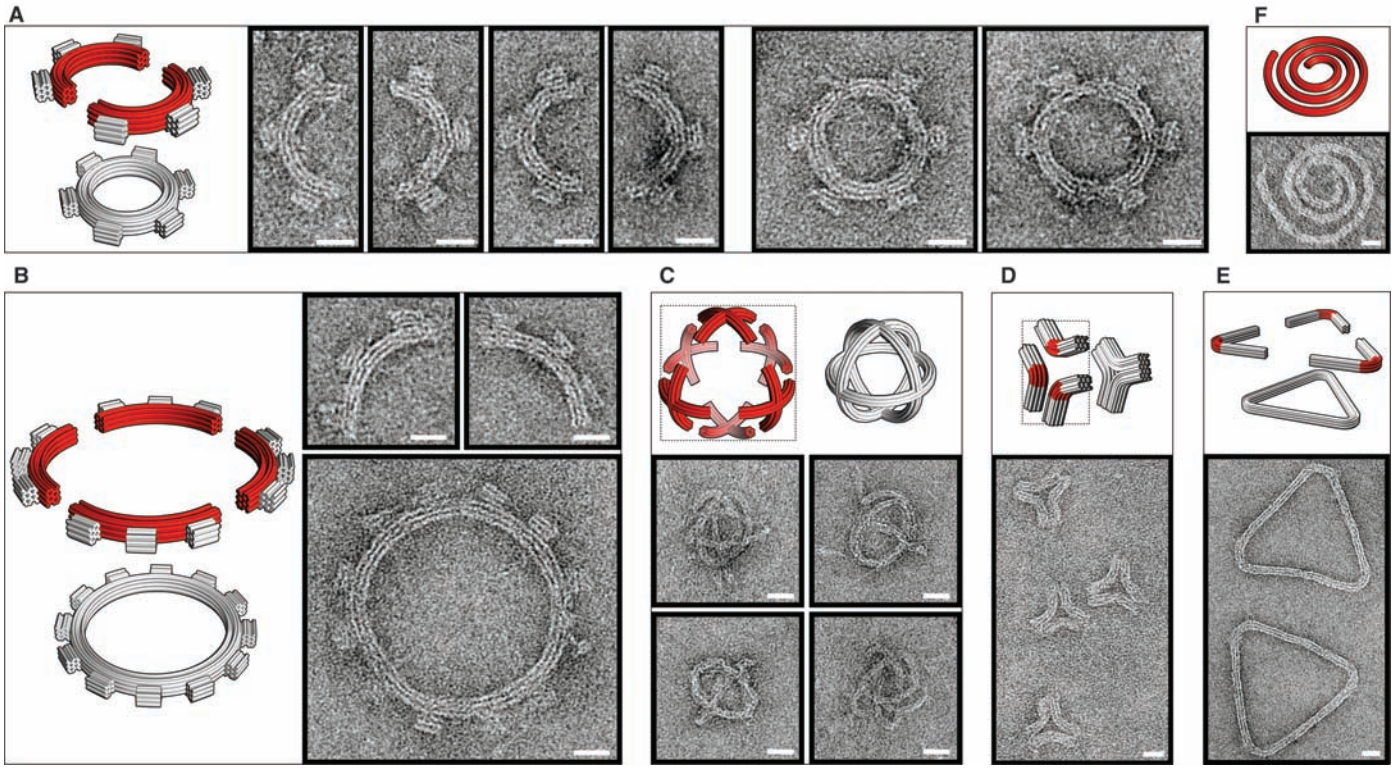

Fig. 4. Bending enables the design of intricate nonlinear shapes. Red segments indicate regions in which deletions and insertions are installed. Scale bars, 20 nm. (**A**) Model of a 3-by-6–helix DNA-origami bundle designed to bend into a half-circle with a 25-nm radius that bears three non-bent teeth. Monomers were folded in separate chambers, purified, and mixed with connector staple strands to form six-tooth gears. Typical monomer and dimer particles visualized by negative-stain TEM. (**B**) 3-by-6–helix bundle as in (A), modified to bend into a quarter circle with a 50-nm radius. Hierarchical assembly of monomers yields 12-tooth gears. (**C**) A single scaffold strand designed to fold into a 50-nm-wide spherical wireframe capsule resembling a beach ball and four typical particles representing different projections of the beach ball. The design folds as six bent crosses (inset) connected on a single scaffold. (**D**) A concave triangle that is folded from a single scaffold strand. The design can be conceptualized as three 3-by-6 bundles with internal segments designed to bend by 60°. (**E**) A convex triangle assembled hierarchically from three 3-by-6 bundles designed with a 120° bend (Fig. 3E). (**F**) A six-helix bundle programmed with varying degrees of bending folds into a spiral-like object.

model parameters. We expect our method for generating DNA shapes with tunable bending to be generally applicable for a wide range of bundle cross-sectional architectures, as long as extreme deviations from canonical B-form DNA twist density (less than 6 bp per turn or more than 15 bp per turn) are avoided.

To illustrate the diversity of curved shapes now accessible, we designed a DNA bundle bearing three "teeth" that is programmed to fold into a half circle with a 25-nm radius (Fig. 4A; also see fig. S19 for design details and fig. S5 for additional zoom-out image data). Using hierarchical assembly, two of these bundles can be combined into a circular object that resembles a nanoscale gear with six teeth. The teeth exhibited a greater frequency of folding defects than the body, at a rate of about one defective tooth out of three, perhaps related to their small size (only 42 bp long per double helix). About one-third of multimeric complexes were observed to be the target cyclic dimers, versus noncyclic dimers and higher-order multimers. By adjusting the gradient of insertions and deletions, the bundle can be tuned to fold into a quarter circle with a 50-nm radius (Fig. 4B; see also fig. S20 for design details). By connecting four of these quarter circles, a gear with 12 teeth can be manufactured. In this case, only about a tenth of the multimeric complexes were observed to be the target cyclic tetramers. In the future, target cyclization may be improved for objects designed with taller interfaces that resist out-of-plane bending and that are more tolerant of folding defects.

3D spherical shapes can be created as well (Fig. 4C). We designed a 50-nm-wide spherical wireframe object that resembles a beach ball by programming six interconnected vertices, each composed of two crossed six-helix bundles, to bend so that a projection of the edges of an octahedron onto a circumscribing sphere is completed (see fig. S21 for design details). We further designed a concave and a convex triangle (Fig. 4, D and E; see figs. S22 and S23 for design details) and a spiral consisting of six segments of a six-helix bundle that are each programmed to bend into a half circle with increasing radii of curvature (Fig. 4F; see fig. S24 for design details). The convex triangle is designed as a hierarchically assembling homotrimer. For this design, about one-third of multimeric complexes were observed to be the target cyclic trimers (additional image data on all objects shown in Fig. 4 is provided in fig. S6).

Precisely arranged bent DNA and associated DNA-binding proteins play an important role in transcriptional regulation and genomic packaging (*24*–*26*). Programmable DNA bending might prove useful as a probe to study the propensity of such proteins to bind pre-bent DNA substrates and also to probe the propensity of different DNA sequences to adopt specifically bent conformations (*27*).

References and Notes

1. N. C. Seeman, *Nature* **421**, 427 (2003).
2. N. C. Seeman, *J. Theor. Biol.* **99**, 237 (1982).
3. T. J. Fu, N. C. Seeman, *Biochemistry* **32**, 3211 (1993).
4. X. J. Li *et al.*, *J. Am. Chem. Soc.* **118**, 6131 (1996).
5. E. Winfree *et al.*, *Nature* **394**, 539 (1998).
6. H. Yan, S. H. Park, G. Finkelstein, J. H. Reif, T. H. LaBean, *Science* **301**, 1882 (2003).
7. P. W. Rothemund *et al.*, *J. Am. Chem. Soc.* **126**, 16344 (2004).
8. F. Mathieu *et al.*, *Nano Lett.* **5**, 661 (2005).
9. S. M. Douglas, J. J. Chou, W. M. Shih, *Proc. Natl. Acad. Sci. U.S.A.* **104**, 6644 (2007).
10. D. Liu *et al.*, *Proc. Natl. Acad. Sci. U.S.A.* **101**, 717 (2004).
11. P. Yin *et al.*, *Science* **321**, 824 (2008).
12. R. P. Goodman *et al.*, *Science* **310**, 1661 (2005).
13. J. H. Chen, N. C. Seeman, *Nature* **350**, 631 (1991).
14. Y. Zhang, N. C. Seeman, *J. Am. Chem. Soc.* **116**, 1661 (1994).
15. Y. He *et al.*, *Nature* **452**, 198 (2008).
16. C. Zhang *et al.*, *Proc. Natl. Acad. Sci. U.S.A.* **105**, 10665 (2008).

17. W. M. Shih, J. D. Quispe, G. F. Joyce, *Nature* **427**, 618 (2004).
18. P. W. Rothemund, *Nature* **440**, 297 (2006).
19. S. M. Douglas *et al.*, *Nature* **459**, 414 (2009).
20. S. M. Douglas *et al.*, *Nucleic Acids Res.*; published online 16 June 2009 (10.1093/nar/gkp436).
21. J. C. Mitchell *et al.*, *J. Am. Chem. Soc.* **126**, 16342 (2004).
22. C. Lin *et al.*, *Nano Lett.* **9**, 433 (2009).
23. K. Luger *et al.*, *Nature* **389**, 251 (1997).
24. J. A. Borowiec *et al.*, *J. Mol. Biol.* **196**, 101 (1987).
25. J. Chang *et al.*, *Structure* **14**, 1073 (2006).
26. H. G. Garcia *et al.*, *Biopolymers* **85**, 115 (2007).
27. S. C. J. Parker, L. Hansen, H. O. Abaan, T. D. Tullius, E. H. Margulies, *Science* **324**, 389 (2009); published online 12 March 2009 (10.1126/science.1169050).
28. H.D. thanks Andres E. Leschziner for training in electron microscopy and generous supply of image processing hardware and software. This work was supported by Claudia Adams Barr Program Investigator, Wyss Institute for Biologically Inspired Engineering, and NIH New Innovator (1DP2OD004641-01) grants to W.M.S. and a Feodor-Lynen Humboldt Fellowship to H.D. H.D., S.M.D., and W.M.S. designed the research for this paper. H.D. developed rules for twisting and bending; H.D. and S.M.D. designed all shapes; H.D. and S.M.D. collected data; H.D. analyzed data; S.M.D. provided caDNAno software support; and H.D., W.M.S., and S.M.D. wrote the manuscript.

Supporting Online Material

www.sciencemag.org/cgi/content/full/325/5941/725/DC1
Materials and Methods
SOM Text
Figs. S1 to S26
References

30 March 2009; accepted 25 June 2009
10.1126/science.1174251

Unexpected Epoxide Formation in the Gas-Phase Photooxidation of Isoprene

Fabien Paulot,[1]* John D. Crounse,[2] Henrik G. Kjaergaard,[3,4] Andreas Kürten,[1]† Jason M. St. Clair,[1] John H. Seinfeld,[1,2] Paul O. Wennberg[1,5]

Emissions of nonmethane hydrocarbon compounds to the atmosphere from the biosphere exceed those from anthropogenic activity. Isoprene, a five-carbon diene, contributes more than 40% of these emissions. Once emitted to the atmosphere, isoprene is rapidly oxidized by the hydroxyl radical OH. We report here that under pristine conditions isoprene is oxidized primarily to hydroxyhydroperoxides. Further oxidation of these hydroxyhydroperoxides by OH leads efficiently to the formation of dihydroxyepoxides and OH reformation. Global simulations show an enormous flux—nearly 100 teragrams of carbon per year—of these epoxides to the atmosphere. The discovery of these highly soluble epoxides provides a missing link tying the gas-phase degradation of isoprene to the observed formation of organic aerosols.

Isoprene is the largest source of nonmethane hydrocarbons to the atmosphere (~500 Tg C/year) (*1*). It is produced by deciduous plants (*2*) and plays a critical role in tropospheric chemistry over large regions of the globe (*3*). In many forested regions, isoprene oxidation by OH occurs far from combustion of biomass and fossil fuel, so nitric oxide (NO) concentrations are very low. Many of the details of the chemical oxidation mechanism under these conditions remain to be elucidated, hindering assessment of the consequences of changes in isoprene emissions from land use and climate variation (*1*, *4*–*6*) or changes in NO emissions. In addition to the uncertainty in the gas-phase chemistry, there is no agreement on the mechanism involved in the formation of secondary organic aerosol (SOA) from isoprene oxidation (*7*).

Where NO is low, isoprene photooxidation is expected to yield the hydroxyhydroperoxides, ISOPOOH = β-ISOPOOH + δ-ISOPOOH (Reaction Series 1, A and B) (*8*, *9*). These series of reactions are expected to strongly depress the concentrations of OH and HO_2 (together known as HO_x) in regions with high isoprene emissions. Observed HO_x levels remain, however, almost unchanged over a wide range of isoprene concentrations, inconsistent with the simulated influence of Reaction Series 1, A and B (*10*–*12*). Simulations and measurements of HO_x have been partly reconciled with substitution of the speculative Reaction Series 1C, where formation of methacrolein (MACR) and formaldehyde is accompanied by OH formation, thus reducing the impact of isoprene on HO_x levels (*11*).

Analogous to Reaction Series 1, A to C, addition of OH on the other double bond yields similar hydroxyhydroperoxides (β1- and δ1-ISOPOOH) and methylvinylketone (MVK)

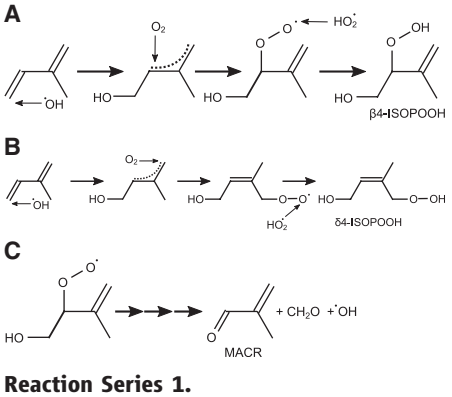

Reaction Series 1.

(*13*). Both unimolecular decomposition of the peroxy radical (*14*) and reaction with HO_2 (*15*) have been proposed in Reaction Series 1C. Although OH reformation (15 to 65%) has been measured for the reactions of HO_2 with acylperoxy and β-carbonyl peroxy radicals, low OH yields (<6%) have been reported from the reactions of HO_2 with β-hydroxy peroxy radicals, structurally more similar to isoprene peroxy radicals (*15*).

We show here that ISOPOOH is formed in large yields (>70%) via the channels shown in Reaction Series 1, A and B, with concomitant formation of MVK and MACR in much smaller yields (<30%) via the channel shown in Reaction Series 1C. The branching through Reaction Series 1C yields OH, although substantially less than required to close the HO_x budget (*11*).

We show below that the oxidation of ISOPOOH by OH produces dihydroxyepoxides (IEPOX = β-IEPOX + δ-IEPOX). This HO_x neutral mechanism produces IEPOX with yields exceeding 75% (Reaction Series 2, A and B). This mechanism is likely specific to isoprene and other polyalkenes. Analogous to liquid phase processes (*16*), it profoundly differs from gas-phase oxidation of simple alkenes by OH (e.g., Reaction Series 1, A and B), which would result in the formation of the dihydroxydihydroperoxides. Formation of these compounds is not observed in these experiments.

The gas-phase formation of IEPOX in high yields provides a suitable gas-phase precursor for Secondary Organic Aerosol from isoprene oxidation (*i*SOA) under low-NO_x conditions (*17*–*19*) and may help resolve an outstanding puzzle in atmospheric aerosol chemistry. Although epoxides have previously been speculated as a possible precursor for *i*SOA (*17*), no mechanism was known to produce them in either the gas or aerosol phase. Consistent with expectation that IEPOX can serve as a precursor to *i*SOA, we

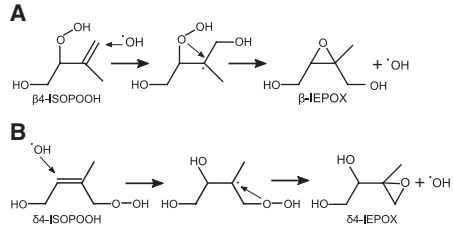

Reaction Series 2.

[1]Division of Engineering and Applied Science, California Institute of Technology, Pasadena, CA 91125, USA. [2]Division of Chemistry and Chemical Engineering, California Institute of Technology, Pasadena, CA 91125, USA. [3]Department of Chemistry, University of Otago, Dunedin, New Zealand. [4]Department of Chemistry, University of Copenhagen, Copenhagen, Denmark. [5]Division of Geological and Planetary Sciences, California Institute of Technology, Pasadena, CA 91125, USA.

*To whom correspondence should be addressed. E-mail: paulot@caltech.edu

†Present address: Institute for Atmospheric and Environmental Sciences, Goethe University, Frankfurt am Main, Germany.

observe rapid and quantitative uptake of 1,4-dihydroxy-2,3-epoxybutane (BEPOX)—a compound structurally similar to IEPOX—on acidic aerosol.

We monitor isoprene photooxidation products in the Caltech environmental chamber by chemical ionization mass spectrometry (CIMS) (*20*), employing a triple-quadrupole mass filter that provides tandem mass spectra (MSMS) (*13*). The reagent anion, CF_3O^-, provides sensitive detection of organic hydroperoxides by formation of ion-molecule clusters (*20*). Detection of BEPOX by CIMS confirms its sensitivity to dihydroxy-epoxides (*13*). In the absence of native standards for many of the compounds described here, the calibration of the instrument was inferred from molecular properties of the analyte (*13*, *21*).

Isoprene is oxidized by OH generated through the photolysis of hydrogen peroxide (H_2O_2) in a Teflon bag filled with 800 standard liters of ultra-zero air. Known amounts of isoprene and H_2O_2 are introduced into the chamber before ultraviolet (UV) lights are energized. Isoprene is quantified using gas chromatography with flame ionization detection (GC-FID) (*13*).

The products formed through Reaction Series 1, A and B, and Reaction Series 2, A and B—ISOPOOH and IEPOX—are isobaric and measured together by CIMS as the cluster of CF_3O^- with these compounds at the mass to charge ratio (*m/z*) 203 (Fig. 1, red curve). However, distinct daughter ions produced through collision-induced dissociation (CID) of these cluster ions allow for quantification of each compound (*22*). Clusters of CF_3O^- with hydroxyhydroperoxides, produced from the oxidation of simple alkenes, fragment to *m/z* = 63, whereas those with BEPOX exhibit loss of hydrofluoric acid (HF). The daughter *m/z* = 63 of 203 (Fig. 1, green curve), associated with the fragmentation of the ISOPOOH cluster clearly precedes the daughter *m/z* = 183 of 203 (Fig. 1, blue curve), associated with IEPOX, consistent with the proposed mechanism. Clusters of CF_3O^- with other plausible isomers of IEPOX are not known to exhibit efficient loss of HF (*13*). The sum of the *m/z* = 63 and *m/z* = 183 daughters (Fig. 1, black dashed line) properly captures the shape of the parent signal (Fig. 1, red curve).

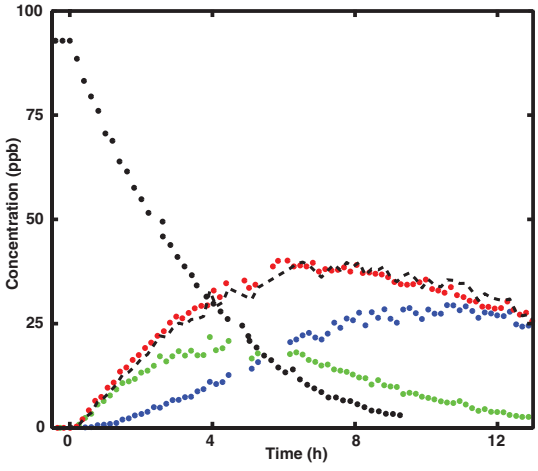

Fig. 1. Consecutive formation of ISOPOOH and IEPOX in the photooxidation of isoprene. Following the time when the photolysis of H_2O_2 [initially 1.66 parts per million by volume (ppmv)] begins (*t* = 0), isoprene (black dotted line) decays quickly. ISOPOOH and then IEPOX are detected as major products of the oxidation of isoprene [because they are isobaric, they both are detected at *m/z* = 203 (red), the cluster of these compounds with CF_3O^-]. Tandem mass spectroscopy provides for separation of the *m/z* = 203 signal: ISOPOOH (green) is observed as the *m/z* = 63 daughter, whereas IEPOX (blue) is observed as the *m/z* = 183 daughter. The sum of IEPOX and ISOPOOH is indicated by the dashed black line.

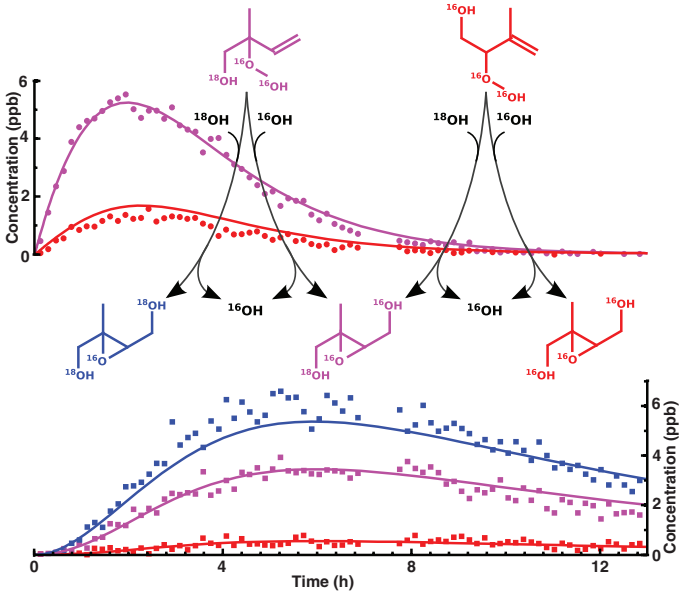

Fig. 2. Formation of light and heavy ISOPOOH and IEPOX in the oxidation of isoprene using $H^{18}O^{18}OH$ as the OH source. Formation of ISOPOOH is monitored via the daughter *m/z* = 63 (circles) of *m/z* = 203 (red) and *m/z* = 205 (magenta). Formation of IEPOX is monitored via the loss of HF (squares) from *m/z* = 203, *m/z* = 205, and *m/z* = 207 (blue). Formation of isotopically light ISOPOOH and IEPOX reflects OH reformation. Solid lines represent the modeled mixing ratios for the different isomers. Isoprene initial concentration was 23.5 parts per billion by volume (ppbv), and ^{18}OH was generated from the photolysis of $H^{18}O^{18}OH$ (1.75 ppmv initial concentration, UV lights on at *t* = 0).

Quantum chemical calculations confirm that, after the addition of OH, ISOPOOH is connected to IEPOX by energetically favorable adiabatic pathways (Fig. 3 and tables S4 and S5). β- and δ-IEPOX lie ~50 kcal/mol below their ISOPOOH parent with the transition state connecting the alkyl radical and IEPOX ~20 kcal/mol below the ISOPOOH reactant. The relative energies and structures of the stationary points along the surface are shown in Fig. 3 for the β4-ISOPOOH to β-IEPOX reaction (Reaction Series 2A). The reaction paths and energetics for the analogous β1-ISOPOOH to β-IEPOX reaction and for the δ4-ISOPOOH to δ4-IEPOX reaction (Reaction Series 2B) are similar (figs. S3 and S4 and tables S6 and S7).

The formation of isotopically light ISOPOOH (*m/z* = 203) (Fig. 2, red circles) and IEPOX (*m/z* = 203 and 205) (Fig. 2, red and magenta squares) in the ^{18}OH-labeled experiment provides additional evidence for Reaction Series 2, A and B, because ^{16}OH is released through formation of IEPOX (Reaction Series 2, A and B). The ^{16}OH quickly reacts with isoprene and ISOPOOH, forming the observed isotopically light compounds. The formation of light ISOPOOH (*m/z* = 203) in the first hour of the experiment cannot, however, be accounted for by Reaction Series 2, A and B, alone, suggesting a small but rapid ^{16}OH formation from Reaction Series 1C. This is consistent with the coincident production of MVK and MACR, measured together by proton transfer mass spectrometry at *m/z* = 89. Very little methyl-butenediol (<2%) is observed, which suggests that cross-peroxy radical reactions (*23*) are unlikely to account for the formation of MVK and MACR. A prompt signal at *m/z* = 201 appears consistent with the recently hypothesized

formation of (2Z)-hydroperoxymethylbutenol by a 1,6 H shift. However, its yield (<10% of ISOPOOH) is much less than predicted theoretically (*14*).

Using a kinetic model constrained by the observed yields of MVK/MACR and the ratios between light and heavy isotopes of ISOPOOH, we estimate that 12 ± 12% of the isoprene peroxy radicals react with HO_2 to recycle OH by Reaction 1C. This estimate accounts for a small initial amount of NO_x present initially in the chamber (*13*). The balance of the isoprene peroxy radicals reacts with HO_2 to form ISOPOOH.

The lifetime of ISOPOOH with respect to OH (3 to 5 hours) is considerably shorter than IEPOX (18 to 22 hours) (calculated for [OH] = 10^6 radicals cm^{-3}). The formation of unlabeled hydroxyacetone as well as singly labeled hydroxyacetone and glycolaldehyde in the photooxidation of isoprene by ^{18}OH suggests that the degradation of IEPOX by OH occurs primarily through hydrogen abstraction α to the alcohol (*13*).

In addition to the gas-phase oxidation, dihydroxyepoxides are lost to aerosol surfaces through reactive uptake. We monitor by CID-CIMS rapid and nearly quantitative uptake of BEPOX onto acidic aerosol seeds ($MgSO_4/H_2SO_4$). The resulting SOA composition can be readily related to the one identified for *i*SOA in pristine environments. In particular, analogs of dihydroxyenols, 2-methyltetrols, alkene-triols, and associated sulfate esters are detected (*13*), which suggests that IEPOX may explain their formation in both field (*7*, *24*) and chamber studies (*17*, *18*). Epoxides are also known to polymerize easily, an essential process for SOA growth (*25*).

The atmospheric yield of IEPOX is directly related to the relative importance of the reactions of isoprene peroxy radicals with HO_2 and NO. Using the chemical transport model GEOS-CHEM (*26*) with an updated chemical mechanism (table S9) (*21*), we find that globally about one-third of isoprene peroxy radicals undergo reaction with HO_2, with the remaining fraction reacting with NO. Over the Amazon, this ratio is almost inverted (fig. S7). Including uncertainties in isoprene emissions, we estimate that 95 ± 45 Tg C/year of IEPOX, a previously unknown class of compounds, are formed each year in the atmosphere. The largest concentrations of IEPOX are localized over the southern tropics, with substantial levels predicted over Canada and the Southeast United States during Northern Hemisphere summer (Fig. 4).

The presence of high concentrations of ISOPOOH and IEPOX in the atmosphere are consistent with recent aircraft-borne observations of isoprene oxidation products (m/z = 203) over southeast Columbia [NASA Tropical Composition, Cloud, and Climate Coupling (TC4) campaign] and (m/z = 203 and its daughters) over Alberta and California [NASA Artic Research of the Composition of the Troposphere from Aircraft and Satellites (ARCTAS) campaign]. Preliminary study of the data collected in the boundary layer is consistent with the concentrations of these compounds calculated with GEOS-CHEM (fig. S8).

The variability in the yield and fate of IEPOX is expected to translate into highly variable *i*SOA yields. In particular, anthropogenic activities depress for IEPOX formation as IEPOX yield drops rapidly with increasing NO. Anthropogenic emissions, however, may enhance the *i*SOA yield from IEPOX because its uptake on surfaces is likely dependent on the aerosol pH and sulfur content (*19*, *27*). This may explain part of the variability of the reported SOA biogenic yields, ranging from negligible (*28*) to potentially dramatic (*29*). Given the enormous flux of IEPOX, the chemistry presented here may also resolve part of the intriguing discrepancy between bottom-up

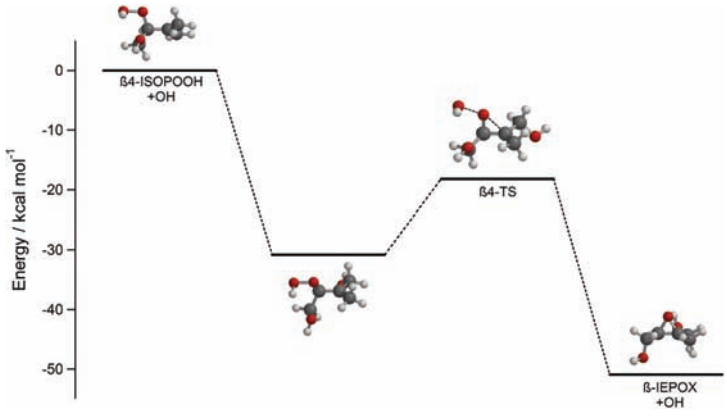

Fig. 3. Relative energies for the formation of β-IEPOX from β4-ISOPOOH (Reaction Series 2A). The alkylradical resulting from the addition of OH onto β4-ISOPOOH double bond is formed with enough excess energy (~30 kcal/mol) that it quickly decomposes to the β-IEPOX + OH via the β4-transition state. Energies are calculated with the CCSD(T)-F12/VDZ-F12 explicitly correlated method at the B3LYP/cc-pVTZ optimized structures (*13*).

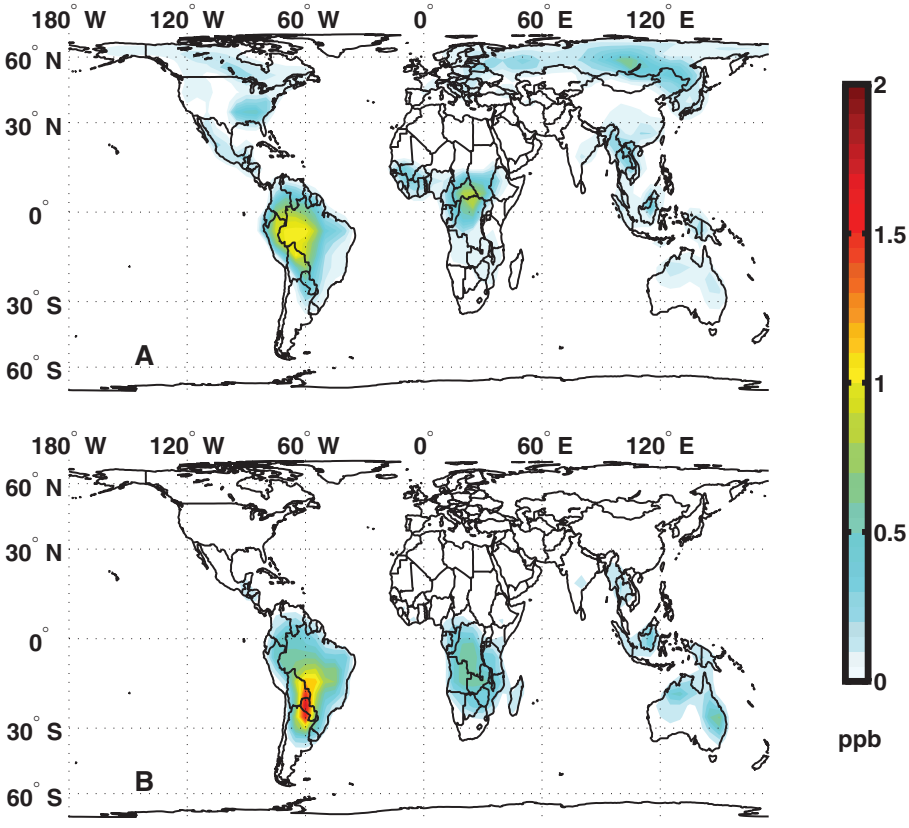

Fig. 4. Simulated daily distribution of IEPOX in the planetary boundary layer during the Northern Hemisphere summer (**A**) and winter (**B**). IEPOX seasonal cycle mirrors the isoprene emissions. The mixing ratio of IEPOX is higher in the tropics than in other isoprene production regions in the northern mid-latitudes (e.g., the southeast United States). This reflects the reduction in the yield of IEPOX from isoprene due to anthropogenic emissions of NO.

(10 to 70 Tg/year) and top-down (140 to 910 Tg/year) estimates of global SOA production (*30*). Nevertheless, IEPOX is expected to undergo hundreds of collisions with aerosol surfaces before reacting with OH, and its detection in the atmosphere (fig. S8) suggests that a complex suite of conditions likely controls its uptake to aerosols (e.g., the pH and chemical composition of aerosol). Furthermore, *i*SOA formation may depend on the unquantified differences in the yields and uptake characteristics of the β- and δ-IEPOX. Quantitative understanding of these complex interactions is required to assess the effect of this chemistry on the overall SOA abundance and its associated impacts [e.g., cloud condensation nuclei (*31*)].

The efficient formation of dihydroxyepoxides, a previously unknown class of gas-phase compounds, addresses many of the issues currently being debated about isoprene chemistry. Because their formation is accompanied by the reformation of OH, this chemistry contributes to the remarkable stability of HO_x in remote regions of the troposphere subjected to high isoprene emissions. The formation of IEPOX also provides a gas-phase precursor for the *i*SOA formation. Further investigation of the multiphase chemistry of IEPOX is needed to elucidate the complex interaction between emissions from the biosphere and atmospheric composition (*32*, *33*). In particular, the development of a proper chemical description of these interactions is essential for assessing the sensitivity of this chemistry to changes in isoprene emissions caused by environmental changes (e.g., climate change and deforestation) and to the further development of anthropogenic activities and the accompanying NO_x emissions in these regions.

References and Notes

1. A. Guenther *et al.*, *Atmos. Chem. Phys.* **6**, 3181 (2006).
2. P. C. Harley, R. K. Monson, M. T. Lerdau, *Oecologia* **118**, 109 (1999).
3. J. D. Fuentes *et al.*, *Bull. Am. Meteorol. Soc.* **81**, 1537 (2000).
4. T. N. Rosenstiel, M. J. Potosnak, K. L. Griffin, R. Fall, R. K. Monson, *Nature* **421**, 256 (2003).
5. C. Wiedinmyer, X. Tie, A. Guenther, R. Neilson, C. Granier, *Earth Interact.* **10**, 1 (2006).
6. R. von Kuhlmann, M. G. Lawrence, U. Pöschl, P. J. Crutzen, *Atmos. Chem. Phys.* **4**, 1 (2004).
7. M. Claeys *et al.*, *Science* **303**, 1173 (2004).
8. P. Crutzen *et al.*, *Atmos. Environ.* **34**, 1161 (2000).
9. C. E. Reeves, S. A. Penkett, *Chem. Rev.* **103**, 5199 (2003).
10. J. A. Thornton *et al.*, *J. Geophys. Res.* **107**, 17 (2002).
11. J. Lelieveld *et al.*, *Nature* **452**, 737 (2008).
12. X. Ren *et al.*, *J. Geophys. Res.* **113**, 5310 (2008).
13. Materials and methods are available as supporting material on *Science* Online.
14. J. Peeters, T. L. Nguyen, L. Vereecken, *Phys. Chem. Chem. Phys.*, **11**, 5935 (2009).
15. T. J. Dillon, J. N. Crowley, *Atmos. Chem. Phys.* **8**, 4877 (2008).
16. E. R. Bell, F. F. Rust, W. E. Vaughan, *J. Am. Chem. Soc.* **72**, 337 (1950).
17. W. Wang *et al.*, *Rapid Commun. Mass Spectrom.* **19**, 1343 (2005).
18. J. D. Surratt *et al.*, *J. Phys. Chem. A* **110**, 9665 (2006).
19. E. C. Minerath, M. J. Elrod, *Environ. Sci. Technol.* **43**, 1386 (2009).
20. J. D. Crounse, K. A. McKinney, A. J. Kwan, P. O. Wennberg, *Anal. Chem.* **78**, 6726 (2006).
21. F. Paulot *et al.*, *Atmos. Chem. Phys.* **9**, 1479 (2009).
22. F. W. McLafferty, *Science* **214**, 280 (1981).
23. L. Ruppert, K. H. Becker, *Atmos. Environ.* **34**, 1529 (2000).
24. J. D. Surratt *et al.*, *J. Phys. Chem. A* **112**, 8345 (2008).
25. S. Gao *et al.*, *Environ. Sci. Technol.* **38**, 6582 (2004).
26. I. Bey *et al.*, *J. Geophys. Res.* **106**, 73 (2001).
27. J. D. Surratt *et al.*, *Environ. Sci. Technol.* **41**, 5363 (2007).
28. J. A. de Gouw *et al.*, *J. Geophys. Res.* **110**, D16305 (2005).
29. P. Tunved *et al.*, *Science* **312**, 261 (2006).
30. A. H. Goldstein, I. E. Galbally, *Environ. Sci. Technol.* **41**, 1515 (2007).
31. V.-M. Kerminen, H. Lihavainen, M. Komppula, Y. Viisanen, M. Kulmala, *Geophys. Res. Lett.* **32**, L14803 (2005).
32. F. W. Went, *Nature* **187**, 641 (1960).
33. M. O. Andreae, P. J. Crutzen, *Science* **276**, 1052 (1997).

34. We thank X. Levine, H. O. T. Pye, and the Harvard GEOS CHEM team (Daniel J. Jacob, principal investigator) for their help in setting up the GEOS-CHEM model; A. J. Kwan, A. W. Chan, P. S. Chhabra, and N. Eddingsaas for experimental assistance; J. D. Surratt for providing the speciation of the SOA resulting from BEPOX reactive uptake; and J. Lane, I. Maxwell-Cameron, and S. Jørgensen for helpful discussions regarding the quantum calculations. F.P. was partially supported by the William and Sonya Davidow fellowship. J.D.C. thanks the EPA Science to Achieve Results (STAR) Fellowship Program (FP916334012) for providing partial support. The mass spectrometer used in this study was purchased as part of a major research instrumentation grant from the National Science Foundation (ATM-0619783). Assembly and testing of the CIMS instrument was supported by the Davidow Discovery Fund. The numerical simulations for this research were performed on Caltech's Division of Geological and Planetary Sciences Dell Cluster. This work was supported by the Office of Science (Biological and Environmental Research), U.S. Department of Energy grant DE-FG02-05ER63983, U.S. Environmental Protection Agency STAR agreement RD-833749, and the Marsden Fund administrated by the Royal Society of New Zealand. The TC4 and ARCTAS campaigns were supported by NASA grants NNX07AL33G and NNX08AD29G. This work has not been formally reviewed by the EPA. The views expressed in this document are solely those of the authors, and the EPA does not endorse any products or commercial services mentioned in this publication.

Supporting Online Material

www.sciencemag.org/cgi/content/full/325/5941/730/DC1
Materials and Methods
Figs. S1 to S9
Tables S1 to S9
References

2 March 2009; accepted 24 June 2009
10.1126/science.1172910

Phylogenetic Conservatism of Extinctions in Marine Bivalves

Kaustuv Roy,[1]* Gene Hunt,[2] David Jablonski[3]

Evolutionary histories of species and lineages can influence their vulnerabilities to extinction, but the importance of this effect remains poorly explored for extinctions in the geologic past. When analyzed using a standardized taxonomy within a phylogenetic framework, extinction rates of marine bivalves estimated from the fossil record for the last ~200 million years show conservatism at multiple levels of evolutionary divergence, both within individual families and among related families. The strength of such phylogenetic clustering varies over time and is influenced by earlier extinction history, especially by the demise of volatile taxa in the end-Cretaceous mass extinction. Analyses of the evolutionary roles of ancient extinctions and predictive models of vulnerability of taxa to future natural and anthropogenic stressors should take phylogenetic relationships and extinction history into account.

Groups of organisms differ in their vulnerability to extinction (*1*–*5*), but the nature and magnitude of that variation is still poorly quantified. Extinction risk of species and lineages is determined by a variety of ecological and life history traits (*2*), as well as emergent properties such as geographic range (*5*–*8*). Many of these extinction-related traits are phylogenetically conserved, suggesting that extinctions should be phylogenetically clustered: Taxa in some clades should be consistently more extinction-prone than others (*3*, *9*, *10*). Consistent with this idea, current extinction risk and documented anthropogenic extinctions are nonrandomly distributed among vertebrate lineages (*9*, *11*–*15*), but whether such phylogenetic selectivity holds in general, including for extinctions in the geologic past, remains poorly known. In this study, we used the Mesozoic-Cenozoic fossil record of marine bivalves, in conjunction with molecular phylogenies, to test for phylogenetic clustering of extinctions within and among bivalve families and how this clustering varies over time.

The fossil record of marine bivalves preserves a rich history of past extinctions, and although this record is not free of taphonomic biases, such biases are increasingly well understood (*16*, *17*). We used a taxonomically standardized database

[1]Section of Ecology, Behavior and Evolution, University of California San Diego, La Jolla, CA 92093–0116, USA. [2]Department of Paleobiology, National Museum of Natural History, Smithsonian Institution, Washington, DC 20013–7012, USA. [3]Department of Geophysical Sciences, University of Chicago, 5734 South Ellis Avenue, Chicago, IL 60637, USA.

*To whom correspondence should be addressed. E-mail: kroy@ucsd.edu

of stratigraphic ranges of marine bivalves (*18*) to calculate background extinction rates (i.e., for times other than the massive end-Cretaceous event) of 1678 genera and subgenera (hereafter termed genera) over the last ~200 million years (Jurassic to Pleistocene). Genera are the preferred units of large-scale paleontological analyses because, relative to species, their taxonomy is better standardized and more stable, and their fossil record is far more complete and more robust to taphonomic biases (*19*, *20*). Furthermore, comparative analyses indicate that morphologically defined molluscan genera generally reflect the topologies of molecular phylogenies (*21*). Taxonomic standardization is clearly a prerequisite for any quantitative analysis of extinction rates, and the data we used were subjected to extensive revisions and standardization (*18*, *19*, *22*). We used the family level for analyses of phylogenetic clustering of extinction rates because families provide the necessary balance between adequate sample size and phylogenetic resolution. In general, families of marine bivalves have proven to be robust taxonomic units, and recent molecular phylogenies suggest that none of the major families of marine bivalves are blatantly polyphyletic (*23*). Although some bivalve families may prove to be paraphyletic when a more complete molecular phylogeny of the group is available, for our analyses, paraphyly is more likely to add noise than to produce artifactual trends.

If extinctions of bivalve genera were random with respect to family membership, then an index of taxonomic clustering for individual extinction events [R_{CL} (*18*)] should not differ systematically from zero across a time series of such events. Positive values of R_{CL} indicate more (and negative values less) clustering than random extinction (*18*). Of the 26 standard time intervals in our data (*18*) for which R_{CL} could be reliably calculated, 21 (81%) have positive values (Fig. 1), a result that is highly unlikely under a model of phylogenetically random extinctions ($P = 0.002$, exact binomial test). When R_{CL} for individual time intervals is compared with the null distribution for that interval (*18*), 8 out of the 26 intervals show significantly positive clustering (i.e., the observed R_{CL} is at least as great as the upper 95% confidence limit), and no interval is significantly less clustered than random (Fig. 1). These eight intervals include the end-Cretaceous event, the only major mass extinction in our data. A ninth interval, the Campanian, is marginally significant. Thus extinctions of marine bivalves over the last 200 million years show a general pattern of phylogenetic conservatism within families, both during background and mass extinctions, but the strength of such clustering varies over time, and not all extinctions show significant clustering.

Our data also reveal that extinction magnitude is not correlated with phylogenetic clustering. The highest R_{CL} value is associated with the end-Cretaceous mass extinction (Fig. 2), but many high-extinction intervals, such as the Late Eocene, lack strong clustering (table S1), and the overall relation between phylogenetic clustering and extinction intensity is not significant (Spearman rank correlation, $r_s = 0.20$, $P = 0.34$). Extinction rates declined significantly over time, but this decline was caused by culling of volatile clades rather than by a decrease in extinction intensity within individual clades. Overall, rates before the end-Cretaceous extinction (excluding the Maastrichtian stage, which ends with the mass extinction) are higher than in the Cenozoic (median for Mesozoic stages = 0.087, median for Cenozoic stages = 0.029; Wilcoxon rank sum test, $W = 157$, $P = 0.054$). For families well-represented in both the Mesozoic and the Cenozoic, extinction rates do not differ significantly before and after the end-Cretaceous event (Wilcoxon paired signed rank test, $V = 61$, $P = 0.74$, $n = 16$ families), and families show high rank-order agreement between Mesozoic and Cenozoic background rates of extinction (Fig. 3) (Spearman rank correlation, $r_s = 0.75$, $P = 0.0008$). The lower Cenozoic extinction rates instead result from preferential losses during the end-Cretaceous extinction in families with inherently high extinction rates (Fig. 4), so that Cenozoic bivalve diversity was dominated by the more extinction-resistant families. The three families with the highest Mesozoic background extinction rates went globally extinct at the end of the Cretaceous, and other high-rate Mesozoic clades (e.g., trigoniids and arcticids, both with background rates >0.15, at least twice the Mesozoic median) (Fig. 4) were severely hit and have since remained minor components of the bivalve fauna. The only family for which background extinction rates were much lower in the Cenozoic than the Mesozoic is the Veneridae, which also suffered major losses at the end of the Cretaceous. Thus, the end-Cretaceous extinction had a filtering effect on lineage-specific extinction rates, removing the most volatile families but not systematically altering within-family extinction rates.

Extinction rates analyzed in conjunction with recently published molecular phylogenies of living bivalve families (*18*) also indicate phylogenetic conservatism at deeper levels in the bivalve tree. Extinction rates of closely related families are significantly more similar to each other than is expected by chance (Fig. 5) [$P = 0.014$ using a permutation test (*18*); the maximum-likelihood estimate of λ, an index of phylogenetic dependence (*24*), for within-family extinction rate is 0.84, a value within the range typically found for ecological and morphological traits (*24*) and significantly different from zero, $P < 0.0004$; see (*18*)]. The phylogenetic signal remains significant ($P = 0.049$) under an alternative model of character change (*18*). Thus, the taxonomic and phylogenetic analyses together suggest that extinction rates in bivalves are conserved at multiple levels of evolutionary divergence, within individual families as well as among related families.

Stratigraphic ranges of taxa can be distorted by preservational and sampling biases (*17*). Our analyses hinged on differences between clades rather than differences between temporal bins, so the primary concern is not temporal variation in the quality of the fossil record (*25*, *26*), but systematic differences in preservation potential across bivalve lineages. Extinction-rate estimates are robust to differences in shell composition (*16*), but other variables known to influence preservation, such as shell size, thickness, and preferred habitats, may be important (*17*). To evaluate the robustness of our results to preservational biases, we repeated all analyses after omitting families identified by Valentine *et al.* (*17*) as having low

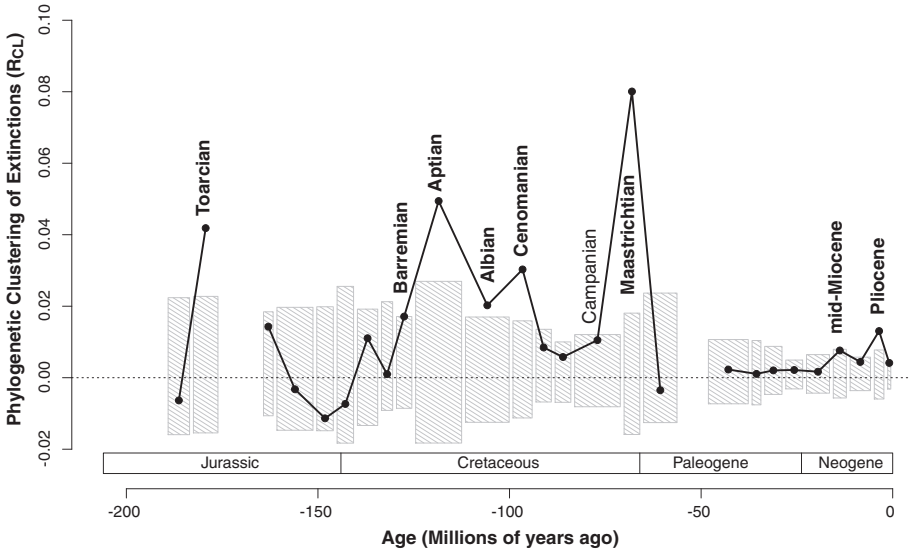

Fig. 1. Temporal trend in phylogenetic clustering of extinctions (R_{CL}). Shaded bars represent 95% confidence intervals around the expected value of R_{CL} (*18*). The intervals showing statistically significant phylogenetic clustering of extinctions are labeled in bold; an additional interval, the Campanian, is marginally significant. Only intervals with enough extinctions to analyze (eight or more) are plotted. The dotted line indicates the value expected if extinctions were not phylogenetically clustered.

preservation potential. The results were qualitatively unchanged (fig. S2). Another potential concern is that the observed differences in extinction rates between the Mesozoic and Cenozoic reflect taxonomic oversplitting of some Cretaceous groups relative to others. However, the families with disproportionate extinction represent a large and ecologically diverse assemblage (table S2), and multiple lines of evidence (*18*) suggest that the Mesozoic-Cenozoic difference is unlikely to simply reflect taxonomic practices. Phylogenetic clustering also does not appear to be driven only by extinctions associated with major environmental changes. For example, the overall signal remains highly significant, even when the Toarcian, Aptian, and Cenomanian stages, all of which include oceanic anoxic events (*27*), are excluded from the analysis, along with the Maastrichtian mass extinction (17 out of 22 extinctions with $R_{CL} > 0$, $P = 0.017$, exact binomial test).

Taken together, our results show that extinction rates of marine bivalve genera tend to be phylogenetically conserved, but the strength of this effect varies over time and can be substantially and permanently changed by a mass extinction. Lineage-level clustering of extinction rates, as seen here, is expected to follow from phylogenetic conservatism of traits that correlate with extinction vulnerability (*28*), making some lineages more prone to extinction than others (*2*, *9*, *10*). As extinction-prone taxa are winnowed out, both the rate of extinction and the associated phylogenetic clustering are expected to decrease. The stronger phylogenetic clustering seen for the Cretaceous extinctions is likely to reflect the prominence during this time of clades with volatile dynamics (table S2). The demise of these high-rate taxa at the end of the Cretaceous shifted the overall distribution to lower values and also reduced the range of variation of within-family extinction rates (Fig. 4). Such hardening of the biota over evolutionary time has been hypothesized before (*29*–*31*). Though we cannot reject the alternative hypothesis that the decline in extinction rates from Mesozoic to Cenozoic is due to a systematic decrease in extinction forcing mechanisms, we see no reason to assume that forcing mechanisms became less intense, especially given that the Cenozoic is characterized by dramatic shifts in climate, occurring on multiple temporal scales (*32*). The Mesozoic-Cenozoic differences also do not reflect differences in statistical power, because each of these eras has similar average numbers of extinctions per time interval (table S1).

Other factors such as the nature of the extinction mechanism can also contribute to the observed variations in phylogenetic clustering. Different kinds of environmental stresses are likely to cause extinctions that are selective with respect to different traits, and we might expect phylogenetic clustering of extinctions to track, in part, the degree to which the relevant traits are conserved over phylogeny. Extinction triggers that disproportionately affect specific regions or environments might also contribute to clustered extinctions in families with restricted distributions. However, virtually all bivalve families are geographically and environmentally widespread (*33*), and such spatial effects are weak in the end-Cretaceous extinction (*5*, *6*). Information on environmental drivers of past extinctions and their spatial heterogeneity is currently insufficient to permit more detailed exploration of these factors. Irrespective of the underlying causes, the influence of previous extinctions on both the magnitude of extinction rates and the pattern of phylogenetic conservatism suggests that attempts to understand the biological basis for differential extinction vulnerabilities of clades should take into account their past history of extinctions. These results also corroborate a peculiarity of the end-Cretaceous mass extinction (and perhaps of major extinctions in general), where the phylogenetic pattern of extinction is consistent with preceding intervals, as shown here, but the functional or ecological selectivity is not (*5*, *29*, *34*).

Phylogenetic nonrandomness and the temporal decline in extinction rates documented here are potentially problematic for calculating speciation and diversification rates from molecular phylogenies because they violate the assumption that extinction rates are stochastically constant over time (*35*, *36*), although recent work has started to

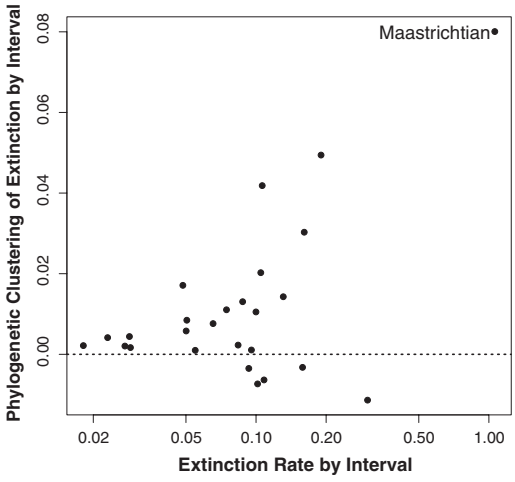

Fig. 2. Phylogenetic clustering of extinctions (R_{CL}) as a function of extinction rate, for each time interval in Fig. 1. The relation is not significant. The dotted line indicates the value expected if extinctions were not phylogenetically clustered.

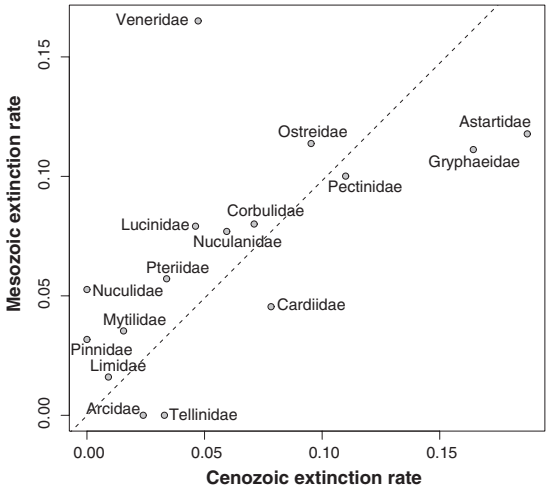

Fig. 3. Mesozoic versus Cenozoic background extinction rates for families well represented in both intervals. The dashed line represents equality in rates between the two eras ($y = x$).

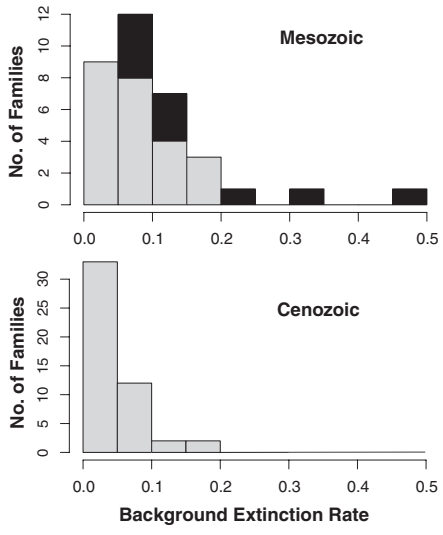

Fig. 4. Distribution of background extinction rates by family during the Mesozoic and Cenozoic eras. Black bars indicate families that went extinct during the end-Cretaceous mass extinction; gray bars indicate surviving families.

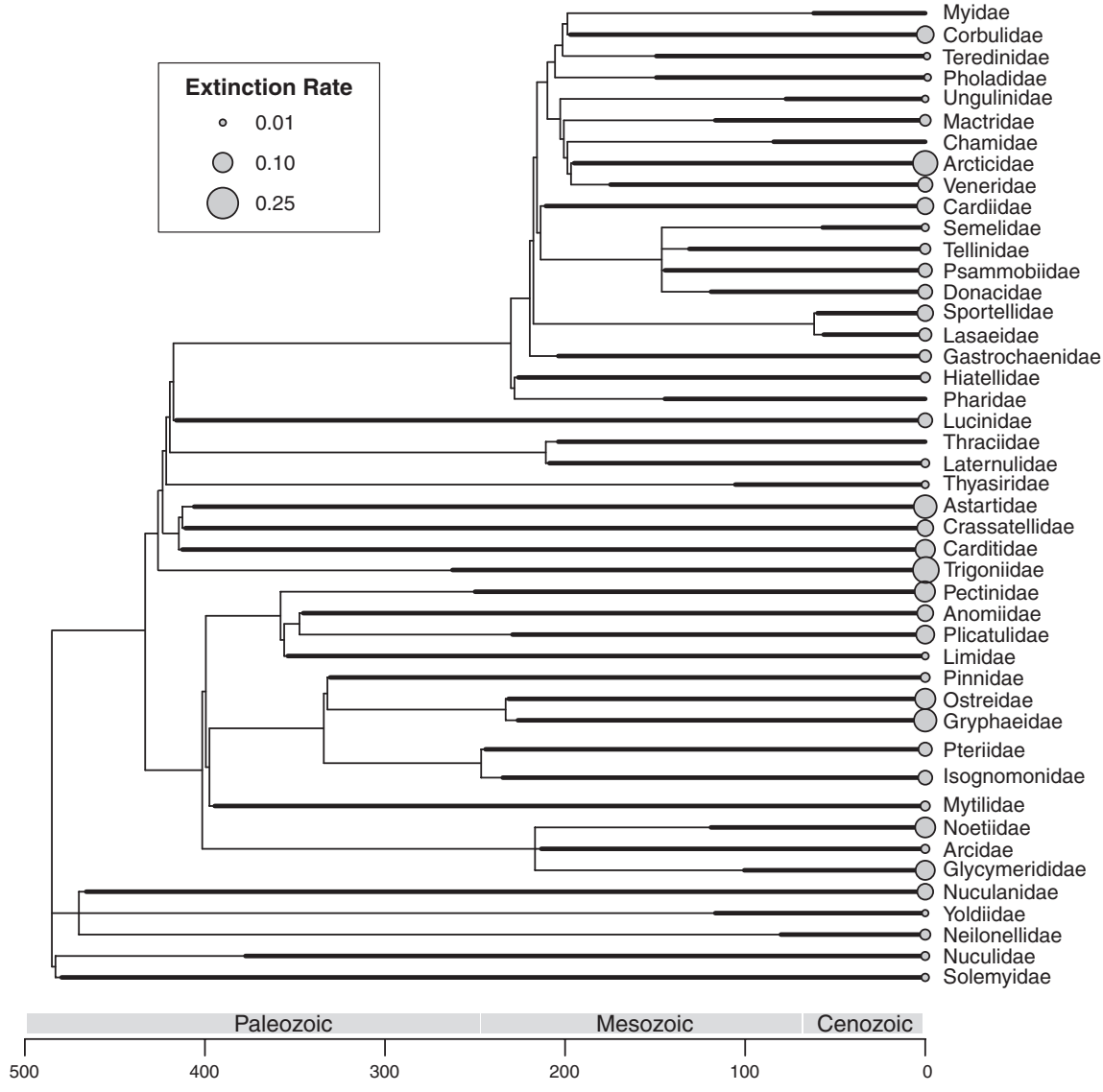

Fig. 5. Mean extinction rates for living families of bivalves mapped on the composite phylogeny used in this study (*18*). Only families for which background extinction rates could be reliably estimated (*18*) are shown. The dark bar along each branch denotes the known stratigraphic range of that taxon, omitting extinct stem groups. The size of the symbol for each family is proportional to its extinction rate. Extinction rates of closely related families are significantly more similar to each other than is expected by chance.

consider less restrictive models (*37*, *38*). On the other hand, if lineages or biotas tend to harden over time, perhaps through the filter of mass extinctions, then the assumption of stochastically constant extinction rates may be more reasonable for later histories of lineages once the more volatile taxa have been winnowed. Caution is needed, however, because such hardening might operate at multiple levels, ranging from the well-documented decline in background extinction rates through the Phanerozoic attributed to the culling of the more volatile Paleozoic fauna in favor of the more resistant Modern fauna (*39*, *40*) to the species-level selectivities seen during the marine extinction pulse near the onset of Pleistocene glacial cycles (*41*). Finally, our results combined with previous studies (*9*, *12*, *14*, *28*) imply that evolutionary histories of individual lineages are important determinants of extinction vulnerabilities of their constituent taxa, under both natural and anthropogenic forcing. This commonality suggests that more detailed studies of phylogenetic selectivity of extinctions in the geological past, and the traits involved, should provide useful insights about the consequences of extinctions unfolding today. For example, if phylogenetic clustering is a general rule, then anthropogenic extinctions are likely to eliminate substantially more evolutionary history in the near future than models based on random extinctions of the same intensity would predict (*15*).

References and Notes

1. D. Jablonski, *Philos. Trans. R. Soc. London Ser. B* **344**, 11 (1994).
2. M. L. McKinney, *Annu. Rev. Ecol. Syst.* **28**, 495 (1997).
3. D. M. Raup, *Extinction. Bad Genes or Bad Luck?* (Norton, New York, 1991).
4. S. C. Wang, A. M. Bush, *Paleobiology* **34**, 434 (2008).
5. D. Jablonski, *Paleobiology* **31** (suppl.), 192 (2005).
6. D. Jablonski, *Proc. Natl. Acad. Sci. U.S.A.* **105**, 11528 (2008).
7. J. L. Payne, S. Finnegan, *Proc. Natl. Acad. Sci. U.S.A.* **104**, 10506 (2007).
8. M. G. Powell, *Paleobiology* **33**, 530 (2007).
9. P. M. Bennett, I. P. F. Owens, D. Nussey, S. T. Garnett, G. M. Crowley, in *Phylogeny and Conservation*, A. Purvis, J. L. Gittleman, T. Brooks, Eds. (Cambridge Univ. Press, Cambridge, 2005), pp. 317–336.
10. A. Purvis, M. Cardillo, R. Grenyer, B. Collen, in *Phylogeny and Conservation*, A. Purvis, J. L. Gittleman, T. Brooks, Eds. (Cambridge Univ. Press, Cambridge, 2005), pp. 295–316.
11. G. J. Russell, T. M. Brooks, M. M. McKinney, C. G. Anderson, *Conserv. Biol.* **12**, 1365 (1998).
12. J. L. Lockwood *et al.*, *Conserv. Biol.* **16**, 1137 (2002).
13. A. Purvis, P.-M. Agapow, J. L. Gittleman, G. M. Mace, *Science* **288**, 328 (2000).
14. J. Bielby, A. A. Cunningham, A. Purvis, *Anim. Conserv.* **9**, 135 (2006).
15. A. Purvis, *Annu. Rev. Ecol. Evol. Syst.* **39**, 301 (2008).
16. S. M. Kidwell, *Science* **307**, 914 (2005).

17. J. W. Valentine, D. Jablonski, S. M. Kidwell, K. Roy, *Proc. Natl. Acad. Sci. U.S.A.* **103**, 6599 (2006).
18. Materials and Methods are available as supporting material on *Science* Online.
19. D. Jablonski, K. Roy, J. W. Valentine, *Science* **314**, 102 (2006).
20. J. J. Sepkoski, *Philos. Trans. R. Soc. London Ser. B* **353**, 315 (1998).
21. D. Jablonski, J. A. Finarelli, *Proc. Natl. Acad. Sci. U.S.A.* **106**, 8262 (2009).
22. D. Jablonski, K. Roy, J. W. Valentine, R. M. Price, P. S. Anderson, *Science* **300**, 1133 (2003).
23. J. D. Taylor, S. T. Williams, E. A. Glover, P. Dyal, *Zool. Scr.* **36**, 587 (2007).
24. R. P. Freckleton, P. H. Harvey, M. Pagel, *Am. Nat.* **160**, 712 (2002).
25. S. E. Peters, *Proc. Natl. Acad. Sci. U.S.A.* **102**, 12326 (2005).
26. A. B. Smith, A. J. McGowan, *Palaeontology* **50**, 765 (2007).
27. R. D. Pancost *et al.*, *J. Geol. Soc. London* **161**, 353 (2004).
28. M. L. McKinney, *Paleobiology* **21**, 300 (1995).
29. D. Jablonski, *Proc. Natl. Acad. Sci. U.S.A.* **98**, 5393 (2001).
30. J. B. C. Jackson, in *Extinction Rates*, J. H. Lawton, R. M. May, Eds. (Oxford Univ. Press, Oxford, 1995), pp. 45–54.
31. S. M. Stanley, *Paleobiology* **16**, 401 (1990).
32. J. Zachos, M. Pagani, L. Sloan, E. Thomas, K. Billups, *Science* **292**, 686 (2001).
33. J. A. Crame, *Paleobiology* **26**, 188 (2000).
34. S. M. Stanley, *Paleobiology* **33** (suppl.), 1 (2007).
35. S. Nee, *Annu. Rev. Ecol. Syst.* **37**, 1 (2006).
36. S. Nee, E. C. Holmes, R. M. May, P. H. Harvey, *Philos. Trans. R. Soc. London Ser. B* **344**, 77 (1994).
37. D. L. Rabosky, I. J. Lovette, *Proc. R. Soc. London Ser. B. Biol. Sci.* **275**, 2363 (2008).
38. D. L. Rabosky, I. J. Lovette, *Evolution* **62**, 1866 (2008).
39. J. J. Sepkoski Jr., in *Global Events and Event Stratigraphy*, O. H. Walliser, Ed. (Springer, Berlin, 1996), pp. 35–51.
40. J. W. Valentine, in *Causes of Evolution: A Paleontological Perspective*, R. M. Ross, W. D. Allmon, Eds. (Univ. of Chicago Press, Chicago, 1990), pp. 128–150.
41. J. T. Smith, K. Roy, *Paleobiology* **32**, 408 (2006).
42. We thank S. M. Kidwell and J. W. Valentine for discussions, I. Tëmkin and T. R. Waller for taxonomic advice, and two anonymous reviewers for insightful comments. This work was supported by a grant from NASA.

Supporting Online Material
www.sciencemag.org/cgi/content/full/325/5941/733/DC1
Materials and Methods
SOM Text
Figs. S1 to S5
Tables S1 and S2
References

4 March 2009; accepted 19 June 2009
10.1126/science.1173073

Genetic Properties of the Maize Nested Association Mapping Population

Michael D. McMullen,[1,2]|| Stephen Kresovich,[3]|| Hector Sanchez Villeda,[2]* Peter Bradbury,[1,3] Huihui Li,[4,5,3] Qi Sun,[6] Sherry Flint-Garcia,[1,2] Jeffry Thornsberry,[7] Charlotte Acharya,[3] Christopher Bottoms,[2] Patrick Brown,[3] Chris Browne,[1] Magen Eller,[1] Kate Guill,[1] Carlos Harjes,[3]† Dallas Kroon,[3] Nick Lepak,[1] Sharon E. Mitchell,[3] Brooke Peterson,[1] Gael Pressoir,[3]‡ Susan Romero,[1] Marco Oropeza Rosas,[8]¶ Stella Salvo,[1] Heather Yates,[3] Mark Hanson,[9] Elizabeth Jones,[10] Stephen Smith,[10] Jeffrey C. Glaubitz,[11] Major Goodman,[8] Doreen Ware,[1,12] James B. Holland,[1,8]|| Edward S. Buckler[1,3,13]||

Maize genetic diversity has been used to understand the molecular basis of phenotypic variation and to improve agricultural efficiency and sustainability. We crossed 25 diverse inbred maize lines to the B73 reference line, capturing a total of 136,000 recombination events. Variation for recombination frequencies was observed among families, influenced by local (cis) genetic variation. We identified evidence for numerous minor single-locus effects but little two-locus linkage disequilibrium or segregation distortion, which indicated a limited role for genes with large effects and epistatic interactions on fitness. We observed excess residual heterozygosity in pericentromeric regions, which suggested that selection in inbred lines has been less efficient in these regions because of reduced recombination frequency. This implies that pericentromeric regions may contribute disproportionally to heterosis.

The majority of phenotypic variation in natural populations and agricultural plants and animals is determined by quantitative genetic traits (*1*). Maize (*Zea mays* L.) exhibits extensive molecular and phenotypic variation (*2*–*4*). Understanding the genetic basis of quantitative traits in maize is essential to predictive crop improvement. However, only slow progress has been made in identifying the genes controlling quantitative agronomic traits because of limitations in the scope of allelic diversity and resolution in available genetic mapping resources. Linkage mapping generally focuses on the construction and analysis of large families from two inbred lines to detect quantitative trait loci (QTLs) (*5*). However, resolution of these QTLs can be poor because of the limited number of recombination events that occur during population development. Association analysis takes advantage of historic recombination from deep coalescent history as linkage disequilibrium (LD) generally decays within 2 kb (*1*, *6*). However, because of the number of single-nucleotide polymorphisms (SNPs) required and the confounding effects of population structure, whole-genome association analysis can be difficult in maize (*4*).

To provide a genetic resource for quantitative trait analysis in maize, we have created the nested association mapping (NAM) population. NAM was constructed to enable high power and high resolution through joint linkage-association analysis, by capturing the best features of previous approaches (*7*, *8*). The genetic structure of the NAM population is a reference design of 25 families of 200 recombinant inbred lines (RILs) per family (fig. S1). The inbred B73 was chosen as the reference inbred line because of its use for the public physical map (*9*) and for the Maize Sequencing Project (www.maizesequence.org). The other 25 parents [named the 25 diverse lines (25DL)] maximize the genetic diversity of the RIL families (*8*, *10*), independent of any specific phenotype. The lines were chosen to represent the diversity of maize—more than half are tropical in origin, nine are temperate lines, two are sweet corn lines (representing Northern Flint), and one is a popcorn inbred line (fig. S2).

The NAM genetic map is a composite map created with 4699 RILs combined across the 25 families, representing 1106 loci, with an average marker density of one marker every 1.3 centimorgans (cM) (fig. S3 and table S1). The proportion of SNP loci from the composite map polymorphic in an individual family ranged from 63 to 74%. Among RILs, 48.7% of all marker genotypes were inherited from B73, 47.6% were inherited from the 25DL parent, and 3.6% were heterozygous, which suggests that they were broadly representative of the parents and fall within the expected range for S5 generation RILs. The NAM population captured ~136,000 crossover events, corresponding, on average, to three crossover events per gene. This allows genetic factors to be mapped to very specific regions of the

[1]United States Department of Agriculture–Agriculture Research Service (USDA–ARS). [2]Division of Plant Sciences, University of Missouri, Columbia, MO 65211, USA. [3]Institute for Genomic Diversity, Cornell University, Ithaca, NY 14853, USA. [4]School of Mathematical Science, Beijing Normal University, Beijing 100875, China. [5]Institute of Crop Science, Chinese Academy of Agricultural Sciences, Beijing 100081, China. [6]Computational Biology Service Unit, Cornell University, Ithaca, NY 14853, USA. [7]Northwest Missouri State University, Maryville, MO 64468, USA. [8]Department of Crop Science, North Carolina State University, Raleigh, NC 27695, USA. [9]Illumina Inc., San Diego, CA 92121, USA. [10]Pioneer Hi-Bred, Johnston, IA 50131, USA. [11]Laboratory of Genetics, University of Wisconsin, Madison, WI 53706, USA. [12]Cold Spring Harbor Laboratory, Cold Spring Harbor, NY 11724, USA. [13]Department of Plant Breeding and Genetics, Cornell University, Ithaca, NY 14853, USA.

*Present address: International Maize and Wheat Improvement Center (CIMMYT), kilometer 45, Carretera Mex-Veracruz, El Batan, Texcoco, Mexico.
†Present address: Monsanto, Leesburg, GA 31763, USA.
‡Present address: Fondation CHIBAS, 30 Rue Pacot, Port-au-Prince, Haiti.
¶Present address: Delta Pine/Monsanto, Post Office Box 194, Scott, MS 38772, USA.
||To whom correspondence should be addressed. E-mail: mcmullenm@missouri.edu (M.D.M.); sk20@cornell.edu (S.K.); james_holland@ncsu.edu (J.B.H.); esb33@cornell.edu (E.S.B.)

genome (*11*) and leads to a higher-resolution anchoring of the physical map of maize.

Recombination varied substantially among the 25 families. The genetic length of the individual family maps relative to the composite map ranged from –104.3 cM (–7.4%) for B73 × Mo18W to +269.4 cM (+19.2%) for B73 × CML228. We attempted to map global recombination controllers by treating the number of crossovers in each individual line as a phenotypic trait (*12*). However, despite our high statistical power and diversity, we found no shared controllers of recombination; in contrast, shared QTLs for other traits were common (*11*). By examining individual families, we found evidence for loci controlling whole-genome or individual chromosome recombination at only a 50% or greater false-discovery rate (FDR). Five of the eight loci showing the strongest effects control recombination in cis, which suggested that they are structural variants that modify recombination for specific chromosomes within specific families. The absence of loci with genome-wide effects on recombination suggests that the observed differences in recombination rates were because of numerous, but localized, regions of variation, as suggested by studies of individual families (*13*–*15*). We used a sliding window (4 to 6 cM) to examine differential recombination across the 25 families. The average interval had a 2.9-fold difference in recombination rate between the highest and lowest families, however, some intervals exhibited as much as 30-fold differences for recombination rate across families (Fig. 1). Overall, 41% of intervals showed significant differences ($P < 0.05$) in the number of recombination events across the 25 families (fig. S4).

Across families, we did not observe a normal distribution in differential recombination frequency; the maximum increase relative to the consensus was twofold, whereas recombination was repressed by more than 20-fold in specific regions among specific families. Although recombination does not occur in retrotransposon clusters between genes, differences in the presence or absence of these clusters (which are ubiquitous among maize inbred lines), can result in at least threefold differences in recombination rates within flanking genes (*16*). Although these differences in non-genic content may explain many of the observed differences in recombination frequency, it seems less likely that they explain the virtual elimination of recombination within 6-cM+ intervals within specific families. Rather, we suspect that previously uncharacterized inversions may be responsible for some of the larger differences observed. For example, for one region on chromosome 5 that represents more than 12 cM of the composite map, we recovered no recombination events in either the B73 × CML322 or B73 × CML52 families, which suggested the presence of a large inversion of this region in CML322 and CML52 relative to B73.

These differences in recombination among families hinder efforts to understand the genetic basis of quantitative traits in maize. All comparisons across mapping populations either by meta-analysis approaches (*17*) or joint-linkage mapping or joint association–linkage mapping, as with NAM, are confounded by this phenomenon, because these methods assume consistent recombination frequencies across families. The differences in recombination rates among families also indicate that map-based gene cloning projects need to be conducted in genetic backgrounds that demonstrate high recombination rates in the target region.

We developed one-third of the lines for each family under different environmental conditions to minimize inadvertent selection (*18*). However, because the final RILs resulted from 50,000 meioses and only 22% of the original F_2 plants produced an S5 RIL, the surviving lines were unavoidably subjected to selection for multiple generations. Of all the chromosomal segments, 97% were represented by parental alleles at 45 to 55% frequency, close to the expectation of 50% (fig. S5). Within individual families, 17% of the markers exhibited segregation distortion at $P < 0.05$, 8.9% at $P < 0.01$, and 4.0% at $P < 0.001$ (Fig. 2), less than has been reported for individual mapping populations (*19*–*21*). Within individual families, only 0.17% of all possible donor-marker combinations had less than 50 donor alleles, which demonstrated that diversity was effectively captured. We saw no bias of selection for temperate alleles, because the 13 families from tropical origin averaged less distorted markers than the total [7.8% for tropical families vs. 8.9% overall, ($P < 0.01$)].

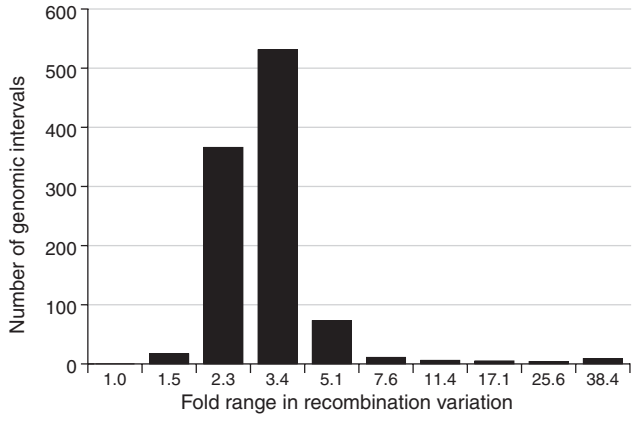

Fig. 1. A sliding window analysis reveals differential recombination rates among the NAM families for synthetic intervals of ~4 cM (*18*).

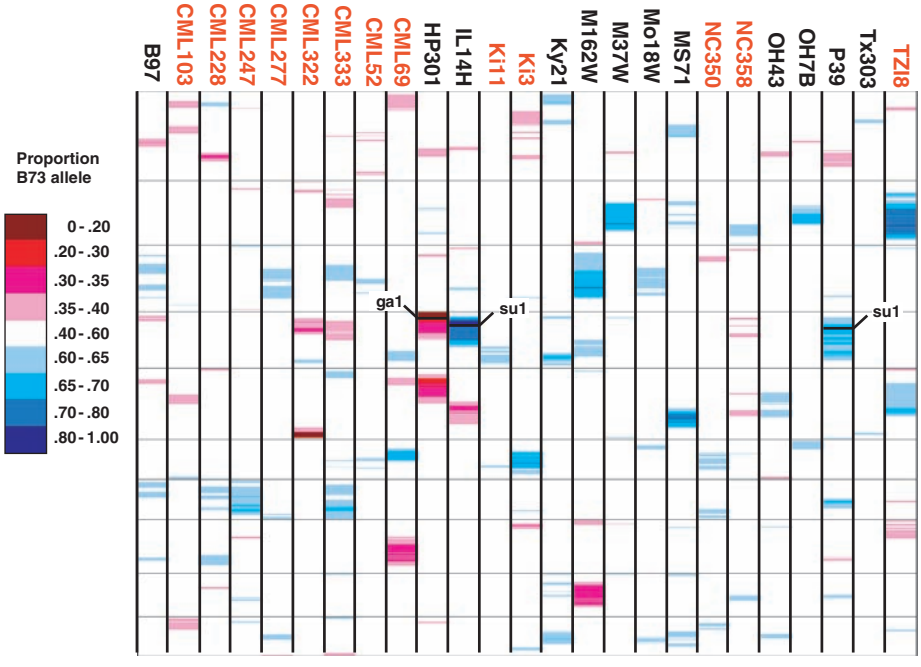

Fig. 2. Segregation distortion within individual NAM families. Each column represents one NAM family, the 25DL parent is indicated above the column. Red family names represent those with the 25DL parent from tropical origin. Each family consists of 1116 intervals, with the values of nonpolymorphic or missing marker data inferred on the basis of flanking marker values. Horizontal lines indicate the positions of chromosome boundaries for chromosomes 1 to 10, top to bottom. The proportion of B73 alleles for an interval is indicated by the color scale. The positions of the *ga1* and *su1* genes (*22*, *24*) are indicated.

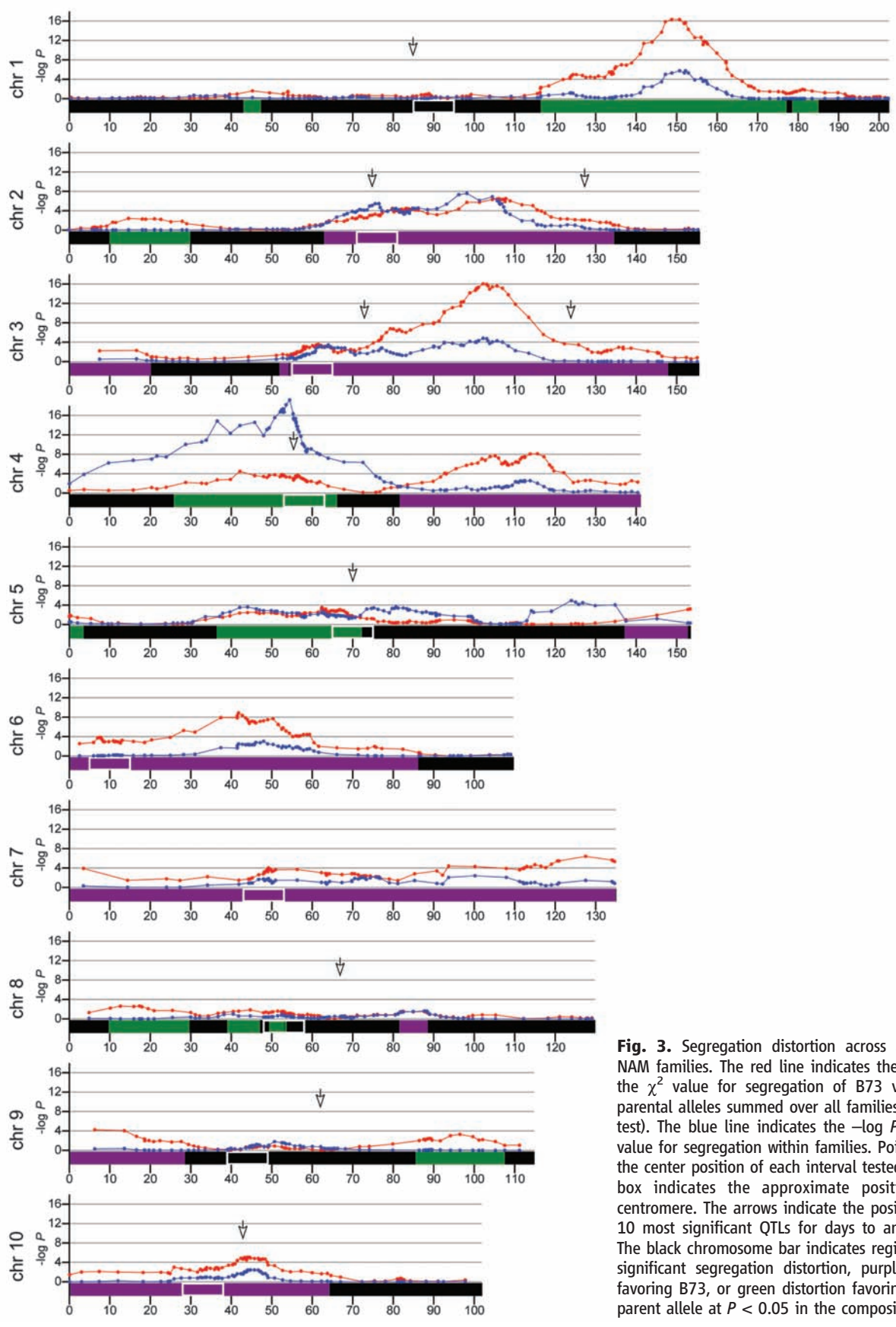

Fig. 3. Segregation distortion across and among NAM families. The red line indicates the –log *P* for the χ^2 value for segregation of B73 versus 25DL parental alleles summed over all families (composite test). The blue line indicates the –log *P* for the χ^2 value for segregation within families. Points indicate the center position of each interval tested. The white box indicates the approximate position of the centromere. The arrows indicate the positions of the 10 most significant QTLs for days to anthesis (*11*). The black chromosome bar indicates regions with no significant segregation distortion, purple distortion favoring B73, or green distortion favoring the 25DL parent allele at $P < 0.05$ in the composite test.

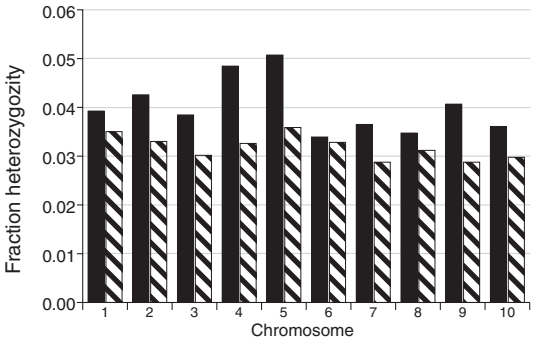

Fig. 4. The proportion of marker genotypes that are heterozygous are shown as calculated for the area within 10 cM on each side of the centromere compared with the remaining chromosome arms. Black bars are within 10 cM on each side of the centromere position; hatched bars represent the rest of the chromosome.

We believe that four of the five most distorted regions within specific families are explained by known genetic factors. *Gametophyte factor 1–strong allele* (*Ga1-S*) (*22*), which excludes *ga1* pollen from fertilizing ovules of *Ga1-S*, causes the distortion on the short arm of chromosome 4 for the Hp301 family (χ^2, $P = 1.7 \times 10^{-19}$) (Fig. 2). The distortion on chromosome 5 of the Hp301 family probably results from a second gametophyte factor, *ga2* (*23*). Two sweet corn lines (Il14H and P39) show distortion on chromosome 4 against the *sugary1* (*su1*) allele, which causes the sweet corn phenotype but can exhibit reduced germination vigor (*24*). We also observed substantial distortion in three families: M37W, Oh7B, and Tzi8 on a 65- to 110-cM region of chromosome 2 with a 2:1 bias favoring the B73 allele, perhaps because of QTLs for delayed flowering (*11*). No candidate for the major distortion on chromosome 5 in the CML322 family was identified. We attempted to map potential QTLs for trans-acting controllers of segregation distortion in individual populations but found none; it seems that selection operates directly on specific blocks of linked alleles.

We also tested whether specific regions of the genome show consistent segregation distortion favoring or disfavoring the B73 allele compared with other parental alleles (Fig. 3). This test includes all 4699 lines, and indeed, we found that 54% of the markers were distorted ($P < 0.05$) by at least slight selection for or against B73 alleles, but few loci were under strong selection. Additionally, among-family segregation with a χ^2 test of B73 versus specific 25DL alleles showed that chromosome 4, containing both the *ga1* and *su1* distortions, creates a large among-family distortion. However, we observed lower overall B73 versus 25DL distortion, most likely because of the different direction of bias of *ga1* and *su1*, which cancel in the composite analysis. We saw little correspondence between flowering-time QTLs and regions of segregation distortion (Fig. 3).

Because these RIL families were derived from inbred lines, one might expect relatively few large single-locus effects for fitness and distortion. However, we expected epistasis to play a role in the creation of these new RILs, such that specific two-locus allelic combinations would be favored, resulting in LD between certain unlinked loci. We surveyed two-locus LD for all pairs of markers on separate chromosomes, first, by comparing B73 alleles to all others from the complete set of 25 families. Marginally significant LD was observed between chromosome 6 and 7, but with a maximum r^2 of only 0.005, a trivially small effect. Second, we tested LD within each population separately; among the 13.6 million tests, the highest level of LD was $r^2 = 0.13$, about what is expected by chance. Despite our tremendous diversity and statistical power, we saw virtually no evidence of epistatic effects on fitness in the NAM population.

The rate of evolution from natural selection or genetic gain from plant breeding for complex traits can be limited by repulsion phase linkages among favorable alleles [Hill-Robertson effect (*25*)]. Although maize has had a very large population size throughout most of its evolution, effective population sizes have been modest during the last century of inbred line development. One prediction of the Hill-Robertson effect is that favorable alleles have a higher chance of being in repulsion LD in regions with limited recombination. If such alleles exhibit dominance, then low-recombination pericentromeric regions should be under higher selective pressure to maintain heterozygosity. In NAM, residual heterozygosity averaged 4.1% for the 343 markers within 10 cM of the centromeres and averaged 3.2% for the 763 markers outside the centromeres, a 30% increase in pericentromeric regions. We found higher levels of heterozygosity near centromeres on all 10 chromosomes ($P < 0.0004$) (Fig. 4), which suggested that selection favors heterozygosity in pericentromeric regions, perhaps because recombination in these regions has been insufficient to combine the optimal alleles. When B73 was mapped to identify heterotic regions (*26*), half of the largest QTL associated with centromeric regions, including a major QTL on chromosome 5 consisting of at least two distinct genes in repulsion phase linkage affecting yield (*27*). We observed high levels of residual heterozygosity in this region as well. We speculate that these data support the dominance theory of heterosis and that the increase in heterozygosity near centromeres is a consequence of heterosis. This heterosis is most likely the product of pseudo-overdominance that is most pronounced in pericentromeric regions, where the Hill-Robertson effect is strongest.

There were two striking and biologically significant discoveries in this project that impact maize breeding. The first was the extensive localized differences in recombination rates among families. We intend to genotype NAM at a much higher density to determine the structural bases of these differences. High-density genotyping in a large human pedigree has revealed extensive variation in use of recombination hotspots among individual families (*28*), similar to the variation we have revealed for maize. The second major finding was strong experimental support for the Hill-Robertson effect and the implications in understanding the basis of heterosis in maize. As similarly structured populations are developed for other model and crop species, it will be of interest to see if these findings are general or more specific to the demographic and breeding history of maize.

References and Notes

1. T. F. Mackay, *Annu. Rev. Genet.* **35**, 303 (2001).
2. M. I. Tenaillon *et al.*, *Proc. Natl. Acad. Sci. U.S.A.* **98**, 9161 (2001).
3. S. I. Wright *et al.*, *Science* **308**, 1310 (2005).
4. S. A. Flint-Garcia *et al.*, *Plant J.* **44**, 1054 (2005).
5. E. S. Lander, D. Botstein, *Genetics* **121**, 185 (1989).
6. D. L. Remington *et al.*, *Proc. Natl. Acad. Sci. U.S.A.* **98**, 11479 (2001).
7. M. Zhang *et al.*, *Genetics* **169**, 2305 (2005).
8. J. Yu, J. B. Holland, M. D. McMullen, E. S. Buckler, *Genetics* **178**, 539 (2008).
9. F. Wei *et al.*, *PLoS Genet.* **3**, e123 (2007).
10. K. Liu *et al.*, *Genetics* **165**, 2117 (2003).
11. E. S. Buckler *et al.*, *Science* **325**, XXX (2009).
12. E. Esch, J. M. Szymaniak, H. Yates, W. P. Pawlowski, E. S. Buckler, *Genetics* **177**, 1851 (2007).
13. W. D. Beavis, D. Grant, *Theor. Appl. Genet.* **82**, 636 (1991).
14. C. G. Williams, M. M. Goodman, C. W. Stuber, *Genetics* **141**, 1573 (1995).
15. H. Yao, P. S. Schnable, *Genetics* **170**, 1929 (2005).
16. H. K. Dooner, L. He, *Plant Cell* **20**, 249 (2008).
17. F. Chardon *et al.*, *Genetics* **168**, 2169 (2004).
18. Materials and methods are available as supporting material on *Science* Online.
19. N. Sharopova *et al.*, *Plant Mol. Biol.* **48**, 463 (2002).
20. A. M. Casa *et al.*, *Proc. Natl. Acad. Sci. U.S.A.* **97**, 10083 (2000).
21. M. Falque *et al.*, *Genetics* **170**, 1957 (2005).
22. R. A. Emerson, *Genetics* **19**, 137 (1934).
23. A. E. Longley, *Genetics* **46**, 641 (1961).
24. H. G. Nass, P. L. Crane, *Crop Sci.* **10**, 139 (1970).
25. W. G. Hill, A. Robertson, *Genet. Res.* **8**, 269 (1966).
26. C. W. Stuber, S. E. Lincoln, D. W. Wolff, T. Helentjaris, E. S. Lander, *Genetics* **132**, 823 (1992).
27. G. I. Graham, D. W. Wolff, C. W. Stuber, *Crop Sci.* **37**, 1601 (1997).
28. G. Coop, X. Wen, C. Ober, J. K. Pritchard, M. Prezeworski, *Science* **319**, 1395 (2008).
29. Supported by National Science Foundation Award DBI0321467 and by research funds provided by USDA–ARS to M.D.M., E.S.B., and J.B.H.

Supporting Online Material

www.sciencemag.org/cgi/content/full/325/5941/737/DC1
Materials and Methods
Figs. S1 to S5
Tables S1 and S2
References

31 March 2009; accepted 18 June 2009
10.1126/science.1174320

Multiscale Mechanics of Fibrin Polymer: Gel Stretching with Protein Unfolding and Loss of Water

André E. X. Brown,[1,2] Rustem I. Litvinov,[3] Dennis E. Discher,[2,4] Prashant K. Purohit,[5] John W. Weisel[3]*

Blood clots and thrombi consist primarily of a mesh of branched fibers made of the protein fibrin. We propose a molecular basis for the marked extensibility and negative compressibility of fibrin gels based on the structural and mechanical properties of clots at the network, fiber, and molecular levels. The force required to stretch a clot initially rises linearly and is accompanied by a dramatic decrease in clot volume and a peak in compressibility. These macroscopic transitions are accompanied by fiber alignment and bundling after forced protein unfolding. Constitutive models are developed to integrate observations at spatial scales that span six orders of magnitude and indicate that gel extensibility and expulsion of water are both manifestations of protein unfolding, which is not apparent in other matrix proteins such as collagen.

Fibrin clots are proteinaceous gels that polymerize in the blood as a consequence of biochemical cascades at sites of vascular injury. Together with platelets, this meshwork stops bleeding and supports active contraction during wound healing (*1*, *2*). Fibrin also provides a scaffold for thrombi, clots that block blood vessels and cause tissue damage, leading to myocardial infarction, ischemic stroke, and other cardiovascular diseases (*3*). To maintain hemostasis while minimizing the impact of thrombosis, fibrin must have suitable stiffness and plasticity (*4*), but also sufficient permeability so that the network can be effectively decomposed (lysed) by proteolytic enzymes (*5*, *6*). It is challenging to meet all of these conditions because open scaffolds would be expected to break at low strains, as is true for collagen gels (*7*). To address how fibrin clots are both permeable and highly extensible, we studied fibrin structures across multiple spatial scales, from whole clots to single fibers and single molecules (Fig. 1).

Fibrin clots were made from purified human fibrinogen under conditions (*8*) that resulted in the formation of long, straight fibers, similar to those found in physiological clots. To simplify the interpretation, the clots were covalently ligated with the use of a transglutaminase (blood clotting factor XIIIa), as naturally occurs in the blood, which prevents protofibrils from sliding past one another, thus eliminating persistent creep (*9*).

Measurements of the extensibility of 2-mm-diameter fibrin clots (Fig. 2A) demonstrated that the clots could be stretched to more than three times their relaxed length before breaking, with an average stretch of 2.7 ± 0.15–fold ($n = 6$) (*10*). This is comparable to the single-fiber extensibility that is observed when a fibrin fiber is laterally stretched with an atomic force microscope (*11*). Qualitatively, the resulting force-strain curve for fibrin is similar to those observed for rubbers and other materials made from flexible chains (*12*). However, for fibrin clots, which are made of longer, straighter fibers than the thermally fluctuating polymer chains in rubber, models of rubber-like elasticity predict a branching density that is wrong by seven orders of magnitude (*4*). Therefore, new models are needed to understand clot mechanics.

In addition to the large extensibility of fibrin clots, these gels also displayed a dramatic decrease in volume upon stretching [supporting online material (SOM) movie S1], unlike most rubbery materials. This unusual effect is quantified in Fig. 2B where the lateral contraction of the gel λ_* allows one to calculate the relative volume ($\lambda_1\lambda_*^2$), which is plotted as function of strain (black circles) and contrasted with a volume-conserving incompressible material (black dashed line). The shrinkage of the stretched clot was due to water expulsion, as confirmed by an ~10-fold increase in the protein content in clots at a strain of 2 (fig. S1B). This protein concentrating effect, or syneresis, is mechanically induced and corresponds to a negative compressibility for the gel (Fig. 2B, inset); the intrinsic compressibility of proteins is usually positive and small, ~2×10^{-4} MPa^{-1} (Fig. 2B inset, open circle) (*13*). This effect might be related to the phenomenon of negative normal stress observed for networks of semiflexible polymers, because even though fibrin fibers are relatively stiff, it is still possible that they buckle more easily than they stretch, thus leading to an effective inward force (*14*). However, our data below support an alternative explanation in which the volume change is associated with protein unfolding and bundling of stretched fibrin fibers.

To understand what makes fibrin so different from other highly extensible polymers, including rubbers and hydrogels, we quantified the structural changes that occur in stretched clots at the network and fiber levels. Unstrained clots imaged with the use of scanning electron microscopy have well-separated fibers with an essentially random orientation (Fig. 3A, top image). When strain is applied (Fig. 3A, lower images), the fibers begin to align and the network orientational order parameter (*15*) increases gradually from 0.1 to 0.7 at a strain of ~2.5 (Fig. 3B).

Transmission electron microscopy of transverse sections through fibrin clots at increasing strain (Fig. 3C, insets) provides a clear picture

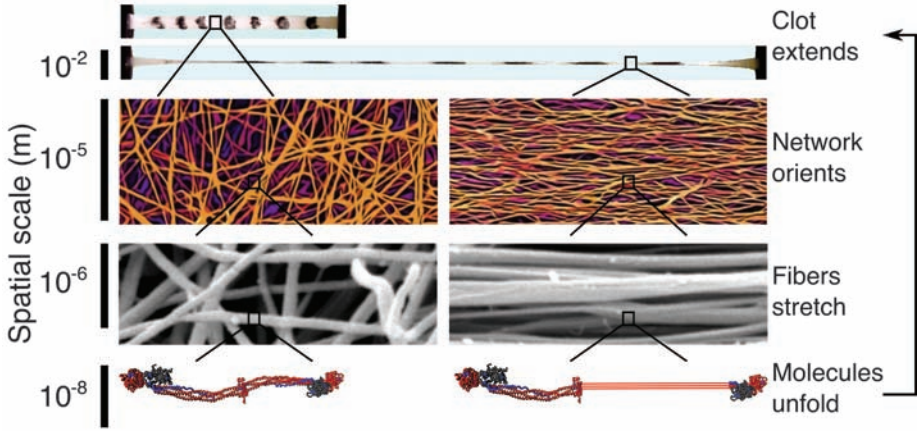

Fig. 1. Blood clots are highly extensible supramolecular protein polymers formed from well-separated, relatively straight and stiff fibers ~200 nm in diameter. When stretched (see movie S1), the fiber network aligns in the direction of the applied strain and the individual fibers stretch, forcing the fibrin monomers that make up the fibers to extend. Ultimately, it is this molecular unfolding that allows clots to stretch so far. Thus, understanding fibrin clot mechanics requires knowledge of the mechanical response and the corresponding structural changes spanning from the centimeter scale to the nanometer scale.

[1]Department of Physics and Astronomy, University of Pennsylvania, Philadelphia, PA 19104, USA. [2]Nano/Bio Interface Center, University of Pennsylvania, Philadelphia, PA 19104, USA. [3]Department of Cell and Developmental Biology, University of Pennsylvania School of Medicine, Philadelphia, PA 19104, USA. [4]Graduate Groups in Physics and Cell Biology and Physiology, University of Pennsylvania, Philadelphia, PA 19104, USA. [5]Department of Mechanical Engineering and Applied Mechanics, University of Pennsylvania, Philadelphia, PA 19104, USA.

*To whom correspondence should be addressed. E-mail: weisel@mail.med.upenn.edu

of how the fibers become thinner, closer together, and bundle. The area occupied by fibers increases from ~5 to 24% at a strain of 2 (Fig. 3C, graph). This increase is smaller than expected given the macroscopic shrinkage of the entire clot (see SOM), indicating that the volume decrease is a combined result of fiber bundling and a decrease in fiber diameter from 185 ± 36 to 74 ± 16 nm (mean ± SD, $P << 0.0001$, Student's t test). Similar transmission electron micrographs (although without corresponding scanning electron micrographs) of fiber ordering have been reported (*16*), but quantifying the strain dependence of these observations proves important below in constraining possible models. Furthermore, knowing the stress applied and the fractional cross section occupied by fibers allows for an estimate of the force per protofibril of ~75 pN at a strain of 2. Given the small loading rate that we used, this force is large enough to result in substantial unfolding of fibrin (*17*). Protein unfolding is generally associated with increased exposure of hydrophobic groups that would tend to interact (e.g., bundle) and expel water, as observed here.

The half-staggered packing of fibrin (Fig. 4A) leads to a ~22-nm repeat that can be measured by small-angle x-ray scattering (SAXS), and this measurement can be used as a readout of the molecular length (*18*). The position of the peak corresponding to the 22-nm spacing does not change substantially as the clot is stretched (Fig. 4B), ruling out a gradual extension of molecules during the stretch, which would otherwise increase this spacing, as suggested by Roska *et al*. (*19*). The marked increase in peak width that we observed indicates an increase in disorder that is consistent with an increasing number of molecules unfolding in response to the large strain. This increase in disorder is captured by the decrease in the Scherrer length L (Fig. 4C): The length over which the 22-nm repeat is correlated (*20*). A decrease in L indicates that the average size of the regions containing a consistent 22-nm repeat becomes smaller because of intervening regions of unfolded molecules. To control for the effect on L of fiber alignment that accompanies strain, we made magnetically prealigned samples in which the fibers were already oriented along the direction of applied strain. In this case, the decrease in L occurs at lower strains because fiber alignment cannot take up as much of the applied strain (Fig. 4C, blue circles). This change is reversible when fibers are allowed to relax (Fig. 4C, blue arrow). Similarly, to control for fiber sliding as an alternative mechanism of strain accommodation, we stretched samples that were not covalently ligated using factor XIIIa. Without ligation, protofibrils slide with respect to each other instead of stretching, and unfolding is suppressed (Fig. 4C, black circles). This behavior is expected for two-state extension in which some molecules extend completely while others remain folded, consistent with our earlier single-molecule observations of the forced unfolding of coiled coils

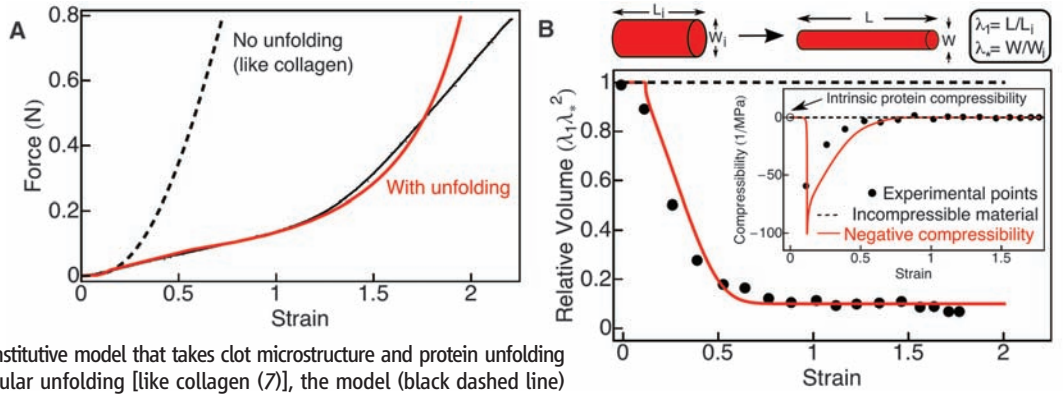

Fig. 2. (**A**) Representative force-extension curve of a cylindrical fibrin clot reaching a threefold longitudinal stretch. The average stretch before breaking was 2.7 ± 0.15–fold (mean ± SEM, $n = 6$ experiments). As the strain (stretched length/initial length − 1) increases, the force on the clot increases linearly until a strain of ~1.2 is reached, at which point the sample hardens and enters a new regime with a steeper slope (black solid line). The force-extension curve (black solid line) is fit using a constitutive model that takes clot microstructure and protein unfolding into account (red line). Without molecular unfolding [like collagen (*7*)], the model (black dashed line) rapidly diverges from the experimental data (black solid line). (**B**) The relative clot volume decreases with strain (black circles), in contrast to the behavior of an incompressible material (dashed black line). This decrease is predicted with the use of the same model and parameters that we used to fit the force-extension data (red line), demonstrating that the volume decrease occurs in parallel with molecular extension (SOM Eq. 29). A decreasing volume with increasing stretch corresponds to a negative compressibility (inset), which indicates that there is a source of free energy to drive contraction, possibly due to fiber bundling when hydrophobic side chains aggregate and bury after exposure during unfolding. The negative compressibility is a property of the network. Proteins in solution have been observed to have intrinsic compressibilities ~2×10^{-4} MPa^{-1} (open circle, inset) (*13*). L, length; L_i, initial length; W, width; W_i, initial width.

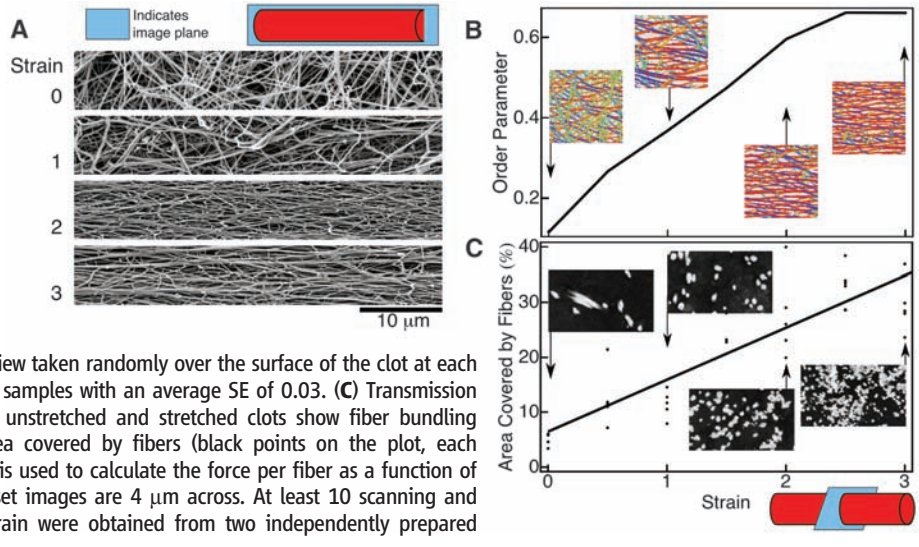

Fig. 3. Structural changes in stretched fibrin clots at the network and fiber levels. Scanning electron micrographs of stretched clots (**A**) show how the fibrin fibers align with strain. (**B**) These scanning electron micrographs are segmented using a Laplace of Gaussian filter that determines which pixels are fibers and which are background and also calculates the orientation θ at each fiber pixel. The inset images show the results of the segmentation with the color at each pixel corresponding to that pixel's orientation. These data are summarized as an orientational order parameter <cos(2θ)> that can range between 0 for randomly oriented fibers and 1 for perfectly aligned fibers (*14*). Data points are averages of five fields of view taken randomly over the surface of the clot at each strain. The order parameter was fairly uniform across samples with an average SE of 0.03. (**C**) Transmission electron micrographs of transverse sections through unstretched and stretched clots show fiber bundling (insets). The plot shows the total cross-sectional area covered by fibers (black points on the plot, each representing a randomly chosen field of view), which is used to calculate the force per fiber as a function of strain from the total force applied to the sample. Inset images are 4 μm across. At least 10 scanning and transmission electron microscope images at each strain were obtained from two independently prepared samples with similar results.

in fibrinogen oligomers (*17*). A more gradual unfolding has been observed in molecular dynamics simulations (*21*), but the coiled-coil spanning αC region is missing from published crystal structures of fibrinogen and is therefore not included in the simulation. Early wide-angle x-ray scattering measurements of fibrin clots support this view of molecular extension (*22*), providing evidence for a folding transition from α helix to β sheet, as has been observed for stretched keratin (*23*, *24*).

When these results are taken together, the following picture of fibrin mechanics emerges (Fig. 1). Because fibrin fibers are straight and relatively stiff, thermally induced bends are negligible, and so there is no slack to be pulled out upon extension. Instead, even at relatively low strains, the fibers themselves must begin to orient and stretch along the direction of the applied strain. The volume fraction of protein within the fibers has been estimated at ~20% (*25*), and the protofibrils that make up the fibers are known to adopt a twisted conformation (*26*) so that, at low strains, fibers could stretch somewhat by having protofibrils straighten and untwist within the fibers. However, to reach even a strain of ~0.15, unfolding must start to play a role. It is this structural transition that allows fibrin clots to maintain their linear response until strains of 1.2, at which point the coiled coils, or perhaps some other compact structures, are stretched to near their unfolded contour lengths, leading to strain hardening. The unfolded domains then interact and expel water, as many denatured proteins do.

To quantitatively test this mechanism, two approaches to model the stress-strain behavior of networks of semi-flexible filaments can be adapted for fibrin. A first model for random networks of folded proteins (*27*) uses a system of connected fibers. Although this model is not explicitly based on the microscopic structure of the network, it has been shown to accurately describe other random networks and serves to connect the microscopic and macroscopic processes. This leads to an expression for the force-extension (or stress-strain) relation of the network in terms of the force-extension relation of a single fiber. The molecules making up the fiber are modeled as two-state systems that can be either folded, in which case the fiber behaves as a linear spring, or unfolded, in which case it is modeled as a wormlike chain (*28*) (see SOM).

An alternative model of filamentous gels starts from the assumption that the networks are homogeneous and isotropic, and strain uniformly (*29*). Such a model can be used to compute the mechanical properties of the network after choosing a fiber force-extension curve as above. This model captures the trend in the data if buckling is taken into account by setting the force on a fiber to zero whenever it is under compression.

With either modeling approach, protein unfolding is required to fit the experimental data. Without unfolding, the fit rapidly diverges from the experimental force-extension curve (Fig. 2A, black dashed line). The fraction of folded domains n_f determined from the model correlates with the decreasing Scherrer length L observed with SAXS (Fig. 4D), providing further evidence that sample disordering is due to molecular extension. The divergence at high strains is probably due to unfolding of structures in the fibrin molecules other than coiled coils, which has been suggested as a possible mechanism to account for the extensibility of single fibrin fibers (*11*) and could be straightforwardly incorporated into our model to fit the force-extension data at the highest strains. In contrast, a linear model without unfolding fits collagen force extension data reasonably well (see SOM). This further highlights the uniqueness of fibrin's ability to balance large extensibility with a large pore size.

To account for the measured volume change in addition to the other results, we modified the first model (*27*) by associating a volume decrease with the unfolding transition. By matching the volume change at high strain, we determined the fractional volume change per domain and then, with no further fitting, the observed volume drop at low strain was captured using the same parameters as those used to fit the force-extension curve (compare Figs. 2B and 4D). The approximate fit to the negative peak in the compressibility (Fig. 2B, inset) further increases confidence in the model and again suggests a connection between clot shrinkage and an unfolding transition (SOM Eq. 29). A likely mechanism is aggregation that buries hydrophobic residues exposed during forced unfolding of protein (fig. S3).

Thus, it is the molecular extensibility of fibrin that allows clots' long straight fibers to extend and that endows them with essential properties, such as large pore sizes and low fibrin volume fraction in combination with extensibility. This allows for efficient permeation and lysis of clots (*5*) and maintenance of mechanical integrity in dynamic environments (e.g., platelet-induced clot retraction, skin and internal wounds that could stretch during healing, arterial thrombi, and pulsatory thrombotic aneurysms). The fact that these molecular transitions occur at small strains that cells can exert (*30*) and are manifested directly in the macroscopic mechanics of fibrin may represent a clear example of an important biological function of forced protein unfolding, as also

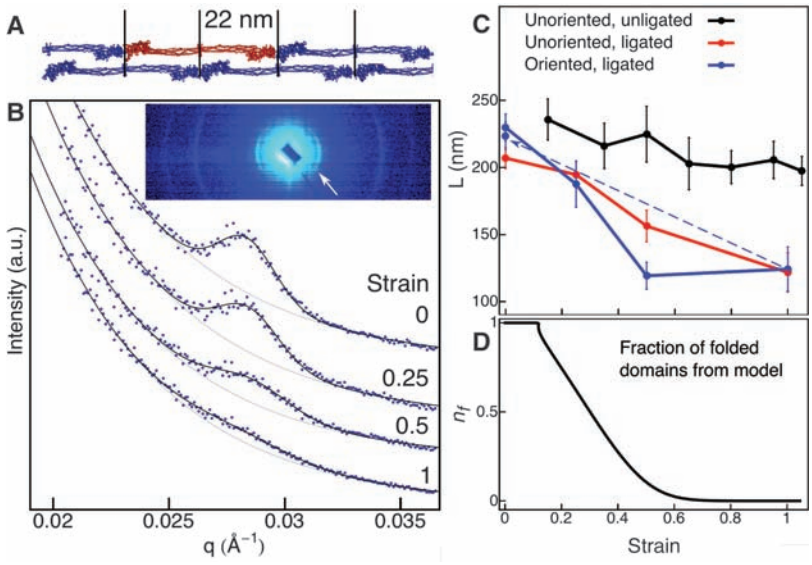

Fig. 4. Structural changes in stretched fibrin clots at the molecular level. (**A**) Schematic of a fibrin protofibril showing the half-staggered pattern that leads to a characteristic 22-nm repeat. A fibrin monomer within the protofibril is shown in red. (**B**) SAXS from fibrin clots leads to a clear first-order peak (white arrow, inset) and to third- and fourth-order peaks. The plots show the peak shape as a function of the wave vector $q = 2\pi/d$, which increases radially from the center (here, d is the fibrin periodicity, 22 nm). The thick lines are fits to the data using the sum of an exponential and a Gaussian with the exponential alone (thin lines) shown for comparison. The width of the peak increases with increasing stretch, which can be understood in terms of a two-state–like extension of fibrin molecules that introduce defects into the sample. a.u., arbitrary units. (**C**) This effect is quantified as the Scherrer length L, which decreases with increasing strain (red). The decrease is more rapid for samples that were prealigned in a magnetic field during polymerization (blue), which implies that network alignment accommodates some strain and delays unfolding. The transition is reversible when samples are allowed to relax, as indicated by the blue arrow. When samples are not ligated using factor XIIIa, protofibril sliding becomes important, and unfolding is decreased. In all cases, the peak position remains relatively constant, implying that there is no gradual lengthening of the whole population of fibrin monomers. Instead, there remains a population that is not unfolded and maintains a fairly constant spacing. Error bars indicate SDs of the distribution of L determined from fits using the bootstrap method. This bootstrap error is similar to the average SE of 15 nm calculated by averaging over results from four samples. (**D**) This behavior is captured by the constitutive model in which the fraction of folded monomers n_f decreases with increasing strain.

demonstrated for some proteins in stressed cells (*31*). Unfolded domains could be promising targets for modification in applications such as tissue engineering and cell biophysics, where stiffness is known to be important (*30*), and for designs of tougher fibrin sealants used in surgeries (*32*). Controlling unfolding could also lead to new strategies for breaking thrombi, perhaps by stabilizing the coiled coil, rendering clots more brittle for thrombectomy, or by destabilizing the coiled coil, making clots softer and less occlusive. Structural transitions observable at multiple scales may also be involved in the mechanics of other protein assemblies.

References and Notes

1. J. W. Weisel, in *Advances in Protein Chemistry*, vol. 70 (Academic Press, London, 2005), pp. 247–299.
2. N. Laurens, P. Koolwijk, M. P. M. DeMaat, *J. Thromb. Haemost.* **4**, 932 (2006).
3. R. W. Colman *et al*., *Hemostasis and Thrombosis: Basic Principles and Clinical Practice* (Lippincott Williams & Wilkins, Philadelphia, 2005).
4. J. W. Weisel, *Biophys. Chem.* **112**, 267 (2004).
5. J. P. Collet *et al*., *Arterioscler. Thromb. Vasc. Biol.* **20**, 1354 (2000).
6. D. A. Gabriel, K. Muga, E. M. Boothroyd, *J. Biol. Chem.* **267**, 24259 (1992).
7. B. A. Roeder *et al*., *J. Biomech. Eng.* **124**, 214 (2002).
8. Materials and methods are available as supporting material on *Science* Online.
9. P. A. Janmey, E. J. Amis, J. D. Ferry, *J. Rheol.* **27**, 135 (1983).
10. The clots typically break where they are clamped, suggesting that the true clot extensibility is larger than that measured here.
11. W. Liu *et al*., *Science* **313**, 634 (2006).
12. L. R. G. Treloar, *The Physics of Rubber Elasticity* (Clarendon, Oxford, 1975).
13. D. P. Kharakoz, *Biophys. J.* **79**, 511 (2000).
14. H. Kang *et al*., *J. Phys. Chem. B* **113**, 3799 (2009).
15. The orientational order parameter is defined as $\langle \cos 2\theta \rangle$, where θ is the angle of the fiber determined at each fiber pixel (see SOM for a description of the analysis algorithm).
16. M. F. Müller, H. Ris, J. D. Ferry, *J. Mol. Biol.* **174**, 369 (1984).
17. A. E. X. Brown, R. I. Litvinov, D. E. Discher, J. W. Weisel, *Biophys. J.* **92**, L39 (2007).
18. L. Stryer, C. Cohen, R. Langridge, *Nature* **197**, 793 (1963).
19. F. J. Roska, J. D. Ferry, J. S. Lin, J. W. Anderegg, *Biopolymers* **21**, 1833 (1982).
20. L. E. Alexander, *X-Ray Diffraction Methods in Polymer Science* (Wiley, Hoboken, NJ, 1979).
21. B. B. C. Lim, E. H. Lee, M. Sotomayor, K. Schulten, *Structure* **16**, 449 (2008).
22. K. Bailey, W. T. Astbury, K. M. Rudall, *Nature* **151**, 716 (1943).
23. W. T. Astbury, H. J. Woods, *Proc. R. Soc. London Ser. B Biol. Sci.* **114**, 314 (1934).
24. J. W. S. Hearle, *Int. J. Biol. Macromol.* **27**, 123 (2000).
25. W. A. Voter, C. Lucaveche, H. P. Erickson, *Biopolymers* **25**, 2375 (1986).
26. J. W. Weisel, C. Nagaswami, L. Makowski, *Proc. Natl. Acad. Sci. U.S.A.* **84**, 8991 (1987).
27. H. J. Qi, C. Ortiz, M. C. Boyce, *J. Eng. Mater. Technol.* **128**, 509 (2006).
28. C. Bustamante, J. F. Marko, E. D. Siggia, S. Smith, *Science* **265**, 1599 (1994).
29. C. Storm *et al*., *Nature* **435**, 191 (2005).
30. D. E. Discher, P. Janmey, Y.-l. Wang, *Science* **310**, 1139 (2005).
31. C. P. Johnson, H.-Y. Tang, C. Carag, D. W. Speicher, D. E. Discher, *Science* **317**, 663 (2007).
32. D. M. Albala, *Cardiovasc. Surg.* **11**, 5 (2003).

33. We thank P. Heiney for help with the x-ray diffraction measurements (NSF–Materials Research Science and Engineering Center partial support); C. Nagaswami for scanning electron microscopy; D. Galanakis for his gift of fibrinogen; S. Pickup for access to the magnet facility; A. Kota for help with the tensile testing; J. Torbet for discussions of x-ray diffraction and magnetic alignment; and P. Janmey, T. Lubensky, H. Shuman, and C. Storm for useful discussions. This work was supported by NIH (grants HL090774 and HL30954 to J.W.W. and grant HL62352 to D.E.D.) and by the Nano/Bio Interface Center through NSF Nanoscale Science and Engineering Center (grant DMR-0425780). A.E.X.B. was supported by a scholarship from the Natural Sciences and Engineering Research Council of Canada.

Supporting Online Material

www.sciencemag.org/cgi/content/full/325/5941/741/DC1
Materials and Methods
SOM Text
Figs. S1 to S11
References
Movie S1

18 February 2009; accepted 19 June 2009
10.1126/science.1172484

The C-Ala Domain Brings Together Editing and Aminoacylation Functions on One tRNA

Min Guo, Yeeting E. Chong, Kirk Beebe,* Ryan Shapiro, Xiang-Lei Yang, Paul Schimmel†

Protein synthesis involves the accurate attachment of amino acids to their matching transfer RNA (tRNA) molecules. Mistranslating the amino acids serine or glycine for alanine is prevented by the function of independent but collaborative aminoacylation and editing domains of alanyl-tRNA synthetases (AlaRSs). We show that the C-Ala domain plays a key role in AlaRS function. The C-Ala domain is universally tethered to the editing domain both in AlaRS and in many homologous free-standing editing proteins. Crystal structure and functional analyses showed that C-Ala forms an ancient single-stranded nucleic acid binding motif that promotes cooperative binding of both aminoacylation and editing domains to $tRNA^{Ala}$. In addition, C-Ala may have played an essential role in the evolution of AlaRSs by coupling aminoacylation to editing to prevent mistranslation.

The algorithm of the genetic code is established in the first reaction of protein synthesis. In this reaction, aminoacyl–transfer RNA (tRNA) synthetases (AARSs) catalyze the attachment of amino acids to their cognate tRNAs that bear the triplet anticodons of the genetic code. When a tRNA is acylated with the wrong amino acid, mistranslation occurs if the misacylated tRNA is released from the synthetase, captured by elongation factor, and used at the ribosome for peptide synthesis. To prevent mistranslation, some AARSs have separate editing activities that hydrolyze the misacylated amino acid from the tRNA (*1*–*3*). Because an editing-defective tRNA synthetase is toxic to bacterial and mammalian cells (*4*, *5*) and is causally linked to disease in animals (*6*), strong selective pressure retains these editing activities throughout evolution.

A particular challenge appears to be avoiding mistranslation of serine or glycine for alanine. All three kingdoms of life contain free-standing editing-proficient homologs of the editing domains found in alanyl-tRNA synthetases (AlaRSs) (*7*). These proteins, known as AlaXps, provide functional redundancy by capturing mischarged $tRNA^{Ala}$ molecules that escape the embedded editing activities of AlaRSs (*8*). Although free-standing editing domains have counterparts in ThrRS and ProRS (*7*, *9*, *10*), they are not as evolutionarily conserved as AlaXps. Moreover, enzymes like LeuRS, IleRS, and ValRS lack any free-standing editing domain counterparts (*1*, *2*, *11*, *12*). Despite the multiple checkpoints to prevent mischarging of $tRNA^{Ala}$, we did not know how the apparatus for preventing confusion of serine and glycine for alanine was assembled. To pursue this question, we focused on a third domain separate from the editing and aminoacylation domains, known as C-Ala, which is found in all AlaRSs and is tethered to their editing domains.

The modular arrangement of domains in AlaRSs is evolutionarily conserved (*13*) (Fig. 1A). The N-terminal aminoacylation domain is active as an isolated fragment, and its three-dimensional structure is that of a typical class II AARS. The central editing domain is homologous to the editing domain of the class II ThrRS (*14*, *15*). Lastly, a linker tethers the third (C-Ala) domain to the editing domain. In contrast to the other two domains, C-Ala is only loosely conserved and its structure is unknown. On the basis of a survey of AlaRS sequences, we predicted that a fragment corresponding to residues 766 to 875 of *Escherichia coli* AlaRS would form a structural unit (Fig. 1B). The corresponding region of *Aquifex aeolicus* AlaRS is the 110–amino acid fragment encompassing residues 758 to 867, which was expressed in *E. coli*, purified, and crystallized (*16*). The structure was solved to a resolution of 1.85 Å

The Skaggs Institute for Chemical Biology and the Department of Molecular Biology, The Scripps Research Institute, BCC-379, 10550 North Torrey Pines Road, La Jolla, CA 92037, USA.

*Present address: Metabolon, Incorporated, 800 Capitola Drive, Suite 1, Durham, NC 27713, USA.

†To whom correspondence should be addressed. E-mail: schimmel@scripps.edu

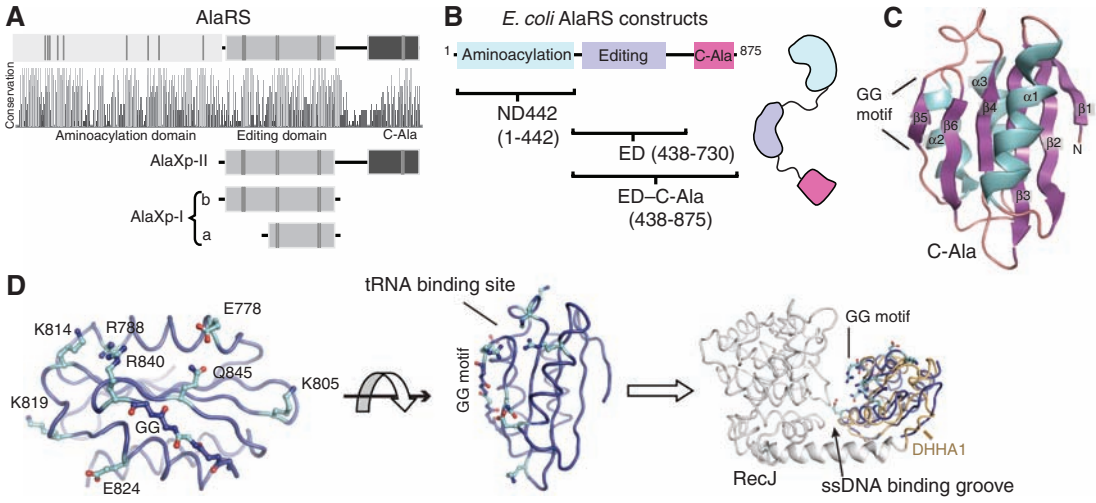

Fig. 1. General design of AlaRS and C-Ala structure. (**A**) Highly conserved AlaRS domain scheme throughout evolution. Conservation panel shows the relative sequence identity of the 410 aligned AlaRS sequences. Some strictly conserved amino acids in each group are shown as gray vertical bars. (**B**) Constructs of *E. coli* AlaRS used in this paper. (**C**) The overall structure of *A. aeolicus* C-Ala. (**D**) The C-terminal half (809 to 879 region) contains relatively conserved surface residues that face the single-strand nucleic acid binding groove (*19*) when C-Ala (blue) is superimposed onto the DHHA1 domain (yellow) of RecJ (gray).

(table S1) and showed a globular domain having an α/β-fold and composed of a central six-stranded β-antiparallel sheet flanked by two α helices on one side and one α helix on the other (Fig. 1C). Although sequences of C-Ala are highly diverged, structural constraints are seen. The highly conserved Gly^{838}-Gly^{839} in β5 (fig. S1A) allows a sharp turn that would be disallowed for non-Gly residues (Fig. 1C and fig. S1B). The following residue (Arg^{840} in *A. aeolicus* C-Ala) is fixed by this sharp turn with its side chain positioned upward, at the center of the proposed nucleic acid binding interface (see below). This Arg (or Lys) is universally conserved in AlaRSs. Given that strand β5 has to be exposed for binding with tRNA, the bulged GG motif additionally prevents intermolecular edge-to-edge aggregation, which occurs easily between solvent accessible β-strand edges (*17*). Except for the GG motif, four well-conserved residues (Val^{812}, Ala^{822}, Gly^{848}, and Ala^{857}) form the hydrophobic core of C-Ala, with other residues only generally conserved in type (fig. S1A). This conservation is consistent with C-Ala domains in all AlaRSs folding into a similar structure.

The distal portion of C-Ala (799 to 869) is annotated as a DHHA1 domain (as seen in the single strand exonuclease RecJ) in the PFAM bioinformatics database (*18*). Although this segment is represented in the C-terminal half of our solved C-Ala structure, the structure of the remainder of C-Ala cannot be estimated from the PFAM database. In spite of low sequence similarity, C-Ala and DHHA1 of RecJ are closely similar structures [root mean squre deviation = 2.0 Å over the 97 Cα positions (fig. S1D)] and are true homologs (fig. S1, B to E). The DHHA1 domain in RecJ binds to single-stranded DNA by forming a central groove with the N-terminal nuclease domain (*19*). Superimposing C-Ala with the phosphoesterase DHH subfamily 1–associated (DHHA1) domain of RecJ revealed that the conserved GG of strand β5 in C-Ala is oriented toward this groove, as is the GG motif of the corresponding β-strand of DHHA1 (Fig. 1D). Relatively conserved surface residues (Glu^{778}, Arg^{781}, Lys^{805}, Arg^{827}, Arg^{840}, and Gln^{845}) in C-Ala are all

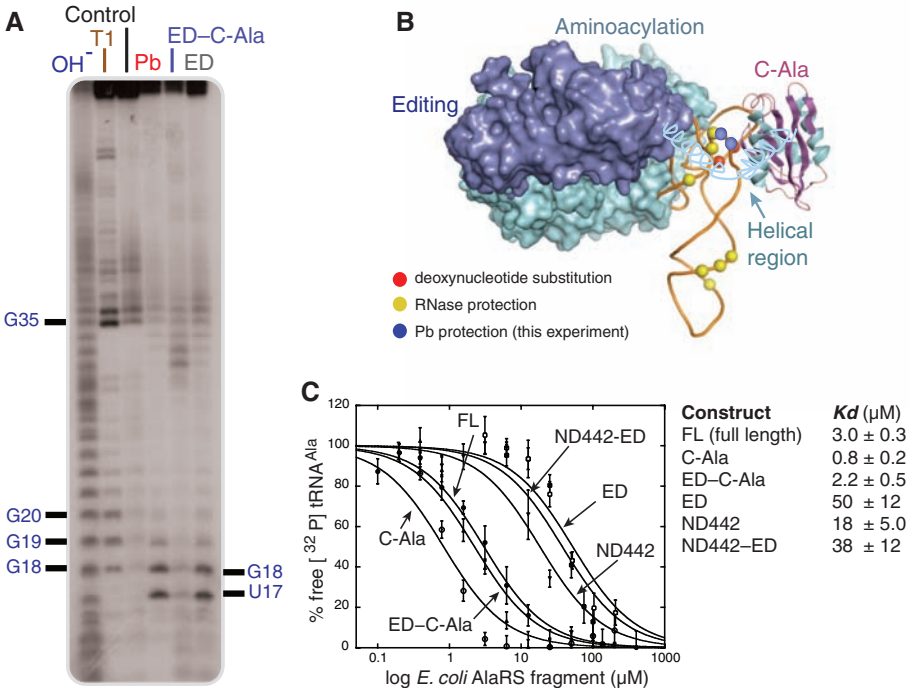

Construct	*Kd* (μM)
FL (full length)	3.0 ± 0.3
C-Ala	0.8 ± 0.2
ED–C-Ala	2.2 ± 0.5
ED	50 ± 12
ND442	18 ± 5.0
ND442–ED	38 ± 12

Fig. 2. C-Ala targets the elbow of tRNA^{Ala} and is the major binding module of AlaRS. (**A**) Lead footprinting of 5′-[^{32}P]-tRNA^{Ala}. Two sites, U17 and G18 on tRNA^{Ala}(UGC) transcript, were cleaved by lead ion and specifically protected by ED–C-Ala but not by ED. (**B**) Model of full-length AlaRS-tRNA^{Ala} complex. The detected contacts are shown as spheres on the tRNA model. (**C**) Retardation of electrophoretic mobility of 3′-[^{32}P]-tRNA^{Ala} by binding of specific fragments of *E. coli* AlaRS. Shown are full-length (FL) AlaRS (●), C-Ala (○), ED–C-Ala (▲), ED (□), ND442 (▼), and ND442–ED (■). The equilibrium response at each concentration was fitted to a single-site binding model. Error bars are SDs from triplicates.

clustered around the side formed by the GG motif (Fig. 1D), and most are restricted to strong hydrogen donors [R, K, or Q (*20*)]. Thus, C-Ala most likely uses this side of the GG motif to bind to tRNA.

We predicted that C-Ala binds to the elbow of the L-shaped tRNA formed by the D and T loops (fig. S2). This prediction was confirmed by footprinting tRNA^{Ala} with use of a lead cleavage as a probe. Fragments of AlaRS comprising the editing domain (ED), with and without tethered C-Ala (ED–C-Ala) (Fig. 1B), were compared by the lead-cleavage pattern of tRNA^{Ala}, which showed that C-Ala specifically protected the D-loop moiety of the tRNA^{Ala} elbow (Fig. 2A). Although mischarged (with Ser or Gly) tRNA^{Ala} is deacylated by AlaRS, a similarly mischarged truncated tRNA^{Ala} substrate lacking the tRNA elbow cannot be deacylated (*21*). Thus, C-Ala appears to specifically recognize the L shape (Fig. 2B).

Electrophoretic mobility shift assays (EMSA) measured binding of all domains and domain combinations to tRNA^{Ala} (Fig. 2C). The binding affinity of full-length AlaRS was modest [K_d = 3.0 ± 0.3 μM

(SEM)] and close to the measured Michaelis constant for tRNA aminoacylation [$tRNA^{Ala}$(UGC), K_M = 2.8 μM] (*22*). Constructs that had either the aminoacylation domain (ND442) or ED alone had lower affinity for $tRNA^{Ala}$, with K_d values of 18 μM and 50 μM, respectively (Fig. 2C). Fusing these two domains together (ND442-ED) gave a K_d that was intermediate to the individual K_d values (38 μM), suggesting that, when the domains are combined, energetic binding contributions of each are partly cancelled out [presumably a conformational change that costs some energy (*23*)]. Furthermore, C-Ala bound to tRNA with a relatively high affinity (K_d = 0.8 μM), and ED–C-Ala bound $tRNA^{Ala}$ with almost the same K_d (2.2 μM) as that of full-length enzyme. Thus, C-Ala is important for binding $tRNA^{Ala}$.

In all AlaRSs, C-Ala is tethered to the ED by a linker that is a predicted α-helical coiled-coil. Without C-Ala, editing activity for ED was reduced to ~1/1000 of *E. coli* AlaRS (*8*). As mentioned above, the linker and C-Ala have high sequence diversity across species. To examine the functional conservation of C-Ala in AlaRS, we fused C-Ala from *A. aeolicus* to ED of *E. coli* AlaRS. The editing activity was boosted from about 0.1% to about 10% of native AlaRS. Including the linker in the swap further boosted the activity to about 20% of the *E. coli* enzyme. Grafting C-Ala and its linker from human AlaRS to ED of *E. coli* AlaRS gave nearly full activity for clearance of Ser-$tRNA^{Ala}$ (Fig. 3). Thus, a conserved function for C-Ala and the linker that tethers it to ED is likely.

The modular arrangement of functional domains along the sequences of AlaRSs (Fig. 1A) might have arisen from fusions of genes encoding separable domains. Selective pressure for fusion would come from advantages of having domains cooperate beneficially. To investigate this question, we split *E. coli* AlaRS into halves: ND442 and ED–C-Ala (Fig. 4A). Consistent with the two domains functioning independently (*8*, *24*), we could detect no interaction between them with two different assays. To investigate whether the two domains could assemble onto one tRNA, we performed gel shift assays with 3′-end radiolabeled *E. coli* $tRNA^{Ala}$ in the presence of ND442, ED–C-Ala, or both. We first established a concentration of ED–C-Ala that allowed formation of a stable binary complex with $tRNA^{Ala}$. Next, we added an amount of ND442 that was insufficient to form a complex with $tRNA^{Ala}$ by itself. Under these conditions, a ternary complex was formed, with the amount of ternary complex increasing with the con-

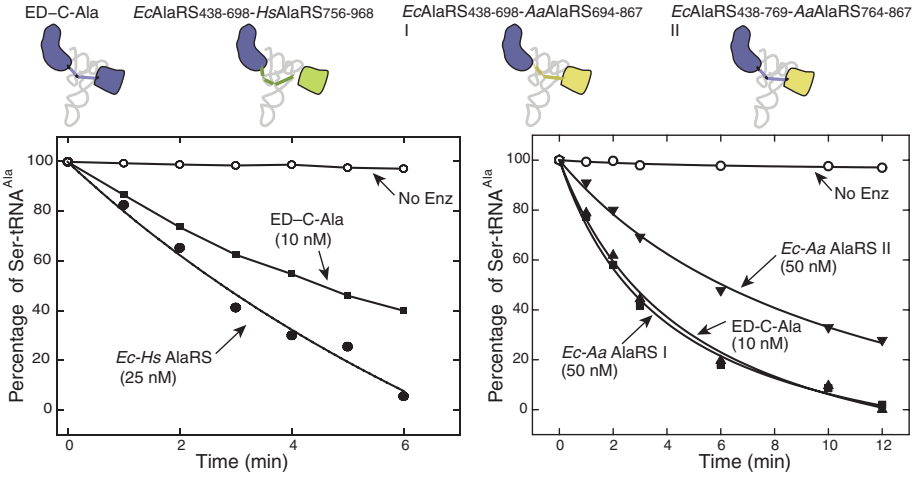

Fig. 3. The C-terminal region is functionally conserved. (**Top**) Four different domain-swapped AlaRS constructs. (**Bottom**) Deacylation of Ser-$tRNA^{Ala}$. Shown are *E. coli* ED–C-Ala (■), *E. coli* $AlaRS_{438-698}$–*Homo sapiens* $AlaRS_{756-968}$ (*Ec-Hs*) (●), *E. coli* $AlaRS_{438-698}$–*A. aeolicus* $AlaRS_{694-867}$ (*Ec-Aa* I) (▼), *E. coli* $AlaRS_{438-769}$–*A. aeolicus* $AlaRS_{764-867}$ (*Ec-Aa* II) (▲), and no enzyme control (○).

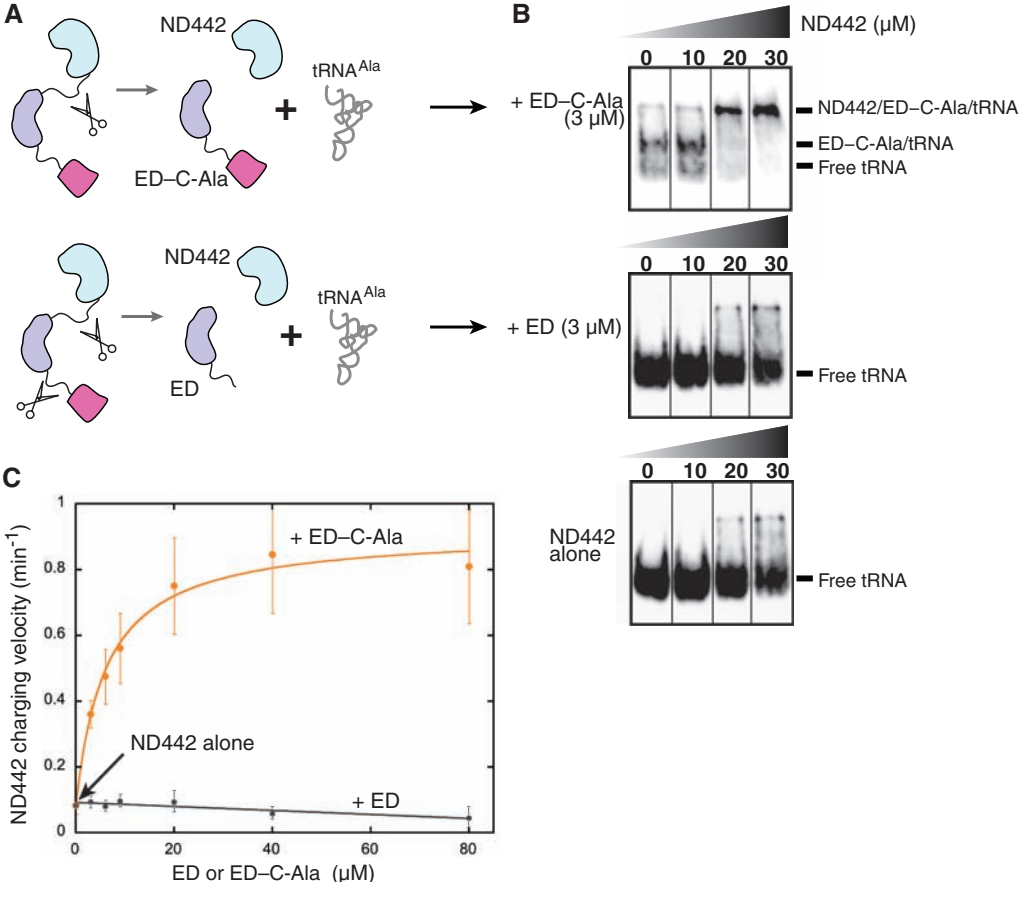

Fig. 4. C-Ala brings together the editing center and aminoacylation domain on $tRNA^{Ala}$. (**A**) Schematic diagrams are shown with *E. coli* AlaRS broken into halves and used for characterizing the possible cooperativity in the experiments below. (**B**) C-Ala–dependent ternary complex formation. Polyacrylamide gel electrophoresis of mixtures containing 0.1 μM of 3′-[^{32}P]-$tRNA^{Ala}$, 3.0 μM ED–C-Ala or ED, and increasing amounts of fragment ND442. (**C**) Specific enhancement of ND442 aminoacylation activity by ED–C-Ala, but not by ED. Error bars are SDs from triplicates.

centration of ND442 (Fig. 4B). Thus, ternary complex formation is cooperative; that is, binding of ND442 is promoted by the presence of ED–C-Ala.

A parallel experiment showed that deletion of C-Ala from ED–C-Ala severely reduced binding of ED to $tRNA^{Ala}$ and thus also eliminated formation of the ternary complex (Fig. 4B). Collectively, these data show that $tRNA^{Ala}$ serves as a bridge to cooperatively bring together editing and aminoacylation centers and that the ability of $tRNA^{Ala}$ to play this role is C-Ala–dependent. To further validate these conclusions, we checked whether C-Ala–dependent ternary complex formation could facilitate the activity of the aminoacylation domain. A series of concentrations of ED–C-Ala (3 to 80 μM) were incubated together with ND442 in the aminoacylation assay (Fig. 4C). Dramatic enhancement of ND442 aminoacylation activity was induced upon addition of ED–C-Ala, with an apparent K_d of 6.1 ± 1.2 μM (this "functional" apparent K_d is comparable to the estimated K_d of 2.2 ± 0.5 μM from EMSA analysis, Fig. 2C). Adding bovine serum albumin (10 μM) to the system slightly decreased the apparent activity in all assays, with no change to the effect of ED–C-Ala on the activity of ND442 (fig. S4A). Although ED is able to bind weakly to $tRNA^{Ala}$ (K_d = 50 μM), when high concentrations (80 μM) of ED were added no enhancement of ND442 aminoacylation activity was seen (Fig. 4C and fig. S4C). Thus, C-Ala brings together aminoacylation and editing domains to bind simultaneously to the acceptor stem (Fig. 4D). Without C-Ala, the binding of tRNA to ND442 and ED is not able to make editing collaborative with aminoacylation.

A docking model positions the aminoacylation and editing domains on opposite sides of the tRNA acceptor stem, where they each make contact with the G3•U70 base pair with use of both major and minor grooves of $tRNA^{Ala}$ (Fig. 2B and fig. S2). Earlier experiments showed that both aminoacylation and editing were sensitive to the same G•U pair (*8*, *25*, *26*), and it is now shown that C-Ala provides the architecture for bringing together the two domains on the same RNA helix. In this way, the editing domain checks for mischarging by picking out tRNAs that have Gly or Ser and a G3•U70 pair. Because G3•U70 is specific to $tRNA^{Ala}$ molecules and thus marks a tRNA as specific for alanine, the editing domain (before being coupled to the aminoacylation domain) could easily pick out in trans those $tRNA^{Ala}$s that are mischarged with Gly or Ser and avoid clearing Gly or Ser from their cognate tRNAs ($tRNA^{Gly}$ and $tRNA^{Ser}$, respectively). C-Ala is distinct from any other tRNA binding domain, including the EMAPII/Trbp111 domain (*27*), C domain of LeuRS (*28*, *29*), and N domain of human LysRS (*30*), which also bind to the elbow region of tRNAs. Additionally, these domains are not linked to both a synthetase and a free-standing editing domain and are not known to promote collaboration between editing and aminoacylation functions.

Three types (Ia, Ib, and II) of free-standing genome-encoded AlaXps are widely distributed in all three kingdoms of life and act in trans to clear $tRNA^{Ala}$ mischarged with Ser or Gly (*7*, *8*, *31*, *32*). Type Ia AlaXp lacks the Gly-rich motif near the N terminus of the editing motif of type Ib and type II AlaXps (*33*). However, unlike types Ia and Ib AlaXps that are composed of just the editing domain, type II AlaXp has the C-Ala domain (Fig. 1A). A highly resolved phylogenetic tree shows the expected canonical patterns of ThrRS and AlaRS, where the bacterial versions are specifically related to, but deeply separated from, eukaryotic lineages (fig. S5) (*34*). This phylogenetic analysis implies that all three forms of AlaXp evolved in the ancestral community. This phylogeny also suggests that AlaXp-II is derived from AlaXp-I. The editing domain of ThrRS is closest to AlaXp-I, thus suggesting an early separation that split the original editing enzyme into two different specificities, one for $tRNA^{Thr}$ and the other for $tRNA^{Ala}$. Most importantly, the phylogenetic analysis indicates that the editing domain of AlaRS appeared concurrently with the ancient, most-developed, and largest free-standing editing enzyme, the C-Ala–containing AlaXp-II. Thus, C-Ala may have been instrumental in bringing together editing and aminoacylation domains on one tRNA to ultimately (through fusion) create AlaRS (fig. S6).

References and Notes

1. O. Nureki *et al.*, *Science* **280**, 578 (1998).
2. S. Fukai *et al.*, *Cell* **103**, 793 (2000).
3. A. Dock-Bregeon *et al.*, *Cell* **103**, 877 (2000).
4. V. Döring *et al.*, *Science* **292**, 501 (2001).
5. L. A. Nangle, C. M. Motta, P. Schimmel, *Chem. Biol.* **13**, 1091 (2006).
6. J. W. Lee *et al.*, *Nature* **443**, 50 (2006).
7. I. Ahel, D. Korencic, M. Ibba, D. Söll, *Proc. Natl. Acad. Sci. U.S.A.* **100**, 15422 (2003).
8. K. Beebe, M. Mock, E. Merriman, P. Schimmel, *Nature* **451**, 90 (2008).
9. F. C. Wong, P. J. Beuning, C. Silvers, K. Musier-Forsyth, *J. Biol. Chem.* **278**, 52857 (2003).
10. D. Korencic *et al.*, *Proc. Natl. Acad. Sci. U.S.A.* **101**, 10260 (2004).
11. L. F. Silvian, J. Wang, T. A. Steitz, *Science* **285**, 1074 (1999).
12. R. Fukunaga, S. Yokoyama, *Nat. Struct. Mol. Biol.* **12**, 915 (2005).
13. L. Ribas De Pouplana, K. Musier-Forsyth, P. Schimmel, in *The Aminoacyl-tRNA Synthetases*, M. Ibba, C. Francklyn, S. Cusack, Eds. (Eurekah, Georgetown, TX, 2005), pp. 241–246.
14. R. Sankaranarayanan *et al.*, *Cell* **97**, 371 (1999).
15. K. Beebe, L. Ribas De Pouplana, P. Schimmel, *EMBO J.* **22**, 668 (2003).
16. Materials and methods are available as supporting material on *Science* Online.
17. J. S. Richardson, D. C. Richardson, *Proc. Natl. Acad. Sci. U.S.A.* **99**, 2754 (2002).
18. R. D. Finn *et al.*, *Nucleic Acids Res.* **36**, D281 (2008).
19. A. Yamagata, Y. Kakuta, R. Masui, K. Fukuyama, *Proc. Natl. Acad. Sci. U.S.A.* **99**, 5908 (2002).
20. Single-letter abbreviations for the amino acid residues are as follows: E, Glu; K, Lys; Q, Gln; and R, Arg.
21. K. Beebe, E. Merriman, P. Schimmel, *J. Biol. Chem.* **278**, 45056 (2003).
22. Y. M. Hou, P. Schimmel, *Biochemistry* **28**, 4942 (1989).
23. A. J. Gale, J. P. Shi, P. Schimmel, *Biochemistry* **35**, 608 (1996).
24. M. Jasin, L. Regan, P. Schimmel, *Nature* **306**, 441 (1983).
25. D. D. Buechter, P. Schimmel, *Biochemistry* **32**, 5267 (1993).
26. M. A. Swairjo *et al.*, *Mol. Cell* **13**, 829 (2004).
27. T. Nomanbhoy *et al.*, *Nat. Struct. Biol.* **8**, 344 (2001).
28. R. Fukunaga, S. Yokoyama, *Biochemistry* **46**, 4985 (2007).
29. J. L. Hsu, S. A. Martinis, *J. Mol. Biol.* **376**, 482 (2008).
30. M. Francin, M. Kaminska, P. Kerjan, M. Mirande, *J. Biol. Chem.* **277**, 1762 (2002).
31. M. Sokabe, A. Okada, M. Yao, T. Nakashima, I. Tanaka, *Proc. Natl. Acad. Sci. U.S.A.* **102**, 11669 (2005).
32. Y. E. Chong, X. L. Yang, P. Schimmel, *J. Biol. Chem.* **283**, 30073 (2008).
33. R. Fukunaga, S. Yokoyama, *Acta Crystallogr.* **D63**, 390 (2007).
34. C. R. Woese, G. J. Olsen, M. Ibba, D. Söll, *Microbiol. Mol. Biol. Rev.* **64**, 202 (2000).

35. Supported by NIH grant GM 15539 and by a fellowship from the National Foundation for Cancer Research. The atomic coordinates have been deposited in the Protein Data Bank (PDB ID:3G98).

Supporting Online Material

www.sciencemag.org/cgi/content/full/325/5941/744/DC1
Materials and Methods
Figs. S1 to S6
Table S1
References

31 March 2009; accepted 23 June 2009
10.1126/science.1174343

Generalized Models Reveal Stabilizing Factors in Food Webs

Thilo Gross,[1]* Lars Rudolf,[1] Simon A. Levin,[2,3] Ulf Dieckmann[4]

Insights into what stabilizes natural food webs have always been limited by a fundamental dilemma: Studies either need to make unwarranted simplifying assumptions, which undermines their relevance, or only examine few replicates of small food webs, which hampers the robustness of findings. We used generalized modeling to study several billion replicates of food webs with nonlinear interactions and up to 50 species. In this way, first we show that higher variability in link strengths stabilizes food webs only when webs are relatively small, whereas larger webs are instead destabilized. Second, we reveal a new power law describing how food-web stability scales with the number of species and their connectance. Third, we report two universal rules: Food-web stability is enhanced when (i) species at a high trophic level feed on multiple prey species and (ii) species at an intermediate trophic level are fed upon by multiple predator species.

Understanding the dynamic properties of food webs is a problem of both theoretical and practical importance (*1*–*16*), especially as concerns about the robustness of natural systems escalate. Further, the discovery of stabilizing factors in food webs can yield much-needed design principles for institutional networks (*17*). Robert May (*1*) showed that randomly assembled webs became less robust (measured in terms of their dynamical stability) as their complexity (measured in terms of the number of interacting species and their connectivity) increased. Although it has often been

pointed out that food webs can persist in nonstationary states, there is growing evidence that May's stability-complexity relationship also holds for nonstationary dynamics (*18*). Moreover, population cycles or external forcing averages out if food webs are considered on longer time scales, so that time-averaged dynamics can be considered as stationary. However, detailed investigations aiming at a deeper understanding of what makes food webs robust have generally been hampered by computational constraints (*12*). We avoided these constraints through the use of generalized modeling (GM) (*19*, *20*).

For a given class of mathematical models, GM identifies parameters that together capture the local stability properties of all stationary states. Some of these parameters (scale parameters) quantify the scaling of biomass fluxes, whereas others (exponent parameters) quantify the nonlinearity of model functions. For any given model, the GM parameters can be expressed as functions of conventional model parameters. More importantly, however, the GM parameters are directly interpretable in their own right. To capture the complexity of real-world problems, the number of GM parameters is often large. Yet, the numerical performance of GM is so favorable that billions of randomly chosen replicates, defined by sample sets of GM parameters, can be analyzed.

Our study focuses on realistic food-web topologies generated by the niche model (*20*, *21*). The dynamics of the population density X_i of each species $i = 1,\ldots,N$ follows a differential equation of the form

$$\dot{X}_i = S_i(X_i) + F_i(X_1, \ldots, X_N) - M_i(X_i) - \sum_{j=1}^{N} G_{ij}(X_1, \ldots, X_N)$$

where S_i, F_i, M_i, and G_{ij} are nonlinear functions describing the gain due to primary production, the gain due to predation, the loss due to natural mortality, and the loss due to predation, respectively. We do not restrict these functions to any specific functional form but rather consider the whole class of such models. The production term is assumed to vanish for all species except producers, whereas the predation gain vanishes for producers. Similarly, the predation loss is 0 for top predators, whereas natural mortality is assumed to be negligible for all species except top predators. Finally, a relationship between the gain of a predator and the loss of its prey species is assumed that is consistent with passive prey switching. GM parameters for this class of models have been derived before (*19*) and are listed together with their interpretations in table S1.

To assess the dependence of food-web stability on the exponent parameters, we generated a sample of 10^8 food webs with a fixed number of species. In this sample, we drew the exponent parameters independently and randomly from suitable uniform distributions, whereas we computed the topological parameters from randomly generated niche-model topologies (*20*, *21*). We estimated the average impact of an exponent parameter on stability by computing the correlation between that parameter and local stability (*20*). Results for food webs with 10, 20, and 30 species, shown in Fig. 1, reveal the following: The sensitivity of predation to prey density (γ) and the sensitivity of top-predator mortality to top-predator density (μ) correlate positively with stability. This corresponds to the well-known fact that low saturation of predators and nonlinear (for example, quadratic) mortality promote stability (*12*). In contrast, the sensitivity of primary production to the number of primary producers (ϕ) and the sensitivity of predation to predator density (ψ) are negatively correlated with stability. This confirms that stability increases when primary production is strongly limited by external factors such as nutrient availability or when predation pressures are not very sensitive to predator density (*22*). The range of turnover rates (α_{scale}) as well as the total range of niche values (n_{range}) do not correlate with stability. However, increasing the average difference between the niche values of a predator and its prey (n_{diff}) has a stabilizing effect (*12*). Our analysis also confirms that the number of links, and therefore a food web's connectivity, is negatively correlated with stability.

As a next step, we set all exponent parameters to realistic values (table S1) and focused on the effects of food-web topology on stability. We began by investigating how stability is affected by the relationship between the number of species (N) and the number of links (L). For better comparison, we express the number of links in terms of the connectance $C = \frac{L}{N(N-1)}$. We generated samples by means of random niche-model topologies, with N and C changing on a logarithmic grid. At every vertex of this grid, we computed the proportion of stable webs (PSW), which describes the probability of randomly drawing a stable food web from our sample. Figure 2 shows PSW results computed from

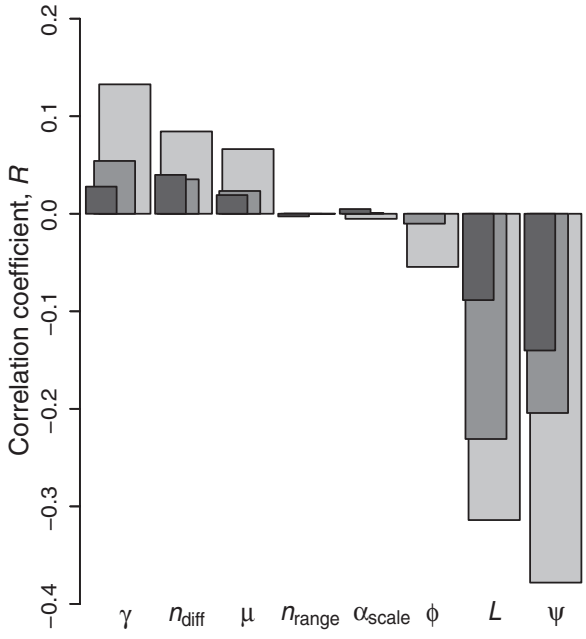

Fig. 1. Dependence of food-web stability on GM parameters. Correlation coefficients R describing the correlation between food-web stability and GM parameters (*20*) are shown for 10^8 randomly generated food webs with 10 (light gray), 20 (medium gray), and 30 species (dark gray). Error bars are too small to be visible. High sensitivities of predation to prey density (γ), large average differences between the niche values of a predator and its prey (n_{diff}), and high exponents of closure (μ) promote stability. High sensitivity of primary production to the number of primary producers (ϕ), large number of links (L), and high sensitivity of predation to the number of predators (ψ) destabilize. The total range of niche values (n_{range}) and the total range of time scales (α_{scale}) have little effect on stability.

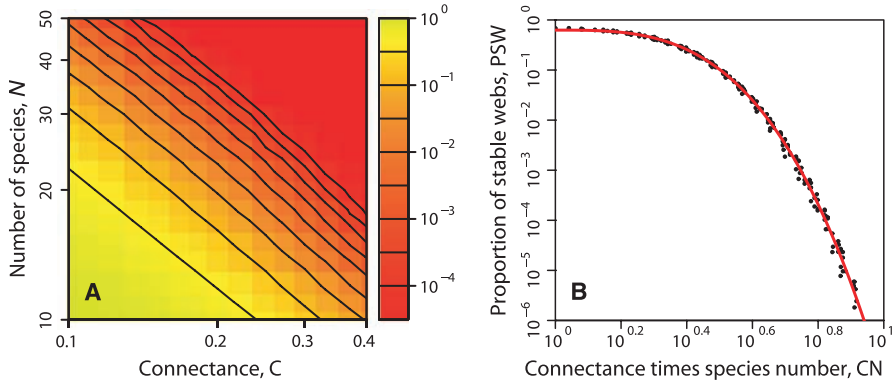

Fig. 2. Dependence of food-web stability on N and C. (**A**) The PSW decreases with increasing N and C, as shown by the color coding and the logarithmically spaced level lines. (**B**) The power law $\log_{10}(\text{PSW}) + a = bx^c$ (red curve) with $x = \log_{10}(CN)$, $a = 0.2090$, $b = -7.025$, and $c = 3.138$ explains 99.64% of the shown variation.

[1]Max Planck Institute for Physics of Complex Systems, Nöthnitzer Straße 38, 01187 Dresden, Germany. [2]Department of Ecology and Evolutionary Biology and Center for BioComplexity, Princeton University, Princeton, NJ 08540, USA. [3]University Fellow, Resources for the Future, 1616 P Street NW, Washington, DC 20036, USA. [4]Evolution and Ecology Program, International Institute for Applied Systems Analysis, Schlossplatz 1, 2361 Laxenburg, Austria.

*To whom correspondence should be addressed. E-mail: thilo.gross@physics.org

35 billion food webs. As expected, the PSW decreases as N and C increase. Moreover, we find that the level lines in Fig. 2A are almost perfectly straight with a slope of 1, so that the PSW is determined almost exclusively by the product of N and C. Figure 2B shows that the dependence of log(PSW) on log(CN) closely follows a power law.

We next turned to the effect of link-strength variability within a food web, which has previously been proposed as a potentially important determinant of food-web stability (*4*, *7*, *9*–*11*, *23*). In order to compare link strength, we had to take into account that, because of allometric scaling, biomass fluxes at higher trophic levels are on average much weaker than at lower trophic levels. We therefore measured link-strength variability in a predator-centric way by determining the coefficient of variation (CV) of all biomass fluxes, which were individually normalized by the total biomass inflow of the flux's recipient. An alternative prey-centric definition, providing independent information, can be devised based on the CV of all biomass fluxes, which were individually normalized by the total biomass outflow of the flux's source.

To explore the impact of link-strength variability, we generated a large ensemble of food webs (~10^7) in which link strengths were drawn from a uniform distribution. Figure 3A shows the PSW as a function of the observed CV of predator-centric link strengths. In very small food webs (such as $N = 5$), large jumps occur in the PSW as a function of the CV. This is due to the relatively low number of feasible topologies, each giving rise to a characteristic range of CVs and PSWs. In larger food webs, the number of topologies grows combinatorially, so that the PSW becomes a smooth function of the CV above approximately $N = 10$. We find that in small and intermediate food webs ($N < 30$), the PSW increases with increasing CV (Fig. 3A), which confirms the stabilizing effect of link-strength variability previously reported in the literature (*4*). However, in larger food webs, this relationship is reversed, so that increasing the CV decreases the PSW.

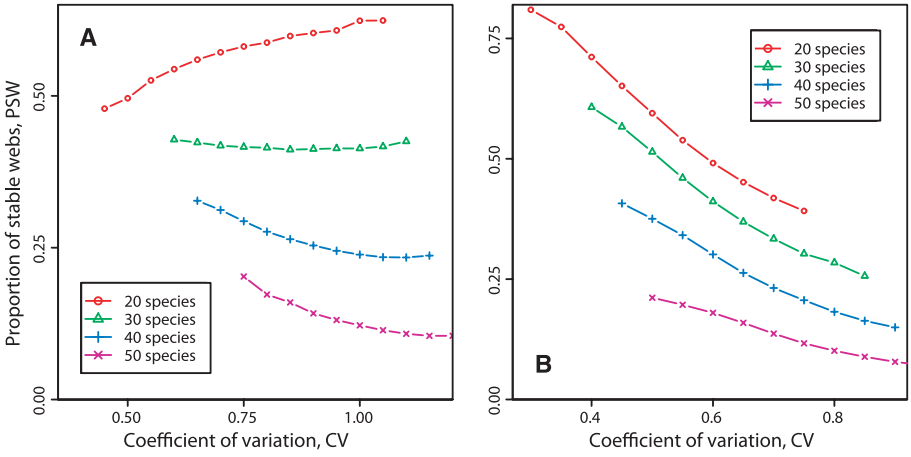

Fig. 3. Dependence of food-web stability on link-strength variability. The former is characterized by PSW and the latter by CV. Link strength is normalized by (**A**) the predator's total influx or (**B**) the prey's total outflux. Link-strength variability enhances stability in small food webs but has a destabilizing effect in larger webs.

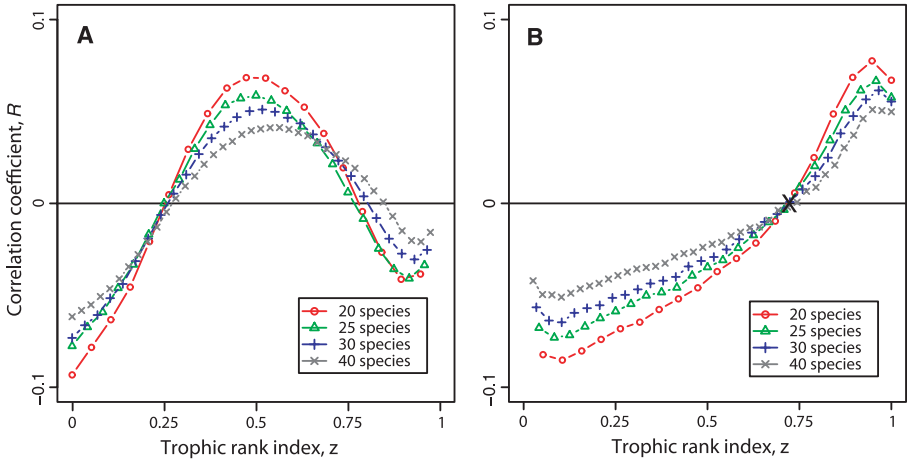

Fig. 4. Dependence of food-web stability on the distribution of links. (**A**) Correlation of stability with the number of predator species preying on a focal species, in dependence on the trophic position of the focal species as measured by its trophic-rank index z. Stability is enhanced if most species prey upon intermediate species, which are characterized by indices around $z = 0.5$. (**B**) Correlation of stability with the number of prey species predated upon by a focal species, in dependence on the trophic position of the focal species. Stability is enhanced if apical predators are generalists, whereas intermediate predators are specialists.

Repeating this investigation with the alternative, prey-centric measure of link variability yields slightly different results. For small food webs ($N < 20$), a local PSW maximum occurs at low CVs. Therefore, increasing the CV has a stabilizing effect if the CV is low. For larger food webs, this maximum becomes less pronounced and eventually disappears so that, also with this alternative measure, we find that increasing the CV destabilizes large food webs (Fig. 3B). Additional investigations (*20*), of lognormally distributed link strengths and of food webs with trophic loops, underscore the robustness of the patterns reported in Fig. 3.

The GM approach can be used to exhaustively search for properties that stabilize food webs. Here, we focus on the stabilizing or destabilizing effects of links depending on the trophic levels they connect. In an ensemble of food webs with fixed connectivity $K = \frac{L}{N}$, a trophic-rank index z is assigned to each species (*20*). This index enumerates species, from lowest to highest trophic position, according to their niche value, which in turn is often interpreted as an indicator of body size. We normalized the index to the interval [0,1], so that the most basal species in a web is always characterized by $z = 0$ and the most apical species by $z = 1$, with all other species occupying an equidistant grid of index values in between. For all focal species with a given z, we then determined the correlations between the PSW and (i) the number of predator species exploiting the focal species and (ii) the number of prey species exploited by the focal species.

Figure 4A shows the correlation of food-web stability with the number of predator species as a function of z. Increasing the number of predator species preying on basal species ($z < 0.25$) has a destabilizing effect on the food web. Likewise, increasing the number of predator species preying on apical species ($z > 0.75$) has a destabilizing effect. In between, there is a large intermediate range ($0.25 < z < 0.75$) in which the correlation is positive, showing that for a given number of links the stability of food webs is enhanced if predators mainly prey upon species of intermediate trophic position.

Figure 4B shows the correlation of food-web stability with the number of prey species as a function of z. For most species ($z < 0.719$), the PSW correlates negatively with the number of prey species, whereas a positive correlation is found for species at high trophic levels ($z > 0.719$). For a given number of links, stability is therefore enhanced by generalist predators at the top of a food web and specialist predators below. The threshold $z = 0.719$ is independent of most GM parameters, including N and K. Additional investigations reveal that the nonlinearity of top-predator mortality is the only parameter in the model that has a detectable impact on this threshold.

Our study adds independent support for some previously proposed stabilizing factors. The mutual reinforcement of similar results obtained with different methods establishes a broader basis for understanding food-web stability. Our analyses show that variability in trophic link strength exerts a stabilizing influence only in relatively small food webs. In contrast, larger food webs are destabilized by in-

creasing the coefficient of variation of normalized link strength. This indicates that large food webs follow qualitatively different rules than smaller webs (*16*) and suggests that extreme link strengths should be rarer in larger food webs. Further, we found a power law for the scaling of food-web stability with species number and connectance and identified two topological rules governing food-web stability: For a given number of species and links, food-web stability is enhanced when (i) species at high trophic levels feed on multiple prey species and (ii) species at intermediate trophic levels are fed upon by multiple predator species. This pattern, with generalist apical predators preying upon intermediate specialist predators, is often encountered in empirical food webs (*7*, *11*, *14*, *15*) and is consistent with reported effects of allometric degree distributions (*15*) and of top predators connecting otherwise separate energy channels (*14*). In comparison with previous results, our study offers more predictive specificity based on a wider ensemble of models, which enhances confidence in the universality of the reported rules. Perhaps most importantly, the GM approach used here has much potential for addressing a large class of related questions.

References and Notes

1. R. M. May, *Nature* **238**, 413 (1972).
2. A. W. King, S. L. Pimm, *Am. Nat.* **122**, 229 (1983).
3. J. E. Cohen, C. M. Newman, *J. Theor. Biol.* **113**, 153 (1985).
4. K. S. McCann, A. Hastings, G. R. Huxel, *Nature* **395**, 794 (1998).
5. K. S. McCann, *Nature* **405**, 228 (2000).
6. J. M. Montoya, S. L. Pimm, R. V. Solé, *Nature* **442**, 259 (2006).
7. A. Neutel, J. A. P. Heesterbeek, P. C. de Ruiter, *Science* **296**, 1120 (2002).
8. M. Kondoh, *Science* **299**, 1388 (2003).
9. V. A. A. Jansen, G. D. Kokkoris, *Ecol. Lett.* **6**, 498 (2003).
10. M. C. Emmerson, D. Raffaelli, *J. Anim. Ecol.* **73**, 399 (2004).
11. S. A. Navarrete, E. L. Berlow, *Ecol. Lett.* **9**, 526 (2006).
12. U. Brose, R. J. Williams, N. D. Martinez, *Ecol. Lett.* **9**, 1228 (2006).
13. N. Rooney, K. S. McCann, G. Gellner, J. C. Moore, *Nature* **442**, 265 (2006).
14. A. Neutel *et al.*, *Nature* **449**, 599 (2007).
15. S. B. Otto, B. C. Rall, U. Brose, *Nature* **450**, 1226 (2007).
16. E. L. Berlow *et al.*, *Proc. Natl. Acad. Sci. U.S.A.* **106**, 187 (2009).
17. R. M. May, S. A. Levin, G. Sugihara, *Nature* **451**, 893 (2008).
18. S. Sinha, S. Sinha, *Phys. Rev. E Stat. Nonlin. Soft Matter Phys.* **71**, 020902 (2005).
19. T. Gross, U. Feudel, *Phys. Rev. E Stat. Nonlin. Soft Matter Phys.* **73**, 016205 (2006).
20. Materials and methods are available as supporting material on *Science* Online.
21. R. J. Williams, N. D. Martinez, *Nature* **404**, 180 (2000).
22. P. A. Abrams, L. R. Ginzburg, *Trends Ecol. Evol.* **15**, 337 (2000).
23. E. L. Berlow *et al.*, *J. Anim. Ecol.* **73**, 585 (2004).

24. T.G. and L.R. thank B. Blasius for extensive discussions and insightful comments. S.L. acknowledges the support of NSF (grant DEB-0083566) and the Defense Advanced Research Projects Agency (grant HR0011-05-1-0057). U.D. acknowledges support by the European Commission, the European Science Foundation, the Austrian Science Fund, and the Vienna Science and Technology Fund.

Supporting Online Material

www.sciencemag.org/cgi/content/full/325/5941/747/DC1
Materials and Methods
Figs. S1 and S2
Table S1
References

13 March 2009; accepted 25 June 2009
10.1126/science.1173536

C3PO, an Endoribonuclease That Promotes RNAi by Facilitating RISC Activation

Ying Liu,[1] Xuecheng Ye,[1] Feng Jiang,[1] Chunyang Liang,[1] Dongmei Chen,[2] Junmin Peng,[2] Lisa N. Kinch,[1,3] Nick V. Grishin,[1,3] Qinghua Liu[1]*

The catalytic engine of RNA interference (RNAi) is the RNA-induced silencing complex (RISC), wherein the endoribonuclease Argonaute and single-stranded small interfering RNA (siRNA) direct target mRNA cleavage. We reconstituted long double-stranded RNA– and duplex siRNA–initiated RISC activities with the use of recombinant *Drosophila* Dicer-2, R2D2, and Ago2 proteins. We used this core reconstitution system to purify an RNAi regulator that we term C3PO (component 3 promoter of RISC), a complex of Translin and Trax. C3PO is a Mg^{2+}-dependent endoribonuclease that promotes RISC activation by removing siRNA passenger strand cleavage products. These studies establish an in vitro RNAi reconstitution system and identify C3PO as a key activator of the core RNAi machinery.

RNA interference (RNAi) is posttranscriptional gene silencing initiated by Dicer, a ribonuclease (RNase) III that processes double-stranded RNA (dsRNA) into 21- to 22-nucleotide (nt) small interfering RNA (siRNA) (*1*–*3*). Nascent siRNA duplex is assembled into the effector RNA-induced silencing complex (RISC), wherein single-stranded siRNA guides the endoribonuclease Argonaute (Ago) to catalyze sequence-specific cleavage of complementary mRNA (*1*–*3*). A minimal RISC can be reconstituted with recombinant Ago2 and single-stranded siRNA, but not duplex siRNA (*4*), which suggests that additional factors are required for loading nascent siRNA onto Ago2. In *Drosophila*, Dicer-2 (Dcr-2) and R2D2 coordinately recruit duplex siRNA to Ago2 to promote RISC assembly (*5*–*7*). Moreover, the Dcr-2–R2D2 complex senses thermodynamic asymmetry of siRNA and facilitates the guide strand selection (*8*). It remains unclear as to what constitutes holo-RISC, how RISC is assembled, and how RISC is regulated. These outstanding questions can be effectively addressed using a classic biochemical fractionation and reconstitution approach.

We took a candidate approach to reconstituting the core RISC activity with the use of recombinant Dcr-2, R2D2, and Ago2 proteins, all of which are essential for *Drosophila* RISC assembly (*6*, *7*, *9*). Besides PAZ and PIWI domains, *Drosophila* Ago2 carries a long stretch of N-terminal polyglutamine (Q) repeats that are absent in most Ago proteins. We generated an active truncated His-Flag–tagged Ago2 that removes most polyQ repeats and fully restores duplex siRNA–initiated RISC activity in *ago2* mutant lysate (fig. S1) (*9*). Furthermore, purified recombinant Dcr-2–R2D2 and Ago2 proteins could successfully reconstitute long dsRNA– and duplex siRNA–initiated RISC activities (Fig. 1A). The RISC activity was abolished when using catalytic mutant Ago2 (Fig. 1A), indicating that Ago2 was responsible for mRNA cleavage in this reconstituted system.

However, recombinant Dicer-2–R2D2 and Ago2 generated lower RISC activities than did S2 extract (Fig. 1A), which suggests that additional factors are required to achieve maximal RISC activity. Therefore, we used this core reconstitution system to search for new RISC-enhancing factors. We found that mild heat treatment (HI, 37°C for 30 min) abolished the RISC activity in S2 extract (fig. S2) and that addition of $S2^{HI}$ extract greatly enhanced the RISC activity of recombinant Dicer-2–R2D2 and Ago2 (Fig. 1B), which suggested the existence of an RNAi activator. We named this factor C3PO (component 3 promoter of RISC) because this is the third component besides Dcr-2 and R2D2 that promotes RISC activity.

We used a seven-step chromatographic procedure to purify C3PO from S2 extract. At the final step, two proteins, ~27 kD and ~37 kD, showed close correlation with the RISC-enhancing activity (Fig. 1C). They were identified by mass spectrometry as the evolutionarily conserved Translin, also known as testis-brain RNA binding protein (TB-RBP), and Translin-associated factor X (Trax). Translin is a single-stranded DNA and RNA binding protein that copurifies with siRNA after cross-linking by ultraviolet light (*10*, *11*), whereas Trax has sequence similarity to and interacts with Translin (*12*). Consistently, recombinant C3PO complex, but not Translin, greatly enhanced the RISC activity of recombinant Dicer-2–R2D2 and Ago2 (Fig. 1D and fig. S3A). Maximal RISC activity was obtained only when Dcr-2–R2D2, C3PO, and Ago2 were present (fig. S3B).

Conversely, genetic depletion of C3PO diminished RISC activity in *Drosophila* ovary extract. Western blotting revealed that Translin and Trax were both missing in *translin* (*trsn*) mutant fly lysate (Fig. 2A) (*11*), which suggests that Trax is unstable

[1]Department of Biochemistry, University of Texas Southwestern Medical Center, Dallas, TX 75390, USA. [2]Department of Human Genetics, Center for Neurodegenerative Diseases, Emory University, Atlanta, GA 30322, USA. [3]Howard Hughes Medical Institute, University of Texas Southwestern Medical Center, Dallas, TX 75390, USA.

*To whom correspondence should be addressed. E-mail: qinghua.liu@utsouthwestern.edu

without Translin. By contrast, the core RNAi components (i.e., Dcr-2, R2D2, and Ago2) remained at wild-type levels in *trsn* mutant lysate (Fig. 2A). Whereas siRNA-generating activity was slightly higher in the mutant lysate (fig. S4), duplex siRNA–initiated RISC activity was at ~25% of wild-type level in *trsn* extract (Fig. 2B), and this defect was rescued by adding recombinant C3PO (Fig. 2C). Thus, C3PO is required for optimal RISC activity in vitro.

To determine whether C3PO is required for RNAi in vivo, we injected wild-type and *trsn* mutant embryos with *fushi tarazu* (*ftz*) siRNA or dsRNA that causes segmentation defects by silencing *ftz* expression (*9*). After injection with *ftz* siRNA, more than 80% of wild-type embryos displayed a severe segmentation phenotype, whereas a substantial portion of *trsn* mutant embryos showed mild or no phenotype (Fig. 2, D and E). A similar phenomenon was observed with *ftz* dsRNA injection (Fig. 2F). These experiments indicate that C3PO is required for efficient RNAi in vivo.

To distinguish whether C3PO enhances RISC assembly or activity, we compared the amount of RISC activity generated by recombinant Dcr-2–R2D2 and Ago2 with C3PO added before or after RISC assembly (fig. S3C). In both cases, C3PO could enhance the core RISC activity; however, the RISC-enhancing effect was greatly diminished when C3PO was added late to preassembled RISC (fig. S3D). Therefore, we conclude that C3PO primarily promotes RISC activation but also enhances RISC-mediated target cleavage. Consistent with the latter, C3PO modestly enhanced single-stranded siRNA–initiated RISC activity (fig. S3E).

To further dissect the role of C3PO in RISC activation, we examined the stepwise process of RISC assembly by native siRNA gel-shift assay. As previously described (*6*, *9*, *13*), three siRNA-protein (siRNP) complexes—B, RISC loading complex (RLC), and RISC—were formed in wild-type ovary extract. RLC contains Dcr-2–R2D2 and siRNA, whose formation precedes and is required for RISC assembly (*6*, *13*). Neither RLC nor RISC could form in *dcr-2* mutant extract, whereas only RISC was absent in *ago2* mutant extract (Fig. 3A). By contrast, all three siRNP complexes could form in *trsn* mutant extract, but the amount of RISC was much less than that in wild-type extract (Fig. 3A). These results suggest that C3PO facilitates the transition from RLC to active RISC.

The central step of RISC activation is the unwinding of duplex siRNA and loading of the guide strand onto Ago2. Thus, we measured the efficiency of RISC assembly by means of the siRNA-unwinding assay (*14*). In the reconstitution system, recombinant C3PO enhanced the siRNA-unwinding activity of Dcr-2–R2D2 and Ago2 (fig. S5A). Conversely, the efficiency of siRNA unwinding was lower in *trsn* mutant extract than in wild-type control extract (fig. S5B). Both results indicate that C3PO promotes siRNA unwinding and RISC activation.

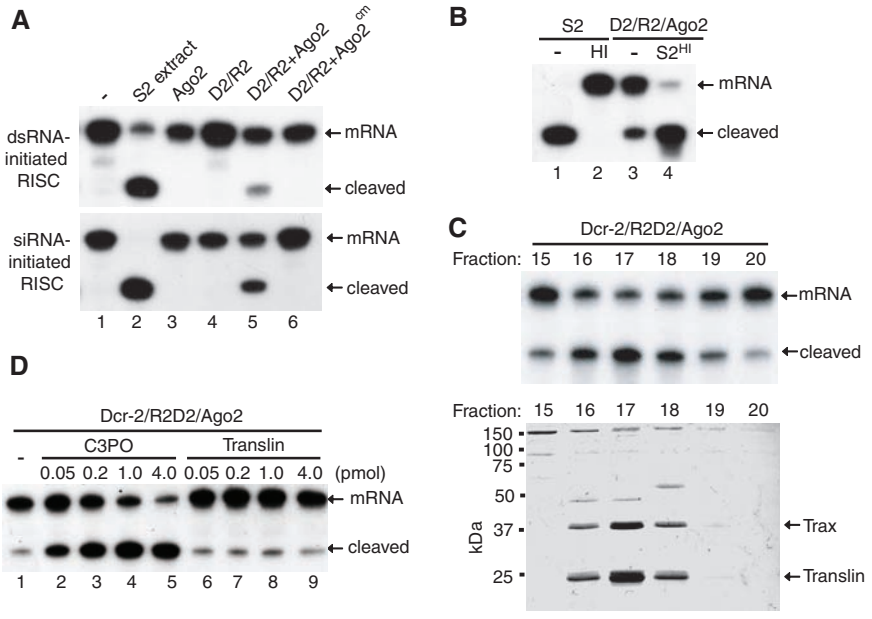

Fig. 1. Purification of C3PO as a RISC activator. (**A**) The dsRNA- and siRNA-initiated RISC assays were performed in buffer, S2 extract, recombinant Ago2, Dcr-2–R2D2 (D2/R2) complex, and D2/R2 plus wild-type or catalytic mutant (cm; $Asp^{965} \rightarrow Ala$) Ago2. All siRNA-initiated RISC assays used duplex siRNA except as noted. (**B**) The siRNA-initiated RISC assays were performed with untreated or heat-inactivated (HI) S2 extract or with recombinant Dcr-2–R2D2 and Ago2 in the absence or presence of $S2^{HI}$ extract. (**C**) Purification of C3PO through a seven-step chromatographic procedure. After the final Mono Q step, individual fractions were assayed with recombinant Dcr-2–R2D2 and Ago2 for the RISC-enhancing activity (top) or resolved by SDS–polyacrylamide gel electrophoresis followed by colloidal staining (bottom). (**D**) The siRNA-initiated RISC assays were performed using recombinant Dcr-2–R2D2 and Ago2 alone or with increasing amounts of recombinant C3PO or Translin.

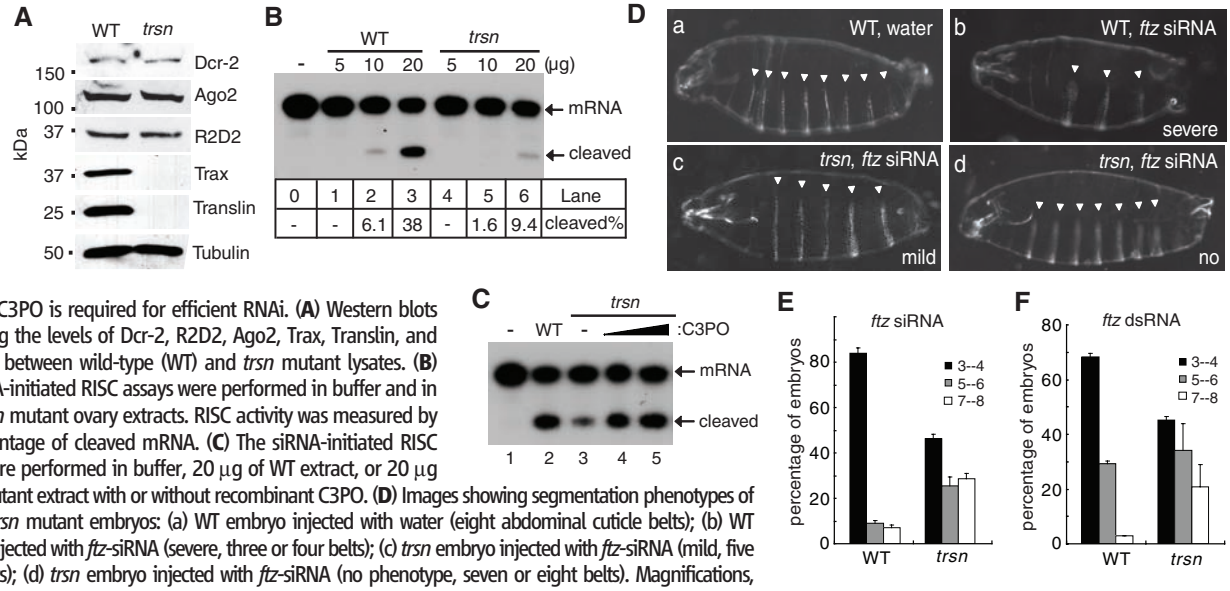

Fig. 2. C3PO is required for efficient RNAi. (**A**) Western blots comparing the levels of Dcr-2, R2D2, Ago2, Trax, Translin, and β-tubulin between wild-type (WT) and *trsn* mutant lysates. (**B**) The siRNA-initiated RISC assays were performed in buffer and in WT or *trsn* mutant ovary extracts. RISC activity was measured by the percentage of cleaved mRNA. (**C**) The siRNA-initiated RISC assays were performed in buffer, 20 μg of WT extract, or 20 μg of *trsn* mutant extract with or without recombinant C3PO. (**D**) Images showing segmentation phenotypes of WT and *trsn* mutant embryos: (a) WT embryo injected with water (eight abdominal cuticle belts); (b) WT embryo injected with *ftz*-siRNA (severe, three or four belts); (c) *trsn* embryo injected with *ftz*-siRNA (mild, five or six belts); (d) *trsn* embryo injected with *ftz*-siRNA (no phenotype, seven or eight belts). Magnifications, 100×. (**E** and **F**) Graphs showing distribution of WT or *trsn* mutant embryos with severe, mild, or no phenotype after injection of *ftz* siRNA [(E), $n > 100$] or *ftz* dsRNA [(F), $n > 150$].

To study the relative contribution of different RISC activation mechanisms, we supplemented $S2^{HI}$ extract, which displayed no siRNA-unwinding activity due to Ago2 inactivation (figs. S2 and S6B), with recombinant wild-type or catalytic mutant Ago2. Only wild-type, but not mutant, Ago2 could effectively rescue siRNA unwinding in $S2^{HI}$ extract (fig. S6C). This result, together with previous studies (*15*–*17*), strongly supports the idea that the catalytic activity of Ago2 is indispensable for siRNA unwinding and RISC activation.

In the "slicer" model, Ago2 cleaves the passenger strand of siRNA into 9- and 12-nt fragments that simply melt away because of low binding energy, leaving the guide strand behind to form an active RISC with Ago2. By passenger strand cleavage assay (*15*, *17*), we observed that both 9- and 12-nt fragments displayed a longer half-life in *trsn* mutant extract than in wild-type extract (Fig. 3, B to E, and fig. S7). Moreover, addition of C3PO complex, but not Translin, resulted in rapid degradation of the 9-nt fragment in the reconstituted system (fig. S8A). Together, these findings suggest that C3PO promotes RISC activation by removing siRNA passenger strand cleavage products.

In further support of this idea, recombinant C3PO displayed potent RNase activity toward single-stranded siRNA but showed little or no activity toward double-stranded siRNA or single-stranded DNA (Fig. 4A and fig. S8, B and C). The RNase activity of C3PO is Mg^{2+}-dependent and could be blocked by EDTA, but not by EGTA (Fig. 4B). In addition, C3PO acts as an endonuclease, because it could degrade circular as well as linear RNA (Fig. 4C). Moreover, the endogenous C3PO complex closely correlated with the RISC-enhancing activity as well as a single-stranded RNase activity after sequential chromatography (Fig. 4D and fig. S8D).

Neither subunit of C3PO shows similarity to any known RNase by bioinformatics and structural analyses (*18*). To identify the catalytic sites of C3PO, we performed a multisequence alignment of Translin and Trax and observed three acidic residues (Glu^{123}, Glu^{126}, and Asp^{204}) that were invariant in Trax but missing in all Translin (Fig. 5A and fig. S9). Furthermore, modeling the structure of *Drosophila* Trax after the crystal structure of human Translin (*18*) revealed that these residues existed in close spatial proximity, which suggests that they may coordinate Mg^{2+} for catalysis (Fig. 5A).

To test this hypothesis, we individually mutated the Glu^{123}, Glu^{126}, and Asp^{204} residues of Trax to alanine. Recombinant mutant C3PO complexes were generated by coexpressing His-tagged wild-type Translin and untagged mutant Trax (fig. S10A). These point mutations did not affect protein folding or complex formation, because wild-type and mutant C3PO displayed the same column behaviors and bound single-stranded siRNA equally well in a noncleaving condition (fig. S10B). Consistently, mutating each putative catalytic residue abolished the RNase activity and the RISC-enhancing activity of C3PO (Fig. 5, B and C, and fig. S10C). By contrast, mutation of other highly conserved Asp or Glu residues in Translin or Trax did not significantly affect

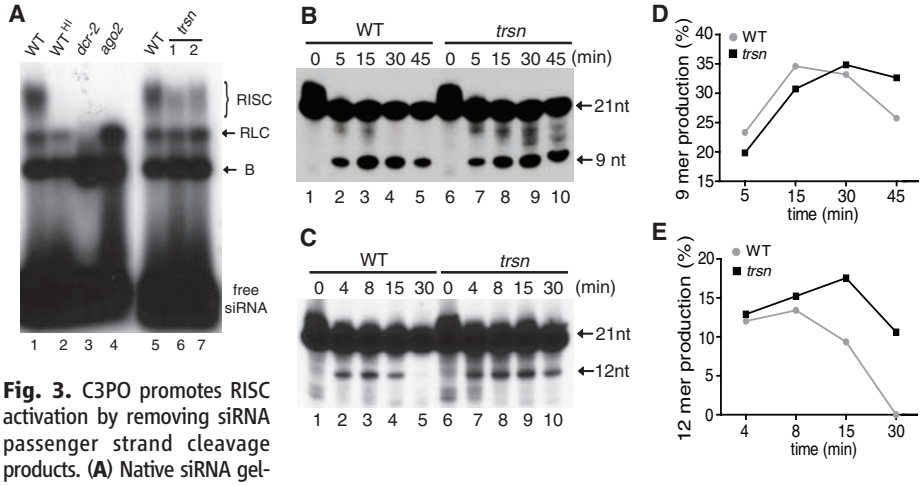

Fig. 3. C3PO promotes RISC activation by removing siRNA passenger strand cleavage products. (**A**) Native siRNA gel-shift assays were performed using radiolabeled *let-7* siRNA with untreated or heat-inactivated (HI) WT, *dcr-2*, or *ago2* mutant ovary extract (lanes 1 to 4), or 40 μg of WT and two preparations of *trsn* mutant ovary extract (lanes 5 to 7). (**B** and **C**) Passenger strand cleavage assays were performed with 40 μg of WT or *trsn* mutant extract. The 9- or 12-nt cleavage products were detected separately using siRNA whose passenger strand was radiolabeled at the 5′ (B) or 3′ (C) end. (**D** and **E**) The data in (B) and (C) were converted into graphs illustrating different stability of the 9- and 12-nt oligomers in WT and *trsn* extracts.

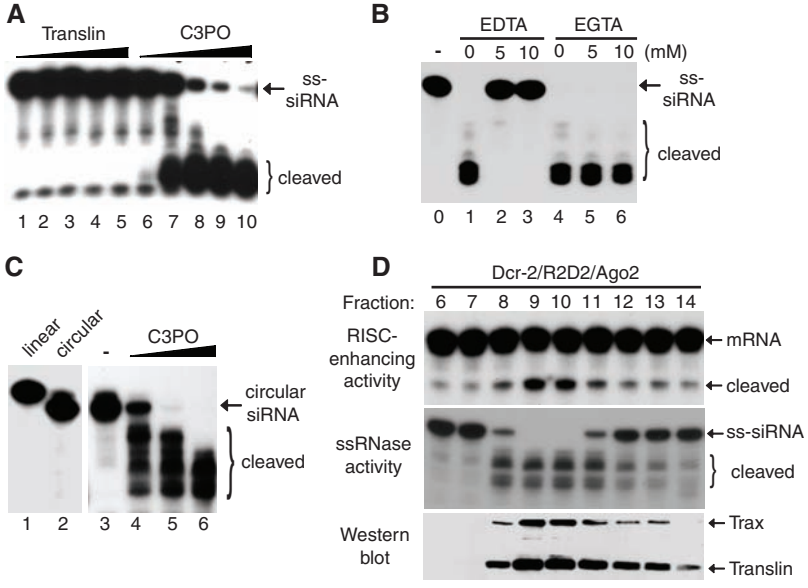

Fig. 4. C3PO is a Mg^{2+}-dependent endoribonuclease. (**A**) 5′-radiolabeled single-stranded (ss) siRNA was incubated with increasing amounts of recombinant Translin or C3PO complex. (**B**) RNase assays were performed with recombinant C3PO in the absence or presence of EDTA or EGTA. (**C**) RNase assays were conducted by incubating circular single-stranded siRNA with increasing amounts of recombinant C3PO. (**D**) After sequential chromatography, fractions were assayed for RISC-enhancing activity (top), RNase activity (middle), or Western blotting to detect Translin and Trax (bottom).

the RNase or RISC-enhancing activity of C3PO (fig. S10, D and E). These studies suggest that the intrinsic RNase activity of C3PO is required for its RISC-enhancing activity.

Our in vitro reconstitution system for dsRNA- and duplex siRNA–initiated RISC activities has revealed that Dcr-2–R2D2 and Ago2 constitute the catalytic core of *Drosophila* RNAi. This reconstitution system enables us to identify C3PO, a multimeric complex of Translin and Trax, as a key activator of the core RNAi machinery. Our biochemical studies indicate that the "slicer" mechanism plays a dominant role in *Drosophila* RISC assembly. C3PO, a Mg^{2+}-dependent endoribonuclease for which Trax is the catalytic subunit, promotes RISC activation by removing siRNA passenger strand cleavage products. The RNase activity of C3PO may be stimulated by Ago2-mediated nick in duplex siRNA and/or fraying of the ends of cleavage products. The exonuclease QIP may function in a similar manner in *Neurospora crassa* (*19*). This robust and progressive reconstitution system should greatly facilitate in-depth mechanistic studies of the assembly, function, and regulation of holo-RISC, the catalytic engine of RNAi.

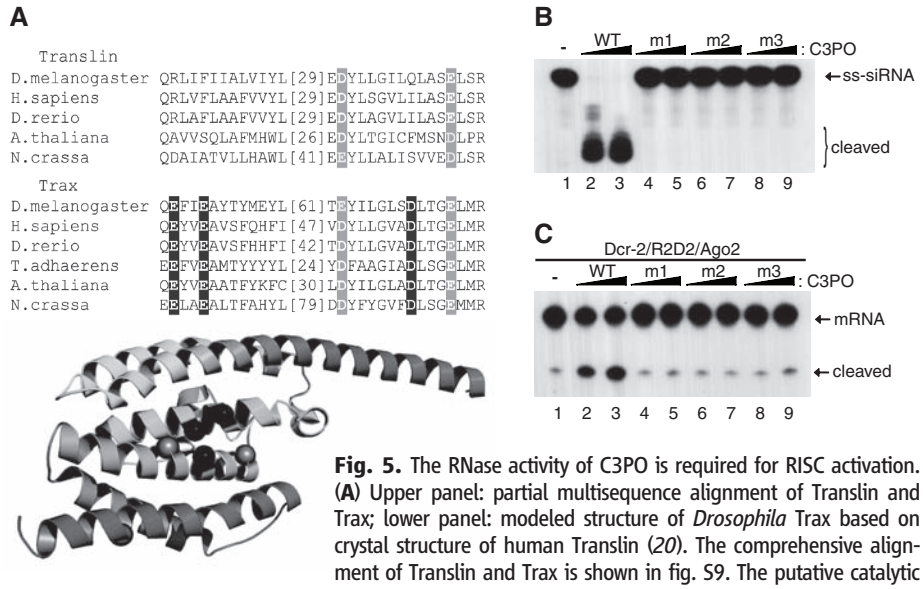

Fig. 5. The RNase activity of C3PO is required for RISC activation. (**A**) Upper panel: partial multisequence alignment of Translin and Trax; lower panel: modeled structure of *Drosophila* Trax based on crystal structure of human Translin (*20*). The comprehensive alignment of Translin and Trax is shown in fig. S9. The putative catalytic Asp and Glu residues are in black; two other highly conserved Glu residues are in gray. (**B**) RNase activity was compared between WT and each of three catalytic mutant C3PO complexes: m1 (Glu^{123} → Ala), m2 (Glu^{126} → Ala), and m3 (Asp^{204} → Ala). (**C**) RISC-enhancing activity was compared between WT and the three catalytic mutant C3PO complexes by assaying together with recombinant Dcr-2–R2D2 and Ago2.

References and Notes

1. R. W. Carthew, E. J. Sontheimer, *Cell* **136**, 642 (2009).
2. H. Siomi, M. C. Siomi, *Nature* **457**, 396 (2009).
3. Z. Paroo, Q. Liu, X. Wang, *Cell Res.* **17**, 187 (2007).
4. J. Liu *et al.*, *Science* **305**, 1437 (2004); published online 29 July 2004 (10.1126/science.1102513).
5. Q. Liu *et al.*, *Science* **301**, 1921 (2003).
6. J. W. Pham, J. L. Pellino, Y. S. Lee, R. W. Carthew, E. J. Sontheimer, *Cell* **117**, 83 (2004).
7. X. Liu, F. Jiang, S. Kalidas, D. Smith, Q. Liu, *RNA* **12**, 1514 (2006).
8. Y. Tomari, C. Matranga, B. Haley, N. Martinez, P. D. Zamore, *Science* **306**, 1377 (2004).
9. K. Okamura, A. Ishizuka, H. Siomi, M. C. Siomi, *Genes Dev.* **18**, 1655 (2004).
10. J. Wang, E. S. Boja, H. Oubrahim, P. B. Chock, *Biochemistry* **43**, 13424 (2004).
11. M. Claussen, R. Koch, Z. Y. Jin, B. Suter, *Genetics* **174**, 1337 (2006).
12. K. Suseendranathan *et al.*, *Eur. J. Cell Biol.* **86**, 173 (2007).
13. Y. Tomari *et al.*, *Cell* **116**, 831 (2004).
14. A. Nykanen, B. Haley, P. D. Zamore, *Cell* **107**, 309 (2001).
15. C. Matranga, Y. Tomari, C. Shin, D. P. Bartel, P. D. Zamore, *Cell* **123**, 607 (2005).
16. K. Miyoshi, H. Tsukumo, T. Nagami, H. Siomi, M. C. Siomi, *Genes Dev.* **19**, 2837 (2005).
17. T. A. Rand, S. Petersen, F. Du, X. Wang, *Cell* **123**, 621 (2005).
18. I. Sugiura *et al.*, *Acta Crystallogr.* **D60**, 674 (2004).
19. M. Maiti, H. C. Lee, Y. Liu, *Genes Dev.* **21**, 590 (2007).

20. Abbreviations for amino acid residues: A, Ala; C, Cys; D, Asp; E, Glu; F, Phe; G, Gly; H, His; I, Ile; K, Lys; L, Leu; M, Met; N, Asn; P, Pro; Q, Gln; R, Arg; S, Ser; T, Thr; V, Val; W, Trp; Y, Tyr.

21. We thank R. Koch, B. Suter, R. Carthew, M. Siomi, and H. Siomi for reagents and Y. Liu, H. Yu, D. Corey, and Z. Paroo for discussion and reading the manuscript. N.V.G. is a Howard Hughes Medical Institute investigator. Supported by a Sara and Frank McKnight fellowship (Y.L.), Welch grant I-1608 and NIH grant AG025688 (J.P.), and NIH grants GM078163 and GM084010 (Q.L.).

Supporting Online Material

www.sciencemag.org/cgi/content/full/325/5941/750/DC1
Materials and Methods
Figs. S1 to S10
References

14 May 2009; accepted 23 June 2009
10.1126/science.1176325

Effects of Antibiotics and a Proto-Oncogene Homolog on Destruction of Protein Translocator SecY

Johna van Stelten,[1] Filo Silva,[2] Dominique Belin,[2] Thomas J. Silhavy[1]*

Protein secretion occurs via translocation by the evolutionarily conserved Sec complex. LacZ hybrid proteins have long been used to study translocation in *Escherichia coli*. Some LacZ hybrids were thought to block secretion by physically jamming the Sec complex, leading to cell death. We found that jammed Sec complexes caused the degradation of essential translocator components by the protease FtsH. Increasing the amounts or the stability of the membrane protein YccA, a known inhibitor of FtsH, counteracted this destruction. Antibiotics that inhibit translation elongation also jammed the translocator and caused the degradation of translocator components, which may contribute to their effectiveness. Intriguingly, YccA is a functional homolog of the proto-oncogene product Bax Inhibitor-1, which may share a similar mechanism of action in regulating apoptosis upon prolonged secretion stress.

Protein translocation is a fundamental process that is essential for the delivery of most extracytoplasmic proteins to their final destination. This process is mediated by an evolutionarily conserved heterotrimeric membrane protein complex called the Sec61 complex (Sec61αβγ) in mammals and the Sec complex (SecY, -E, and -G) in prokaryotes (*1*). In *Escherichia coli*, two pathways target proteins to the Sec complex (*2*): the posttranslational Sec pathway, which targets most outer membrane (OM) and periplasmic proteins (*3*), and the cotranslational pathway, which is used primarily by inner membrane (IM) proteins, where the ribosome-nascent chain complex is targeted to the Sec complex by the signal recognition particle (SRP) (*4*). In both cases, proteins are initially directed to the SecY translocator via an amino-terminal signal sequence, which may or may not be cleaved upon translocation. The nature of this signal sequence determines which targeting pathway is used (*2*).

Genetic analysis of protein secretion is facilitated by *lacZ* (which specifies β-galactosidase) gene fusions (*5*, *6*). When the signal sequence of the OM protein LamB is fused to LacZ, the resulting hybrid protein is targeted for the posttranslational translocation pathway (*5*). Upon induction with maltose, large amounts of hybrid protein are made, and rapid folding of LacZ sequences in the cytoplasm causes a lethal jamming of the Sec complex (Fig. 1A), as evidenced by the accumulation in the cytoplasm of the precursor forms of wild-type secreted proteins (*7*). Under noninducing conditions (in the absence of maltose) in which low amounts of hybrid protein are made, lethal jamming does not occur. But because the hybrid protein is inefficiently secreted, some LacZ remains in the cytoplasm, where it is active, and strains carrying this fusion exhibit a Lac^+ phenotype. When the signal sequence of this hybrid is changed to increase its hydrophobicity, the resulting H*LamB-LacZ hybrid is directed instead to the alternative cotranslational SRP pathway (*4*). Because full-length LacZ is never exposed to the cytoplasm when secretion occurs cotranslationally, the H*LamB-LacZ hybrid is translocated efficiently to the periplasm, and jamming does not occur (Fig. 1B). In the oxidizing environment of the periplasm, LacZ misfolds. Thus, under noninducing conditions, strains carrying this fusion are Lac^-. Under inducing conditions, toxic hybrid protein aggregates accumulate in the periplasm so that even though no Sec complex jamming is observed, these strains are as maltose-sensitive as strains producing LamB-LacZ (*4*).

The Cpx two-component system regulates gene expression in response to misfolded proteins in the cell envelope. Dominant mutations, called *cpxA**, ac-

[1]Department of Molecular Biology, Princeton University, Princeton, NJ 08544, USA. [2]Department of Pathology and Immunology, Faculty of Medicine, University of Geneva, Geneva, Switzerland.

*To whom correspondence should be addressed. E-mail: tsilhavy@princeton.edu

tivate this system and suppress the inducer-sensitivity caused by periplasmic LacZ aggregates (*8*). Suppression of this toxicity was due solely to the induction by the Cpx system of the periplasmic protease DegP. Indeed, increasing production of DegP by cloning the structural gene on a multi-copy plasmid suppresses toxicity caused by H*LamB-LacZ (*4*). The protease degrades the toxic periplasmic LacZ aggregates. Activation of the Cpx system also relieves the inducer-sensitive phenotype caused by LamB-LacZ (*7*). This was surprising because this hybrid protein exerts its toxic effects in the cytoplasm by jamming the Sec complex. Indeed, overproduction of DegP is necessary but not sufficient to relieve the toxicity caused by LamB-LacZ (*4*). Activation of the Cpx system by use of *cpxA** alleles results in the efficient translocation of LamB-LacZ to the periplasm, where it can then be degraded by DegP (*7*). This reduced LacZ activity in uninduced cells (Fig. 2). Apparently, a Cpx-inducible gene product(s) other than DegP facilitates translocation of LamB-LacZ.

To search for this Cpx-inducible factor(s), we utilized the uninduced Lac phenotype of LamB-LacZ strains. Under these conditions, artificially increasing the production of the relevant factor in fusion strains that are $cpxA^+$ should increase the efficiency of LamB-LacZ secretion and thus decrease LacZ activity. Alternatively, inactivating the Cpx-regulated gene responsible for the efficient secretion of LamB-LacZ in a strain carrying the *cpxA** allele should increase LacZ activity. We began by testing genes regulated by Cpx (*9*).

The *yccA* gene is regulated in a Cpx-dependent fashion (*9*, *10*), and we confirmed this with reverse transcription polymerase chain reaction (fig. S1) (*11*). Overexpression of *yccA* from an isopropyl-β-D-thiogalactopyranoside (IPTG)–inducible promoter with a construct integrated at the lambda attachment site in a $cpxA^+$ fusion strain reduced LacZ activity comparable with that seen in *cpxA** fusion strains (Fig. 2) (*11*). Conversely, deletion of *yccA* in the *cpxA** fusion strain caused a modest increase in LacZ activity. The fact that $yccA^-$ is not completely epistatic to *cpxA** indicates that there are other Cpx-regulated factors that function to enhance translocation. Here, we focused on YccA because its increased production is sufficient to relieve jamming.

When SecY is not in a complex with SecE and SecG, it is degraded by FtsH, an essential, adenosine 5′-triphosphate–dependent, membrane-bound protease (*12*). In a search for mutants in which SecY was stabilized, a mutant form of the IM protein YccA, which lacks eight amino acids in the amino-terminus, was identified (*13*). This mutant protein, YccA11, binds to FtsH, but unlike wild-type YccA it is resistant to FtsH-mediated degradation (*13*). We replaced the chromosomal copy of *yccA* with *yccA11* in a $cpxA^+$ *lamB-lacZ* fusion strain and found that YccA11 was even more effective than overexpressed wild-type YccA at reducing LacZ activity (Fig. 2). Thus, YccA and even more so YccA11 can apparently stimulate secretion of the LamB-LacZ hybrid protein under noninducing conditions.

It had long been thought that the toxicity caused by high-level production of LamB-LacZ was due to a physical "jamming" of the Sec complex (*7*, *8*). Our results suggested an alternative hypothesis; perhaps the cell responds to jamming by promoting the energy-dependent degradation of SecY by FtsH. Translocator destruction would also cause the accumulation of the precursor forms of secreted proteins and result ultimately in cell death. Induction caused the degradation of SecY in strains carrying LamB-LacZ (Fig. 3A) but not in strains carrying the LamBΔ60-LacZ fusion in which the signal sequence is deleted (Fig. 3B) (*11*). Moreover, this degradation was prevented by

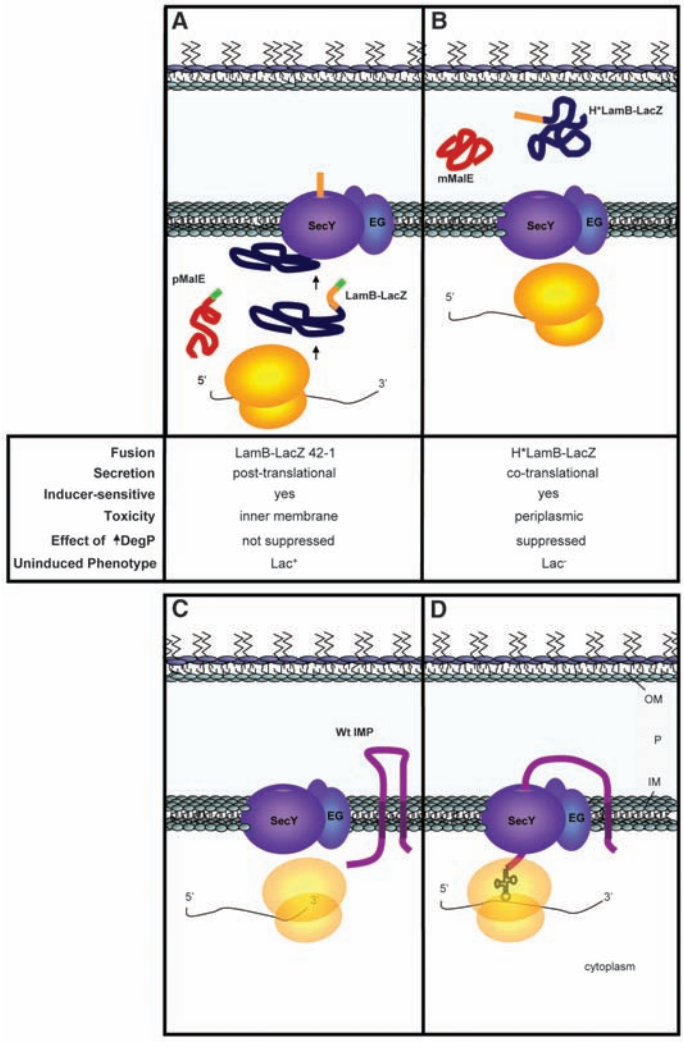

Fig. 1. Protein translocation in *E. coli*. (**A**) Jamming of SecY occurs during posttranslational translocation of the LamB-LacZ hybrid, resulting in accumulation of precursor proteins such as pMalE (red) with their signal sequence (green) still attached. (**B**) When the hybrid is targeted for cotranslational translocation (H*LamB-LacZ), it is secreted into the periplasm. Properties of the LacZ fusion strains are summarized in the text box. (**C**) Cotranslational translocation of a wild-type SRP substrate (purple). (**D**) During cotranslational translocation, antibiotics that inhibit peptide chain elongation jam the translocator. Orange circles, translating ribosome; IMP, IM protein; P, periplasm.

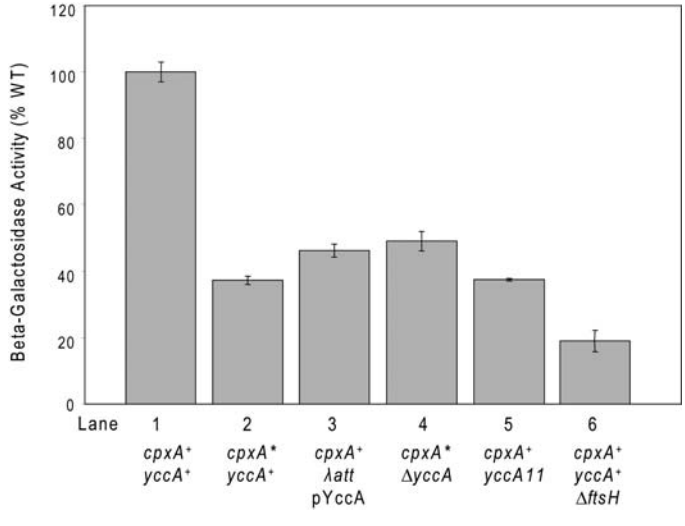

Fig. 2. YccA affects translocation of LamB-LacZ. Shown is LacZ activity of *lamB-lacZ* strains assayed in the absence of maltose induction so as to determine the efficiency of translocation. Lane 1, Pop3186 ($cpxA^+$ $yccA^+$); lane 2, WBS226 (*cpxA** $yccA^+$); lane 3, JVS724 ($cpxA^+$ *λatt* pYccA); lane 4, JVS621 (*cpxA** Δ*yccA*); lane 5, JVS716 ($cpxA^+$ *yccA*11); lane 6, JVS679 ($cpxA^+$ $yccA^+$ Δ*ftsH*). See table S1 for complete genotypes. Activities are expressed as a percent of wild type (WT). Error bars indicate SD (n = 3 experiments).

the *cpxA** mutation (Fig. 3A). As noted above (*7*), this mutation prevents jamming, as evidenced by the lack of accumulation of the precursor form of MalE in induced *cpxA** *lamB-lacZ* fusion strains (Fig. 3C). Overproduction of YccA alone was sufficient to prevent jamming in the *lamB-lacZ cpxA*$^+$ strain (Fig. 3C) and to prevent SecY destruction (Fig. 3B). The mutant YccA11 protein also stabilizes SecY (Fig. 3B). Thus, the toxicity associated with high-level production of LamB-LacZ is not entirely due to a physical jamming but rather is due, at least in part, to the proteolytic destruction of SecY.

YccA inhibits the protease FtsH (*13*). If this is the protease that degrades jammed SecY, then mutations that inactivate FtsH should result in hybrid protein secretion into the periplasm even better than do the *cpxA** mutations. Although the *ftsH* gene is essential, we could test this prediction using a strain that carries *sfhC21* (*14*). This allele suppresses the lethality of *ftsH* null but by itself does not dramatically alter the LacZ phenotype (fig. S2). Removing FtsH strongly reduced LacZ activity (Fig. 2), reflecting an enhanced secretion of LamB-LacZ to the periplasm.

SRP-mediated cotranslational secretion couples the processes of translation and translocation (Fig. 1) (*2*). Antibiotics that block translation elongation should produce proteins that are effectively fused to a ribosome by an unhydrolyzed, unreleased tRNA (*15*). We found that antibiotics that block translation elongation, such as chloramphenicol (Cm) and tetracycline (Tc), caused proteolytic destruction of SecY, whereas antibiotics that affect other stages of gene expression, such as translation initiation (kasugamycin) or transcription (rifamycin) did not (Fig. 4) (*11*). Furthermore, destruction of SecY upon treatment with Cm was FtsH-dependent (Fig. 4C). We have also investigated the fate of SecE and SecG. SecE was also degraded in the presence of Cm, although more slowly than SecY, whereas SecG was not (Fig. 4, C and D). Lastly, in agreement with the notion that SRP-dependent substrates define the target for FtsH-mediated translocon destruction upon treatment with antibiotics that inhibit translation elongation, high-level production of PhoA, a protein that is secreted in SRP-independent fashion, increased the stabililty of SecY upon treatment with Cm (fig. S3).

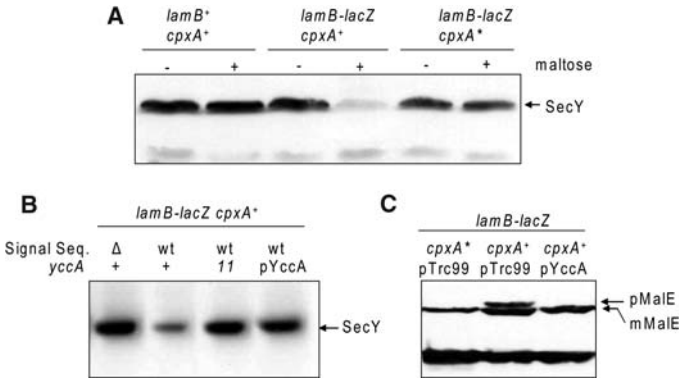

Fig. 3. Increased YccA stabilizes SecY and enables translocation of LamB-LacZ. (**A**) Immunoblot of SecY from strains carrying either wild-type *lamB* or the *lamB-lacZ* fusion and with either wild-type *cpxA* or the constitutive *cpxA** allele incubated in the presence (+) or absence (–) of maltose for 4 hours. (**B**) Immunoblot of SecY from strains incubated in the presence of maltose for 6 hours, of *cpxA*$^+$ strains carrying the *lamB-lacZ* fusion with (wt; Pop3186) and without (Δ; BZR60) its signal sequence, and expressing either endogenous levels of YccA (+), wild-type *yccA* on a multi-copy plasmid (pYccA), or the protease-resistant form of YccA (*yccA11*) from the chromosomal gene. (**C**) Immunoblot of MalE from cultures incubated in the presence of maltose for 1.5 hours. The empty vector (pTrc99a) and the *yccA* overexpression plasmid (pYccA) were induced with 2 μM IPTG 4 hours before and during induction with maltose.

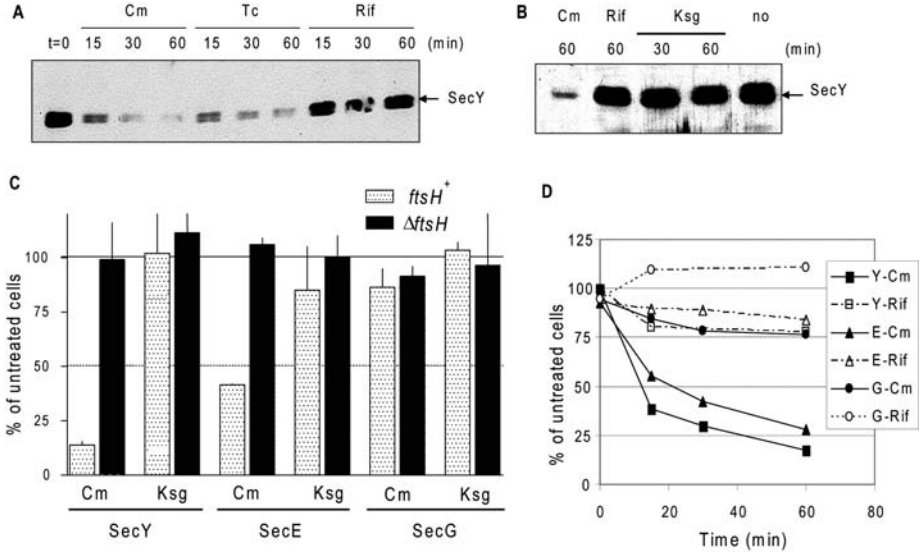

Fig. 4. Antibiotic inhibition of translation elongation results in SecY degradation. (**A**) Immunoblot of SecY from cultures untreated (t = 0) or incubated for the indicated times with 30 mg/L Cm, 10 mg/L Tc, or 100 mg/L rifampicin (Rif). (**B**) Immunoblot of SecY from cultures untreated (no) or incubated for the indicated times with 30 mg/L Cm, 100 mg/L Rif, or 200mg/L kasugamycin (Ksg). (**C**) Normalized levels of SecY, SecE, and SecG in an *ftsH*$^+$ strain (Pop3186, stippled bars) and an *ftsH* null strain (JVS679, solid bars), as determined by means of immunoblotting in cultures incubated for 30 min with Cm or Ksg. Values of untreated cultures have been set to 100%; each value is the mean of duplicate cultures, and the range is indicated. (**D**) The levels of SecY (squares), SecE (triangles), and SecG (circles) were determined by means of immunoblotting in cultures incubated for the indicated times with Cm (solid lines) or Rif (dashed lines).

Our results reveal a new activity for several old antibiotics. Because the secretion of many proteins occurs in a cotranslational fashion, agents that inhibit translation elongation will result in jammed translocators, and this will lead to the proteolytic destruction of these translocators. The suicidal nature of SecY destruction reflects the fact that SecY is required to insert newly synthesized SecY in the membrane (*16*). This chicken-and-the-egg–like problem may help explain why antibiotics that inhibit translation elongation exhibit bactericidal effects much sooner in some bacteria than in others (*17*, *18*). Perhaps the most susceptible bacteria have lower amounts of functional SecY.

We propose that *E. coli*, and perhaps all cells, have mechanisms that respond to SecY (or Sec61) translocators that are struggling with difficult substrates by degrading the stressed translocator. Clearly, such degradative activities can have dire consequences, and thus cells also have mechanisms to limit this suicidal activity. In *E. coli*, this limiting activity is controlled, at least in part, by the Cpx envelope stress response and YccA.

YccA is homologous to human Bax Inhibitor-1 (BI-1), an anti-apoptotic protein that restrains the activity of the tumor-suppressor Bax (*19*). BI-1 is so highly conserved that YccA from *E. coli* protects yeast cells against ectopically expressed human Bax (*20*). BI-1 is a proto-oncogene and is overexpressed in various types of cancer. Although Bax function is not fully understood, it contributes to cellular apoptosis caused by prolonged stress in the protein secretion pathway in eukaryotes (*21*), a pathway that involves the endoplasmic reticulum (ER) and is clearly related to the secretion stress caused by LacZ hybrids in bacteria. Moreover, Lisbona *et al.* (*22*) recently reported that BI-1 is a negative regulator of ER stress. Despite its obvious importance, the mechanism of action of BI-1 remains unknown, in part because of the inherent difficulty of studying the effects of Bax and its inhibitors in eukaryotic cells (*20*, *23*). Owing to the highly conserved function of BI-1 and YccA, studies of the bacterial counterpart may shed light on the mechanistic role of this important cell death regulator in human cells.

References and Notes

1. T. A. Rapoport, *Nature* **450**, 663 (2007).
2. R. S. Hegde, H. D. Bernstein, *Trends Biochem. Sci.* **31**, 563 (2006).
3. A. K. Veenendaal, C. van der Does, A. J. Driessen, *Biochim. Biophys. Acta* **1694**, 81 (2004).
4. C. W. Bowers, F. Lau, T. J. Silhavy, *J. Bacteriol.* **185**, 5697 (2003).
5. T. J. Silhavy, H. A. Shuman, J. Beckwith, M. Schwartz, *Proc. Natl. Acad. Sci. U.S.A.* **74**, 5411 (1977).
6. P. Bassford, T. J. Silhavy, J. Beckwith, *J. Bacteriol.* **139**, 19 (1979).
7. C. L. Cosma, P. N. Danese, J. H. Carlson, T. J. Silhavy, W. B. Snyder, *Mol. Microbiol.* **18**, 491 (1995).
8. W. B. Snyder, L. J. Davis, P. N. Danese, C. L. Cosma, T. J. Silhavy, *J. Bacteriol.* **177**, 4216 (1995).
9. N. L. Price, T. L. Raivio, *J. Bacteriol.* **191**, 1798 (2008).
10. K. Yamamoto, A. Ishihama, *Biosci. Biotechnol. Biochem.* **70**, 1688 (2006).
11. Materials and methods are available as supporting material on *Science* Online.
12. A. Kihara, Y. Akiyama, K. Ito, *Proc. Natl. Acad. Sci. U.S.A.* **92**, 4532 (1995).
13. A. Kihara, Y. Akiyama, K. Ito, *J. Mol. Biol.* **279**, 175 (1998).
14. T. Ogura *et al.*, *Mol. Microbiol.* **31**, 833 (1999).
15. C. Walsh, *Antibiotics: Actions, Origins, Resistance* (ASM Press, Washington, DC, 2003).
16. Y. Akiyama, K. Ito, *J. Biol. Chem.* **264**, 437 (1989).
17. W. E. Feldman, N. S. Manning, *Antimicrob. Agents Chemother.* **23**, 551 (1983).
18. J. J. Rahal Jr., M. S. Simberkoff, *Antimicrob. Agents Chemother.* **16**, 13 (1979).
19. Q. Xu, J. C. Reed, *Mol. Cell* **1**, 337 (1998).
20. H. J. Chae *et al.*, *Gene* **323**, 101 (2003).
21. M. I. Smith, M. Deshmukh, *Cell Death Differ.* **14**, 1011 (2007).
22. F. Lisbona *et al.*, *Mol. Cell* **33**, 679 (2009).
23. R. Huckelhoven, *Apoptosis* **9**, 299 (2004).

24. We thank I. Collinson for SecY antisera and T. Ogura for strains. This work was supported by the National Institute of General Medical Sciences (T.J.S.), the New Jersey Commission on Cancer Research (J.v.S.), and the Canton de Genève and the Swiss National Science Foundation (F.S. and D.B.).

Supporting Online Material

www.sciencemag.org/cgi/content/full/325/5941/753/DC1
Materials and Methods
Figs. S1 to S3
Table S1
References

12 February 2009; accepted 23 June 2009
10.1126/science.1172221

Synaptic Integration in Tuft Dendrites of Layer 5 Pyramidal Neurons: A New Unifying Principle

Matthew E. Larkum,[1]*† Thomas Nevian,[1]* Maya Sandler,[2] Alon Polsky,[2] Jackie Schiller[2]†

Tuft dendrites are the main target for feedback inputs innervating neocortical layer 5 pyramidal neurons, but their properties remain obscure. We report the existence of *N*-methyl-D-aspartate (NMDA) spikes in the fine distal tuft dendrites that otherwise did not support the initiation of calcium spikes. Both direct measurements and computer simulations showed that NMDA spikes are the dominant mechanism by which distal synaptic input leads to firing of the neuron and provide the substrate for complex parallel processing of top-down input arriving at the tuft. These data lead to a new unifying view of integration in pyramidal neurons in which all fine dendrites, basal and tuft, integrate inputs locally through the recruitment of NMDA receptor channels relative to the fixed apical calcium and axosomatic sodium integration points.

The pyramidal neuron is the basic computational unit of the cortex. Its distal tuft dendrite is heavily innervated by horizontal fibers coursing through layer 1 (L1), which provide long-range corticocortical and thalamocortical associational input (*1*–*6*). In the standard view of dendritic electrogenesis of L5 pyramidal neurons, the basal and apical tuft dendrites are quite different (*7*–*9*). Whereas thin basal dendrites of neocortical pyramidal neurons initiate local *N*-methyl-D-aspartate (NMDA) and weak Na^+ spikes (*10*–*12*), the apical dendrite is able to initiate calcium spikes (*13*–*17*). However, this view is based mostly on recordings from the thick apical dendrite, and little information is presently available with regard to the actual properties of the tuft dendrites, which are thin dendrites branching from the main bifurcation forming a tree that resembles more closely the basal dendritic tree. It has been suggested that the properties that give rise to calcium spikes are restricted to an apical band (*18*) beyond which the initiation of Ca^{2+} spikes becomes progressively more difficult (*19*) [but see Rhodes and Llinás (*20*)]. This raises questions about the active and passive properties of the tuft dendrites, which are vital to understanding how and where feedback inputs to the pyramidal neuron are integrated (*21*). To overcome the difficulties in recording from these fine dendrites, we combined two-photon excitation fluorescence microscopy and infrared-scanning gradient contrast (*10*).

Using multiple simultaneous patch-clamp recordings from near the main apical bifurcation point (658 ± 110 μm from the soma; $n = 28$) and secondary and tertiary/quaternary tuft branches (775 ± 98 μm from the soma, $n = 14$; and 859 ± 60, $n = 8$) to within 50 μm of the pia of L5 pyramidal neurons, we directly tested the local spiking capabilities of fine tuft dendrites. Recordings from higher-order branches mostly in L1 or near the border of L1/L2 are referred to as "distal tuft" recordings. We first investigated local integration of synaptic input using visually guided focal stimulation at preselected distal tuft dendrites while recording simultaneously the voltage from nearby locations (Fig. 1A). Recordings made from two distal tuft dendrites simultaneously while focally stimulating each of the branches revealed local, all-or-none spikes that failed to propagate to neighboring tuft branches (Fig. 1, B and C). On average, the spike attenuated by 86 ± 2.3% as it spread from one branch to another ($n = 3$).

Simultaneous recordings from distal and proximal tuft branches revealed that these all-or-none potentials originated in the fine distal tuft branches and attenuated as they spread proximally (Fig. 1, D to F). The voltage threshold for initiation of synaptically evoked dendritic spikes at the distal tuft branches was 9.67 ± 4.69 mV, and the amplitude of the spike at the distal tuft branch recording site was an additional 17.39 ± 5.87 mV from threshold and 27.07 ± 9.62 mV from baseline (*22*, *23*). These spikes attenuated further as they spread toward the main bifurcation point (by a factor of 2.25 ± 0.58; $n = 6$; average distance between the recording sites 189 ± 74 μm) (Fig. 1F) but still could contribute substantial depolarization. The cable-filtered distal tuft dendritic spike attenuated on average to 7.74 ± 2.8 mV at the proximal tuft recording site.

Because of their localization to the activated branch, we considered the possibility that, similar to basal dendrites, the main regenerative current of the distal tuft dendrites is carried through the synaptic currents themselves, that is, NMDA receptor channels (*11*). The specific NMDA receptor blocker AP5 (100 μM) completely abolished the dendritic spike and linearized the relationship between the synaptic stimulus intensity and the excitatory postsynaptic potential (EPSP) amplitude observed under control conditions ($n = 7$) (Fig. 1, G to I). To rule out the possibility that blockade of NMDA receptors simply increased the threshold for local spikes, we also used ultraviolet (UV) laser uncaging of glutamate (MNI-glutamate) directed to a specific location in the distal tuft dendrites while recording the nearby dendritic voltage (recordings at 832 ± 61.5 μm from the soma passed second bifurcation and mostly at third bifurcations; uncaging site was 18 ± 2.7 μm distal to recording site; $n = 8$) (Fig. 1J) (*24*). Gradually increasing the UV laser intensity evoked gradual EPSP-like potentials until a threshold value

[1]Department of Physiology, University of Berne, Bühlplatz 5, 3012 Berne, Switzerland. [2]Department of Physiology, The Rappaport Faculty of Medicine and Research Institute, Technion-Israel Institute of Technology, Bat-Galim, Haifa 31096, Israel.

*These authors contributed equally to this work.
†To whom correspondence should be addressed. E-mail: matthew.larkum@gmail.com (M.E.L.); jackie@tx.technion.ac.il (J.S.)

beyond which a spike was initiated (Fig. 1J). With this stimulation method, we could test the contribution of Na^+ and Ca^{2+} voltage-gate channels with application of tetrodotoxin (TTX) (1 μM), cadmium (100 μM), and nickel (100 μM). These blockers had only a minor effect on the spike amplitude and threshold (spike amplitude from baseline 53.5 ± 7 mV and 51.2 ± 7.4 mV; spike threshold 18.7 ± 4.1 mV and 19.2 ± 4.6 mV before and after application of cadmium, nickel, and TTX, respectively; $n = 5$). In contrast, it was not possible to evoke a spike in the presence of AP5 (50 μM; $n = 4$).

Our uncaging experiments suggested that distal tuft dendrites cannot support calcium electrogenesis but can support weak sodium spikes in addition to NMDA spikes. To further investigate this point, we used direct current injection through dendritic patch electrodes (Fig. 2A). In agreement with previous reports (*14*, *19*), current injection (300 pA to 1900 pA, 800 ms) to the proximal tuft dendrites (main bifurcation and primary tuft branches) nearly always initiated a calcium spike at the site of injection (Fig. 2, B and F) ($n = 39/43$; average threshold 1003 ± 346 pA). These calcium spikes propagated well into the distal tuft branches (including to tertiary and quaternary branches), only attenuating to 92.6 ± 7% of the proximal tuft amplitude (see also fig. S1). In contrast, current injection to distal tuft dendrites rarely initiated dendritic Ca^{2+} spikes. In distal tuft branches, Ca^{2+} spikes were evoked in only 4 out of 36 cases (Fig. 2F). However, in 24 out of 36 recordings, small regenerative events were initiated (average 20 ± 7 mV as measured from baseline; $n = 24$), and in the rest (8/36), no regenerative events could be elicited with up to 2400 pA current injection (Fig. 2F). The dichotomy between distal versus proximal electrogenesis was confirmed statistically using Fisher's exact test ($P < 0.001$). The threshold of the small regenerative event was 1008 ± 475 pA in secondary branches and 736 ± 238 pA in tertiary or more distal branches, and its forward propagation was poor (attenuation between 2 and 3 branch points to 33% ± 14% of its original value; $n = 9$).

Addition of TTX (1 μM) (Fig. 2D) did not block the initiation of regenerative potentials at the proximal tuft dendrites [which in some cases even became longer (e.g., Fig. 2D, black)] but

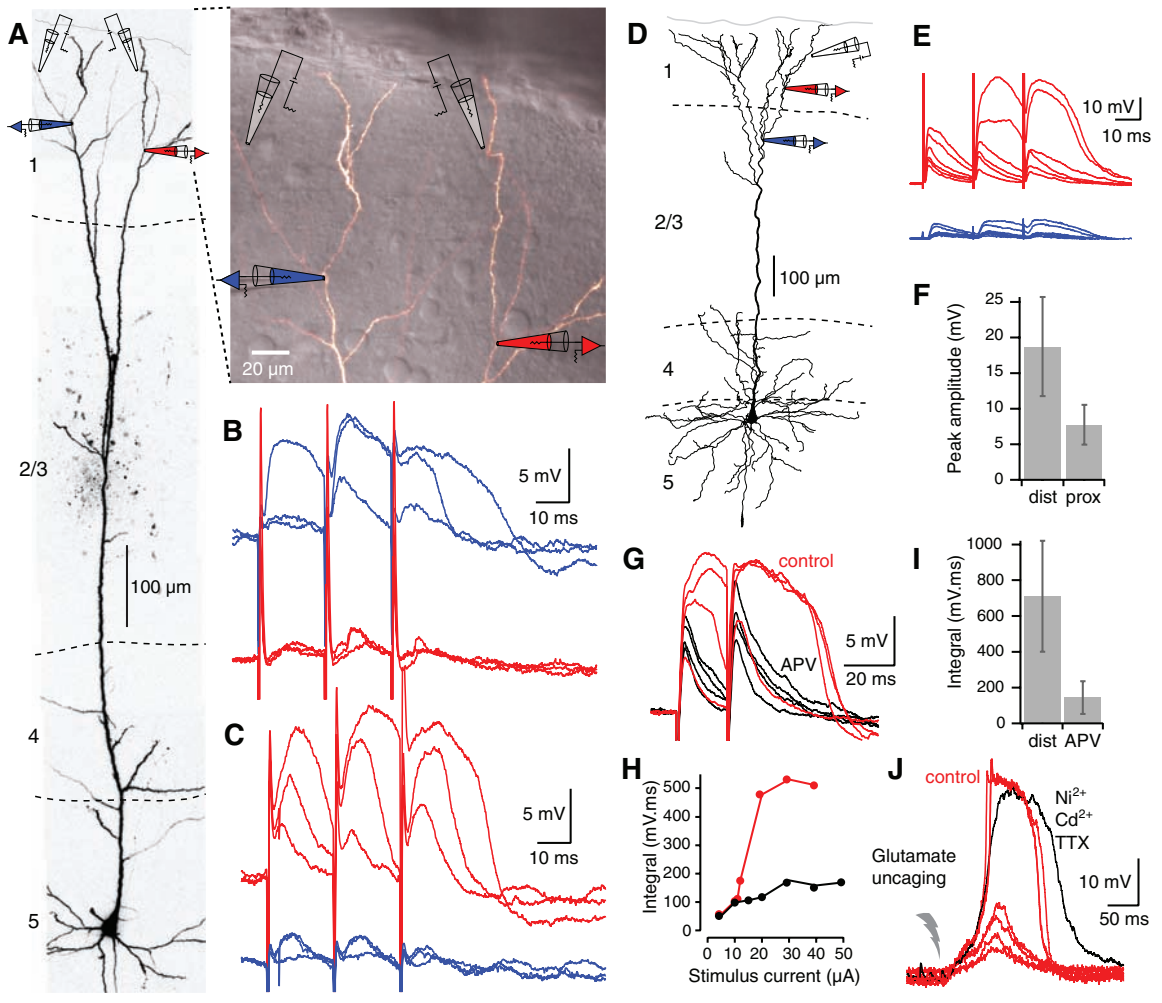

Fig. 1. NMDA spikes in fine tuft dendrites of L5 pyramidal neurons. (**A**) Two-photon fluorescence image of an L5 pyramidal neuron (left) and fluorescence image overlayed with scanning gradient contrast image (right). (**B** and **C**) Parallel recordings were performed from two tuft dendrites simultaneously (blue electrode, 4th bifurcation, 975 μm from the soma; red electrode, 3rd bifurcation, 944 μm from the soma) while separately focally (gray electrodes) each of the recorded sub-branches sequentially with gradually increasing stimulus intensity until an NMDA spike was evoked. Simultaneous responses are shown from both locations, with increasing stimulation intensity near the blue electrode (B) and the red electrode (C). (**D**) Reconstruction of a biocytin-filled L5 pyramidal neuron showing the experimental setup. Dendritic recording pipettes are shown near the third bifurcation (875 μm from the soma, red) and near the second bifurcation (715 μm from the soma, blue). An extracellular stimulation electrode (black) was positioned ~100 μm distal to the distal recording electrode. (**E**) Responses to gradual increase of the extracellular stimulus (from 4 to 9 μA) recorded in both electrodes. (**F**) Summary of the size of extracellularly evoked dendritic spikes recorded in the distal tuft and proximal tuft shaft for six neurons (distance between the two recording electrodes 189.2 ± 74 μm). Peak responses were measured from threshold. (**G**) Dendritic recording from another pyramidal neuron after the second bifurcation (807 μm from the soma, red), similar to the recording shown in (D). An extracellular synaptic stimulation electrode was positioned ~100 μm from the recording electrode. Gradually increasing extracellular stimulation strength (10 to 40 μA) led to broad regenerative spikes that were blocked by the addition of 50 μM AP5. (**H**) Integral of the voltage responses to a paired stimulation before (red) and after application of AP5 for recordings shown in (G). The integral was measured over the entire response. (**I**) Summary of results in (G) and (H) showing the blockade of the spike by AP5. (**J**) Uncaging MNI-glutamate near another tuft dendrite (recording electrode 830 μm from the soma, uncaging 40 μm from recording site) also led to a prolonged spike (red) which was not blocked by a combination of 100 μM Ni^{2+}, 100 μM Cd^{2+}, and 1 μM TTX (black). Note the blockade of a small sodium component in the spike by TTX (black).

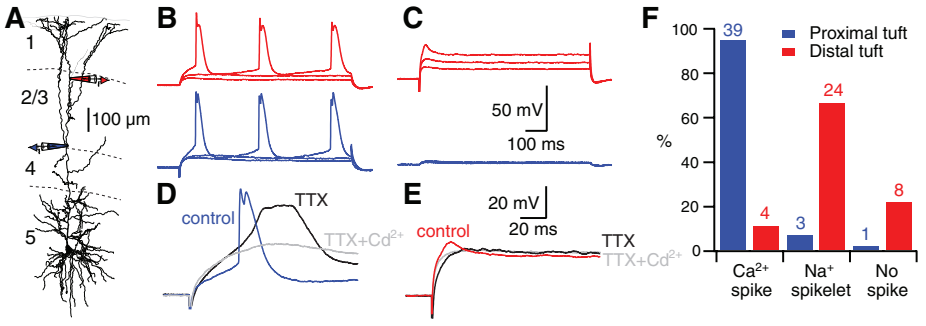

Fig. 2. Properties of the L5 pyramidal distal apical tuft dendrite revealed by current injection. (**A**) Reconstruction of biocytin-filled L5 pyramidal neuron showing the experimental setup. Two dendritic tuft recording pipettes are shown (blue electrode, 550 μm at main bifurcation point; red electrode at distal tuft, 850 μm from the soma). (**B**) Long current injection (400-ms steps) at the more proximal tuft electrode resulted in broad dendritic spikes first at the proximal (blue) and then distal (red) electrode. (**C**) Current injection at the distal tuft electrode (red) evoked only a small spikelet that did not propagate to the proximal tuft electrode (blue). (**D**) Suprathreshold spike response to same current injection shown in (B) in control conditions and after consecutive application of 1 μM TTX (black) and 100 μM Cd^{2+} (gray) to the extracellular solution. (**E**) Same as (D) for distal current injection. (**F**) Summary of responses to suprathreshold current injection in different L5 pyramidal cells when current was injected in dendrites of branch order 1 (blue, i.e., on or after the main bifurcation) compared with responses to injection in higher-order branches (red).

completely abolished the local regenerative events in distal tuft branches (Fig. 2E, red) (n = 4). Addition of extracellular cadmium (100 μM), however, blocked the regenerative event at the proximal tuft dendrites but had no further effect on the response seen in the distal tuft branches (n = 4) (Fig. 2E). Dendrite thickness was a good predictor of Na^+ spikelet versus Ca^{2+} spike electrogenesis, thicker (3.0 ± 1.1 μm; n = 26) dendrites supporting calcium spikes and thinner (1.6 ± 0.5 μm; n = 19) dendrites supporting pure sodium electrogenesis only (fig. S4).

Several properties, including the existence of local NMDA spikes and the weak electrogenesis of both sodium and calcium spikes, suggest that the relationship of the fine distal tuft branches to the apical Ca^{2+} initiation zone is similar to the relationship of the basal dendrites to the axosomatic initiation zone (*10*). However, one of the most notable remaining differences between the distal tuft and basal dendrites is the presence of hyperpolarization-activated current (I_h) (*25*–*27*). This current, which is active at resting potentials, acts like a leak and could potentially determine

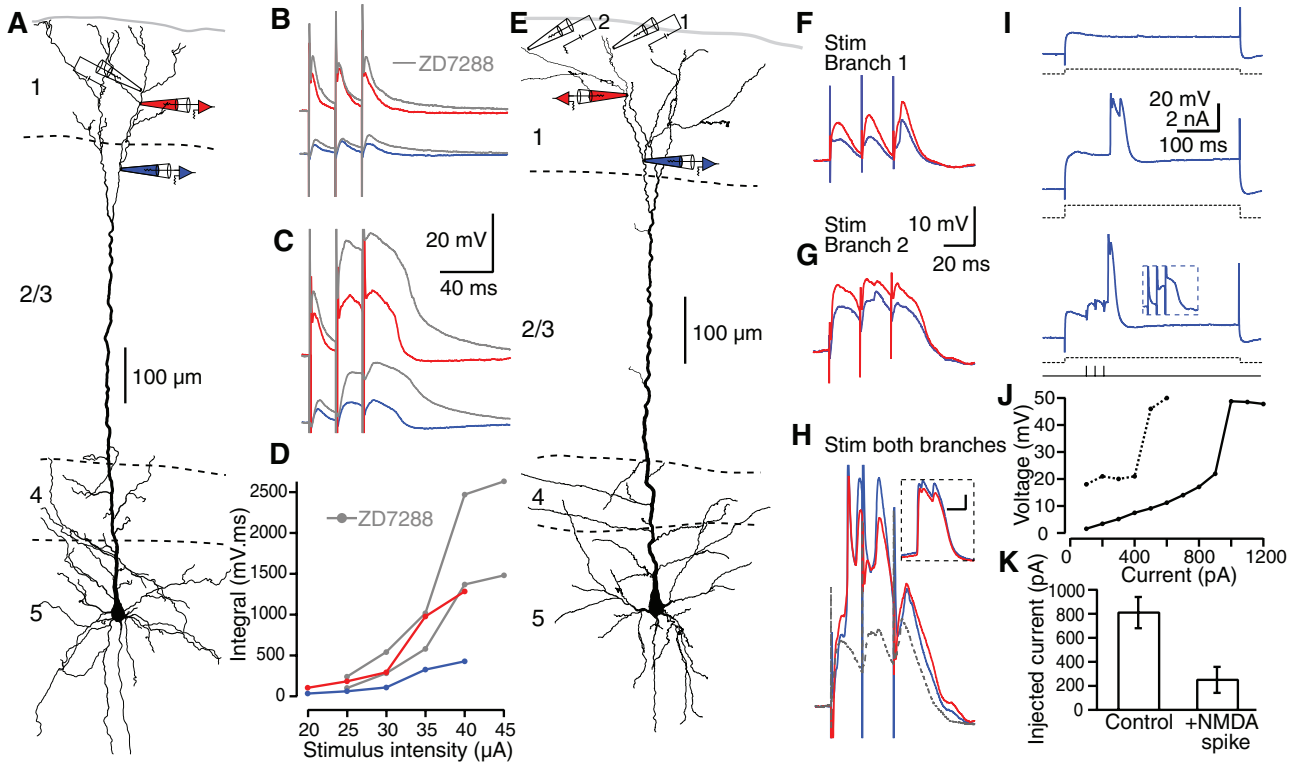

Fig. 3. Compartmentalization and interactions of NMDA spikes in the tuft. (**A** to **D**) Recordings were made from proximal tuft dendrite electrodes at 790 μm (blue) and at distal tuft dendrite 930 μm (red) from the soma (A). The effect of the I_h-channel blocker ZD7288 on the EPSPs (B) and NMDA spikes (C) evoked by extracellular synaptic stimulation (black electrode) at tuft dendrites. (D) Integral of the responses as a function of the stimulus intensity. For (B) to (D), colored traces show control responses, and gray traces indicate the same responses after application of ZD7288 (D). (**E** to **H**) Simultaneous activation of two tuft branches evoked a calcium spike. (E) Experimental setup. Simultaneous stimulation at site 1, which alone evoked an EPSP (F), and at site 2, which alone evoked an NMDA spike (G), summated and crossed the threshold in the calcium spike initiation zone (H). (Inset) The calcium spike evoked by current injection at the proximal electrode (no calcium spike could be evoked at the distal site, red). Recording electrodes at 640 μm (blue) and 750 μm (red) from the soma (E). (**I**) Subthreshold current injection (350 nA, top, black dashed line) in the calcium spike initiation zone (top, blue trace) reached threshold at 900 nA (middle), which was also reached by 350 nA current injection with a simultaneous NMDA spike in a branch (evoked at the 4th bifurcation and recorded at the 3rd bifurcation; reconstructed cell not shown). (**J**) Maximum depolarization in the presence (dashed line) and absence (solid line) of NMDA spike initiation at a third-order bifurcation. (**K**) Average current threshold at the site proximal to the main bifurcation site needed to evoke a Ca^{2+} spike with and without an NMDA spike.

the degree of compartmentalization of the tuft tree and lead to substantial current loss of signals propagating toward the apical Ca^{2+} spike dendritic initiation zone. Addition of the I_h channel blocker ZD7288 to the bath solution (50 to 100 μM) led to an increase in the size and integral of NMDA spikes at both tuft dendrites and the main apical bifurcation point (Fig. 3, A to D). In the presence of ZD7288, the average amplitude of NMDA spikes increased by 221 ± 35% in the tuft and by 298 ± 63% (n = 4) in the proximal tuft dendrites. Our findings show that I_h currents had dramatic effects on the characteristics and spread of NMDA spikes, and thus on the degree of compartmentalization of the tuft tree.

The calcium initiation zone is considered to be an integration zone conveying pre-integrated apical information to the axosomatic initiation zone (*28*–*31*). Thus, we were interested in the summation process of NMDA spikes at the level of the calcium spike initiation zone. The attenuation of the NMDA spike initiated at a single distal tuft branch meant that the threshold for a Ca^{2+} spike was never reached at the Ca^{2+} initiation zone by a single distal NMDA spike at threshold stimulation (n = 20) (*32*). However, the voltage of two distal tuft branches could sum to initiate an apical calcium spike. Dual-site focal synaptic stimulation of identified thin tuft dendrites showed that the generation of NMDA spikes in two different distal tuft branches, or even an NMDA spike in one branch and an EPSP in the second, was sufficient to reach threshold at the Ca^{2+} initiation zone (Fig. 3, E to G; n = 7). Furthermore, small depolarization near the Ca^{2+} spike initiation zone enabled NMDA spikes in single distal tuft branches to evoke Ca^{2+} spikes (Fig. 3, I to K). Pairing current injections at the calcium initiation zone with NMDA spikes at distal tuft branches lowered significantly the current injection required for calcium spike initiation (current threshold changed from 820 ± 130 pA at control to 260 ± 108 pA during pairing; P = 0.0001).

How crucial are NMDA spikes in firing the calcium initiation zone? To evaluate the impact tuft inputs may have at the apical calcium spike initiation zone without the influence of NMDA spikes, we characterized the size and propagation of the unitary synaptic events at the distal tuft branches. Spontaneous and sucrose-evoked synaptic inputs to the distal tuft branches were severely attenuated after propagating to the calcium spike initiation zone (Fig. 4, A to D). Next, we used computer simulations in the NEURON simulation platform to investigate the contribution of tuft NMDA spikes versus tuft AMPA-EPSPs in initiating apical calcium spikes. Active and passive parameters were varied until a good agreement with our experimental data was obtained (fig. S2). To fit the experimental data, voltage-gated potassium channel density in the tuft region was made an order of magnitude lower than the apical trunk. In addition, we inserted low calcium conductance into the tuft region, combined with a "hot zone" of calcium conductance situated at the main bifurcation zone extending 500 to 800 μm from the soma. When the calcium conductance was evenly distributed throughout the tuft, we could not fit the experimental data regardless of the amount of potassium conductance inserted. The model either could not evoke calcium spikes (low calcium) or evoked ripples (high calcium). Spine density was determined from reconstructed biocytin-labeled cells used in this study. The unitary synaptic conductance was estimated from both sucrose-evoked EPSPs and excitatory postsynaptic currents (EPSCs) (17.32 ± 8.6 pA) (Fig. 4, A to E), with

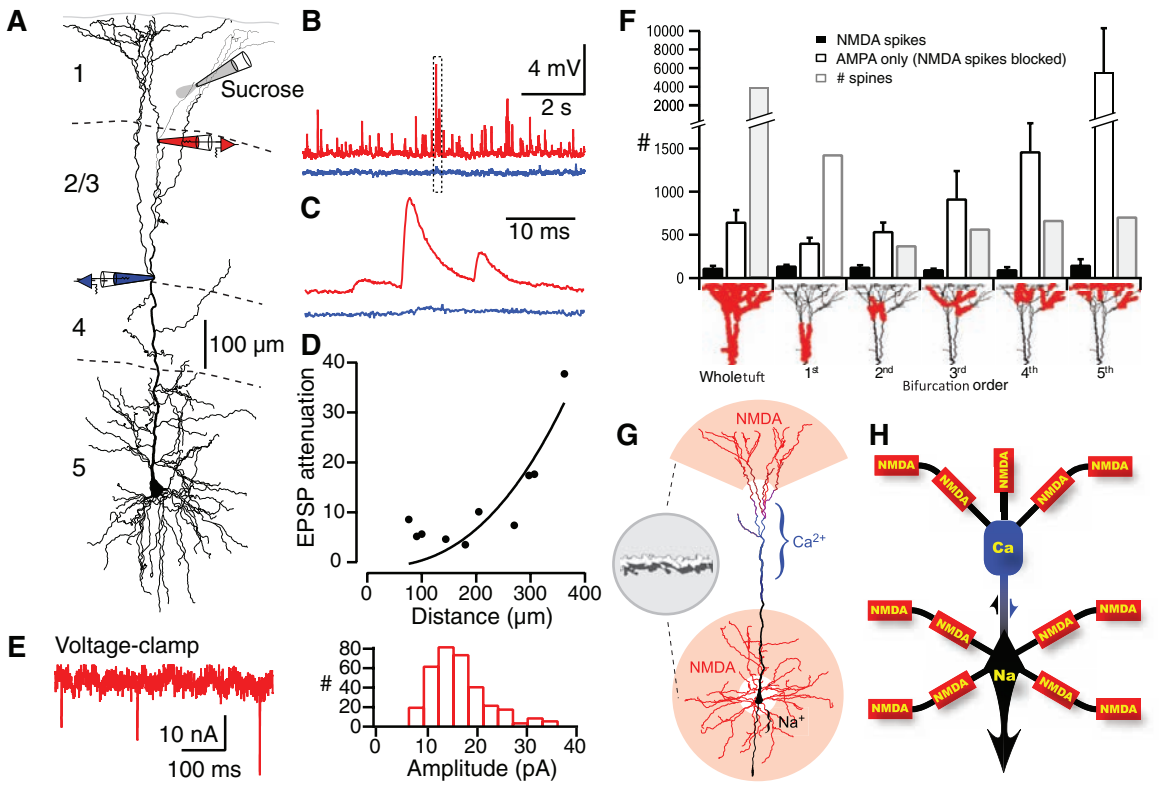

Fig. 4. General scheme for the integration of synaptic input to the tuft. (**A**) Reconstruction of biocytin-filled L5 pyramidal neuron showing the experimental setup. Two tuft recording pipettes are shown (blue electrode, 550 μm from the soma; red electrode, 850 μm from the soma). Another pipette for locally applying a high-sucrose solution is shown near a distal tuft branch (black, 915 μm from the soma.) (**B**) Spontaneous activity after local application of sucrose to the distal tuft. (**C**) Same as (B) for the time indicated by the box in (B). (**D**) Attenuation of EPSPs (spontaneous and sucrose-evoked pooled) versus distance from the distal (higher branch order) recording electrode to the proximal (first-order branch) electrode for 10 neurons. Here, zero marks the position of the proximal recording electrode. (**E**) Voltage-clamp recordings at a distal tuft branch 950 μm from the soma in a different neuron. (Left) Examples of unitary EPSCs evoked by local sucrose application (10 μm distal to the recording site). (Right) Amplitude histogram distribution of unitary EPSC from the same recording (175 events). (**F**) Results of simulations in NEURON predicting the number of active synapses at the tuft needed to generate a Ca^{2+} spike near the main bifurcation point (activated randomly at different locations). The results are binned according to the region with active synapses (shown schematically underneath). Indicated for each bin is the number of active synapses required under control conditions (NMDA spikes, black), without NMDA receptors (AMPA only, white), and also the total number of spines per activated region (gray). (**G**) Reconstructed pyramidal neuron showing the regions of the dendritic tree where NMDA (red), Ca^{2+} (blue), and Na^+ (black) electrogenesis can be initiated. (Inset) Enlargement of typical thin branch with a higher density of synapses than thicker dendrites (*33*). (**H**) Schematic representation of the important subcompartments of a typical L5 pyramidal neuron showing the relationship of multiple local sites for NMDA spikes to the Ca^{2+} and Na^+ initiation zones, which can signal each other through active propagation along the main apical trunk (arrows).

4.25 ±1.9 pA of NMDA current at resting membrane potential. In addition, we measured directly (830 to 950 μm from the soma) the total and NMDA just-suprathreshold current needed for NMDA spike initiation using glutamate uncaging (total current of 187 ± 43 pA; NMDA current of 88 ± 19 pA; $n = 5$) (fig. S2D). Using these parameters, NMDA spikes could be initiated at all locations on the tuft tree; however, the number of synapses needed was far lower in the very distal tuft branches. Just 8.75 ± 2.21 synapses were needed to evoke NMDA spikes near the ends of the tuft branches, whereas up to 43 ± 4.54 synapses were needed at 250 μm from the pia, leading to a depolarization of 1.07 ± 0.25 mV and 9.22 ± 1.4 mV, respectively, at the calcium spike initiation zone (fig. S2). The contribution of voltage-gated calcium channels was negligible at the tuft regions (fig. S2) but became prominent at the apical calcium initiation zone (extending ~340 μm from the first bifurcation), where a full-blown calcium spike was evoked (fig. S2).

When we activated randomly distributed synapses at the tuft dendrites, which usually leads to NMDA spike initiation at multiple branches, we found that 116.66 ± 25.59 randomly distributed synapses (2.9% of total synapses) over the whole tuft region are sufficient to trigger a calcium spike (Fig. 4F). Interestingly, when we redistributed the activated synapses based on bifurcation order, calcium spikes were most readily initiated by third- and fourth-order branches (100.83 ± 11.64 and 99 ± 28.75 synapses, respectively) (Fig. 4F). Blocking NMDA receptors caused a dramatic increase in the number of synapses at tuft branches needed for calcium spike initiation. In this scenario, the number of synapses increased exponentially with branch order, from 408.33 ± 59.69 synapses near the main bifurcation to 5550 ± 4749 synapses at the terminal branches (exceeding the total spine number at these dendrites) (*33*) (Fig. 4F). In contrast, NMDA spikes only modestly contributed to the initiation of calcium spikes when synapses were activated at the calcium initiation zone itself (Fig. 4F, first bifurcation). On the other hand, uniformly increasing calcium conductance in tuft branches (up to a factor of 3) did not change the requirement for an exponential increase in the number of pure AMPA synapses needed to initiate a calcium spike at the main bifurcation point.

Thus, there are three stages (thresholds) in the integration of top-down associative information terminating at distal tuft branches: (i) NMDA spike initiation at the distal tuft branches, (ii) Ca^{2+} spike initiation near the main bifurcation, and (iii) sodium spike initiation at the axon hillock (Fig. 4, G and H).

Taking all the properties together, a new unifying principle emerges as to how pyramidal neurons integrate synaptic information. The thin distal tuft and basal dendrites of pyramidal neurons, which receive the overwhelming majority of synaptic inputs (*33*), appear to constitute a class of dendrite in which NMDA spikes are the predominant regenerative events summing synaptic inputs in semi-independent compartments. The output of each subunit in this class of dendrite is passed on to the major sites of integration at the axon and apical calcium initiation zones, which can all interact via actively propagated signals (*34*), enabling the interactions between top-down and bottom-up information.

References and Notes

1. D. J. Felleman, D. C. Van Essen, *Cereb. Cortex* **1**, 1 (1991).
2. K. S. Rockland, D. N. Pandya, *Brain Res.* **179**, 3 (1979).
3. J. M. Budd, *Proc. R. Soc. London Ser. B Biol. Sci.* **265**, 1037 (1998).
4. B. Kuhn, W. Denk, R. M. Bruno, *Proc. Natl. Acad. Sci. U.S.A.* **105**, 7588 (2008).
5. L. Petreanu, T. Mao, S. M. Sternson, K. Svoboda, *Nature* **457**, 1142 (2009).
6. P. Rubio-Garrido, F. Pérez-de-Manzo, C. Porrero, M. J. Galazo, F. Clascá, *Cereb. Cortex*; published online 2 February 2009 (10.1093/cercor/bhn259).
7. O. Bernander, C. Koch, R. J. Douglas, *J. Neurophysiol.* **72**, 2743 (1994).
8. M. Häusser, N. Spruston, G. J. Stuart, *Science* **290**, 739 (2000).
9. N. Spruston, *Nat. Rev. Neurosci.* **9**, 206 (2008).
10. T. Nevian, M. E. Larkum, A. Polsky, J. Schiller, *Nat. Neurosci.* **10**, 206 (2007).
11. J. Schiller, G. Major, H. J. Koester, Y. Schiller, *Nature* **404**, 285 (2000).
12. B. A. Milojkovic, J. P. Wuskell, L. M. Loew, S. D. Antic, *J. Membr. Biol.* **208**, 155 (2005).
13. H. G. Kim, B. W. Connors, *J. Neurosci.* **13**, 5301 (1993).
14. J. Schiller, Y. Schiller, G. Stuart, B. Sakmann, *J. Physiol. London* **505**, 605 (1997).
15. M. E. Larkum, K. M. Kaiser, B. Sakmann, *Proc. Natl. Acad. Sci. U.S.A.* **96**, 14600 (1999).
16. M. E. Larkum, J. J. Zhu, B. Sakmann, *Nature* **398**, 338 (1999).
17. A. Polsky, B. W. Mel, J. Schiller, *Nat. Neurosci.* **7**, 621 (2004).
18. R. Yuste, M. J. Gutnick, D. Saar, K. R. Delaney, D. W. Tank, *Neuron* **13**, 23 (1994).
19. M. E. Larkum, J. J. Zhu, *J. Neurosci.* **22**, 6991 (2002).
20. P. A. Rhodes, R. R. Llinás, *J. Physiol.* **536**, 167 (2001).
21. S. R. Williams, G. J. Stuart, *Trends Neurosci.* **26**, 147 (2003).
22. J. Bullier, *Brain Res. Brain Res. Rev.* **36**, 96 (2001).
23. The dendritic spike was probably larger than this at the site of initiation, which was most likely closer to the stimulating electrode.
24. Distal dendritic recording sites were chosen on the basis of dendritic thickness and the lack of Ca^{2+} spike initiation.
25. T. Berger, M. E. Larkum, H. R. Lüscher, *J. Neurophysiol.* **85**, 855 (2001).
26. S. R. Williams, G. J. Stuart, *J. Neurophysiol.* **83**, 3177 (2000).
27. A. Lörincz, T. Notomi, G. Tamás, R. Shigemoto, Z. Nusser, *Nat. Neurosci.* **5**, 1185 (2002).
28. P. A. Rhodes, in *Cerebral Cortex, Vol. 13*, P. S. Ulinski, E. G. Jones, A. Peters, Eds. (Plenum, New York, 1999), pp. 139–200.
29. C. Koch, I. Segev, *Nat. Neurosci.* **3** (suppl.), 1171 (2000).
30. N. Spruston, W. L. Kath, *Nat. Neurosci.* **7**, 567 (2004).
31. M. London, M. Häusser, *Annu. Rev. Neurosci.* **28**, 503 (2005).
32. With the I_h-blocker ZD7288, single NMDA spikes sometimes caused Ca^{2+} spikes.
33. A. U. Larkman, *J. Comp. Neurol.* **306**, 332 (1991).
34. M. E. Larkum, J. J. Zhu, B. Sakmann, *J. Physiol. London* **533**, 447 (2001).

35. We thank B. Sakmann for generous support and comments on the manuscript and Y. Schiller for helpful comments and discussions on the manuscript. We thank K. Fischer for Neurolucida reconstructions of the biocytin-filled neurons. This study was supported by NIH, the Israel Science Foundation, and the Rappaport Foundation (J.S.); by the Swiss National Science Foundation (M.L., grant PP0033-119159; T.N., grant 3100A0-118395); and by SystemsX.ch (M.L., Neurochoice). The authors declare that they have no competing financial interests.

Supporting Online Material

www.sciencemag.org/cgi/content/full/325/5941/756/DC1
Materials and Methods
Figs. S1 to S4
References

6 February 2009; accepted 24 June 2009
10.1126/science.1171958

Spinal Endocannabinoids and CB_1 Receptors Mediate C-Fiber–Induced Heterosynaptic Pain Sensitization

Alejandro J. Pernía-Andrade,[1]*† Ako Kato,[1,9]* Robert Witschi,[1,9]* Rita Nyilas,[2] István Katona,[2] Tamás F. Freund,[2] Masahiko Watanabe,[3] Jörg Filitz,[4] Wolfgang Koppert,[4]‡ Jürgen Schüttler,[4] Guangchen Ji,[5] Volker Neugebauer,[5] Giovanni Marsicano,[6] Beat Lutz,[7] Horacio Vanegas,[8] Hanns Ulrich Zeilhofer[1,9]§

Diminished synaptic inhibition in the spinal dorsal horn is a major contributor to chronic pain. Pathways that reduce synaptic inhibition in inflammatory and neuropathic pain states have been identified, but central hyperalgesia and diminished dorsal horn synaptic inhibition also occur in the absence of inflammation or neuropathy, solely triggered by intense nociceptive (C-fiber) input to the spinal dorsal horn. We found that endocannabinoids, produced upon strong nociceptive stimulation, activated type 1 cannabinoid (CB_1) receptors on inhibitory dorsal horn neurons to reduce the synaptic release of γ-aminobutyric acid and glycine and thus rendered nociceptive neurons excitable by nonpainful stimuli. Our results suggest that spinal endocannabinoids and CB_1 receptors on inhibitory dorsal horn interneurons act as mediators of heterosynaptic pain sensitization and play an unexpected role in dorsal horn pain-controlling circuits.

Activity-dependent central hyperalgesia can be induced in the absence of any inflammation or nerve damage by selective activation of glutamatergic C-fiber nociceptors; for example, with the specific transient receptor potential channel (TRP) V1 agonist capsaicin. Local subcutaneous injection of capsaicin induces primary hyperalgesia at the site of injection and a purely mechanical secondary hyperalgesia in the surrounding healthy skin (*1*). This secondary hyperalgesia originates from changes in the central processing of input from mechano-

sensitive A fibers and is characterized by an exaggerated sensitivity to painful stimuli and by pain evoked by light tactile stimulation (allodynia or touch-evoked pain). These symptoms are mimicked by the blockade of inhibitory γ-aminobutyric acid–mediated (GABAergic) and glycinergic neurotransmission in the spinal dorsal horn (*2*, *3*), suggesting that a loss of synaptic inhibition also accounts for C-fiber–induced secondary hyperalgesia. Activity-dependent hyperalgesia can thus be regarded as a correlate of heterosynaptic depression of inhibition (*4*). In many neuronal circuits of the central nervous system, endocannabinoids [2-arachidonoyl glycerol (2-AG) and anandamide (AEA)] are released upon intense activation of metabotropic glutamate receptors and serve as retrograde messengers mediating either homosynaptic feedback inhibition or heterosynaptic depression of (GABAergic) inhibition (*5*, *6*). Type 1 cannabinoid (CB_1) receptors are densely expressed in the superficial dorsal horn of the spinal cord (*7*), where they exert anti-hyperalgesia in different inflammatory or neuropathic disease states (*8*, *9*).

To define the role of CB_1 receptors in dorsal horn neuronal circuits, we first characterized the effects of CB_1 receptor activation on neurotransmission in mouse transverse spinal cord slices (Fig. 1). Excitatory and inhibitory postsynaptic currents (EPSCs and IPSCs) were evoked by extracellular electrical field stimulation at a frequency of four per minute and recorded from visually identified neurons in the superficial spinal dorsal horn (laminae I and II) (*10*). The mixed CB_1/CB_2 receptor agonist WIN 55,212-2 (3 μM) reversibly reduced the amplitudes of glycine receptor IPSCs to 64.3 ± 3.5% of control amplitudes (mean ± SEM, $n = 13$ neurons, $P < 0.001$, paired Student's t test) (Fig. 1A). Similarly, $GABA_A$ receptor IPSCs were reduced to 64.7 ± 3.0% ($P < 0.001$, $n = 8$ neurons, paired Student's t test) (Fig. 1B). The inhibition of IPSCs by WIN 55,212-2 was confined to the superficial dorsal horn, reversed by the CB_1 receptor antagonist/inverse agonist AM 251 (5 μM) (Fig. 1, A and B), and absent in global CB_1 receptor–deficient mice ($CB_1^{-/-}$ mice) (*11*) and in mice lacking CB_1 receptors specifically in dorsal horn inhibitory interneurons (*ptf1a*-$CB_1^{-/-}$ mice) (*12*) (fig. S1). WIN 55,212-2 had virtually no effect on EPSCs mediated by glutamate receptors of the α-amino-3-hydroxy-5-methylisoxazole (AMPA) subtype (AMPA-EPSCs) [Fig. 1C, see also (*13*)]. It did, however, reduce the amplitudes of monosynaptic AMPA-EPSCs evoked by stimulation of dorsal root primary afferent nerve fibers at C-fiber intensity by 34.5 ± 3.3% ($n = 9$ neurons). This inhibition was not reversed by AM 251 (fig. S2). We next tested whether stimulation of endogenous endocannabinoid production through the activation of group I metabotropic glutamate receptors (mGluR1/5) would have a similar effect on inhibitory synaptic transmission. These experiments were carried out in GlyT2–enhanced green fluorescent protein (GlyT2-EGFP) transgenic mice, which allowed targeted recordings from glycinergic (EGFP-positive) and nonglycinergic (EGFP-negative), presumed excitatory, interneurons (*14*). (*S*)-3,5-dihydroxyphenylglycine (DHPG, 10 μM), an agonist at mGluR1/5, reduced IPSC amplitudes in nonglycinergic presumed excitatory superficial dorsal horn neurons by 40.6 ± 4.5% ($n = 8$ neurons) (Fig. 1D). This inhibition was reversed by AM 251 (5 μM) (Fig. 1D) and partially prevented by mGluR1 and mGluR5 antagonists (LY

[1]Institute of Pharmacology and Toxicology, University of Zurich, Winterthurerstrasse 190, CH-8057 Zurich, Switzerland. [2]Institute of Experimental Medicine, Hungarian Academy of Sciences, H-1083 Budapest, Hungary. [3]Department of Anatomy, Hokkaido University School of Medicine, Sapporo 060-8638, Japan. [4]Department of Anesthesiology, University of Erlangen-Nürnberg, Krankenhausstrasse 12, D-91054 Erlangen, Germany. [5]Department of Neuroscience and Cell Biology, University of Texas Medical Branch, Galveston, TX 77555–1069, USA. [6]U862 Centre de Recherche INSERM François Magendie, 33077 Bordeaux, France. [7]Institute of Physiological Chemistry and Pathobiochemistry, Johannes Gutenberg-University Mainz, D-55099 Mainz, Germany. [8]Instituto Venezolano de Investigaciones Cientificas, Apartado 20632, Caracas 1020A, Venezuela. [9]Institute of Pharmaceutical Sciences, ETH Zurich, Wolfgang Pauli Strasse 10, CH-8093 Zurich, Switzerland.

*These authors contributed equally to this work.
†Present address: Institute of Physiology, University of Freiburg, Engesserstrasse 4, D-79108, Freiburg, Germany.
‡Present address: Department of Anesthesiology, Medical School Hannover, D-30625 Hannover, Germany.
§To whom correspondence should be addressed. E-mail: zeilhofer@pharma.uzh.ch

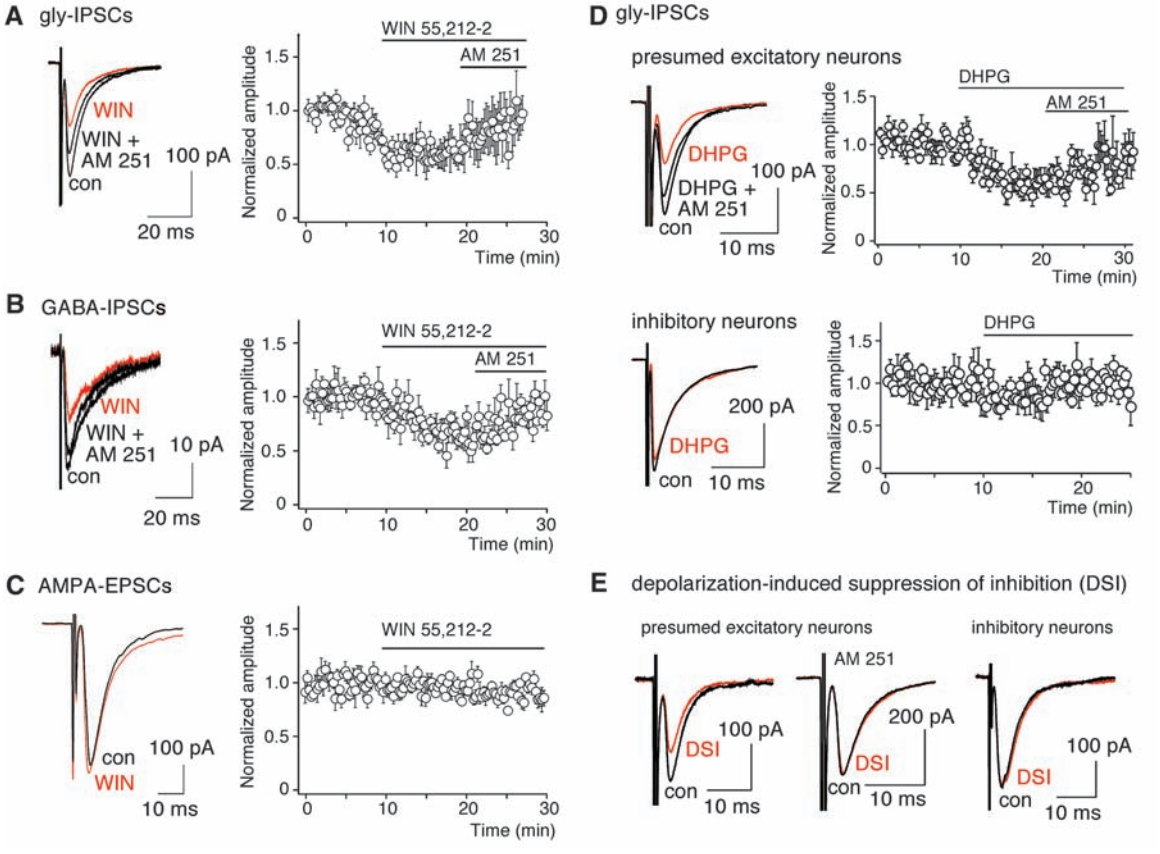

Fig. 1. Synaptic effects of CB_1 receptor activation in dorsal horn neuronal circuits. (**A** to **C**) Effects of the mixed CB_1/CB_2 receptor agonist WIN 55,212-2 (3 μM) on glycinergic IPSCs (A), GABAergic IPSCs (B), and AMPA-EPSCs (C). Left panels: Current traces averaged from 10 consecutive stimulations under control conditions, after addition of WIN 55,212-2 and after the additional application of AM 251 (5 μM). Right panels: Time course. Mean ± SEM, n = 7 to 13 neurons. (**D**) Inhibition of glycinergic IPSCs in nonglycinergic (EGFP-negative) neurons ($n = 8$ neurons) by the mGluR1/5 agonist DHPG (10 μM) and its reversal by AM 251 (5 μM). Only a minor inhibition was observed in glycinergic (EGFP-positive) neurons ($n = 8$ neurons). (**E**) DSI (1-s depolarization of the postsynaptic neuron to 0 mV) in nonglycinergic neurons (six out of eight neurons) and its prevention by AM 251 (5 μM). No DSI occurred in glycinergic neurons ($n = 5$ neurons). Glycinergic IPSCs were evoked at a frequency of 0.2 Hz.

367,385, 100 μM, remaining inhibition 21.0 ± 3.9%, n = 5 neurons; and MPEP, 10 μM, 25.0 ± 3.4%, n = 5 neurons) (fig. S3). Glycinergic input to EGFP-positive (glycinergic) neurons was less sensitive to DHPG, with an average reduction of only 10.3 ± 3.6% (n = 8 neurons) (Fig. 1D). Depolarization-induced suppression of inhibition (DSI) could be induced in six out of eight non-glycinergic neurons but was not seen in glycinergic neurons (n = 5 neurons) (Fig. 1E).

The reduction of inhibitory synaptic transmission by endocannabinoids was due to dimin-

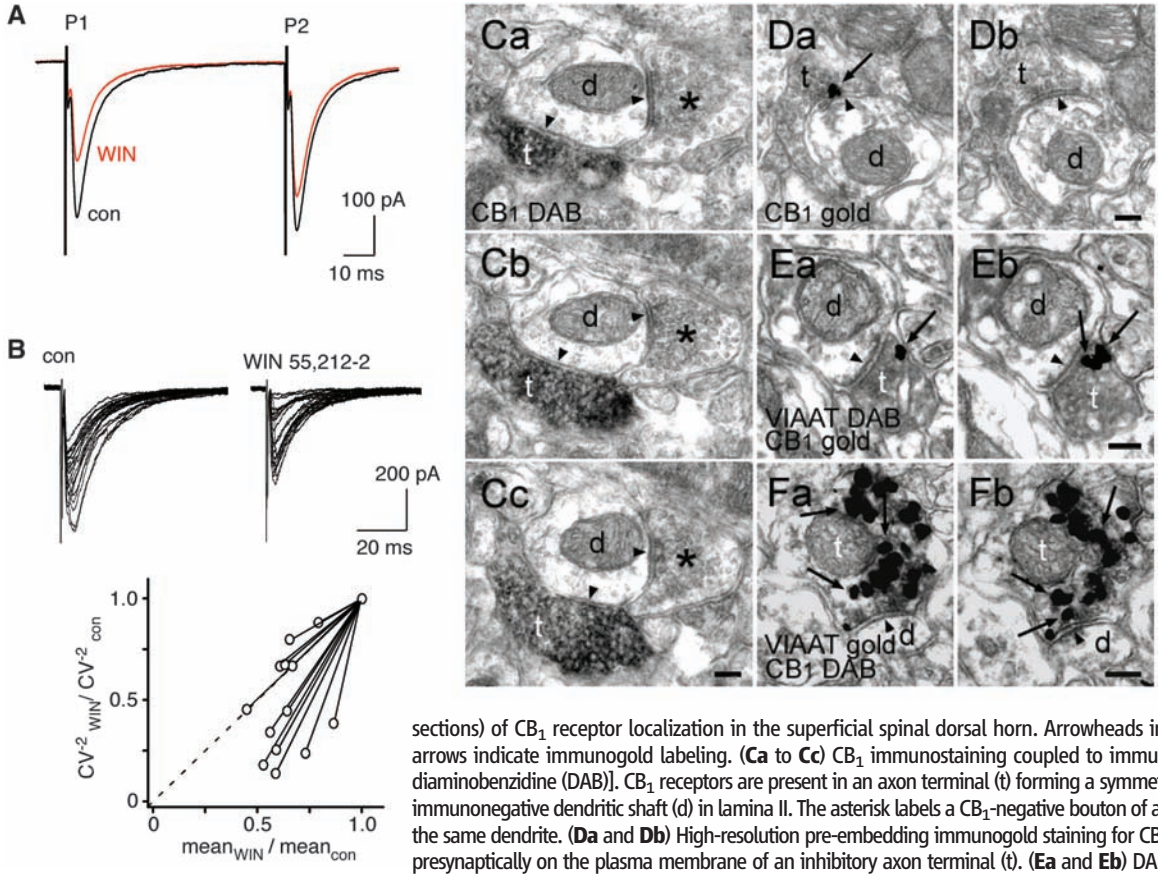

Fig. 2. Inhibition of glycinergic and GABAergic synaptic transmission via presynaptic CB_1 receptors. (**A**) Paired pulse experiments. Current traces of two consecutive glycinergic IPSCs (P1 and P2) under control conditions (black) and in the presence of 3 μM WIN 55,212-2 (red) are shown. (**B**) Variation analysis. Top panel: Individual traces of glycinergic IPSCs recorded under control conditions and in the presence of WIN 55,212-2 (3 μM). Bottom panel: Changes in the CV in 13 cells are plotted versus changes in the mean amplitude induced by WIN 55,212-2. (**C** to **F**) Electron microscopic analysis (**a** to **c** and **a** and **b** are serial sections) of CB_1 receptor localization in the superficial spinal dorsal horn. Arrowheads indicate symmetric synapses; arrows indicate immunogold labeling. (**Ca** to **Cc**) CB_1 immunostaining coupled to immunoperoxidase reaction [3,3′-diaminobenzidine (DAB)]. CB_1 receptors are present in an axon terminal (t) forming a symmetric (inhibitory) synapse on an immunonegative dendritic shaft (d) in lamina II. The asterisk labels a CB_1-negative bouton of another symmetric synapse on the same dendrite. (**Da** and **Db**) High-resolution pre-embedding immunogold staining for CB_1. The CB_1 receptor is located presynaptically on the plasma membrane of an inhibitory axon terminal (t). (**Ea** and **Eb**) DAB staining for VIAAT and pre-embedding immunogold labeling for CB_1. CB_1 cannabinoid receptors (indicated by arrows) are on an inhibitory (VIAAT-positive) axon terminal (t). In this reaction, silver intensification results in weaker electron density of the DAB precipitate. (**Fa** and **Fb**) Immunoperoxidase staining for CB_1 combined with pre-embedding immunogold labeling for VIAAT demonstrates colocalization of the two proteins. Similar results were obtained in four animals. Scale bar, 0.1 μm.

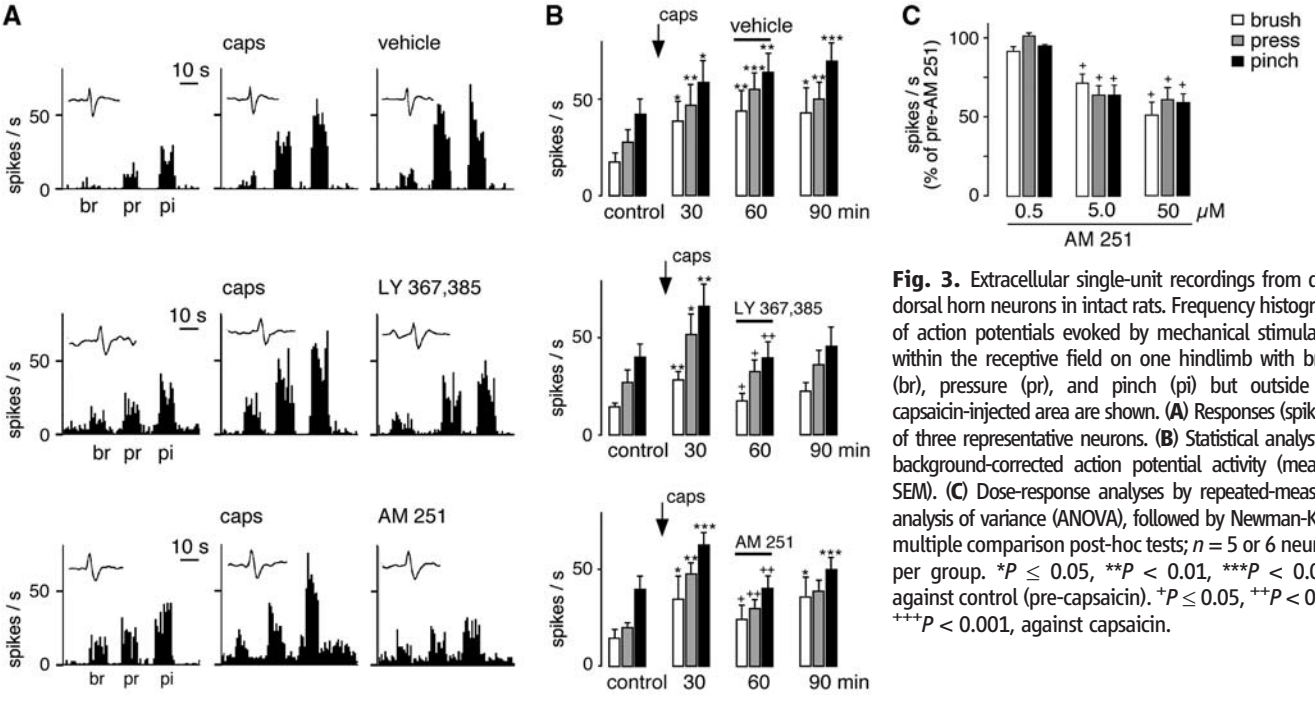

Fig. 3. Extracellular single-unit recordings from deep dorsal horn neurons in intact rats. Frequency histograms of action potentials evoked by mechanical stimulation within the receptive field on one hindlimb with brush (br), pressure (pr), and pinch (pi) but outside the capsaicin-injected area are shown. (**A**) Responses (spikes/s) of three representative neurons. (**B**) Statistical analysis of background-corrected action potential activity (mean ± SEM). (**C**) Dose-response analyses by repeated-measures analysis of variance (ANOVA), followed by Newman-Keuls multiple comparison post-hoc tests; n = 5 or 6 neurons per group. $^{*}P \leq 0.05$, $^{**}P < 0.01$, $^{***}P < 0.001$, against control (pre-capsaicin). $^{+}P \leq 0.05$, $^{++}P < 0.01$, $^{+++}P < 0.001$, against capsaicin.

ished release of GABA and glycine from inhibitory nerve terminals. In paired pulse experiments, WIN 55,212-2 (3 μM) increased the amplitude ratio of two consecutive IPSCs, 70 ms apart, from 1.14 ± 0.07 to 1.61 ± 0.15 (n = 5 neurons, $P < 0.05$, paired Student's t test) (Fig. 2A). Accordingly, the coefficient of variation [CV = $(SD^2/mean^2)^{1/2}$] of IPSC amplitudes (*15*) increased from 0.190 ± 0.012 under control conditions to 0.306 ± 0.031 in the presence of WIN 55,212-2, again indicative of a presynaptic action (n = 13 neurons, $P < 0.01$, paired Student's t test) (Fig. 2B). We directly demonstrated the presence of CB_1 receptors on the presynaptic terminals of inhibitory mouse superficial dorsal horn neurons by electron microscopy (EM) (Fig. 2, C to F). Peroxidase-based and immunogold labeling of CB_1 receptors and high-resolution EM unequivocally showed the presence of CB_1 receptors on presynaptic terminals of symmetrical (inhibitory) synapses (Fig. 2, C and D) and the colocalization of CB_1 with the vesicular inhibitory amino acid transporter (VIAAT) (Fig. 2, E and F), a marker of inhibitory axon terminals (*16*).

We next studied the role of endocannabinoids in secondary hyperalgesia in intact rats and performed in vivo extracellular single-unit recordings (*10*) from neurons with a wide dynamic range (that is, neurons responding to both noxious and innocuous stimulation) with receptive fields in the hindpaw and located in the deep lumbar dorsal horn (Fig. 3). Intracutaneous injection of capsaicin (200 μg) into the receptive field of the recorded neuron led to a robust increase in action potential firing in response to mechanical stimulation in an area surrounding the capsaicin injection site, akin to secondary hyperalgesia and allodynia. This increase was reversed by local spinal application not only of the mGluR1 antagonist LY 367,385 (10 μM, n = 5 neurons) but also of the CB_1 receptor blocker AM 251 (5 and 50 μM, n = 5 or 6 neurons).

In mice, we tested the effects of pharmacological and genetic manipulation of the endocannabinoid system on capsaicin-induced secondary hyperalgesia (Fig. 4). Subcutaneous injection of capsaicin (30 μg) into one hindpaw of wild-type mice led to a reduction in paw withdrawal thresholds in response to mechanical stimulation with dynamic von Frey filaments from 2.85 ± 0.04 g under control conditions to 0.53 ± 0.10 g (mean ± SEM, n = 6 mice) at 2 hours after capsaicin injection (*10*). Intrathecal injection (injection into the lumbar spinal canal) of the mGluR1 antagonist LY 367,385 (1.0 nmol per mouse) 2 hours after capsaicin reduced mechanical sensitization by 64.9 ± 2.9% (n = 6 mice) (*17*). Consistent with the role of CB_1 receptors in synaptic disinhibition, intrathecal AM 251 (0.5 nmol) reversed mechanical sensitization by 71.2 ± 9.0% (n = 6 mice). Accordingly, inhibition of endocannabinoid degradation with URB 597 or of endocannabinoid reuptake with UCM 707 (each 1.0 nmol) (*18*) prolonged secondary hyperalgesia (Fig. 4A). In naïve mice, all five compounds exerted only minor effects on mechanical sensitivity (fig. S4).

Global $CB_1^{-/-}$ mice and *ptf1a*-$CB_1^{-/-}$ mice were protected from capsaicin-induced mechanical sensitization. In contrast, mice devoid of CB_1 receptors only in primary afferent nociceptors (*sns*-$CB_1^{-/-}$ mice) (*19*) developed normal secondary hyperalgesia (Fig. 4B), indicating that the CB_1 receptors on inhibitory dorsal horn neurons, and not those on primary nociceptors, mediated capsaicin-induced secondary hyperalgesia. The unchanged responses of *sns*-$CB_1^{-/-}$ mice also indicate that possible direct interactions of CB_1 receptors with TRPV1 channels (*20*, *21*) expressed on the spinal terminals of primary nociceptors were not involved.

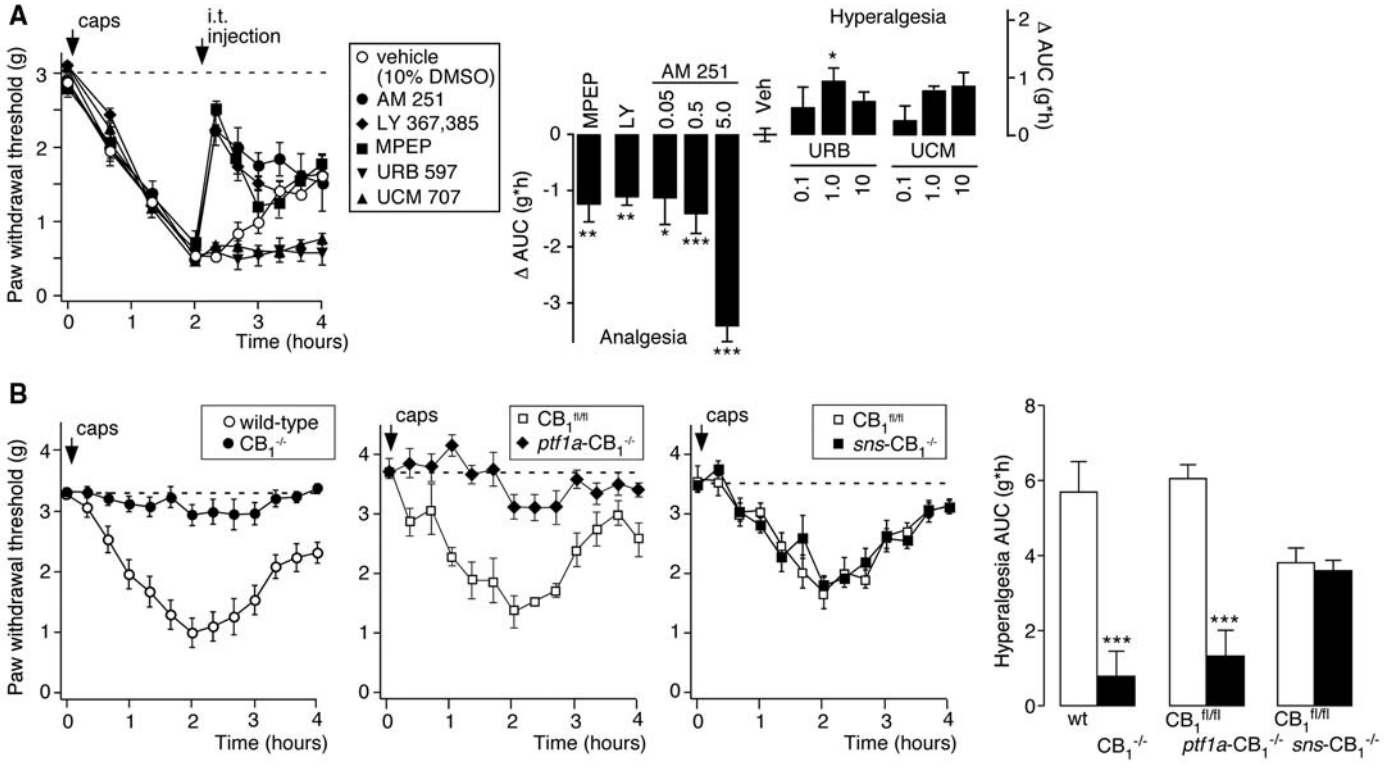

Fig. 4. Effects of pharmacological and genetic manipulations of the endocannabinoid system on capsaicin-induced mechanical hyperalgesia in mice. (**A**) Mechanical paw withdrawal thresholds (mean ± SEM) were determined with dynamic von Frey filaments at 20-min intervals for 2 hours after capsaicin injection into the left hindpaw and for another 2 hours after intrathecal injections of vehicle (10% dimethyl sulfoxide), AM 251 (0.5 nmol per mouse), URB 597 (1.0 nmol), UCM 707 (1.0 nmol), LY 367,385 (1.0 nmol), or MPEP (150 nmol). Left panel: Time course (mean ± SEM). Right panel: Treatment-induced changes in hyperalgesia. Areas under the curve (AUC) were integrated over time from 2 to 4 hours after capsaicin injection. The time course of sensitization in wild-type mice treated with intrathecal vehicle is the same as in wild-type mice that did not receive intrathecal injections (B). n = 5 or 6 mice per group; for statistical analyses, three groups of vehicle-injected mice were pooled. Analyses were by one-way ANOVA followed by Dunnett's post-hoc test $F(11,74) = 21.18$; $^*P \leq 0.05$, $^{**}P < 0.01$, $^{***}P < 0.001$. (**B**) Capsaicin-induced secondary hyperalgesia in wild-type mice versus $CB_1^{-/-}$ mice (n = 9 mice per group) and in *ptf1a*-$CB_1^{-/-}$ mice (n = 7 and 11 mice per group) and *sns*-$CB_1^{-/-}$ mice versus mice carrying a CB_1 receptor gene flanked by two *loxP* sites ($CB_1^{fl/fl}$ mice) (n = 5 mice per group). Left: Time course. Right: AUC (0 to 4 hours after capsaicin injection). $^{***}P < 0.001$, unpaired Student's t test.

Mechanical sensitization could also be evoked by intrathecal injection of the CB_1/CB_2 agonist CP 55,940 (fig. S5). Intrathecal CP 55,940 (10 nmol) significantly decreased the thresholds of mechanical stimulation with von Frey filaments in wild-type ($CB_1^{fl/fl}$) and *sns*-$CB_1^{-/-}$ mice and rendered both types of mice extremely sensitive to touch. In both tests, mechanical sensitization by CP 55,940 was absent in global $CB_1^{-/-}$ mice. The pronociceptive effects of endocannabinoids suggested here are specific for C-fiber–mediated, activity-dependent hyperalgesia. In models of mild inflammatory pain (produced by subcutaneous injection of zymosan A) (*10*) and neuropathic pain (produced by chronic constriction injury) (*10*), $CB_1^{-/-}$ mice behaved normally (fig. S6, A and B). AM 251 had only negligible effects (fig. S6, C and D), whereas CP 55,940 exerted anti-hyperalgesic actions in these models (fig. S6, E and F). Both of these models also involve spinal disinhibitory processes, but the underlying mechanisms are most likely different and involve the spinal release of pronociceptive prostaglandin E_2 (*22*) and changes in the transmembrane chloride gradient (*23*).

Finally, we tested the effect of CB_1 receptor blockade on C-fiber–induced secondary hyperalgesia and allodynia in human volunteers (fig. S7). Secondary hyperalgesia was induced by intracutaneous electrical stimulation at C-fiber strength (2 Hz, 15 to 100 mA) of a small skin area of the left forearm (*10*). In the first session, the intensity of electrical stimulation was adjusted to yield a value of 6 on a numeric rating scale ranging from 0, no pain, to 10, maximum imaginable pain, and pain ratings and the sizes of hyperalgesic skin areas surrounding the site of electrical stimulation were determined for 100 min at regular intervals. In a second session, 28 days later, the volunteers were tested again after a 10-day treatment with either placebo or rimonabant (20 mg/day, aken rally), a CB_1 receptor antagonist/inverse agonist closely related to AM 251. Rimonabant treatment had no effect on acute pain ratings induced by electrical stimulation (–2.0 ± 5.7%, $n = 8$ volunteers per group) but decreased the sizes of hyperalgesic and allodynic skin areas to 53.7 ± 5.2 and 57.4 ± 5.0%, respectively.

The contribution of endocannabinoids to activity-dependent pain sensitization, which we propose here, builds on a model of secondary hyperalgesia and allodynia (fig. S8), in which normally pain-specific dorsal horn neurons receive not only monosynaptic input from C-fiber nociceptors but also polysynaptic input from non-nociceptive fibers (*24*). The suprathreshold activation of these neurons by such non-nociceptive input is normally prevented by the activity of dorsal horn inhibitory interneurons. The present study shows that intense glutamatergic input from C-fiber nociceptors diminishes this inhibitory control through endocannabinoids acting at CB_1 receptors located on dorsal horn inhibitory interneurons. Our findings thus attribute to endocannabinoids an unexpected role in dorsal horn neuronal circuits as mediators of spinal activity–dependent pain sensitization. They are also an example of a distinctive phenotype of mice lacking CB_1 receptors specifically in inhibitory interneurons, whereas most previously reported phenotypes of global CB_1 receptor–deficient mice could be ascribed to the lack of CB_1 receptors on glutamatergic neurons (*25*).

References and Notes

1. R. Meyer, M. Ringkamp, J. Campbell, S. Raja, in *Textbook of Pain*, S. B. McMahon, M. Koltzenburg, Eds. (Elsevier, Churchill Livingstone, 2006), pp. 3–34.
2. L. Sivilotti, C. J. Woolf, *J. Neurophysiol.* **72**, 169 (1994).
3. T. L. Yaksh, *Pain* **37**, 111 (1989).
4. R. D. Treede, W. Magerl, *Prog. Brain Res.* **129**, 331 (2000).
5. M. Kano, T. Ohno-Shosaku, Y. Hashimotodani, M. Uchigashima, M. Watanabe, *Physiol. Rev.* **89**, 309 (2009).
6. V. Chevaleyre, K. A. Takahashi, P. E. Castillo, *Annu. Rev. Neurosci.* **29**, 37 (2006).
7. W. P. Farquhar-Smith *et al.*, *Mol. Cell. Neurosci.* **15**, 510 (2000).
8. P. Pacher, S. Batkai, G. Kunos, *Pharmacol. Rev.* **58**, 389 (2006).
9. V. Di Marzo, *Nat. Rev. Drug Discov.* **7**, 438 (2008).
10. Materials and methods are available as supporting material on *Science* Online.
11. G. Marsicano *et al.*, *Nature* **418**, 530 (2002).
12. S. M. Glasgow, R. M. Henke, R. J. Macdonald, C. V. Wright, J. E. Johnson, *Development* **132**, 5461 (2005).
13. E. A. Jennings, C. W. Vaughan, M. J. Christie, *J. Physiol.* **534**, 805 (2001).
14. H. U. Zeilhofer *et al.*, *J. Comp. Neurol.* **482**, 123 (2005).
15. R. Malinow, R. W. Tsien, *Nature* **346**, 177 (1990).
16. F. A. Chaudhry *et al.*, *J. Neurosci.* **18**, 9733 (1998).
17. V. Neugebauer, P. S. Chen, W. D. Willis, *J. Neurophysiol.* **82**, 272 (1999).
18. D. Piomelli, *Nat. Rev. Neurosci.* **4**, 873 (2003).
19. N. Agarwal *et al.*, *Nat. Neurosci.* **10**, 870 (2007).
20. B. Fioravanti *et al.*, *J. Neurosci.* **28**, 11593 (2008).
21. M. Maccarrone *et al.*, *Nat. Neurosci.* **11**, 152 (2008).
22. R. J. Harvey *et al.*, *Science* **304**, 884 (2004).
23. J. A. Coull *et al.*, *Nature* **424**, 938 (2003).
24. C. Torsney, A. B. MacDermott, *J. Neurosci.* **26**, 1833 (2006).
25. K. Monory *et al.*, *PLoS Biol.* **5**, e269 (2007).

26. This research was supported in part by grants from the Schweizerischer National Fonds to H.U.Z. (3100A0-116064/1), from the Deutsche Forschungsgemeinschaft to W.K. (KO 1878/2-2) and H.U.Z. (ZE 377/8-2), from NIH (NS38261 and NS11255) to V.N., from the European Union (LSHM-CT-2004-005166) to T.F.F., and from the OTKA (F046407) and ETT (561/2006) to I.K. A.J.P.A. was supported partly by scholarships from the German DAAD and the Venezuelan FONACIT for graduate study at IVIC. I.K. was supported by a János Bolyai scholarship. The authors thank R. Kuner and C. V. Wright for providing *sns*-cre and *ptf1a*-cre mice, respectively; J.-M. Fritschy, H. Handwerker, H. Möhler, and M. Schmelz for critical reading of the manuscript; T. Müller for very valuable suggestions; and I. Camenisch and L. Scheurer for genotyping of the mice.

Supporting Online Material

www.sciencemag.org/cgi/content/full/325/5941/760/DC1
Materials and Methods
Figs. S1 to S8
Table S1
References

4 February 2009; accepted 24 June 2009
10.1126/science.1171870

An Alternative DNA Structure Is Necessary for Pilin Antigenic Variation in *Neisseria gonorrhoeae*

Laty A. Cahoon and H. Steven Seifert*

Pathogens can use DNA recombination to promote antigenic variation (Av) of surface structures to avoid immune detection. We identified a cis-acting DNA sequence near the antigenically variable pilin locus of the human pathogen, *Neisseria gonorrhoeae*. This 16–base pair guanine (G)–rich sequence was required for pilin Av and formed a guanine quartet (G4) structure in vitro. Individual mutations that disrupted the structure also blocked pilin Av and prevented nicks required for recombination from occurring within the G4 region. A compound that binds and stabilizes G4 structures also inhibited pilin Av and prevented nicks from occurring on the G-rich strand. This site constitutes a recombination initiation sequence/structure that directs gene conversion to a specific chromosomal locus.

DNA recombination is a process that is shared by all DNA-carrying organisms and used for a variety of cellular processes, including DNA repair, genetic exchange, and meiotic chromosome segregation (*1*). Additionally, recombination mediates many high-frequency gene-diversification systems, including yeast mating-type switches, immunoglobin diversity, and pathogenesis-associated antigenic variation (Av) (*2*–*4*). Most recombination reactions occur at a low frequency, but several diversity-generating systems can enact programmed recombination reactions between specific loci at relatively high frequencies (*2*, *3*, *5*, *6*).

Neisseria gonorrhoeae is the sole causative agent of gonorrhea and has evolved three high-frequency, diversity-generation systems to avoid immune surveillance (*7*). This antigenic variability of gonococcal populations is one reason that natural immunity to re-infection has never been demonstrated and has prevented the development of an effective vaccine. One of these Av systems is mediated by high-frequency gene-conversion events between one of many silent pilin loci and the single expressed pilin locus,

Northwestern University Feinberg School of Medicine, 303 East Chicago Avenue, Chicago, IL 60611, USA.

*To whom correspondence should be addressed. E-mail: h-seifert@northwestern.edu

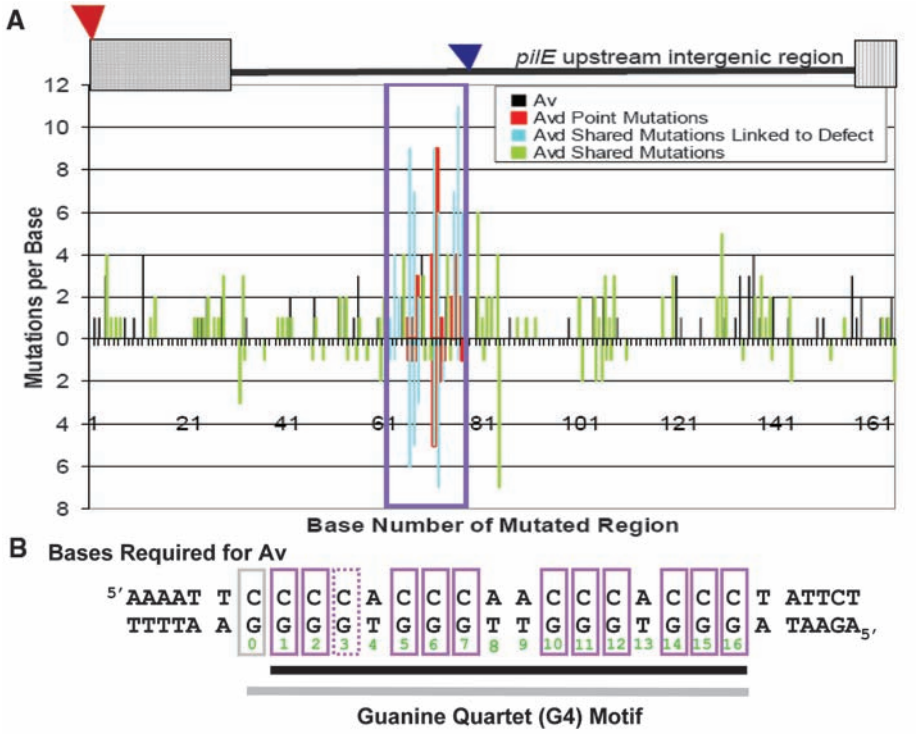

Fig. 1. Identification of a DNA sequence in the intergenic region upstream of *pilE* required for gonococcal pilin Av. (**A**) Mutational spectrum of genetic screens. Cartoon of the mutagenized region from the transposon insertion (red triangle) that has no effect on pilin Av (*13*) to 165 bp downstream showing the location of the previously identified Av-disrupting transposons (blue triangle) (*11*, *13*). The *x* axis indicates the base number, whereas the *y* axis indicates the number of mutations isolated per base. Screen 1 (bottom axis) represents 103 Avd mutants (only mutants with mutations <9 are shown) (table S1A). Screen 2 (top axis) represents 204 Av transformants and 106 Avd mutants (only mutants with mutations <17 are shown) (table S1B). The region linked to the Avd phenotype is shown with a purple box. Bars indicate mutations that allow Av (black), single mutations that cause an Avd phenotype (red), and Avd mutants that have mutations within the boxed region (blue) but have mutations elsewhere (green). (**B**) Bases required for pilin Av. Mutation of individual purple-boxed base pairs results in an Avd phenotype. Solid purple boxes indicate a complete block of pilin Av, whereas the G-3 mutant shows residual activity (fig. S2). The DNA element on the bottom strand forms a G4 motif (black underlined bases 1 to 16); when G-3 is mutated, the alternative G4 using G-0 (gray box) is shown underlined in gray.

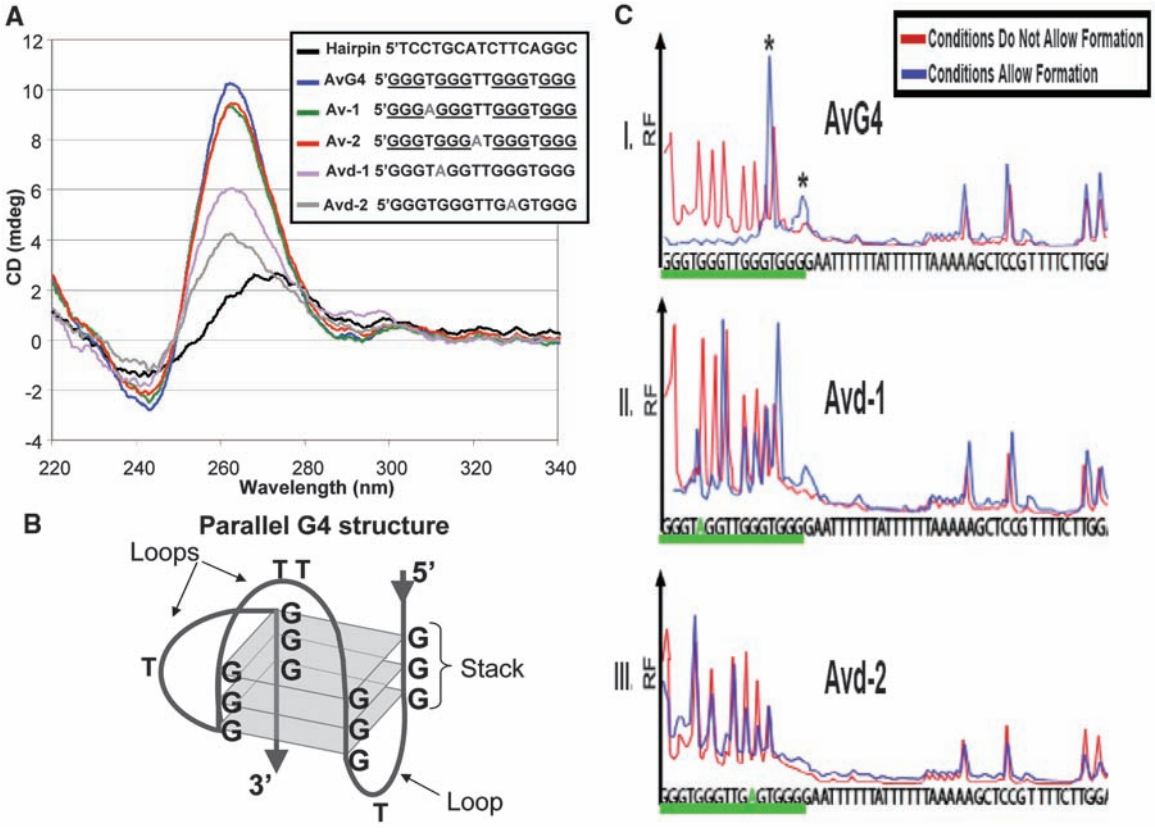

Fig. 2. Analysis of G4 structure formation in vitro. (**A**) Circular dichroism (CD) spectrometry. The hairpin oligonucleotide forms a double-stranded DNA molecule producing a B-form DNA CD spectrum (*26*). The AvG4 oligonucleotide has the *pilE* G4 sequence that allows pilin Av; Av-1 and Av-2 oligonucleotides have A-to-T (gray) mutations that do not alter Av, and all produce parallel G4 structure CD spectrums (*26*). Avd-1 and Avd-2 oligonucleotides contain G-to-A (gray) transversions that block pilin Av and show altered CD spectrums. (**B**) Parallel G4 structure. Three G-quartets (squares) in a parallel G4 configuration. G, guanine; T, thymine. (**C**) Dimethyl sulfate (DMS) methylase-protection assay. Formed G4 guanines are protected from DMS attack (*27*). Representative electropherograms of a FAM-labeled oligonucleotide are shown. The oligonucleotide contains I, the wild-type G4 sequence (AvG4 underlined), or II and III, two mutations that block pilin Av (Avd-1 and Avd-2, underlined) (three independent repeats). The *x* axis shows a 52-base region, and the *y* axis shows relative fluorescence (RF). Blue and red traces indicate G4-forming and nonforming conditions, respectively. Under G4-forming conditions, AvG4 forms two alternative G4 structures (5′GGGTGGGTTGGGTGGGG or 5′GGGTGGGTTGGGTGGG; guanines forming the structure are underlined; asterisks), whereas mutant oligonucleotides do not form either structure.

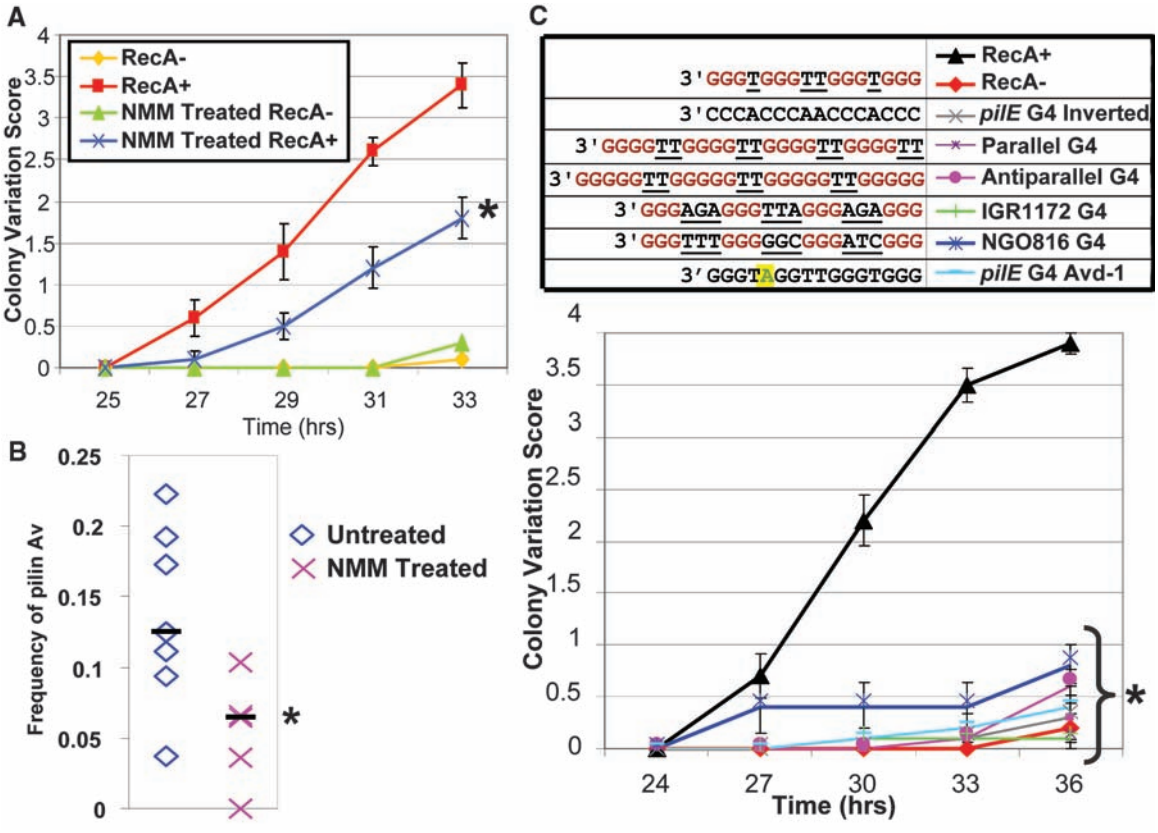

Fig. 3. Stabilization, substitution, or inversion of the *pilE* G4 structure inhibits Av. (**A**) Kinetic pilus-dependent colony phase-variation assay. A representative assay ($n = 3$) of NMM-treated or untreated RecA+ and RecA– bacteria (RecA is required for pilin Av) with a mean phase-variation score (*11*) and SEM (error bars) of 10 colonies is shown. The mean phase variation of NMM-treated RecA+ is different from untreated RecA+ by Student's *t* test, $P < 0.05$ (asterisk). (**B**) DNA sequencing assay for pilin Av frequency (*2*). 28 piliated progeny from seven founder colonies of untreated and NMM-treated bacteria were analyzed. Blue diamonds and pink x marks show the mean frequency of untreated and NMM-treated founders, respectively. Horizontal bars show the median of the means. The pilin Av frequency of NMM-treated bacteria is less than that for untreated bacteria by Wilcoxon rank-sum test, $P < 0.05$ (asterisk). (**C**) G4 substitution colony phase-variation assay. RecA+ and RecA– strains have the wild-type *pilE* G4 sequence. The *pilE* G4 inverted strain has the identical G4 sequence inverted in the same location with no other sequence changes. The *pilE* G4 Avd-1 mutant has a G-to-A transversion at G-5 that blocks pilin Av. The other mutants contain different G4-forming sequences: a parallel G4 from *T. thermophila* (*28*), an in vitro characterized antiparallel G4 (*29*), and two G4s (IGR1172 G4 and NGO816 G4) found in other locations in the gonococcal chromosome. A representative assay ($n = 3$) with mean phase variation score (*11*) and SEM (error bars) of 10 colonies is shown. All mutants are different than RecA+ by Student's *t* test, $P < 0.05$ (asterisk).

pilE. This produces variant pilin proteins (*2*) that form antigenically divergent pili, which are the hairlike appendages expressed by many bacteria.

This system uses normal homologous recombination factors to mediate specialized gene-conversion reactions (*8*–*12*), but no DNA element required for pilin Av has been described. Previous work showed that some transposon insertions in the intergenic region upstream of *pilE* block pilin Av without altering pilin expression (*11*, *13*). To define the DNA element being disrupted by these transposons, the *pilE* upstream region was randomly mutagenized, and the mutations were introduced into the gonococcal chromosome by DNA transformation and linkage to a transposon insertion that does not affect pilin Av (fig. S1A) (*13*, *14*). Two independent screens were performed. In both screens, mutants unable to undergo pilin Av were selected by screening for a stable, piliated colony morphology (Avd phenotype, fig. S1B), whereas in the second screen, both Av deficient (Avd) and Av transformants were analyzed (table S1) (*15*). Coupled with site directed mutagenesis, DNA sequence analysis of the transformants revealed that alteration of any one of 12 guanine-cytosine (GC) base pairs within a 16–base pair (bp) region each inhibits pilin Av, whereas mutation of the other base pairs within or surrounding this region did not (Fig. 1, A and B, fig. S2, and table S2). The 12 GC base pairs defining this DNA element are conserved in 14 sequenced gonococcal isolates and three *Neisseria meningitis* genomes upstream of *pilE*, but they are not found in commensal *Neisseria* (table S3). The ability of the single-nucleotide mutations to replicate the genetic behavior of the pilin Av–disrupting transposon insertions was determined by introducing one of the GC base pair mutations into a *recG/ruvB* double mutant. Previously, the RecG and RuvABC Holliday junction processing pathways were both found to be required for pilin Av (*10*). RecA expression in a *recG/ruvB* double mutant is synthetically lethal but can be overcome by a pilin Av–disrupting transposon insertion (*10*). Introduction of one of the GC base pair mutations also rescued the RecA-dependent synthetically lethal phenotype, showing that these mutants have the identical phenotypes as the neighboring transposon insertions that act upstream of homologous recombination factors (fig. S3).

The G-rich sequence defined by the genetic screens conforms to a guanine-quartet (G4) motif (Fig. 1B) (*16*, *17*). G4-forming sequences have been implicated in many biological processes (*18*–*21*), but their existence within a cell has yet to be proven. To test whether the *pilE*-linked G4 motif forms a G4 structure, we synthesized a series of oligonucleotides and evaluated their ability to form a G4 structure. CD spectrum analysis showed that the DNA sequence required for pilin Av adopts a parallel G4 structure and that mutation of two thymines in the loop regions has no effect on the structure (Fig. 2, A and B). A methylase-protection assay revealed two alternative G4 structures (Fig. 2C). Mutation of the G-3 residue yielded a mutant with residual pilin Av, suggesting that this alternate G4 structure can form when the G-3 site is mutated (Fig. 1B and fig. S2). Replication-stop assays with three different DNA polymerases confirmed that the G4 structure forms and can halt replication (fig. S4). Individual mutations that block pilin Av were also found to block structure formation in all three assays (Fig. 2, A and C, and fig. S4).

There are 46 predicted G4-forming sequences in the gonococcal chromosome (*16*, *17*), and none of these sequences are identical to the *pilE*-linked G4, nor are they located near any gene involved in pilin Av. Mutation of two irrelevant G4-forming sequences in the genome had no effect on pilus phase variation, thus ruling out a nonspecific role for other G4 sequences in pilin Av (fig. S5). When a copy of

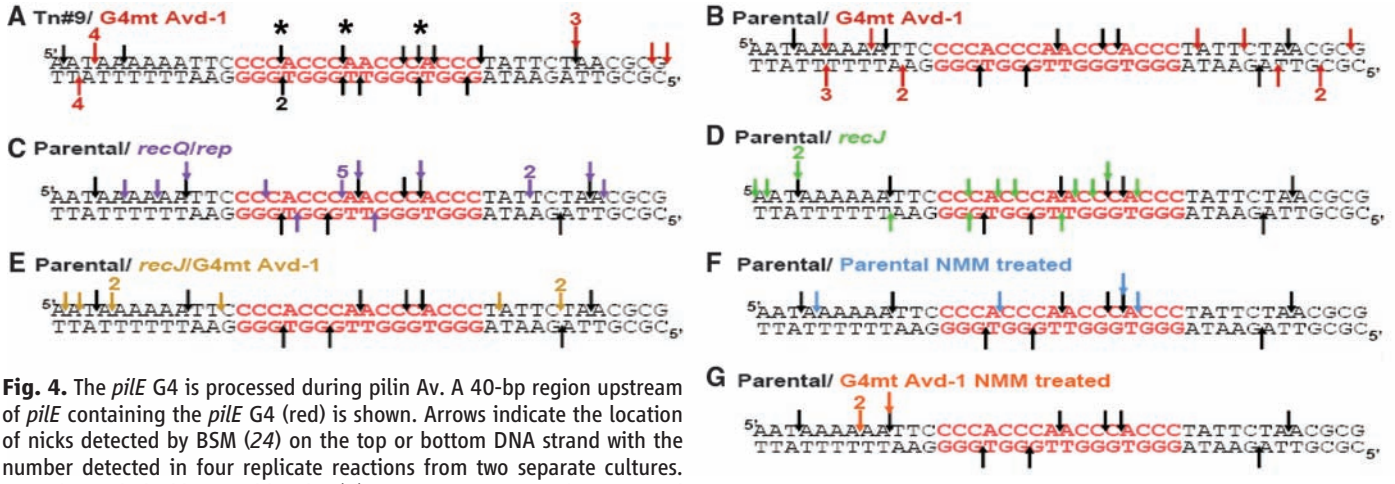

Fig. 4. The *pilE* G4 is processed during pilin Av. A 40-bp region upstream of *pilE* containing the *pilE* G4 (red) is shown. Arrows indicate the location of nicks detected by BSM (*24*) on the top or bottom DNA strand with the number detected in four replicate reactions from two separate cultures. Asterisks mark double-strand breaks. (**A**) Tn#9 is an Av strain that was used in the genetic screen (black arrows) with an isogenic G4 mutant strain, Avd-1 (red arrows). (**B** to **G**) Parental strain nicks (black arrows). (B) G4 mutant-strain Avd-1 nicks (red arrows). (C) *recQ/rep* double-mutant nicks (purple arrows). (D) *recJ* mutant-strain nicks (green arrows). (E) G4 Avd-1/ *recJ* double-mutant nicks (yellow arrows). (F) NMM-treated parental-strain nicks (blue arrows). (G) NMM-treated G4 mutant-strain Avd-1 nicks (orange arrows).

the *pilE*-linked G4 sequence was introduced upstream of the *pilS7* silent pilin locus at a position similar to the *pilE*-linked copy in a strain where the *pilE*-linked copy was mutated (fig. S6), there were no observed changes at *pilS7* or *pilE*, even though 4 to 31 *pilE* variants carrying *pilS7* sequences would normally be found in a pool of 374 progeny (table S4) (*2*). Moreover, when the *pilE*-linked G4 was replaced with four other G4-forming sequences or an inverted copy, pilin Av was lost (Fig. 3C). Thus, the specific G4-forming sequence, its position, and its orientation are all essential to allow pilin Av.

To directly probe for a role of the G4 structure in live gonococci, we used N-methyl mesoporphyrin IX (NMM) (fig. S7, A and B), a compound that can enter live cells and specifically bind G4 DNA, but not duplex DNA (*22*, *23*). Gonococci grown on a concentration of NMM that did not alter growth (fig. S7C) were assayed for pilin phase and Av. Bacterial growth on NMM showed significantly decreased pilus phase and Av (Fig. 3, A and B). Surprisingly, ~70% of piliated antigenic variants arising on NMM were produced by recombination with *pilS3* copy 1, which normally contributes to ~20% of variants produced from the same parental variant (table S4) (*2*). These results are consistent with formation and further processing of the G4 structure being required for pilin Av.

Because homologous recombination is initiated by a nick or break, we used break-site mapping (BSM) (*24*) to assay for G4-dependent nicks or breaks in this chromosomal region. We detected nicks throughout the *pilE* upstream region that were at a higher concentration per base pair in the G4-forming sequence in antigenically variant bacteria (table S5) and in a higher density throughout the region as compared with the analogous region in *pilS7* (table S6). Occasionally, we also detected double-strand breaks in the G4-forming sequence (Fig. 4A). We did not detect any nicks or breaks in the G-rich sequence in the Avd-1 G4 point mutant, suggesting that nicks are the result of the G4 structure (Fig. 4, A and B). NMM-treated bacteria had a similar pattern of nicks as untreated bacteria on the top strand, but we did not detect any nicks on the bottom strand (Fig. 4, F and G). To test whether specific proteins required for pilin Av process the *pilE* G4, we performed BSM of selected mutants. A *recJ* exonuclease mutant and *recQ/rep* helicase double mutant are both deficient in pilin Av. BSM of the *recJ* mutant showed an increase in nicks at the G4-forming sequence, but all G4 localized nicks were lost in a *recJ*/Avd-1 mutant (Fig. 4, D and E). A *recQ/rep* double mutant showed a slight increase in the number of nicks (Fig. 4C). Thus, an intact G4-forming sequence is required to produce nicks in the G4 DNA, and these nicks are processed by RecJ exonuclease and RecQ and Rep helicases. The involvement of RecQ in pilin Av (*9*, *11*) is consistent with the established affinity of RecQ helicases for G4 structures (*23*, *25*).

Our data suggest that formation of the *pilE* G4 structure is required for pilin Av. It is likely that the structure forms only when the DNA duplex is melted, possibly during DNA replication, because the G-rich sequence is on the lagging strand. As only the *pilE* G4-forming sequence can mediate pilin Av, we propose that this G4 structure is a specialized recombination initiation sequence/structure (G4-RIS). The recognition that some G4-forming sequences are important for transcription (G4-TSC) and telomere maintenance (G4-TEL) suggests divergent evolution of these sequences/structures for diverse molecular processes.

References and Notes

1. X. Li, W. D. Heyer, *Cell Res.* **18**, 99 (2008).
2. A. K. Criss, K. A. Kline, H. S. Seifert, *Mol. Microbiol.* **58**, 510 (2005).
3. J. E. Haber, *Annu. Rev. Genet.* **32**, 561 (1998).
4. N. Maizels, *Annu. Rev. Genet.* **39**, 23 (2005).
5. B. B. Finlay, G. McFadden, *Cell* **124**, 767 (2006).
6. J. Stavnezer, J. E. Guikema, C. E. Schrader, *Annu. Rev. Immunol.* **26**, 261 (2008).
7. K. A. Kline, E. V. Sechman, E. P. Skaar, H. S. Seifert, *Mol. Microbiol.* **50**, 3 (2003).
8. K. A. Kline, H. S. Seifert, *J. Bacteriol.* **187**, 2903 (2005).
9. I. J. Mehr, H. S. Seifert, *Mol. Microbiol.* **30**, 697 (1998).
10. E. V. Sechman, K. A. Kline, H. S. Seifert, *Mol. Microbiol.* **61**, 185 (2006).
11. E. V. Sechman, M. S. Rohrer, H. S. Seifert, *Mol. Microbiol.* **57**, 468 (2005).
12. E. P. Skaar, M. P. Lazio, H. S. Seifert, *J. Bacteriol.* **184**, 919 (2002).
13. K. A. Kline, A. K. Criss, A. Wallace, H. S. Seifert, *J. Bacteriol.* **189**, 3462 (2007).
14. Materials and methods are available as supporting material on *Science* Online.
15. J. Swanson, S. Bergstrom, J. Boslego, M. Koomey, *Antonie van Leeuwenhoek* **53**, 441 (1987).
16. O. Kikin, L. D'Antonio, P. S. Bagga, *Nucleic Acids Res.* **34**, W676 (2006).
17. V. Scaria, M. Hariharan, A. Arora, S. Maiti, *Nucleic Acids Res.* **34**, W683 (2006).
18. K. Muniyappa, S. Anuradha, B. Byers, *Mol. Cell. Biol.* **20**, 1361 (2000).
19. K. Paeschke *et al.*, *Nat. Struct. Mol. Biol.* **15**, 598 (2008).
20. A. Siddiqui-Jain, C. L. Grand, D. J. Bearss, L. H. Hurley, *Proc. Natl. Acad. Sci. U.S.A.* **99**, 11593 (2002).
21. M. Fry, *Front. Biosci.* **12**, 4336 (2007).
22. J. Ren, J. B. Chaires, *Biochemistry* **38**, 16067 (1999).
23. X. Wu, N. Maizels, *Nucleic Acids Res.* **29**, 1765 (2001).
24. Q. Kong, N. Maizels, *Nucleic Acids Res.* **29**, E33 (2001).
25. M. D. Huber, M. L. Duquette, J. C. Shiels, N. Maizels, *J. Mol. Biol.* **358**, 1071 (2006).
26. S. Burge, G. N. Parkinson, P. Hazel, A. K. Todd, S. Neidle, *Nucleic Acids Res.* **34**, 5402 (2006).
27. J. Tang *et al.*, *Nucleic Acids Res.* **36**, 1200 (2008).
28. T. Schierer, E. Henderson, *Biochemistry* **33**, 2240 (1994).
29. P. A. Rachwal, T. Brown, K. R. Fox, *Biochemistry* **46**, 3036 (2007).

30. We thank A. Chen and P. Schook for reading the manuscript and the Seifert laboratory members and W. Anderson for input. This work was supported by NIH grants R37AI033493, R01AI055977, and R01AI044239 to H.S.S. L.A.C. was partially supported by NIH grant T32GM08061.

Supporting Online Material

www.sciencemag.org/cgi/content/full/325/5941/764/DC1
Materials and Methods
Figs. S1 to S7
Tables S1 to S8
References

30 April 2009; accepted 25 June 2009
10.1126/science.1175653

New Products Focus: RNAi

In Vivo siRNA Delivery

MaxSuppressor RNA-LANCEr II is a nonviral transfection agent optimized for the efficient in vivo introduction of small interfering RNA, microRNA, and other RNA interference (RNAi) agents. The new agent is comprised of a neutral hydrophobic emulsion that encapsulates and delivers RNAi agents directly into tissues. Users simply mix the agent with their RNAi agent, extrude or sonicate the mixture, and inject into an animal. It offers consistent, reliable silencing using minimal amounts of RNAi agents.

Bioo Scientific
For information 512-707-8993
www.biooscientific.com

Blood miRNA Kit

The PAXgene Blood miRNA Kit lets researchers minimize preanalytical variables for RNA and microRNA (miRNA). PAXgene Blood RNA Tubes used in combination with the new miRNA kit comprise the first system for collecting and stabilizing whole human blood and copurifying total RNA enriched for miRNA. Systems such as the PAXgene Blood RNA System inhibit RNA degradation and gene induction in vitro, resulting in preservation of the gene expression profile that is essential for accurate analysis, but researchers cannot easily extract and purify the miRNA from these samples. The PaxGene Blood miRNA Kit provides this ability. Both manual and automated protocols are available.

Qiagen
For information 800-362-7737
www.qiagen.com

Reference Control Tool

The microRNA-specific miRXplore Universal Reference is a synthetic microRNA (miRNA) pool that comprises more than 950 miRNA oligonucleotides from human, mouse, rat, and virus. It allows direct comparison of large numbers of samples, independent of the time of the experiment, and allows the user to save control sample material. The Universal Reference also serves as a hybridization control or as a quality control to monitor miRNA microarray hybridization efficiency. It can also be used as a positive control for real-time polymerase chain reaction, cloning, and sequencing experiments.

Miltenyi Biotec
For information +49-2204-8306-6591
www.miltenyibiotec.com

Target Expression Vector

The pmirGLO Dual-Luciferase miRNA Target Expression Vector provides researchers in microRNA (miRNA) study both the ability to measure a wide dynamic range of miRNA activity in a vast number of cell types and the option to create a stable cell line from one genetic construct for further research. The pmirGLO vector makes use of optimized firefly luciferase gene as the readout for activity, while also offering a Renilla luciferase/neomycin resistance gene for data normalization. The pmirGLO vector allows a luciferase reporter gene assay to measure the function of endogenous or exogenous miRNA and enables functional studies of sequence variations in 3'-untranslated gene regions.

Promega
For information 608-274-4330
www.promega.com

Transcriptome Tools

The ExactStart tools for transcriptome discovery and analysis enable the user to selectively tag the exact 5′ end of any class of RNA molecules in a total RNA preparation. The tagged RNA is then converted to complementary DNA (cDNA) with unique tagging sequencing on both ends that are customizable based on the intended application, such as next generation sequencing. Kits are available for small-RNA discovery and analysis, full-length cDNA cloning, and rapid amplification of cDNA ends.

Epicentre Biotechnologies
For more information 800-284-8474
www.EpiBio.com/exactstart

Inert Pipette Tips

High-quality BioClean pipette tips are completely inert and do not influence experimental outcome in any way. They have been tested by independent analysts for the absence of bioactive components and boast a proven lack of external contaminants, including DNA, deoxyribonuclease, ribonuclease, adenosine triphosphate, pyrogens, and polymerase chain reaction inhibitors in the production and packaging process.

Rainin Instrument
For information 510-564-1600
www.rainin.com

Electronically submit your new product description or product literature information! Go to **www.sciencemag.org/products/newproducts.dtl** for more information.

Newly offered instrumentation, apparatus, and laboratory materials of interest to researchers in all disciplines in academic, industrial, and governmental organizations are featured in this space. Emphasis is given to purpose, chief characteristics, and availabilty of products and materials. Endorsement by *Science* or AAAS of any products or materials mentioned is not implied. Additional information may be obtained from the manufacturer or supplier.

POSITIONS OPEN

The George Washington University

FACULTY POSITIONS
in Molecular Cancer Research

The Department of Biochemistry and Molecular Biology at The George Washington University Medical Center invites applications for tenure-track **ASSISTANT/ASSOCIATE PROFESSORS.** We seek outstanding candidates with demonstrated excellence in cancer research. Areas of research interest include nuclear and growth factor receptors, signal transduction, transcription, and chromatin remodeling. The Medical Center is located on the main campus of The George Washington University. The presence of basic and applied science departments and the proximity of the NIH, Children's National Research Institute, and other medical centers in the Washington, D.C., metropolitan area offers ample opportunities for collaborations. The GW University will provide a competitive startup package to successful candidates. Basic qualifications: Applicants must hold a Ph.D. and/or M.D. degree in an appropriate discipline and shall have extramural funding for consideration of Associate Professorship.

Application process: Interested applicants must send complete curriculum vitae, a statement of current and future research interests (limited to three pages), and the names and addresses of three references to: **Rakesh Kumar, Ph.D., Professor and Chair, Department of Biochemistry and Molecular Biology, Faculty Search, The George Washington University Medical Center, Suite 530, 2300 Eye St., N.W., Washington, DC 20037 or via e-mail: bcmdjm@gwumc.edu.** Review of applications by the Search Committee began on March 6, 2009, and will continue until positions are filled. Only complete applications will be considered.

The George Washington University is an Affirmative Action/Equal Opportunity Employer.

ASSISTANT PROFESSOR
The University of Chicago, Department of Chemistry

The Department of Chemistry of the University of Chicago invites applications from outstanding individuals for the position of Assistant Professor of chemistry. This search is in the areas broadly defined as inorganic, organic, and physical chemistry. Applicants must apply online at the University of Chicago academic job **website: https://academiccareers.uchicago.edu.** Applicants must upload a cover letter, curriculum vitae with a list of publications, and a succinct outline of research plans. The cover letter should be addressed to the Inorganic Search Committee, Organic Search Committee, or Physical Search Committee, depending on the applicant's discipline of interest. Applicants must also arrange to have three letters of recommendation sent to: **Department of Chemistry, Office of the Chairman (SCL 119), The University of Chicago, 5735 S. Ellis Avenue, Chicago, IL 60637.** The recommendation letters will be accepted by mail only. Review of completed applications will begin October 1, 2009; to ensure full consideration, all material should be submitted by that date. *The University of Chicago is an Affirmative Action/Equal Opportunity Employer.*

YALE UNIVERSITY
DEPARTMENT OF CHEMISTRY

The Department of Chemistry at Yale University invites applications for tenure-track positions at the **ASSISTANT PROFESSOR** level to commence July 1, 2010. We seek creative teacher-scholars who show promise for developing outstanding research programs in any area of chemistry. Applicants should send their curriculum vitae along with a statement of research plans and arrange for the submission of three letters of recommendation. All materials should be received by October 15, 2009. Send applications to: **Chair, Junior Faculty Search Committee, Department of Chemistry, Yale University, P.O. Box 208107, New Haven, CT 06520-8107.** *Yale University is an Equal Opportunity/Affirmative Action Employer and applications from women and underrepresented minority group members are especially encouraged.*

POSITIONS OPEN

California State University Northridge

ASSISTANT PROFESSORSHIPS

California State University, Northridge invites applications for three tenure-track positions in the Department of Biology, starting August 2010. Applicants must have a Ph.D. and postdoctoral experience. Each successful candidate will develop a vigorous research program involving undergraduate and M.S. students, seek extramural research funding, and demonstrate teaching excellence.

MICROBIOLOGIST. Focusing on prokaryotic biology relating to any aspect of the health sciences. Teaching options include medical microbiology, principles of microbiology, a specialty course, and introductory biology.

EVOLUTIONARY BIOLOGIST. Explaining patterns or processes of diversification among species or populations. Teaching options include a course on the diversity of a group of terrestrial organisms, molecular systematics, evolution, and introductory biology.

MOLECULAR GENETICIST. Emphasizing genomic or proteomic approaches to problems in eukaryotic genetics. Teaching options include molecular genetics, genetics, introductory biology, and a specialized graduate course.

Applicants should submit a cover letter to the respective search committee, including curriculum vitae, a summary of teaching experiences, statements of research interests and teaching philosophy, and three publications. Applicants should arrange to have three letters of recommendation sent to **e-mail: biology.dept@csun.edu or Department of Biology, California State University, 18111 Nordhoff Street, Northridge, CA 91330-8303.** Screening will begin on October 1, 2009.

UNIVERSITY OF MINNESOTA

TENURE-TRACK FACULTY POSITIONS
in Cardiovascular Physiology

The Department of Integrative Biology and Physiology at the University of Minnesota Medical School seeks outstanding faculty candidates in integrative systems biology of the cardiovascular system open to all ranks (**ASSISTANT, ASSOCIATE, FULL PROFESSOR**). Successful candidates will have an innovative research program that embraces biological complexity from molecular building blocks to the living organism with a focus on cardiovascular biology in health and disease. A commitment to excellence in teaching is essential. Minimum requirements are a Ph.D., M.D., or M.D.-Ph.D. with two or more years of postdoctoral training. Applicants should apply on-line (**website: http://employment.umn.edu – requisition number 156389;** curriculum vitae, cover letter, and references). *The University of Minnesota is an Equal Opportunity Educator and Employer.*

FACULTY POSITION
Institute of Molecular and Cellular Biology
National Taiwan University

The Institute is seeking an outstanding individual to fill a full-time Faculty position available on August 1, 2010. The level of appointment is open. The specific research area should be related to molecular biology and/or cellular biology of plant and animal. Candidate must have a Ph.D. degree, and a postdoctoral experience is preferred. Applicant should submit curriculum vitae, a brief statement of research and teaching course(s), and three recommendation letters prior to November 30, 2009, to: **Chair, Faculty Search Committee, Institute of Molecular and Cellular Biology, National Taiwan University, No.1, Section 4, Roosevelt Road, Taipei, Taiwan 10617. Website: http://cell.lifescience.ntu.edu.tw/english/index.htm.**

MRC Medical Research Council

The MRC provides support through a broad portfolio of personal award schemes for talented individuals who wish to pursue a career in the biomedical sciences, public health and health services research. These schemes range from studentships for early research training, through to postdoctoral research training fellowships and career development opportunities for more senior investigators.

Applications are invited for:

Special Research Training Fellowships in Biomedical Informatics (Bioinformatics, Neuroinformatics and Health Informatics)

These fellowships provide specialist multidisciplinary research training aimed at creating highly skilled researchers able to take forward new developments in the fields of bioinformatics, neuroinformatics, health informatics and computational biology. The special fellowship also provides the opportunity to further enhance research training by allowing Fellows to undertake a Masters degree in full or in part, or other taught courses during the fellowship and/or spend up to one year in an overseas research centre, a second UK research centre or in UK industry.

Who can apply?

The fellowships are aimed at those with non-biological, biological, non-clinical or clinical backgrounds who wish to undertake training and research in biomedical informatics. Applications are encouraged from those with advanced training in the physical or mathematical sciences or in information technology, who wish to apply their expertise to biomedical problems. Science graduates should hold either a PhD or DPhil in a relevant discipline or expect to have received their doctorate by the time they intend to take up the award. Medical and dental applicants holding a PhD can apply at any stage in their careers from immediately post-registration up to specialist registrar grade or be at the equivalent level in general practice or dentistry.

What funding is provided?

An MRC Special Research Training Fellowship in Biomedical Informatics is usually awarded for three years but can be four years where there is special justification. The fellowship provides the fellow's personal salary, research training support costs (for example, for taught statistics courses), annual travel costs, and all other relevant costs under Full Economic Costs. Support is also available where a period of training at an overseas/second UK/UK industry research centre forms a critical part of your proposal. All applications must include a formal training component in addition to a research project.

The deadline for applications for the above scheme is 4pm on Friday 25th September 2009.

As part of the Council's Equal Opportunities policy, consideration will be given to applicants returning to science following a career break. There are no age limits for any of our schemes and all fellowships may be held part-time to accommodate domestic responsibilities.

Further information on this and other funding opportunities provided by the MRC, can be found on our website at www.mrc.ac.uk/index.htm and additional details can be requested by e-mail from fellows@headoffice.mrc.ac.uk

'Leading Science for Better Health'

MRC is a equal opportunity employer.

Seeking a Standing Vice Editor-in-chief for the *Journal of Biomedical Research*

The *Journal of Biomedical Research (JBR)* publishes biomedical research from both life and health sciences. The journal is published bimonthly, in English, and is sponsored by Nanjing Medical University in China. The *JBR* features peer-reviewed, original research articles and review articles relating to basic, clinical and preventive medical sciences. Authors represent a range of institutions including medical institutes, research centers, universities and hospitals worldwide.

The *JBR* evolved from the Journal of Nanjing Medical University (English Edition), which has historically been one of the most influential biomedical journals in China, and is indexed by several authority indexes, including Chemical Abstracts of America, Abstract Journal of VINITI and the Chinese Core Journals Index. The *JBR* is currently published both in China and abroad through ScienceDirect. In order to further establish an international scientific medium for biomedical researchers and doctors, we are recruiting a Standing Vice Editor-in-chief to be responsible for the continued development and advancement of the *JBR*.

Requirements for consideration:

1. Native Chinese speaker and fluent in English
2. Professional biomedical background
3. Experience of being Editor-in-chief or Vice Editor-in-chief in a biomedical journal with impact factor of more than 3.0
4. Enthusiasm to work with a multi-disciplinary, international team

This position is based in Nanjing, China and the individual will be considered as a Distinguished Professor in Nanjing Medical University with an annual compensation of RMB 200,000. To apply, or learn more about the position, please contact the **Personnel Division of Nanjing Medical University** at **0086-25-86862023** (phone) and send a curriculum vitae to **ghz@njmu.edu.cn**.

COMPUTATIONAL BIOLOGIST in Signaling and Cancer

THE BEN MAY DEPARTMENT FOR CANCER RESEARCH
THE UNIVERSITY OF CHICAGO

The University of Chicago is seeking outstanding individuals for a tenure-track position at the Assistant Professor level in the Ben May Department for Cancer Research (**http://ben-may.bsd.uchicago.edu/**), the Institute for Genomics and Systems Biology (**http://www.igsb.uchicago.edu**) and the University of Chicago Cancer Research Center (**http://uccrc.uchicago.edu**). We are a basic research department whose faculty is committed to an interdisciplinary approach to investigate fundamental problems in signal transduction and cancer. We are seeking computational biologists interested in signaling mechanisms relevant to diverse aspects of tumor biology, including but not limited to tumor microenvironment, tumor metabolism, EMT, stem cells, epigenetics, in vivo imaging, drug discovery, cancer nanotechnology, systems biology and genomics.

Departmental faculty have access to outstanding Ph.D. and M.D./Ph.D. students affiliated with graduate degree-granting programs in the Biological and Physical Sciences including the Committees on Cancer Biology, and Genetics and Systems Biology. Candidates should have sufficient research experience to demonstrate both significant accomplishments and outstanding potential. The successful recruit will be expected to teach undergraduate and graduate students. Curriculum vitae, bibliography, a brief statement of research interest and three letters of recommendation should be sent to: **Geoffrey Greene, Search Committee Chair, Ben May Department for Cancer Research, Gordon Center for Integrative Sciences, 929 East 57th Street, Room W421, Chicago, IL 60637**.

THE UNIVERSITY OF CHICAGO
The University of Chicago is an Affirmative Action/Equal Opportunity Employer.

Director, Division of Intramural Research
(Scientific Director)
National Center on Minority Health and Health Disparities

THE POSITION: The National Center on Minority Health and Health Disparities (NCMHD) is seeking exceptional candidates for the position of Director, Division of Intramural Research (DIR). The incumbent serves as the principal advisor to the NCMHD Director on biomedical and scientific affairs involving the intramural research programs conducted by basic and clinical research investigators in the field of minority health and health disparities research. This position offers a unique and exciting opportunity for an extremely capable individual to evaluate research efforts and establish program priorities; direct training of pre- and post doctoral fellows; collaborate with other NIH programs; and advise the NCMHD Director and senior staff of the DIR in areas of science of interest to the Center. The Division of Intramural Research will have staff of approximately 10 employees and a current annual budget of $4.3 million dollars. In addition to the managerial/administrative responsibilities outlined above, the Scientific Director is expected to carry out his/her own research program. Resources commensurate with the proposed program will be provided. The NCMHD seeks candidates who have a commitment to scientific excellence and the energy, enthusiasm, and innovative thinking necessary to lead and direct the DIR's research efforts at the forefront of science.

QUALIFICATIONS: Applicants must possess an M.D., Ph.D., or equivalent degree, and have demonstrated scientific leadership and research experience in either a basic or clinical research program of national and international standing in one or more of the areas of research that has or will contribute new knowledge in biomedical and behavioral issues recognized as part of the NCMHD mandate.

SALARY/BENEFITS: Salary is very competitive and will be commensurate with the experience of the candidate. A full package of Civil Service benefits is available including: retirement, health and life insurance, long term care insurance, annual and sick leave and the thrift savings plan (401K equivalent). The position is subject to a background investigation.

HOW TO APPLY: Interested candidates should send a letter of interest, including a brief description of research and administrative experience; curriculum vitae and bibliography; and full contact information for three to five individuals who may be contacted to provide letters of reference. Application packages should be sent to the **National Institutes of Health (NIH), National Center on Minority Health and Health Disparities, 6707 Democracy Blvd., Suite 800, Bethesda, Maryland 20892, or electronically to white1@mail.nih.gov.** For further information about the position, please contact **Dr. John O'Shea on (301) 496-2612 or e-mail at osheaj@arb.niams.nih.gov**. All information provided by the candidates will remain confidential and will not be released outside the NCMHD search process without a signed release from candidate.

DEPARTMENT OF HEALTH AND HUMAN SERVICES
NATIONAL INSTITUTES OF HEALTH (NIH)
National Center for Complementary and Alternative Medicine

The National Center for Complementary and Alternative Medicine (NCCAM), a component of the National Institutes of Health (NIH), Department of Health and Human Services, seeks an accomplished, innovative neuroscientist to serve as Scientific Director of its Intramural Research Program (IRP) and as senior investigator responsible for developing a new research program in mind-body medicine. This individual reports to the Director, NCCAM, and will serve as a member of the NCCAM leadership team.

As Scientific Director, you will articulate and implement a vision and oversee research infrastructure for highly unified and mutually supportive laboratory and clinical programs in the conduct of bench-to-bedside and bedside-to-bench research related to complementary and alternative medicine (CAM) therapies.

As Senior Investigator, you will have substantial committed resources to create a cutting-edge program of clinically oriented laboratory research and/or clinical studies that exploit the best current methods from the neuroscience disciplines to define the nature, mechanisms of action, safety, and efficacy of the CAM modalities that affect actions and interactions linking mind, body, and behavior.

This exceptional opportunity is available to an accomplished neuroscientist who has a demonstrated record of senior-level management of a large, nationally recognized research program, a commitment to both basic and clinical research, and leadership skills to forge team efforts with colleagues within intramural programs across the NIH.

The candidate will be given the necessary resources (space, budget, staff) to build the intramural research program anticipated to encompass three to five laboratory groups.

Applicants must possess an M.D., Ph.D., or equivalent degree in a biomedical field related to the mission of NCCAM and have professional experience reflecting a broad scientific background and experience in basic and/or clinical investigation. Applicants must be able to interact with full authority; have the demonstrated capability to plan and direct research programs of national and international importance; and have the ability to communicate with and obtain the cooperation of national and international organizations and individuals who represent wide-ranging views and competing priorities. Salary is commensurate with qualifications and experience. Full Federal benefits including leave, health and life insurance, long-term care insurance, retirement, and a savings plan (401k equivalent). Qualified individuals are encouraged to email their CV, bibliography, list of three references, and cover letter outlining their relevant experience and vision for leading the NCCAM IRP to: **nccamsrrecruits@mail.nih.gov, Subject Line: Scientific Director Search**. **Email receipt of applications and inquiries is preferred; however, candidates needing reasonable accommodation may fax application materials to 301-402-4741**.

Nanotechnologies for Biomolecular Physics

Eindhoven University of Technology (The Netherlands) invites candidates to apply for the positions of:

Full Professor

and

Assistant Professor (tenure track)

in the focus area Nanotechnologies for Biomolecular Physics.
For more information:
www.phys.tue.nl/hrm

www.tue.nl/jobs

TU/e Technische Universiteit **Eindhoven** University of Technology

Where innovation starts

Tenure Track Positions (3rd Term))
Nanoscience and Nanotechnology Research Center
Osaka Prefecture University, Osaka, Japan

Osaka Prefecture University is seeking applications for two tenure track positions at the Nanoscience and Nanotechnology Research Center. This recruitment is being carried out under the "Leading University in the Region as a Base for Human Resource Development in Nanoscience and Nanotechnology" program. Applicants should hold a PhD degree acquired within the past 10 years; a track record of three or more years as an assistant professor, postdoctoral fellow or an equivalent title as of April 1, 2010; and excellent research achievements in the fields of nanoscience or nanotechnology.

- **Number of tenure track positions available:** Two tenure-track special lecturers.
- **Research areas:** A wide range of research areas related to nanoscience and nanotechnology
- **Appointment duration:** From April 1, 2010 to March 31, 2015.
- **Annual salary:** Approximately 8,000,000 yen.
- **Research fund:** During the first fiscal year, 10,000,000 yen will be provided as a start-up fund, and from the second year onward, 5,000,000 yen per annum will be ensured.
- **Promotion to tenured associate professors:** Tenure track lecturers hired through this recruitment program will be promoted to tenured associate professors of Osaka Prefecture University—or tenured full professors if they have shown an excellent record of accomplishment—starting from April, 2015 after successfully passing the final evaluation. In such cases, those who have been promoted may be positioned to their preferred department and faculty at the university.
- **Submission deadline:** September 29, 2009, 5 p.m. Japan Standard Time. All documents must be submitted online through our website by the deadline, with hard-copy documents to follow.

Please refer to our official website below for a complete description of the position and application information:

http://www.nanosq.21c.osakafu-u.ac.jp/
http://www.nanosq.21c.osakafu-u.ac.jp/en/

Unil
UNIL | Université de Lausanne

| live knowledge |

THE FACULTY OF BIOLOGY AND MEDICINE OF THE UNIVERSITY OF LAUSANNE, SWITZERLAND INVITES APPLICATIONS FOR A POSITION OF

Associate Professor in Microbiology
in the Department of Fundamental Microbiology

Targeted starting date : August 1st, 2010.

The candidate must pursue a strong and independent research program in any non-clinical field of microbiology or microbial ecology, and have a proven track record of excellence in research and extramural funding. He or she will join the Department of Fundamental Microbiology (www.unil.ch/dmf) to reinforce and complement current research, training and teaching in prokaryotic microbiology.

The DMF offers a highly stimulating and collegial environment. Current research topics include bacterial cell-cycle control, microbial-host interactions, environmental and evolutionary microbiology. The Department has excellent experimental facilities and access to the latest imaging and genomics platforms on campus. The Lausanne academic area further offers excellent possibilities for new and exciting collaborations.

Teaching at the Faculty of Biology and Medicine of the University of Lausanne involves contributing to the Bachelor and Master curriculums of the School of Biology and to directing PhD students of the Doctoral School. With an optional period for adaptation, the successful candidate will need to be capable of teaching in both French and English.

The job description is available on the Internet site www.unil.ch/fbm/page64812.html. Further information may be obtained from vice-Dean Prof. Béatrice Desvergne (beatrice.desvergne@unil.ch).

Applicants should send their curriculum vitae, a list of publications in which the five most significant ones are identified, a description of present and future research interests, past and current funding, and complete postal and e-mail addresses of five reference persons before October 9th, 2009 to Prof. Patrick Francioli, Dean of the Faculty of Biology and Medicine, rue du Bugnon 21, 1011 Lausanne, Switzerland.

The University of Lausanne wishes to promote the access of women to academic careers and encourages applications from women.

Science Careers is the stage that showcases your talent.

Visit our ENHANCED WEBSITE!

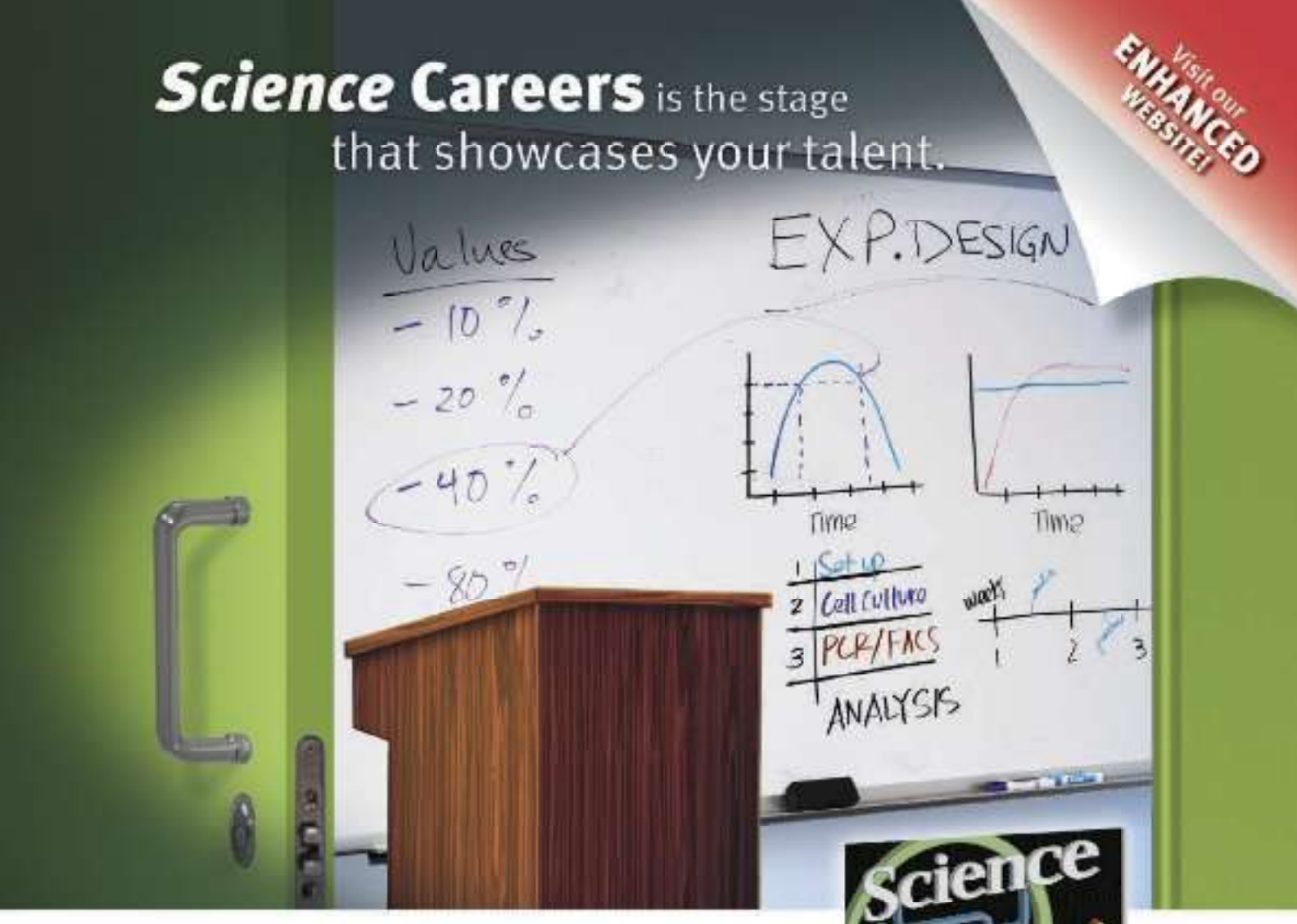

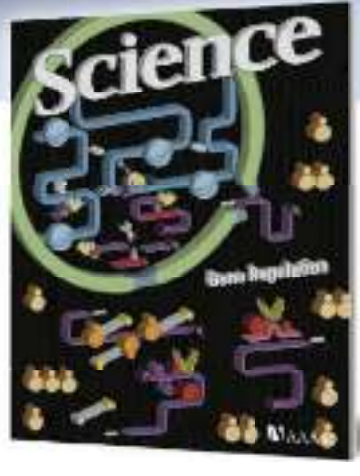

Showcasing your talent is our forte. We're your source for connecting with top employers in industry, academia, and government. We're the experts and platform for accessing the latest and most relevant career information across the globe.

Our newly designed website offers a set of tools that help you discover career opportunities and your personal potential. Whether you're seeking a new job in academia, career advancement in your chosen field, or ways to stay current on industry trends, *Science* Careers is your first stage toward a fulfilling future.

Your Future Awaits.

Improved Website Features:

- Relevant Job E-mail Alerts
- Improved Resume Uploading
- Content Specific Multimedia Section
- Facebook Profile

Job Search Functionality:

- Save and Sort Jobs
- Track Your Activity
- Search by Geography
- Enhanced Job Sorting

Science Careers
From the Journal *Science* AAAS

ScienceCareers.org

BBSRC Genome Analysis Centre

ifr Institute of Food Research

John Innes Centre

Independent Research Fellowships Addressing Food Security

The John Innes Centre (JIC), a world leading centre of excellence in plant and microbial sciences, the Institute of Food Research (IFR), a world leader in research into harnessing food for health and controlling food-related diseases, and The Genome Analysis Centre (TGAC), an international centre for DNA sequencing and analysis for plants, animals and microbes, are based on the Norwich Research Park, Norwich, UK. We are inviting applications from outstanding researchers who wish to apply for a BBSRC Institute Career Path Fellowship (ICPF) focussed on food security research. Appropriate research areas would include:

- Genomic approaches to plant breeding
- Genes for traits in crops
- Improving crops for human nutrition
- Plant-microbe interactions
- Food-related diseases

We particularly encourage applications from scientists proposing novel approaches to take advantage of the breadth of expertise across the Institutes. Candidates with a background in model plant systems and an interest in crop improvement are encouraged to apply. Successful applicants will be invited to attend a Conference at the JIC on 28th September 2009.

At the meeting you will be able to present a talk about your proposed area of research and to discuss your proposals, the development of your group and your future career plans in depth with senior scientists. After the Conference, we will select and mentor outstanding candidates in writing Fellowship applications. Those winning an ICPF from the BBSRC will be made tenure-track project leaders.

Further details and particulars can be found at http://www.jic.ac.uk/corporate/opportunities/vacancies/fellows.htm http://www.ifr.ac.uk/info/about/Vacancies/default.html and http://www.tgac.bbsrc.ac.uk/

Please e-mail a 2-page summary of your research plan, a copy of your CV and arrange for three letters of recommendation to be emailed to dawn.barrett@bbsrc.ac.uk by Friday 4th September 2009.

The John Innes Centre and Institute of Food Research are institutes of the Biotechnology and Biological Sciences Research Council and are registered charities (No 223852 & 1058499). These institutes, together with the Sainsbury Laboratory (No 106550) and The BBSRC Genome Analysis Centre are Equal Opportunity Employers.

POSITIVE ABOUT DISABLED PEOPLE

ORNL NEUTRON SCIENCES

Career Development Program

The Neutron Sciences Career Development Program was founded to nurture the creative development of neutron scattering instrumentation at ORNL. This initiative is viewed as a critical part of keeping the neutron scattering instruments at ORNL on the cutting edge of design and scientific functionality, keeping them competitive worldwide. This program is designed to provide an environment in which early-career scientists and technicians can be a part of innovative concepts for neutron-related instrumentation, while helping end users develop proposals, conduct experiments, and analyze data.

Position Overviews

- **Neutron Scattering Instrument Scientist**—will provide operational support for a specific instrument at the Spallation Neutron Source and High Flux Isotope Reactor. This will include developing a vigorous scientific program associated with the instrument. (Please see online posting for more details.)
- **Neutron Scattering Instrument Associate**—will serve as the technical specialist in assisting users and Neutron Scattering Science Division (NSSD) personnel in the performance of experiments and analysis of the results conducted on NSSD instruments. (Please see online posting for more details.)
- **Neutron Scattering Technician**—will serve as technical operational support to end users and instrument scientists and associates at the Spallation Neutron Source. (For more info: Marie Woodly, marie.woodly@orau.org)

For more information and apply online visit: http://www.orau.org/ornl/neutrons

To learn more about Neutron Sciences at ORNL visit: http://neutrons.ornl.gov

These appointments are offered through the ORNL Postgraduate Research Participation Program and are administered by the Oak Ridge Institute for Science and Education (ORISE).

FACULTY POSITION
YALE UNIVERSITY
DEPARTMENT OF MOLECULAR BIOPHYSICS AND BIOCHEMISTRY

The Department of Molecular Biophysics and Biochemistry at Yale University seeks applications for a tenure-track appointment at the Assistant Professor level in all areas of molecular biophysics that entail imaging and reconstruction, spectroscopic, diffraction, and computational approaches. The new faculty member will contribute to the department's undergraduate and graduate teaching and mentoring programs. Current faculty research interests encompass biochemistry, biophysical chemistry, structural biology, molecular biology and molecular genetics.

Applicants should provide a curriculum vitae, a statement of research interests, three letters of reference, and reprints or preprints. Completed applications should be sent to:

Search Chair
Faculty Search Committee
Department of Molecular Biophysics and Biochemistry
Yale University
260 Whitney Avenue
P.O. Box 208114
New Haven, Connecticut 06520-8114

Telephone: (203) 432-5593

Review of applications will begin **October 15, 2009**.

Yale is an Affirmative Action/Equal Opportunity Employer. Yale University values diversity among its students, staff, and faculty and strongly encourages applications from women and underrepresented minorities.

POSITIONS OPEN

University of Tennessee at Chattanooga, LECTURER/LABORATORY COORDINATOR, Human Anatomy and Physiology (nine-month, nontenure-track), M.S. or Ph.D. required. Responsibilities include teaching lecture and laboratory courses and coordinating laboratory courses in human anatomy and physiology. Position requires commitment to teaching excellence, responsiveness to student needs, and effective communication skills. Advising students and participation in department matters required. Preference is given to candidates with demonstrated excellence in college or university teaching. Position available for January 1, 2010, start. Screening will begin September 1, 2009, and will continue until the position is filled. Submit curriculum vitae, transcripts, and three current reference letters to: **Dr. John C. Tucker, Head, Department of Biological and Environmental Sciences, 615 McCallie Avenue, Department #2653, The University of Tennessee at Chattanooga, Chattanooga, TN 37403. Telephone: 425-423-4341; e-mail: john-tucker@utc.edu.** *The University of Tennessee at Chattanooga is an Equal Employment Opportunity/Affirmative Action/Title VI+IX/Section 504/ADA/ADEA Institution.*

Case Western Reserve University (CWRU) and University Hospitals through the newly formed Institute for Transformative Molecular Medicine (ITMM) seek outstanding research scientists for the development of its research programs.

The research programs of the ITMM are located in the state-of-the-art Wolstein Research Building. Investigators will work in close proximity to multiple NIH-funded investigators and will have access to outstanding core research facilities. Areas of interest include (but are not limited to) cell signaling, genetic and epigenetic regulation of cardiac and vascular cell development and function, stem cell biology, cancer biology, regenerative medicine, and human genetics and models of disease. Available positions include:

(1) **ASSISTANT PROFESSOR OF MEDICINE,** nontenure or tenure track (three positions). Candidates must have a doctoral degree and a clearly defined research focus in: (a) proteomics and/or chemical biology; (b) redox systems and skeletal/muscle biology; or (c) G potein-coupled receptor signaling and cellular/molecular biology.

(2) **ASSOCIATE PROFESSOR OF MEDICINE,** nontenure or tenure track (three positions). Candidates must have a doctoral degree and a clearly defined research focus in: (a) proteomics, protein biochemistry, and/or redox systems biology; (b) cell biology and neurobiology with an emphasis on redox regulation; or (c) animal models of disease and clinical practice.

CWRU and the ITMM offer excellent compensation and benefit packages that are commensurate with the applicant's training and experience. Please send curriculum vitae, a statement of current and future research interests/goals, and three letters of support to:

c/o Robert Jenkins
Division of Cardiovascular Medicine
University Hospitals Case Medical Center
Harrington-McLaughlin Heart & Vascular Institute
11100 Euclid Avenue
Cleveland, OH 44106-5038

CWRU is a Diversity and Equal Opportunity/Affirmative Action Employer.

POSTDOCTORAL POSITION to study a novel replication origin binding protein, using human cell culture and *Xenopus* egg extracts (**Leffak** laboratory; **website: http://www.med.wright.edu/bmb/ml/ml.htm**). Applicants must have relevant experience in molecular and cell biology research and a Ph.D. in a life science discipline (or have advanced to Ph.D. candidacy). Please apply at **website: https://jobs.wright.edu.** *Wright State University is an Affirmative Action/Equal Opportunity Employer.*

Science Careers is the key that opens doors.

Visit our ENHANCED WEBSITE!

Opening doors is what we do. We're the key to connecting with the industry's top employers. We're the experts and source for accessing the latest and most relevant career information across the globe.

Our newly designed website offers a set of tools that help you unlock career opportunities and your personal potential. Whether you're seeking a new job, career advancement in your chosen field, or ways to stay current on industry trends, *Science* Careers is your key to a brighter future.

Improved Website Features:

- Relevant Job E-mail Alerts
- Improved Resume Uploading
- Content Specific Multimedia Section
- Facebook Profile

Job Search Functionality:

- Save and Sort Jobs
- Track Your Activity
- Search by Geography
- Enhanced Job Sorting

Your Future Awaits.

Science Careers
From the Journal *Science* AAAS

ScienceCareers.org

POSITIONS OPEN

杭州师范大学
Hangzhou Normal University

MULTIPLE FACULTY POSITIONS

The College of Life and Environmental Sciences at Hangzhou Normal University is seeking candidates to fill several faculty positions at open ranks, ranging from **INSTRUCTORS** to **ASSOCIATE PROFESSOR** to **FULL PROFESSOR.** The candidates should have a Ph.D. degree and postdoctoral research experience in animal development, stem cell biology, or plant molecular biology. Publications in peer-reviewed international journals as the first or corresponding author are required. Preferences will be given to those who study mammalian organogenesis or plant molecular biology. Positions are commensurate with academic qualifications. Salaries and startup funds are extremely generous and internationally competitive.

The college has recently acquired state-of-the-art research equipment and animal/plant facilities, and is well positioned to conduct world-class research in the most beautiful and best-living city in China.

Candidates should send their curriculum vitae, research statement, and the names of three references electronically to **e-mail: hnusearch@gmail.com.**

ADVISER

McKenna Long & Aldridge, LLP, is seeking one Adviser to join our life sciences and public health preparedness practice in Washington, D.C.

Candidates should be science-focused with a Master's degree or higher in industrial biotechnology, green technology, biofuels, and/or climate change.

Ideal candidates will be motivated, creative, smart, resourceful, and independent. They will also possess a demonstrated entrepreneurial spirit with a desire to engage industry and government across a variety of cleantech/greentech issues, the initiative to build and sustain client and government relationships, and maintain scientific credibility.

Candidates should be able to prioritize competing deadlines and manage their own schedule. High degree of writing and public speaking proficiency required. Relevant business experience is highly desired. All inquiries will be kept confidential.

Please send resume and school transcripts to:

Ms. Megan C. McGrath
Legal Recruitment Manager
1900 K Street, N.W.
Washington, DC 20006
E-mail: mcmcgrath@mckennalong.com

Candidate submissions only.

McKenna Long & Aldridge is an Equal Opportunity Employer.

LECTURER, MARINE SCIENCE

Stony Brook University's School of Marine and Atmospheric Sciences (SoMAS) seeks to hire a full-time Lecturer with expertise in any aspect of marine biology or marine chemistry to work at the Stony Brook Southampton campus. The initial review of applications will begin on October 1, 2009, and will continue until the position is filled. For a full position description, application procedures, or to apply online visit **website: http://www.stonybrook.edu/jobs (jobs reference # F-5948-09-07).** *Equal Opportunity/ Affirmative Action Employer.*

CAREER OPPORTUNITY

Doctor of Optometry (O.D.) degree in 27 months for Ph.D.s in science and M.D.s. Excellent career opportunities for O.D./Ph.D.s and O.D./M.D.s in research, education, industry, and clinical practice. This unique program starts in March 2009, and features small classes and 12 months devoted to clinical care.

Contact the **Admissions Office, telephone: 800-824-5526** at the **New England College of Optometry, 424 Beacon Street, Boston, MA 02115.** Additional information at **website: http://www.neco.edu, e-mail: admissions@neco.edu.**

POSITIONS OPEN

STANFORD UNIVERSITY
Department of Chemical Engineering

The Department of Chemical Engineering at Stanford University is seeking applicants for a tenure-track faculty position at the junior level (**ASSISTANT** or untenured **ASSOCIATE PROFESSOR**). Applicants are expected to have earned a Ph.D. degree in chemical engineering or related disciplines.

We will consider applicants knowledgeable in the general area of chemical engineering science. There are several broad areas of interest, including hydrocarbon chemistry, surface reactivity and catalysis, fuel cells, environmental or atmospheric studies, molecular transport processes and mechanics, soft materials physics and chemistry, computation and simulation, biochemical and biomolecular engineering, and nanomaterials processing. In general, we give higher priority to the overall originality and promise of the candidate's work rather than to the subarea of specialization. Researchers with programs that emphasize the production and storage of energy are particularly encouraged to apply.

The successful candidate will be expected to teach at the graduate and undergraduate levels, to develop advanced graduate courses in a research specialty, as well as to develop a world-class research program with an emphasis on the fundamental physical, chemical, and engineering aspects of chemical engineering science. Applicants should be seeking a stimulating interdisciplinary environment in which to pursue teaching and research. We anticipate that the faculty members will contribute to and develop leadership roles and interactions among faculty not only in chemical engineering, but also electrical, mechanical, civil and environmental, and material science and engineering in the school of engineering; in physics, chemistry, and biology in the School of Humanities and Sciences; in the departments and programs in the School of Medicine; as well as bioengineering located in the Schools of Engineering and Medicine; and at the Stanford Synchrotron Radiation Laboratory.

Applicants should send curriculum vitae (including research accomplishments, teaching experience, and publications) a transcript of doctoral graduate study, a detailed research and teaching plan, and supporting letters from three references to: **Professor Gerald G. Fuller, Chair, Search Committee, Department of Chemical Engineering, Stanford University, Stanford, CA 94305-5025.** Applications are due by December 1, 2009, but we will continue to accept applications until the position is filled.

Stanford University is an Equal Opportunity Employer and is committed to increasing the diversity of its faculty. It welcomes nominations of and applications from women and members of minority groups, as well as others who would bring additional dimensions to the university's research and teaching missions.

POSITIONS OPEN

ASSISTANT PROFESSOR, ICHTHYOLOGY
Texas A&M University

The Department of Wildlife and Fisheries Sciences seeks an Assistant Professor and Curator of Ichthyology. Candidates must have a doctorate and demonstrate capacity for excellence in research in evolutionary biology, systematics, genetics, ecology, or conservation biology. The position is tenure-track with a 12-month annual appointment. The successful candidate will teach ihthyology, a graduate course in their specialty, and contribute occasionally to a course in vertebrate zoology. The successful candidate will be Curator of the TCWC fish collection, consisting of 630,000 specimens (**website: http://wfsc.tamu.edu/TCWC).** Many opportunities exist for interdisciplinary collaborations among departments and programs including Ecology and Evolutionary Biology **(website: http://eeb.tamu.edu**), Genetics (**website: http://gene.tamu.edu**), and Renewable Natural Resources. Applicants may address their ability to contribute to the mission of the university's diversity plan (**website: http://diversity.tamu.edu/plan/index.asp**). To apply: Submit electronically curriculum vitae, statements of teaching, research, and curation, plus contact information for three references to: **Dr. Kirk O. Winemiller, Ichthyologist Search Committee Chair, e-mail: k-winemiller@tamu.edu.** Review of applications will begin October 5, 2009.

The Texas A&M University System is an Equal Opportunity Employer committed to building a diverse faculty, staff, and student body reflecting the population and educational needs of Texas and the nation.

MARKETPLACE

Put yourself in the picture by entering the **2010 AAAS Student Poster Competition.** Winners receive a cash prize, framed award certificate, and a one-year AAAS membership—including a subscription to *Science!*

CALL FOR ENTRIES

AAAS Student Poster Competition

American Association for the Advancement of Science
Annual Meeting

18-22 February 2010 San Diego

"Bridging Science and Society"

Submission Deadline: Friday, 23 October 2009

- Don't miss out on this opportunity to put your research in the spotlight and discuss your work with leading scientists and engineers from across the country and around the world.
- All submissions will be peer reviewed. Accepted posters will be listed in the 2010 Annual Meeting Poster Book.
- Winners will be published in *Science* and at www.aaas.org/meetings.
- The competition is open to college undergraduate and graduate students only.

To learn more, including how you can volunteer and attend the Annual Meeting for free, visit

www.aaas.org/meetings

R&D Systems Bioactive Proteins

High quality proteins aren't a luxury, they are a necessity.

WHAT'S THE RISK? ✓ Missed opportunities ✓ Non-specific results ✓ Experiments that can't be repeated ✓ Weeks or months of wasted time

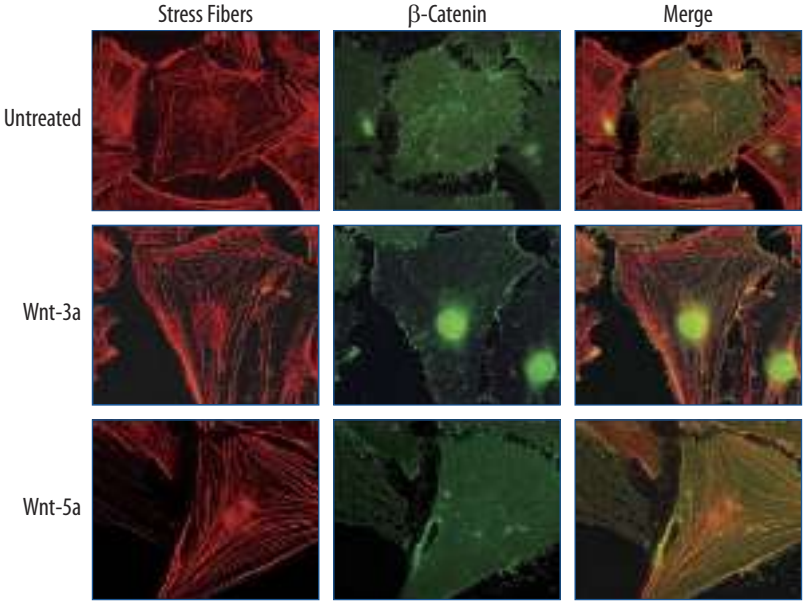

R&D Systems recombinant mouse Wnt-3a (Catalog # 1324-WN) and Wnt-5a (Catalog # 645-WN) promote stress fiber formation in NIH-3T3 cells, while only Wnt-3a promotes nuclear β-Catenin accumulation. Please visit our website for information about our new high purity human Wnt-3a (Catalog # 5036-WNP). *Images Courtesy of Dr. Raymond Habas, Robert Wood Johnson School of Medicine.*

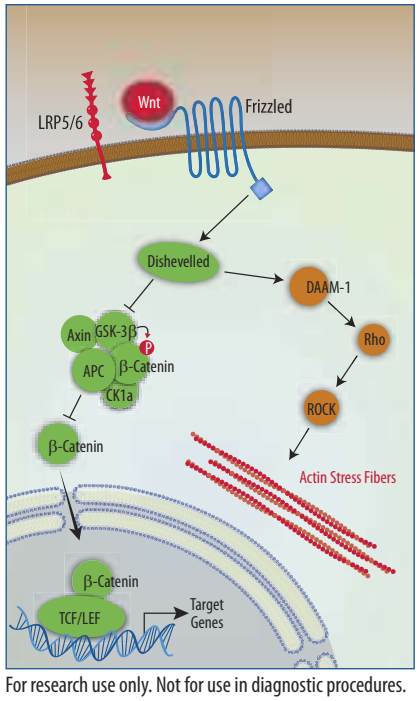

For research use only. Not for use in diagnostic procedures.

R&D Systems has spent almost 25 years building its reputation as a source for high quality proteins.

Every stage of protein development takes place in R&D Systems' laboratories, from cloning of the gene, to protein purification and testing for bioactivity. Because we control all aspects of protein manufacturing, R&D Systems can better control the quality of our products and the technical assistance we offer. Please visit our website at **www.RnDSystems.com/go/Proteins** for more information.

Cancer Development Endocrinology Glycobiology Immunology Neuroscience Proteases Signal Transduction Stem Cells

R&D Systems Tools for Cell Biology Research™

USA & Canada **R&D Systems, Inc.** Tel: (800) 343-7475 info@RnDSystems.com
Europe **R&D Systems Europe, Ltd.** Tel: +44 (0)1235 529449 info@RnDSystems.co.uk
China **R&D Systems China Co., Ltd.** Tel: (800) 988-1270 info@RnDSystemsChina.com.cn

Selection expanding weekly—visit **www.RnDSystems.com/go/request** to sign up for weekly new product updates.

R&D SYSTEMS®